Transformation and sublimation of interstellar ices

Insights from laboratory experiments and astronomical observations

Proefschrift

Julia de Carvalho Santos

geboren te Rio de Janeiro, Brazilië
in 1995

It is again among us, in a glass of milk. It is inserted in a very complex, long chain, yet such that almost all of its links are acceptable to the human body. It is swallowed; and since every living structure harbors a savage distrust toward every contribution of any material of living origin, the chain is meticulously broken apart and the fragments, one by one, are accepted or rejected. One, the one that concerns us, crosses the intestinal threshold and enters the bloodstream: it migrates, knocks at the door of a nerve cell, enters, and supplants the carbon which was part of it. This cell belongs to a brain, and it is my brain, the brain of me who is writing; and the cell in question, and within it the atom in question, is in charge of my writing, in a gigantic minuscule game which nobody has yet described. It is that which at this instant, issuing out of a labyrinthine tangle of yeses and nos, makes my hand run along a certain path on the paper, mark it with these volutes that are signs: a double snap, up and down, between two levels of energy, guides this hand of mine to impress on the paper this dot, here, this one.

Carbon
– The Periodic Table, by Primo Levi

TABLE OF CONTENTS

1. INTRODUCTION

If you wish to make a Ph.D. thesis from scratch, you must first invent the Universe.

It all began with the Big Bang. One second later, the Universe consisted of matter and radiation enmeshed in an extremely hot (10^{10} K) primordial soup. As it expanded and cooled, subatomic particles collided and formed the nuclei of the first atoms—hydrogen, helium, and traces of lithium and beryllium. This brief era of primordial nucleosynthesis ended within minutes, as the Universe became too cool for neutrons and protons to fuse. What remained was a dense, opaque plasma made of nuclei, free electrons, and light.

After 380 thousand years, the Universe had cooled enough for atomic nuclei and electrons to recombine, finally forming neutral atoms. This process, which itself generated a significant amount of radiation, allowed light and matter do decouple, rendering the Universe (momentarily) transparent. Light from that time is observed today as the cosmic microwave background (CMB)[1].

Within 200 million years, clumps of gas that accumulated in cooler areas of the Universe had grown massive enough to ignite nuclear fusion in their cores, giving rise to the first stars. It is through the life cycle of stars that most of the elements in the periodic table are formed—whether via nuclear fusion in stellar cores, via explosive events at the end of a star's life, or even from the collision of supermassive star core remnants known as neutron stars (Figure 1.1; Johnson 2019). These elements combine through a multitude of bonding arrangements to form molecules, some of which eventually coalesce into structures such as the planet we now call Earth.

Over the course of 4.5 billion years, the molecules that constitute the Earth underwent multiple cycles of destruction and reformation as the planet and its inhabitants were shaped into their current state. The work shown in this thesis is the result of the fraction of these elements and molecules that found their way to Earth, and ultimately became part of the cells that compose the writer's body, driving the exploration of the origins and fate of the other fractions that still permeate the interstellar medium.

To achieve this goal, this thesis combines laboratory simulations of interstellar ice processes—particularly, reactions and desorption—with observations of the gas surrounding protostars. The focus is on molecules containing carbon, hydrogen, oxygen, and sulfur, which, along with nitrogen and phosphorus, constitute the six major biogenic elements essential to virtually all life-related processes. By examining how such molecules form and evolve, this work provides insight into the chemical history of our own Solar System and beyond.

---

[1]Although the CMB was initially highly energetic, with the expansion of space its wavelength has increased, and its effective temperature has cooled off to just 2.7 K. After the CMB, the universe became opaque again due to light absorption by neutral atomic hydrogen—a period known as the Dark Ages. With the ignition of the first stars, hydrogen was reionized, making the universe transparent to light once more.
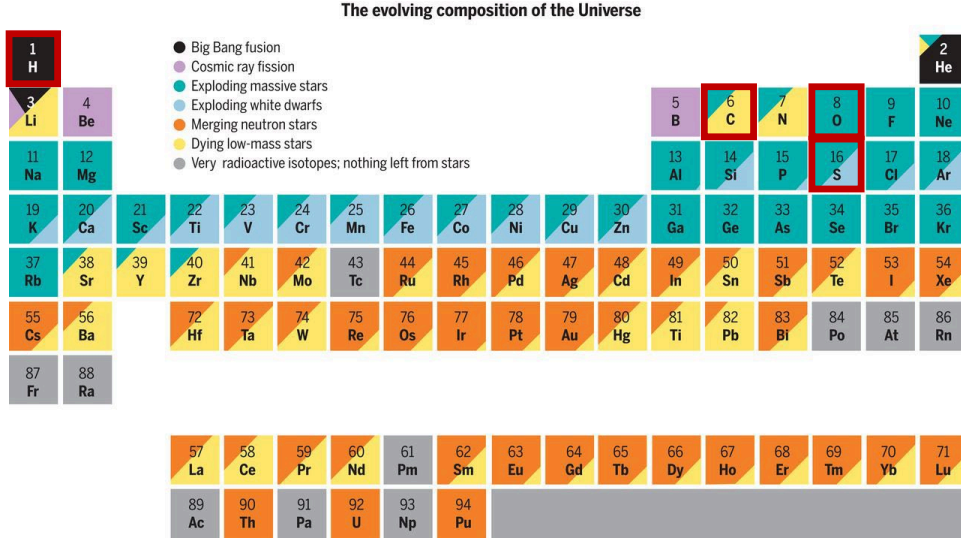
Figure 1.1: Periodic table of elements color-coded by their relative contributions from different nucleosynthesis sources. Carbon (C), hydrogen (H), oxygen (O), and sulfur (S) are particularly important for this thesis, and are highlighted in red. Artificially synthesized elements and those produced exclusively through the radioactive decay of long-lived nuclei are shaded in gray. Elements that do not occur naturally in the Solar System are omitted. Figure adapted from Johnson (2019).

1.1   Star and planet formation

To date, over 320 molecules have been detected in the interstellar medium or in circumstellar shells[2], with new detections increasing at an incredibly fast and possibly accelerating rate of $\sim$4.9 molecules per year (see McGuire 2022). The formation and destruction pathways of these molecules are shaped by the physical and chemical conditions of their environments, which in turn change dramatically throughout the different stages of star and planet formation (e.g., Herbst & van Dishoeck 2009). As a result, astrochemistry is inherently connected to the interstellar cycle of matter. The progression of this cycle depends on the mass of the star that is ultimately formed and can be broadly categorized into the evolution of low-mass and high-mass stars. In this thesis, the focus is primarily on low-mass stars due to their relevance to planetary systems capable of supporting life. Nevertheless, massive protostars are explored in Chapters 8 and 9, and therefore their formation is also briefly addressed.

1.1.1   Low-mass stars

Low-mass stars ($<$2 $M_\odot$) are the prevalent type of stars in the Galaxy and, consequently, the most frequent hosts of planetary systems. Their long main-sequence lifetimes provide the extended timescales thought to be necessary for life to emerge (i.e., $\sim$10^9 yr, based on geological records tracing Earth's earliest organisms; Hol-

---

[2]https://cdms.astro.uni-koeln.de/classic/molecules

land 1997; Schopf 1993, 1994). As such, these stars are key to understanding the chemical evolution of planet-forming regions, and are frequently the objects of astrochemical studies. Figure 1.2 (Öberg & Bergin 2021) illustrates the different stages of star and planet formation in low-mass systems. It begins with dense molecular clouds, which are inhomogeneous structures measuring $2-15$ pc and with typical densities of $\sim 10^2 - 10^4$ cm^{-3} and temperatures of $\sim 10 - 20$ K (Bergin & Tafalla 2007). Within these clouds, there are substructures of even higher densities ($\sim 10^6$ cm^{-3}) called cores, with scales of ~ 0.1 pc and where temperatures typically remain at $8-12$ K (Bergin & Tafalla 2007). When these cores accumulate sufficient mass, gravitational forces overtake thermal and magnetic pressures, as well as turbulence, causing the core to collapse and form a protostar. Centrally concentrated dense cores that are fated to collapse, but have not yet done so, are called prestellar cores.
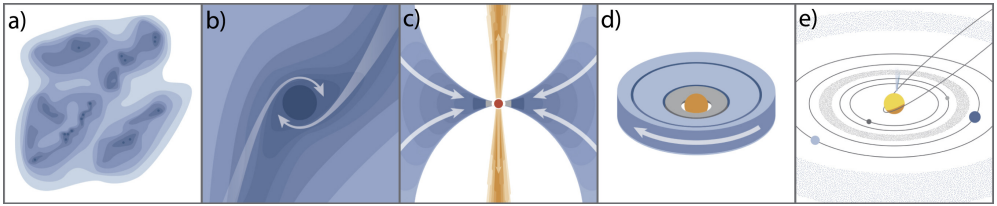
Figure 1.2: Schematic of the star- and planet-formation stages in low-mass systems. a) Dense cores form within molecular clouds. (b) These cores start to collapse under gravity to form a protostar. (c) As the protostar emerges, remnant cloud material continues to accrete by funneling through a circumstellar disk, while outflows and jets remove angular momentum from the system. (d) The envelope gradually dissipates, leaving behind a pre-main-sequence star surrounded by a protoplanetary disk. (e) After the disk material is depleted through accretion and dispersal, a planetary system remains. Figure from Öberg & Bergin (2021).

Once a protostar is born, it continues to accrete material from the surrounding envelope, which in turn experiences positive temperature and density gradients towards the accreting star. Due to the conservation of angular momentum, a portion of this material settles in a disk around the star (Tobin & Sheehan 2024). Angular momentum is further transferred out of the system via protostellar outflows and jets, while the disk facillitates accretion by chanelling matter onto the star. Over time, the star and disk continue to accrete mass as the surrounding envelope gradually dissipates, eventually dispersing completely within timescales of $\sim 10^6$ yr. This process leaves behind a pre-main-sequence star surrounded by a Keplerian disk (Williams & Cieza 2011). This remaining structure, known as a protoplanetary disk, serves as the birthplace of planets and planetesimals—though recent evidence points to the onset of giant planet formation taking place as early as the embedded protostellar phases (Harsono *et al.* 2018; Tychoniec *et al.* 2020). Eventually, the disk material is completely depleted through accretion and dispersal, leaving behind a planetary system that may continue to evolve through collisions between its constituent bodies.

1.1.2 High-mass stars

In contrast to low-mass stars, high-mass stars ($\gtrsim 4$ M$_\odot$) form on much shorter timescales ($\sim 10^4 - 10^5$ yr) and are typically located farther away ($d \gtrsim 1$ kpc), making their observation and the development of a formation paradigm more challenging (Beuther

et al. 2007; Mottram *et al.* 2011). Several models have been proposed to explain massive star formation, with the two most prominent ones being a core accretion model, which is a scaled-up version of the model for low-mass stars, and the competitive accretion model, where protostellar seeds form through gravitational collapse and grow by tidally-modified Bondi-Hoyle accretion[3] (Bonnell & Bate 2006; Tan *et al.* 2014; Beuther *et al.* 2025). In this latter scenario, the gas is initially not gravitationally bound to any individual star, and the protostellar seeds compete for the mass available within the clump. Still, no clear consensus has been reached on the dominant mechanism driving massive star formation, with alternative (though less likely) scenarios, such as the merging of low-mass protostars, also being proposed (e.g., Bonnell *et al.* 1998).

Due to the shorter timescales of high-mass star formation, these stars do not exhibit visible pre-main-sequence phases[4]. Nonetheless, like their low-mass counterparts, massive protostars originate within clouds and undergo an embedded phase during which they heat their surrounding envelopes, giving rise to regions known as hot cores (Kurtz *et al.* 2000). Additionally, massive protostars are predicted to host disks where planets may form via gravitational instability (Boss 1997), though their short main-sequence lifespans are too brief to support the emergence of life.

1.2 Interstellar chemistry

As matter progresses through the different stages of star and planet formation—from clouds to protostars, to protoplanetary disks, and eventually planetary systems—it encounters a wide range of physical conditions (e.g., densities, temperatures, radiation fields) that can affect its molecular composition and distribution (Herbst & van Dishoeck 2009). Understanding the physicochemical processes at play in these environments, and consequently how chemistry evolves across these stages, is essential not only for interpreting observations but also for accurately predicting the outcomes of planet formation.

1.2.1 Gas vs ice reactions

Interstellar chemistry can be broadly separated into two different types of processes: gas-phase reactions and solid-phase reactions. In the former case, the low densities typical of most phases of star and planet formation inhibit three-body reactions of the form $A + B + C \rightarrow ABC^\star \rightarrow AB + C$, which require densities $\gtrsim 10^{13}$ cm^{-3}. Such conditions are only found in a few exceptionally dense environments, such as the atmospheres of AGB stars and the inner midplanes of protoplanetary disks. This limitation has significant implications for gas-phase chemistry: three-body reactions assist in the stabilization of the reaction product (AB) by having the third body (C) carry away the bond formation energy. In their absence, many systems must rely on alternative stabilization mechanisms, such as the emission of a photon or an electron, which are often inefficient. As a result, gas-phase reactions are constrained in their ability to form chemical bonds (Herbst & Klemperer 1973). Some bond-rearrangement

---

[3]Bondi-Hoyle accretion describes the spherical accretion onto a compact object moving through a uniform gas free of self gravity.

[4]Intermediate-mass cases ($2M_\odot \lesssim M_\star \lesssim 15M_\odot$) are an exception, as pre-main-sequence stars in this range are observed and classified as Herbig Ae/Be (Brittain *et al.* 2023).

gas-phase reactions, of the form $A + BC \rightarrow AB + C$, can proceed efficiently because the excess energy is carried by the C product, eliminating the need for radiative stabilization. Ion-molecule reactions are an example of bond-rearrangement processes that play an important role in astrochemical networks, primarily because they are typically exothermic, and can proceed at high rates even at temperatures as low as 10 K due to long-range charge interactions between the reactants (van Dishoeck 2014; Öberg & Bergin 2021). For ions reacting with symmetric molecules with no permanent dipoles, the charge interactions occur via induced dipoles and rates are temperature independent, typically around 10^{-9} cm^{-3} s^{-1}. For neutral species with a permanent dipole, reaction rates are temperature dependent and can be enhanced by one to two orders of magnitude at low temperatures. In addition, neutral-neutral routes involving radicals as reactants can contribute significantly to form certain species, such as H$_2$O (when $T_{\text{gas}} > 400$ K; Wagner & Graff 1987) and a few organic molecules (when in cold environments, Shannon $et\ al.$ 2013; Balucani $et\ al.$ 2015). Nonetheless, generally speaking, gas-phase reactions are less effective at driving chemical complexity in space.

In solid-phase reactions, on the other hand, the substrate (consisting of interstellar dust grains or frozen molecular layers coating these grains) act as the third body through which the excess energy from product formation can be dissipated, thus stabilizing the reaction products. In fact, abundant species such as H$_2$ and CH$_3$OH can only be attributed to solid-phase formation mechanisms, as their gas-phase formation is either highly inefficient or entirely prohibitive due to the inability to stabilize the reaction products (Geppert 2006; Vidali 2013). Additionally, these grains are typically at very low temperatures ($<$10 K in prestellar cores and $<$30 K in the more extended regions, like the outskirts of starless cores; Crapsi $et\ al.$ 2007; Pagani $et\ al.$ 2007). Under such conditions, sticking coefficients are nearly unity, meaning that most molecules—except for H$_2$ and He—will readily freeze out onto dust grains upon contact. As a result, these grains act as chemical reservoirs, facilitating encounters among reactants and promoting a rich solid-state chemistry. Given the key role played by ices in driving interstellar chemical complexity, this thesis focuses on solid-state phenomena and its contribution to the chemical evolution of the interstellar medium.

1.2.2 Ice processes

Once an atom or molecule adsorbs onto a dust grain, it can undergo three different types of processes: (i) desorption, (ii) diffusion, and (iii) reaction. An overview of these processes is provided in Figure 1.3.

The first process, desorption, occurs when a species overcomes its binding energy (E$_{\text{bind}}$) to the surface and is released into the gas phase. Sources of energy that can lead to desorption include thermal heating (e.g., from a protostar), energetic particles such as UV photons, or the excess heat released by highly exothermic reactions.

The second process, diffusion, involves the movement of species across the grain surface upon overcoming their diffusion energy barrier (E$_{\text{diff}}$). Diffusion can proceed via thermal hopping—when a species has enough energy to overcome the diffusion barrier classicaly—or via quantum tunneling through the barrier. Some light species (namely, H and O atoms) have been suggested to diffuse efficiently via quantum tunneling under specific conditions (e.g., at very low temperatures of $\lesssim$10 K, and on relatively smooth surfaces like polycristalline water ice; Congiu $et\ al.$ 2014; Kuwahata $et\ al.$ 2015). However, for most astrophysical contexts, thermal hopping is expected to
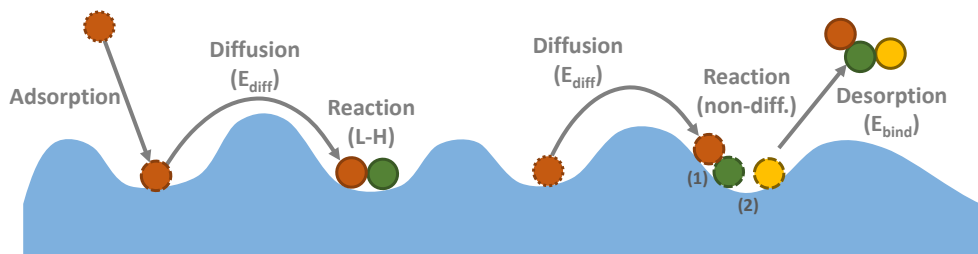
Figure 1.3: Illustration of the various processes experienced by chemical species on icy grain surfaces. The chronological order of events is indicated by species with dotted contours, followed by dashed contours, and finally solid-line contours. In one scenario, a species adsorbs onto the ice and diffuses by overcoming its diffusion energy (E_{diff}) until it encounters another molecule in a different binding site, where they react via the Langmuir-Hinshelwood (L-H) mechanism. In another scenario, a species diffuses to a new binding site and reacts via L-H with a second species (event denoted as (1) in the figure). The newly formed molecule then undergoes a second reaction (event (2)), forming a more complex species via the non-diffusive mechanism. The excess heat released from event (2) allows the molecule to overcome its binding energy (E_{bind}) and desorb from the ice.

dominate. Consequently, the mobility of a species is highly temperature-dependent, with most molecules remaining immobile at the low temperatures typical of prestellar environments.

The third process, reaction, takes place when species encounter one another under conditions conducive to chemical reactions. These have been historically thought to proceed through three primary mechanisms: Langmuir-Hinshelwood, Eley-Rideal, and hot atom. In the Langmuir-Hinshelwood mechanism, both reactants are thermalized on the grain surface, diffuse, meet, and react. The Eley-Rideal mechanism involves one reactant remaining stationary on the surface while another from the gas phase collides with it, triggering a reaction. In the hot-atom mechanism, a non-thermalized species briefly diffuses across the surface before encountering another molecule and reacting. In astrophysical ices, thermalization typically occurs on much shorter timescales than chemical reactions, rendering the hot atom mechanism largely irrelevant. The Eley-Rideal mechanism could potentially play a role under conditions of high surface coverages or low surface mobility (Cuppen *et al.* 2017)—conditions that can arise during events like the catastrophic CO freeze-out in prestellar cores (see Section 1.3.1). For most astrophysical environments, however, the Langmuir-Hinshelwood mechanism is thought to dominate among the three.

While diffusion has long been considered the standard scenario in astrochemical models and is a key limiting factor for chemical reactions, its absence does not entirely preclude molecule formation. At the extremely low temperatures typical of prestellar cores and the cold envelopes of protostars ($\lesssim$10 K), only atomic hydrogen can diffuse efficiently. Under such conditions, hydrogenation reactions are expected to dominate, producing simple species such as CH_4, NH_3, and CH_3OH from C, N, and CO. The formation of more complex species, however, requires that radical-radical and radical-molecule associations become competitive with the hydrogenation of these radicals. In a diffusive scenario, these conditions would only be met at $T \gtrsim 20$ K, where radicals become mobile. Yet, gas-phase observations towards cold interstel-

lar environments have revealed the presence of complex organic molecules (COMs) such as acetaldehyde (CH$_3$CHO), methyl formate (CH$_3$OCHO), and dimethyl ether (CH$_3$OCH$_3$) (Öberg *et al.* 2010a; Bacmann *et al.* 2012; Cernicharo *et al.* 2012; Vastel *et al.* 2014), challenging this view. Given that these COMs are likely formed via solid-state chemistry, such findings suggest that diffusion is not the sole pathway for the formation of larger molecules in ices. To explain these observations, Jin & Garrod (2020) proposed a new non-diffusive mechanism—inspired in part by experimental results (e.g., Fedoseev *et al.* 2015a, 2017)—in which radicals react with nearby molecules to produce complex organics. In this scenario, the initial radical formation might proceed, for instance, through the hydrogenation of a closed-shell species via a standard Langmuir-Hinshelwood process, but the subsequent formation of complex organics occurs without requiring the radicals to be mobile. This non-diffusive mechanism is relevant to both bulk-ice and surface-ice reactions, and is likely responsible for much of the chemistry under molecular cloud conditions explored in this thesis (for which $T \leq$20 K).

Regardless of whether reactions proceed via diffusive or non-diffusive mechanisms, astrophysical ice chemistry relies heavily on atoms and radicals, with only a limited number of feasible reactions involving strictly closed-shell species (such as the formation of ammonium and hydronium salts; e.g., Theule *et al.* 2011; Mispelaer *et al.* 2012; Loeffler *et al.* 2015; Bergner *et al.* 2016). Open-shell species can populate ices through adsorption from the gas phase or via in-situ formation. In the latter case, radicals can form within the ice through "non-energetic" processes, such as atom addition and abstraction reactions (e.g., Linnartz *et al.* 2015), or via molecular dissociation induced by energetic particles like UV photons and electrons (e.g., Öberg 2016). While energetic pathways are certainly relevant for generating radicals in ices, this thesis primarily focuses on non-energetic processes, which are thought to dominate under the shielded conditions characteristic of molecular clouds.

The low temperatures in astrophysical ices suppress endothermic reactions, thus only exothermic reactions (i.e., with a negative enthalpy change; ΔH < 0) can proceed in the environments explored in this thesis. When these reactions have an activation energy barrier (E$_a$), they can proceed via either thermal hopping or quantum tunneling (Figure 1.4)—similar to the case of diffusion. In most astrochemical contexts, tunneling rates (k_{tunn}) are described by using the Wentzel-Kramers-Brillouin (WKB) approximation[5] and assuming a rectangular barrier (Cuppen *et al.* 2017):

$$k_{\mathrm{tunn}} = \nu \exp\left(-\frac{2a}{h}\sqrt{2\mu E_a} \right), \qquad (1.1)$$

where ν is an attempt frequency (see, e.g., Cuppen *et al.* 2017), a is the width of the barrier, h is the Planck's constant, μ is the effective mass of the system, and E_a is the reaction energy barrier. Quantum tunneling becomes particularly relevant for light species such as H atoms, and is thought to dominate hydrogen addition and abstraction reactions in clouds and prestellar cores, where the classical solution is not thermally viable (e.g., Cuppen *et al.* 2017 and references therein). Notably, the efficiency of quantum tunneling decreases significantly when a species is replaced by its heavier

---

[5]The WKB method approximates a non-linear second order ordinary differential equation (in this case, the Schrödinger equation), which has no analytical solution, by assuming a slowly varying potential. In the context of tunneling it works by assuming the wavefunction to be an exponential function that is semiclassicaly expanded and with either amplitude or phase taken to be slowly changing relative to the de Broglie wavelength.

isotope. This phenomenon, known as the kinetic isotope effect, arises because the heavier isotope tunnels less efficiently through the barrier than its lighter counterpart (see equation 1.1). In the case of hydrogen, the twofold increase in mass from protium ($_1^1$H) to deuterium ($_1^2$H) results in a particularly pronounced effect, which was leveraged in Chapter 2 of this thesis as a tool to pinpoint the contributions of specific reaction pathways to methanol ice formation.
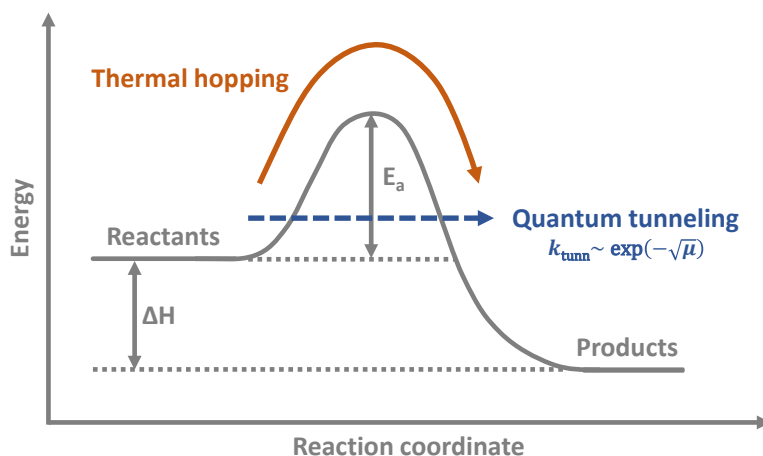
Figure 1.4: Illustration of the energy landscape along the reaction coordinate for an exothermic reaction (ΔH $<$ 0) with an activation energy (E_a). The activation barrier can be overcome through thermal hopping or quantum tunneling. Tunneling rates (k_{tunn}) are heavily dependent on the effective mass of the system (μ, see equation 1.1), giving rise to the kinetic isotope effect.

In the cases where quantum tunneling is inefficient (e.g., for heavier species), any activation barrier must be overcome through thermal hopping, making the reaction temperature dependent. In fact, even for barrierless reactions or those that proceed via tunneling, the temperature of the environment still influences how efficiently a reaction can occur. This is because temperature affects the diffusion and desorption rates of the reactants, which in turn influence how often they encounter one another and how long they remain in proximity before diffusing away. At higher temperatures, increased diffusion can enhance the likelihood of encounters among reactants, but the reduced residence time of reactants in each other's vicinity may be insufficient for the reaction to occur (Cuppen *et al.* 2017). Even in low-temperature environments, where only atomic hydrogen can diffuse, temperature remains a key factor in chemical networks. It directly influences the efficiency of hydrogenation reactions, which not only generate the simple species that constitute the bulk of the ice but also acts as the main trigger of non-diffusive chemistry by producing radicals that drive the formation of complex molecules.

1.3   Chemical evolution through star and planet formation

Interstellar clouds, where stars form, are composed of approximately 99% gas by mass, with elemental abundances dominated by hydrogen ($\sim$90% by number) and helium ($\sim$8%). All other elements in the periodic table are present in significantly lower quantities. For instance, elemental abundances of oxygen, carbon, and nitrogen—the next most abundant elements—correspond to 4.9×10^{-4}, 2.7×10^{-4}, and 6.8×10^{-5} relative to hydrogen, as derived from the Solar photosphere (Asplund *et al.* 2009), with minimal variation expected for the interstellar medium. Dust accounts for only $\sim$1% of the total mass of clouds, and is composed of silicates and carbonaceous material (Draine 2003; Chiar *et al.* 2013; Jones *et al.* 2013). Despite its small mass fraction, as discussed in the previous sections, dust plays a crucial role in the chemical evolution of star- and planet-forming regions by promoting a rich solid-state chemistry. The resulting chemical structures of molecular clouds and protostellar envelopes are briefly outlined in this Section. Here, we focus on the chemical evolution of low-mass star-forming systems, and refer to them as protostars for simplicity.

1.3.1   Prestellar phase

Figure 1.5 shows the chemical evolution of gas and ices along the prestellar phase. In the earliest stages of star formation—the diffuse cloud phase—densities are low ($\sim 10^2$ cm^{-3}) and temperatures range from $\sim 30-100$ K (e.g., Snow & McCall 2006). These regions are surrounded by diffuse atomic gas that provides some shielding to the radiation, allowing the interstellar radiation field to be sufficiently attenuated for molecular hydrogen to form in significant amounts ($> 10\%$ of the hydrogen fraction). Elements with lower ionization potentials, such as carbon, remain predominantly in their ionized form. As these clouds become more compact, the interstellar radiation field is further attenuated, allowing ionized carbon to transition to its neutral state or partake in ion-molecule reactions to form CO efficiently (van Dishoeck & Black 1986). This marks the start of the translucent cloud stage, characterized by densities of $\sim 10^3$ cm^{-3} and visual extinctions of $A_V \sim 1-2$ mag. In this stage, the dominant carbon reservoir is no longer C$^+$, as it is progressively converted into the its neutral atomic and molecular forms. With increasing compaction and extinction, a sufficiently thick CO column builds up to allow self-shielding against interstellar radiation (van Dishoeck & Black 1988). This leads to a dramatic increase in the CO formation efficiency, effectively locking up most of the available carbon. This transitions defines the dense molecular cloud stage, characterized by densities $> 10^4$ cm^{-3}, visual extinctions of $A_V \sim 5-10$ mag, and temperatures of $\sim 10-50$ K (Snow & McCall 2006). At even higher densities and extinctions within the cloud, gaseous nitrogen atoms undergo neutral-neutral reactions to form N$_2$ (Pineau des Forets *et al.* 1990; Gerin *et al.* 1992b), effectively sequestering most of the volatile nitrogen.

Ices begin to form early in the evolution of a cloud, once extinction levels reach a few mag (e.g., Whittet *et al.* 2013). At this stage, atomic and molecular oxygen on the surface of dust grains are efficiently hydrogenated to produce H$_2$O ice (Tielens & Hagen 1982; Hiraoka *et al.* 1998; Mokrane *et al.* 2009; Dulieu *et al.* 2010; Ioppolo *et al.* 2010; Cuppen *et al.* 2010)—a process so efficient that most of the available volatile oxygen becomes locked into it. Simultaneously, interactions between CO and OH on
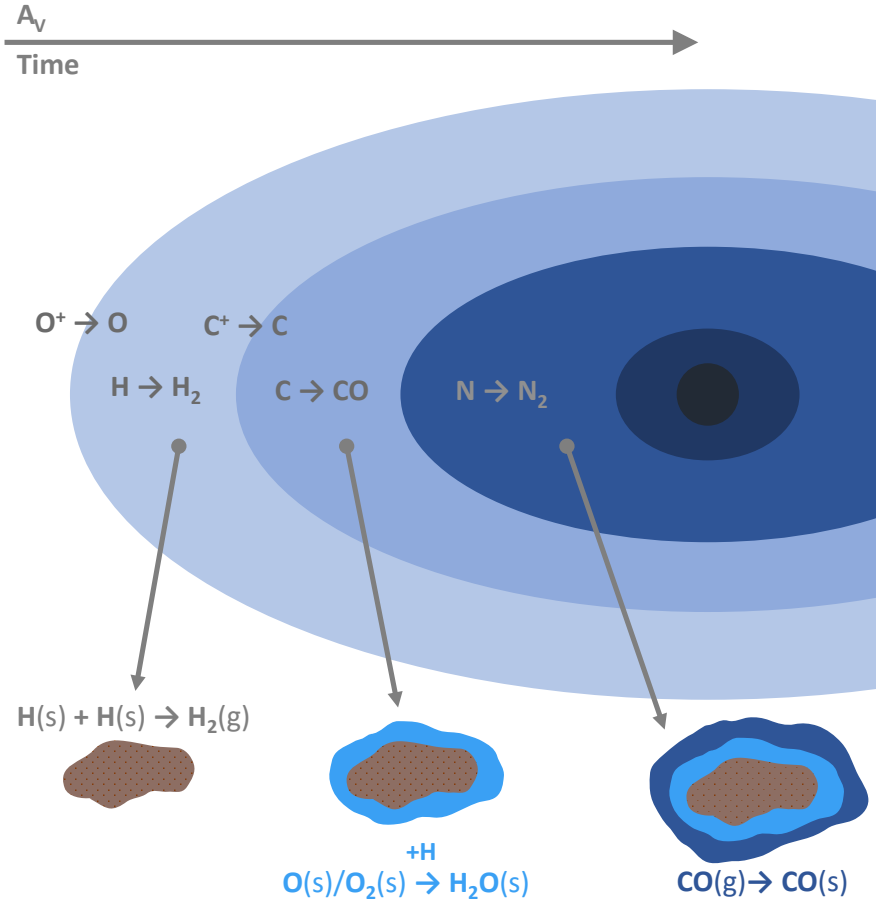
Figure 1.5: Illustration of the chemical evolution during the cloud stages preceding star formation. Gas-phase species are labeled with (g), while species in the solid are labeled with (s). The top arrow represents increasing cloud depth (corresponding to greater extinction) or time elapsed since the start of the compaction of diffuse cloud material. Adapted from Öberg & Bergin (2021).

dust grains lead to the formation of CO_2 (Ioppolo *et al.* 2011; Garrod & Pauly 2011). Other, less abundant species such as NH_3, CH_4, and H_2S also form via hydrogenation reactions on dust grains (respectively, of N, C, and S; e.g., Garrod *et al.* 2007; Garrod & Pauly 2011; Linnartz *et al.* 2015). The bulk of these molecules are produced on similar timescales as H_2O, coexisting as mixtures within a water-rich ice. However, small differences in their adsorption timescales, reactant mobility, and relative gas-phase abundances of their precursors may lead to local differences in ice mixing ratios.

Closer to the cloud core, once densities and extinction levels become sufficiently high ($> 10^5$ cm^{-3}, $A_V \geq 9$ mag), gas-phase CO begins freezing out onto dust grains at a rate that surpasses H-atom-activated surface reactions. This leads to the buildup of a CO-rich ice layer on top of the existing H_2O-rich one, a process known as catastrophic CO freeze-out (e.g., Pontoppidan 2006; Boogert *et al.* 2015). Within this ice layer, CO interacts with hydrogen atoms to form CH_3OH, the simplest COM (Watanabe &

Kouchi 2002; Fuchs *et al.* 2009; and Santos *et al.* 2022b—Chapter 2 of this thesis). Similarly, gaseous N_2 is expected to freeze-out around the same time or slightly later than CO (e.g., Öberg *et al.* 2005; Bisschop *et al.* 2006; Nguyen *et al.* 2018), leading to N_2 ice that is either mixed with or on top of CO ice. This results in a stratified ice structure, with a water-rich layer beneath a CO-rich counterpart, each containing additional molecular components in complex mixtures. Throughout the cloud stage, radicals are produced via atom-induced reactions (Linnartz *et al.* 2015; Chuang *et al.* 2016) or through energetic processing by cosmic rays, secondary electrons, or low-level UV fields generated by electronically-excited H_2 molecules (Prasad & Tarafdar 1983; Öberg 2016). Some of these radicals will form complex species via the non-diffusive mechanism (Jin & Garrod 2020), but a fraction will remain unreacted within the ice, and later will take part in a rich diffusive chemistry when heated in the envelopes surrounding protostars. The resulting main constituents of interstellar ices are shown in Figure 1.6, whose interactions drive the formation of even more complex molecules, which are the main topic of Chapters 4, 6, and 7 of this thesis.
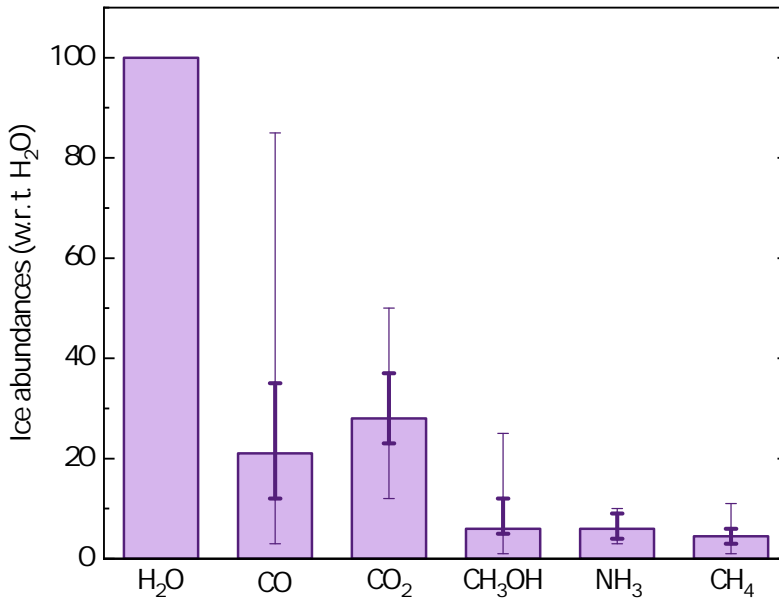
Figure 1.6: Median bulk abundances of the main components of interstellar ices observed towards low-mass protostars. The values are normalized to the most abundant ice species, water, with thick error bars representing the lower and upper quartiles of the detections, and thin error bars corresponding to the full range of detections. For CO and CH_3OH, the lower bounds of the full range of observations (thin errors) correspond to observed upper limits. Figure adapted from Öberg (2016), based on data summarized by Boogert *et al.* (2015).

1.3.2   Protostellar phase and beyond

Figure 1.7 shows the chemical evolution of ices along the protostellar phase. With the gravitational collapse of the prestellar core, a protostar emerges, surrounded by a large envelope of infalling cloud material. This protostar creates a temperature gradient that increases inwards, triggering a range of chemical and physical processes

(Herbst & van Dishoeck 2009). In the outer envelope (thousands of au from the central protostar), conditions remain similar to those of prestellar cores (with $T < 20$ K), and ice chemistry proceeds as a continuation of the previous prestellar stage. Closer to the protostar, increasing temperatures gradually enable molecules to become mobile, triggering a diffusive chemistry regime that leads to the production of a wide range of organic molecules (Garrod *et al.* 2008). Species also begin to desorb from the ice, with more volatile molecules (such as N_2, CO, and CH_4) sublimating at larger distances from the protostar, unless trapped within less volatile ice matrices. Sublimation alters the pool of available reactants in both the solid and gas phases, affecting the chemistry taking place in each. In particular, the sublimation of methane (at $\sim 20 - 30$ K) has been proposed to initiate a network of gas-phase reactions in warm protostellar envelopes, leading to the formation of carbon-chain species in a process known as warm carbon chain chemistry (WCCC; Sakai & Yamamoto 2013).
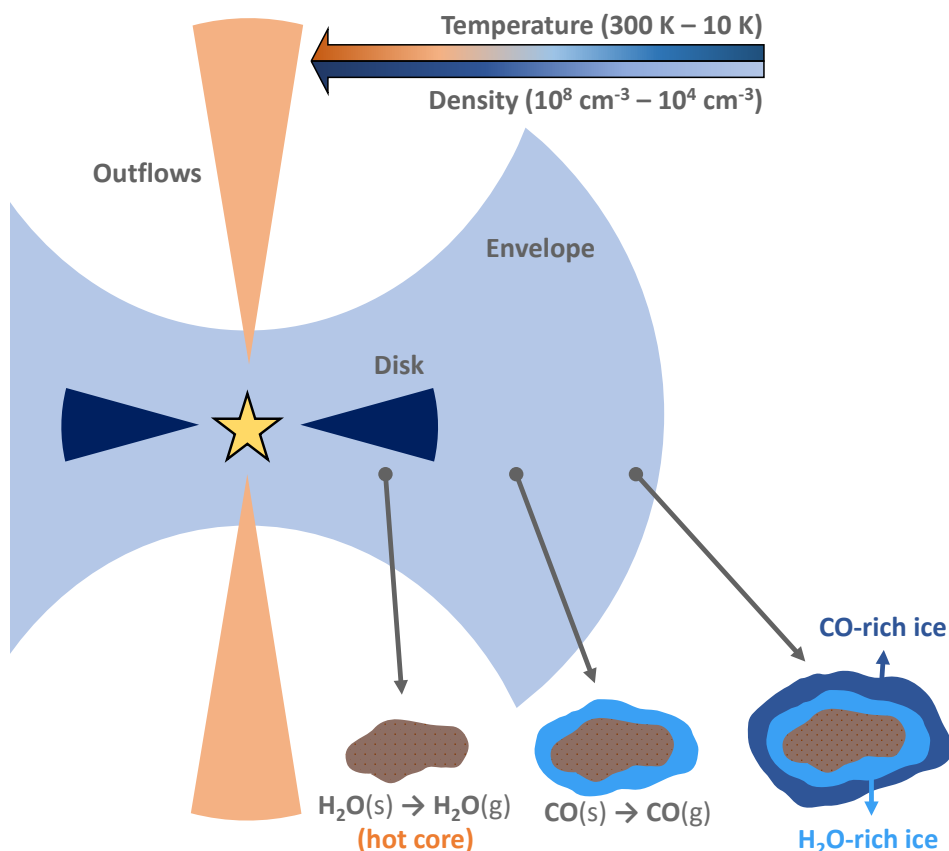
Figure 1.7: Illustration of the chemical structure of protostellar envelopes. As in Figure 1.5, (g) denotes gas-phase species, while (s) denotes solid-state species. As dust grains move closer to the protostar, rising temperatures drive diffusion, reactions, and desorption, with more volatile species sublimating at greater distances than less volatile ones—unless trapped. Where temperatures exceed 100 K, water ice and volatile COMs sublimate, giving rise to the hot core region. Figure adapted from Herbst & van Dishoeck (2009).

Within the region where temperatures exceed 100 K (at tens of au from the proto-star during the embedded phases), the entire volatile ice reservoir sublimates, releasing its constituents into the gas phase. These regions, whose boundaries are defined by the sublimation of water ice, are often called hot corinos in low-mass protostars and hot cores in high-mass counterparts. Here, we use "hot core" as an umbrella term encompassing both. Hot cores are excellent environments to investigate ice composition, as molecules initially formed in ices become detectable through gas-phase techniques—which are much more sensitive and suffer less from line confusion than solid-state observations. However, hot cores may also undergo further chemical evolution (Caselli & Ceccarelli 2012), meaning that gas-phase observations towards such regions may not always directly reflect the original ice composition. Whether they do depends on the molecule and its chemical timescales. Observations of water, for instance, indicate a high degree of inheritance from the prestellar stage, with its gas-phase abundances in warm protostellar envelopes closely mirroring its icy precursors (Jensen *et al.* 2021; Slavicinska *et al.* 2024). In addition to thermal sublimation, ices in protostellar envelopes might also desorb as a result of shocks, for instance from the interactions with protostellar outflows (e.g., Arce *et al.* 2008; Lefloch *et al.* 2017).

Already during the embedded protostellar phases, disks may form at scales similar to those of the hot core. Initially, these disks are expected to be hot, potentially fully dissociating any molecule into its atomic constituents. Over time, however, the centrifugal radius of the disk expands, and infalling material from larger radii start to supply the disk. There is an ongoing discussion regarding the extent to which the material in these disks is inherited from the prestellar and protostellar phases versus being reset during the disk stage. In general, a combination of both is required to explain observational evidence from protostellar disks, as well as data from meteoritic samples and comets (see, e.g., Öberg & Bergin 2021; Öberg *et al.* 2023, and references therein). Eventually, the envelope will be fully dispersed, and the disk—now referred to as protoplantary disk—will be actively undergoing planet formation. Ice processes, such as diffusion, chemistry, and sublimation, will continue to shape the chemical composition and structure of these disks. They will determine which species, and in what physical state, will be incorporated into forming planets and planetesimals. For instance, the locations at which volatiles transition from ice to gas, known as snowlines, play an important part in determining planetary composition. Within them, molecules exist as gases, and might contribute to planet atmospheres. Beyond them, they remain solid and may be incorporated into planetesimal cores. Snowlines, particularly of hydrogen sulfide (H_2S), are a central topic of Chapter 5.

1.3.3   The missing sulfur problem

A significant portion of this thesis focuses on the formation and destruction of sulfur-bearing ice molecules. Interstellar sulfur has been a long-standing topic of discussion in the astrochemical community due to its conspicuously low detectable abundances compared to cosmic values—a discrepancy known as the "missing sulfur problem". While identifying potential reservoirs for this missing sulfur is not a central focus of this thesis, it is closely related to the topics explored in Chapters 4, 5, 6, 7, and 8. Therefore, it is relevant to briefly summarize the current state of this discussion here.

Among the over 320 molecules detected in the interstellar medium to date, at least 30 contain one or more sulfur atoms (McGuire 2022). Sulfur is one of the most common

elements in space (S/H$\sim$1.35$\times$10^{-5}; Asplund *et al.* 2009), and S-bearing species are observed in the gas phase throughout most stages of star and planet formation: in clouds (e.g., Drdla *et al.* 1989; Agúndez *et al.* 2025), protostars (e.g., Blake *et al.* 1987; Drozdovskaya *et al.* 2018), and protoplanetary disks (e.g., Fuente *et al.* 2010; Rivière-Marichalar *et al.* 2021; Le Gal *et al.* 2021), as well as in Solar System bodies such as comets (e.g., Calmonte *et al.* 2016; Altwegg *et al.* 2022), and satellites (e.g., Moullet *et al.* 2008; Cartwright *et al.* 2020). Extragalactic sulfur-bearing species have also been detected (e.g., Martín *et al.* 2003, 2005). Identified molecules range in complexity, from simple diatomic species such as CS and SO to complex organics such as thioacetaldehyde (CH_3CHS), methanethiol (CH_3SH), and ethanethiol (CH_3CH_2SH) (e.g., Linke *et al.* 1979; Kolesniková *et al.* 2014; Agúndez *et al.* 2025). Note that the references provided here represent only a small subset of the broader literature, as numerous other studies have reported detections of sulfur-bearing molecules, from simple to complex, across a wide range of astrophysical environments.

In spite of this widespread detection, derived abundances in dense starless cores, protostars, and protoplanetary disks can only account for up to a few percent of the total expected cosmic value (e.g., Tieftrunk *et al.* 1994; Wakelam *et al.* 2004; Anderson *et al.* 2013; Vastel *et al.* 2018; Fuente *et al.* 2019; Le Gal *et al.* 2019; Rivière-Marichalar *et al.* 2019, 2020; Le Gal *et al.* 2021; Bouscasse *et al.* 2022; Fuente *et al.* 2023), with the bulk of the sulfur content remaining elusive. In diffuse clouds, however, sulfur is undepleted. One of the main hypothesis to explain the missing sulfur is that it is locked away in or underneath the ice mantles that shroud interstellar dust grains, in a state that is difficult to detect. H_2S could be a good candidate to explain the depletion of sulfur since it is efficiently formed on ices via the hydrogenation of S atoms (see, e.g., Garrod *et al.* 2007; Vidal *et al.* 2017). However, solid-phase interstellar H_2S has not been unequivocally detected yet, and only upper limits are available so far (e.g., Jiménez-Escobar & Muñoz Caro 2011a; McClure *et al.* 2023). These upper limits are not sufficient to account for the bulk of the missing sulfur, meaning that H_2S ice is likely undergoing effective solid-state destruction pathways that prevent it from accumulating onto dust grains (see, e.g., Garrod *et al.* 2007; Jiménez-Escobar & Muñoz Caro 2011a; Oba *et al.* 2018; Cazaux *et al.* 2022; as well as Santos *et al.* 2023b, 2024a,b—Chapters 4, 6, and 7 of this thesis—and references therein). Other proposed solid reservoirs are in the form of sulfur chains (e.g., S_n, H_2S_n; Wakelam *et al.* 2005; Calmonte *et al.* 2016; Shingledecker *et al.* 2020; Cazaux *et al.* 2022), sulfide minerals (e.g., FeS; Keller *et al.* 2002; Köhler *et al.* 2014; Kama *et al.* 2019), or even a combination of a wide range of simple organosulfur compounds hardly observable on their own (Laas & Caselli 2019). More recently, ammonium hydrosulfide salt (NH_4SH) has been invoked as a promising semirefractory sulfur reservoir candidate due to its high detected abundances in comet 67P/Churyumov-Gerasimenko (Altwegg *et al.* 2022) and tentatively in protostars, where it could account for up to 20% of the missing sulfur (Slavicinska *et al.* 2025). Although important advances surrounding the sulfur depletion problem have been achieved in the last decades, the state of the bulk of the interstellar sulfur content is ultimately still under debate. This distinctive characteristic unique to sulfur-bearing species makes them prominent puzzle pieces in understanding the evolution of volatile and refractory components throughout the different stages of star and planet formation, and particularly interesting cases for direct comparisons between interstellar ice and gas.

1.4   Laboratory astrochemistry

The field of astrochemistry is built upon three foundational pillars: observations, models, and experiments. Both observations and models fundamentally rely on laboratory experiments, alongside theoretical calculations, to derive meaningful interpretations of the phenomena under investigation (Cuppen *et al.* 2024). While calculations offer their own unique avenues of exploration that are certainly valuable the field, this thesis focuses on the laboratory component of experimental astrochemistry—whose indispensable role is briefly outlined here.

In the context of observations, laboratory-derived spectra of solid and gas-phase species are essential for identifying molecular features and interpreting telescope data (see, e.g., Boogert *et al.* 2015; Widicus Weaver 2019). While *ab initio* computational methods can help narrow down possible identifications for unknown spectral features, only laboratory measurements provide the level of precision required for definitive assignments. Similarly, determining column densities from observations depends on prior laboratory measurements of fundamental molecular properties. In the solid state, comprehensive measurements of infrared absorption band strengths across a range of relevant temperatures and ice mixing conditions are necessary for accurately quantifying ice abundances (e.g., Bouilloud *et al.* 2015). Additionally, laboratory measurements of optical constants for astrophysically-relevant solid media are necessary to properly model the scattering of light interacting with astronomical objects (e.g., Gerakines & Hudson 2020). In the gas phase, molecular excitation levels in interstellar environments often deviate from local thermodynamic equilibrium (LTE), where a single temperature characterizes the population distribution of rotational levels. In such cases, accurately determining column densities requires knowledge of collision rate coefficients to account for the interplay between collisional and radiative processes governing molecular excitation. While most collisional rate coefficients come from theory (e.g., van der Tak *et al.* 2020), laboratory experiments on selected transitions and systems are needed to benchmark the accuracy of calculated rate coefficients (Smith 2011).

Similarly, astrochemical models rely on key parameters, such as reaction rate coefficients and product branching ratios, which must be determined both for the solid and the gas phases. While theoretical predictions can provide useful estimates, in many instances these parameters must be determined experimentally. For example, gaseous neutral-neutral reaction rate coefficients often exhibit temperature dependencies that contradict theoretical predictions (Smith 2011). In the solid state, reactions rates and branching ratios are not the sole factors governing surface chemistry. Adsorption, desorption, and diffusion processes are also intertwined and collectively shape the chemical evolution of interstellar ices. These processes are difficult to fully constrain from first principles, making laboratory experiments essential for determining these convoluted parameters (Cuppen *et al.* 2017, 2024).

1.4.1   An overview of ice experiments

Much of this PhD thesis involves experiments on the chemical evolution of interstellar ices, which are performed using apparatuses designed to simulate the conditions typical of space environments. First, the common features of these setups, including the analytical techniques employed, are described. The specific details of each setup are

then provided in the subsequent subsections. For better context, an example setup is shown in Figure 1.8, which was used for the largest fraction of the experimental works presented in this thesis (Chapters 2, 4, 6, and 7). In a nutshell, ice analogue experiments involve growing thin ($\sim 0.1-100$s monolayers, ML) ice films via freeze-out of gas onto a cold (typically $\sim 10-15$ K) substrate, and studying the physicochemical behavior of these ices under controlled conditions. To simulate as well as possible the low pressure conditions of interstellar space, experiments are performed under ultra-high vacuum (UHV; $\lesssim 10^{-9}$ mbar), achieved through dedicated vacuum pumping systems. At such pressures, the residual atmosphere consist mostly of H_2, with minimal water contamination (i.e., residual water deposition rates of $\lesssim 0.01$ ML/h). Interstellar temperature conditions are reproduced using cryogenic techniques. In all experimental setups used in this thesis, this is achieved with closed-cycle helium cryostats attached (either directly or via an interface) to the substrate. These systems allow a controlled manipulation of the substrate temperature using resistive heating wires. While the exact temperature ranges vary across the different setups used here, and even over time within the same setup, the typical range explored in this thesis remains within $\sim$ 10–300 K. The physicochemical processes of interest can then be induced by a variety of triggers. This thesis primarily focuses on atom- and radical-induced reactions, particularly those initiated by thermalized atomic hydrogen interacting with the other ice constituents (Chapters 2, 4, 6, and 7). Additionally, heat-driven processes are explored in Chapter 5, while ice processing induced by infrared radiation is examined in Chapter 3.

Ices can be grown sequentially to form distinct layers or concomitantly to produce ice mixtures. Furthermore, experimental deposition conditions can be categorized into two types: predeposition and codeposition, each serving a distinct purpose in terms of phenomena being probed. In predeposition, a species or mixture is first deposited onto the cold substrate and subsequently exposed to a trigger. This method allows for the changes in the ice to be monitored as a function of time, or of trigger fluence, enabling the determination of kinetic properties by fitting the time-resolved data with rate equations. For instance, this approach was used in Chapter 4 to investigate the product formation and the non-thermal sublimation kinetics of H_2S ice exposed to H atoms. However, a key limitation of the predeposition method is that it is restricted by the penetration depth of the trigger, which is typically just one or two monolayers for atomic hydrogen. As a result, this method is less suited for studying low-yield processes, for instance when the goal is to investigate multi-step reaction pathways. In codeposition, by contrast, the ice is grown on the substrate while simultaneously being exposed to the trigger. The continuous supply of reactants enables a steady formation of reaction products proportional to the duration of the deposition, facilitating their production above instrumental detection limits. Additionally, by controlling the relative deposition rates of different reactants and monitoring their impact on product yields, it is possible not only to optimize experimental conditions for better data interpretation but also to infer details about the underlying chemical networks. This strategy was employed, for instance, in Chapters 2, 6, and 7 to investigate how variations in atomic hydrogen abundance influence the equilibrium of product yields.

In terms of analytical techniques, this thesis primarily employs infrared spectroscopy and mass spectrometry. The former is used to monitor the ice composition and abundance *in situ*, and in all cases for this thesis, is performed using a Fourier-transform infrared spectrometer (FTIR) combined with a mercury cadmium telluride
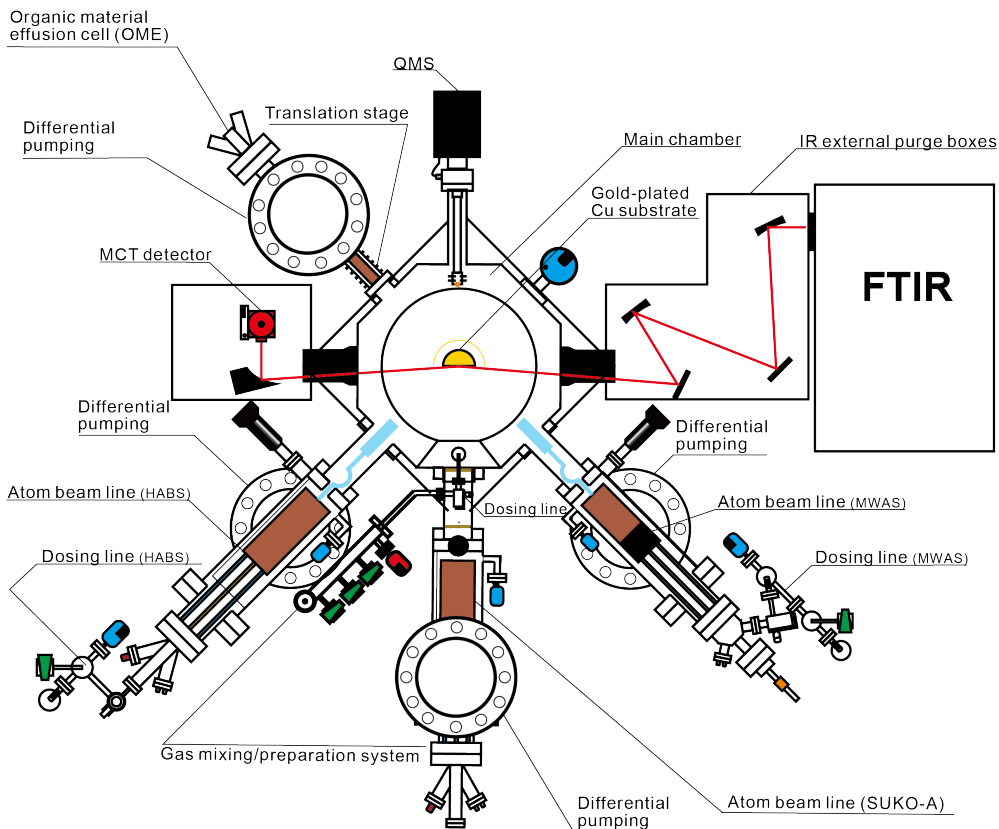
Figure 1.8: Top-view schematic of SURFRESIDE³ in the configuration used for this thesis. Adapted from the earlier versions shown in Ioppolo *et al.* (2013) and Chuang (2018).

(MCT) detector cooled by liquid nitrogen. The FTIR emits infrared light, typically covering the range of $4000-700$ cm^{-1} with a resolution of 1 cm^{-1}[6], which then either reflects off the substrate (when in reflection mode) or passes through it (when in transmission mode) before reaching the detector. More information on these two modes are presented in Sections 1.4.2 and 1.4.4, as they depend on the setup geometry and the choice of substrate material. Ice films grown on top of the substrate may interact with infrared radiation, producing absorption features in the spectra if they are infrared active. For a molecular vibration to be infrared active, it must induce a change in the dipole moment function (i.e., $d\mu/dQ \neq 0$, where μ is the dipole moment and Q is the vibrational coordinate), and the intensity of the absorption feature will be proportional to $(d\mu/dQ)^2$. Homonuclear diatomic species, for instance, have $d\mu/dQ = 0$ and therefore lack electric-dipole allowed infrared transitions, thus their infrared transitions are typically not detectable via conventional IR spectroscopy[7].

Infrared features in the solid state are often broad as a result of the range of molec-

---

[6]While higher resolution (0.5 cm^{-1}) is possible, it was not required for the scientific goals of this thesis.

[7]One notable exception is H_2, which due to its high abundance, is detectable by infrared observatories in astrophysical environments through its weak second-order electric quadrupole transitions.

ular interactions that produce variations in vibrational mode strengths. This effect is especially pronounced in amorphous solids, which exhibit a higher degree of structural disorder. The chemical environment of a species—such as its mixing conditions and the nature of the surrounding molecules—also strongly influences the shape of its infrared bands. Solid-state IR features are thus typically highly degenerate, especially for molecules with similar functional groups. As a result, laboratory assignments based solely on infrared spectroscopy performed at ∼10 K can be challenging, particularly for complex ice mixtures containing structurally similar molecules. One approach to produce an assignment is to compare the relative intensities of different absorption features that are thought to originate from the same molecule in the ice, as these tend to be less degenerate across different species. However, this method remains difficult in complex mixtures, where absorption features blend and it is not trivial to isolate individual contributions to the overall feature intensity. Isotope-labeled control experiments provide another strategy to mitigate these issues. Changes in a molecule's reduced mass, particularly for the moieties directly involved in a given vibrational transition, alter vibrational strengths and thus shift its frequencies. Heavier isotopologues exhibit a redshift in their infrared spectrum, which can help confirm spectral assignments in the laboratory. Additionally, differences in the volatilities of ice species can also be leveraged for spectral identification, provided that the molecules are not fully entrapped in less-volatile matrices. This can be achieved through temperature-programmed desorption (TPD) experiments, where the substrate is gradually heated at a constant rate. As the ice film reaches the sublimation temperatures of its components, they desorb, and the disappearance of absorption features at specific temperatures can provide information about the sublimation temperature of its carriers. This approach also allows for the isolation of spectral features from less volatile constituents within an ice mixture through a distillation-like process: as the ice film reaches the sublimation temperatures of the more volatile components, they sublimate first, leaving behind the less volatile species that can then be assigned via their infrared features (see Figure 1.9 for an example of distillation-facilitated assignment).

The integrated absorbance of an infrared feature ($\int Abs(\nu)\mathrm{d}(\nu)$) can be used to determine the column density of its carrier species via a modified Beer-Lambert law (see, e.g., Bouilloud $et\ al.$ 2015 for a derivation of this relation):

$$N_X = \ln 10 \frac{\int Abs(\nu)\mathrm{d}(\nu)}{A_X}, \tag{1.2}$$

where N_X is the species' column density in molecules cm^{-2} and A_X is its absorption band strength in cm molecule^{-1}. The $\ln 10$ factor is employed to convert the integrated absorbance to optical depth scales. As discussed previously, band strength values are influenced by factors such as the ice mixing environment and ice morphology. Additionally, in setups utilizing reflection mode, the band strength is further affected by the optical properties of the infrared beam, which depend on the system's optical geometry. This introduces setup-dependent variations in the band strength, so literature values measured in transmission mode should not be directly applied to reflection-mode experiments. Instead, band strength measurements should be performed under the same experimental conditions, or a reflection-to-transmission conversion factor must be determined for the setup. These considerations will be addressed further in Section 1.4.2, which discusses a setup operating in reflection mode.

The other analytical tool employed throughout this thesis is mass spectrometry,
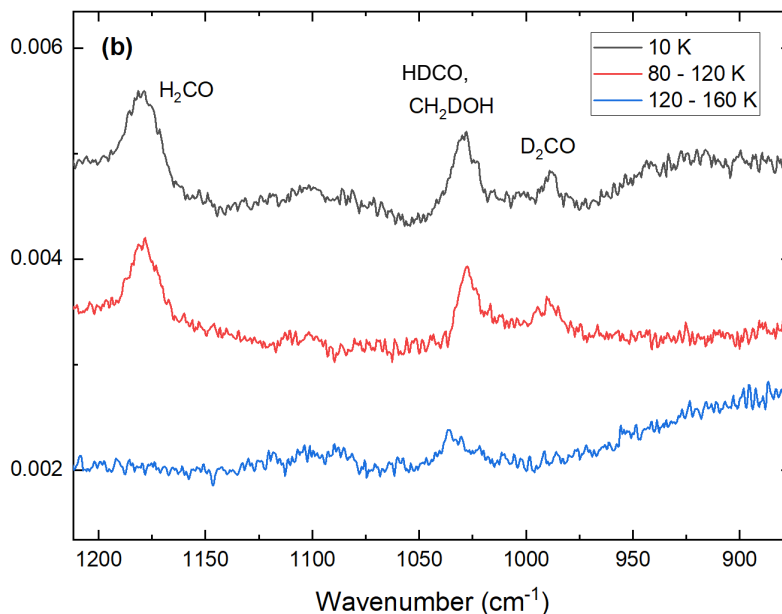
Figure 1.9: Infrared spectra measured during a TPD experiment. At 10 K, the absorption feature of CH$_2$DOH cannot be unambiguously identified due to blending with a HDCO feature. However, after formaldehyde fully desorbs (below 120 K), the absorption feature of the less volatile CH$_2$DOH becomes isolated. Figure from Chapter 2 (Santos *et al.* 2022b).

specifically using quadrupole mass spectrometers (QMS). In these instruments, gaseous species in the chamber are ionized via 70 eV electron impact from electrons generated by a hot filament at the tip of the QMS. While other electron energies are allowed, 70 eV is the stardard and the only value used here. The resulting ionized species are guided to the quadrupole mass filter, which selects for ions with specific mass-to-charge (m/z) ratios based on preset parameters. The filter consists of four parallel cylindrical rods, with each opposing rod pair electrically connected. An RF voltage with a DC offset is applied between the pairs of rods, allowing only ions with a particular m/z ratio to maintain a stable trajectory and reach the detector, while others develop unstable trajectories and collide with the rods.

Quadrupole mass spectrometers are powerful tools for molecular identification of desorbed ices. For instance, during a TPD experiment, when the substrate temperature reaches the sublimation range for a given molecule (provided it is not trapped in a less volatile ice matrix), it transitions into the gas phase and may be detected by the QMS. Upon electron impact ionization at 70 eV, molecules fragment into characteristic, energy-dependent patterns that serve as molecular fingerprints. Databases such as NIST[8] provide extensive mass fragmentation patterns for 70 eV electron bombardment, which can be used as reference standards to identify molecules desorbing from the ice at specific temperatures. This approach can be further strengthened by correlating QMS detections with the simultaneous disappearance of infrared features, providing robust assignments of ice species. Additionally, QMS measurements are

---

[8]https://webbook.nist.gov/chemistry/

typically at least an order of magnitude more sensitive than infrared spectroscopy of ice analogues, enabling the detection of less abundant reaction products.

Beyond serving as an assignment tool, the QMS can also be used as a quantification method under the high pumping speeds typical of UHV chambers. The integrated ion current from the mass fragments m/z of a species desorbing during a TPD experiment is related to the column density of that species by (Martín-Doménech *et al.* 2015):

$$N_X = k_{\text{QMS}} \frac{a(m/z)}{\sigma_X^+ \cdot I_F(z) \cdot F_F(m) \cdot S(m/z)}, \tag{1.3}$$

where N_X is the total column density of desorbed species X, k_{QMS} is a proportionality constant, $a(m/z)$ is the integrated area of the desorption peak corresponding to a given mass fragment m/z from species X, σ_X^+ is the molecule's first ionization cross section at 70 eV, $I_F(z)$ is the fraction of ionized molecules with charge z, $F_F(m)$ is the fraction of molecules leading to a fragment of mass m, and $S(m/z)$ is the QMS sensitivity to the mass fragment of interest. For most molecules studied in this thesis, the ionization cross section σ_X^+ is either available in the literature or can be inferred from other molecular properties (see, e.g., Chapter 7). Under the experimental conditions explored here, only singly-charged mass fragments are relevant, so $I_F(z) = 1$. $F_F(m)$ can be derived if the fragmentation pattern of the molecule is known, while $S(m/z)$ must be measured for a given mass spectrometer under a specific setup configuration. The proportionality constant, k_{QMS}, depends on the fraction of desorbed molecules that can reach the QMS and is thus a setup-dependent value that must be calibrated in order to derive absolute column density measurements. To determine relative abundances, Equation 1.3 for species X can be divided by the same equation for species Y. Assuming analogous pumping speeds for both molecules X and Y (a reasonable assumption, see e.g. Martín-Doménech *et al.* 2015), the k_{QMS} constant cancels out, enabling relative abundances to be determined without it.

The desorption rate of a given species as a function of temperature, measured by the QMS in units of current per Kelvin during TPD, can also be used to derive the species' sublimation parameters—such as its binding energies and desorption attempt frequencies under specific coverage regimes and substrate condition (e.g., Minissale *et al.* 2022). Coverage regimes can be broadly categorized into two cases: the multilayer regime, where desorption follows zeroth-order kinetics due to a constant number of adsorbates available for desorption at any given time, and the submonolayer regime, where the varying number of adsorbates results in first-order kinetics. In the former, binding energies are primarily dictated by intermolecular interactions between adsorbates of the same kind, whereas in the latter, they are dominated by interactions between the adsorbate and the substrate. This analysis is explored in detail in Chapter 5, where sublimation parameters and the corresponding snowline positions of H_2S in protoplanetary disk midplanes are determined. Furthermore, non-thermal desorption processes can also be studied by analyzing the QMS signal of a molecule's mass fragment—proportional to its desorption rate—as a function of trigger fluence. This is done in Chapter 4, where the kinetics of the non-thermal desorption of H_2S due to its excess heat of formation are explored using both infrared spectroscopy and mass spectrometry. Although QMS analyses have some limitations, the most notable being the destruction of the sample, they remain a powerful and versatile tool in astrochemical research.

1.4.2 SURFRESIDE³

Chapters 2, 4, 6, and 7 of this thesis present work conducted using the SURFRESIDE[39] experimental setup, located at the Laboratory for Astrophysics at Leiden University, the Netherlands. This setup is specifically designed to investigate atom- and radical-induced reactions in interstellar ice analogues and is described in detail by Ioppolo *et al.* (2013) and Qasim *et al.* (2020b). A top-view schematic of the current system is shown in Figure 1.8.

The base pressure in the main chamber is of $\sim 10^{-9}$ mbar at room temperature and $\sim 10^{-10}$ mbar at 10 K. At its center, a gold-plated copper substrate is mounted on the tip of a closed-cycle helium cryostat (CH-204 SF; compressor HC-4E1). The substrate temperature can be controlled between $\sim 9 - 450$ K using resistive heating wires, and is monitored by two silicon diode sensors with an absolute accuracy of 0.5 K. The setup includes three atom source chambers and an organic material effusion cell chamber, each differentially pumped to UHV pressures. These chambers are connected to the main chamber with UHV shutter valves and/or gate valves. Additionally, a high vacuum ($\lesssim 10^{-5}$ mbar) manifold is used to prepare and introduce vapors and gases into the main chamber. Vapors from liquid or solid samples are admitted into the manifold through an ultratorr connection, while gases enter via swagelock valves. The admitted species can then be stored in two separate dosing line reservoirs, and then be inlet into the main chamber through two capillary tubes controlled by two high-precision leak valves that enable ice deposition with submonolayer precision.

The hydrogen atom beam source (HABS; Dr. Eberl MBE-Komponenten GmbH; Tschersich 2000) produces atomic hydrogen or deuterium via thermal cracking of H_2 or D_2 molecules using a tungsten filament. The molecular gas is admitted into a dedicated dosing line, then introduced into the HABS chamber by a leak valve. The chamber pressure is adjusted to control the atomic flux reaching the substrate, typically on the order of 10^{12} atoms cm^{-2} s^{-1}. The microwave atom source (MWAS, Oxford Scientific Ltd; Anton *et al.* 2000) operates by generating free electrons with sufficient kinetic energy to break apart and ionize molecules, creating a plasma. Consequently, it can be used to generate atomic species such as O and N, as well as radicals such as OH, depending on the gases inlet into the MWAS chamber. It is powered by a 2.45 GHz microwave power supply (Sairem) delivering up to 200 W, coupled into a microwave cavity. An ion trap deflects ions to prevent them from entering the main chamber. Like HABS, gases are admitted into the MWAS chamber via a dedicated dosing line controlled by a leak valve, with attainable atom/radical fluxes also around 10^{12} atoms cm^{-2} s^{-1}. In the case of H or D atoms, both HABS and MWAS can be used simultaneously to maximize the atom flux, as is done in Chapter 2. On the exit path of both the HABS and the MWAS, nose-shaped quartz pipes are placed to cool the species through multiple collisions with their walls. This allows the species to quench and thermalize before reaching the substrate, and also shields the substrate from any UV light produced by the MWAS plasma. The carbon atom source (SUKO-A, Dr. Eberl MBE-Komponenten GmbH; Krasnokutski & Huisken 2014) generates ground state $C(^3P_0)$ atoms by resistively heating a tantalum filament packet with graphite powder. This design is advantageous because it predominantly produces atomic carbon, unlike conventional carbon rod heating methods that generate clusters. A dosing line is not required, but filaments must be replaced after $\sim 10 - 15$ hours

---

[9]SURFace REaction SImulation DEvice³

of operation under standard conditions. Finally, the organic material effusion cell (OME Dr. Eberl MBE-Komponenten GmbH) allows the deposition of high-vapor-pressure organic materials such as sugars and aminoacids by heating a conical quartz crucible containing the sample at temperatures up to 300 °C. The source is mounted on a 10-inch linear translator (Hositrad HOBLT27S-10), allowing precise positioning near the substrate during deposition. Like for SUKO-A, the OME does not require a dosing line. All three atomic sources, as well as the effusion cell, are equipped with water-cooled shrouds to prevent overheating.

SURFRESIDE[3] features two analytical tools: an FTIR spectrometer (Agilent Cary 640/660) with a liquid-nitrogen-cooled MCT detector and a QMS (Hidden Analytical 3F RGA). The IR pathway is purged of atmospheric H_2O and CO_2 using filtered compressed air. In this setup, IR light is emitted from the FTIR and focused by external optics onto the sample, where it reflects off the gold-plated substrate before being collected by the MCT detector. It thus operates in reflection mode, also known as Reflection Absorption Infrared Spectroscopy (RAIRS). RAIRS is chosen over transmission spectroscopy because of its higher sensitivity: the IR path passes through the ice twice—upon incidence and reflection—and the p-polarized electric field intensity of the IR light is enhanced due to the shallow grazing angle ($\sim 10°$ to the surface place) on the gold substrate (see the discussion in Qasim 2020). However, the shape and relative intensities of absorption features in RAIRS spectra can vary significantly depending on experimental conditions (e.g., ice thickness, IR path geometry, and the instrument setup), making them unsuitable for direct comparison with observational infrared data, which is acquired in transmission mode (see, e.g., Rocha *et al.* 2022). Moreover, band strength values measured in transmission mode cannot be directly applied to SURFRESIDE[3] experiments. To address this, the band strengths of H_2S—the most frequently used species in this thesis—and CO were experimentally determined for this setup. This was done by depositing ice at a constant rate while simultaneously measuring its thickness via laser interference (using a HeNe laser) and recording its absorption spectra with RAIRS. The detailed procedure for H_2S is discussed in Chapter 4, and is repeated with CO. Their resulting estimated band strengths are: A_{CO}(C-O str.) $= (4.2\pm0.3)\times10^{-17}$ cm molecule^{-1} and A_{H_2S} (S-H str.) $= (4.7\pm0.1)\times10^{-17}$ cm molecule^{-1}. From these values, a mean reflection-to-transmission conversion factor of ~ 3.2 is derived based on their corresponding transmission band strengths (Bouilloud *et al.* 2015; Yarnall & Hudson 2022). Setup-dependent calibrations of the QMS sensitivity are also necessary. Here, we adopt the calibration values provided by Chuang (2018) for the same experimental setup.

1.4.3   LISA

The work presented in Chapter 3 was conducted using the LISA[10] experimental setup located at the HFML-FELIX Laboratory, Radboud University, the Netherlands. The setup has been rebuilt multiple times in recent years, and details on the version used in this thesis can be found in Ioppolo *et al.* (2022). It consists of an UHV end station coupled to the tunable, high-power, short-pulsed radiation from the free-electron lasers (FEL) at the HFML-FELIX: FELIX-1 ($\sim 30-150$ μm), and FELIX-2 ($\sim 3-45$ μm). The main chamber operates at a base pressure of $\sim10^{-9}$ mbar at room temperature, at the center of which a gold-plated copper substrate is in thermal contact with a

---

[10]Laboratory Ice Surface Astrophysics

closed-cycle helium cryostat head (Sumitomo, CH-204SB) supported by a compressor (HC-4E). The substrate temperature can be controlled between $\sim 20 - 300$ K via resistive heating, and is measured by a silicon diode. Pure gas and vapors, as well as mixtures, are prepared in a manifold with a base pressure of 10^{-4} mbar and admitted into the main chamber through a dosing line controlled by an all-metal leak valve. The substrate position can be adjusted vertically using a z-translation stage with a 2-inch stroke, allowing for different spots in the ice to be probed during experiments.

The LISA end station is coupled to the FEL beamline so that the beam path reaches the substrate. Three gate valves are installed in series along the FEL beam path before it enters the main chamber. The first two contain CsI and TPX windows, which are transparent in the IR and THz ranges, respectively. Their intent is to optimize switching between FELIX-1 and FELIX-2 during a shift (8 hours). The third gate valve is a blank, used to block the FEL beam when irradiation is not required. For analytical techniques, LISA is equipped with an FTIR spectrometer (VERTEX 80v, Bruker) coupled to a liquid-nitrogen-cooled MCT detector for infrared spectra acquisition in reflection mode. A QMS (MKS Instruments) is also positioned facing the gold substrate for analysis of the gas phase.

1.4.4   SPACE-KITTEN

The experimental setup SPACE-KITTEN[11], located at the Öberg Astrochemistry Lab at the Center for Astrophysics, Harvard University, was used in Chapter 5 of this thesis. This setup is dedicated to studying thermal processes in interstellar ice analogues and is described in detail elsewhere (Simon *et al.* 2019, 2023). It consists of a UHV chamber with a base pressure of $\sim 10^{-9}$ Torr at room temperature. At the center of the chamber, a CsI window is mounted on an optical ring sample holder attached to a closed-cycle helium cryostat (Advanced Research Systems model DE204S). To minimize vibration transfer from the cryocooler to the CsI window, the cryostat is integrated with a DMX-20B interface that uses helium exchange gas to decouple the window from the cold tip. The substrate temperature is controlled via resistive heating over a range of $12 - 350$ K, with a precision of ± 0.1 K and an absolute accuracy of ~ 2 K, monitored by silicon diode sensors. Gas and vapor samples are prepared in a manifold maintained at base pressures of $< 5 \times 10^{-4}$ Torr before deposition. After preparation, species are introduced into the main chamber via a stainless steel tube doser (4.8 mm diameter) positioned 2 inches from the substrate. The doser is connected to the manifold through a variable leak valve and is mounted on a compact z-translation stage (MDC Vacuum Products, LLC), allowing to approach the doser to the substrate during deposition.

SPACE-KITTEN is equipped with an FTIR spectrometer (Bruker Vertex 70) with a liquid-nitrogen-cooled MCT detector operating in transmission mode. The UHV chamber is housed within the FTIR's sample compartment, with the IR optical path aligned with the horizontal axis of the chamber. The chamber and the FTIR are interfaced on each side with two IR transparent KBr windows that are differentially pumped, as well as with vibrational damping mounts. The optical path of the IR is purged with pure, dry nitrogen gas to prevent atmospheric interference. Additionally, the setup includes a QMS (QMG 220M2, PrismaPlus Compact) positioned near the sample holder. For the scientific objectives of Chapter 5, it was not necessary to

---

[11]Surface Processing Apparatus for Chemical Experimentation–Kinetics of Ice Transformation in Thermal ENvironments

determine the sensitivity of the QMS as a function of m/z.

1.5   Observational astrochemistry

Telescopes offer another fundamental avenue for astrochemical research, providing the only means to obtain direct empirical evidence of the chemistry in star- and planet-forming regions beyond our Solar System. Throughout this thesis, observations of interstellar ices and gas serve to contextualize and motivate the investigations presented in each chapters. Additionally, in Chapters 8 and 9, we utilize radio telescopes to observe emission lines from the rotational transitions of relevant molecules, which provide insights into their chemical evolution and origins.

1.5.1   Submilimeter and millimeter observations

Observations at submillimeter and millimeter wavelengths have led to the detection of the vast majority of interstellar molecules (McGuire 2022). This is largely because of the low energies associated with the levels whose transitions fall on such large wavelengths, which are more easily populated compared to higher-energy transitions. The primary type of molecular transition probed in these wavelengths are rotational lines, often in the ground vibrational state ($\nu = 0$)—though, in some instances, vibrationally-excited pure rotational lines are also observed. When sufficient energy is available to populate a molecule's rotational levels above the background radiation field, emission lines are observable. This occurs in warm regions such as hot cores, which are known for their rich spectra with forests of molecular emission lines (e.g., Belloche *et al.* 2013; Jørgensen *et al.* 2020), but emission lines are also observable even in much colder environments like dark clouds (e.g., Kaifu *et al.* 2004). In extremely cold environments where there is not enough energy to populate rotational energy levels, molecules can still be observed in absorption against the background continuum (e.g., Neufeld *et al.* 2012; Gerin *et al.* 2016). As a result, molecules can be observed in millimeter and submillimeter wavelengths across virtually all types of interstellar regions.

To observed these lines, millimeter-wave telescopes are employed. These instruments use antennas, typically consisting of paraboloid reflectors that focus incoming radiation onto a receiver. They can operate as either single-dish telescopes, which use a single antenna, or as interferometric arrays of antennas. In an interferometric array, multiple antennas are combined to form a synthesized aperture with an effective diameter much larger than that of an individual antenna. The separation between antennas, combined with Earth's rotation, introduces differences in the path length of incoming light from the observed source. These path length variations produce interference patterns that can be reconstructed into an image of the observed source (Thompson *et al.* 2017). Spatial resolution is inversely proportional to the effective antenna diameter, so interferometry is a powerful technique for achieving high spatial resolution by synthesizing an aperture much larger than would be possible with a single dish antenna. For instance, in its most extended configuration, the Atacama Large Millimeter/submillimeter Array (ALMA) can space its antennas up to ∼16 km apart, yielding spatial resolutions on the order of tens of milliarcseconds. However, because the gaps between antennas do not collect radiation, interferometers gather less total light than a single dish of equivalent size. Additionally, the sensitivity of an interferometer depends on the signal received by each individual antenna. As a result,

even if the total collecting area of an array exceeds that of a single-dish telescope, its sensitivity may be lower if the individual antennas are too small. Nonetheless, other factors, such as receiver noise, also play a role in determining sensitivity. Ultimately, both single-dish and interferometric telescopes offer distinct advantages and limitations, and this thesis employs both techniques to study molecular emission lines toward massive young stellar objects.

1.5.1.1 ALMA

ALMA is an interferometer comprising 66 antennas located in the Atacama Desert in northern Chile. It includes 54 antennas with individual diameters of 12 m, which can be arranged in various configurations to achieve angular resolutions ranging from $\sim 0.01''$ to $\sim 9''$. Large-scale observations are also possible using ALMA's compact configuration, which employs its 12 7-m dishes. ALMA operates over a broad frequency range of $\sim 35-950$ GHz, with spectral resolution as high as ~ 0.03 MHz (corresponding to $\sim 0.26-0.01$ km s^{-1}, depending on frequency). This coverage is achieved using 10 different receivers, known as bands, each designed to capture a specific frequency range. In Chapter 8 of this thesis, publicly available ALMA Band 6 observations ($\sim 1.1-1.4$ mm, or $\sim 211-275$ GHz) with spatial resolutions of $0.5-1.5''$ and spectral resolutions of ~ 0.5 MHz (~ 0.7 km s^{-1}) are used to investigate the abundances of key sulfur-bearing molecules in the inner envelopes of 26 massive young stellar objects.

1.5.1.2 APEX

The Atacama Pathfinder Experiment (APEX) is a 12-m single-dish telescope based on an ALMA prototype antenna, and like ALMA is also located in the Atacama desert in northern Chile. APEX currently operates over a spectral range of $157-850$ GHz, with spatial resolutions between $6''$ to $39''$, depending on the instrument. In Chapter 9, APEX observations with the Swedish-ESO PI Instrument (SEPIA180; Belitsky *et al.* 2018) alongside the Swedish Heterodyne Facility Instrument (SHeFI, decommissioned; Vassilev *et al.* 2008a) are used to conduct a spectral survey of methyl acetylene (CH_3CCH) towards the hot molecular core system G331.512-0.103 (R.A., decl. [J2000] $= 16^h12^m10.^s1$, $-51°28'38.''1$). We observe nine frequency setups within $170-205$ GHz and $222-307$ GHz, respectively, with spectral resolution of $0.06-0.13$ km s^{-1} and spatial resolution of $\sim 17-39''$.

1.5.2 Infrared observations

In emission, molecules can also be observed through their vibrational transitions, which typically occur at infrared wavelengths, provided sufficient energy is available to populate these excited levels. This is the case, for instance, in inner disk regions, where high gas densities and temperatures allow the detection of molecular emission lines from rovibrational transitions (e.g., Salyk *et al.* 2011). Other mechanisms, such as radiative pumping from a strong radiation field, can also help populate these energy levels (e.g., van Gelder *et al.* 2024). In the absence of such mechanisms, vibrational transitions can still be observed in absorption if a background radiation source is present and the environment is optically thin enough to allow some light to pass through and reach the telescope.

For the purpose of this thesis, infrared observations of interstellar ices are particularly interesting. Since molecules in the solid state lack the degrees of freedom necessary for rotational transitions, their vibrational modes provide the only direct means of observing ices. These observations typically occur in absorption, as the energy required for emission would generally lead to desorption of the molecules. The exceptions are torsion and lattice modes ($\sim 25-300$ μm), which have excitation energies below the ice binding energies and thus might be observed in emission (Boogert *et al.* 2015).

Following the first observation of the 3.1 μm feature associated with H_2O ice towards the Orion BN/KL region (Gillett & Forrest 1973), numerous ice features have been identified, with profiles that reflect the complexities of their composition, mixing conditions, thermal history, and grain shape effects (Boogert *et al.* 2015). Such observations can be carried out using ground-based, airborne, or space telescopes. While ground-based telescopes were responsible for much of the early infrared investigations of the universe, and continue to offer powerful insights into interstellar ice composition (e.g., Boogert *et al.* 2022), they are inherently limited by light absorption and distortion caused by Earth's atmosphere. In contrast, airborne and space-based telescopes either mitigate or bypass these issues entirely, and have thus been instrumental in study of interstellar ices. The Kuiper Airborne Observatory (KAO; Haas *et al.* 1995) was a pioneering tool in this regard, allowing observations to be performed from above almost all of the water vapor in the Earth's atmosphere and thus providing unprecedented insights on the composition of ices (e.g., Willner *et al.* 1982). The subsequent launch of the Infrared Space Observatory (ISO), particularly through its short wavelength spectrometer (SWS), opened up the full mid-infrared spectrum to observations, offering the first comprehensive inventory of major interstellar ice features and providing the first glimpse of these ices in low-mass sources (van Dishoeck 2004). With the advent of the James Webb Space Telescope (JWST), the field has entered a new golden age, with observations confirming ice species that were previously undetected or only tentatively identified—including a range of complex organic molecules (Rocha *et al.* 2024) as well as deuterated water ice (Slavicinska *et al.* 2024).

1.5.3 Fundamentals of radiative transfer

To extract information from observed spectra, it is necessary to accurately describe how light propagates through a medium before reaching the telescope. The variation of specific intensity along the light path (dI_ν/ds) is described by (Rybicki & Lightman 1985):

$$\frac{dI_\nu}{ds} = -\alpha_\nu I_\nu + j_\nu. \tag{1.4}$$

where ds is the distance traveled by the beam, α_ν is the absorption coefficient, defined as the product of the density n of absorbing particles times their absorption cross section σ_ν, and j_ν is the monochromatic emission coefficient. In other words, energy emission increases the beam intensity, while absorption of radiation reduces it. Equation 1.4, known as the radiative transfer equation, provides a framework for modeling light-matter interactions. It serves as the basis for methods used to derive physical properties from observed molecular absorption and emission in space.

When molecular excitation and de-excitation are primarily driven by collisions, as is typical in high-density environments, the system is said to be in local thermodynamic

equilibrium (LTE). Under these conditions, the population of a molecule's energy levels follows a Boltzmann distribution characterized by a single excitation temperature, and the population of each level is given by (Goldsmith & Langer 1999):

$$N_u = \frac{N_\text{tot}}{Q(T_\text{ex})} g_u e^{-E_u/k_\text{B}T_\text{ex}} \tag{1.5}$$

where N_u is the molecule's column density in the upper energy level of a given transition, N_tot is the total column density of the species in question, $Q(T_\text{ex})$ is its partition function (i.e., the sum of the populations across all energy levels), g_u is the statistical weight of the upper energy level, and E_u is its energy. Thus, in LTE, the total molecular column density can be derived from the column density of any individual transition if the excitation temperature is known, and the excitation temperature corresponds to the kinetic temperature of the gas.

By solving the radiative transfer equation under LTE conditions, one can fit molecular emission lines with a Gaussian function to extract both the total column density and excitation temperature (see, e.g., Vastel 2014; Nazari 2024, for a more detailed explanation). However, if only a single transition from a given molecule is observed, excitation temperature and column density become degenerate, meaning one can only be determined by fixing the other. This is the case in Chapter 8, where excitation temperatures are set to an average value typical of hot cores to allow column density determination. If transitions are optically thick, part of the emission will not be accounted for, leading to an underestimation of the column density. Moreover, if the telescope beam size is much larger than the size of the source, the measured intensity will be reduced by beam dilution, also underestimating the column density. The latter effect is particularly relevant for single-dish observations, for which beam sizes are larger.

In this thesis, we use the CASSIS software (Vastel *et al.* 2015) to solve the radiative transfer equation under LTE assumptions and fit the observed molecular emission lines to extract column densities and, where applicable, excitation temperatures. An example of such fits is shown in Figure 1.10 (Nazari 2024). Additionally, assuming LTE, the natural logarithm of the column density per statistical weight of different molecular energy levels is linearly correlated with the level's energy above ground state over k_B, with the slope of this relation yielding the excitation temperature and the y-intercept yielding the total column density (Figure 1.11; Goldsmith & Langer 1999). These plots, known as population diagrams, are used in Chapter 9 to determine the temperature and column density of the CH_3CCH gas surrounding a massive protostar.

1.6   This thesis

1.6.1   Chapter summary

Once thought to be chemically barren, the interstellar medium is now known to host a large variety of chemical species. Many of these, including simple molecules like H_2, and especially more complex organic molecules, result from processes taking place on icy dust grains. This thesis combines experimental and observational approaches to explore the physicochemical transformation of interstellar ices throughout the stages of star and planet formation—from clouds, to protostars, to protoplanetary disks.
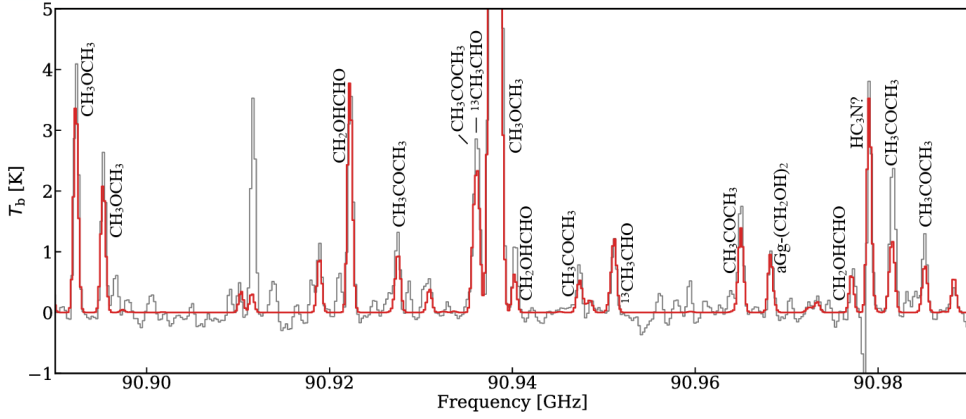
Figure 1.10: ALMA Band 3 observations towards IRAS 16293-2422 B (gray) superimposed by Gaussian fittings to a subset of the molecular emission lines (red). Figure from Nazari (2024).
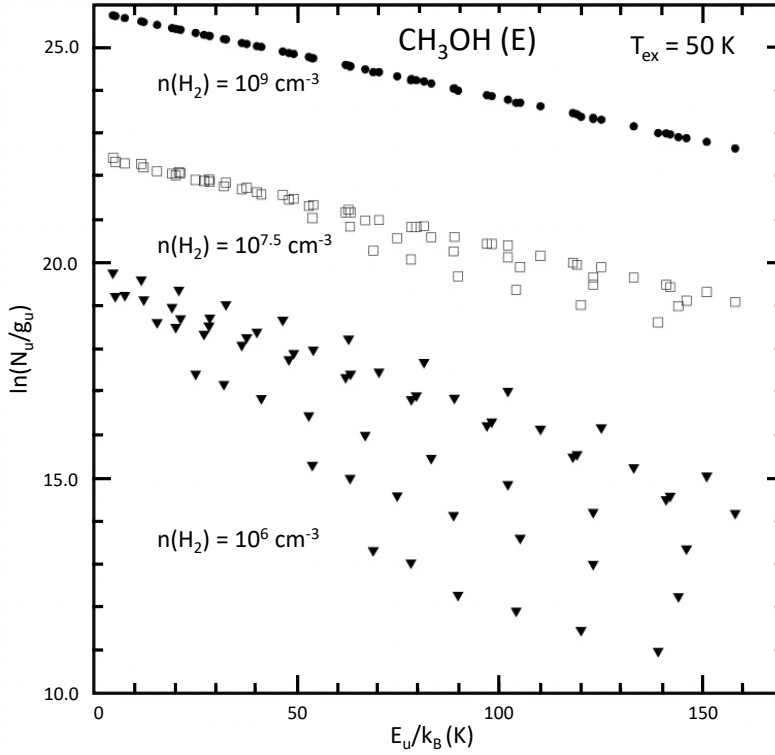
Figure 1.11: Population diagram of modeled optically thin CH_3OH rotational lines at varying hydrogen densities for $T_K = 50$ K. At low densities, sub-thermal excitation heavily affects the slope of the plot, particularly at high energies. For densities of 10^9 cm^{-3}, all modeled transitions are thermalized, and the data points follow a linear trend with no scattering. Figure adapted from Goldsmith & Langer (1999), see Figure 6 in Johnstone *et al.* (2003) for an alternative version.

The central question guiding this work is: *How do ice molecules form, transform, and desorb?*

To address this question, we explore how ices evolve under the influence of various phenomena throughout different stages of star and planet formation. We investigate the chemical networks that dominate in the cold environments of molecular clouds, where reactions are largely driven by "non-energetic" atom- and radical-induced processes. We also explore the stability of ices in these clouds, as well as potentially relevant non-thermal sublimation processes. Once gravitational collapse has begun, we turn to the thermal desorption of ices as they are heated by the protostar. We characterize sublimation front locations in disk midplanes, and leverage gas-phase observations of sublimated ices to gain insights into the chemical evolution and the physical properties of the sources. The main conclusions of each chapter are as follows:

On the formation and stability of O-bearing ices: the case of CO and CH$_3$OH

Chapter 2: Methanol (CH$_3$OH), a major component of interstellar ices and a key precursor of larger complex organic molecules, has long been thought to form through successive hydrogen addition to CO. However, recent kinetic Monte Carlo models have challenged this view, particularly regarding the final reaction step. Leveraging the kinetic isotope effect as a tool, we provide the first experimental confirmation that the reaction CH$_3$O + H$_2$CO $\rightarrow$ CH$_3$OH + HCO is the dominant final step to form methanol ice under laboratory conditions. The experimentally derived contributions from this pathway, along with the traditionally proposed hydrogen addition route (CH$_3$O + H $\rightarrow$ CH$_3$OH), agree with kinetic Monte Carlo models under laboratory conditions. These models, when extended to molecular cloud conditions, confirm that this abstraction pathway dominates in the interstellar medium.

Chapter 3: Infrared photons from the interstellar radiation field can penetrate deep into molecular clouds, yet their interactions with ices remain largely unexplored experimentally. We utilize a free-electron laser large facility to irradiate pure CO and CH$_3$OH ices, as well as mixtures of the two, with near-monochromatic mid-infrared photons to explore the effects of resonant infrared irradiation on ice morphology. We find that ices undergo structural rearrangement as a result of on-resonance irradiation. In the cases of pure CO and ice mixtures, this rearrangement cannot be solely explained by thermal processing. We also find evidence for the loss of ice material, which we attribute to single-photon, non-thermal infrared-induced desorption mechanisms, particularly for indirect CO desorption resulting from resonant CH$_3$OH irradiation. Although this process is far less efficient than UV-induced desorption, its potential impact may be non-negligible due to the greater penetration depth of infrared photons in molecular clouds.

On sulfur-bearing ice chemistry and desorption

Chapter 4: H$_2$S ices are predicted to form very efficiently and were once considered strong candidates for the main interstellar sulfur reservoir in the solid state. However, its observed upper limits contradict this idea, suggesting that H$_2$S ice must undergo effective solid-state destruction mechanisms. To explore some of its most promising destruction pathways, we experimentally investigate the interaction of H$_2$S ice with thermalized hydrogen atoms. We show that HS radicals, formed *in situ* via the reaction H$_2$S + H $\rightarrow$ HS + H$_2$, can initiate a sulfur-bearing chemical network,

demonstrated here by the formation of H_2S_2 as a proof-of-concept. Additionally, we directly quantify the chemical desorption efficiency of H_2S formed via $HS + H \rightarrow H_2S$ by analyzing the gaseous signal recorded by the QMS. This direct approach is complemented by indirect measurements of the chemical desorption efficiency, derived from the loss of H_2S signal from the ice after accounting for H_2S_2 formation. The dominant destruction mechanism of H_2S ice under our experimental conditions is chemical desorption. However, as temperatures rise from 10 to 16 K, the formation of H_2S_2 becomes increasingly more significant, arguably due to enhanced diffusion.

Chapter 5: Although H_2S is unlikely to be the main sulfur reservoir in ices, there is still compelling evidence for its presence in non-negligible amounts ($\sim 1\%$ relative to water). Understanding its desorption behavior is crucial for interpreting the sulfur chemical network and predicting in what physical state it may be incorporated by forming planets and planetesimals. For the first time, we experimentally characterize the sublimation dynamics of H_2S ice and derive its corresponding desorption temperatures and snowline positions in a representative T-Tauri disk midplane. We determine binding energies in the multilayer regime, where H_2S primarily interacts with other H_2S molecules, as well as in the submonolayer regime on top of a compact amorphous solid water substrate, that is, where H_2S interacts primarily with H_2O. Both cases lead to sublimation fronts located just interior to the CO_2 snowline. However, we find that the entrapment of H_2S in water ice is highly efficient ($\gtrsim 75\%$), effectively shifting its snowline position closer to the H_2O snowline, assuming it forms mixed with water. Therefore, H_2S is expected to remain in the solid phase throughout the entire region where comets and icy asteroids form.

Chapter 6: Building on the results of Chapter 4, we present compelling experimental evidence that HS radicals can efficiently react with CO and H in the solid state to form OCS ice. We propose a formation mechanism involving the HSCO complex: $HS+CO \rightarrow HSCO+H \rightarrow OCS+H_2$, similar to the formation of CO_2 ice. This reaction proceeds efficiently even under conditions of significant H_2S dilutions (5% with respect to CO) and low hydrogen abundances (H:CO=1.5:1). That, combined with the fact that HS radicals can be produced through both bottom-up ($S + H \rightarrow SH$) and top down ($H_2S + H \rightarrow SH + H_2$) pathways, makes this route a promising mechanism to forming OCS throughout various stages of cloud evolution.

Chapter 7: Further expanding on the ice sulfur network initiated by HS radicals, we find that its interaction with C_2H_2 and atomic H leads to the formation of a large number of species. We identify at least six sulfurated products: CH_3CH_2SH, CH_2CHSH, $HSCH_2CH_2SH$, H_2S_2, and tentatively CH_3CHS and CH_2CS. Experimental mixing ratios, as well as quantum chemical calculations, are employed to help pinpoint the underlying reactions driving this network. At higher H abundances, CH_3CH_2SH is preferentially formed due to a series of barrierless hydrogenation reactions leading to it—largely at the expense of other organic products. It thus acts as a sink in this chemical network.

Chapter 8: SO_2 and OCS are major volatile sulfur carriers and the only sulfur-bearing molecules detected in interstellar ices to date, making them the ideal candidates for directly comparing the volatile sulfur content in the gas and ices across star and planet formation. In this observational work, we derive the column densities of SO_2 and OCS towards the hot cores of 26 line-rich massive young stellar objects,

observed as part of the ALMA Evolutionary study of High Mass Protocluster Formation in the Galaxy (ALMAGAL) survey. We derive their abundance with respect to methanol, which are compared among themselves and to gas-phase observations from low mass sources, as well as ice observations in clouds, protostars, and comets. For OCS, the abundances suggest ice formation during the high-density prestellar core stage, with minimal gas-phase reprocessing upon thermal sublimation in the hot core phase. It also appears to be largely inherited by comets. In contrast, SO_2 seems to also form in ices prior to star formation, but likely at earlier stages before the catastrophic CO freeze-out. It is more subject to gas-phase reprocessing upon sublimation and is only moderately inherited by comets.

On the physical conditions probed by gas-phase hydrocarbons: the case of CH$_3$CCH

Chapter 9: Methyl acetylene (CH_3CCH) is widely observed in star-forming regions and is known to be a reliable tracer of physical conditions such as density and temperature. It is thought to form from a combination of gas and solid-state processes. In this work, we conduct a spectral survey of the CH_3CCH gas towards the hot molecular core G331.512-0.103 using observations from the Atacama Pathfinder Experiment (APEX). By analyzing its temperature-sensitive spectral features, we derive the small-scale temperature distribution of the gas from single-dish observations. Based on the relative intensities of the $K = 2$ and $K = 3$ lines, we probe a temperature gradient in the gas ranging from $45 \lesssim T_{\mathrm{ex}} \lesssim 60$ K. The $K = 0$ transitions exhibit a distinct kinematic signature compared to the other lines in the K-ladders, suggesting they trace a different gas component. We hypothesize that this may correspond to a colder gas, as the spectra at low temperatures are dominated by low K-level lines.

1.6.2   Main conclusions and future directions

A significant portion of this thesis explores the formation of ice molecules under molecular cloud conditions, where temperatures are low ($\sim 10 - 20$ K) and chemistry is primarily driven by radical- and atom-induced reactions. The key reaction pathways identified in this work are summarized in Figure 1.12. Beyond these, the main takeaways of this thesis are outlined below, which also reveal some interesting new directions for future explorations:

1. The main formation mechanisms of interstellar ices may not always be the most intuitive ones (Chapter 2). As solid-state chemical networks depend on numerous convoluted effects whose final outcomes are challenging to predict, laboratory experiments that evaluate the contributions of different reaction pathways to interstellar ice complexity are essential. These can be achieved, for instance, by leveraging physicochemical principles such as the kinetic isotope effect.

2. While, over the past 20 years, significant progress has been made in understanding entrapment efficiencies for various matrix-volatile combinations, many open questions still remain regarding the underlying mechanisms governing volatile entrapment (Chapter 5). Elucidating these mechanism is crucial for accurately translating laboratory measurements to realistic disk conditions.

3. A prolific ice sulfur chemistry can be initiated by HS radicals, which form both via hydrogenation of S atoms in early cloud stages and via hydrogen abstraction
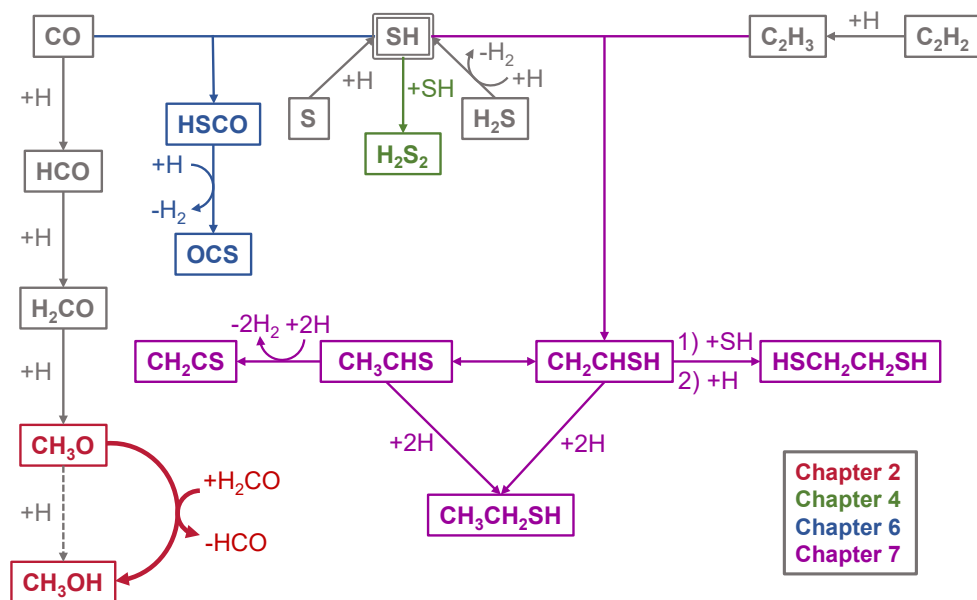
Figure 1.12: Summary of the new ice reaction pathways experimentally uncovered in this thesis.

from H_2S at later stages (Chapters 4, 6, 7). Solid-state reactions involving this radical offer a promising avenue for building a complex sulfur-bearing interstellar molecular inventory, and may also help explain why observationally-constrained H_2S ice upper limits are lower than expected based on its predicted formation efficiency.

4. The chemical environment of an icy molecule dictates the shape of its spectral signatures, available reaction partners, and desorption dynamics. It is thus paramount to understand not only *how*, but also *when* molecules are formed. Gas-phase observations of sublimated ices offer an interesting avenue to probing the formation history of less abundant species that are challenging to detect in ices. This approach reveals, for instance, that while both SO_2 and OCS predominantly form in ices during prestellar stages, SO_2 likely forms much earlier than OCS and/or is considerably more subject to post-sublimation reprocessing (Chapter 8).

5. The temperature-sensitive K-ladders of symmetric rotors, particularly those with different nuclear spin statistics (as is the case, e.g., for molecules with three equivalent hydrogen atoms like CH_3CCH), can be leveraged to infer the small-scale temperature gradients in the gas. This is particularly useful for single-dish observations, which lack the angular resolution to directly resolve these gradients (Chapter 9).

Overall, this thesis demonstrates how experiments and observations work in synergy to advance our understanding of the chemical evolution of volatiles in star- and

planet-forming regions. This field is now experiencing a golden age, with state-of-the-art telescopes such as ALMA and JWST offering unprecedented sensitivity and resolution to probe both the gaseous and solid molecular inventory of interstellar space. By combining the capabilities of these telescopes, observations are now able to provide strong, direct empirical evidence for the interplay between gas and ice in these environments. Laboratory experiments are, arguably now more than ever, essential for accurately interpreting these observations. Furthermore, as experiments push the limits of *in-situ* detection of complex ice species forming under molecular cloud and protostellar envelope conditions, developing experimental pipelines that integrate *ex-situ* analysis techniques (such as gas chromatography-mass spectrometry) while preserving the sample in vacuum conditions or inert atmospheres for as long as possible becomes increasingly relevant. Finally, with JWST enabling better benchmarking of volatile materials in planet-forming zones, the combined power of observations, experiments, and modeling will be more capable than ever of uncovering the ice composition in disk midplanes, where planet formation is actively underway.

2. First experimental confirmation of the CH_3O + H_2CO → CH_3OH + HCO reaction: expanding the CH_3OH formation mechanism in interstellar ices

The successive addition of H atoms to CO in the solid phase has been hitherto regarded as the primary route to form methanol in dark molecular clouds. However, recent Monte Carlo simulations of interstellar ices alternatively suggested the radical-molecule H-atom abstraction reaction $CH_3O + H_2CO \rightarrow CH_3OH + HCO$, in addition to $CH_3O + H \rightarrow CH_3OH$, as a very promising and possibly dominating (70–90%) final step to form CH_3OH in those environments. Here, we compare the contributions of these two steps leading to methanol by experimentally investigating hydrogenation reactions on H_2CO and D_2CO ices, which ensures comparable starting points between the two scenarios. The experiments are performed under ultrahigh vacuum conditions and astronomically relevant temperatures, with H:H_2CO (or D_2CO) flux ratios of 10:1 and 30:1. The radical-molecule route in the partially deuterated scenario, $CHD_2O + D_2CO \rightarrow CHD_2OD + DCO$, is significantly hampered by the isotope effect in the D-abstraction process, and can thus be used as an artifice to probe the efficiency of this step. We observe a significantly smaller yield of $D_2CO + H$ products in comparison to $H_2CO + H$, implying that the CH_3O-induced abstraction route must play an important role in the formation of methanol in interstellar ices. Reflection-Absorption InfraRed Spectroscopy (RAIRS) and Temperature Programmed Desorption-Quadrupole Mass Spectrometry (TPD-QMS) analyses are used to quantify the species in the ice. Both analytical techniques indicate constant contributions of ∼80% for the abstraction route in the 10-16 K interval, which agrees well with the Monte Carlo conclusions. Additional $H_2CO + D$ experiments confirm these conclusions.

2.1   Introduction

Methanol (CH_3OH) is abundantly detected in interstellar environments and is one of the main components of interstellar ices. Its formation is tightly connected to the evolution of molecular clouds. In these dense and cold regions, CO molecules present in the gas phase freeze-out and form an apolar coating on top of icy grains, largely comprising of H_2O and CO_2 ice. Methanol is then efficiently formed through the hydrogenation of CO in the solid phase (Tielens & Hagen 1982; Charnley *et al.* 1992; Hiraoka *et al.* 1994; Watanabe & Kouchi 2002; Fuchs *et al.* 2009). The presence of methanol in CO-rich ice is supported by a series of comparisons between laboratory and observational evidence (e.g., Bottinelli *et al.* 2010; Cuppen *et al.* 2011; Penteado *et al.* 2015). Furthermore, as opposed to CO hydrogenation, neither gas-phase nor alternative solid-phase routes can explain the observed CH_3OH abundances (Geppert *et al.* 2005; Garrod *et al.* 2006; Watanabe *et al.* 2007). As a secondary mechanism, it has also been shown to form in H_2O-rich ices prior to the heavy CO freeze-out—thus in an earlier evolutionary stage of the cloud (Bergner *et al.* 2017; Qasim *et al.* 2018; Potapov *et al.* 2021; Molpeceres *et al.* 2021).

So far, the main proposed hydrogenation route to form methanol is through successive addition reactions of H atoms to CO ice, as follows:

$$CO + H \rightarrow HCO \tag{2.1}$$

$$HCO + H \rightarrow H_2CO \tag{2.2}$$

$$H_2CO + H \rightarrow CH_3O \tag{2.3}$$

$$CH_3O + H \rightarrow CH_3OH. \tag{2.4}$$
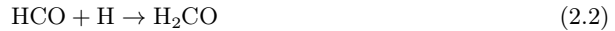
Here, abstraction reactions induced by H atoms also take place, converting CH_3OH into CO through H_2CO (Hidaka *et al.* 2009; Chuang *et al.* 2016). However, recent theoretical works that combine a full reaction network for the hydrogenation of CO and microscopic kinetic Monte Carlo simulations of interstellar ices suggest a dominating alternative to reaction (2.4), that is the radical-molecule route (Álvarez-Barcia *et al.* 2018; Simons *et al.* 2020):

$$CH_3O + H_2CO \rightarrow CH_3OH + HCO, \tag{2.5}$$

with a contribution of 70–90% with respect to the remainder of the routes to form methanol. Reaction (2.5) can take place upon only one hydrogen-atom addition to H_2CO, as long as another H_2CO molecule lies in the vicinity of the formed CH_3O. Comparatively, reaction (2.4) warrants that an additional H atom diffuses through the ice and reacts with CH_3O. The overall contribution from each route will therefore be dictated by the availability of H, CH_3O, and H_2CO in the ice. Although the theoretical results represent a significant paradigm change in the final step of the CO hydrogenation formation pathway of methanol in interstellar ices, they have not yet been systematically investigated in the laboratory. Experimental verification is however possible by exploring the kinetic isotope effect of the reactions involving deuterated species (i.e., D_2CO and D), as will be discussed below.

At the typical low temperatures of molecular clouds, quantum-mechanical tunneling governs the activation of chemical reactions. Under these conditions, D-abstraction reactions are significantly hampered in comparison to their H-abstraction counterparts (e.g., Nagaoka *et al.* 2005; Hidaka *et al.* 2007; Goumans 2011), on account of the so-called "kinetic isotope effect". Reaction (2.5) is a radical-molecule route that involves an H-abstraction reaction from H_2CO with an activation barrier of $\Delta E \sim 2670$ K (Álvarez-Barcia *et al.* 2018). Thus, it most likely proceeds through quantum-tunneling at such low temperatures. As a consequence, the rate constant of the analog reaction with the deuterated formaldehyde (i.e., D-atom abstraction from D_2CO) is expected to be severely hindered. In the present work, we take advantage of this isotope effect to quantify the respective contributions from the mechanisms (2.4) and (2.5) in forming methanol under molecular-cloud conditions. We then confirm the dominance of the radical-molecule route through complementary $H_2CO + D$ experiments.

2.2   Experimental

All experiments are performed using the setup SURFRESIDE[3], which has been described in detail elsewhere (Ioppolo *et al.* 2013; Qasim *et al.* 2020b). It consists of an ultrahigh vacuum (UHV) chamber with a base pressure of $\sim 5 \times 10^{-10}$ mbar. At its center, a gold-plated copper substrate is mounted on the tip of a closed-cycle He cryostat that allows the temperature of the substrate to vary between 8 and 450 K through resistive heating. The temperature is monitored by two silicon diode sensors with a relative accuracy of 0.5 K. We deposit either H_2CO or D_2CO simultaneously with thermalized H and D atoms during the so-called codeposition experiments. The H_2CO and D_2CO vapors are produced from paraformaldehyde (purity 95%, Sigma-Aldrich) and paraformaldehyde-d_2 (purity 98%, Sigma-Aldrich) powders heated to $\sim 60 - 100°$ C in glass vacuum tubes. The hydrogen and deuterium atoms are simultaneously generated by both a Hydrogen Atom Beam Source (HABS, Tschersich 2000) and a Microwave Atom Source (MWAS, Anton *et al.* 2000), and are thermally cooled to room temperature by colliding with the walls of nose-shaped quartz pipes that are placed along the beam path in both atom sources. A set of experiments comprising of 360 minutes of $H_2CO + H$ or $D_2CO + H$ codepositions is performed at temperatures of 10, 12, 14 and 16 K. Additionally, analogous codeposition experiments of $H_2CO + D$ are also reported. The full complementary set of H_2CO + D and D_2CO + D codepositions are not performed due to the low efficiency of the D-atom addition reactions resulting from the kinetic isotope effect caused by the slower rate of quantum tunneling of D atoms over H atoms (Hidaka *et al.* 2009; Goumans 2011).

During the experiments, the ices are monitored *in situ* by means of Fourier-Transform Reflection-Absorption Infrared Spectroscopy (RAIRS) in the range of 700 to 4000 cm^{-1}, with a resolution of 1 cm^{-1}. After the codeposition experiments, the sample is heated at a ramping rate of 5 K min^{-1}. The desorbed species are monitored by a Quadrupole Mass Spectrometer during Temperature-Programmed Desorption experiments (TPD-QMS). To derive the column densities of the species in the ice, we employ the modified Beer-Lambert law to convert absorbance area to absolute abundance. We use band-strength values of $A(H_2CO)_{\nu=1727} \sim 3.6 \times 10^{-17}$ cm molecule^{-1} and $A(CH_3OH)_{\nu=1030} \sim 3.1 \times 10^{-17}$ cm molecule^{-1}, which were calibrated in the same setup by laser-interference measurements (Chuang *et al.* 2018). For CHD_2OH (ν=1037 cm^{-1}), the band strength is estimated by multiplying $A(CH_3OH)$ by a calibration factor of 0.43 (Nagaoka *et al.* 2007). Finally, the band strength of D_2CO is obtained by comparing the IR absorbance areas of the same amount of pure H_2CO and D_2CO ices. We experimentally derive $A(D_2CO)_{\nu=1679} \sim 2.8 \times 10^{-17}$ cm molecule^{-1}. More details on this procedure are given in Appendix 2.5.1. For a specific flux configuration, the relative uncertainties of the molecule and H-atom fluxes are, respectively, <9% and <4%. The error-bar estimation due to the instrumental uncertainties of the RAIRS and TPD-QMS measurements is derived from the integrated noise signals of blank experiments in the same band width. Table 2.1 in Appendix 2.5.2 lists the experiments performed in this study and the relative abundance of CHD_2OH/CH_3OH derived from the RAIRS and QMS-TPD analyses.

2.3   Results and Discussion

In Figure 2.1, we present a schematic view of the reaction routes probed in our experiments. To focus on reactions (2.4) and (2.5), we skip steps (2.1) and (2.2) and start by directly depositing formaldehyde. This way, comparable starting points between the two scenarios are obtained.

By using different isotope-labeled reactants (H_2CO and D_2CO), the importance of reactions (2.4) and (4') can be directly assessed. The yields of methanol from H_2CO through

$$H_2CO \xrightarrow[\text{(3)}]{+ H} CH_3O \xrightarrow{+ H} CH_3OH \qquad (4)$$

$$CH_3O \xrightarrow{+ H_2CO} CH_3OH + HCO \qquad (5)$$

$$D_2CO \xrightarrow[\text{(3')}]{+ H} CHD_2O \xrightarrow{+ H} CHD_2OH \qquad (4')$$

$$CHD_2O \dashrightarrow[\text{}]{+ D_2CO} CHD_2OD + DCO \qquad (5')$$
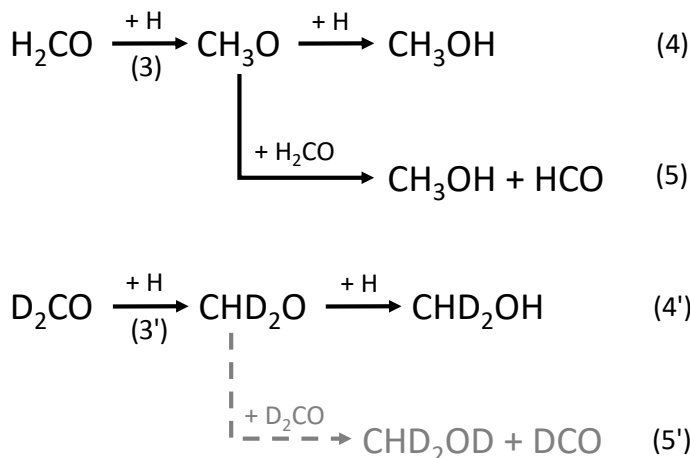
Figure 2.1: CH_3OH formation scheme involving H_2CO and D_2CO. The gray dashed line indicates the smaller efficiency of the deuterated radical-molecule reaction with relation to route (5).

reaction (2.4) and from D_2CO through (4')—see Figure 2.1—should be identical, since both radical-radical routes are barrierless. Conversely, the formation of the isotope-labeled CHD_2OD through reaction (5') is expected to be strongly affected by the isotope effect and to become negligible, whereas (2.5) still takes place. Moreover, the hydrogen-addition steps $H_2CO + H$ and $D_2CO + H$ have similar activation barriers of 2318 and 2253 K, respectively, and similar rate constants (Hidaka *et al.* 2009; Goumans 2011). Thus, they yield comparable amounts of CH_3O and CHD_2O. The contributions of the two competing routes are hence obtained by comparing the relative abundances between the total CH_3OH yield of the H_2CO ice (reactions (2.4) and (2.5)) and that of CHD_2OH in the D_2CO ice (reaction (4')).

The final infrared spectra of both $H_2CO + H$ and $D_2CO + H$ codepositions after 360 minutes at 12 K are shown in Figure 2.2. IR features of H_2CO are observed at 1167 (CH_2 wag., $\nu = 6$), 1249 (CH_2 rock., $\nu = 5$), 1500 (CH_2 scis., $\nu = 3$) and 1727 cm^{-1} (CO str., $\nu = 2$). In the analog deuterated experiments, D_2CO peaks are detected at 988 (CD_2 wag.), 1101 (CD_2 scis.) and 1679 cm^{-1} (CO str.). In both cases the hydrogenated products CH_3OH and CHD_2OH are detected by their CO stretching ($\nu = 8$) features at 1030 and 1037 cm^{-1}, respectively (Shimanouchi 1972; Hidaka *et al.* 2009), which indicates that the H-addition routes in Figure 2.1 proceed at a considerable rate.

Even in the experimental configuration with the highest product yield, no CHD_2OD peaks (OD str. at $\nu_1 \sim 2420$ cm^{-1}, Nagaoka *et al.* 2007) could be observed in the $D_2CO + H$ spectrum. The detection of CHD_2OH and non-detection of CHD_2OD are in line with the expected low efficiency of the radical-molecule route for deuterated species and are consistent with the results by Hidaka *et al.* (2009) on the exposure of H atoms to D_2CO ice. That, in addition to the fact that the CHD_2OH peak is much smaller than the CH_3OH counterpart in the H_2CO+H experiment at equivalent conditions, strongly suggests that reaction (2.4) is not the dominant route to form methanol under the investigated experimental conditions. Instead, reaction (2.5) must play a more prominent role in the formation of methanol. This observation remains valid after converting the integrated peak areas from the RAIR spectra to the species' abundances, as shown in Table 2.1. From the RAIRS analyses, we do not detect any bands related to the radicals HCO or CH_2OH—nor their deuterated isotopes—reinforcing the
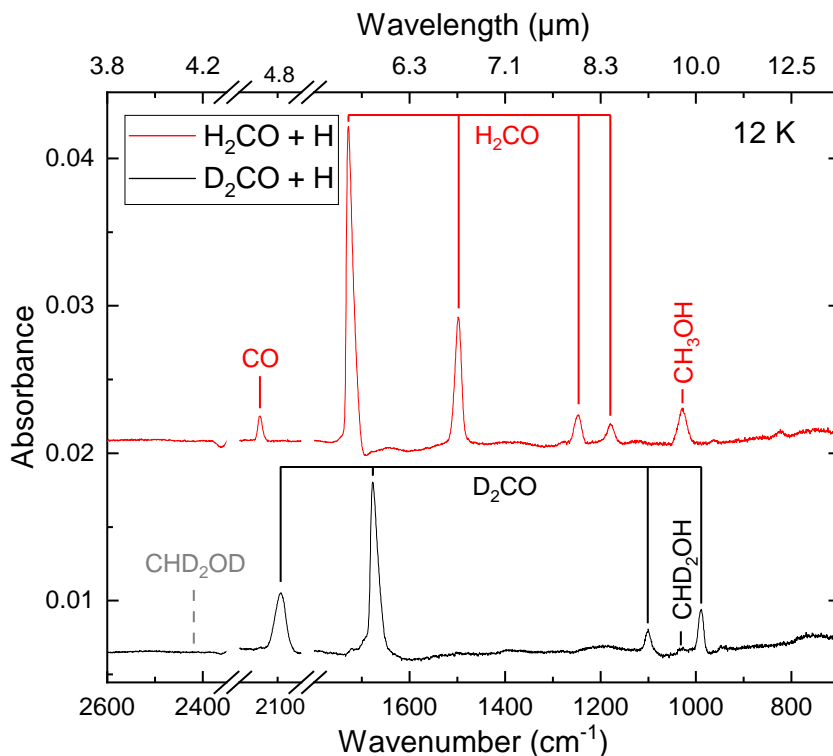
Figure 2.2: Final IR spectra of the $H_2CO + H$ (red) and $D_2CO + H$ (black) codeposition experiments performed at 12 K. The spectra were obtained after 360 minutes of deposition and are artificially offset for clarity. Peak assignments are indicated with solid red (for $H_2CO + H$) and black (for $D_2CO + H$) lines, while the dashed gray line shows the absence of the CHD_2OD $\nu \approx 2420$ cm^{-1} peak.

findings from previous studies that their high reactivity results in low abundances (Watanabe & Kouchi 2002; Fuchs *et al.* 2009). The radical CH_3O is also not observed in the $H_2CO + H$ experiments. It should be noted, though, that the most intense IR features of its isotopologue CHD_2O overlap with those of the other reactants and products in the spectra (see, e.g., Haupa *et al.* 2017), and therefore we cannot rule out its presence in the $D_2CO + H$ experiments. Moreover, we observe a clear CO peak ($\nu = 2138$ cm^{-1}) in the $H_2CO + H$ experiment, as well as HDCO ($\nu = 1694$ cm^{-1}) and H_2CO ($\nu = 1727$ cm^{-1}) peaks in the $D_2CO + H$ counterpart, in agreement with the results by, e.g., Hidaka *et al.* (2009) and Chuang *et al.* (2016) that H-atom induced abstraction reactions take place for the studied conditions (see, e.g., Figure 5 in Hidaka *et al.* 2009).

The TPD-QMS results of the experiments at 12 K are presented in Figure 2.3 as a typical example of the obtained spectra. Since trying to account for the mass-fragmentation patterns induced by electron impact may complicate the interpretation of the data, only the ion signals of the products' molecular masses are selected to quantify their formation yield. For example, the CH_3OH formation is quantified by the mass signal m/z = 32, while the deuterated species CHD_2OH and CHD_2OD are depicted by m/z = 34 and 35, respectively. All methanol (-d_0-d_3) mass signals peak at ∼140 K. The small m/z = 32 signal that peaks at 160 K could be due to either CH_3OH trapped in background water or fragments originating from complex organic molecules (Fedoseev *et al.* 2015a; Chuang *et al.* 2016; He *et al.* in press). The flux of

background water deposited throughout the experiment is estimated to be 5.2×10^{10} molecules $cm^{-2} s^{-1}$, being a minor component of the ice that does not affect the final results. The TPD spectra show that a much smaller yield of CHD_2OH is observed in comparison to CH_3OH, and no CHD_2OD is detected above the instrumental detection limit, thereby confirming the RAIRS analysis.
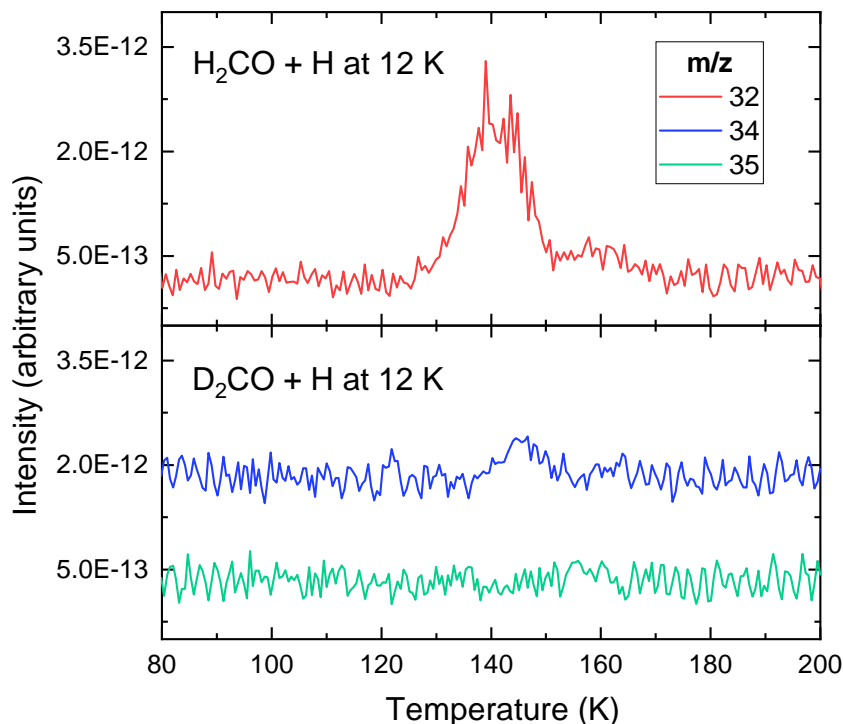
Figure 2.3: Spectra of the TPD-QMS experiments obtained after codeposition of $H_2CO + H$ (upper) and $D_2CO + H$ (lower) at 12 K for 360 min. The m/z signals of 32 (red), 34 (blue) and 35 (green) correspond to, respectively, CH_3OH, CHD_2OH and CHD_2OD. No signal is detected for m/z = 35 at the desorption temperature of methanol ($\sim$140 K).

Figure 2.4 presents the relative yields of CH_3OH and CHD_2OH derived from the RAIRS and QMS-TPD analyses at 10, 12, 14 and 16 K. The methanol yield of the hydrogenation reactions varies with the surface temperature, showing the effective result of the competition between the increase in the diffusion of H atoms and the decrease in their residence time on the ice as a function of temperature from 10 to 16 K. The highest abundances of methanol in both experiments $H_2CO + H$ and $D_2CO + H$ are found at 12 K, and drop with increasing temperatures. A set of experiments performed at 20 K results in CHD_2OH yields that are not measurable, and thus is not reported here. Therefore, the abundances are normalized to that of CH_3OH at 12 K. Similar observations have been reported in a previous study on the hydrogenation of H_2CO at temperatures up to 25 K (Chuang *et al.* 2016).

For the entire set of experiments, the RAIRS data show a considerably lower abundance of CHD_2OH from the $D_2CO + H$ experiments compared to that of CH_3OH from $H_2CO + H$. In fact, the abundance ratios of CHD_2OH/CH_3OH between analogous experiments yield a constant value of ~ 0.16 for the temperature range between 10 and 16 K (see Table 2.1). This is confirmed by the QMS-TPD data, which agree well within their uncertainties with the results from the RAIRS analysis ($CHD_2OH/CH_3OH \sim 0.17$). The contributions of the

reactions probed here are therefore independent of these temperatures (10–16 K), which are of relevance to molecular clouds. This observation is in accordance with the predictions of the models by Simons *et al.* (2020). The similarity between both the RAIRS and TPD ratios also excludes the possibility of the former being influenced by the heating of the substrate.
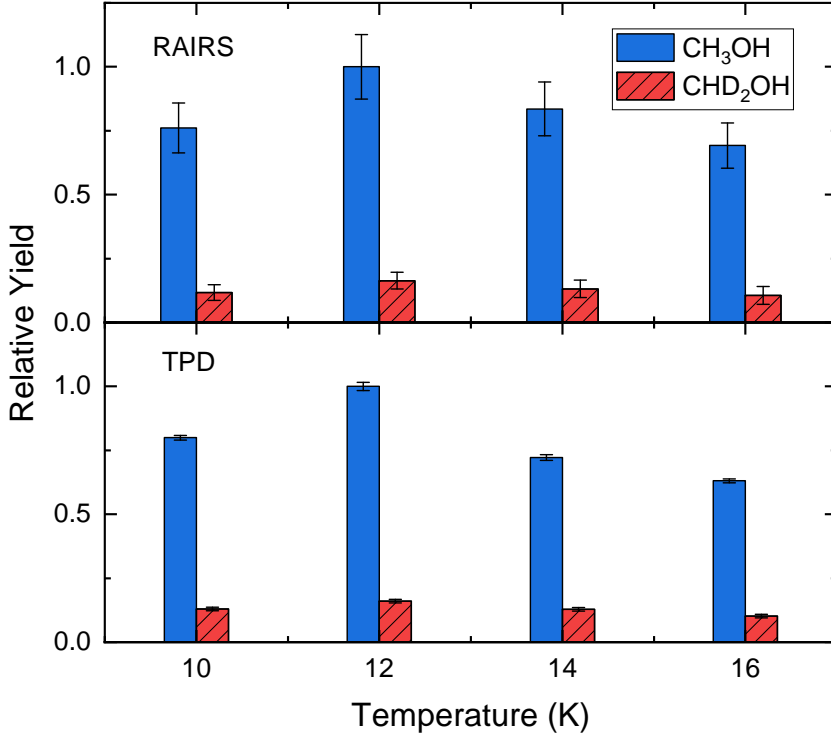
Figure 2.4: *Upper panel:* Yields of CH_3OH and CHD_2OH relative to the column density of CH_3OH after 360 minutes of $H_2CO + H$ codeposition at 10, 12, 14, and 16 K, as derived from the RAIRS data. *Lower panel:* Same as the upper panel, but for the TPD-QMS data. The reported values are normalized to the most abundant yield at 12 K.

Under the assumption that reactions (2.3) and (3') result in similar amounts of CH_3O and CHD_2O respectively, and since both reactions (2.4) and (4') are barrierless, the methanol yields from the abstraction route should be similar in both $H_2CO + H$ and $D_2CO + H$ experiments;

$$(4) \sim (4'), \tag{2.6}$$

where the parentheses denote the methanol yield of the reactions. The discrepancy between the yields of CH_3OH and CHD_2OH under our experimental conditions can therefore be used to estimate the contribution $C4$ of reaction (2.4) with respect to the total yield of methanol:

$$C4 = \frac{(4)}{(4) + (5)} \sim \frac{(4')}{(4) + (5)}$$
$$\sim \frac{(CHD_2OH)}{(CH_3OH)} \sim [0.16 - 0.17]. \tag{2.7}$$

The estimation described here assumes that the formation of CHD_2OH and CH_3OH takes place predominantly through the reactions presented in Figure 2.1. Other routes to form methanol, such as $CH_2OH + H$, have very minor contributions and are hence disregarded

based on the inefficient formation of CH_2OH from H_2CO hydrogenation (Song & Kästner 2017 and, e.g., Table 6 in Simons *et al.* 2020). Accordingly, the contribution $C5$ of reaction (2.5) corresponds to:

$$C5 = 1 - C4 \sim [0.83 - 0.84]. \qquad (2.8)$$

The experimentally derived value of $C5$ agrees well with the contribution of $\sim 90\%$ reported by Simons *et al.* (2020) from kinetic Monte Carlo simulations of the hydrogenation of H_2CO ices.

The H/H_2CO flux ratios employed here were chosen based on the conditions of the models by Simons *et al.* (2020) ($H:H_2CO = 20:1$). A higher H flux could potentially favor the atom-addition route and thus lead to a lower product ratio. To verify whether the contributions $C4$ and $C5$ depend on the hydrogen-to-molecule ratio, a set of experiments using $H/H_2CO(D_2CO)=30$ was performed at 10 K (see Table 2.1). The resulting CHD_2OH/CH_3OH ratios derived from the RAIRS and TPD-QMS data are 0.18 ± 0.03 for $C4$ and 0.82 ± 0.03 for $C5$. These values are negligibly different considering the detection error. Thus, a higher hydrogen flux affects only slightly the contributions derived above, and reaction (2.5) still governs the formation of CH_3OH. This implies that both flux ratios employed here represent an overabundance of H atoms, and therefore the product yield is limited by either H_2CO or D_2CO.

In our experiments, the dominance of the radical-molecule route is likely due to the higher availability of H_2CO in the environment, as opposed to H atoms, to react with CH_3O. Both CH_3O and H are very reactive species; when a CH_3O radical is formed in the vicinity of a H_2CO molecule, it readily reacts with H_2CO to form CH_3OH + HCO. On the other hand, the accreted H atoms on the surfaces are required to diffuse in order to react with the CH_3O radicals. Therefore, they will mostly react with the broadly available H_2CO, and less likely with CH_3O, which is a minor ice component. Moreover, the diffusion of hydrogen atoms also competes with its reaction with CH_3O, whereas both CH_3O and H_2CO do not diffuse and therefore have more time available to react. As a result, the higher likelihood of the two reactants in reaction (2.5) to meet overpowers reaction (2.4), despite the latter being barrierless.

Although the ice composition explored here is not fully representative of interstellar ices, the foregoing reaction routes are nonetheless relevant to their chemistry. In more realistic ices, there is a lower availability of formaldehyde, and the formed CH_3O radicals can also react with other species. Nevertheless, the aforementioned reasoning still applies, since the H atoms will mostly react with CO and HCO, additionally to H_2CO. Indeed, route (2.5) was observed to dominate the formation of methanol even in simulations starting from the hydrogenation of CO ice (Simons *et al.* 2020). Moreover, the radical-molecule route forms HCO as a byproduct, which will then be hydrogenated again to H_2CO, replenishing and thus favoring the chemical network. Additional formaldehyde formed in the gas phase in the ISM can also subsequently accrete onto ice grains and take part in the radical-molecule route.

It is noteworthy that the hydrogenation of pure D_2CO ice is not perfectly equivalent to that of pure H_2CO ice. The rate constant of reaction (3') is in fact slightly higher than that of reaction (2.3) (Hidaka *et al.* 2009; Goumans 2011). Moreover, reaction (5') is inhibited by the isotope effect. Thus, there should be an increase in the availability of CHD_2O in the ice during the deuterated experiments, which in turn favors the formation of CHD_2OH through route (4'). The surplus of CHD_2O is either consumed through H-induced abstraction reactions or preserved in the ice. Furthermore, the isotope effect also hampers the D abstraction reaction $D_2CO + H \rightarrow DCO + HD$, which is why the formation of CO is much less efficient in these scenarios (see Figure 2.2). This results in a higher availability of H atoms in the surface of the ice in the deuterated experiments, compared to the non-deuterated counterparts where the abstraction reaction $H_2CO + H \rightarrow HCO + H_2$ is faster. As a consequence, the formation of CHD_2OH is also favored by the surplus of hydrogen atoms. Therefore, the contribution from reaction (4') to forming methanol under the present experimental conditions should be

regarded as an upper limit to that of reaction (2.4), which puts a lower limit to reaction (2.5) as being at least roughly four times more efficient than reaction (2.4).

Aiming to directly confirm the occurrence of the radical-molecule route forming methanol, an experiment of $H_2CO + D$ and a control experiment of D-atom beam exposure to the bare substrate are performed at 10 K for six hours. The codeposition experiment is followed by a TPD with a ramping rate of 5 K/min. These experiments are designed to probe the following competing reactions:

$$H_2CO \xrightarrow{+D} CH_2DO \xrightarrow{+D} CH_2DOD, \tag{2.9}$$

$$H_2CO \xrightarrow{+D} CH_2DO \xrightarrow{+H_2CO} CH_2DOH + HCO. \tag{2.10}$$
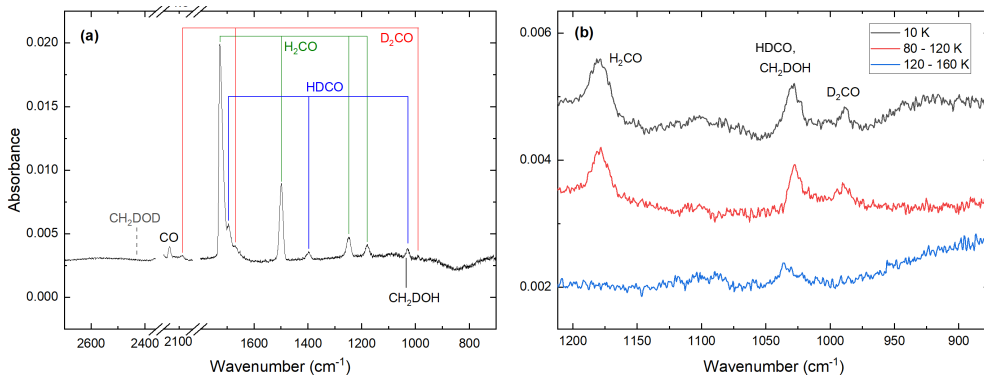
Figure 2.5: (a) Difference spectrum of the final spectra acquired after 360 minutes of H_2CO + D codeposition minus that of the analogous D-atom beam deposition for the same time, both performed at 10 K. The dashed line indicates the absence of the CH_2DOD feature at $\nu \sim 2430$ cm^{-1}. (b) Infrared spectra obtained during the ramp-up after the H_2CO + D 360-minutes codeposition. The gray, red and blue spectra were measured at 10 K, $80 - 120$ K, and $120 - 160$ K, respectively.

The difference of the spectra acquired after the H_2CO + D experiment and the D deposition is shown in panel (a) of Figure 2.5. In agreement with Hidaka *et al.* (2009), we observe spectral features of HDCO and D_2CO as a result of D-substitution (abstraction + addition) reactions on H_2CO. Moreover, a signal at $\nu = 1034$ cm^{-1} is in line with the CO stretching band of CH_2DOH, which would indicate that the radical-molecule route (i.e., reaction (2.10)) proceeds. However, this feature is (at least partially) blended with the CH_2 rocking mode of HDCO ($\nu = 1029$ cm^{-1}), to an extent where deconvolution is not possible. Nonetheless, given the lower desorption temperature of HDCO ($\sim$100 K) with respect to that of CH_2DOH ($\sim$140 K), it is possible to isolate the contribution from CH_2DOH by analyzing the infrared spectra obtained during the TPD experiment. The spectra acquired at 10 K and in the temperature intervals of $80 - 120$ K and $120 - 160$ K are shown in panel (b) of Figure 2.5.

In the IR spectrum acquired in the temperature range of $80 - 120$ K, the peak at $\nu \sim$1029 cm^{-1} contains the contributions from both HDCO and CH_2DOH. However, at the interval of $120 - 160$ K, the peak slightly shifts to $\nu \sim$1034 cm^{-1}, and only accounts for the CH_2DOH left on the substrate. Based on the obtained area of this peak and its reported band strength (Nagaoka *et al.* 2007), we derive a CH_2DOH column density of $\sim (3.0 \pm 0.3) \times 10^{14}$ molecules cm^{-2}. This yield is ~ 4 times smaller than that of CH_3OH from the H_2CO + H experiment at 10 K (H/$H_2CO = 10$), which is consistent with a lower rate for the D-addition reaction to H_2CO over the H-addition counterpart.

During TPD, the mass signal m/z = 33 is detected at $\sim$150 K. However, whereas the spectroscopic signals are quite unambiguous, this does not apply to the mass spectromet-

ric data. Since the mass signals of CH$_2$DOH (m/z = 33, 32, 31...) overlap with those of CH$_2$DOD (m/z = 34, 33, 32, ...), and since their fragmentation patterns are unknown, the interpretation of the mass spectrometry data is impeded.

The product of the D-addition route, CH$_2$DOD (reaction (2.9)), was not observed in its OD stretching mode ($\nu \sim 2430$ cm^{-1}) within the detection limit of the instrument, as shown by the dashed line in panel (a) of Figure 2.5. Given that the band strength of this feature is expected to be around 1.5 times that of the CO stretching mode of CH$_2$DOH (Nagaoka *et al.* 2007), the abundance of CH$_2$DOD must be appreciably smaller than that of CH$_2$DOH. This result provides additional compelling evidence that the radical-molecule route dominates the formation of methanol under the present conditions.

2.4   Conclusions

In the present work, we experimentally examine the contribution from the conventional route to the formation of methanol (reaction (2.4)) with reaction (2.5), and provide the respective impact of the two proposed last steps of relevance to the chemistry of molecular clouds. This was done by focusing on the specific reaction step in question, as more realistic experiments with CO ices would be much more difficult to interpret. Our main conclusions are the following:

- We derive a contribution of $\gtrsim 83\%$ for the radical-molecule route (2.5), which is independent of the H/H$_2$CO ratios (i.e., 10 and 30) and the temperatures (i.e., $10 - 16$ K) experimentally investigated in this work. This temperature range is typical of dense clouds, where H atoms are expected to be overabundant in comparison with H$_2$CO. Our experiments confirm the results in Simons *et al.* (2020), who performed simulations for conditions as used in the laboratory work presented here. Their model, in turn, extends to the interstellar medium, and concludes that this route dominates the formation of interstellar methanol. Our results corroborate with this finding. Comparatively, reaction (2.4) should account for $\lesssim 17\%$ of the methanol formation under the present conditions.

- Additional codeposition experiments of H$_2$CO and D yield measurable amounts of CH$_2$DOH, whereas CH$_2$DOD is not detectable within the IR experimental limits. This further confirms the dominance of the radical-molecule route to form methanol under our experimental conditions.

- The conclusion drawn here does not affect the consensus that methanol is mainly formed through the hydrogenation of CO in the solid phase, albeit by means of a different mechanism than originally thought. Nonetheless, this finding represents an important change in the perspective of methanol formation in space, and could affect astrochemical models that involve this key species.

- The expected deuterium fractionation of methanol will likely be affected, with a possibly smaller abundance of deuterated species due to the kinetic isotope effect.

- Furthermore, the HCO radical is an important astrochemical intermediate since it can react to further form H$_2$CO or recombine with other radicals (e.g., CH$_3$O and CH$_2$OH) to produce complex organic molecules (COMs). The alternative route probed here forms HCO radicals as a byproduct, which enriches an icy surface with this species and therefore affects the COM distribution in interstellar ices, likely enhancing the predicted formation rate of, e.g., glycolaldehyde and ethylene glycol in previous astrochemical models that did not consider reaction (2.5) as a dominant channel. Models of the radical-radical reactions driven by the warming of the ice at later stages of star-formation will also be affected by the additional HCO that eventually remains preserved in the ice and that becomes mobile and reacts.

- The inclusion of deuterium atoms to microscopic kinetic Monte Carlo simulations would be a logical next step, as it could provide additional insight on the chemical network involving methanol. This, however, is beyond the scope of the present work.

Acknowledgments

2.5 Appendix

2.5.1 D$_2$CO band strength estimation

The column densities (N_X) of the species in the ice are calculated by means of the modified Beer-Lambert equation:

$$N_X = \ln 10 \frac{\int Abs(\nu)d\nu}{A_X}, \tag{2.11}$$

in which $\int Abs(\nu)d\nu$ is the integrated absorbance of a given infrared band and A_X is its corresponding band strength. To estimate the band strength of D$_2$CO, the same deposition conditions (i.e., exposure time and dose) are applied to both pure H$_2$CO and D$_2$CO, ensuring identical abundances of both types of ices. This is achieved by using the same leak valve while keeping the same flow-rate setting. Previously, Nagaoka *et al.* (2007) used this method to determine the relative integrated band strengths of CH$_3$OH and isotopes. We plot the integrated areas of the D$_2$CO $\nu_2 = 1679$ cm^{-1} band versus those of H$_2$CO $\nu_2 = 1727$ cm^{-1} for different accumulated abundances performed at three different flux configurations, as shown in Figure 2.6.

After performing a linear fit to the points in the plot, we derive an average slope of $a = 0.78 \pm 0.03$. This slope corresponds to the conversion factor between $A(H_2CO)$ and $A(D_2CO)$:

$$A(D_2CO)_{\nu 2} = a \times A(H_2CO)_{\nu 2} \tag{2.12}$$

Given that $A(H_2CO)$ for the $\nu = 1727$ cm^{-1} peak has been previously measured to be $\sim 3.6 \times 10^{-17}$ cm molecule^{-1} (Chuang *et al.* 2018), we estimate the D$_2$CO $\nu = 1679$ cm^{-1} band strength to be $A(D_2CO) \sim 2.8 \times 10^{-17}$ cm molecule^{-1}.

2.5.2 Experiment list

Table 2.1: Overview of the experiments performed in this work, as well as the resulting CHD_2OH/CH_3OH abundance ratios between each set of experiments derived from the RAIRS and TPD-QMS analyses. The former was calculated from the CO stretching bands ($\nu=8$) of CHD_2OH and CH_3OH, and the latter from the m/z = 32 and m/z = 34 mass signals.

Experiment	T_{sample} (K)	Molecule Flux ($cm^{-2} s^{-1}$)	H (D) flux ($cm^{-2} s^{-1}$)	Time (min)	CHD_2OH/CH_3OH (RAIRS, $\nu = 8/\nu = 8$)	CHD_2OH/CH_3OH (TPD)
D_2CO+H	10	6×10^{11}	6×10^{12}	360	0.15 ± 0.04	0.16 ± 0.01
H_2CO+H	10	6×10^{11}	6×10^{12}	360		
D_2CO+H	12	6×10^{11}	6×10^{12}	360	0.16 ± 0.04	0.16 ± 0.01
H_2CO+H	12	6×10^{11}	6×10^{12}	360		
D_2CO+H	14	6×10^{11}	6×10^{12}	360	0.16 ± 0.04	0.18 ± 0.01
H_2CO+H	14	6×10^{11}	6×10^{12}	360		
D_2CO+H	16	6×10^{11}	6×10^{12}	360	0.15 ± 0.04	0.16 ± 0.01
H_2CO+H	16	6×10^{11}	6×10^{12}	360		
D_2CO+H	10	6×10^{11}	1.8×10^{13}	360	0.18 ± 0.03	0.18 ± 0.01
H_2CO+H	10	6×10^{11}	1.8×10^{13}	360		
H_2CO+D	10	4×10^{11}	6×10^{12}	360		
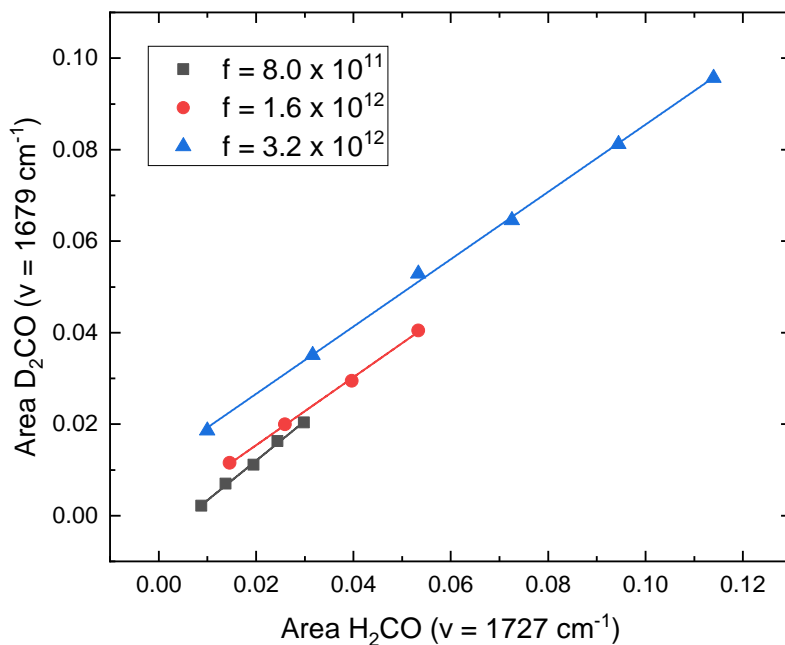
Figure 2.6: Plot of the integrated area of the D_2CO ($\nu_2 = 1679$ cm^{-1}) infrared absorption band versus that of H_2CO ($\nu_2 = 1727$ cm^{-1}) for three different molecule fluxes, f: 8×10^{11}, 1.6×10^{12}, and 3.2×10^{12} cm^{-2} s^{-1}.

3. Resonant infrared irradiation of CO and CH$_3$OH interstellar ices

Solid-phase photo-processes involving icy dust grains greatly affect the chemical evolution of the interstellar medium by leading to the formation of complex organic molecules and by inducing photodesorption. So far, the focus of laboratory studies has mainly been on the impact of energetic ultraviolet (UV) photons on ices, but direct vibrational excitation by infrared (IR) photons is expected to influence the morphology and content of interstellar ices as well. However, little is still known about the mechanisms through which this excess vibrational energy is dissipated, as well as its implications for the structure and ice photochemistry. In this work, we present a systematic investigation of the behavior of interstellar relevant CO and CH$_3$OH ice analogs following the resonant excitation of vibrational modes using tunable IR radiation. We seek to quantify the IR-induced photodesorption and gain insights into the impact of vibrational energy dissipation on ice morphology. We utilized an ultrahigh vacuum setup at cryogenic temperatures to grow pure CO and CH$_3$OH ices, as well as mixtures of the two. We exposed the ices to intense, near-monochromatic mid-IR (MIR) free-electron-laser radiation using the LISA end-station at the FELIX free electron laser facility to selectively excite the species. Changes to the ice are monitored by means of reflection-absorption IR spectroscopy combined with quadrupole mass-spectrometry. These methods also allowed us to characterize the photodesorption efficiency. The dissipation of vibrational energy is observed to be highly dependent on the excited mode and the chemical environment of the ice. All amorphous ices undergo some degree of restructuring towards a more organized configuration upon on-resonance irradiation. Moreover, IR-induced photodesorption is observed to occur for both pure CO and CH$_3$OH ices, with interstellar photodesorption efficiencies on the order of 10 molecules cm^{-2} s^{-1}. This result is comparable to or higher than what is found for UV-induced counterparts. An indirect photodesorption of CO upon vibrational excitation of CH$_3$OH in ice mixtures is also observed to occur, particularly in environments that are rich in methanol. Here, we discuss the astrochemical implications of these IR-induced phenomena.

3.1   Introduction

Interstellar icy dust grains are continuously exposed to both energetic and non-energetic triggers that initiate solid-state processes, such as chemical reactions. The consequent association of induced fragments (e.g., in exothermic reactions) has been reported to result in larger molecules containing excess energy. The ejection of solid-state chemical products to the gas phase through so-called "reactive desorption" and "photo-induced chemical desorption" is a direct consequence of this process (Minissale & Dulieu 2014; Minissale *et al.* 2016a; Muñoz Caro & Martín Doménech 2018; Chuang *et al.* 2018; Oba *et al.* 2018). This extra energy (which can take a vibrational form) must, in turn, be dissipated within the ice itself. Understanding the mechanisms through which this energy is dissipated and its consequences for the content and morphology of the ice is of special relevance when constructing accurate astrochemical models. Over recent decades, the focus has been on ultraviolet (UV) photons, given their ability to break chemical bonds. However, impacting infrared (IR) photons are also expected to have substantial effects, specifically in dense molecular clouds. The infrared interstellar radiation field (ISRF) is most intense in the inner galaxy, generated both by stellar emission (mainly for $\lambda \lesssim 8\ \mu$m) and by re-emission from dust grains (dominant for $\lambda \gtrsim 8$ μm). The former is accounted for by a combination of blackbody radiation fields, while the latter requires a model of the interstellar dust as described in Draine & Li (2001) and Li & Draine (2001). Within clouds, the integrated flux of secondary UV photons resulting from the excitation of H_2 upon interactions with cosmic rays is expected to be on the order of $\sim 10^4$ photons cm^{-2} s^{-1} (Cecchi-Pestellini & Aiello 1992). However, that of IR photons with wavelengths in the range of $1-10\ \mu$m is currently estimated to be substantially higher and on the order of $\gtrsim 10^9$ photons cm^{-2} s^{-1} (e.g., Mathis *et al.* 1983; Porter & Strong 2005; Roueff *et al.* 2014). The response of ices upon direct vibrational excitation has been scarcely investigated in the laboratory and is typically not included in models (e.g., Cuppen *et al.* 2017). For instance, vacuum ultraviolet radiation is known for resulting in a rich photochemistry (see, e.g., the review by Öberg 2016 and references therein), transforming the ice structure (Kouchi & Kuroda 1990), as well as leading to photodesorption induced by electronic transitions (Fayolle *et al.* 2011, 2013; van Hemert *et al.* 2015), whereas laboratory investigations of potential photodesorption and structural changes upon direct vibrational excitation are still limited. Structural changes are typically reflected in the spectral appearance of such ices (e.g., Cuppen *et al.* 2011; Cooke *et al.* 2016; Müller *et al.* 2021) and therefore changes in ice morphology and content due to energy-dissipation processes will play a part in interpreting observational data from IR facilities, such as the James Webb Space Telescope (McClure *et al.* 2023).

Silicates and carbonaceous materials are the main components of (sub)micron-sized dust grains present in the interstellar medium (ISM) (Millar & Williams 1993). During the earlier stages of star formation, H and O atoms adsorbed onto these grains react to form H_2O, resulting in a water-rich "polar-ice" layer (Ioppolo *et al.* 2010; Cuppen *et al.* 2010; Linnartz *et al.* 2015). In addition to water, carbon dioxide (CO_2) is a very abundant solid-phase ISM species, and is mainly present in the aforementioned interstellar polar-ice layer mixed with H_2O (Goumans *et al.* 2008; Oba *et al.* 2010a; Ioppolo *et al.* 2011; Noble *et al.* 2011). As the density of the collapsing cloud increases, carbon monoxide (CO) molecules present in the gas phase (catastrophically) freeze-out on top of the polar ice, forming a second coating known as the "apolar-ice" layer (Tielens *et al.* 1991; Boogert *et al.* 2002; Pontoppidan *et al.* 2003). Through hydrogenation reactions of solid-state CO, methanol (CH_3OH) is efficiently formed (Tielens & Hagen 1982; Charnley *et al.* 1992; Hiraoka *et al.* 1994; Watanabe & Kouchi 2002; Fuchs *et al.* 2009; Santos *et al.* 2022c). This alcohol is abundantly present in interstellar ices mixed with CO, as shown by various laboratory and observational works (e.g., Bottinelli *et al.* 2010; Cuppen *et al.* 2011; Penteado *et al.* 2015). Follow-up studies have shown that along the same hydrogenation scheme also larger complex organic molecules (COMs), such as

glycerol, can be formed involving radical reactions (Chuang *et al.* 2016; Fedoseev *et al.* 2017). Alternatively, CH_3OH can also be formed less efficiently during stages prior to CO-freeze out through reactions involving CH_4 and OH (Qasim *et al.* 2018).

The IR irradiation of crystalline water ice has been previously studied with a focus on its resonant desorption at elevated temperatures ($\gtrsim 100$ K) (Krasnopoler & George 1998; Focsa *et al.* 2003). These first studies suggested that on-resonance irradiation of crystalline ices leads to selectivity effects, with a strong wavelength-dependent H_2O desorption as a result of IR-photon absorption. Infrared-induced matrix-assisted laser desorption and ionization (MALDI) experiments ensued, evincing the photodesorption of polycyclic aromatic hydrocarbons (PAHs), as well as their hydrated clusters, embedded in water ice matrices and subjected to resonant vibrational excitation (Focsa *et al.* 2006; Mihesan *et al.* 2006; Henderson & Gudipati 2014). More recently, porous amorphous solid water (pASW) has been studied in works combining IR-free electron laser (FEL) irradiation experiments and molecular dynamics simulations, which revealed a reorganization of the ice structure towards a more ordered configuration upon the absorption of photons in the broad IR regime (Noble *et al.* 2020; Coussan *et al.* 2022; Cuppen *et al.* 2022). Amorphous CO_2 ices have shown a similar behavior as a result of IR-FEL irradiation, whereas this effect was barely observed in the crystalline counterparts (Ioppolo *et al.* 2022). Moreover, both Noble *et al.* (2020) and Ioppolo *et al.* (2022) hint at possible photodesorption upon resonant irradiation of the pure ices.

Vibrational energy pooling (VEP) is also an interesting phenomenon that takes place as a result of vibrational excitation. In VEP, vibrationally excited CO molecules pool their energy through a base-camp mechanism, resulting in highly excited CO species that constitute a small portion of the group (DeLeon & Rich 1986; Corcelli & Tully 2002; Chen *et al.* 2017; Chen *et al.* 2019; DeVine *et al.* 2022). DeVine *et al.* (2022) have explored the effects of VEP of crystalline CO under interstellar conditions in a combined laboratory and theoretical work, and reported the formation of CO_2 and C_2O_3 species as a result of spin-forbidden reactions involving highly vibrationally excited CO molecules. The reaction pathways they explored also led to CO desorption due to the energy release from the dissociation of an intermediate CO dimer species only accessible at extremely high vibrational excitation levels.

Infrared spectroscopic properties such as band width and peak position can provide powerful information on the mixing and layering conditions of ices (Boogert *et al.* 2015). With the James Webb Space Telescope (JWST), IR observations of interstellar ices are available at a wide spectral range ($0.6 - 28.3$ μm) and with unprecedented spatial resolution and sensitivity, enabling us to focus on specific areas in a proto-planetary disk or to investigate dense interstellar clouds for extinction values as high as 90 (McClure *et al.* 2023). The interpretation of these observations requires highly detailed laboratory data on the spectroscopic properties, morphology, and dynamics of ices. Moreover, understanding the effects of vibrational energy on the structure and dynamics of the CO-rich ice layer plays a key role in developing thorough models of the chemical evolution of the interstellar medium.

In the present work, we explore the effects of IR-photon irradiation and the consequences of vibrational-energy release in interstellar apolar ice analogues. We provide the first selective IR-FEL irradiation study on pure amorphous and crystalline CO ices (henceforth aCO and cCO), as well as pure amorphous CH_3OH ices and mixtures of the two species. In Section 3.2, the experimental setup and procedures employed in this work are detailed. The main results are described and discussed in Section 3.3. In Section 3.4 we explore the astrophysical implications and our main findings are summarized in Section 3.5.

3.2   Experimental methods

The experiments are performed at the HFML-FELIX laboratory at Radboud University, the Netherlands, directing tunable free electron laser radiation towards the laboratory ice sur-

Table 3.1: Overview of the experiments performed in this work.

Experiment	$T_{deposition}$ [a] (K)	$T_{irradiation}$ [a] (K)	N(CO) [b] (molecules cm^{-2})	N(CH$_3$OH) [b] (molecules cm^{-2})	FEL irradiation (μm)
CH$_3$OH	20	20		6×10^{17}	2.96, 3.07, 3.14, 4.67, 9.62
aCO	20	20	1×10^{17}		4.67, 5.20
cCO	29	20	1×10^{17}		4.67, 5.20
CO:CH$_3$OH = 1:0.3	20	20	2×10^{17}	6×10^{16}	3.07, 4.67, 9.62
CO:CH$_3$OH = 1:3.0	20	20	2×10^{17}	5×10^{17}	3.07, 4.67, 9.62

[a] Measured temperature values varied by ± 0.8 K.
[b] Upper limits derived using transmission band strengths.

face astrophysics (LISA) ultrahigh vacuum (UHV) end station. At HFML-FELIX, LISA is connected to FELIX-2 and -1 to perform selective irradiation experiments in the broad IR ($3700 - 220$ cm^{-1}, $2.7 - 45$ μm) and terahertz (THz, $10 - 2$ THz, $30 - 150$ μm) spectral ranges, respectively, shedding light on the relaxation mechanisms that follow the excitation of particular vibrational modes within solid matter. LISA has been described in detail elsewhere (Noble *et al.* 2020; Ioppolo *et al.* 2022) and here we provide a brief explanation of the experimental procedure. The experiments described here have been obtained during four 7.5-hour-long beam shifts, focusing on the basic concept of (off/on) resonant IR photodesorption of interstellar ices. Extended measurements are scheduled for later this year in another run of four beam shifts.

A gold-plated optically-flat copper substrate in the center of the UHV chamber is in thermal contact with the head of a closed-cycle helium cryostat, which allows to control the substrate temperature in the range of $20 - 300$ K through resistive heating. The temperature is monitored by a silicon diode thermal sensor fixed at the bottom of the substrate. At room temperature, the base pressure in the chamber is $\sim 2 \times 10^{-9}$ mbar. Gaseous CO (Hoekloos/Praxair, purity 99.9%) and CH$_3$OH (Sigma-Aldrich, purity 99.9%) vapor are introduced in the dosing line, either separately (in the case of pure ices) or simultaneously for a binary ice. Beforehand, the methanol sample is purified through multiple freeze-pump-thaw cycles. The ices are then grown on the substrate through background deposition by admitting the pure species or mixtures into the main chamber via an all-metal leak valve that faces the walls of the chamber. This deposition method leads to more uniform ices and better simulates the deposition conditions on interstellar dust grains. Amorphous CO ice is deposited at the lowest substrate temperature of 20 K, while crystalline CO is grown at 29 K (see, e.g., Kouchi 1990). The different solid-state configurations are confirmed by the clearly sharper CO-stretching feature of the cCO IR spectra. After deposition, all ices are maintained at 20 K during the irradiations.

The ice growth and the effects of the IR irradiation are monitored in situ through reflection-absorption IR spectroscopy (RAIRS) using a Fourier Transform IR spectrometer. The FTIR spectra cover a range of $5000 - 600$ cm^{-1} with a resolution of 0.5 cm^{-1}. To calculate the column density (N_X) of the species in the ice, a modified Beer-Lambert law is applied to convert the IR integrated absorbance ($\int Abs(\nu)d\nu$) to the absolute abundance:

$$N_X = \ln 10 \frac{\int Abs(\nu)d\nu}{A'_X},\tag{3.1}$$

where A'_X is the absorption band strength of a given species. Since the band strengths of CO and CH$_3$OH have not been estimated for the LISA setup in reflection mode, we use the transmission values from the literature instead. Specifically, we have $A(\text{CO})_{\nu_1=2142} = 1.1 \times 10^{-17}$ cm molecule^{-1} (Jiang *et al.* 1975) and $A(\text{CH}_3\text{OH})_{\nu_8=1032} = 1.8 \times 10^{-17}$ cm molecule^{-1} (Hudgins *et al.* 1993). Since the RAIRS technique is more sensitive than transmission IR spectroscopy, the column densities derived here should be regarded as upper limits. The details of each experiment performed in this work are listed in Table 3.1.

For the IR irradiation of the ice, we used the IR-FEL source FELIX-2 to generate nearly monochromatic mid-IR photons in the ranges of $2.9 - 4.5$ μm (fundamental mode) and $4.5 - 9.7$ μm (third harmonic mode). The photons are bunched in $5 - 10$ microseconds-long macropulses with a repetition rate of 5 Hz, consisting of a train of micropulses of several picoseconds spaced out by 1 nanosecond. Unless otherwise specified, at longer wavelengths ($\gtrsim 4.5$ μm), the energy of the macropulses is attenuated to a constant value of $\sim$20 mJ, as measured at the diagnostic station located before the LISA end-station area of the facility. At shorter wavelengths ($\lesssim 4.5$ μm), the laser energy is kept at its highest attainable value of $\sim$5 mJ, as it is generated in the third harmonic mode. The fluence of IR photons with wavelength λ in each experiment can be calculated via the expression:

$$\text{Fluence}_\lambda = \frac{E_\lambda * r * t}{S}, \qquad (3.2)$$

where E_λ is the energy and r is the repetition rate of the macropulses, S is the area of the FELIX-2 beam spot on the substrate, and t is the duration of the irradiation. The FEL beam impinges the gold-plated flat substrate at an angle of $45°$ with respect to the surface, resulting in an elliptical spot size of $\sim$1.0 x $\sim$1.5 mm in semi-axes. In comparison, the FTIR beam angle with the gold substrate is of $13°$, resulting in an elliptical spot size of $\sim$1.5 x $\sim$6.5 mm in semi-axes. Consequently, the FTIR RAIRS beam fully covers the region irradiated by the FEL beam, with a FTIR/FEL area ratio of $\gtrsim$6. The spectral FWHM of FELIX-2 is estimated to be $\sim$0.8% $\delta\lambda/\lambda$ for the entire wavelength range.

A z-translator allows the movement of the substrate in height, providing multiple ice spots for systematic IR irradiation. In this work, we utilize seven different substrate positions, each separated by 4 mm from the neighboring spot. Each FEL irradiation is thereby performed at an unirradiated ice spot (unless otherwise specified). With the exception of the long aCO and cCO experiments, the irradiations are subsequently repeated, on average, two additional times for each spot. This is done to ensure reproducible results. As stated above, the FTIR beam is $\gtrsim$6x larger in area than the FEL beam, thus part of the ice probed by the FTIR is not exposed to FEL irradiation. As a result, the difference FTIR spectra acquired before and after FEL irradiation are utilized to visualize changes in the ice. During the irradiation experiments, any possible desorption of species from the ice was monitored by a quadrupole mass spectrometer (QMS). Control temperature-programmed desorption (TPD) experiments with analogous deposition conditions and a ramping rate of 2.5 K min^{-1} were performed to assist in interpreting the IR-FEL irradiation results. In this work, we discuss FEL irradiations in terms of wavelength and FTIR spectra in wavenumbers (both in vacuum) to reflect the higher spectral resolution of the FTIR data, as opposed to the transform-limited bandwidth of the FEL photons.

3.3 Results and discussion

Figure 3.1 shows the spectra of the ices of pure CH$_3$OH (panel a), pure CO (both aCO and cCO, panel b), and 1:0.3 and 1:3.0 mixtures of CO:CH$_3$OH in panels c and d, respectively. Also indicated in this figure are the involved vibrational modes. The wavelengths of FELIX-2 used during the irradiations are marked by the dashed vertical lines and their respective FWHMs are shown by the shadowed areas. Given the broad wavelength coverage of the FTIR measurements, the laser bandwidths are hard to see in panels a, c, and d, but the shadowed area is substantially larger in panel b because of the smaller spectral range shown here. For each experiment (i.e., pure CO, pure CH$_3$OH, and mixtures), we use the same color scheme throughout the paper. The individual ices are discussed below.

3.3.1 CH$_3$OH

3.3.1.1 Morphology

Figure 3.2 shows the difference spectra obtained before and after continuous exposure for five minutes, of pure CH$_3$OH ice to the FEL light at 2.96 (ν_1), 3.07 (ν_1), 3.14 (ν_1), 4.67 (off-resonance), and 9.62 (ν_8) μm. Intermolecular interactions give rise to the OH-stretching features of CH$_3$OH at 3.07 and 3.14 μm (see, e.g., Jakobsen *et al.* 1967; Hudgins *et al.* 1993), while the shoulder feature at 2.96 μm has been suggested to originate from molecules with weakly bound O-H bonds, or potentially dangling bonds, due to pores in the ice (Luna *et al.* 2018). The macropulse energies of all irradiations are adjusted to a constant value of $\sim$5 mJ. Modifications to the CH$_3$OH band profiles are clearly observed for all exposures in which the
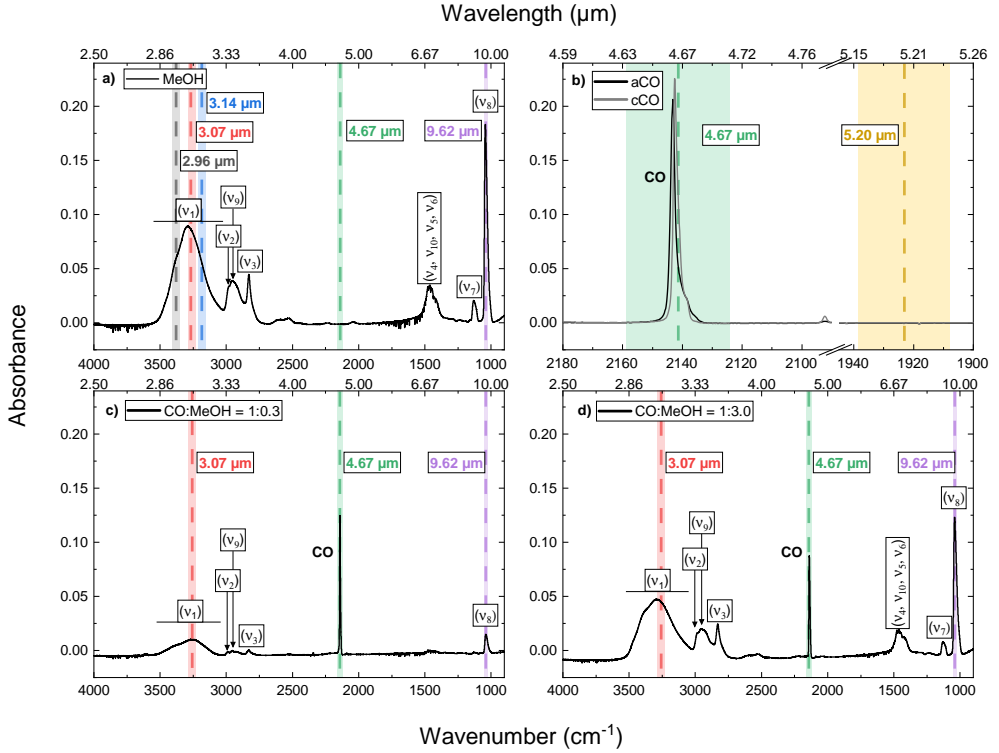
Figure 3.1: Spectra and irradiation maps of the ices explored in this work, all taken at 20 K. Panel a) Pure amorphous CH_3OH. Panel b) Pure amorphous and crystalline CO. Panel c) Mixture of CH_3OH and CO with a CO:CH_3OH ratio of 1:0.3. Panel d) Same as c), but with a 1:3.0 ratio. All spectra are taken after deposition and before irradiation. The wavelengths of FELIX-2 used later for on and off-resonance irradiation are shown with dashed lines, and the FWHM is visible from the shadowed areas. The fundamental mode of CO is denoted in boldface, and the other labels correspond to the (ν_X) vibrational modes of CH_3OH.

IR wavelength is on resonance with absorption bands of methanol. Comparatively, no differences are observed after the off-resonance irradiation (i.e., at 4.67 μm). Thus, the observed spectral changes are a consequence of the absorption of IR radiation by the methanol ice, and not by the golden substrate underneath—in agreement with what has been previously observed for pASW and CO_2 ices (Noble *et al.* 2020; Ioppolo *et al.* 2022). Overall, each CH_3OH absorption feature shows similar spectral changes in the difference spectra of all on-resonance irradiations, with variations only appearing in their intensities. The most pronounced effects are observed for the irradiations at the OH-stretching region. Indeed, we may expect that irradiations at the OH-stretch—which has a higher band strength—would result in more photon-absorption events than those on resonance with the CO-stretching mode. Furthermore, the exposure at the CH_3OH ν_1 band at 2.96 μm, in particular, yields changes that are significantly stronger than the other OH stretches. The fact that neighboring irradiations in the OH-stretching region yield such varying results highlights the high dependence of the energy-dissipation mechanisms on the type of vibrational mode excited, even within similar energy ranges. Irradiations at the CH-stretching modes of CH_3OH are also performed (not shown) and result in similar spectral changes to the other on-resonance spectra, albeit with lower intensities.
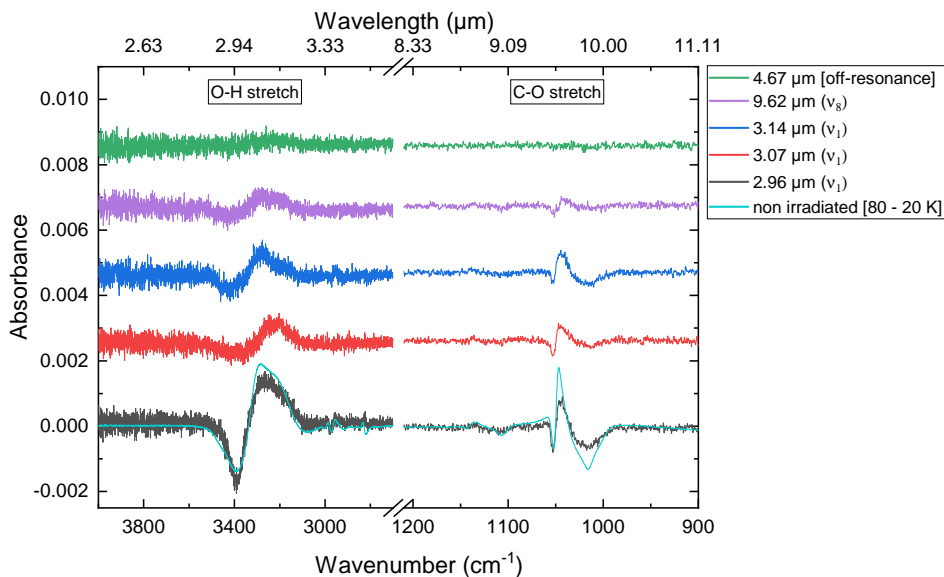
Figure 3.2: Difference spectra obtained before and after five minutes of IR-FEL irradiation on methanol ice at 20 K. The difference between spectra acquired at 80 K and 20 K (without IR irradiation) during a TPD control experiment is also shown in cyan and included in the 2.96 um plot. To allow for a direct comparison, all spectra are plotted for the same scale; the differences in the noise level between 3 μm and 9 μm are due to the intrinsic wavelength-dependent S/N of the FTIR. The irradiation spectra are offset for clarity.

The features around the OH- and CO-stretching bands of methanol in the difference spectra show both positive and negative components that yield a negligible net integral absorbance. Those features are thus attributed to the restructuring of the ice upon exposure to the IR-FEL with a power of ~ 5 mJ, leading to an overall loss of the weakly bound O-H modes at 2.96 μm and corresponding gain of bulk O-H modes at 3.07 and 3.14 μm. A similar behavior was observed for O-H dangling modes versus bulk modes of IR-FEL irradiated pASW (Coussan *et al.* 2022). Moreover, the CO-stretching band profiles show an overall narrowing trend, typically on the order of 0.2%. It should be noted that the significantly larger area of the FTIR beam in comparison with the IR-FEL beam results in an appreciable ($\gtrsim$6x) dilution of the laser effect on the recorded IR band shapes, meaning that the aforementioned percentage is, in fact, a lower limit.

To investigate the character of the morphological changes induced by the IR-FEL, we performed a control TPD experiment of unirradiated pure CH_3OH ice deposited under the same conditions as in the irradiation study. Such an experiment allows to compare controlled thermally induced morphology changes with those induced upon IR irradiation. The IR spectra acquired during the TPD experiments are reported in Appendix 3.7.1. The spectra, as obtained for different temperatures, were compared to the difference spectra before and after irradiation. The best qualitative fit to the most effective irradiation at ν_1 (i.e., the TPD result that best reproduces the irradiation) is obtained by the difference between the spectra taken at 80 K and 20 K, as shown in Figure 3.2. The profile of the IR spectrum obtained during the TPD experiment reproduces that of the irradiation spectrum for the OH-stretching modes quite well, whereas discrepancies arise in the intensity of the changes for the CO-stretching counterpart. Nonetheless, the overall profiles of both difference spectra acquired during irradiation and the TPD experiment are remarkably similar. This is a strong indication that for pure methanol ices, the excess vibrational energy is efficiently dissipated throughout the bulk of the ice in an equivalent manner to thermal heating of an extended area. This energy dissipation leads to restructuring toward a more organized morphology, as observed previously for pASW and CO_2 ices (Noble *et al.* 2020; Ioppolo *et al.* 2022; Coussan *et al.* 2022).

The polarity of the ice could play a role in the effectiveness of the vibrational energy dissipation through restructuring: similarly to the case of methanol ice reported here, Noble *et al.* (2020) observed that the difference spectra upon IR-FEL irradiation of pASW can be satisfactorily reproduced by the subtraction of theoretical spectra simulating a restructuring of the ice. However, Ioppolo *et al.* (2022) found that for CO_2 ices, local restructuring alone is not sufficient to explain the changes induced by the IR-FEL. Alternatively, this difference could also be related to the type of intermolecular interactions within the ice, in which H-bonding networks could potentially facilitate the vibrational energy dissipation through restructuring, while generally weaker van der Waals interactions could be less efficient in doing so. Indeed, transfer of vibrational energy has been shown to occur in H_2O ices through hydrogen-bonded water molecules with resonant O-H stretches, which leads to local heating and restructuring of the ice (Cuppen *et al.* 2022).

3.3.1.2   Power-dependence analysis and photodesorption

It is possible to assess whether the changes to the CH_3OH ice are due to single- or multi-photon processes through a power-dependence analysis. We performed IR-FEL irradiations of a pure CH_3OH ice sample at 9.62 μm with three different power settings (5.76 mJ, 57.6 mJ, and 115 mJ) for five minutes and compared the resulting integrated net areas around the ν_8 absorption band of methanol as a function of IR-FEL power. Figure 3.3 shows a fairly linear ($R^2 = 0.98$) correlation between beam power and area, further suggesting that the effect of the IR-FEL laser on the ice morphology is due to single-photon processes (Noble *et al.* 2020; Ioppolo *et al.* 2022; Coussan *et al.* 2022). The decreasing trend in the integrated absorption signal at the ν_8 band with increasing beam power suggests that photodesorption might be

observed in the IR spectra once enough vibrational excitations take place in the ice. The extent of the desorption is however not high enough to be detectable with the sensitivity of the current QMS. From the integrated absorption signal of the CH_3OH ν_8 band lost after the 115 mJ irradiation and the total beam fluence ($\sim 1.8 \times 10^{23}$ photons cm^{-2}), we derived a tentative upper limit to the photodesorption rate of $r = (1.6 \pm 0.5) \times 10^{12}$ molecules J^{-1}, or $r = (3 \pm 1) \times 10^{-8}$ molecules photon^{-1}. We considered only the uncertainties in the band strength to derive the errors in the photodesorption rates, although other error sources could also have an influence. The restructuring of the ice is expected to have a minor effect on the band strength of CH_3OH, as it was shown to only change appreciably at temperatures above the crystallization of methanol (Luna *et al.* 2018).

The resulting rate is several orders of magnitude lower than typical (non-dissociative) CH_3OH UV photodesorption counterparts, of 10^{-5} molecules photon^{-1} (Bertin *et al.* 2016), but it is still measurable because of the much higher IR flux of FELIX-2 compared to the UV-broadband flux of a microwave H_2 discharge lamp (Ligterink *et al.* 2015; Cruz-Diaz *et al.* 2016) or monochromatic radiation of a synchrotron VUV beam (Fayolle *et al.* 2011). At a first glance, the astronomical relevance of such a low photodesorption rate may be considered negligible, but it is important to realize that in dense interstellar clouds, the IR photon fluxes are $\gtrsim 10^4$ times higher than that of the secondary UV, resulting in comparable efficiencies for IR-induced photodesorption phenomena in the interstellar medium. These efficiencies and their impacts on astrochemical models are further discussed in Section 3.4. Furthermore, while UV studies show that CH_3OH largely fragments upon electronic excitation (Bertin *et al.* 2016), it is likely that upon IR excitation desorption follows a non-dissociative pathway, further influencing the predicted abundance of CH_3OH in the gas phase.
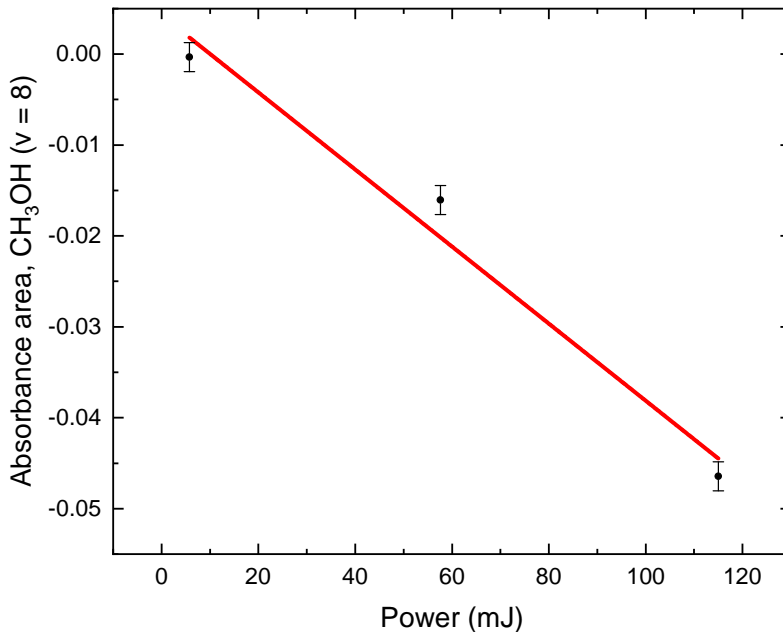
Figure 3.3: Power-dependence analysis of the IR-FEL effect on CH_3OH ice. The three different power settings, i.e., 5.76, 57.6, and 115 mJ, are controlled by attenuating a 115 mJ beam with 13, 3, and 0 dB, respectively. Error bars correspond to the three sigma limit of the instrumental error as derived from the integrated noise signal of the off-resonance difference spectrum in the same band width.

3.3.2   CO

3.3.2.1   Morphology
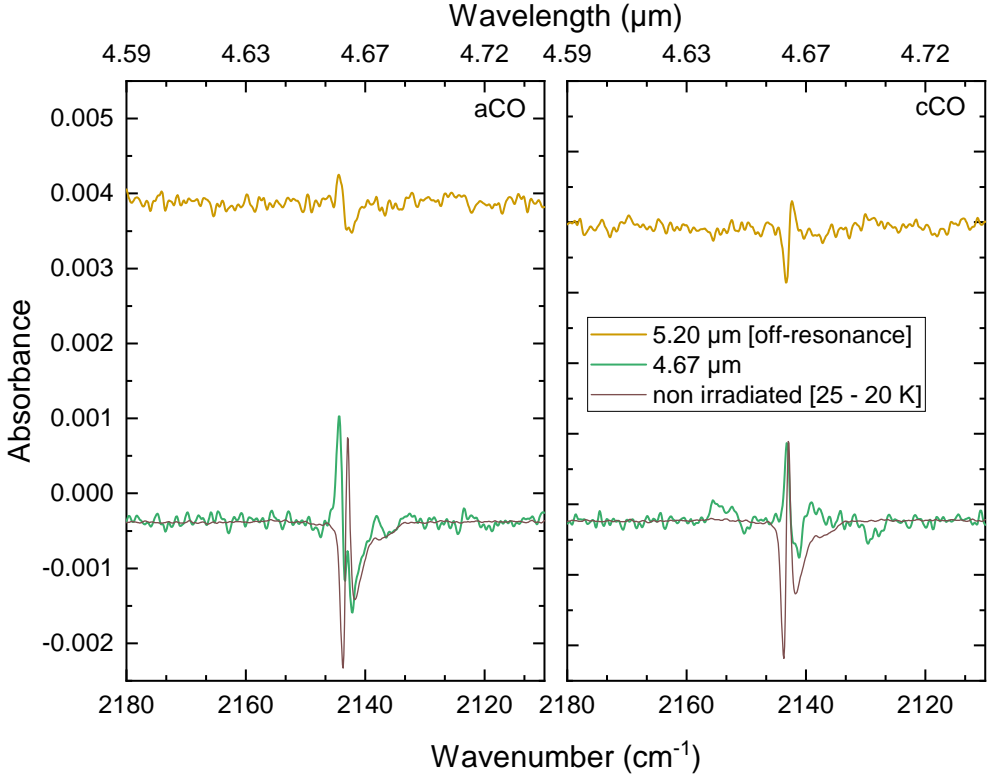
Figure 3.4: Difference spectra obtained before and after ten minute of IR-FEL irradiation on aCO ice (left panel) and cCO ice (right panel), both at 20 K. The difference between spectra acquired at 25 K and 20 K during a TPD control experiment is shown in brown. The irradiation spectra are offset for clarity.

The difference spectra obtained before and after ten minute of IR-FEL exposure of amorphous and crystalline CO ice at 4.67 and 5.2 μm are shown in Figure 3.4. Since there is only one vibrational absorption band available to resonant irradiation in the CO-ice case, thereby limiting the number of excitations to perform and leaving more time to perform longer irradiations, we opted for a higher IR-FEL fluence (i.e., ten instead of five minutes of irradiation) in order to further increase the signal-to-noise ratio (S/N) in the IR difference spectra. Irradiations of CO ice at wavelengths off-resonance (i.e., at 5.20 μm) show a feature that turns out to be due to the ongoing stabilization of the ice—a process that extends to a time frame of several hours after deposition. This is confirmed by recording spectra taken ten minutes apart (without any exposure to the IR-FEL) directly before performing the irradiations. Their difference spectra show similar features with identical intensities to the one observed in the 5.20 μm case. For direct comparison, the IR spectra of the 4.67 μm and 5.20 μm irradiations (corrected for the artifacts due to ice stabilization) are shown in Appendix 3.7.2.

Due to the intrinsic bandwidth, the irradiation at 4.67 μm overlaps with both the longitudinal optical (LO) and transverse optical (TO) phonons of the vibrational mode of CO

at ∼2142 and ∼2138 cm^{-1}, respectively. The on-resonance FEL exposure at 4.67 μm yields
more pronounced (∼2x) modifications to the ice in the amorphous case than in the crystalline
counterpart. This is in line with the hypothesis that the ice undergoes some degree of restruc-
turing toward a more organized configuration, in which case cCO would reach a saturation
point more quickly, as its structure is already largely organized. Similar saturation effects
have been reported in previous studies on crystalline H_2O and CO_2 ices (Noble *et al.* 2020;
Ioppolo *et al.* 2022).

The beam exposure at 4.67 μm is compared to the TPD difference spectrum between 25
K and 20 K, also shown in both panels in Fig. 3.4. As shown by the difference spectrum
from the TPD experiment, heating of the ice causes the CO molecules to reorganize in
a more compact configuration, resulting in a narrower band profile. Additionally to the
narrowing effect, the irradiation spectrum also shows a slight overall blueshift of the CO band,
suggesting that repulsive interactions between the molecules might become more prominent
upon restructuring. Concomitant ice stabilization could contribute to the apparent blueshift,
albeit to a smaller extent. Ultimately, the spectral changes induced by the IR-FEl cannot
be simply reproduced by the TPD-IR results—in contrast to the case of CH_3OH shown in
Figure 3.2. This suggests that the dissipation of vibrational energy throughout the CO ice is
not as efficient as for CH_3OH and thus the effects of the IR-FEL exposure in the former case
cannot be described solely by an extended heating that transforms the structure of the ice.

3.3.2.2 Photodesorption

To thoroughly investigate the temporal effects of vibrational energy injection into pure CO
ice and the possibility of photodesorption, we systematically irradiated both the amorphous
and crystalline samples at 4.67 μm for different irradiation durations. In Figure 3.5, the
integrated net area around the CO stretching mode obtained from the difference spectra
before and after each irradiation are shown as a function of irradiation time (i.e., fluence).
The error bars include the fluctuations in integrated absorbance area due to the stabilization
of the ice, such as the artifacts seen after the irradiation at 5.20 μm in Figure 3.4.

The overall absorbance area of the stretching feature of aCO decreases linearly with
irradiation fluence, strongly suggesting a continuous loss of material upon exposure to the
beam due to IR-induced photodesorption. On the contrary, there is no significant loss in the
intensity of the stretching mode of crystalline CO due to irradiation for the fluences explored
in this work. Thus, cCO does not seem to photodesorb (as effectively) as a result of IR-
photon absorption to the same extent that aCO does. This contrasts with results on H_2O
ices irradiated by IR-FEL reported by Noble *et al.* (2020), in which case pASW was observed
to mainly restructure upon vibrational excitation, with only a minor potential contribution
from photodesorption. On the other hand, irradiated cubic crystalline ices underwent pure
photodesorption, totaling a loss of ∼15% of the deposited material. The different nature
of the intermolecular interactions among CO and H_2O ices could be the reason behind this
discrepancy. van Hemert *et al.* (2015) predicted the UV-induced photodesorption probability
of cCO to be around five times smaller than that of aCO, which they attributed to the stronger
binding of the molecules in the crystalline structure. This value is remarkably consistent with
experimental measurements of CO photodesorption as a function of deposition temperature
(Öberg *et al.* 2009b). Likewise, the same effect could also contribute to the significantly
lower desorption efficiency of cCO upon FEL irradiation. Since the observed decrease in the
CO band intensity does not happen at the precise wavelength of irradiation (which is shifted
from the CO peak), we can rule out the contribution from hole-burning effects to the negative
integrated areas.

The transfer of vibrational energy to translational energy (i.e., vibrationally induced
photodesorption) by CO molecules has been previously predicted to be inefficient (van Hemert
et al. 2015; Fredon *et al.* 2021). In this work, we observe a total absolute loss of ∼ 2.6 × 10^{15}
molecules cm^{-2} of aCO as a result of 80 minutes of irradiation, which yields a relatively
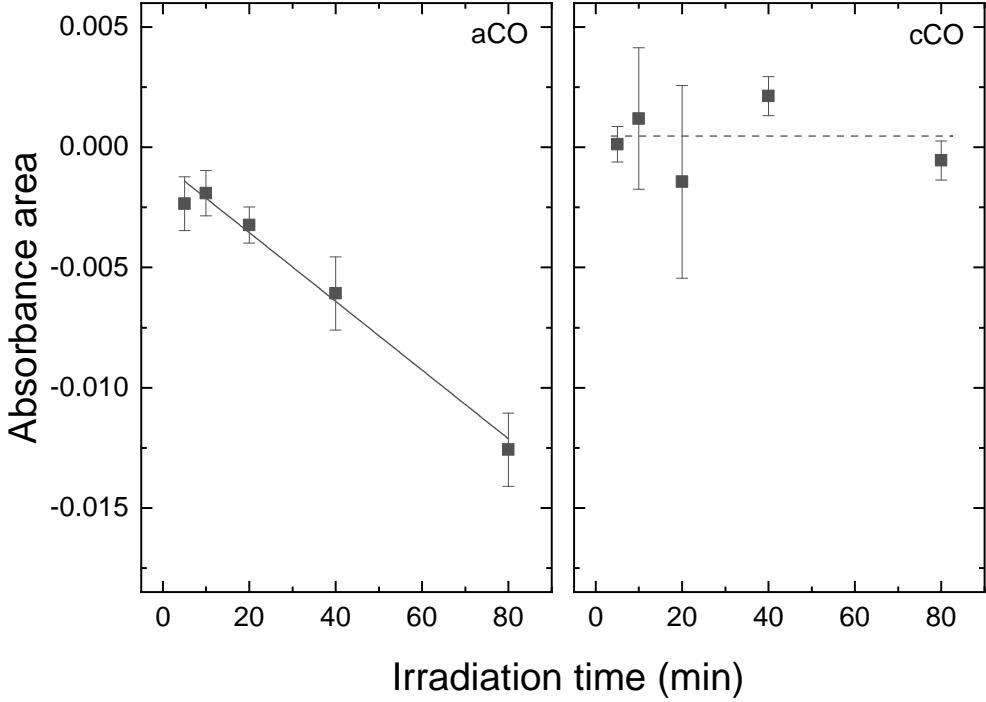
Figure 3.5: Plot of the integrated area of the stretching mode of CO in the difference spectra obtained as a function of irradiation time. Left panel: Irradiation of amorphous CO ice. The solid line shows the linear fit to the points. Right panel: Irradiation of crystalline CO ice. The averaged integrated noise is denoted by the dashed line.

small amount of desorbed species that is below the detection limit of the QMS, rendering the mass spectrometry data inconclusive. Nonetheless, our IR spectroscopy data provide clear evidence of a CO photodesorption process that has not been predicted by the aforementioned models. From the total column density loss of aCO after 80 minutes of irradiation and the total beam fluence integrated over the entire exposure time ($\sim 2.4 \times 10^{23}$ photons cm^{-2}), we derive a tentative upper limit to the photodesorption rate of $r \sim (2.6 \pm 0.8) \times 10^{11}$ molecules J^{-1} or $\sim (1.1 \pm 0.3) \times 10^{-8}$ molecules photon^{-1}. The errors were estimated from the band strength uncertainties. Similarly to CH$_3$OH, changes in the band strength of CO due to restructuring are expected to be minor, and the derived rate translates to a CO desorption efficiency induced by IR photons comparable to the UV value under interstellar conditions (see Section 3.4). Moreover, the linear trend between the decrease in integrated absorption signal and photon fluence is further evidence of a zeroth-order, single-photon interaction of the IR beam with the ice leading to desorption, as has been observed before for the UV-induced photodesorption of CO (Öberg *et al.* 2007; Muñoz Caro *et al.* 2010; Fayolle *et al.* 2011; Chen *et al.* 2014; Muñoz Caro *et al.* 2016; Paardekooper *et al.* 2016). Similar to this work, other studies of FEL exposure to pASW and CO$_2$ ices suggest the occurrence of IR-induced photodesorption (see, e.g., Noble *et al.* 2020; Ioppolo *et al.* 2022; Coussan *et al.* 2022).

In the case where multiple CO species are vibrationally excited simultaneously, effects such as VEP phenomena can arise. In the interstellar medium this is rather unlikely, but for the high fluxes used in the laboratory this should not be a priori neglected. As a consequence, some desorption mechanisms could in principle become accessible to CO molecules

that collect energy from their neighbors and reach higher vibrational levels (DeVine *et al.* 2022). Differently from DeVine *et al.* (2022), however, we do not detect any photoinduced products upon irradiation of aCO nor cCO. This is likely due to the differences between the experimental conditions of both studies (e.g., ice morphology, thickness, IR-photon generation method) that result in a significant quenching of the pooling effect during our experiments in comparison to DeVine *et al.* (2022). Indeed, simultaneously excited species at any given time are expected to be very diluted within the ice in this work, as the number of absorption events per IR-FEL pulse is estimated to be much lower ($\sim$0.1%) than the total ice column density. Excited species are therefore expected to be sufficiently apart to prohibit effective interactions. Moreover, it is worth emphasizing that multi-photon excitations are unlikely under our experimental conditions, as shown by the linear trend in Figure 3.3.

3.3.3 Mixtures

3.3.3.1 Morphology

To further explore the impact of the chemical environment on the dissipation of vibrational energy, we performed irradiation experiments on ice mixtures of CO and CH_3OH with ratios of $CO:CH_3OH$ = 1:0.3 (CO-rich) and 1:3.0 (CH_3OH-rich). As methanol is expected to form through CO hydrogenation, such mixtures are of direct astronomical relevance (Watanabe & Kouchi 2002; Fuchs *et al.* 2009; Cuppen *et al.* 2011). The difference spectra of both mixtures obtained before and after five minutes of FEL exposure at 20 K are shown in Figure 3.6. For comparison, we maintain the same absolute column densities of CO in both CO-rich and methanol-rich ices (see Table 3.1).
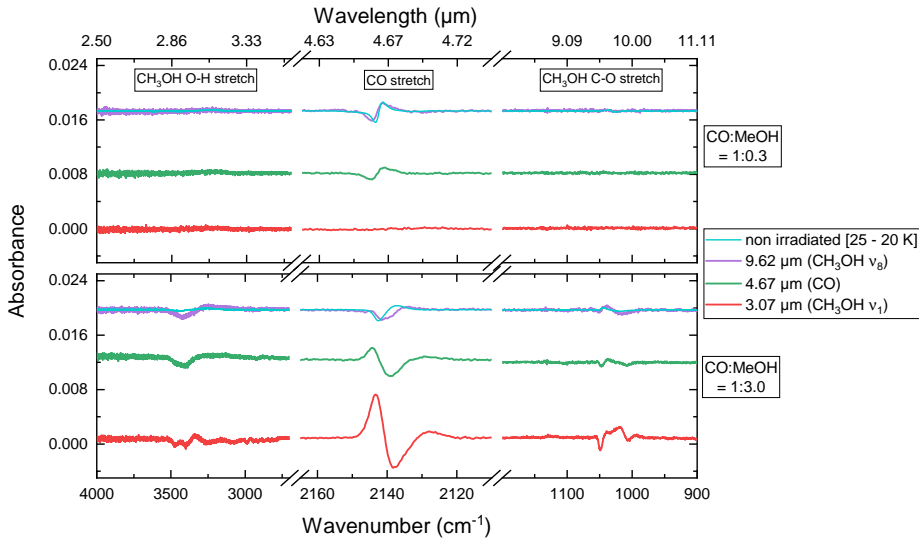
Figure 3.6: Difference spectra obtained before and after five minutes of IR-FEL irradiation on ice mixtures of CO and CH_3OH at 20 K. Upper panel: Mixture ratio of $CO:CH_3OH$ = 1:0.3. Lower panel: Mixture ratio of $CO:CH_3OH$ = 1:3.0. The control TPD difference spectra between 25 K and 20 K are also shown in cyan. The irradiation spectra are offset for clarity.

The FEL exposures of the CO-rich ice do not result in any significant changes around the methanol features (i.e., CO and OH stretches), namely, above the detection limit (top panel of Figure 3.6). This is likely because the impact of restructuring changes of the deposited

amount of methanol remains within the spectral noise level. The CO feature, conversely, is modified by the IR-FEL irradiation at both 4.67 and 9.62 μm, displaying the same spectral profile in both cases. After five minutes of irradiation with $\sim$20 mJ, the ice becomes saturated to the IR-FEL effects (see Figure 3.13 in Appendix 3.7.3). This indicates that the absorption of photons by either CO or CH$_3$OH molecules (at 4.67 and 9.62 μm, respectively) leads to similar modifications of the ice, which result in a slight redshift of the overall CO band profile. The IR difference spectrum obtained during TPD between 25 K and 20 K reproduces the CO shape reasonably well (see upper graph in the top panel), meaning that most ice changes can be explained by an extended heating-like event upon photon absorption that leads to a more organized configuration. However, the negative features in the irradiation spectra are not completely reproduced by the TPD control experiment, which suggests that additional desorption could also be taking place. It is worth noting that both the irradiation and TPD difference spectra of the CO-rich mixture display a different profile around the CO band compared to the pure aCO ice. In the TPD experiments, pure amorphous CO becomes narrower with higher temperatures as a result of an increasingly ordered configuration, but no change in peak position is observed. In the binary ice, conversely, the CO stretching mode becomes slightly redshifted at higher temperatures, indicating that (more) attractive interactions dominate the new CO sites. These observations highlight the crucial role played by the surrounding species on solid-state IR band shapes. Moreover, the on-resonance irradiation at the ν_1 vibrational mode of CH$_3$OH at 3.07 μm results in no apparent changes around the CO feature, despite it yielding the most pronounced effects in the case of pure methanol ice. These observations provide further evidence of the strong dependence of the dissipation of vibrational energy on the involved excited vibrational mode and on interactions with the surrounding ice matrix.

In the case of the methanol-rich ice, modifications to both species' bands upon irradiation are observed above the detection limit of the instrument (bottom panel of Figure 3.6). The higher absolute abundance of methanol in this case compared to the CO-rich ice allows for more IR photons to be absorbed when irradiation is on resonance with methanol absorption wavelengths. As a consequence, the exposures at 9.62 μm and especially at 3.07 μm result in significantly more intense changes to the CO band than in the CO-rich ice. In the latter case, the irradiation at the ν_1 mode of CH$_3$OH leads to no differences in the CO band, while in a more methanol-rich environment (likewise in pure methanol ice), it yields the most pronounced profile changes. The methanol features in this mixture, however, display a remarkably different behavior upon irradiation at its OH stretching mode in comparison to the pure methanol case. Clearly, the changes in the band profiles of both CH$_3$OH and CO species are highly dependent on the excited vibrational mode, as found by the differences of the shapes resulting from the three irradiation frequencies. Interestingly, when irradiated at 3.07 μm and 4.67 μm, the profile of the stretching feature of CO in the methanol-rich mixture is the inverse of what is observed for the CO-rich counterpart: while the IR excitation of the former leads to a blueshift of the peak, in the latter it results in its redshift. In fact, the blueshifted profile better resembles the one observed in the irradiation of pure aCO, despite their very different surrounding conditions. These profiles are repeatedly observed during additional measurements of the CH$_3$OH-rich ice mixture (see Figure 3.14 in Appendix 3.7.3). However, the mechanisms that result in such effects are still unclear. Further systematic investigation of the dissipation of vibrational energy by CO:CH$_3$OH ice mixtures with various ratios are warranted to fully understand these observations.

Both irradiations at 3.07 and 4.67 μm lead mainly to a decrease in the area of the OH-stretching band of methanol, as well as a narrowing of its CO stretching mode. Comparatively, the irradiation at 3.07 μm results in a more complex difference spectrum, which shows methanol vibrational modes that do not follow a clear trend in overall band shift nor width change. Furthermore, despite both ices containing the same column density of CO molecules, the higher abundance of surrounding CH$_3$OH species in the methanol-rich ice results in more intense changes to the CO band, even upon irradiation at 4.67 μm. As was observed by Cup-

pen *et al.* (2022) in H_2O ices, it is likely that the higher fraction of hydrogen-bonded species in the CH_3OH-rich mixture facilitates the vibrational energy transfer in comparison to the CO-rich counterpart, thus resulting in more intense spectral changes. In both ice mixtures, irradiations at the CH-stretching bands of methanol (not shown) yield similar changes to the other modes, but less intense.

Fredon *et al.* (2021) have explored the dissipation of different types of energy (i.e., vibrational, rotational and translational) by admolecules on top of an ASW surface using molecular dynamics simulations. They observed that the distribution of vibrational energy among the species' vibrational modes heavily impacts the energy dissipation channels, in agreement with our experimental results and those of previous IR-FEL exposure works (Noble *et al.* 2020; Ioppolo *et al.* 2022; Coussan *et al.* 2022; Cuppen *et al.* 2022). They also concluded that the dissipation of vibrational energy from the admolecule to the surface occurs through the excitation of a surface-admolecule bond. Thus, intermolecular interactions clearly play a key role in this process and this is corroborated by our experimental results. Further theoretical works on the dissipation of vibrational energy in ice mixtures are needed to fully understand the profile changes observed in Figure 3.6.

As for the CO-rich case, the irradiation spectrum of the methanol-rich ice at 9.62 μm is best reproduced by the corresponding TPD difference spectrum between 25 and 20 K. Yet, neither the band profiles nor the relative intensities can satisfactorily match that of the 9.62 μm irradiation spectrum, which displays more negative features than the TPD control experiment overall. This indirectly implies that consumption of the ice material should take place, for instance, through the photodesorption of CO, CH_3OH, or both. We do not detect any new signals in the IR spectra after irradiation, and therefore IR-induced photochemistry is unlikely to contribute to this effect. Additionally, the irradiations at 3.07 μm and 4.67 μm yield difference spectra that cannot be reproduced by any combination of the TPD control spectra and, thus, it must be dominated by a process other than extended heating.

3.3.3.2 Photodesorpion

As discussed above, the 9.62 μm difference spectrum of the methanol-rich mixture hints at the possibility of photodesorption taking place. We further investigate this hypothesis by performing successive FEL five-minute exposures at 9.62 μm on a same spot and varying the power settings. For the first irradiation, the $\sim$60 mJ beam is attenuated by 5 dB to yield a total power of $\sim$20 mJ. The second irradiation is performed at the full beam power of $\sim$60 mJ. The resulting difference IR spectra and corresponding QMS data are presented in Figure 3.7.

The difference spectrum of the first irradiation is consistent with the 9.62 μm irradiation spectrum shown in the lower panel of Figure 3.6, which was performed at similar conditions. In the case of UV experiments, photo-induced codesorption (i.e., the excitation of one species leading to the desorption of another) has been observed in the past for $CO:N_2$ and $CO:CO_2$ ice mixtures (Bertin *et al.* 2013; Fillion *et al.* 2014), but did not proceed following the excitation of CO in $CO:CH_3OH$ mixtures (Bertin *et al.* 2016). In contrast, both CH_3OH and CO seem to potentially desorb from the ice to some extent upon IR excitation of methanol, given by the decrease in the intensity of their vibrational modes after the exposure to the free-electron laser. This desorption, however, is expected to be small, as no signals of CO nor CH_3OH were detected in the QMS (see the right panel in Figure 3.7). From the areas of the negative peaks in the IR difference spectrum, we estimated an absolute loss in column density of $\sim 1.1 \times 10^{15}$ and $\sim 0.6 \times 10^{15}$ molecules cm^{-2} for CO and CH_3OH, respectively. Upon increasing the beam power to its highest attainable value of $\sim$60 mJ, the second irradiation results in a difference spectrum with much more pronounced features. The CO stretching mode decreases in intensity drastically, as shown by its prominently negative peak. Moreover, we detected an increase in the mass signal of CO clearly above noise level upon the start of the irradiation. Comparatively, no increase in mass signal was detected for CH_3OH (not shown),
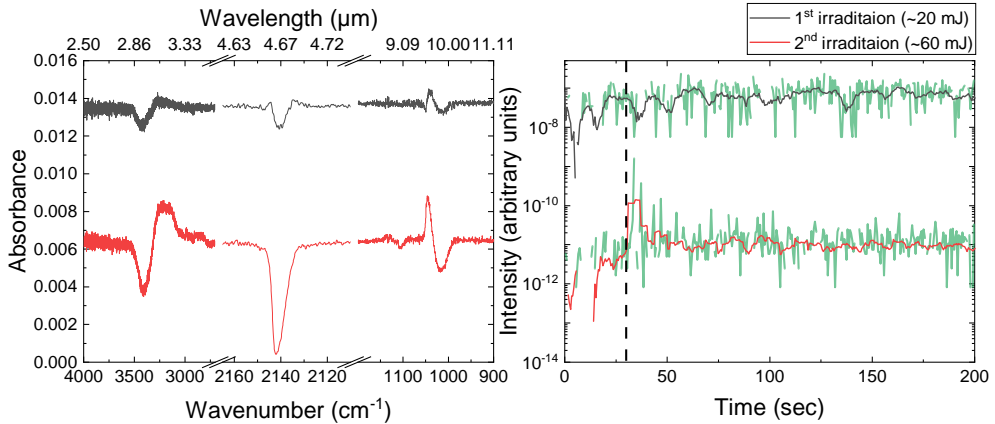
Figure 3.7: IR and QMS data obtained for two successive 9.62 μm FEL exposures of the methanol-rich ice performed at the same substrate position (i.e., without moving the translation stage) and at 20 K. The first (black) irradiation was attenuated to a power of $\sim$20 mJ, whereas the second (red) is performed at the full attainable power of $\sim$60 mJ. Left panel: Difference of the spectra acquired before and after the irradiations. The spectra are offset for clarity. Right panel: Superposition of the QMS data for the mass signal of CO (m/z = 28) measured concomitantly to the IR spectra during the FEL exposures (green lines) and their corresponding smoothed signal (black and red lines). The dashed line indicates the beginning of the irradiations.

and no new signals were observed in the IR spectrum. These two techniques together confirm the IR-induced photodesorption of CO from the methanol-rich ice. The negative peaks in the IR difference spectrum after the five-minute irradiation yield CO and CH_3OH absolute losses, respectively, of $\sim 8.7 \times 10^{15}$ and $\sim 1.3 \times 10^{15}$ molecules cm^{-2} for a fluence of $\sim 9.2 \times 10^{22}$ photons cm^{-2}. This corresponds to photodesorption rates of $\sim (9 \pm 3) \times 10^{-8}$ molecules photon^{-1} and $\sim (1.4 \pm 0.4) \times 10^{-8}$ molecules photon^{-1}, respectively. The former is $\sim$ 8x higher than the estimated photodesorption rate of pure CO, whereas the latter is $\sim$ 2x lower than pure CH_3OH. Since the irradiation frequency (9.62 μm) is on resonance with the ν_8 vibrational mode of CH_3OH, its energy dissipation mechanisms must lead to the desorption of CO in a more effective way than by direct vibrational excitation. This can happen, for instance, as a result of the reorganization of the methanol species towards a more stable configuration, which might spatially force CO species out of the ice. Alternatively, energy transfer effects between interacting neighboring CO and CH_3OH could also play a part in the sublimation of CO; for example, through the higher density of H-bond interactions among species in a CH_3OH-rich ice. In contrast, the photodesorption of methanol becomes less effective in the mixture than in the pure ice. These hypotheses will be investigated more deeply in future IR-FEL studies with interstellar ice analogues.

3.4 Astrophysical implications

In this work we have focused on the IR irradiation of interstellar ice analogues. We observe that, upon resonant vibrational irradiation, the ices of pure CO, pure CH_3OH, and mixtures of the two will generally undergo restructuring towards a more compact configuration as a result of vibrational energy dissipation. Thus, even in regions with low typical temperatures (such as dense molecular clouds), we would nonetheless expect the icy grains to contain some

degree of organization, either as a result of IR photon absorption or other phenomena leading to vibrational excitation in the ice. This could potentially influence not only the IR band profiles of the species in the mantle, but also their diffusion, adsorption, desorption, and reaction rates, which in turn can significantly impact astrochemical models and observations. Evidently, the extent of this effect strongly depends on how localized the changes are in the ice and how frequently it is being processed. The implications of this will therefore be increasingly intense in regions with higher radiation fluxes.

We also provide compelling evidence of the desorption of carbon monoxide induced by both vibrationally excited CO and CH_3OH molecules, as well as the IR-induced photodesorption of pure CH_3OH ice. Those species are the main constituents of the apolar ice layer that shrouds interstellar dust grains and therefore their photoprocesses are of great relevance to the chemistry of the interstellar medium. Given the available specific fluxes of IR photons with ~4.7 and ~9.6 μm inside interstellar clouds: $\sim 3 \times 10^9$ and $\sim 4 \times 10^8$ photons cm^{-2} s^{-1}, respectively (Mathis *et al.* 1983), and the upper limits to the photodesorption rates for pure aCO and CH_3OH ices estimated here, we derived tentative IR-induced photodesorption efficiencies of $\sim 3.3 \times 10^1$ molecules cm^{-2} s^{-1} for carbon monoxide and $\sim 1.2 \times 10^1$ molecules cm^{-2} s^{-1} for methanol in molecular cloud conditions. Comparatively, the total UV flux (i.e., integrated for all frequencies) inside molecular clouds is estimated to be on the order of $\sim 10^4$ photons cm^{-2} s^{-1} (Cecchi-Pestellini & Aiello 1992). When multiplied by the derived UV-induced non-dissociative photodesorption rates of CO and CH_3OH, this result yields respective efficiencies of $\sim (1.4 - 89) \times 10^1$ and $\sim 1.0 \times 10^{-1}$ molecules cm^{-2} s^{-1}. These values are summarized in Table 3.2. Notably, the UV-induced photodesorption efficiencies for CO are comparable to the IR-induced counterparts and for CH_3OH, they are two orders of magnitude lower. The former values are, on the one hand, presented as upper limits due to the utilization of transmission instead of reflection band strengths to derive the photodesorption rates. On the other hand, the fact that the specific IR fluxes at the species' peak absorption frequencies (instead of the integrated flux over the IR absorption width) are used in the calculations leads to an underestimation of the photodesorption efficiencies. The values listed in Table 3.2 should be considered tentative and a more thorough quantification of such efficiencies is warranted.

A caveat to these estimations is that the density of excitations (i.e., the number of simultaneously excited species in the ice) is considerably higher in laboratory experiments compared to the interstellar medium, which could play a part in the mechanisms that lead to IR-induced desorption. Still, only ~0.1% of the species in the ice are estimated to be excited per IR-FEL pulse, and therefore they should be sufficiently diluted that their interactions will have a minor effect. Moreover, the total photon fluence employed here correspond to $10^6 - 10^7$ yrs of exposure in interstellar conditions, thus within molecular cloud timescales. Therefore, we expect that IR-induced photodesorption can greatly affect the abundance of CO and CH_3OH in both the solid and gas phase, and we advise for this aspect to be taken into consideration when modeling the chemistry of interstellar environments. In particular, IR-induced photodesorption can potentially lead to an enhanced abundance of larger species, possibly even COMs, being preserved as they are ejected to the gas-phase from the ice, since the lower-energy IR photons are less likely to result in dissociation compared to UV rays. This could then help explain the observed abundances of CH_3OH in the gas phase. More systematic works focused on the quantification of the IR-induced photodesorption rates of interstellar ice analogues are evidently of high interest and more research is needed, both to learn about the processing taking place at a molecular level and to extrapolate these findings to interstellar environments and timescales.

Table 3.2: Comparison of the estimated fluxes, desorption rates, and desorption efficiencies of CH_3OH and CO species induced by IR and UV photons.

		Interstellar flux (photons cm^{-2} s^{-1})	Rate (molecules photon^{-1})	Estimated efficiency (molecules cm^{-2} s^{-1})
CO	IR	$> 3 \times 10^9$ [a]	$\lesssim (1.1 \pm 0.3) \times 10^{-8}$ [c]	$\sim 3.3 \times 10^1$
	UV	$\sim 1 \times 10^4$ [b]	$\sim (0.14 - 8.9) \times 10^{-2}$ [d]	$\sim (1.4 - 89) \times 10^1$
CH_3OH	IR	$> 4 \times 10^8$ [a]	$\lesssim (3 \pm 1) \times 10^{-8}$ [c]	$\sim 1.2 \times 10^1$
	UV	$\sim 1 \times 10^4$ [b]	$\sim 1 \times 10^{-5}$ [e]	$\sim 1.0 \times 10^{-1}$

[a] Mathis $et\ al.$ (1983).
[b] Cecchi-Pestellini & Aiello (1992).
[c] This work.
[d] Öberg $et\ al.$ (2007); Muñoz Caro $et\ al.$ (2010); Fayolle $et\ al.$ (2011); Chen $et\ al.$ (2014); Paardekooper $et\ al.$ (2016).
[e] Bertin $et\ al.$ (2016); Cruz-Diaz $et\ al.$ (2016).

3.5   Conclusions

In the present work, we use FELIX-2 with the LISA end station at the HFML-FELIX Laboratory to perform selective MIR irradiations of CO and CH_3OH ices, as well as mixtures of the two, under interstellar conditions. The results are monitored using both reflection-absorption IR spectroscopy and mass spectrometry techniques. Additionally, control temperature-programmed desorption experiments on identical ices are performed to assist in the data interpretation. This study, using both resonant and off-resonance IR irradiation, offers tools to elucidate the physico-chemical processes that take place in the ice as a result of vibrational energy dissipation. Our main findings are summarized below:

- The vibrational excitation of the species in the ice and the subsequent dissipation of this excess energy affects the ice morphology.

- The ices explored here are restructured to a more organized configuration upon irradiation.

- In the case of pure CH_3OH ice, most of the changes in the irradiation spectra can be attributed to restructuring. However, for the pure CO ices and mixtures with methanol, additional phenomena such as photodesorption are needed to fully explain the difference spectra.

- The changes in band shape upon irradiation are highly dependent on the FEL wavelength and the composition of the ice. Thus, the excited vibrational mode and the surrounding species must strongly affect the mechanism through which the excess vibrational energy is dissipated.

- We find compelling evidence of IR-induced photodesorption of pure CO ice with a tentative estimated rate of $\sim (1.1 \pm 0.3) \times 10^{-8}$ molecules photon^{-1} upon excitation of its stretching mode. The photodesorption of CH_3OH is also suggested upon excitation of it ν_8 mode, with a tentative estimated rate of $\sim (3 \pm 1) \times 10^{-8}$ molecules photon^{-1}. Both (low) rates yield desorption efficiencies up to two orders of magnitude higher than UV-induced counterparts inside molecular clouds, because of the much higher IR fluxes in such environments. So even though the absolute rate is lower in the IR, the overall effect is expected to be around the same order of magnitude or greater.

- Furthermore, the indirect photodesorption of CO upon IR irradiation on resonance with CH_3OH is strongly suggested.

Given the influence of the ice morphology and composition in the rates of the processes that take place on icy grains, chemical models that involve solid-phase reactions would especially benefit from the inclusion of vibrational-energy dissipation mechanisms into the network. The tentative rates presented here will be further investigated in a follow-up study whereby time is made available to derive accurate absorption cross-sections for the applied reflection mode settings.

3.6   Acknowledgements

3.7 Appendix

3.7.1 Control IR spectra

The difference IR spectra of the CO, CH_3OH, $CO:CH_3OH = 1:0.3$, and $CO:CH_3OH = 1:3$ ices acquired during the control TPD experiments are shown in Figures 3.8, 3.9, 3.10, and 3.11, respectively. Differences are taken between a temperature T (as labeled in the legend) and the deposition temperature of 20 K.
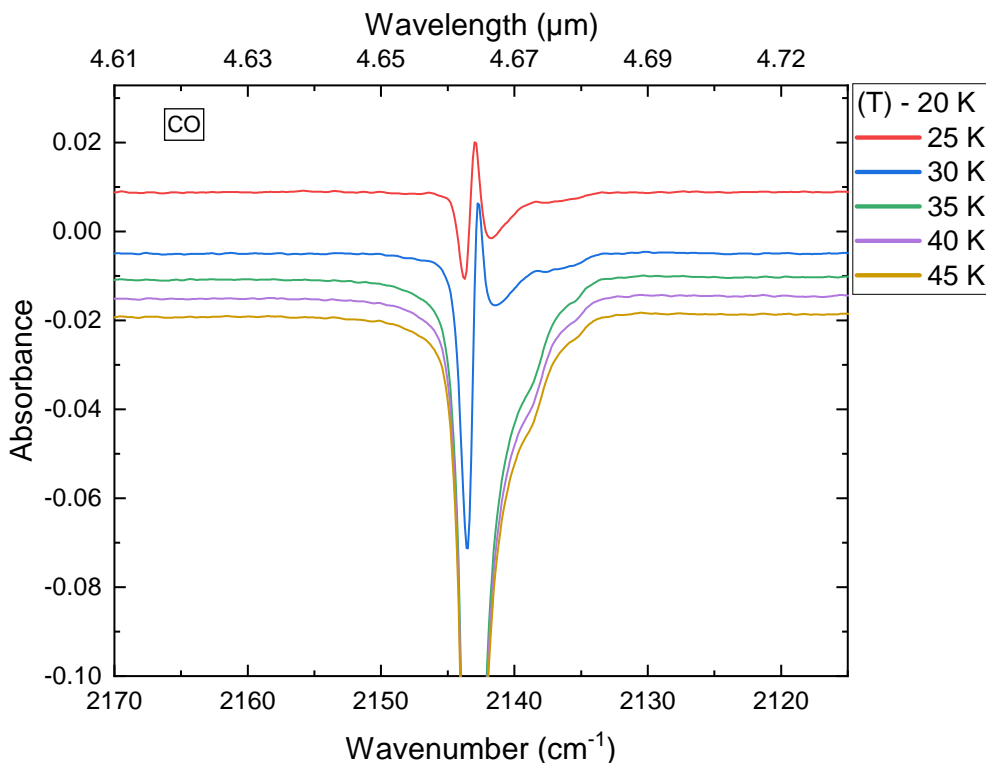
Figure 3.8: Control IR difference spectra of pure CO ice acquired during TPD.

3.7.2 aCO ice stabilization

The difference IR spectra before and after irradiation of aCO ice corrected for stabilization are shown in Figure 3.12. The correction is made by subtracting the signal due to ice stabi-
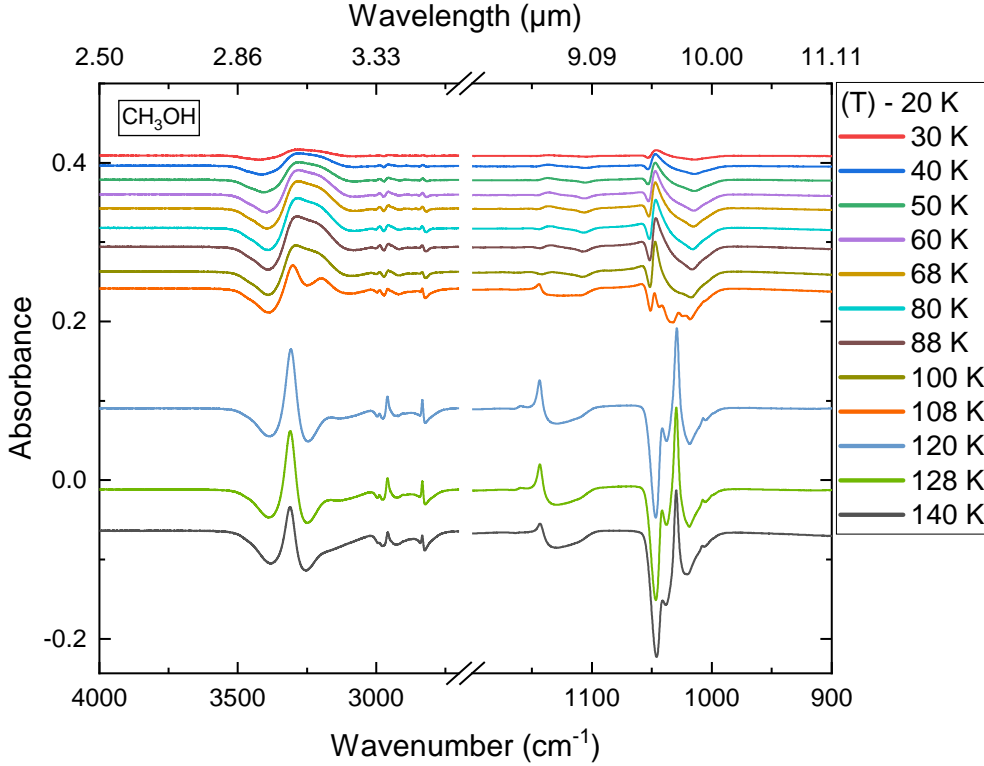
Figure 3.9: Control IR difference spectra of pure CH$_3$OH ice acquired during TPD.

lization,as obtained from two spectra taken ten minutes apart and without IR-FEL exposure, from the irradiation difference spectra.

3.7.3 Repeated irradiations on ice mixtures

The irradiations of the ice mixtures were performed a total of three times in a same substrate position each, namely, the translator stage was only used when the irradiation wavelength was changed. The difference spectra of the CO-rich and CH$_3$OH-rich ice mixtures are shown in Figures 3.13 and 3.14, respectively. In the CO-rich case, the ice becomes saturated after the first irradiation at each frequency, and no significant effect (besides ice stabilization) can be seen in the repeated measurements. The irradiation at 9.62 μm was performed significantly later in the experiment shift, in which case the ice had had appreciably more time to stabilize, hence the smaller signal in its second and third measurements. In the CH$_3$OH-rich ice case, saturation takes higher fluences to occur and the effects of the IR-FEL are still observable in the repeated irradiations.
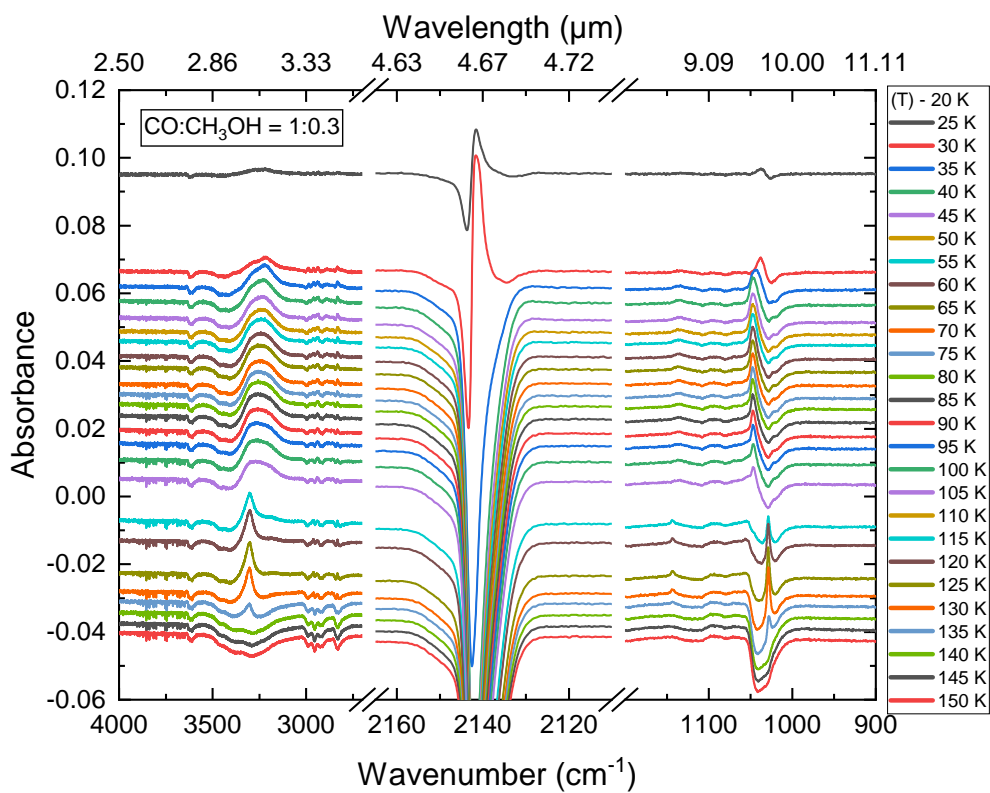
Figure 3.10: Control IR difference spectra of the CO:CH$_3$OH = 1:0.3 ice mixture acquired during TPD.
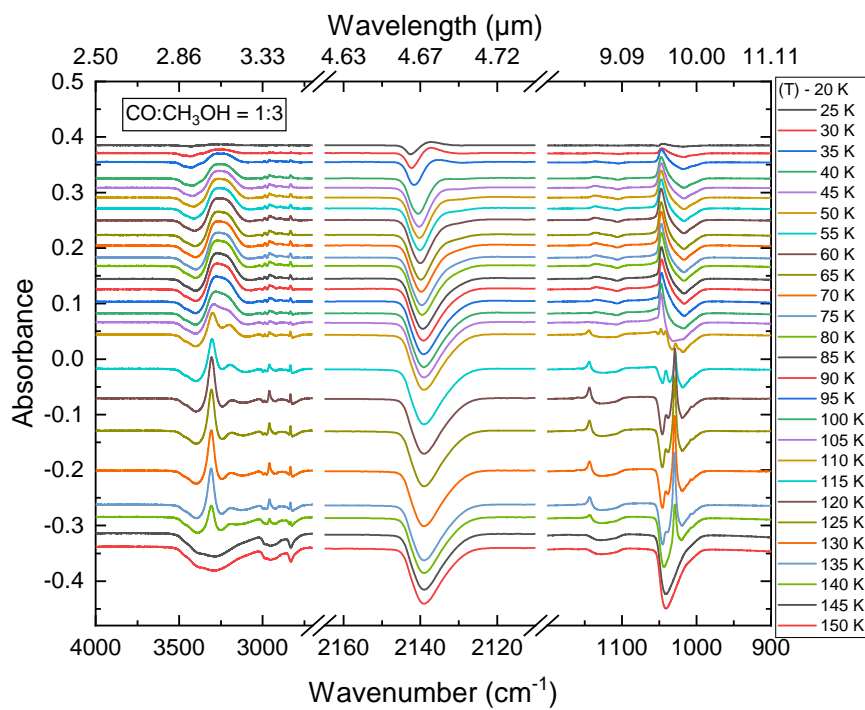
Figure 3.11: Control IR difference spectra of the CO:CH$_3$OH = 1:3 ice mixture acquired during TPD.
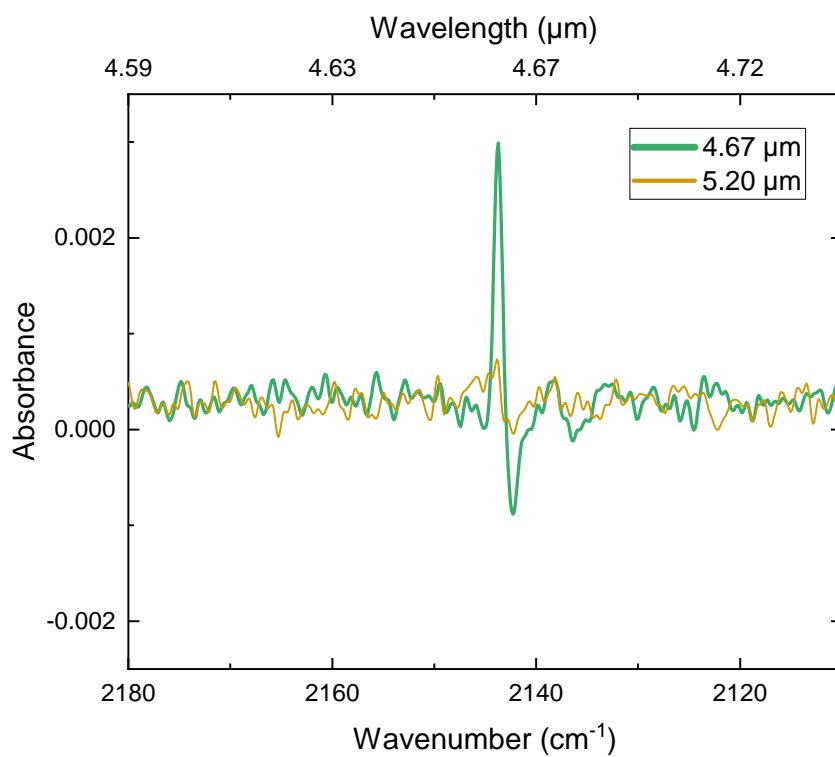
Figure 3.12: Difference spectra obtained before and after ten minutes of IR-FEL irradiation on aCO ice at 20 K, corrected for ice stabilization.
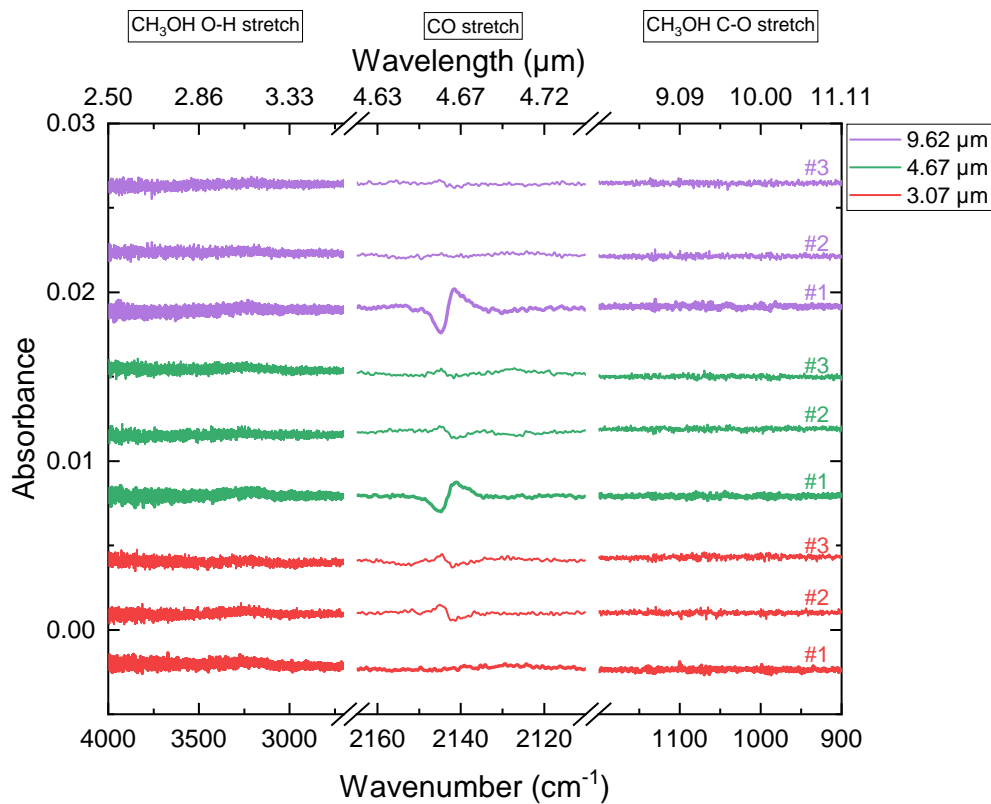
Figure 3.13: Difference irradiation spectra of repeated measurements on the CO-rich ice mixture. Irradiations at the same frequency were performed at the same substrate position and the ice is already saturated on each second and third measurements.
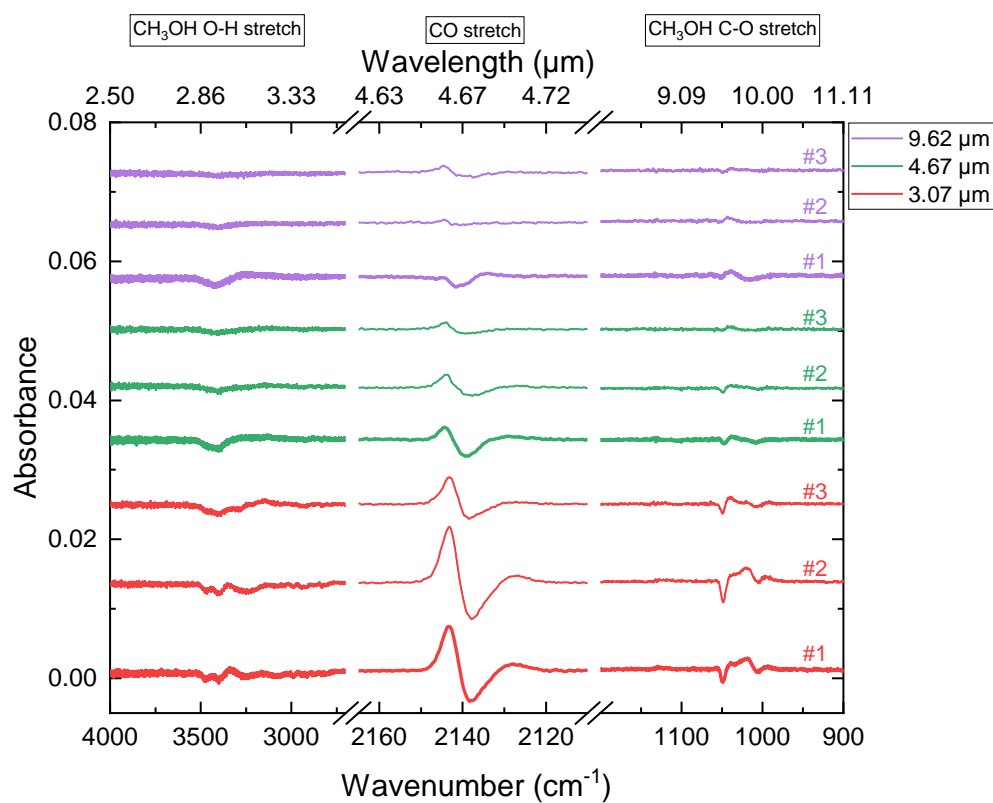
Figure 3.14: Difference irradiation spectra of repeated measurements on the CH_3OH-rich ice mixture. Irradiations at the same frequency were performed at the same substrate position.

4. INTERACTION OF H_2S WITH H ATOMS ON GRAIN SURFACES UNDER MOLECULAR CLOUD CONDITIONS

Hydrogen sulfide (H_2S) is thought to be efficiently formed on grain surfaces through the successive hydrogenation of sulfur atoms. Its non-detection so far in astronomical observations of icy dust mantles thus indicates that effective destruction pathways must play a significant role in its interstellar abundance. While chemical desorption has been shown to remove H_2S very efficiently from the solid phase, in line with H_2S gas-phase detections, possible ice chemistry triggered by the related HS radical have been largely disregarded so far, despite it being an essential intermediate in the H_2S + H reaction scheme. We aim to thoroughly investigate the fate of H_2S upon H-atom impact under molecular cloud conditions, providing a comprehensive analysis combined with detailed quantification of both the chemical desorption and ice chemistry that ensues. We performed experiments in an ultrahigh vacuum chamber at temperatures between $10 - 16$ K in order to investigate the reactions between H_2S molecules and H atoms on interstellar ice analogs. The changes in the solid phase during H-atom bombardment were monitored in situ by means of reflection absorption infrared spectroscopy (RAIRS), and desorbed species were complementarily measured with a quadrupole mass spectrometer (QMS). We confirmed the formation of H_2S_2 via reactions involving H_2S + H and quantified its formation cross section under the employed experimental conditions. Additionally, we directly assessed the chemical desorption of H_2S by measuring the gas-phase desorption signals with the QMS, providing unambiguous desorption cross sections. Chemical desorption of H_2S_2 was not observed. The relative decrease of H_2S ices by chemical desorption changed from $\sim 85\%$ to $\sim 74\%$ between temperatures of 10 and 16 K, while the decrease as the result of H_2S_2 formation was enhanced from $\sim 15\%$ to $\sim 26\%$, suggesting an increasingly relevant sulfur chemistry induced by HS radicals at warmer environments. The astronomical implications are further discussed.

4.1   Introduction

Interstellar dense clouds are known for harboring a lavish chemical inventory spanning from simple ions and radicals to a large variety of complex organic molecules (COMs). At the temperatures and densities typical of these environments (T = $10 - 20$ K and $\rho = 10^4 - 10^5$ cm^{-3}, respectively; van Dishoeck *et al.* 2013), thermal desorption cannot take place, and most species—except for H_2 and He—should be fully depleted into interstellar icy dust grains (Collings *et al.* 2004). Yet, observations with radio-astronomical facilities have detected copious amounts of COMs such as methanol (CH_3OH), acetaldehyde (CH_3CHO), methyl formate (CH_3OCHO), among others, in the gas phase toward dense and cold clouds (see, e.g., Öberg *et al.* 2010a; Bacmann *et al.* 2012; Cernicharo *et al.* 2012; Jiménez-Serra *et al.* 2016; Scibelli & Shirley 2020). Especially given that these hydrogen-rich species are most likely formed in the ice mantles that shroud interstellar dust grains, such observations reveal that non-thermal desorption mechanisms must play a significant role in balancing gas- and solid-phase chemical abundances. For smaller species, such as CO, photodesorption induced by UV photons through the (in-)direct desorption induced by electronic transitions (DIET) mechanism is an efficient desorption process that could explain, in part, the observed abundances of gaseous species (Öberg *et al.* 2007; Muñoz Caro *et al.* 2010; Fayolle *et al.* 2011; Chen *et al.* 2014; Paardekooper *et al.* 2016; Sie *et al.* 2022). However, larger molecules are increasingly susceptible to fragmentation upon UV photon impact, which can then be followed by photochemical desorption (Bertin *et al.* 2016; Cruz-Diaz *et al.* 2016). Moreover, recent studies have shown that the photodesorption of CO and CH_3OH ices induced by IR photons might be astronomically relevant (Santos *et al.* 2023a), shedding light on potential new processes to help explain gas-phase abundances of COMs.

Complementarily, another promising non-thermal desorption mechanism that proceeds without fragmentation is the so-called chemical desorption, or reactive desorption. This phenomenon involves the ejection of products upon formation in an exothermic reaction. It has been consistently shown to improve gas-phase abundances predicted by chemical models (Garrod *et al.* 2006, 2007; Cazaux *et al.* 2010; Vasyunin & Herbst 2013; Vidal *et al.* 2017; Cuppen *et al.* 2017; Fredon *et al.* 2021) and has been explored in the laboratory for a range of astronomically relevant species and substrates (Dulieu *et al.* 2013; Minissale & Dulieu 2014; Minissale *et al.* 2016b; He *et al.* 2017; Chuang *et al.* 2018; Oba *et al.* 2018, 2019; Nguyen *et al.* 2020, 2021a). Yet, efforts to experimentally quantify chemical desorption efficiencies are still limited, and modelers typically assume a universal input value between 0.01 and 0.1 (Garrod *et al.* 2007; Cuppen *et al.* 2017).

Among the species whose observed abundances cannot be explained by gas-phase processes alone, hydrogen sulfide (H_2S) is perhaps one of the most broadly studied in the recent literature. It has been detected toward various interstellar sources and in the comae of comets (Thaddeus *et al.* 1972; Minh *et al.* 1989; van Dishoeck *et al.* 1995; Hatchell *et al.* 1998; Vastel *et al.* 2003; Wakelam *et al.* 2004; Neufeld *et al.* 2015; Le Roy *et al.* 2015; Biver *et al.* 2015; Calmonte *et al.* 2016; Phuong *et al.* 2018; Navarro-Almaida *et al.* 2020). It was also tentatively identified on the surface of the Galilean satellites Io, Ganymede, and Callisto (Nash & Howell 1989; McCord *et al.* 1998). However, solid-phase interstellar H_2S has not been unequivocally detected yet, and only upper limits are available in ices so far (Smith 1991; van der Tak *et al.* 2003; Jiménez-Escobar & Muñoz Caro 2011a).

The main proposed route to form H_2S is through the successive hydrogenation of sulfur on icy grains (S $\xrightarrow{+H}$ HS $\xrightarrow{+H}$ H_2S). Once formed, H_2S can undergo an H-induced abstraction reaction to form the radical HS

$$H_2S \xrightarrow{+H} HS + H_2 \tag{4.1}$$

by quantum tunneling through an effective barrier of ~ 1500 K (Lamberts & Kästner 2017). The HS radical can subsequently be hydrogenated to reform H_2S. Alternatively, H_2S can also be energetically processed to form species such as H_2S_2 and a wide range of S allotropes

(Moore *et al.* 2007; Garozzo *et al.* 2010; Jiménez-Escobar & Muñoz Caro 2011a; Jiménez-Escobar *et al.* 2014a; Chen *et al.* 2015; Shingledecker *et al.* 2020; Cazaux *et al.* 2022; Mifsud *et al.* 2022).

Laboratory studies have reported the hydrogenation of a thin layer (0.7 monolayers; ML) of H_2S on top of both porous and non-porous amorphous solid water as well as on top of polycrystalline water ice (Oba *et al.* 2018, 2019). The experimental data has demonstrated that the excess energy generated by the cycle of H-induced abstraction and H_2S reformation results in chemical desorption with high effectiveness. Kinetic Monte Carlo simulations of such experiments suggest the chemical desorption efficiency to be of $\sim 3\%$ per hydrogenation event (Furuya *et al.* 2022). Contrary to energetically processed ices, however, new species formed by the HS radicals were not reported—possibly due to the relatively low abundance of H_2S species in their experiments. In this work, we aim to further constrain the chemical desorption efficiency of H_2S by incorporating the chemistry involving HS radicals resulting from the (de-)hydrogenation of hydrogen sulfide, in particular to form disulfane (H_2S_2). Moreover, for the first time, we present a comprehensive experimental analysis of the H_2S chemical desorption phenomenon supported by a strong gas-solid correlation using infrared spectroscopy and mass spectrometry techniques concomitantly.

The experimental setup and techniques employed are described in Section 4.2. The results are shown and discussed in Section 4.3, where we provide effective cross sections for the chemical desorption of H_2S and H_2S_2 formation. In Section 4.4, the astrochemical implications of this work are considered, and our main findings are summarized in Section 4.5.

4.2   Experimental methods

We performed our experiments using the ultrahigh vacuum setup SURFRESIDE,[3] which has been described in detail elsewhere (Ioppolo *et al.* 2013; Qasim *et al.* 2020b). Thus, we only provide the relevant information in this work. The main chamber operates at a base pressure of $\sim 5 \times 10^{-10}$ mbar. In its center is a gold-plated copper substrate mounted on the tip of a closed cycle He cryostat. The temperature of the substrate can vary between 8 and 450 K through resistive heating and is monitored by two silicon diode sensors with a relative accuracy of 0.5 K. Ices of H_2S (Linde, purity 99.5%) are deposited either prior to or simultaneously with H atoms generated by a hydrogen atom beam source (HABS; Tschersich 2000) during what is referred to in this work as pre- and codeposition experiments, respectively. The hydrogen atoms are cooled to room temperature through collision with a nose-shaped quartz pipe before reaching the substrate. As described in detail by Ioppolo *et al.* (2013), the determination of the absolute H-atom flux is done by placing a quadrupole mass spectrometer (QMS) at the exact position of the substrate and monitoring its signal in a series of systematic experiments with varying filament temperatures and inlet gas flow. Such a measurement is not a trivial procedure, but it serves as a reference guide for regular calibrations of the relative H flux at different operation conditions through the HO_2 peak intensity formed in the barrierless reaction $H + O_2 \rightarrow HO_2$. To infer the temperature-dependent kinetics of the processes explored in this work, we performed predeposition experiments at a range of temperatures of relevance to interstellar molecular clouds (10, 12, 14, and 16 K). Due to its low sticking coefficient at the studied temperatures, the presence of H_2 molecules on the ice (either incoming from the atom source or formed through H recombination) was not expected to significantly affect the outcome of our experiments (Watanabe & Kouchi 2002; Ioppolo *et al.* 2010).

Ice growth through vapor deposition is monitored by Fourier-transform reflection absorption infrared spectroscopy (FT-RAIRS). The IR spectra are acquired in the range of 700 to 4000 cm^{-1}, with a resolution of 1 cm^{-1}. Concurrently, species in the gas phase are ionized upon electron impact with 70 eV and recorded by a QMS. Once the depositions are finished, temperature-programmed desorption (TPD) experiments are performed by heating the sam-

ple at a ramping rate of 5 K min^{-1} while concomitantly monitoring the solid and gas phases with the RAIRS and QMS techniques, respectively.

The column densities (N_X) of the species in the ice are derived by converting the IR integrated absorbance ($\int Abs(\nu)d\nu$) to absolute abundance using a modified Beer-Lambert law:

$$N_X = \ln 10 \frac{\int Abs(\nu)d\nu}{A'(X)}, \tag{4.2}$$

where $A'(X)$ is the apparent absorption band strength of a given species. For H$_2$S, band strength values measured by infrared transmission spectroscopy are available in the literature. However, signals obtained in reflection mode are systematically higher than transmission counterparts due to substrate dipole couplings and a typically longer IR pathway in the ice. Thus, to ensure high accuracy in the derivation of the H$_2$S ice column density, we performed calibration experiments using the laser interference technique that yield a band strength value of $A'(\mathrm{H_2S})_{\sim 2553\ \mathrm{cm}^{-1}} \sim (4.7 \pm 0.1) \times 10^{-17}$ cm molecule^{-1} for our specific experimental settings (see Appendix 4.7.1).

Since direct determination of the H$_2$S$_2$ band strength is challenging, we estimate $A'(\mathrm{H_2S_2})$ in a similar way to what has been described by Cazaux *et al.* (2022). The column density ratio $(N_{\mathrm{H_2S_2}})/(N_{\mathrm{H_2S}})$ can be derived from the QMS data by the expression (Martín-Doménech *et al.* 2015)

$$\frac{N_{\mathrm{H_2S_2}}}{N_{\mathrm{H_2S}}} = \frac{A(66)}{A(34)} \cdot \frac{\sigma^+(\mathrm{H_2S})}{\sigma^+(\mathrm{H_2S_2})} \cdot \frac{I_F([\mathrm{H_2S}]^+)}{I_F([\mathrm{H_2S_2}]^+)} \cdot \frac{F_F(34)}{F_F(66)} \cdot \frac{S(34)}{S(66)}, \tag{4.3}$$

where $A(\mathrm{m/z})$ is the integrated area of a given mass fragment; $\sigma^+(X)$ is the molecule's electronic ionization cross section; $I_F(\mathrm{z})$ is the ionization fraction of charge z (in this work, corresponding to unity); $F_F(\mathrm{m/z})$ is the fragmentation fraction; and $S(\mathrm{m/z})$ is the sensitivity of the QMS at a specific mass. As there are no values for $\sigma^+(\mathrm{H_2S_2})$ reported in the literature, we estimated its value based on the molecule's polarizability volume ($\alpha(X)$) by the empirical correlation (Hudson *et al.* 2006; Bull *et al.* 2012):

$$\sigma^+_{\max}(X) = c \cdot \alpha(X), \tag{4.4}$$

where X denotes a given species and c is a correlation constant of 1.48 Å^{-1}. The maximum ionization cross section ($\sigma^+_{\max}$) of organic species typically occurs around 90 eV and varies only slightly ($< 5\%$) in intensity from ionizations with 70 eV (Hudson *et al.* 2003; Bull & Harland 2008). Thus, we utilized this method to derive both $\sigma^+(\mathrm{H_2S_2})$ and $\sigma^+(\mathrm{H_2S})$ from $\alpha(\mathrm{H_2S_2})$ and $\alpha(\mathrm{H_2S})$ as calculated by group additivity.[1] The $F_F(\mathrm{m/z})$ of the relevant mass fragments are inferred from the QMS data acquired during the TPD experiments after codeposition of H$_2$S and H, and we obtained the sensitivity from previous calibrations performed with the same setup (Chuang 2018). The employed values are summarized in Table 4.1.

By combining $(N_{\mathrm{H_2S_2}})/(N_{\mathrm{H_2S}})$ from Equation 4.3 and $N_{\mathrm{H_2S}}$ from Equation 4.2, one can obtain $N_{\mathrm{H_2S_2}}$, which in turn can be used to estimate $A'(\mathrm{H_2S_2})$ from the integrated absorbance area of the IR spectra:

$$A'(\mathrm{H_2S_2}) = \frac{\int Abs(\nu)d\nu}{N_{\mathrm{H_2S_2}}}. \tag{4.5}$$

The average between two independent experiments yields an estimated $A'(\mathrm{H_2S_2})_{\sim 2490\ \mathrm{cm}^{-1}} \sim (9.9 \pm 0.2) \times 10^{-17}$ cm molecule^{-1}.

---

[1]Values have been taken from the NIST Computational Chemistry Comparison and Benchmark Database (CCCBDB),
NIST Standard Reference Database Number 101,
http://cccbdb.nist.gov/.

Table 4.1: List of parameters used in the estimation of $A'(H_2S_2)$.

Species	α [Å^3] [a]	F_F (m/z) [b]	S (m/z) [b]
H_2S	3.776	0.52	0.28
H_2S_2	6.828	0.31	0.08

[a] CCCBDB

[b] Values are given for the molecular ions.

The details of the experiments performed in this work are summarized in Table 4.2. The relative errors of both H_2S and H fluxes are estimated to be $\sim 5\%$.

Table 4.2: Overview of the experiments performed in this work.

Experiment	T_{sample} (K)	H_2S flux (cm^{-2} s^{-1})	H flux (cm^{-2} s^{-1})	Time (min)
Codeposition experiments				
H_2S	10	$\sim 1 \times 10^{13}$		60
$H_2S + H$	10	$\sim 1 \times 10^{13}$	$\sim 8 \times 10^{12}$	60
Predeposition experiments				
$H_2S \rightarrow +H$	10	$\sim 1 \times 10^{13}$	$\sim 8 \times 10^{12}$	60 + 120
$H_2S \rightarrow +H$	12	$\sim 1 \times 10^{13}$	$\sim 8 \times 10^{12}$	60 + 120
$H_2S \rightarrow +H$	14	$\sim 1 \times 10^{13}$	$\sim 8 \times 10^{12}$	60 + 120
$H_2S \rightarrow +H$	16	$\sim 1 \times 10^{13}$	$\sim 8 \times 10^{12}$	60 + 120

4.3   Results and discussion

4.3.1   H$_2$S + H ice chemistry

The left panel of Figure 4.1 shows the spectra obtained after deposition of pure H_2S and codeposition of $H_2S + H$ at 10 K in the frequency region characteristic of SH stretching modes. A strong IR feature is observed at ~ 2553 cm^{-1}, corresponding to the ν_1 (symmetric) and ν_3 (anti-symmetric) SH stretching modes of H_2S. In comparison, when H atoms are also present, a new feature peaking at ~ 2490 cm^{-1} appears on the red wing of the $\nu_{1,3}$ mode of H_2S—consistent with the SH stretching band (ν_1, sym.; and ν_5, anti-sym.) of H_2S_2 (Isoniemi *et al.* 1999). During the TPD experiment performed after codepositing $H_2S + H$, the main bands at ~ 2553 cm^{-1} and ~ 2490 cm^{-1} fully disappear in the temperature ranges of $10-100$ K and $100-140$ K, respectively (Figure 4.1, right panel), which coincides with previously measured desorption temperatures of H_2S and H_2S_2 (Jiménez-Escobar & Muñoz Caro 2011a; Chen *et al.* 2015; Cazaux *et al.* 2022).

The assignments of H_2S and H_2S_2 are substantiated by their respective mass fragments induced by electron impact during the TPD experiments in Figures 4.2 and 4.3, respectively. As shown in Figure 4.2a, a desorption peak of fragments m/z = 32 and 34 can be observed at ~ 85 K in both H_2S and $H_2S + H$ cases, amounting to relative intensities consistent
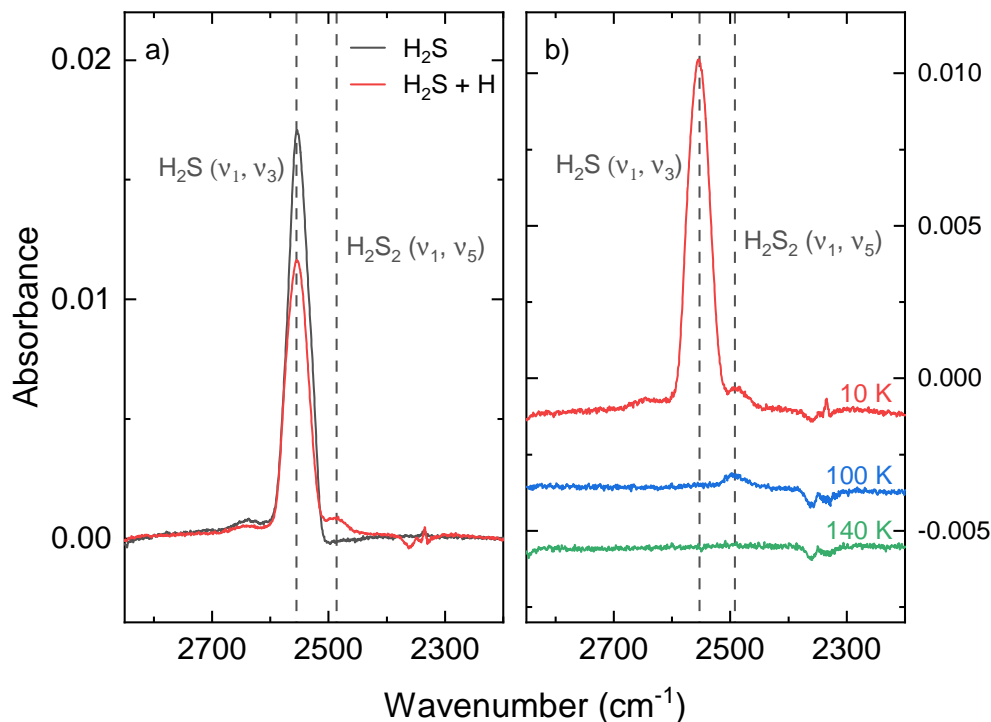
Figure 4.1: Infrared spectra of the codeposition experiments. Panel a): Comparison between the final infrared spectra after deposition of a pure H_2S ice (black) superimposed by the final spectrum after codeposition of H_2S and H atoms (red) with analogous experimental conditions. Panel b): Infrared spectra acquired during the warming up of the H_2S ice codeposited with H atoms, offset for clarity. In both panels, the assignments of the H_2S and H_2S_2 vibrational bands are shown with dashed lines.

with the standard for H_2S as provided by the NIST database.[2] This desorption temperature matches the disappearance of the ~ 2553 cm^{-1} bands in the IR spectra. In Figure 4.3, the desorption peak of the mass fragments associated with H_2S_2 is detected solely in the H_2S + H experiment at 126 K—coinciding with the disappearance of the feature at ~ 2490 cm^{-1} in the IR spectra. Thus, the assignment of the new peak as H_2S_2 is confirmed by both RAIRS and QMS techniques combined with TPD experiments. Given the lack of laboratory data on its mass fragmentation pattern, we provide for the first time—to the best of our knowledge—the relative intensities of m/z = 32, 34, 64, 65, and 66 as generated by 70 eV electron ionization of H_2S_2 and corrected for the sensitivity of the QMS in the right panel of Figure 4.3. The contribution from the $^{3}_{4}$S isotope (natural abundance of 4.29%) is included in the fragmentation pattern.

When H_2S is deposited simultaneously with H atoms, HS radicals formed by the hydrogen abstraction of H_2S (Reaction 4.1) can thus further associate either with H atoms, reforming H_2S, or with HS radicals, forming H_2S_2:

$$HS \xrightarrow{+H} H_2S \text{ (solid or gas)} \tag{4.6a}$$

$$HS + HS \rightarrow H_2S_2. \tag{4.6b}$$

---

[2]https://webbook.nist.gov/chemistry/
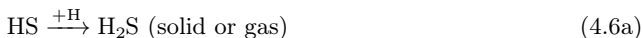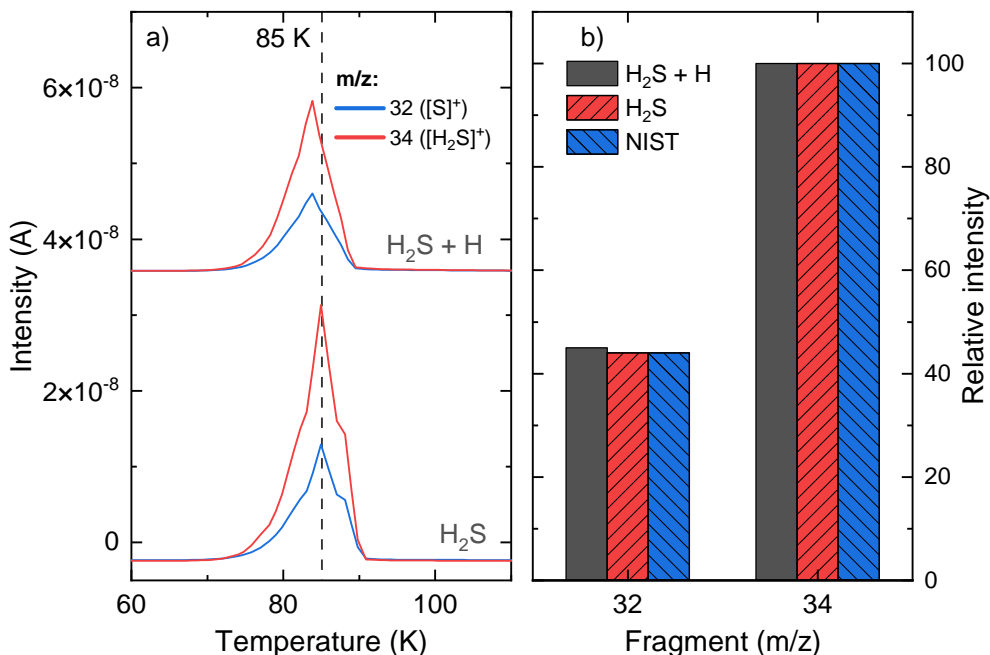
Figure 4.2: TPD-QMS results for the detection of H_2S. Panel a): TPD-QMS spectra of $m/z = 32$ (blue) and $m/z = 34$ (red) after deposition of a pure H_2S ice and codeposition of $H_2S + H$ with analogous experimental conditions. Spectra are offset for clarity and shown in the temperature range relevant to H_2S thermal desorption. Panel b): Comparison between the relative intensities of $m/z = 32$ and 34 desorbing at 85 K in both H_2S and $H_2S + H$ experiments together with the standard fragmentation pattern of H_2S from NIST.

Reaction 4.6a proceeds barrierlessly and can result in chemical desorption due to its high exothermicity ($\sim$ 6980 K, based on the gas-phase enthalpies of formation of reactants and products). Reaction 4.6b is also barrierless and has been proposed in previous studies on the energetic processing of H_2S-containing ices (Jiménez-Escobar & Muñoz Caro 2011a; Jiménez-Escobar *et al.* 2014a; Chen *et al.* 2015; Cazaux *et al.* 2022; Mifsud *et al.* 2022).

4.3.2   H-atom bombardment on H_2S ice

The left panels in Figures 4.1 and 4.2 show that the amount of H_2S ice after the codeposition experiment with H atoms is smaller than that of the pure ice deposition with the same experimental conditions, thus signaling that the interaction of H_2S with hydrogen leads to a net loss of material as a result of both Reactions 4.6a and 4.6b. While the efficiency of the former reaction has been explored in detail (Oba *et al.* 2018, 2019; Furuya *et al.* 2022), the contribution from H_2S_2 formation to depleting H_2S from the solid phase has not been considered so far. In this work, we explore the effectiveness of both reactions thoroughly and assess their respective relevance to the destruction of the H_2S ice.

To quantify the efficiencies of Reactions 4.6a and 4.6b, we monitored the abundance of H_2S and H_2S_2 as a function of H-atom fluence during predeposition experiments in which a deposited H_2S ice was subsequently bombarded by a constant H-atom flux. The difference spectra after the H-atom bombardment for 20, 40, and 60 minutes at 10 K together with the pure H_2S sample prior to hydrogenation are shown in Figure 4.4. Both H_2S and H_2S_2 features can be resolved in the difference spectra by deconvolution using Gaussian profiles,
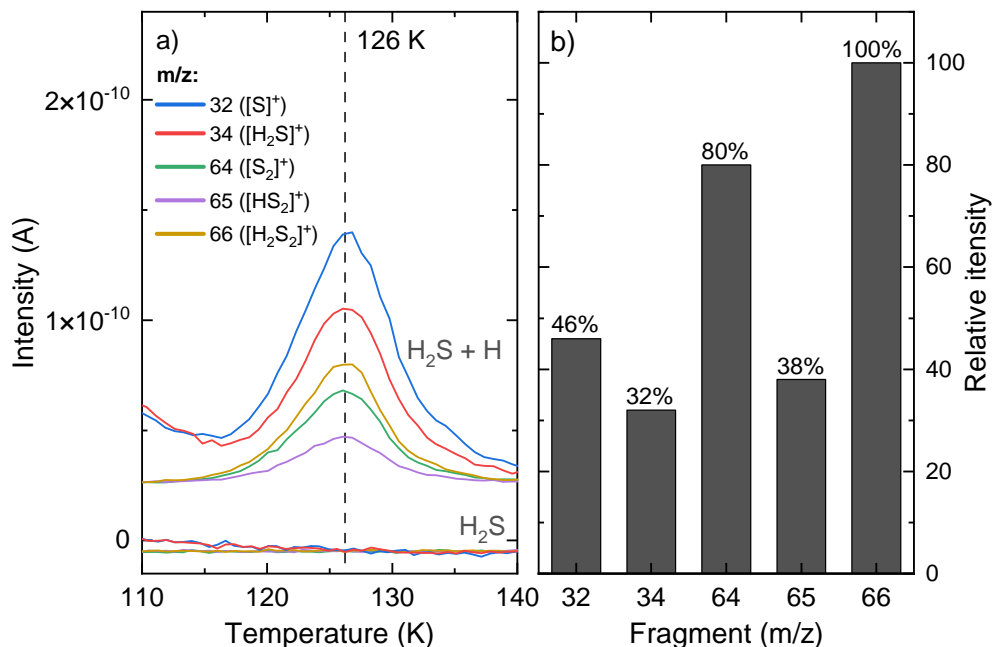
Figure 4.3: TPD-QMS results for the detections of H_2S_2. Panel a): TPD-QMS spectra of m/z = 32 (blue), 34 (red), 64 (green), 65 (purple), and 66 (yellow) after deposition of a pure H_2S ice and codeposition of H_2S + H with analogous experimental conditions. Spectra are offset for clarity and shown in the temperature range relevant to H_2S_2 thermal desorption. Panel b): Mass fragmentation pattern of H_2S_2 generated by 70 eV electron ionization as measured in this work.

as shown by the superimposing lines. The interaction with H atoms leads to a loss of H_2S, as evinced by the decrease in its SH stretching band at ~ 2553 cm^{-1} (purple dashed line). Concomitantly, a feature due to the SH stretching modes of H_2S_2 appears on the red wing of the H_2S band and becomes increasingly evident at longer H-atom exposure times (yellow dashed line). The results of the predeposition experiments are therefore consistent with the codeposition counterparts, and they indicate a non-negligible contribution to the H_2S depletion from Reaction 4.6b. In contrast, neither Oba *et al.* (2018) nor Oba *et al.* (2019) have detected any other sulfur-bearing species apart from hydrogen sulfide during similar $H_2S \rightarrow +H$ predepositions at $10 - 30$ K followed by TPD experiments. Such a discrepancy might be due to the limited abundance of H_2S in the aforementioned works (0.7 ML) compared to the present experiments ($\sim$20 ML), as they might not yield product amounts above the instrumental detection limit.

To directly probe the chemical desorption of H_2S as a result of reactions with H atoms, we monitored the gas-phase signals via the relevant mass fragments (m/z = 34, $[H_2S]^+$; m/z = 33, $[HS]^+$) with a QMS during the H-exposure experiments. In Figure 4.5, data acquired by both the RAIRS and QMS techniques while intermittently bombarding the predeposited H_2S ice with H atoms (i.e., in three intervals of 20 minutes, ending with 60 minutes) are presented in the upper and lower panels, respectively. In the first 20 minutes of bombardment, we observed a steep decrease in the H_2S IR absorbance area coinciding with an abrupt increase in the m/z = 34 readout by the QMS. Once bombardment was stopped, the area of the H_2S band remained fairly constant, and the QMS signal dropped to the base value. Such results provide unambiguous evidence of the effective chemical desorption of H_2S upon H-atom

exposure. Following the first bombardment, a similar behavior was observed through both RAIRS and QMS techniques for the rest of the exposure periods, albeit to a diminishing extent of H_2S loss due to saturation of the ice layer within the penetration depth of the hydrogen atoms—typically of a few monolayers (see, e.g., Watanabe & Kouchi 2008; Fuchs *et al.* 2009). No increase in signal was detected for $m/z = 66$ ($[H_2S_2]^+$), indicating that relative to H_2S, disulfane does not undergo chemical desorption effectively upon formation. This is quite expected, as H_2S_2 contains more degrees of freedom and, as inferred from its higher desorption temperature, a higher binding energy than H_2S. Consequently, H_2S_2 does not contribute significantly to the measurement of $m/z = 34$ during H-atom exposure, which can therefore be solely attributed to H_2S.

We measured the intensity of the $m/z = 33$ signal relative to $m/z = 34$ to be ~ 0.55 throughout the H-atom exposure, whereas the expected fragmentation pattern of H_2S corresponds to $33/34 \sim 0.42$. The excess of $[HS]^+$ fragments detected during the bombardment is consistent with the transfer of HS radicals to the gas phase through chemical desorption as a result of Reaction 4.1. This fraction, however, is significantly smaller than the detected gaseous H_2S and could therefore be neglected. Indeed, due to the high exothermicity of Reaction 4.6a and the fact that its excess energy is concentrated in a single product, we expected
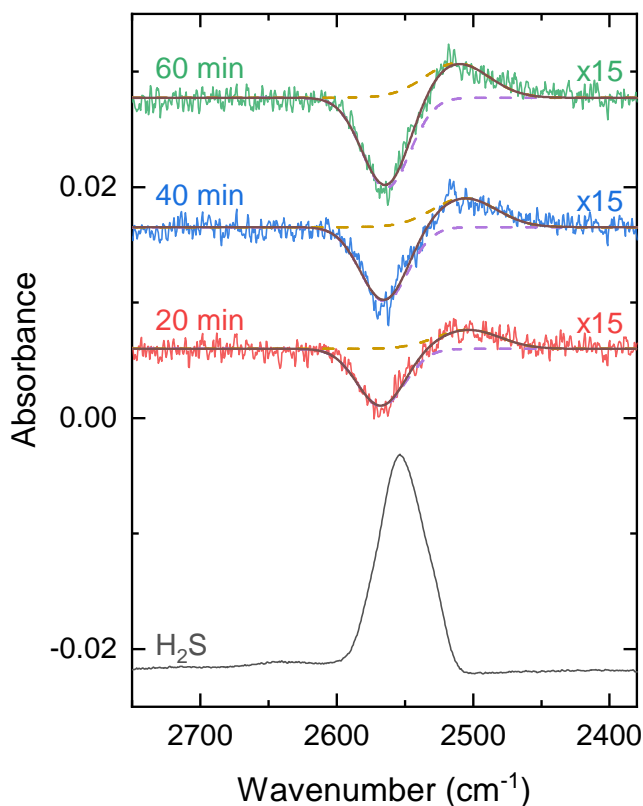
Figure 4.4: Infrared spectrum after deposition of a pure H_2S ice (black) and the difference spectra after exposure to H atoms for 20 minutes (red), 40 minutes (blue), and 60 minutes (green). Superimposed onto the difference spectra are the corresponding Gaussian fittings of the H_2S band (purple), H_2S_2 band (yellow), and the resulting convoluted feature (brown). The spectra have been offset for clarity.
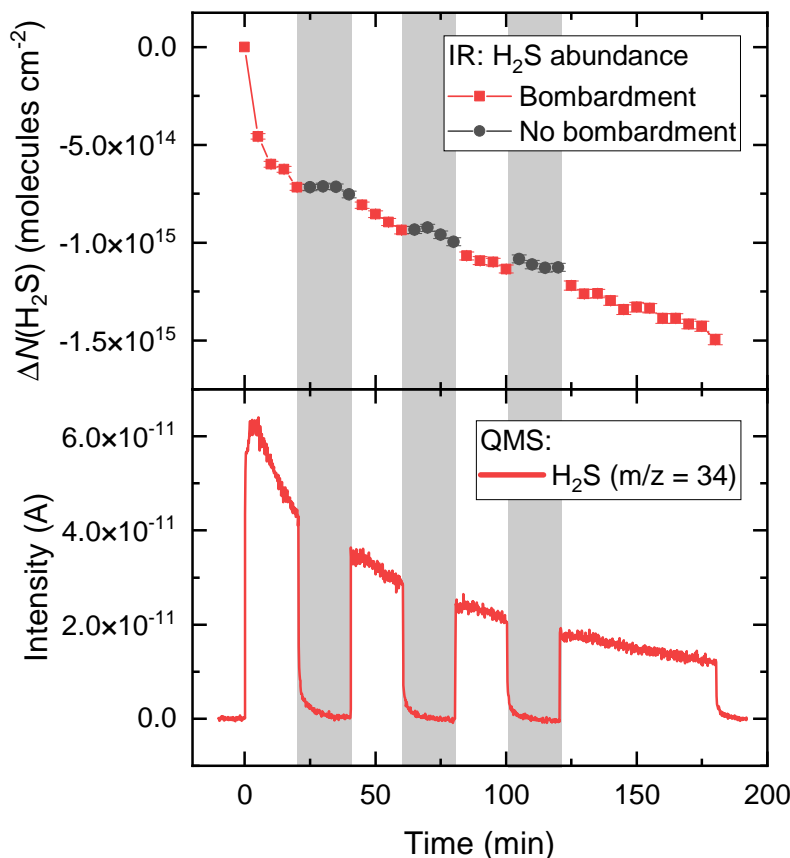
Figure 4.5: Monitoring of H_2S in the solid and gas phases during H-atom bombardment. Upper panel: Variation in H_2S column density measured from the ~ 2553 cm^{-1} band in the IR spectra as a function of time. Lower panel: Scan of the m/z = 34 ($[H_2S]^+$) as measured by the QMS as a function of time. The shadowed areas denote the periods during which the H-atom flux was stopped.

H_2S to be the most susceptible species to chemical desorption during the hydrogenation sequence—as was also suggested by Oba *et al.* (2018).

In addition to experiments at 10 K, we performed predeposition experiments with analogous conditions at 12 K, 14 K, and 16 K in order to investigate the effects of different temperatures on H_2S_2 formation and H_2S chemical desorption. The percentage of H_2S lost either to chemical desorption or H_2S_2 formation by the end of the predeposition experiments can be derived by comparing the final ΔN of both species, assuming that other potential processes have a minor contribution in decreasing the H_2S band. The derived efficiencies are temperature dependent, as shown in Figure 4.6; the overall H_2S loss due to chemical desorption varies from $\sim 85\%$ to $\sim 74\%$ when the ice temperature increases from 10 K to 16 K. Accordingly, the percentage loss due to the formation of H_2S_2 varies from $\sim 15\%$ to $\sim 26\%$. We note that these values are respective to the relative H_2S loss at each specific temperature and are not the absolute amount of formed H_2S_2 or chemically desorbed H_2S in each experiment. At higher temperatures, the fraction of H_2S consumed to form H_2S_2 increases relatively to the loss due to chemical desorption, suggesting that the former process becomes increasingly relevant in warmer environments. This observation is possibly related

to a significant increase in diffusion rates of HS radicals enhancing the overall H_2S_2 formation at the expense of chemical desorption by H_2S reformation. In summary, by taking into account this chemical loss channel, it is possible to further constrain the fate of H_2S molecules upon H-atom bombardment, thus expanding the results from previous works in which H_2S_2 formation was not observed.
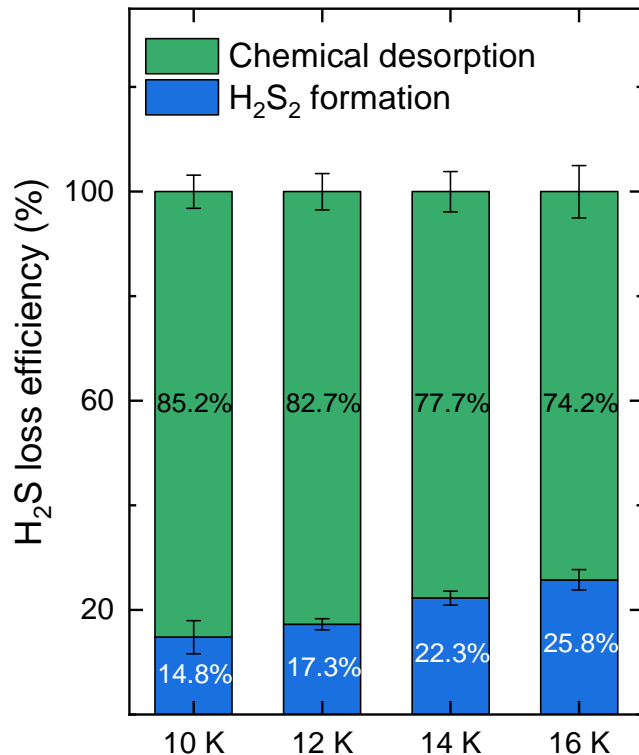
Figure 4.6: Derived contributions from H_2S_2 formation and H_2S chemical desorption to the measured loss in $N(H_2S)$ after 120 minutes of H-atom exposure at 10, 12, 14, and 16 K.

4.3.3   Kinetic analysis

Information on the kinetics of H_2S_2 formation and H_2S consumption can be derived from predeposition experiments. In the upper panel of Figure 4.7, the variation in column density (ΔN) of H_2S_2 as a function of H-atom fluence measured from the IR spectra at 10 K is shown. The curve is fitted by a single exponential function:

$$\Delta[X]_t = [H_2S]_0 \cdot a(1 - \exp(-\sigma \cdot F)), \qquad (4.7)$$

where $\Delta[X]$ and $[H_2S]_0$ are, respectively, the abundance of species X at a given time and the initial abundance of H_2S. Here, a is the saturation value, F is the incident H-atom fluence, and σ is the effective formation cross section of H_2S_2. From this fitting, we derived $\sigma \sim (9.8 \pm 0.9) \times 10^{-17}$ cm^2 for H_2S_2 formation at 10 K. We note, however, that the rate law of H_2S_2 formation is far from trivial, as both Reactions 4.1 and 4.6b contribute to the effective cross section, with the latter requiring two HS radicals to occur. Therefore, it cannot be simplified by the pseudo first-order approximation. Moreover, the accurate amount of

H atoms available on the surface of the ice is very difficult to quantify, as a fraction will recombine to form H_2—hence the use of the "effective" term. The σ value derived here is thus not suited to be directly employed in chemical models as a rate constant, but it is very useful for comparison purposes with other effective cross sections derived with similar conditions.

In the lower panel of Fig. 4.7, the effective variation in the column density of H_2S as a function of H-atom fluence measured from the infrared spectra is shown. In this case, the plot is better fitted by a two-term exponential function:

$$\Delta[H_2S]_t = [H_2S]_0(a_1(1 - \exp(-\sigma_1 \cdot F)) + a_2(1 - \exp(-\sigma_2 \cdot F))), \tag{4.8}$$

where a_n is the saturation value and σ_n is the effective destruction cross section. The interpretation of such a fitting is not straightforward, as it incorporates the contribution from all the processes leading to a decrease in $N(H_2S)$. Nonetheless, the double exponential fitting suggests that the processes dominating the observed decrease in $N(H_2S)$ can be separated into two different timescales with $\sigma_1 \sim 10^{-16}$ cm^2 and $\sigma_2 \sim 10^{-17}$ cm^2.

The fast process with $\sigma_1 \sim 10^{-16}$ cm^2 is likely due to startup effects, such as collision-induced desorption of the weakly bound topmost molecules (Chuang *et al.* 2018). Accordingly, the effective destruction cross section of H_2S can be approximated as the second exponential term with $\sigma_2 \sim 10^{-17}$ cm^2. Control experiments with neutral helium bombardment of H_2S ices show that material loss due to collisional impact should account for $\lesssim 10\%$ of the total H_2S desorption from the QMS. In comparison, the saturation point of the fast exponential curve (blue line in the lower panel of Figure 4.7) corresponds to ~ 0.3 of the total loss of H_2S and should thus be regarded as an upper limit to the real value.

Given that the interaction of H_2S with H atoms mostly results in chemical desorption via Reaction 4.6a and H_2S_2 formation via Reaction 4.6b, it is possible to isolate the H_2S chemical desorption curve by subtracting the minimum amount of H_2S consumed to form H_2S_2 (i.e., twice the column density of H_2S_2). The resulting isolated H_2S chemical desorption curve is shown in the upper panel of Figure 4.8 and yields an effective cross section of $\sigma \sim (1.7 \pm 0.2) \times 10^{-17}$ cm^2. We emphasize, however, that this value was derived using a series of assumptions and is therefore only a rough estimation.

In addition to the IR approach, it is possible to directly probe the chemical desorption of hydrogen sulfide by utilizing mass spectrometry data acquired during hydrogen exposure. The lower panel of Figure 4.8 shows the integrated signal for the m/z = 34 ($[H_2S]^+$) fragment as a function of H-atom fluence (i.e., the area of the plot in the lower panel of Figure 4.5). Similar to H_2S_2, this curve can be fitted by an exponential function as described in Equation 4.7, yielding $\sigma \sim (3.7 \pm 0.3) \times 10^{-17}$ cm^2, which is quite compatible with the IR approach. Assuming similar chemical desorption efficiencies for both $^{3}_{2}S$ and $^{3}_{4}S$ isotopes of H_2S, the contribution from $[^{3}_{4}S]^+$ to m/z = 34 does not affect the exponential factor in the fitting and can therefore be neglected. We find it is important to note that the cross section from the QMS data is likely more accurate than the IR counterpart, as the former is a direct fitting of the measurements, whereas the latter involves a number of presumptions. Both values are similar to the chemical desorption cross sections of $(2.1 \pm 0.2) \times 10^{-17}$ cm^2 derived by Oba *et al.* (2019) from the exposure of H_2S ice to H atoms at 10 K and reinforce the relevance of H_2S chemical desorption to interstellar gas-grain chemistry. Small discrepancies between the two studies are expected due to the different experimental conditions, such as ice thicknesses, growth surfaces, and H-atom fluxes.

We performed similar experiments at 12, 14, and 16 K, and the derived effective cross sections are summarized in Table 4.3. The estimated $\sigma(H_2S_2)$ values suggest that the effectiveness of H_2S_2 formation remains fairly consistent (within the uncertainty range) for temperatures between 10 K and 14 K. At 16 K, the cross section is slightly reduced. This behavior is likely the outcome of competing elementary processes involved in synthesizing H_2S_2 on ice. While diffusion can be facilitated at higher temperatures, thus enhancing encounters between two HS radicals and favoring Reaction 4.6b, the sticking coefficient of H atoms on
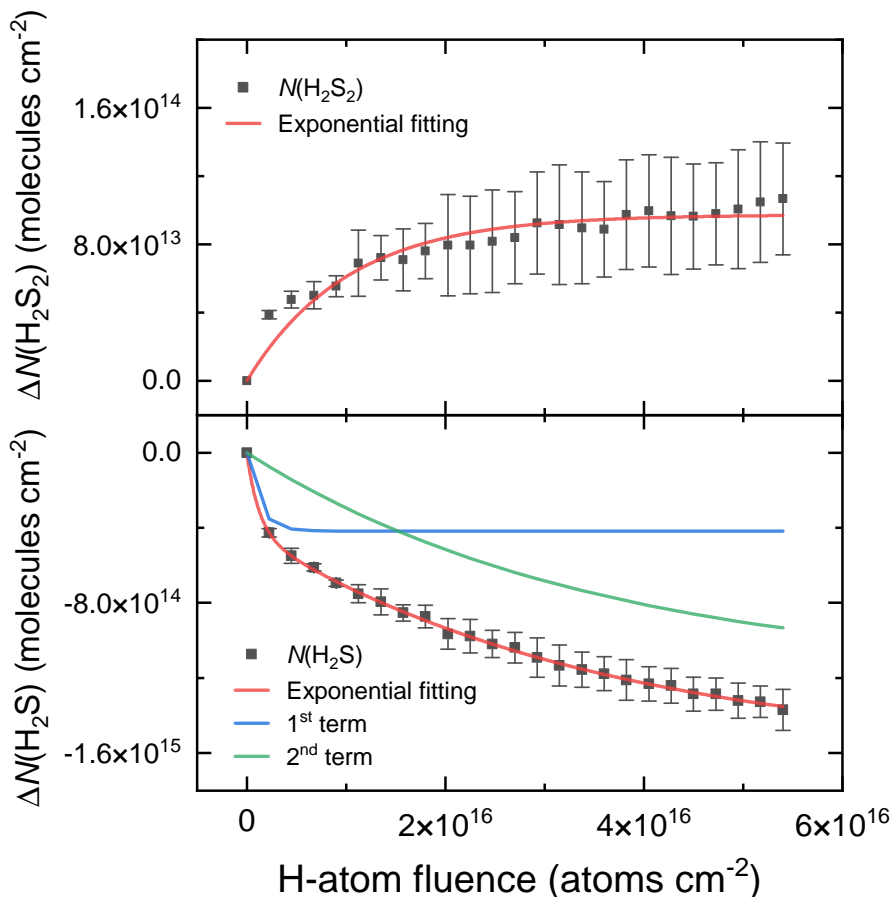
Figure 4.7: Column densities of H_2S and H_2S_2 in the ice during H-atom bombadrment. Upper panel: Variation in H_2S_2 column density during H-atom exposure of an H_2S ice at 10 K. Lower panel: Variation in H_2S column density as a function of H-atom fluence during bombardment of an H_2S ice at 10 K. The two-term exponential fitting to the points is shown in red, while the fast and slow components of the fitting are plotted in blue and green, respectively.

ices diminishes, thus hindering the formation of reactants in the first place. Moreover, faster diffusion rates also imply that H atoms might not have enough available time in the vicinity of an H_2S molecule to overcome the ~1500 K barrier in Reaction 4.1. Similar findings were described in other H-atom addition experiments (e.g., in the hydrogenation of O_2; Ioppolo *et al.* 2008, 2010; Cuppen *et al.* 2010).

We obtained the effective cross sections of H_2S chemical desorption from the QMS data, and they show a slight decreasing trend between the temperatures of 10, 12, 14, and 16 K. A similar behavior was also observed by Oba *et al.* (2019) with measurements at 10, 20, and 30 K, which they attributed to the combination of the H atom availability at $T \geqslant 20$ K and the true efficiency of H_2S chemical desorption at higher temperatures. The slightly lower effective cross sections, they argue, would in reality indicate an increase of the true value at warmer environments, balancing out the considerably diminishing sticking coefficient of H. In the present work, we probe a much smaller temperature range where the availability of H
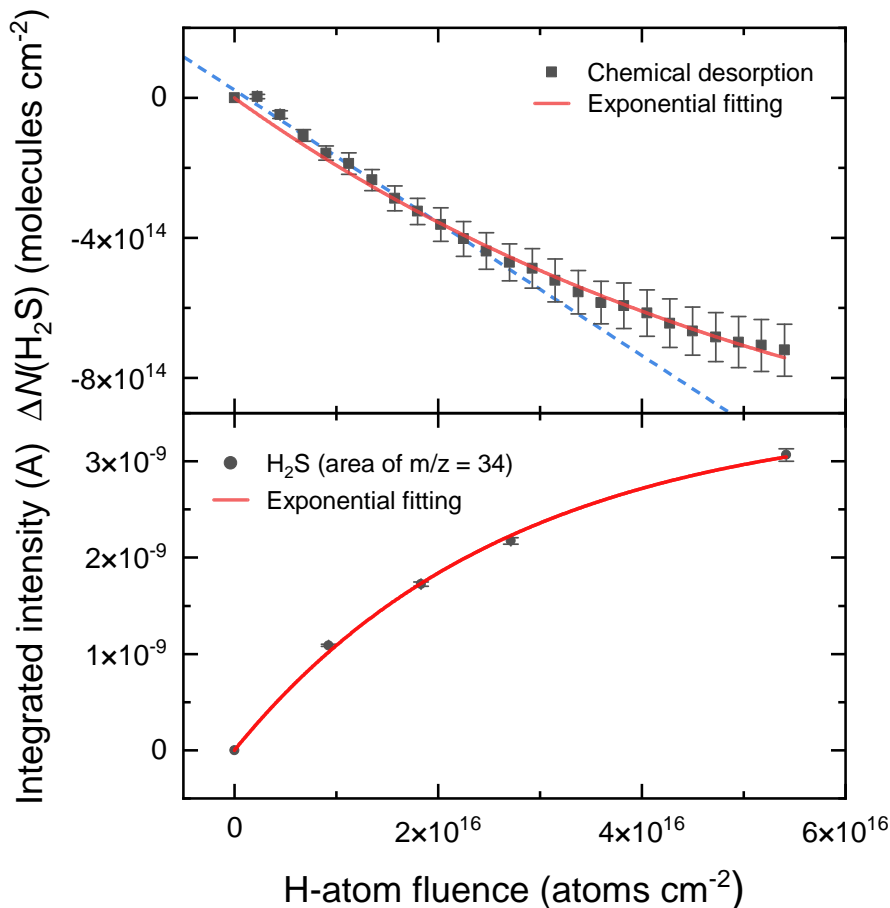
Figure 4.8: Chemical desorption curves for H_2S as a function of H-atom fluence. Upper panel: Estimated contribution from chemical desorption to the decrease in $N(H_2S)$ as a function of fluence. The simple exponential fitting to the points is shown in red, and the linear fitting to the first 55 minutes of bombardment is shown in blue (dashed line). Lower panel: Integrated intensity of the m/z = 34 signal measured by the QMS as a function of H-atom fluence during the same experiment. The red line shows the exponential fitting to the points.

Table 4.3: Effective cross sections of H_2S_2 formation ($\sigma(H_2S_2)$) and H_2S chemical desorption ($\sigma_{CD}(H_2S)$) derived from the predeposition experiments performed at 10, 12, 14, and 16 K.

Temperature (K)	$\sigma(H_2S_2)$ ($\times 10^{-17} cm^2$)	$\sigma_{CD}(H_2S)$ ($\times 10^{-17} cm^2$)
10	9.8 ± 0.9	3.7 ± 0.3
12	7.8 ± 0.9	2.8 ± 0.1
14	8.3 ± 0.7	2.7 ± 0.2
16	5.2 ± 0.6	2.6 ± 0.2

atoms on the surface is not expected to drop as significantly. Nonetheless, some effect of the smaller sticking coefficient of hydrogen at higher temperatures could in principle influence the measured effective cross sections—albeit to a smaller extent than in Oba *et al.* (2019). Although speculating the effect of the ice temperature on the real $\sigma_{CD}(H_2S)$ is challenging, it seems as though a measurable change occurs only from 10 K to 12 K within the range explored in this work.

4.4   Astrophysical implications

Hydrogen sulfide is thought to be efficiently formed on the surface of interstellar dust through the hydrogenation of S atoms (see, e.g., Tielens & Hagen 1982; Laas & Caselli 2019). It is also the major sulfur-bearing species found in the comae of comets (Calmonte *et al.* 2016 and references therein), which in turn are thought to harbor the content of prestellar ices. The (so far) non-detection of solid-phase H_2S in interstellar clouds thus poses a question regarding the fate of H_2S in interstellar icy mantles. One likely explanation for its absence in observations is that solid-phase H_2S is effectively destroyed by, for instance, energetic processing, which is known to result in solid-phase sulfur chemistry (e.g., Moore *et al.* 2007; Garozzo *et al.* 2010; Jiménez-Escobar & Muñoz Caro 2011a; Jiménez-Escobar *et al.* 2014a; Chen *et al.* 2015; Shingledecker *et al.* 2020; Cazaux *et al.* 2022; Mifsud *et al.* 2022). In fact, the photochemistry of H_2S induced by UV photons has been suggested as a potential sulfur sink, as it has been shown to produce allotropic forms of S (S_n) that are largely refractory (especially for $n > 4$). In addition to energetic processing, non-energetic routes to remove H_2S from the solid phase are also essential, as they are the dominant processes taking place within dense clouds. Indeed, recent observations with the James Webb Space Telescope aimed at highly shielded regions within interstellar clouds (with $A_V > 50$) have still been unable to detect H_2S ices, providing only upper limits of 0.6% with respect to H_2O (McClure *et al.* 2023). Especially in such environments, chemical desorption due to hydrogenation seems to be a particularly prominent mechanism to transfer H_2S to the gas phase (Oba *et al.* 2018, 2019). In this work, the cross sections derived directly from the chemically desorbed H_2S as measured by the QMS—and thus not influenced by additional H_2S destruction phenomena such as chemical reactions—is fully in line with this proposition.

Another relevant value that can be derived from predeposition experiments is the efficiency of chemical desorption per incident H atom. The reason for deriving a value per incident atom instead of per reactive event is because the true value of H atoms involved in the reactions under our experimental conditions is unknown, as a fraction of them will recombine into H_2 molecules through diffusion. The efficiency derived per incident atom can therefore be regarded as a lower limit to the value per reaction event. After isolating the variation in the H_2S column density due to chemical desorption (as described in Section 4.3.3; see also Figure 4.8), a linear fit to the points within the first 55 minutes of bombardment at 10 K (blue dashed line in the lower panel of Figure 4.8) yielded an efficiency of $\sim 0.019 \pm 0.001$, which is around four times higher than the values reported by Oba *et al.* (2018) and Oba *et al.* (2019) and consistent with the calculated value per reaction event (i.e., $(3 \pm 1.5)\%$) in Furuya *et al.* (2022). Similar to the cross sections, such a discrepancy could be due to the different ice compositions (pure H_2S versus H_2S on top of amorphous solid water) and thicknesses ($\sim$20 ML versus 0.7 ML). Nonetheless, this estimated efficiency reinforces the key role of H_2S chemical desorption as a non-thermal mechanism of transferring hydrogen sulfide to the gas phase within dark clouds. Indeed, by combining gas-grain chemical models with millimeter observations, Navarro-Almaida *et al.* (2020) found that chemical desorption is the main mechanism responsible for gas-phase H_2S formation.

Complementary to chemical desorption, the interaction of H_2S with H atoms can also kick-start non-energetic chemistry to form larger sulfur-bearing molecules. The detection of H_2S_2 under our experimental conditions is one example of how HS radicals produced by Reaction

4.1 can lead to a higher sulfur-bearing chemical complexity. In fully representative interstellar ices, the probability of two HS radicals meeting is rather low, given the small abundance of H_2S relative to other ice components, such as H_2O or CO. However, these radicals can react with more widespread ice species, potentially leading to the formation of sulfur-bearing COMs. This present work therefore serves as a proof of concept that non-energetic sulfur chemistry can be initiated by the formation of HS radicals through Reaction 4.1 with the simplest example of H_2S_2. We find that it is also noteworthy that the contributions from each process to the consumption of H_2S varies significantly with temperature, as an appreciable increase in sulfur-bearing species formed at 16 K compared to 10 K. This is likely due to the enhanced radical diffusion within warmer ices and signifies that sulfur chemistry could be significantly intensified at regions closer to the edges of dark clouds—where temperatures can approach 20 K.

4.5   Conclusions

In the present work, we experimentally investigated the interaction of H_2S ices with H atoms under ultrahigh vacuum pressures and astronomically relevant temperatures $(10-16$ K$)$. Our main findings are summarized below:

- We verified that solid-phase hydrogen sulfide is destroyed and H_2S_2 is formed as a result of the interaction between H_2S and H atoms.

- The chemical desorption of H_2S was directly probed by quantifying the material ejected into the gas phase during H-atom exposure experiments. The calculated effective cross sections for ice temperatures of 10, 12, 14, and 16 K are, respectively, $(3.7\pm0.3)\times10^{-17}$ cm^2, $(2.8\pm0.1)\times10^{-17}$ cm^2, $(2.7\pm0.2)\times10^{-17}$ cm^2, and $(2.6\pm0.2)\times10^{-17}$ cm^2.

- From the RAIRS data, we estimate the chemical desorption efficiency per incident H atom at 10 K to be $\sim 0.019\pm0.001$.

- The derived values for the effective chemical desorption cross sections and efficiency per incident H strengthen the argument that H_2S ice is effectively transferred to the gas phase through the excess energy generated by reactions with hydrogen atoms.

- The confirmation of H_2S_2 formation as a result of HS radical recombination proves that non-energetic sulfur chemistry can take place at temperatures as low as 10 K through radical-radical reactions, which could potentially lead to the formation of sulfur-bearing COMs in more representative interstellar ice mixtures.

- We derived the effective formation cross sections for H_2S_2 of $(9.8\pm0.9)\times10^{-17}$ cm^2, $(7.8\pm0.9)\times10^{-17}$ cm^2, $(8.3\pm0.7)\times10^{-17}$ cm^2, and $(5.2\pm0.6)\times10^{-17}$ cm^2 at 10, 12, 14, and 16 K, respectively.

- No chemical desorption was observed upon formation of H_2S_2 above the current detection limit.

- Approximately 85% to 74% of the H_2S ice destruction observed under our experimental conditions can be associated with chemical desorption, whereas $\sim 15\%$ to 26% is due to H_2S_2 formation. The relative consumption of H_2S by the latter process grows with temperature, implying that sulfur chemistry induced by HS radicals becomes increasingly more relevant in warmer environments.

4.6   Acknowledgements

4.7 Appendix

4.7.1 Determination of IR band strengths

The derivation of $A'(\text{H}_2\text{S})$ for our specific experimental settings was performed in a manner similar to what was described by Chuang *et al.* (2018). Infrared spectra are acquired during deposition of an H_2S ice at 10 K while simultaneously measuring the interference pattern of a HeNe laser that hits the ice sample at an incident angle of $\sim 1.7°$. The thickness of the ice (d_X) is derived from the laser fringe pattern by the equation (Hollenberg & Dows 1961; Westley *et al.* 1998):

$$d_X = k \times \frac{\lambda}{2n_X \cdot \cos(\theta_f)},$$ (4.9)

where k is the number of fringes, λ is the laser wavelength (i.e., 632.8 nm), n_X is the refractive index of the ice species, and θ_f is the angle of refraction in degrees. From the thickness measurements, it is possible to derive the absolute column density of the ice by the equation:

$$N_X = \frac{d_X \cdot \rho_X \cdot N_a}{M_X},$$ (4.10)

where ρ_X is the density in grams per cubic centimeter, N_a is the Avogadro's constant, and M_X is the molar mass of a given species.

In the left panel of Figure 4.9, the HeNe laser interference pattern is shown as a function of time and fit with a sinusoidal function. This pattern arises from the growing H_2S ice being deposited on the sample. The corresponding increase in the IR absorption area of the SH stretching mode of H_2S (i.e., ~ 2553 cm^{-1}) as a function of ice column density is shown in the right panel of Figure 4.9. A linear fit to the points yields a band strength value in reflection mode and is specific to our experimental setup of $A'(\text{H}_2\text{S})_{\sim 2553 \text{ cm}^{-1}} \sim (4.7 \pm 0.1) \times 10^{-17}$ cm molecule^{-1}. For this calculation, we utilized $\rho = 0.944 \pm 0.005$ g cm^{-3} and $n = 1.407 \pm 0.005$, as reported by Yarnall & Hudson (2022).
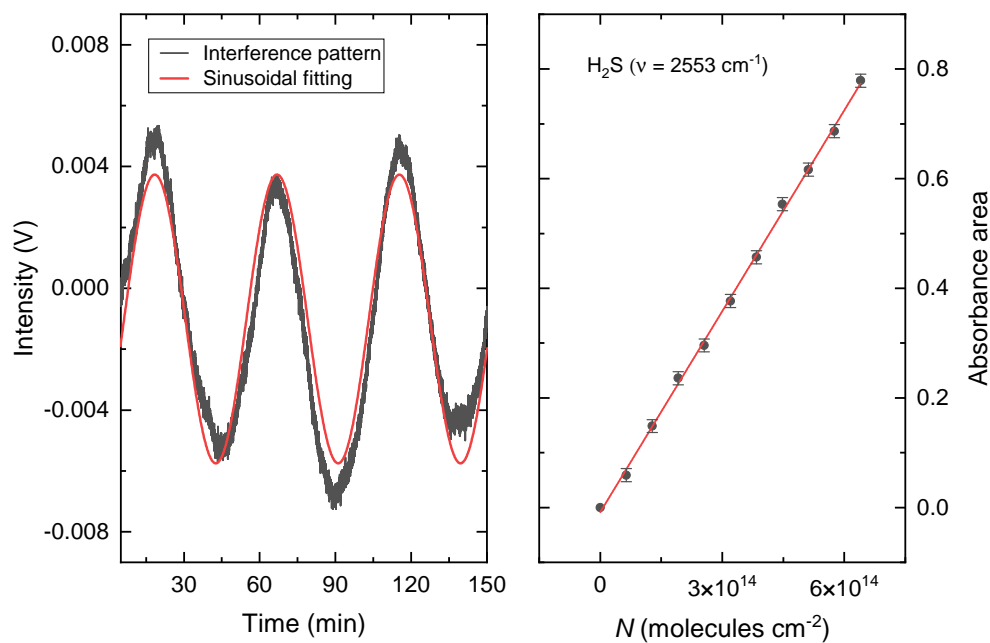
Figure 4.9: Derivation of $A'(H_2S)$. Left panel: HeNe laser interference pattern obtained from the growing H_2S ice at 10 K (black) together with its sinusoidal fitting (red). Changes in the amplitude of the fringes are attributed to laser instabilities. Right panel: Integrated absorbance area of the SH stretching mode of H_2S as a function of column density as derived from the fringe patter. A linear fit to the points is also shown in red.

5.   H₂S ICE SUBLIMATION DYNAMICS: EXPERIMENTALLY CONSTRAINED BINDING ENERGIES, ENTRAPMENT EFFICIENCIES, AND SNOWLINES

Hydrogen sulfide (H_2S) is thought to be an important sulfur reservoir in interstellar ices. It serves as a key precursor to complex sulfur-bearing organics, and has been proposed to play a significant role in the origin of life. Although models and observations both suggest H_2S to be present in ices in non-negligible amounts, its sublimation dynamics remain poorly constrained. In this work, we present a comprehensive experimental characterization of the sublimation behavior of H_2S ice under astrophysically-relevant conditions. We used an ultrahigh vacuum chamber to deposit pure multilayer H_2S ice, submonolayer H_2S ice on top of compact amorphous solid water (cASW), as well as ice mixtures of H_2S and H_2O. The sublimation behavior of H_2S was monitored with a quadrupole mass spectrometer (QMS) during temperature-programmed desorption (TPD) experiments. These experiments are used to determine binding energies and entrapment efficiencies of H_2S, which are then employed to estimate its snowline positions in a protoplanetary disk midplane. We derive mean binding energies of 3159 ± 46 K for pure H_2S ice and 3392 ± 56 K for submonolayer H_2S desorbing from a cASW surface. These values correspond to sublimation temperatures of around 64 K and 69 K in the disk midplane, placing its sublimation fronts at radii just interior to the CO_2 snowline. We also investigate the entrapment of H_2S in water ice and find it to be highly efficient, with $\sim 75 - 85\%$ of H_2S remaining trapped past its sublimation temperature for H_2O:H_2S mixing ratios of $\sim$5−17:1. We discuss potential mechanisms behind this efficient entrapment. Our findings imply that, in protoplanetary disks, H_2S will mostly be retained in the ice phase until water crystallizes, at radii near the water snowline, if it forms mixed into water ice. This has significant implications for the possibility of H_2S being incorporated into icy planetesimals and its potential delivery to terrestrial planets, which we discuss in detail.

5.1   Introduction

The interchange between solids and gas plays a major role in the chemical composition and structure of star- and planet-forming regions (Bergin & Langer 1997; Aikawa *et al.* 2002; Viti *et al.* 2004; Henning & Semenov 2013; He *et al.* 2016b; Öberg *et al.* 2023). At the cold temperatures of interstellar clouds (typically $\sim 10-20$ K), most molecules adsorb onto dust grains, forming ice mantles that undergo rich solid-state chemical processes. The result is a lavish icy chemical reservoir—spanning from simple molecules such as CO and H_2O to complex organics (Herbst & van Dishoeck 2009; van Dishoeck 2014; Linnartz *et al.* 2015; Öberg 2016; Cuppen *et al.* 2024). As this interstellar material collapses into an emerging young stellar object, increasing temperatures caused by the heat from the protostar enable the diffusion of ice species—further facilitating chemical reactions (see, e.g., Cuppen *et al.* 2017)—and eventually lead to their thermal sublimation. The locations of these sublimation fronts, or snowlines, determine the physical state in which specific molecules are available for incorporation into forming planets and planetesimals, thus shaping their solid and atmospheric constitution (Öberg *et al.* 2011b; Henning & Semenov 2013; Madhusudhan 2019). Such locations are dictated by a combination of desorption kinetics, set by a species' binding energies, and the efficiencies with which it is trapped within less volatile ice matrices. It is thus paramount to characterize the thermal sublimation behavior of ice species in order to understand the chemical evolution of environments where young solar system bodies are forming.

One particularly riveting volatile interstellar molecule is hydrogen sulfide (H_2S). Following its first detection by Thaddeus *et al.* (1972) in seven Galactic sources, it has since been observed in the gas phase towards a range of interstellar and protoplanetary environments: from clouds (Minh *et al.* 1989; Neufeld *et al.* 2015) to dense cores and protostars (Minh *et al.* 1990; van Dishoeck *et al.* 1995; Hatchell *et al.* 1998; Vastel *et al.* 2003; Wakelam *et al.* 2004) to protoplanetary disks (Phuong *et al.* 2018; Rivière-Marichalar *et al.* 2021, 2022). On the other hand, interstellar H_2S ice has yet to be observed, with abundance upper limits in prestellar cores and protostellar envelopes estimated as $\lesssim 1\%$ with respect to H_2O (Smith 1991; Jiménez-Escobar & Muñoz Caro 2011a; McClure *et al.* 2023). This non-detection is likely associated with the intrinsic limitations of astronomical observations in the solid state (e.g., the broadness of the ice features and their high degeneracy). Indeed, the strongest IR feature of H_2S ice (its S-H stretching modes at 3.93 μm) is particularly challenging to unequivocally observe due to its broad profile and because it overlaps both with CH_3OH combination modes (a major ice component) and with the S-H stretching modes of simple thiols (Jiménez-Escobar & Muñoz Caro 2011a; Hudson & Gerakines 2018). While the latter are less concerning due to the low expected abundances of thiols, both factors still complicate confidently assigning absorption features in this region to H_2S. Nevertheless, H_2S is predicted by chemical models to be very efficiently formed in ices via the successive hydrogenation of S atoms (see, e.g., Garrod *et al.* 2007; Druard & Wakelam 2012; Esplugues *et al.* 2014; Vidal *et al.* 2017; Vidal & Wakelam 2018):

$$S \xrightarrow{+\,H} HS \xrightarrow{+\,H} H_2S. \tag{5.1}$$

Indeed, it has been observed to be a major sulfur carrier in the comae of comets (Mumma *et al.* 2011; Le Roy *et al.* 2015; Biver *et al.* 2015; Calmonte *et al.* 2016), which are thought to (at least partially) inherit the ice material from the prior pre- and protostellar evolutionary stages (e.g., Bockelée-Morvan *et al.* 2000a; Altwegg *et al.* 2017; Rubin *et al.* 2018; Drozdovskaya *et al.* 2019). Cometary H_2S abundances relative to H_2O range between $\sim 0.13-1.75\%$ (Calmonte *et al.* 2016 and references therein), with measurements from the coma of comet 67P/Churymov-Gerasimenko (hereafter 67P) by the Rosetta Orbiter Sensors for Ion and Neutral Analysis (ROSINA) instrument on board of the Rosetta spacecraft yielding H_2S/H_2O abundances of $1.06 \pm 0.05\%$ (Calmonte *et al.* 2016). These findings point to H_2S as the

main volatile sulfur carrier in 67P. Consequently, while the upper limits on H_2S ice are sufficient to rule it out as the main interstellar sulfur reservoir (see, e.g., Jiménez-Escobar & Muñoz Caro 2011a), cometary inheritance from interstellar ices remains a plausible hypothesis within current observational constraints. Moreover, observed gas-phase H_2S abundances toward solar-mass protostars—attributed to the sublimation of ices in the hot core region—suggest H_2S to be an important gaseous sulfur carrier (Drozdovskaya *et al.* 2018). Given that gas-phase routes to H_2S cannot account for its detected gaseous abundances, all evidence point to it being present in interstellar ices at a level of $\sim$1% with respect to H_2O.

Irrespective of its physical state, H_2S can serve as a important source of sulfur during the chemical evolution of star- and planet-forming regions. As a solid, it has been shown both experimentally and by chemical models to initiate a prolific sulfur network by producing HS radicals and S atoms—induced either by energetic processing or interactions with H atoms—that readily react with other ice species (Moore *et al.* 2007; Ferrante *et al.* 2008; Garozzo *et al.* 2010; Jiménez-Escobar *et al.* 2014a; Chen *et al.* 2015; Laas & Caselli 2019; Santos *et al.* 2024a,b). Solid H_2S and its reaction products might then be incorporated into icy planetesimals, which in turn might deliver them to terrestrial planets during events such as our Solar System's late heavy bombardments. This is particularly relevant to theories on the origins of life, as H_2S has been proposed as a key energy source for early metabolic pathways predating oxygenic photosynthesis (Olson & Straub 2016). More broadly, sulfur-bearing compounds have long been recognized as fundamental to biological systems. Additionally, H_2S can also undergo solid-state acid-base reactions with NH_3 to form ammonium hydrosulfide ($NH_4^+SH^-$) at temperatures as low as 10 K (Loeffler *et al.* 2015; Vitorino *et al.* 2024; Slavicinska *et al.* 2025). This salt has been detected at very high abundances in the grains of comet 67P by the ROSINA instrument (Altwegg *et al.* 2022), and is proposed to be a major carrier of the 6.85 μm band assigned to NH_4^+ in ices, as well as a significant sink to the conspicuous missing sulfur problem (Slavicinska *et al.* 2025). As a gas, H_2S can contribute to the elemental abundance of sulfur in planetary atmospheres—which in turn might help tracing the planet's formation history (Öberg *et al.* 2011b; Polman *et al.* 2023; Tsai *et al.* 2023).

Despite its pivotal role in the sulfur network of star- and planet-forming regions, a comprehensive characterization of the thermal sublimation behavior of H_2S is still lacking from the literature, with no experimentally-determined binding energies or entrapment efficiencies available to date. We aim to bridge this gap with this work. The paper is outlined as follows: in Section 5.2, the experimental setup and procedures are described. In section 5.3, we report and discuss our results, including experimentally-derived binding energies as well as entrapment efficiencies in H_2O ice. The corresponding locations of the H_2S sublimation fronts and their astrophysical implications are discussed in Section 5.4. Finally, in Section 5.5 we summarize our main findings.

5.2   Methods

5.2.1   The setup

This work utilized the experimental setup SPACE-KITTEN[1], which has been described in detail elsewhere (Simon *et al.* 2019, 2023). Briefly, the setup consists of an ultrahigh vacuum (UHV) chamber with base pressure at room temperature of $\sim$4$\times10^{-9}$ Torr. At the center of the chamber, an IR-transparent CsI window is mounted on a sample holder attached to a closed-cycle helium cryostat with a DMX-20B interface (which decouples the sample holder from the cryostat's cold tip, thus preventing vibrations). The substrate temperature can be varied between 12 and 300 K using a resistive thermofoil heater, and is monitored by

---

[1]Surface Processing Apparatus for Chemical Experimentation–Kinetics of Ice Transformation in Thermal ENvironments

two silicon diode sensors with a precision of ± 0.1 K and absolute accuracy of ~ 2 K. H_2S (Sigma-Aldrich, purity $\geq 99.5\%$) and H_2O are admitted into the chamber, either individually or as a mixture, through a stainless steel tube doser with a diameter of 4.8 mm at normal incidence to the substrate. The doser outlet is located at 1 inch from the substrate during deposition and the base pressure of the gas line is $\sim 10^{-4}$ Torr. The H_2O sample was prepared by purifying deionized water through multiple freeze-pump-thaw cycles in a liquid nitrogen bath. Moreover, $^{13}CO_2$ (Sigma-Aldrich, purity 99%; <3 atom % ^{18}O, 99 atom % ^{13}C) is also utilized for a control experiment mixed with H_2O. The minor isotopologue is chosen to avoid any potential residual atmospheric contamination from interfering with the analysis. Ice growth is monitored by a Bruker Optics Vertex 70 Fourier-transform infrared spectrometer (FTIR) in transmission mode, while the gas-phase composition in the chamber is sampled by a Pfeiffer Vaccum Inc. PrismaPlus QMG 220 quadrupole mass spectrometer (QMS).

5.2.2 The experiments

The experiments performed in this work are summarized in Table 5.1. We derive binding energies of H_2S in two scenarios: for pure multilayer H_2S ice and for submonolayer H_2S on top of multilayer compact amorphous solid water (cASW). The latter was chosen as a substrate because it is generally thought to be more representative of interstellar water ice than porous counterparts (e.g., Accolla et $al.$ 2013). In order to grow cASW, the substrate is kept at 100 K during the H_2O ice deposition (Bossa et $al.$ 2012), and is subsequently cooled down to 15 K before depositing H_2S. The pure multilayer H_2S ices are deposited at 15 K directly. Entrapment experiments are performed for water-dominated ice mixtures of H_2S or $^{13}CO_2$ deposited at 15 K. Prior to dosing, the mixtures are prepared in a gas manifold within one hour of the experiment. In all cases, after the deposition is completed, temperature programmed desorption (TPD) experiments are performed by heating up the substrate temperature linearly at a rate of 2 K min^{-1}. The desorbed species are immediately ionized by 70 eV electron impact and are monitored by the QMS. Their desorption rates are then used to derive the binding energies and entrapment efficiencies. Any contamination from background H_2O deposition is negligible. Based on the infrared absorption features of H_2O observed after H_2S deposition in the pure ice experiments, the background H_2O deposition rate is at most 0.1 ML/min. This is at least one order of magnitude lower than the H_2S deposition rate in the multilayer experiments and a factor of ~ 5 lower in the submonolayer experiments. Even in the latter case, we find no evidence of significant H_2O codeposition with H_2S, as no additional desorption feature is observed with the QMS following the submonolayer desorption of H_2S—which would be expected if a non-negligible amount of porous ASW were forming due to background deposition at 15 K.

The surface coverage of the ice species is quantified by two approaches. For ices with thicknesses $\gtrsim 1$ ML, taken as the typical approximation of 1 ML $= 10^{15}$ molecules cm^{-2}, their infrared absorbance bands are reliably detected above the instrumental limit of the spectrometer. In such cases, the IR integrated absorbance ($\int Abs(\tilde{\nu})d\nu$) of the species is converted to absolute abundance using a modified Beer-Lambert law:

$$N_X = \ln 10 \frac{\int Abs(\tilde{\nu})\mathrm{d}\tilde{\nu}}{A(X)}, \tag{5.2}$$

where N_X is the species' column density in molecules cm^{-2} and $A(X)$ is its absorption band strength in cm molecule^{-1}. We use $A(H_2S)_{\text{S-H str}} = 1.69 \times 10^{-17}$ cm molecule^{-1} for pure H_2S ices and $A(H_2S)_{\text{S-H str}} = 1.66 \times 10^{-17}$ cm molecule^{-1} for H_2S mixed with H_2O, as derived by Yarnall & Hudson (2022). For H_2O and $^{13}CO_2$, we use $A(H_2O)_{\text{O-H str}} = 2.2 \times 10^{-16}$ cm molecule^{-1} and $A(^{13}CO_2)_{\text{C=O str}} = 1.15 \times 10^{-16}$ cm molecule^{-1}, taken from Bouilloud et $al.$ (2015) based on the values reported by Gerakines et $al.$ (1995). Uncertainties in the band strengths are the main source of error in the ice coverage estimation, and are assumed

Table 5.1: List of experiments.

Experiment[a]	X coverage (ML)	H_2O coverage (ML)	Total mixture coverage (ML)	H_2O:X
		$X = H_2S$		
H_2S	90	—	—	—
H_2S	73	—	—	—
H_2S	45	—	—	—
H_2S	32	—	—	—
H_2S	19	—	—	—
$H_2O{\rightarrow}H_2S$	1.6	42	—	—
$H_2O{\rightarrow}H_2S$	1.2	40	—	—
$H_2O{\rightarrow}H_2S$	0.6	40	—	—
$H_2O{\rightarrow}H_2S$	0.5	39	—	—
$H_2O{\rightarrow}H_2S$	0.3	39	—	—
$H_2O{\rightarrow}H_2S$	0.2	47	—	—
H_2O:H_2S	7.0	36	43.0	5.1:1
H_2O:H_2S	5.1	38	43.1	7.5:1
H_2O:H_2S	4.2	39	43.2	9.3:1
H_2O:H_2S	2.3	40	42.3	17:1
		$X = {}^{13}CO_2$		
H_2O:${}^{13}CO_2$	2.6	37	39.6	14:1

Notes. [a] Arrows ($H_2O{\rightarrow}$X) denote sequential depositions (X on top of H_2O); colons (H_2O:X) denote ice mixtures of H_2O and X.

to be 10% to account for possible variations caused by temperature and mixing conditions. This uncertainty is then propagated throughout the analysis. For the cases in which ices are deposited with submonolayer coverages, IR absorption bands are not or barely detected and the coverage is estimated by the species' integrated QMS signal during TPD corrected by a scaling factor (see Appendix 5.7.1 for more details).

5.2.3   The analysis

The H_2S binding energies are derived by fitting the measured TPD curves with the Polanyi-Wigner equation:

$$-\frac{d\theta}{dT} = \frac{\nu}{\beta}\theta^n e^{-E_{\mathrm{des}}/T}, \tag{5.3}$$

where θ is the ice coverage in monolayers, T is the ice temperature in K, β is the heating rate in K s^{-1}, ν is the preexponential factor, n is the kinetic order, and E_{des} is the desorption energy in K. The kinetic order is a dimensionless quantity that indicates the influence of the species' concentration on its desorption rate. In the multilayer regime, desorption is independent of the ice thickness ($n = 0$), whereas in the submonolayer regime it is proportional to the ice coverage ($n = 1$). This reflects the constant number of adsorbates available for desorption at any given time in the former case, as opposed to the varying number in the latter. The preexponential factor is associated with the molecule's frequency of vibration in the adsorbate−surface potential well, and its units depend on the kinetic order (ML^{1-n} s^{-1}). For a given temperature T, we derive the preexponential factor following the transition state theory (TST) approach and approximating the partition function of the species in the adsorbed state to unity (that is, assuming it to be fully immobile; Tait *et al.* 2005; Minissale *et al.* 2022):

$$\nu_{\mathrm{TST}} = \frac{k_{\mathrm{B}}T}{h}q^{\ddagger}_{\mathrm{tr,2D}}q^{\ddagger}_{\mathrm{rot,3D}}. \tag{5.4}$$

Where k_{B} is the Boltzmann constant, h is the Planck constant, and $q^{\ddagger}_{\mathrm{tr,2D}}$ and $q^{\ddagger}_{\mathrm{rot,3D}}$ are the transitions state's partition functions of translation and rotation, respectively. All constants used here are in the MKS unit system. The translational motion perpendicular to the surface can be neglected, resulting in a translational partition functional parallel to the surface plane:

$$q^{\ddagger}_{\mathrm{tr,2D}} = \frac{A_S 2\pi m k_{\mathrm{B}}T}{h^2}, \tag{5.5}$$

where m is the mass of the species in kg and A_S is the surface area per adsorbed molecule, fixed to the typical value of 10^{-19} m^2. The rotational partition function is given by:

$$q^{\ddagger}_{\mathrm{rot,3D}} = \frac{\sqrt{\pi}}{\sigma h^3}(8\pi^2 k_{\mathrm{B}}T)^{3/2}\sqrt{I_x I_y I_z}, \tag{5.6}$$

where σ is the species' symmetry number (i.e., the number of indistinguishable rotated positions) and $I_x I_y I_z$ is the product of its principal moments of inertia. The choice of T values used to derive ν_{TST} will be discussed in Sections 5.3.1.1 and 5.3.1.2 for their respective coverage regimes, while the rest of the parameters employed in equations 5.5 and 5.6 are listed in Table 5.2. The inertia moments of H_2S were calculated using Gaussian 16e (Frisch *et al.* 2016) at the M06-2X/aug-cc-pVTZ level of theory (Dunning Jr 1989; Zhao & Truhlar 2008a). The resulting ν_{TST} are then used to fit equation 5.3 to the TPD curves and derive the corresponding binding energies.

When a more volatile species is embedded within a less volatile ice matrix, it can remain trapped in the solid phase beyond its expected sublimation temperature. The entrapment behavior of H_2S in H_2O-dominated ices is also investigated here, with $^{13}CO_2$ mixed into a water-rich ice included as a control experiment. As water ice crystallizes, it creates new

Table 5.2: Summary of parameters used to derive ν_{TST} for H_2S.

Parameter	Value
m (kg)	5.66×10^{-26}
σ	2
I_x (amu Å^2)	5.81066
I_y (amu Å^2)	6.71494
I_z (amu Å^2)	12.52560

Notes. See equations 5.4, 5.5, and 5.6.

channels that allow trapped species to reach the surface, producing the so-called "molecular volcano" desorption peaks (Smith *et al.* 1997). Entrapment efficiencies are calculated as the ratios of the integrated volcano-desorption TPD peak of the more volatile species (H_2S or $^{13}CO_2$) over the integrated area of its entire TPD curve. The integration bounds for the volcano peaks are defined by the temperature range of the water desorption peak, thus accounting for all volatiles sublimating concurrently with water. All mixed-ice experiments were conducted with a fixed total coverage of ∼40 ML to eliminate the influence of the ice thickness and isolate the effect of the mixing ratio on the entrapment efficiencies.

5.3   Results and discussion

5.3.1   Binding energies

5.3.1.1 H_2S−H_2S

Figure 5.1 shows the IR spectra obtained after completing the deposition of the pure H_2S ice in the multilayer experiments. The figure focuses on the frequency range of the S-H stretching modes of H_2S—its most prominent IR feature. Five different thicknesses (19, 32, 45, 73, and 90 ML) were used to derive the H_2S−H_2S binding energy; that is, the binding energy dominated by H_2S interactions with other H_2S molecules. The TPD curves for each coverage are shown in gray in Figure 5.2, measured from the mass-to-charge (m/z) ratio of 34, which corresponds to the molecular ion of H_2S and represents its dominant mass signal in electron-impact mass spectrometry at 70 eV ionization energy[2].

To fit the TPD curves with the Polanyi-Wigner equation (eq. 5.3), we must first determine the preexponential factor ν_{TST} of H_2S using equations 5.4, 5.5, and 5.6. Since these equations are temperature dependent, we opt to derive ν_{TST} at the maximum temperature where the experimental curve is still well described by an exponential behavior. This is to ensure consistency in the data analysis: by choosing the maximum temperature within the exponential range, we ensure that ν_{TST} is consistent with the region within which the model is fitted. This temperature is determined on the basis of its adjusted R^2 value, a coefficient that measures the proportion of variation in outcomes explained by the model, while adjusting for the number of predictors used. This adjustment is particularly important in this context, as R^2 naturally increases with the temperature, even without an improvement in model fit. The maximum temperatures are 79.2, 78.9, 80.5, 80.6, and 81.5 K for the respective coverages of 19, 32, 45, 73, and 90 ML.

---

[2]https://webbook.nist.gov
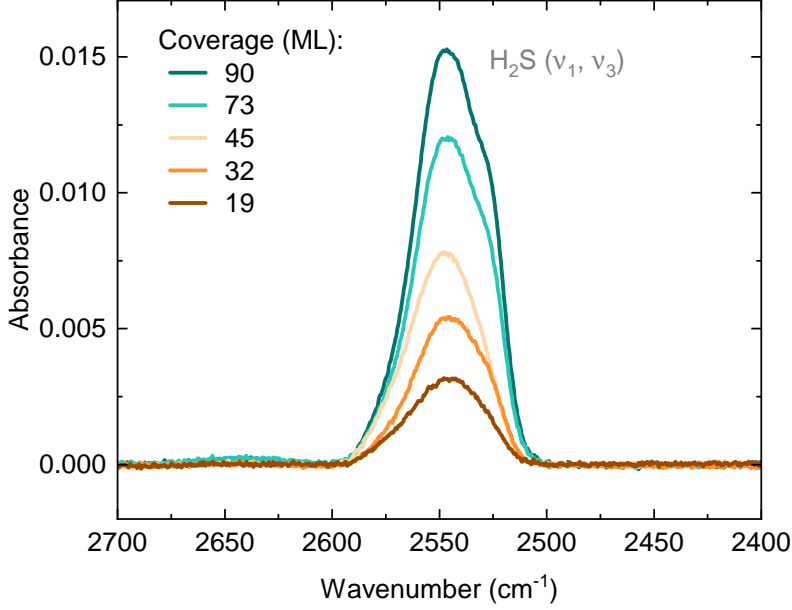
Figure 5.1: Infrared spectra recorded after the deposition of the five different multilayer H$_2$S ice thicknesses on top of the CsI window. The spectra are centered on the frequency range of the S-H stretching modes of H$_2$S (ν_1 and ν_3).
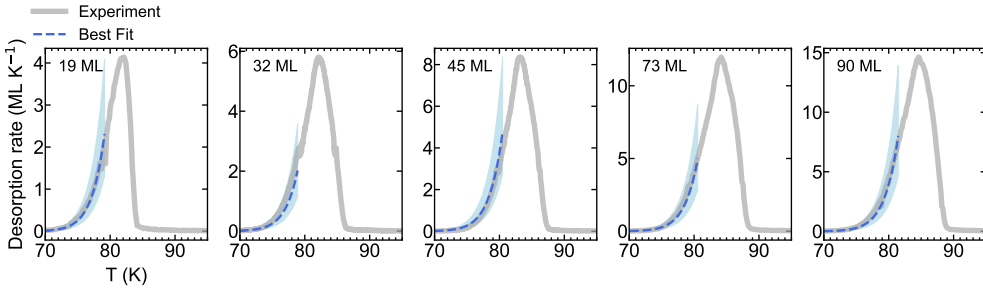
Figure 5.2: TPD curves of the multilayer H$_2$S ice experiments. The experimental data is shown in gray, while the zeroth-order Polanyi-Wigner models are shown with the dashed blue curve. The shaded blue region indicates the 1σ uncertainty.

As the substrate is warmed up, the morphology of the H$_2$S ice gradually changes toward more ordered configurations, with amorphous-to-crystalline transitions beginning at temperatures as low at $\sim$30 K, and nearing completion by $\sim$60 K (Fathe *et al.* 2006; Mifsud *et al.* 2024). Although the crystallization process appears to be largely finalized by the onset of desorption ($\gtrsim$70 K), the S-H stretching modes of the H$_2$S ice continue to blueshift as the temperature rises beyond this threshold (see Appendix 5.7.2 and Mifsud *et al.* 2024), indicating an ongoing reorientation of the ice until its complete desorption. This continued reorientation may contribute to deviations from zeroth-order kinetics near the desorption peak, disrupting the exponential trend. Our approach to the choice of temperature reduces the contribution from these confounding factors to the calculation of the preexponential factor.

An alternative, commonly-employed approach is to instead use the peak desorption tem-

perature of the TPD curve. In the case of H_2S, the temperature differences between the two approaches and their overall impact on the desorption parameters are small: the ν_{TST} values derived from the peak desorption T for each coverage (respectively, 82.1, 82.2, 83.0, 84.2, and 84.6 K) deviate by $\lesssim 16\%$ from the values derived by our preferred method, resulting in a less than 3% variation in the corresponding binding energies. Uncertainties in the derived ν_{TST} values stemming from the absolute error of 2 K in the temperature readout are of $\sim 1\%$. We emphasize that the H_2S-H_2S binding energy derived in this work corresponds to crystalline H_2S. However, given that the crystallization of H_2S is largely complete by temperatures much lower than its onset of desorption, any thermal desorption of pure H_2S from interstellar ices is expected to occur from its crystalline phase.

The ν_{TST} values derived for each coverage are used to fit their respective TPD curves with the zeroth-order Polanyi-Wigner equation. Following the above reasoning, the fit is performed for the temperature range where the curve maintains an exponential behavior; that is, until the same maximum temperature for which ν_{TST} was calculated. We performed a Monte Carlo analysis using 10,000 independent trials to incorporate and quantify the uncertainties in the ice coverage, absolute substrate temperature, and ν_{TST}. In each trial, temperature, coverage, and ν_{TST} values were randomly sampled from Gaussian distributions defined by their respective uncertainties. A least-squares fit was then applied to the logarithm of the molecule's desorption rate versus the inverse of the temperature, optimizing all five experimental curves simultaneously to derive the binding energy (E_b). This transformation, known as an Arrhenius plot, allows the data to be fitted with a straight line, thus mitigating temperature-dependent fitting biases that can arise when applying Monte Carlo sampling to exponential trends.

This analysis yields a mean best-fit H_2S-H_2S binding energy of $E_b = 3159 \pm 46$ K, shown in the original exponential format by the blue curves in Figure 5.2. The log-transformed Arrhenius fits are shown in Appendix 5.7.3. The uncertainties in E_b are primarily driven by errors in the absolute substrate temperature and in ν_{TST}, as the errors in ice coverage and from the fitting are $\lesssim 1$ K. Given that the uncertainties in ν_{TST} due to temperature readout errors are small ($\sim 1\%$), we adopt the standard deviation from the five experiments (7×10^{14} ML s^{-1}, or $\sim 4\%$) as the ν_{TST} error in the fits, which yields uncertainties of $\lesssim 5$ K in the binding energy. Consequently, most of the uncertainty in E_b are due to the absolute temperature error. Another approach could be to adopt as uncertainties in ν_{TST} the full range of values derived for the temperatures within the limits encompassed by the fit. However, this also does not affect the results appreciably: while, in this case, ν_{TST} uncertainties correspond to approximately 20%, the resulting mean E_b value remains unchanged, and the error is only increased by 1 K. Additionally, it is also possible to incorporate a temperature-dependent ν_{TST} value into the fit, but this approach produces a poorer fit to the data and was thus not preferred (see Appendix 5.7.4). In some instances, small artifacts are observed at the leading edge, and occasionally symmetrically at the trailing edge of the TPD curves. However, these artifacts have an insignificant impact on the results, with masked fits yielding E_b values that differ by less than 1 K. Table 5.3 summarizes the recommended desorption parameters derived experimentally for the multilayer H_2S ice. The recommended preexponential factor is the mean value between all five thicknesses, with its uncertainty corresponding to their standard deviation: $\nu_{TST} = (1.76 \pm 0.07) \times 10^{16}$ ML s^{-1}.

5.3.1.2 H_2S-H_2O

Figure 5.3 shows the TPD curves of the low-coverage H_2S ice grown on top of a cASW substrate. In total, six coverages are depicted: 1.6, 1.2, 0.6, 0.5, 0.3, and 0.2 ML (see Appendix 5.7.1 for details on the submonolayer coverage estimation). The two largest thicknesses, 1.6 and 1.2 ML, show nearly overlapping leading edges that culminate in sharp peaks at ~ 77 and ~ 76 K, respectively—in accordance with the expected dominating zeroth-order desorption behavior. In contrast, the submonolayer coverages display a markedly different

Table 5.3: Summary of the H_2S desorption parameters derived experimentally in this work

Regime	Substrate	n	Coverage (ML)	E_b (K)	ν_{TST} $(ML^{1-n}\ s^{-1})$
H_2S-H_2S	CsI window	0	$19-90$	3159 ± 46	$(1.76 \pm 0.07) \times 10^{16}$
H_2S-H_2O	cASW	1	0.6	3355 [179] [a]	$(1.69 \pm 0.04) \times 10^{16}$
H_2S-H_2O	cASW	1	0.5	3368 [172] [a]	$(1.72 \pm 0.04) \times 10^{16}$
H_2S-H_2O	cASW	1	0.3	3401 [169] [a]	$(1.83 \pm 0.05) \times 10^{16}$
H_2S-H_2O	cASW	1	0.2	3443 [191] [a]	$(1.85 \pm 0.05) \times 10^{16}$

Notes. [a] Square brackets denote the FWHMs of the binding energy distributions.

profile, with misaligned leading edges and peak desorption temperatures that increase slightly with decreasing coverages ($T_{peak} \sim$ 79.3, 79.6, 81.1, and 81.3 K for 0.6, 0.5, 0.3, and 0.2 ML). This behavior is consistent with pure first-order desorption, and therefore the $0.6-0.2$ ML coverages are used to derive the H_2S-H_2O binding energy (dominated by H_2S interactions with water).
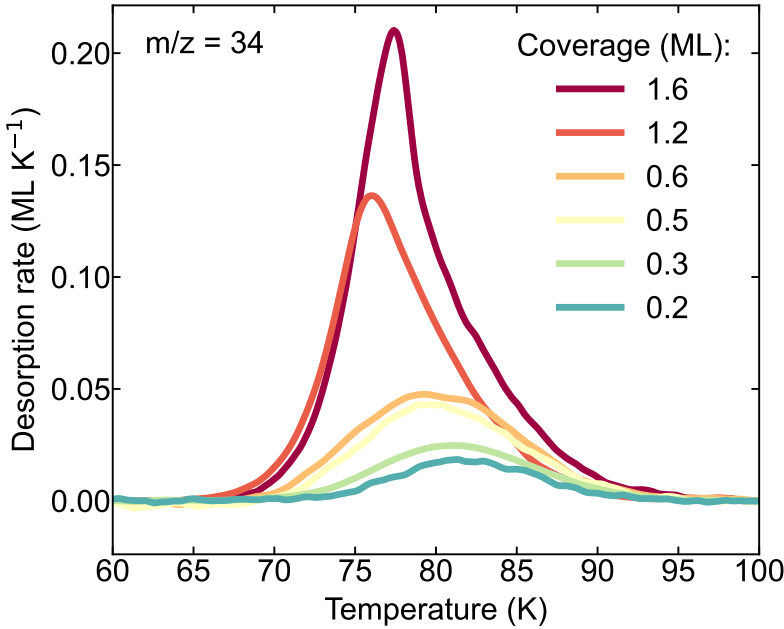
Figure 5.3: TPD curves of the low-coverage H_2S ice experiments deposited on top of a cASW substrate. The transition from zeroth-order to pure first-order sublimation behavior is seen for coverages <1.2 ML. The experimental data is smoothed for clarity.

In the case of the submonolayer TPD curves, unlike the multilayer curves, the entire desorption profile is fitted to find E_b. As a result, the peak desorption temperature of the curve is encompassed by the model, and thus we calculate ν_{TST} at the peak value for each coverage—which reflects the transition state of the largest parcel of desorbed H_2S molecules. Also differently from the multilayer regime, the TPD curves of the submonolayer H_2S ice cannot

be described by a single binding energy (see Appendix 5.7.5 for an example of an attempted fit). This is a direct consequence of the non-homogeneous nature of the cASW substrate, which generates multiple binding sites that result in a range of H_2S-H_2O desorption energies. To account for that, we fit a linear combination of first-order Polanyi-Wigner equations (eq. 5.3) to the curves, with statistical weights normalized to the initial ice coverages for each experiment. This allows us to determine the relative population of each binding site. The same approach has been used in the past to derive submonolayer binding energies of hypervolatiles such as N_2 and CO, as well as less volatile molecules such as 2-C and 3-C hydrocarbons and methanol, on varying substrates (from water ice to graphite; Doronin et al. 2015; Fayolle et al. 2016; Behmard et al. 2019). Since the preexponential factor is calculated using equations 5.4, 5.5, and 5.6, it is treated as a fixed parameter when fitting the curves with a linear combination of Polanyi-Wigner equations. Our sampled desorption energies range from 2000 to 4500 K in steps of 90 K, chosen to balance fit resolution and degeneracies associated with smaller bin sizes. Figure 5.4 shows the resulting fits to the submonolayer TPD curves and their corresponding binding energy distributions, plotted as fractional coverages as a function of the energy.

The population histograms can be approximated by a normal distribution and are thus fitted by a Gaussian curve to allow for more straightforward interpretation (red dashed line in the right panels in Figure 5.4). The mean binding energy and FWHM values for each coverage are listed in Table 5.3 and can be regarded as representative desorption energies for each ice thickness. The corresponding ν_{TST} values used in the fits are also listed, with their uncertainties stemming from the absolute error in the substrate temperature. Among the four coverages, the average binding energy and preexponential factor are $E_b = 3392 \pm 56$ K and $\nu_{TST} = (1.7 \pm 0.1) \times 10^{16}$ s^{-1}. The uncertainty of E_b encompasses the relative error due to the step size in the binding energy sampling and the standard deviation among the four coverages, while for ν_{TST} it is taken solely from its standard deviation.

5.3.1.3   Binding energies vs coverage

In Figure 5.5, we show a comparison of all H_2S binding energies derived in this work as a function of coverage. The multilayer binding energy ($E_b \sim 3159$ K) is slightly lower than the submonolayer values, with a difference of $\sim 7\%$ w.r.t the average submonolayer E_b (~ 3392 K). This small difference suggests that the H_2S-H_2S interactions are only moderately weaker than the H_2S-H_2O counterparts. This is rather expected: both H_2S and H_2O interact via hydrogen bonding networks—known as one of the strongest intermolecular forces—where hydrogen atoms are covalently bonded to an electronegative atom. Since sulfur is larger than oxygen, it is less electronegative, and therefore the H-bonding networks are weaker for H_2S than for H_2O. Indeed, the fact that pure first-order desorption could be achieved at coverages of ~ 0.6 ML (as evinced by the profile of the TPD curves in Figure 5.3, see section 5.3.1.2) suggests that wetting of the H_2S on the cASW surface proceeds relatively uniformly, as opposed to having a tendency to form H_2S islands (for comparison, Bergner et al. 2022 found that a dose of 0.04 ML was required to achieve the first-order desorption regime for HCN on cASW). This is in line with a (modest) preference of H_2S to interact with H_2O.

In the submonolayer regime, the mean H_2S-H_2O binding energy increases with decreasing ice coverage, in line with other laboratory measurements for various adsorbate-substrate combinations (e.g., Noble et al. 2012; Fayolle et al. 2016; He et al. 2016a; Nguyen et al. 2018; Behmard et al. 2019). This generalized phenomenon can be explained by two effects: 1. lateral interactions influencing the binding energy of the adsorbates, or 2. a preference of the adsorbates to occupy deeper binding sites (caused by their diffusion from shallower sites)— with the most likely explanation being a combination of the two. The weaker H_2S-H_2S interactions relative to H_2S-H_2O may manifest as a slight decrease in binding energy caused by lateral H_2S interactions compared to isolated H_2S adsorbates fully interacting with H_2O, in support of explanation 1. Complementarily, the alignment of the trailing edges in the
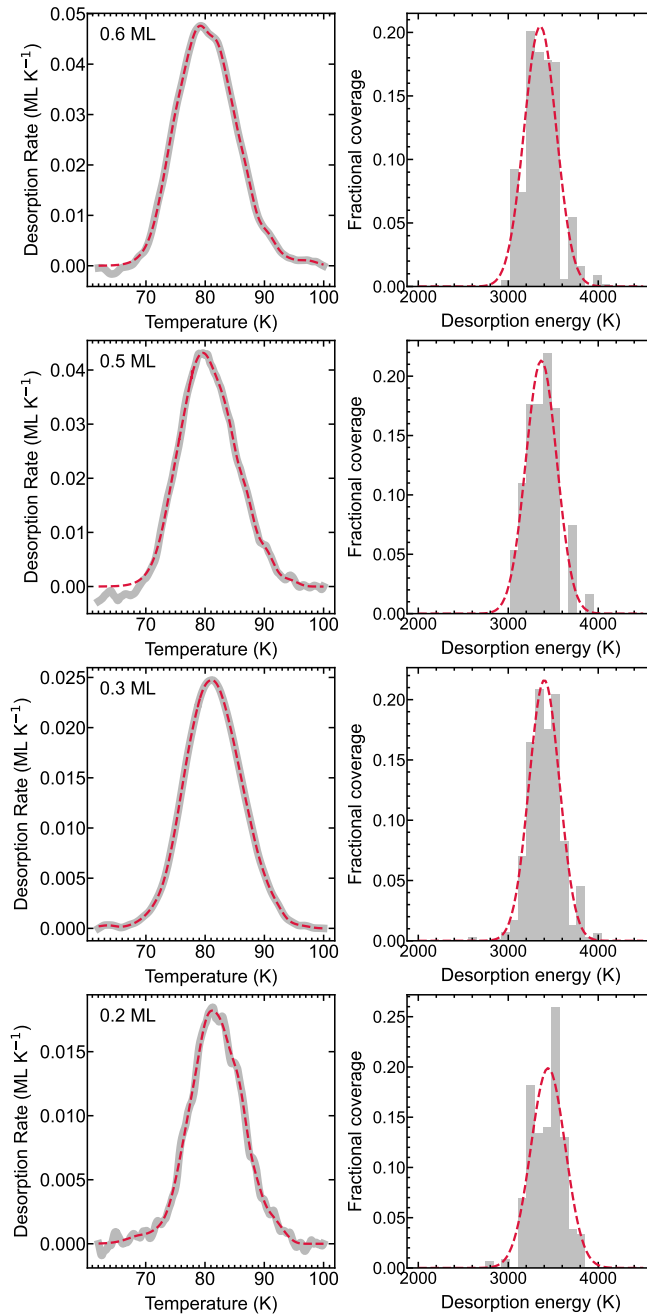
Figure 5.4: Results of the fits to the submonolayer H$_2$S ice data. Each row corresponds to a different H$_2$S ice thickness: ∼0.6, ∼0.5, ∼0.3, and ∼0.2 ML (from top to bottom). Left panels show the TPD curves with the experimental data in gray and the fits with a linear combination of first-order Polanyi-Wigner equations in red. Right panels show the corresponding binding energy distribution: normalized fractional coverages are shown as a functional of the binding energy (gray histogram), superimposed by a Gaussian fit to the distribution (red dashed line).
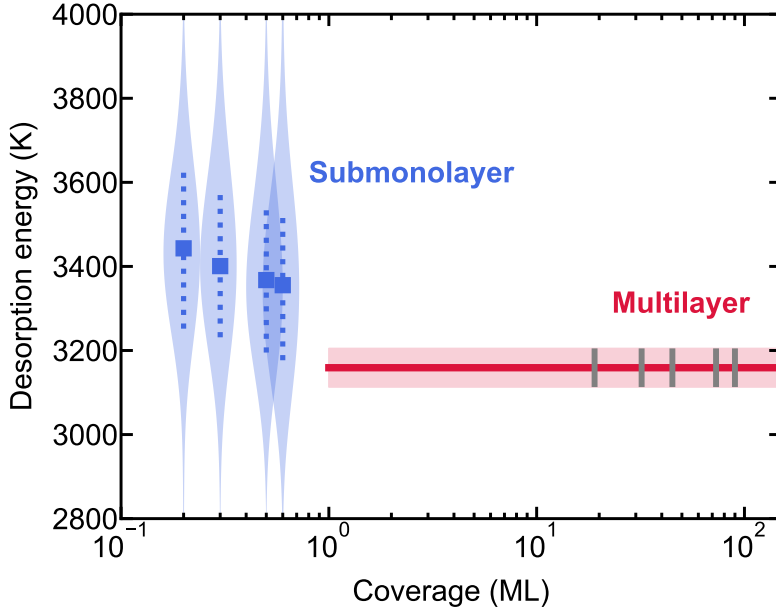
Figure 5.5: Desorption energies derived experimentally in this work as a function of H_2S ice thickness. For the submonolayer regime, the binding energies are represented by blue violin plots, where the square markers indicates the mean binding energies, and the vertical dotted lines show the FWHMs of the Gaussian fits to the binding energy distributions for each coverage. The contour of each violin plot reflects the full range of the sampled binding energy distribution, with its thickness normalized according to the statistical weights (or fractional coverages) of each E_b value. The multilayer binding energy is depicted as a red solid line with its uncertainty shown by the light-red shadowed area. The five different ice coverages used to derive the multilayer E_b are shown as gray vertical lines.

submonolayer experiments suggests that the deeper binding sites are similarly occupied for all explored thicknesses, reinforcing explanation 2.

To the best of our knowledge, this is the first study to experimentally determine binding energies for H_2S ice analogues. Nonetheless, estimations based on laboratory data have been proposed in the past. Minissale *et al.* (2022) recommend a value of $E_b = 3426$ K for H_2S on a cASW substrate based on the peak desorption temperature of H_2S and the associated ν obtained using the TST formalism—in good agreement with our measurements. In contrast, the E_b value of 2296±9 K estimated by Penteado *et al.* (2017), based on the relative peak desorption temperature of H_2S with respect to H_2O and the binding energy of the latter, differs significantly from our measurements. Computational efforts have also been made to estimate the binding energies of H_2S. In general, computed E_b distributions for H_2S on water substrates range between ∼ 2000 − 3600 K (Wakelam *et al.* 2017; Das *et al.* 2018; Ferrero *et al.* 2020; Piacentino & Öberg 2022), but some studies predict much lower ranges, with upper limits closer to 2000 K (Oba *et al.* 2018; Bariosco *et al.* 2024). The experimental values reported here for H_2S-H_2O (and H_2S-H_2S) are generally not well reproduced by the computations, often falling within their upper bounds or, in some cases, being entirely underpredicted. This discrepancy is likely due to the limitations in the computational methods to incorporate diffusion as part of their binding energy calculations, which can lead to systematic underestimations by failing to account for the tendency of adsorbates to settle into deeper binding sites prior to sublimating. In an astrophysical context, icy mantles shrouding

dust grains are gradually heated by protostellar radiation, in which case adsorbates in shallow sites become free to diffuse throughout the ice and find deeper binding sites before eventually sublimating. The binding energies derived from TPD experiments are therefore expected to better reproduce the conditions in space.

5.3.2   Entrapment in H_2O

The entrapment behavior of H_2S in water-dominated ice was investigated by TPD experiments of H_2O:H_2S ice mixtures with four different ratios (5.1:1, 7.5:1, 9.3:1, and 17:1, determined from the final IR spectra measured after deposition) and constant total ice thicknesses ($\sim$40 ML). These mixing conditions are chosen to ensure that H_2S is mostly surrounded by H_2O molecules while still allowing for measurements with good signal-to-noise ratios, particularly for the more water-dominated cases. Additionally, a control experiment consisting of $^{13}CO_2$ mixed in H_2O ice with a ratio of H_2O:$^{13}CO_2$=14:1 was also performed with the goal of testing the potential role of intermolecular interactions on the entrapment efficiencies. Both H_2S and CO_2 have similar volatilities, with desorption temperatures typically falling in similar ranges for the same pressure and substrate conditions. However, CO_2 is an apolar molecule and its intermolecular interactions with H_2O are markedly different from those of H_2S. The resulting TPD curves of the H_2O:H_2S = 9.3:1 experiment, as well as the control H_2O:$^{13}CO_2$ = 14:1 experiment, are shown in the upper and lower panels of Figure 5.6, respectively.

Two desorption features are observed for H_2S ice mixed in H_2O: a monolayer desorption peak at $\sim$84 K, and a molecular volcano feature at $\sim$150 K. The former is consistent with H_2S desorption characterized by the H_2S-H_2O binding energy (see Appendix 5.7.6), and includes contributions from H_2S adsorbates on the uppermost ice layer, as well as H_2S molecules occupying channels within the H_2O matrix with access to the surface. The molecular volcano is the strongest desorption peak, and corresponds to H_2S being released from the H_2O ice matrix as the ice crystallizes and cracks, creating new channels to the surface. In the case of $^{13}CO_2$, a third desorption regime is observed ranging from $\sim 90 - 140$ K. Following its monolayer desorption feature at $\sim$80 K, the TPD curve does not return to zero desorption rate, but instead shows a relatively steady desorption of $^{13}CO_2$ until the molecular volcano feature at $\sim$150 K—after which it appears to be completely sublimated. This continuous desorption between the two main features might be related to the diffusion of $^{13}CO_2$ through the H_2O ice.

Table 5.4 lists and Figure 5.7 depicts the entrapment efficiencies of H_2S and $^{13}CO_2$ measured from our mixed-ice experiments (see section 5.2.3 for details on how these are determined). The uncertainties are dominated by experimental variability and are thus taken as 10% of the entrapment efficiency, based on the estimations derived by Simon *et al.* (2023) with the same experimental setup for H_2O:hypervolatile mixtures with ratios 3:1. In comparison, the error due to stochastic instrumental noise amounts to $\lesssim$2%. Overall, H_2S experiences very efficient entrapment in the H_2O-ice matrix, with $\sim 76 - 85\%$ of the H_2S unable to escape to the gas phase until H_2O undergoes significant structural changes. This efficient entrapment of H_2S has been alluded to in the past by Jiménez-Escobar & Muñoz Caro (2011a) based on experiments using H_2O:H_2S ice mixtures with roughly 10% H_2S concentrations. Larger water abundances relative to H_2S result in higher entrapment efficiencies, consistent with the behavior observed for many other species mixed in H_2O and CO_2-dominated ices (Fayolle *et al.* 2011; Martín-Doménech *et al.* 2014; Simon *et al.* 2019, 2023; Kruczkiewicz *et al.* 2024; Pesciotta *et al.* 2024). Fayolle *et al.* (2011) propose two explanations for this phenomenon: 1. there is a reduction in porous channels connected to the surface for higher dilutions of the volatile; and/or 2. higher volatile concentrations increase its diffusion lengths. The two highest dilutions (H_2O:H_2S $\sim$9:1 and 17:1) yield analogous efficiencies within their uncertainties, signaling that the trapping capacity of H_2S in the H_2O ice saturates at $\sim$85% for our deposition conditions and a total ice thickness of $\sim$40 ML. Similarly, Pesciotta *et al.* (2024) recently reported a leveling-off of the entrapment efficiencies of CO in both H_2O and
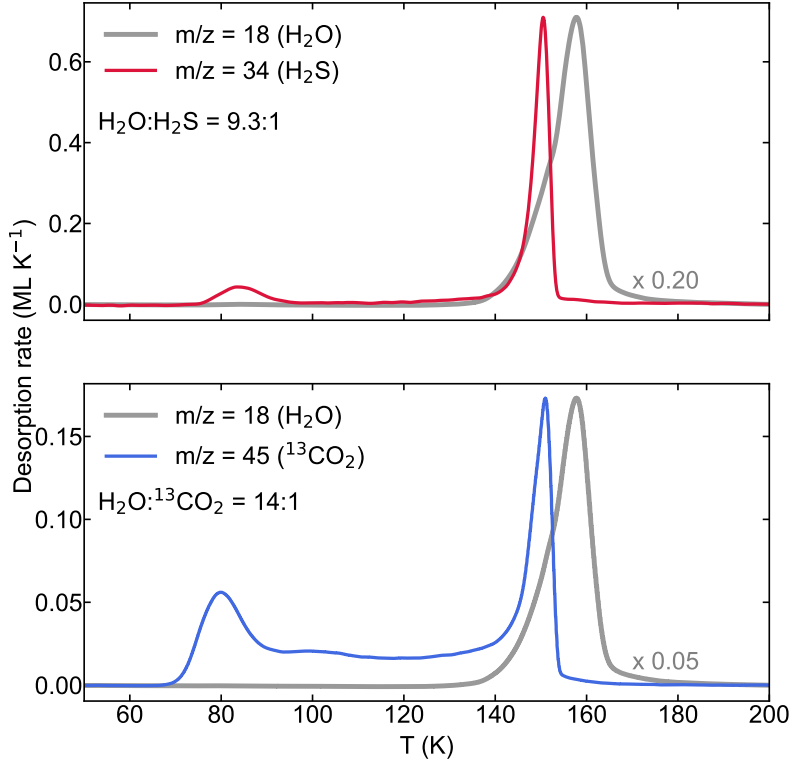
Figure 5.6: TPD curves of two mixed-ice experiments, $H_2O:H_2S = 9.3:1$ (top) and $H_2O:^{13}CO_2 = 14:1$ (bottom). The desorption data of H_2O, H_2S, and $^{13}CO_2$ are shown in gray (m/z = 18, $[H_2O]^+$), red (m/z = 34, $[H_2S]^+$), and blue (m/z = 45, $[^{13}CO_2]^+$), respectively. Two desorption regimes are seen for H_2S: a submonolayer H_2S-H_2O desorption feature and a molecular volcano desorption peak. For $^{13}CO_2$, a third regime is observed between its submonolayer and volcano peaks, indicating constant sublimation within that temperature range.

CO_2 dominated binary ice mixtures starting at concentrations of $\lesssim$1:10 volatile:matrix. We emphasize, however, that the CO entrapment saturation measured in their work occurred at significantly lower efficiencies than the saturation point for H_2S in H_2O measured here (they find $\sim$69% and $\sim$61% for CO_2 and H_2O matrices, respectively, in 1:15 CO:matrix ratios and ice thicknesses $\gtrsim$50 ML).

In comparison to H_2S, $^{13}CO_2$ is significantly less entrapped in the H_2O ice, with an efficiency of $\sim$ 52% for a $H_2O:^{13}CO_2$ ratio of $\sim$14:1. This stark difference between two similarly volatile molecules might be explained by the nature of their interactions with the water matrix. For $^{13}CO_2$, the oxygen atoms may serve as hydrogen bond acceptors; however, their very low partial negative charges result in exceptionally weak hydrogen bonds (Zukowski *et al.* 2017). Interactions between $^{13}CO_2$ and H_2O are thus primarily governed by weaker van der Waals forces. In contrast, the hydrogen bonds between H_2S and H_2O, while not as strong as H_2O-H_2O counterparts (Craw & Bacskay 1992), still offer significant energetic stabilization. This is reflected in the mean H_2S-H_2O binding energy measured here at 3392 ± 56 K, which surpasses the CO_2-H_2O binding energies measured in the literature by

Table 5.4: Summary of the entrapment efficiencies derived experimentally in this work.

Mixture	Ratio	Entrapment efficiency (%)
$H_2O{:}H_2S$	5.1:1	76±8
$H_2O{:}H_2S$	7.5:1	80±8
$H_2O{:}H_2S$	9.3:1	86±9
$H_2O{:}H_2S$	17:1	85±9
$H_2O{:}^{13}CO_2$	14:1	52±5

Notes. All experiments kept a constant total ice thickness of $\sim$40 ML.

$\sim$50$-$60%[3]. In fact, both Noble *et al.* (2012) and Edridge *et al.* (2013) reported CO_2-CO_2 binding energies to be higher than the mean value for those of CO_2-H_2O, in clear contrast with the behavior observed here for H_2S and water. The difference in the interaction energetics between the two systems ($H_2O{:}^{13}CO_2$ vs $H_2O{:}H_2S$) may result in H_2S diffusing less readily through H_2O ice compared to $^{13}CO_2$, leading to more efficient trapping of H_2S. Indeed, the steady desorption of $^{13}CO_2$ between its monolayer and volcano peaks may suggest that it is more mobile than H_2S, for which this behavior is minimal. Specifically, this temperature range accounts for $\lesssim$ 5% of the integrated QMS signal in all H_2S experiments, and corresponds to only $\sim$ 2% in the $H_2O{:}H_2S$ = 9.3:1 mixture, compared to $\sim$ 21% for $^{13}CO_2$ in a higher dilution.

In addition to intermolecular interactions, the mass and size of the molecule may also influence its diffusion and entrapment. Based on their molecular masses and kinetic diameters, $^{13}CO_2$ is $\sim$30% heavier and $\sim$9% smaller than H_2S ($m_{^{13}CO_2} \sim 45$ amu vs $m_{H_2S} \sim 34$ amu; $d_{^{12}CO_2} \sim 3.3$ vs $d_{H_2S} \sim 3.6$, Matteucci *et al.* 2006; Ismail *et al.* 2015). Considering the mass effect alone, the attempt frequency for diffusion of $^{13}CO_2$ would be smaller than that of H_2S, resulting in the former diffusing slower (see, e.g., Cuppen *et al.* 2017) and consequently being more efficiently trapped. The fact that the inverse is observed in our experiments signals that the mass effect is overpowered by other factors favoring the entrapment of H_2S. In contrast, the size difference could result in H_2S molecules being more efficiently trapped if the mean pore size is smaller than the kinetic diameter of H_2S, but larger than that of $^{13}CO_2$. This size mismatch may create a geometrical limitation, with the pores acting similarly to a net that restricts diffusion. For instance, gas permeance through microporous silica membranes (pore size between $3.8 - 5.5$) has been shown to decrease steeply with the species' kinetic diameter, with the permeance of N_2 ($d \sim 3.6$, similar to H_2S; Ismail *et al.* 2015) being roughly one order of magnitude lower than that of CO_2 (De Vos & Verweij 1998). ASW ices are typically found to be microporous (pore width $\leq$ 20), with no lower limits estimation for the pore sizes and little to no incidence of mesopores (Mayer & Pletzer 1986; Raut *et al.* 2007; Cazaux *et al.* 2015; Carmack *et al.* 2023). This is particularly true for ices grown through collimated deposition—the technique employed in this work. The possibility of a pore effect therefore cannot be ruled out. Pore effects could also play a role in the constant sublimation regime of CO_2, observed between its monolayer and volcano features. The same behavior is seen for $^{12}CO_2{:}H_2O$ ice mixtures in Kruczkiewicz *et al.* (2024), though they note that this is not observed for other, more volatile species (such as Ar and CO) trapped in H_2O-dominated binary ices. Since both Ar and CO have larger kinetic diameters than CO_2 ($d_{Ar} \sim 3.4$ and $d_{CO} \sim 3.8$; Breck 1973; Matteucci *et al.* 2006), the fact that they do not display the constant

---

[3]Noble *et al.* (2012) and Edridge *et al.* (2013) measured the mean monolayer CO_2 binding energy on ASW to be $\sim$2247 K and $\sim$2100 K, respectively. The former was measured on a nonporous ASW substrate, while the latter was measured on porous ASW.
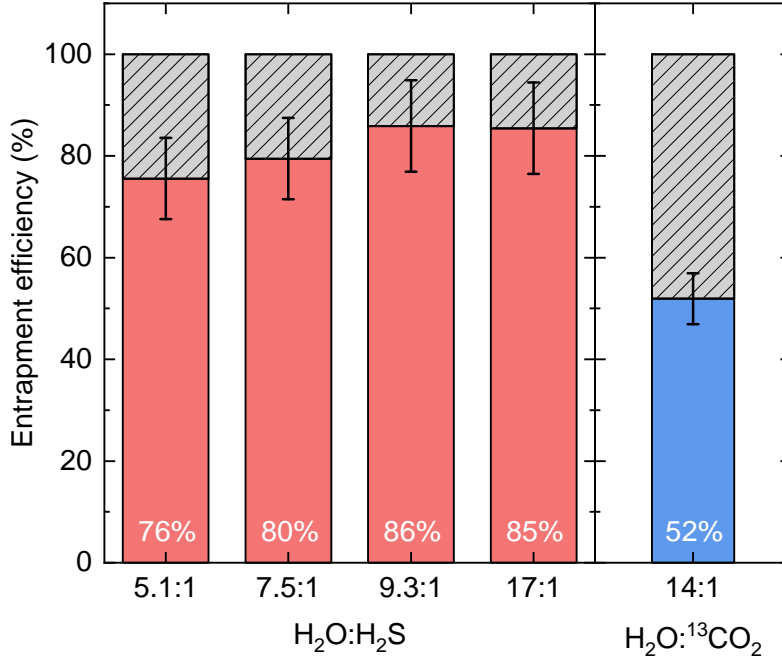
Figure 5.7: Efficiencies with which H_2S (red) and $^{13}CO_2$ (blue) are trapped in water-rich binary ice mixtures as derived from our experiments (see also Table 5.4).

sublimation regime in the experiments by Kruczkiewicz *et al.* (2024) does not preclude this possibility. Dedicated experimental investigations are necessary to fully constrain the effect of the species' size and intermolecular interactions to entrapment. Nonetheless, the overall result is that H_2S is very efficiently entrapped in H_2O ice, more so than other similarly volatile molecules, which has significant implications to its gas vs ice distribution in planet-forming regions.

5.4   Astrophysical implications

The binding energies derived experimentally in this study are used to estimate the locations of the H_2S sublimation fronts in the midplane of a representative protoplanetary disk. First, we calculate the desorption temperatures of H_2S for its two binding energies (H_2S-H_2S and H_2S-H_2O) following the formalism by Hollenbach *et al.* (2009), in which the desorption temperature is found by equating the flux of molecules adsorbing on the grain surface to the flux of molecules desorbing from it:

$$T_i \sim (E_{b,i}/k) \left[\ln \left(\frac{4 N_i f_i \nu}{n_i v_i} \right) \right]^{-1}, \tag{5.7}$$

where T_i is the sublimation temperature of species i, $E_{b,i}$ is its binding energy, N_i is the number of adsorption sites (assumed to be $\sim 10^{15}$ cm^{-2}), f_i is the fraction of such sites occupied by species i, and ν_i is its vibrational frequency in the surface potential well (i.e., the preexponential factor in equation 5.3). In the denominator, n_i is the number density of species i in the gas phase, and v_i is its thermal speed. We estimate f_i based on the cometary abundance of H_2S relative to water, $H_2S/H_2O = 1.10\pm0.05\%$, as measured by the

Rosetta mission on the coma of comet 67P (Calmonte *et al.* 2016); and assuming a cometary composition of $\sim 80\%$ water (e.g., Delsemme 1991). The number density n_i is estimated by multiplying the cometary H_2S/H_2O by the water abundance with respect to H and the number density of hydrogen nuclei in a disk midplane (taken as $H_2O/H \sim 10^{-4}$, e.g., Drozdovskaya *et al.* 2015; Boogert *et al.* 2015; and $n_H \sim 10^{10}$ cm $^{-3}$, e.g., Walsh *et al.* 2014). This yields sublimation temperatures for H_2S-H_2S and H_2S-H_2O of ~ 64 K and ~ 69 K, respectively. For the latter, the mean H_2S-H_2O binding energy value was used ($E_b \sim 3392$ K). We note that the desorption temperatures in the disk model differ from those in the laboratory due to variations in physical conditions between the two environments.

To derive the locations of the sublimation fronts, we assume a representative disk midplane radial temperature profile:

$$T = 200 \times r^{-0.62}, \tag{5.8}$$

where r is the radial distance in a.u. This corresponds to the median midplane temperature distribution found for a sample of 24 T-Tauri disks (Andrews & Williams 2007). The resulting sublimation front locations are shown in Figure 5.8.
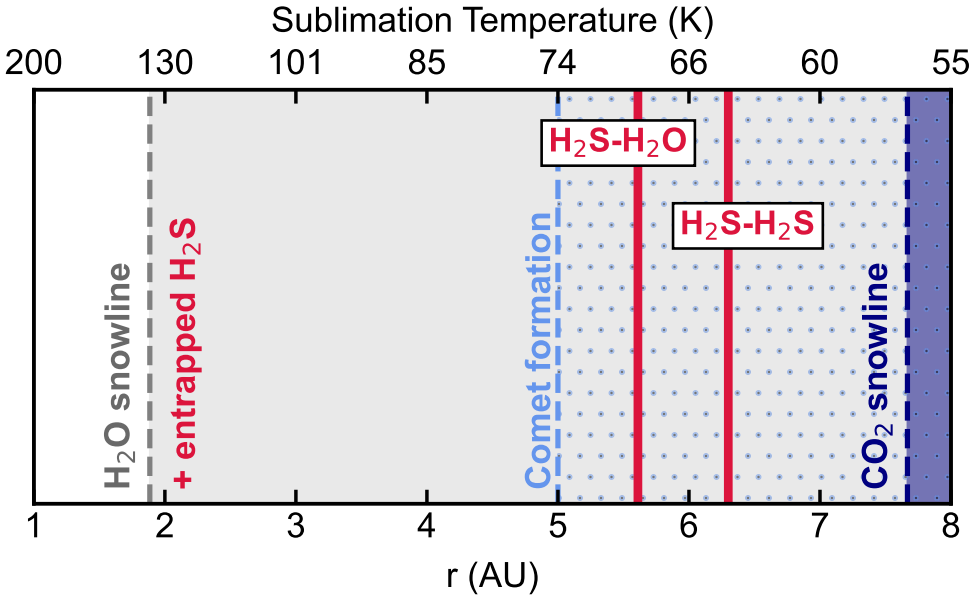
Figure 5.8: Sublimation front locations for the H_2S-H_2S and H_2S-H_2O binding energies estimated for a representative T-Tauri disk midplane. Most of the H_2S will remain entrapped in the ice past its sublimation front radii, and will only be released to the gas phase close to the water snowline. The CO_2 snowline location is also shown for comparison. It was estimated based on the mean binding energy derived by Noble *et al.* (2012) for (sub)monolayer CO_2 ice on a nonporous ASW surface and their adopted preexponential factor of 10^{12} s^{-1}, while assuming ice abundances $N(CO_2)/N(H_2O) \sim 0.28$ (median value observed in low-mass young stellar objects; Boogert *et al.* 2015).

The sublimation fronts for the H_2S-H_2S and H_2S-H_2O binding energies occur at ~ 6.3 au and ~ 5.6 au, respectively. The former corresponds to pure H_2S ice desorption, while the latter is relevant for H_2S desorbing from a H_2O-rich surface. In the case of H_2S entrapped in water ice, its sublimation will be delayed to much closer to the water snowline at ~ 1.9 au (assuming $E_{b,H_2O} \sim 5600$ K, Wakelam *et al.* 2017; and a typical $\nu \sim 10^{13}$ s^{-1}). The precise location of this sublimation front will depend on the water crystallization kinetics, but will

generally occur at slightly lower temperatures than H_2O desorption, placing it just beyond the H_2O snowline.

The deuterium fractionation of gaseous H_2S observed towards Class 0 protostars suggests that it is formed in ices during early prestellar cloud timescales, before the onset of the catastrophic CO freeze-out (Ceccarelli *et al.* 2014). Most of the water ice is also formed during similarly early timescales, resulting in H_2S likely inhabiting a H_2O-rich ice environment—the so-called polar ice layer. The sublimation behavior of H_2S will therefore be likely dominated by its entrapment within H_2O ice, given its high efficiency as measured in this work ($\sim 85\%$ for H_2S concentrations of $\sim 5-10\%$ in H_2O). In more representative interstellar scenarios, the bulk H_2S concentration in H_2O ice is expected to be considerably smaller ($\lesssim 1\%$ based on observationally-constrained H_2S ice upper limits), and ice thicknesses larger ($\gtrsim 0.01$ μm; Dartois *et al.* 2018) than our experimental conditions. Like for higher dilutions, entrapment efficiencies have been shown to increase with ice thickness (Fayolle *et al.* 2011; Simon *et al.* 2019; Bergner *et al.* 2022; Simon *et al.* 2023; Kruczkiewicz *et al.* 2024), though this dependency might break down for thicknesses $\gtrsim 50$ ML (Pesciotta *et al.* 2024). Moreover, the deposition temperatures used in our entrapment experiments generate porous amorphous water ice matrices, whereas more representative cASW might trap volatiles more efficiently than porous counterparts (Kruczkiewicz *et al.* 2024).[4] These three factors (mixing ratios, thicknesses, and water ice morphology) thus point to real H_2S entrapment efficiencies being higher than the values measured here, further highlighting the shift in the H_2S sublimation front closer to the water snowline. At the same time, differences between the heating rates used in the laboratory and those occurring in astrophysical timescales could result in an overestimation of the measured entrapment efficiencies (Cuppen *et al.* 2017). Moreover, since sulfur atoms are heavier and less abundant than oxygen, the bulk of the H_2S ice has been predicted to form at slightly later timescales (by ~ 1.4 A_V) than H_2O (Goicoechea *et al.* 2021). This differential formation could result in a concentration gradient for H_2S within the polar ice layer, meaning that a fraction of H_2S could exists in higher local concentrations than the estimated $\lesssim 1\%$. In any case, the very efficient entrapment of H_2S in water, with measured efficiencies of $\gtrsim 75\%$ for H_2S concentrations even as high as $\sim 20\%$, means that even in these scenarios, a significant portion of H_2S will remain entrapped in water.

Some ice species, such as CO_2 and potentially HCN, exhibit a segregation behavior upon heating, where diffusion leads to the formation of pockets of pure ice instead of a homogeneous mixture (e.g., Öberg *et al.* 2009a; Boogert *et al.* 2015; Bergner *et al.* 2022). For H_2S, segregation appears to be less energetically favorable than for the archetypal case of CO_2. Unlike CO_2, the H_2S-H_2O binding energies exceed that of H_2S-H_2S, and H_2S appears to wet the cASW surface effectively. However, the significantly stronger stabilization among H_2O molecules themselves compared to H_2S-H_2O interactions ($E_b(H_2O-H_2O) \sim 5600$ K; Wakelam *et al.* 2017) may still drive some degree of segregation, as a system with separate water-rich and H_2S-rich pockets can be energetically more favorable than a fully mixed one. Similar energetic considerations are required in the kinetic Monte Carlo simulations performed by Öberg *et al.* (2009a) to reproduce the segregation behavior they observed experimentally for CO_2:H_2O mixed ices. [5] Consequently, in an astrophysical context, a fraction of H_2S within channels with access to the surface might desorb at the sublimation fronts defined by

---

[4]Previously, Burke & Brown (2010) suggested that more compact ASW should result in lower entrapment efficiencies due to a reduction in available trapping sites. This interpretation was based on earlier experiments by Bar-Nun *et al.* (1988), which observed lower entrapment efficiencies of hypervolatiles in binary mixtures with water ice as the deposition temperature increased. However, this decline is more likely dominated by the reduced surface residence time of hypervolatiles at higher deposition temperatures (Zhou *et al.* 2024), rather than due to the water ice morphology. Recently, Kruczkiewicz *et al.* (2024) deposited cASW ices at 10 K using well-collimated beams, and found that trapping capacities were actually higher for the compact ice structure.

[5]Öberg *et al.* (2009a) find that segregation in CO_2:H_2O ice mixtures is not precluded by CO_2-CO_2 binding energies being lower than those of CO_2-H_2O. Rather, it might occur when a CO_2 molecule from a water-dominated environment is swapped with a H_2O molecule from a CO_2-dominated en-

H_2S-H_2S and H_2S-H_2O interactions, depending on the extent of segregation.

Nonetheless, the primary sublimation front of H_2S is driven by its entrapment. This effectively shifts the H_2S sublimation front closer to the protostar by nearly threefold, fully retaining H_2S in the ice throughout and beyond the comet-formation zone (> 5 au; Mandt *et al.* 2015), and across the region where other H_2O-rich bodies, such as icy asteroids, are formed. Consequently, H_2S may be incorporated into planetesimal cores formed beyond the water snowline (~ 1.9 au), which in turn may deliver it to terrestrial planets. In fact, Rosetta measurements of the H_2S/H_2O ratios in the coma of comet 67P remained remarkably constant over several months, strongly suggesting that H_2S desorbs from the comet nucleus along with H_2O (Calmonte *et al.* 2016). This supports the hypothesis that H_2S is incorporated into cometary cores mixed with H_2O, where it remains preserved beyond its sublimation temperature, until water ice desorption.

Additionally, solid-state H_2S can react with NH_3 to form the ammonium salt $NH_4^+SH^-$——a likely major carrier of both nitrogen and sulfur in comets (Altwegg *et al.* 2022; Slavicinska *et al.* 2025). Upon sublimation, this salt decomposes back into its neutral reactants, releasing H_2S (and NH_3) into the gas phase. The desorption temperature of the salt is nearly identical to that of water, meaning that the gaseous H_2S released from the decomposition of the salt will have a sublimation front similar to that of neutral H_2S entrapped in H_2O. Distinguishing the contribution from the neutral H_2S and the salt to the gas-phase distribution of H_2S in disks presents a challenge, but it could be an interesting avenue for future exploration. We emphasize that the neutral H_2S component within interstellar ices is likely significant, as the $NH_4^+SH^-$ salt detected by the Rosetta mission is found in the comet's grains, while the ice predominantly contains H_2S in its neutral form (Altwegg *et al.* 2022).

5.5 Conclusions

In this work, we provide a comprehensive characterization of the thermal sublimation dynamics of H_2S ice. We investigate its binding energies both dominated by interactions with other H_2S molecules (H_2S-H_2S) and with H_2O molecules (H_2S-H_2O), as well as the efficiency with which it is entrapped in water-rich ices. This information is used to estimate the different snowline positions of H_2S in the midplane of a representative T-Tauri protoplanetary disk. Our main findings are as follows:

1. We derive $E_b = 3159 \pm 46$ K for the H_2S-H_2S binding energy, with a mean preexponential factor of $\nu = (1.76 \pm 0.07) \times 10^{16}$ ML s^{-1}.

2. For H_2S-H_2O, we find four sets of desorption parameters for four different H_2S coverages (0.6, 0.5, 0.3, and 0.2 ML). The mean binding energy and preexponential factor are $E_b = 3392 \pm 56$ K and $\nu = (1.7 \pm 0.1) \times 10^{16}$ s^{-1}.

3. Theoretical H_2S binding energies generally underpredict the experimental values derived in this work. We propose this mismatch is due to a limitation in the computations to account for adsorbate diffusion causing a preference for occupying deeper surface biding sites. In interstellar and protoplanetary conditions, diffusion plays an important role in a molecule's sublimation dynamics, and therefore our experimentally-derived binding energies are expected to be more representative values.

4. H_2S is very efficiently entrapped in H_2O ice, with efficiencies of $\sim 75-85\%$ for H_2O:H_2S mixing ratios of 1:$\sim 5-17$ (more diluted cases yielding more efficient entrapment). In comparison, $^{13}CO_2$ is much less efficiently entrapped, with an efficiency of $\sim 52\%$ for a H_2O:$^{13}CO_2$ ratio of 1:14. We suggest this might be due to the hydrogen bonding networks between H_2S and H_2O, which are stronger intermolecular interactions that

---

vironment. This process only requires that $0.5 \times E_b(H_2O-H_2O) + 0.5 \times E_b(CO_2-CO_2)$ is greater than $E_b(H_2O-CO_2)$.

the induced dipoles between $^{13}CO_2$ and H_2O. Pore effects could also play a role in entrapping H_2S more efficiently than $^{13}CO_2$.

5. Our measured H_2S-H_2S and H_2S-H_2O binding energies yield H_2S sublimation temperatures at $\sim$64 K and $\sim$69 K, respectively. This corresponds to a radial distance of $\sim$6.3 au and $\sim$5.6 au in the midplane of a representative T-Tauri disk.

6. The vast majority of H_2S will remain entrapped in the ice until water crystallizes at radii close to the H_2O snowline, shifting its sublimation front inward by nearly a factor of three. As a result, most of the H_2S will remain in ices throughout the region where water-rich icy planetesimals form.

5.6   Acknowledgements

5.7   Appendix

5.7.1   Submonolayer coverage estimation

The submonolayer H_2S coverages were estimated based on a QMS-to-column density scaling factor, f, derived from the multilayer H_2S experiments. Figure 5.9 shows the correlation between the H_2S ice column density obtained from the integrated absorbance of its S-H stretching feature (see Equation 5.2) and the integrated signal of the H_2S desorption feature as measured by the QMS for m/z = 34.

A linear fit to the plot gives the conversion factor $f = (3.2 \pm 0.4) \times 10^{26}$ A^{-1} K^{-1}. In the low coverage experiments, where H_2S was deposited on top of cASW, the H_2S ices with approximately 1.6 ML and 1.2 ML (determined from their infrared absorbance bands) produced S-H stretching features detectable above our instrumental noise. By comparing the measured and predicted H_2S coverages in these experiments, we estimate that the submonolayer coverages might be underpredicted by up to a factor of 2 using our scaling method. However, this discrepancy does not impact our analysis, as the higher coverages (by a factor of two) yield binding energy distributions with mean E_b values differing by less than 2 K from those derived for the predicted coverages—well within their FWHMs.

5.7.2   Pure H_2S ice infrared features vs temperature

Figure 5.10 shows the IR spectra recorded during the TPD experiment of a multilayer H_2S ice with an initial coverage of 73 ML. The splitting between its symmetric (ν_1) and antisymmetric (ν_3) S-H stretching modes signals that ice crystallization starts to occur at temperatures as low as $\sim$30 K. By $\sim$65 K, the transition to phase III crystalline H_2S is nearly complete. However, from $\sim$65 K up to the point of complete desorption, a continuous blueshift in the S-H stretching features is observed, suggesting ongoing structural reorganization within the ice. While higher-energy crystalline phases of H_2S exist (phase II transitioning at $\sim$100 K and phase I transitioning at $\sim$125 K, see Fathe *et al.* 2006 and references therein), these transitions are observed under ambient pressure and occur above the sublimation temperature of H_2S in UHV conditions. They are therefore not relevant to our experiments.
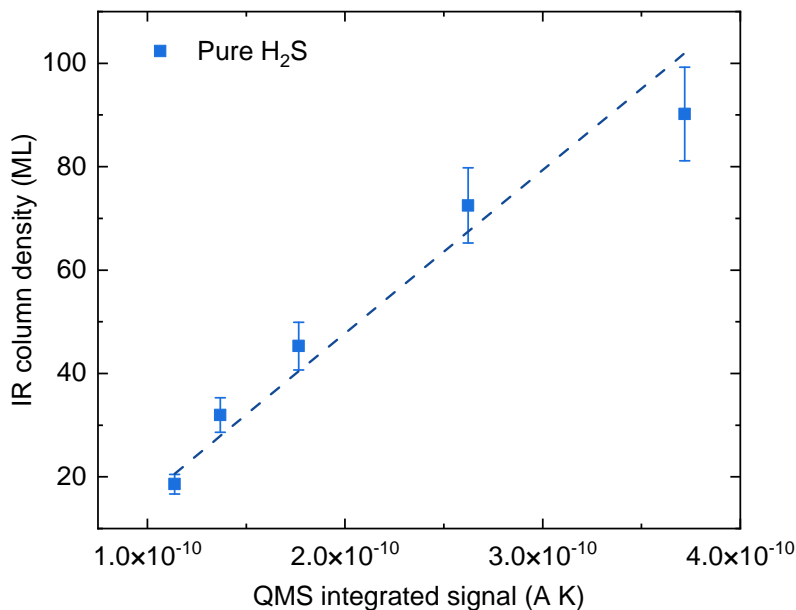
Figure 5.9: H_2S column densities derived from the integrated absorbance of its S-H stretching modes at 15 K for each multilayer ice thickness as a function of its corresponding integrated desorption feature as measured by the QMS. The dashed blue line shows the linear fit to the points from which the QMS-to-column density scaling factor was derived.

5.7.3   Arrhenius plots

Figure 5.11 shows the Arrhenius plots of the TPD experiments of all multilayer H_2S ice coverages. The desorption rate data (gray) for all five thicknesses was fit simultaneously following a Monte-Carlo sampling approach with 10,000 trials. The mean best-fit model corresponds to an H_2S-H_2S binding energy of $E_b = 3159 \pm 46$ K (blue dashed lines).

5.7.4   Multilayer H_2S ice fits with a temperature-dependent ν_{TST}

Figures 5.12 and 5.13 show the fits to the log-transformed multilayer TPD curves of H_2S with a temperature-dependent ν_{TST}. The former presents the data as the original TPD profile, while the latter shows the corresponding Arrhenius plots. This approach yields $E_b = 3141 \pm 49$ K (blue dashed lines).

5.7.5   Submonolayer fit with a single energy component

Figure 5.14 illustrates an attempted fit of the 0.2 ML H_2S ice using the Polanyi-Wigner equation (eq. 5.3) with a single temperature component. The fit fails to capture the experimental data, highlighting the presence of a distribution of binding energies caused by the inherent inhomogeneity of the cASW substrate.
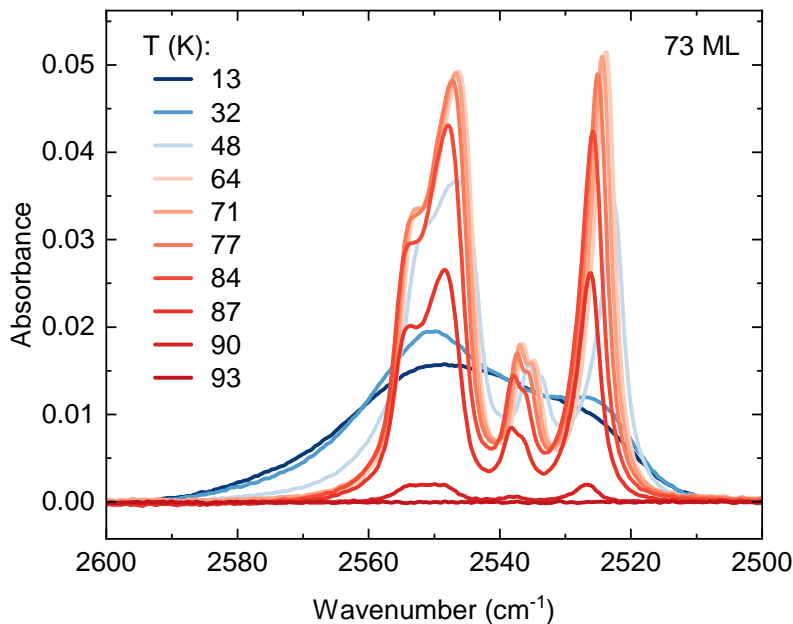
Figure 5.10: Infrared spectra taken during the TPD experiment of the 73 ML H_2S ice, centered on the frequency range of its S-H stretching modes. For clarity, only a subset of spectra collected at the relevant temperatures are shown.
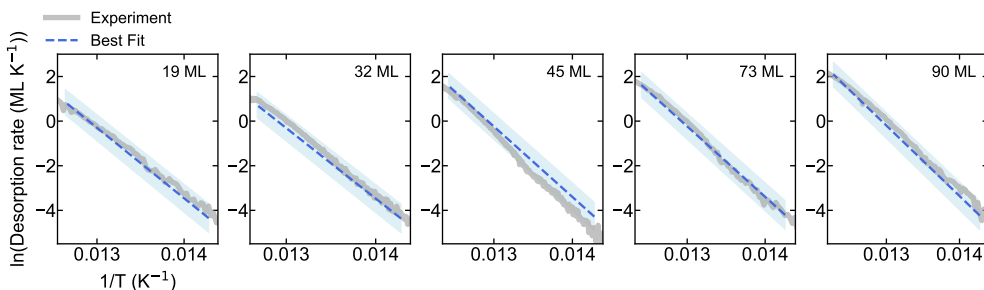
Figure 5.11: Arrhenius plots of the multilayer H_2S TPD curves used to derive the H_2S-H_2S binding energy. The experimental data is shown in gray, while the linear fits to the plots, performed simultaneously for the five ice thicknesses, are shown by the blue dashed lines. The shaded blue region indicates the 1σ uncertainty. The fit is performed for the temperature range where the original curve follows an exponential trend (see section 5.3.1.1).

5.7.6 QMS-TPD results for mixed H_2O:H_2S ices

Figure 5.15 presents the QMS data collected for m/z = 34 during the TPD experiments with mixed H_2O:H_2S ices. In all cases, the first desorption feature (panel a) corresponds to monolayer desorption characterized by the H_2S-H_2O binding energies. This is evinced by the peak desorption temperatures, which increase with decreasing coverages, and by the desorption profiles consistent with first-order desorption kinetics for all mixing ratios. The second desorption feature (panel b) corresponds to the molecular volcano.
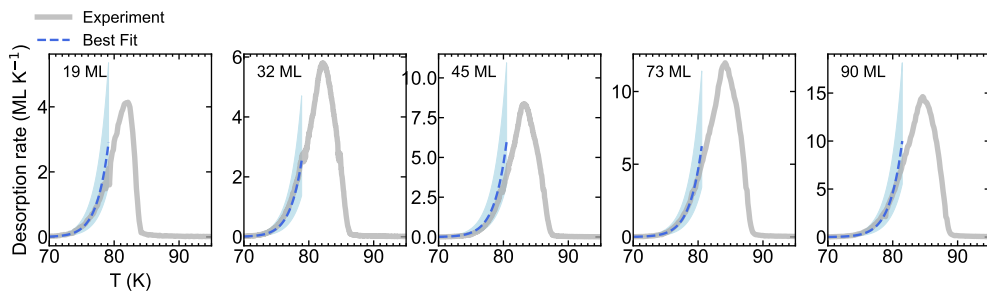
Figure 5.12: Same as Figure 5.2, but with fits performed using a temperature-dependent ν_{TST}.
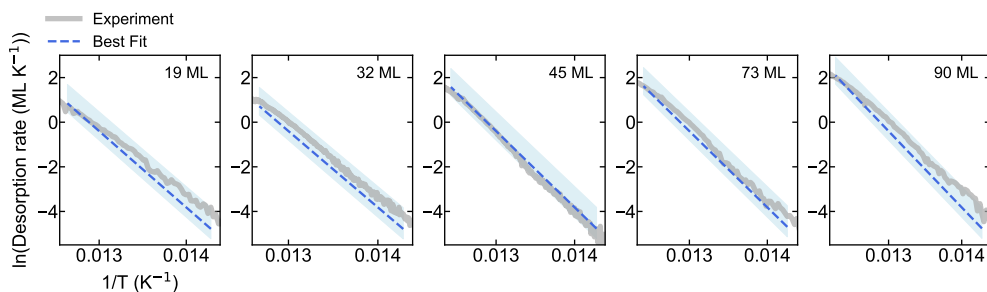
Figure 5.13: Same as Figure 5.11, but with fits performed using a temperature-dependent ν_{TST}.
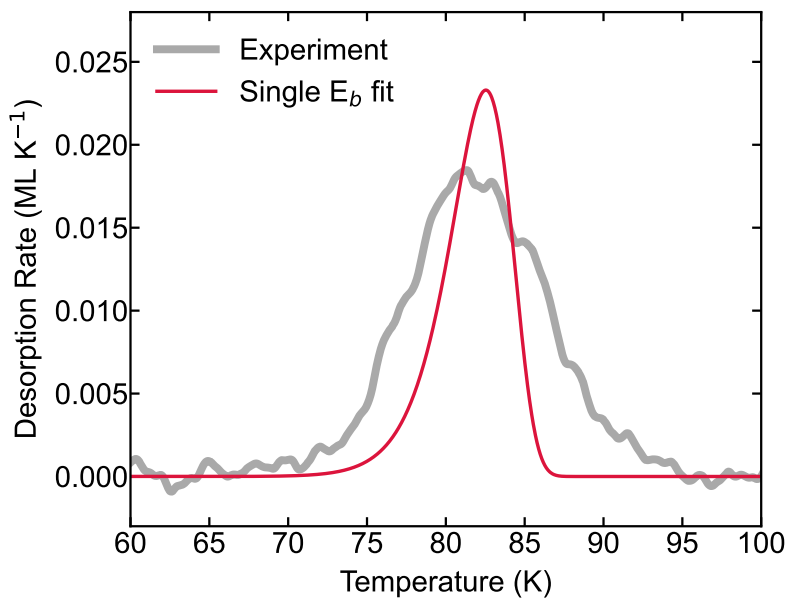
Figure 5.14: TPD curve of the 0.2 ML H_2S ice experiment deposited on top of a cASW substrate. The experimental data is show in gray, while the attempted fit to the data with a first-order Polanyi-Wigner curve with only one temperature component is shown in red.
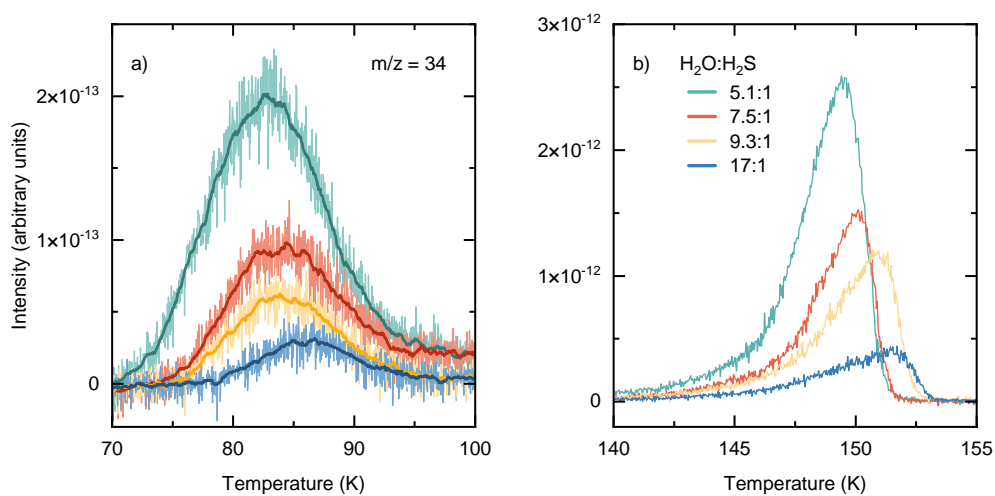
Figure 5.15: TPD data measured by the QMS for m/z = 34 in the experiments with mixed $H_2O:H_2S$ ices. Panel a shows the monolayer desorption of H_2S molecules with access to the surface, and panel b depicts the molecular volcano feature due to H_2S entrapped in the H_2O ice matrix.

6. FORMATION OF CARBONYL SULFIDE (OCS) VIA SH RADICALS IN INTERSTELLAR CO-RICH ICE UNDER DENSE CLOUD CONDITIONS

Carbonyl sulfide (OCS) is widely observed in the gas phase toward star-forming regions and was the first of the only two sulfur-bearing species to be detected in interstellar ices so far. However, the chemical network governing its formation is still not fully understood. While the sulfurization of CO and the oxidation of CS are often invoked to form OCS, other mechanisms could have a significant contribution. In particular, the multistep reaction involving CO and SH is a good candidate for forming a significant portion of the OCS in dense cloud environments. We aim to constrain the viability of the $CO + SH$ route for forming solid OCS in the interstellar medium, in a similar manner as $CO+OH$ is known to produce CO_2 ice. This is achieved by conducting a systematic laboratory investigation of the targeted reactions on interstellar ice analogs under dense cloud conditions. We used an ultrahigh vacuum chamber to simultaneously deposit CO, H_2S, and atomic H at 10 K. SH radicals produced in situ via hydrogen abstraction from H_2S reacted with CO to form OCS. We monitored the ice composition during deposition and subsequent warm-up by means of Fourier-transform reflection absorption infrared spectroscopy (RAIRS). Complementarily, desorbed species were recorded with a quadrupole mass spectrometer (QMS) during temperature-programmed desorption (TPD) experiments. Control experiments were performed to secure the product identification. We also explored the effect of different H_2S:CO mixing ratios—with decreasing H_2S concentrations—on the OCS formation yield. OCS is efficiently formed through surface reactions involving CO, H_2S, and H atoms. The suggested underlying mechanism behind OCS formation is $CO + SH \rightarrow HSCO$, followed by $HSCO + H \rightarrow OCS + H_2$. The OCS yield reduces slowly, but remains significant with increasing CO:H_2S mixing ratios (CO:H_2S = 1:1, 5:1, 10:1, and 20:1). Our experiments provide unambiguous evidence that OCS can be formed from $CO + SH$ in the presence of H atoms. This route remains efficient for large H_2S dilutions (5% with respect to CO), suggesting that it is a viable mechanism in interstellar ices. Given that SH radicals can be created in clouds over a wide evolutionary timescale, this mechanism could make a non-negligible contribution to the formation of interstellar OCS ice.

6.1   Introduction

Among the over 300 molecules detected in the interstellar medium to date[1], those that contain sulfur constitute a particularly conspicuous chemical family. They are observed in the gas phase throughout a wide evolutionary time span, from clouds (e.g., Drdla *et al.* 1989; Navarro-Almaida *et al.* 2020; Spezzano *et al.* 2022; Esplugues *et al.* 2022) to protostars (e.g., Blake *et al.* 1987, 1994; van der Tak *et al.* 2003; Li *et al.* 2015; Drozdovskaya *et al.* 2018; Codella *et al.* 2021; Artur de la Villarmois *et al.* 2023; Fontani *et al.* 2023; Kushwahaa *et al.* 2023), protoplanetary disks (Fuente *et al.* 2010; Phuong *et al.* 2018; Semenov *et al.* 2018; Le Gal *et al.* 2019; Rivière-Marichalar *et al.* 2021; Le Gal *et al.* 2021; Booth *et al.* 2024), and Solar System bodies (Smith *et al.* 1980; Bockelée-Morvan *et al.* 2000a; Hibbitts *et al.* 2000; Jessup *et al.* 2007; Moullet *et al.* 2008, 2013; Cartwright *et al.* 2020; Biver *et al.* 2021a,b; Calmonte *et al.* 2016; Altwegg *et al.* 2022). The species detected so far range in size, from simple diatomic molecules such as CS and SO to the thiols CH_3SH and CH_3CH_2SH (Linke *et al.* 1979; Gibb *et al.* 2000; Cernicharo *et al.* 2012; Kolesniková *et al.* 2014; Zapata *et al.* 2015; Müller *et al.* 2016; Majumdar *et al.* 2016; Rodríguez-Almeida *et al.* 2021a).

As opposed to gas-phase observations, however, only two sulfurated molecules have been detected in interstellar ices to date: OCS and SO_2 (Palumbo *et al.* 1995; Boogert *et al.* 1997; Palumbo *et al.* 1997; Öberg *et al.* 2008; Boogert *et al.* 2022; McClure *et al.* 2023; Rocha *et al.* 2024). This is probably in large part due to their low abundances, combined with the intrinsic limitations of solid-state observations, such as the broadness of the features and their high degeneracy. Nonetheless, these confirmed ice species already bring vast chemical ramifications, as they can act as reactants to form more complex organosulfur compounds, some of which have key biochemical roles (see, e.g., McAnally *et al.* 2024). However, despite their astrochemical significance, many open questions remain regarding the formation pathways of these small sulfur-bearing molecules in the solid state.

One particularly important case is that of carbonyl sulfide (OCS), a major gaseous sulfur carrier commonly detected toward young stellar objects (e.g., van der Tak *et al.* 2003; Herpin *et al.* 2009; Oya *et al.* 2016; Drozdovskaya *et al.* 2018; Kushwahaa *et al.* 2023; López-Gallifa *et al.* 2024; Santos *et al.* 2024c). OCS is also frequently detected in interstellar ices (see, e.g., Palumbo *et al.* 1997; Boogert *et al.* 2022), in part facilitated by the characteristically large absorption band strength of its 4.9 μm feature in comparison to other ice species (e.g., $\sim 1.2 \times 10^{-16}$ cm molecule^{-1} as measured by Yarnall & Hudson 2022 for pure OCS ice at 10 K; See also Hudgins *et al.* 1993). Observed OCS abundances in both protostellar ices and hot-core gas point to a solid-state formation mechanism occurring predominately during the high-density pre-stellar core stage ($A_V > 9$, $n_H \gtrsim 10^5$ cm^{-3}) after the onset of the CO catastrophic freeze-out (Palumbo *et al.* 1997; Boogert *et al.* 2022; Santos *et al.* 2024c). This proposed icy origin of OCS is corroborated by gas-phase astrochemical models, which fail to reproduce observed OCS abundances (Loison *et al.* 2012). In the inner regions of the protostellar envelope, thermal heating by the protostar causes the volatile ice content to fully sublimate, enabling the bulk of the gaseous OCS observations.

So far, the two most commonly proposed routes to OCS involve either the oxidation of CS or the sulfurization of CO in the solid state (Palumbo *et al.* 1997; Ferrante *et al.* 2008; Adriaens *et al.* 2010; Chen *et al.* 2015; Laas & Caselli 2019; Shingledecker *et al.* 2020; Boogert *et al.* 2022):

$$CS + O \rightarrow OCS, \tag{6.1}$$

$$CO + S \rightarrow OCS. \tag{6.2}$$

---

[1]https://cdms.astro.uni-koeln.de/
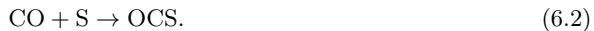
However, CS abundances are considerably smaller ($\lesssim$ 2.5%) than those of OCS, casting doubts on the extent of the contribution from Reaction 6.1 to the interstellar OCS content (Boogert *et al.* 2022). Reaction 6.2 is more often invoked as the dominant route to OCS, especially due to the large availability of solid-state CO as a reactant in the post freeze-out stage.

Hydrogen in its atomic form is also abundant in pre-stellar cores (H/CO$\sim$1$-$10, Lacy *et al.* 1994; Goldsmith & Li 2005) and can trigger solid-state reactions of relevance to the sulfur network. Following adsorption onto dust grains, sulfur atoms are subject to successive hydrogenation reactions to form SH and H_2S via the steps:

$$S + H \rightarrow SH, \tag{6.3}$$

$$SH + H \rightarrow H_2S, \tag{6.4}$$

both of which are predicted by astrochemical models to proceed very efficiently (see, e.g., Garrod *et al.* 2007; Druard & Wakelam 2012; Esplugues *et al.* 2014; Vidal *et al.* 2017). Once H_2S ice is formed, it can further react with another hydrogen atom via an abstraction route (Lamberts & Kästner 2017; Oba *et al.* 2018, 2019; Santos *et al.* 2023b), or be dissociated through energetic processing (e.g., Jiménez-Escobar *et al.* 2014a; Chen *et al.* 2015; Cazaux *et al.* 2022):

$$H_2S + H \rightarrow SH + H_2, \tag{6.5a}$$

$$H_2S + h\nu \rightarrow SH + H, \tag{6.5b}$$

thus partially replenishing the SH ice content. As a result, SH radicals will likely be present in the ice throughout a wide evolutionary time span, and could potentially serve as an alternative source of sulfur in the formation of OCS.

A particularly promising pathway is the reaction between SH and CO followed by a hydrogen abstraction step (Adriaens *et al.* 2010; Chen *et al.* 2015):

$$SH + CO \rightarrow HSCO, \tag{6.6}$$

$$HSCO + H \rightarrow OCS + H_2, \tag{6.7}$$

which involves the formation of the intermediate complex HSCO. This pathway is analogous to the case of CO_2 ice formation from CO and OH through the HOCO complex (e.g., Oba *et al.* 2010b; Ioppolo *et al.* 2011; Noble *et al.* 2011; Qasim *et al.* 2019; Molpeceres *et al.* 2023). In the case of CO_2, Molpeceres *et al.* (2023) find that the spontaneous dissociation of HOCO into H and CO_2 is not energetically viable, and thus the formation of the latter is only possible through the interaction of the HOCO intermediate with a hydrogen atom. Similarly, HSCO is also prevented from spontaneously dissociating into OCS and H (Adriaens *et al.* 2010). In the laboratory, OCS is readily formed in energetically processed CO:H_2S ice mixtures (Ferrante *et al.* 2008; Garozzo *et al.* 2010; Jiménez-Escobar *et al.* 2014a; Chen *et al.* 2015), for which both reactions involving CO + S and CO + SH have been suggested as possible formation routes. Moreover, Nguyen *et al.* (2021b) allude to the possibility of forming OCS through reactions 6.6 and 6.7 in a CO:H_2S ice mixture exposed to hydrogen atoms, but without exploring this pathway further. Dedicated laboratory studies assessing this particular reaction pathway to OCS formation are therefore still highly warranted.

In the present experimental work, we investigate the viability of OCS formation via Reactions 6.6 and 6.7 under dark cloud conditions by simultaneously depositing H_2S, CO, and H atoms at 10 K. The SH radicals are produced via Reaction 6.5a, and are subsequently subject to reaction with neighboring species. The experimental methods used in this work are described in Sect. 6.2. In Sect. 6.3 we present and discuss our main results. Their astrophysical implications are elaborated in Sect. 6.4, followed by a summary of our main findings in Sect. 6.5.

6.2   Experimental methods

Table 6.1: Experiments performed in this work.

Experiment	Label	CO flux (cm^{-2} s^{-1})	H$_2$S flux (cm^{-2} s^{-1})	H flux (cm^{-2} s^{-1})	CO:H$_2$S:H
CO + H$_2$S + H	1	1.8×10^{11}	1.8×10^{11}	5.5×10^{12}	1:1:30
CO + H$_2$S	2	1.8×10^{11}	1.8×10^{11}	–	1:1:0
^{13}C^{18}O + H$_2$S + H	3	1.8×10^{11}	1.8×10^{11}	5.5×10^{12}	1:1:30
CO + H$_2$S + H	4	9.3×10^{11}	1.8×10^{11}	5.5×10^{12}	5:1:30
CO + H$_2$S + H	5	1.8×10^{12}	1.8×10^{11}	5.5×10^{12}	10:1:30
CO + H$_2$S + H	6	3.7×10^{12}	1.8×10^{11}	5.5×10^{12}	20:1:30

This work uses the ultrahigh vacuum (UHV) setup SURFRESIDE[3], for which detailed descriptions are provided elsewhere (Ioppolo *et al.* 2013; Qasim *et al.* 2020b). Briefly, this setup contains a main chamber that operates at base pressures of $\sim 5 \times 10^{-10}$ mbar, and at the center of which a gold-plated copper substrate is mounted on the tip of a closed-cycle helium cryostat. Resistive heaters are used to vary the substrate temperature between 8 and 450 K, as monitored by two silicon diode sensors with a relative accuracy of 0.5 K. A hydrogen atom beam source (HABS Tschersich 2000) generates H atoms that are subsequently cooled down by colliding with a nose-shaped quartz pipe before reaching the substrate. As H atoms are injected into the chamber, gases of H$_2$S (Linde, 99.5% purity) and CO (Linde, 99.997% purity) are concomitantly admitted through two separate all-metal leak valves. The heavier isotopolog ^{13}C^{18}O (Sigma-Aldrich, 95% purity ^{18}O, 99% purity ^{13}C) is also used to assist in the product identification. Fourier-transform reflection-absorption infrared spectroscopy (FT-RAIRS) is used to monitor ice growth in the range of 700 to 4000 cm^{-1} with 1 cm^{-1} spectral resolution. When the deposition is complete, temperature-programmed desorption (TPD) experiments are performed by heating the sample at a constant rate of 5 K min^{-1}. During TPD, the solid phase is monitored by RAIRS, while the sublimated species are immediately ionized by 70 eV electron impact and are recorded by a quadrupole mass spectrometer (QMS). The variation of the substrate temperature during the collection of each IR TPD spectrum is of $\sim$10 K.

The absolute abundance of the ice species can be derived from their integrated infrared absorbance ($\int Abs(\nu)d\nu$) using a modified Beer-Lambert law:

$$N_X = \ln 10 \frac{\int Abs(\nu)d\nu}{A'(X)}, \tag{6.8}$$

where N_X is the column density in molecules cm^{-2} and $A'(X)$ is the apparent absorption band strength in cm molecule^{-1} of a given species. We use $A'(CO)_{\sim 2142cm^{-1}} \sim (4.2 \pm 0.3) \times 10^{-17}$ cm molecule^{-1} and $A'(H_2S)_{\sim 2553cm^{-1}} \sim (4.7 \pm 0.1) \times 10^{-17}$ cm molecule^{-1}, as measured for our reflection-mode IR settings using the laser-interference technique (see Santos *et al.* 2023b for the case of H$_2$S). For the target product, OCS, we employ the band strength of $A'(OCS)_{\sim 2043cm^{-1}} \sim (1.2 \pm 0.1) \times 10^{-16}$ cm molecule^{-1} measured in transmission mode by Yarnall & Hudson (2022), and correct it by an averaged transmission-to-reflection conversion factor of 3.2 derived with our experimental setup (see Santos *et al.* 2023b for the case of H$_2$S, which was later combined with CO ice depositions to derive the averaged setup-specific conversion factor).

Table 6.1 summarizes the experiments performed in this work. All depositions are carried out for 180 minutes with a constant substrate temperature of 10 K. The relative errors of

the H-atom flux, as well as both molecule fluxes, are estimated to be $\lesssim 5\%$. The latter are estimated from evaluating the ice growth rate in multiple pure-ice deposition experiments. To estimate the former, multiple experiments to calibrate the relative H-atom flux are conducted. These consist of trapping H atoms inside O_2 ice matrices and monitoring the formation of HO_2, which is proportional to the H-atom flux provided that O_2 is overabundant relative to H (Ioppolo *et al.* 2013; Fedoseev *et al.* 2015b). The instrumental uncertainties in the integrated QMS and IR signals are derived from the corresponding integrated spectral noise for the same band width.

6.3   Results and discussion

6.3.1   OCS formation

Panel (a) of Fig. 6.1 shows the infrared spectra obtained after codeposition of CO, H_2S, and H atoms (1:1:30, experiment 1) at 10 K, as well as after a control experiment of only CO and H_2S (1:1, experiment 2). When CO and H_2S are exposed to hydrogen atoms, a new feature appears at ~ 2043 cm^{-1} (~ 4.89 μm) with a full-width at half maximum (FWHM) of $\sim$15 cm^{-1} (~ 0.03 μm). Based on its peak position and the ice elemental composition (i.e., C, O, S, and H), this feature is assigned as the CO-stretching mode of OCS (ν_1, Yarnall & Hudson 2022)[2]. The band's FWHM and peak position are also consistent with previously reported values for OCS in CO-rich ices measured in reflection mode (Ferrante *et al.* 2008). To confirm this assignment, an analogous experiment is performed with a heavier isotopolog of carbon monoxide, $^{13}C^{18}O$ (experiment 3: blue spectrum in Fig. 6.1). In this case, the $^{18}O^{13}CS$ ν_1 feature appears at ~ 1954 cm^{-1} (~ 5.12 μm) in accordance with the expected redshift of the heavier isotopolog. During TPD, both features at ~ 2043 cm^{-1} and ~ 1954 cm^{-1} disappear from the ice in the same temperature interval of $70 - 100$ K (Panels b) and c) in Fig. 6.1), thus signaling that the two bands correspond to the same molecule.

Complementarily to the infrared spectra, data obtained by the QMS during TPD can also be used to strengthen the OCS identification. Panel (a) of Fig. 6.2 displays the signal for m/z = 60 recorded during the warm-up of the ice sample in the CO + H_2S + H experiment. This mass-to-charge ratio corresponds to the molecular ion of OCS, its strongest signal resulting from 70 eV electron impact as listed in NIST[3]. A desorption feature appears peaking at $\sim$89 K, in agreement with previously reported desorption temperatures of OCS (Ferrante *et al.* 2008; Nguyen *et al.* 2021b). In the isotope-labeled experiment, a similar desorption peak is observed for m/z = 63, consistent with the mass shift corresponding to the molecular ion of $^{18}O^{13}CS$. Moreover, no peak signal is detected for m/z = 60, indicating that this same feature appearing in experiment 1 corresponds uniquely to carbonyl sulfide. The desorption temperature of OCS as measured by the QMS correlates with the disappearance of the ~ 2043 cm^{-1} feature in the infrared spectra taken during TPD, as indicated by the area of this infrared band as a function of substrate temperature (Fig. 6.2 panel b). Both the infrared and QMS data therefore provide unequivocal evidence for the formation of OCS as a result of interactions between H_2S, CO, and H atoms in the solid state.

Aside from OCS, another S-bearing species that could presumably be formed under our experimental conditions is thioformic acid, HCOSH. Indeed, formation routes via either the hydrogenation of the HSCO intermediate or the interaction between HCO + SH have been proposed by Rodríguez-Almeida *et al.* (2021a) to explain HCOSH observations toward the giant molecular cloud G+0.693–0.027, with the former subsequently verified theoretically by Molpeceres *et al.* (2021). Although HCOSH has been shown to form upon keV electron

---

[2]The numbers assigned to the CS and CO stretches of OCS are interchangeable. In this work, we adopt the notation from Yarnall & Hudson (2022).

[3]https://webbook.nist.gov/chemistry/
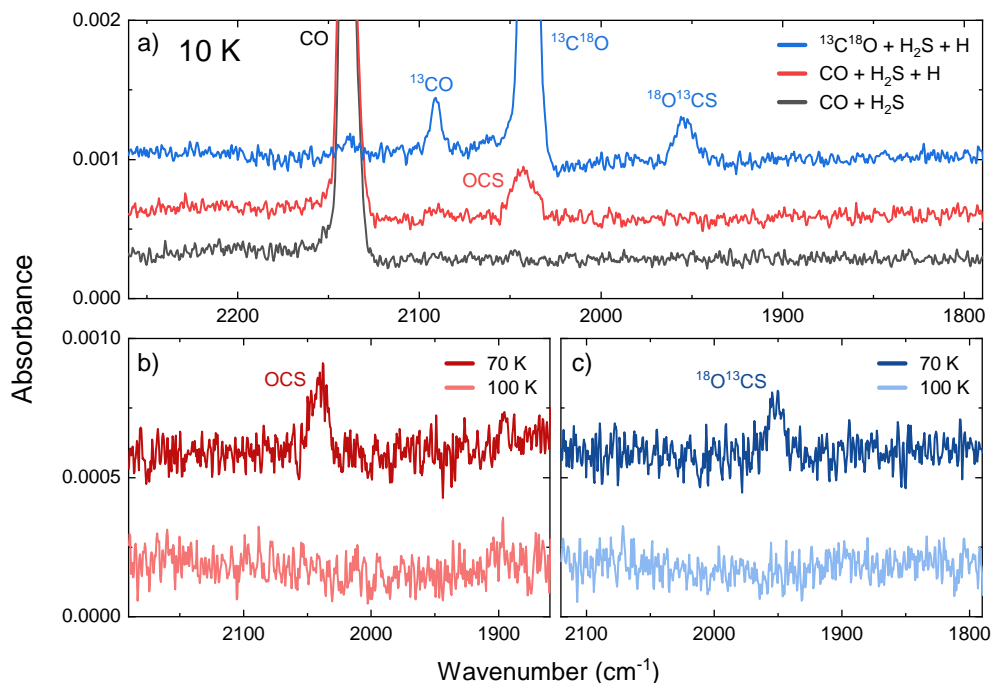
Figure 6.1: Infrared data confirming the formation of OCS from CO, H$_2$S, and H atoms. Panel (a): Spectrum collected after deposition of CO + H$_2$S + H (experiment 1, red) together with the control experiment without H atoms (experiment 2, gray) and the isotope-labeled experiment with ^{13}C^{18}O (experiment 3, blue). Small features assigned to ^{13}CO and ^{12}CO are due to minor contaminations from the gas bottle (respectively, $\sim 4\%$ and $\sim 2\%$ with respect to ^{13}C^{18}O). Panel (b): Infrared spectra acquired during TPD following the deposition of experiment 1. The spectrum in dark red (upper) is taken at $\sim$70 K, and the one in light red (lower) is taken at $\sim$100 K. Panel (c): Same as panel (b), but for the isotope-labeled experiment. In all panels, only the relevant frequency range is shown and the spectra are offset for clarity.

irradiation of H$_2$S:CO ices (Wang *et al.* 2022), Nguyen *et al.* (2021b) only tentatively identify this product in similar hydrogenation experiments on H$_2$S:CO ices. No evidence for this species is observed in our experiments above the instrumental detection limit. Likewise, we do not detect any signal of volatile sulfur allotropes such as S$_2$ or S$_3$, nor of hydrogenated sulfur chains such as H$_2$S$_2$ or H$_2$S$_3$—which could presumably be formed from the association of sulfur atoms produced via hydrogen abstraction reactions from SH radicals. This leads to the conclusion that the potential production of the atomic S does not proceed efficiently under our experimental conditions. Moreover, as no H$_2$S$_2$ is detected, the recombination of two SH radicals is also likely not efficient in the present experiments—signaling that HS radicals are efficiently consumed, both by reacting with CO leading to OCS and by reacting with H to reform H$_2$S.

Reactions 6.6 and 6.7 are therefore the predominant contributors to the formation of OCS in our experiments. As shown by Nguyen *et al.* (2021b), however, the backward reactions are also viable. Once formed, OCS can be hydrogenated into the complex intermediate HSCO, which in turn can further react with another H atom to yield CO and H$_2$S, as well as dissociate back into the reactants SH and CO (Adriaens *et al.* 2010; Nguyen *et al.* 2021b; Molpeceres *et al.* 2021). The effective amount of OCS detected will therefore be subject to these two
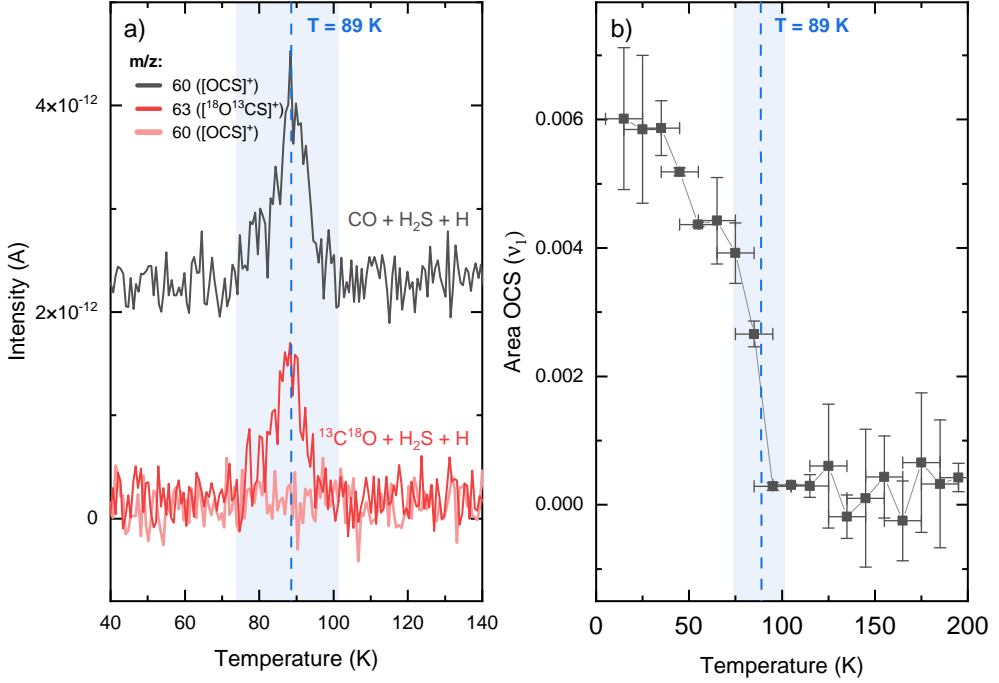
Figure 6.2: Complementary QMS and infrared data acquired during TPD confirming the OCS detection. Panel (a): TPD-QMS signal recorded for m/z = 60 after the deposition of CO + H$_2$S + H (experiment 1, gray), as well as those for m/z = 63 (dark red) and m/z = 60 (light red) after the deposition of ^{13}C^{18}O + H$_2$S + H (experiment 3). The blue shadowed region denotes the range of desorption, and the dashed line highlights the peak desorption temperature. Signals from different experiments are offset for clarity. Panel (b): Area of the OCS ν_1 band as a function of temperature during TPD following the deposition of experiment 1. The uncertainties in the horizontal axis are due to the substrate temperature variation of ~10 K during the collection of each IR TPD spectrum. The blue shadowed area and dashed line are reproductions of the range and peak position shown in Panel (a).

competing directions.

6.3.2   Effects of larger CO fractions

Once the possibility of forming OCS from CO and SH is ascertained, the next question to arise is that regarding the viability of this route in more astronomically representative ice mixing ratios. To date, there are no convincing detections of H$_2$S in interstellar ices, with upper limits estimated to be ≤0.7% with respect to water (Jiménez-Escobar & Muñoz Caro 2011b). This would translate to ice abundance upper limits of roughly a few percent with respect to CO (e.g., $N(\mathrm{H_2S})/N(\mathrm{CO}) \lesssim 0.035$ if assuming $N(\mathrm{CO})/N(\mathrm{H_2O}) \sim 0.21$ according to the median CO ice abundance value with respect to H$_2$O derived for low-mass young stellar objects (LYSOs) in Boogert *et al.* 2015). Accordingly, we performed similar depositions with larger fractions of CO with respect to H$_2$S in order to assess how the dilution of the latter affects the yields of OCS. The deposition fluxes of H$_2$S and atomic H are kept the same in all experiments, with only variations in the CO flux (see Table 6.1). Figure 6.3 compares the relative intensities of the OCS signals obtained from both the IR and QMS data for the

different mixing ratios explored here (i.e., CO:H$_2$S = 1:1, 5:1, 10:1, and 20:1). The areas of the OCS ν_1 vibrational modes for each mixing ratio after deposition are normalized to that of experiment 1, which yielded the largest absolute amount of products. Similarly, the areas of the m/z = 60 desorption band at $\sim$ 89 K are also normalized to that of experiment 1.
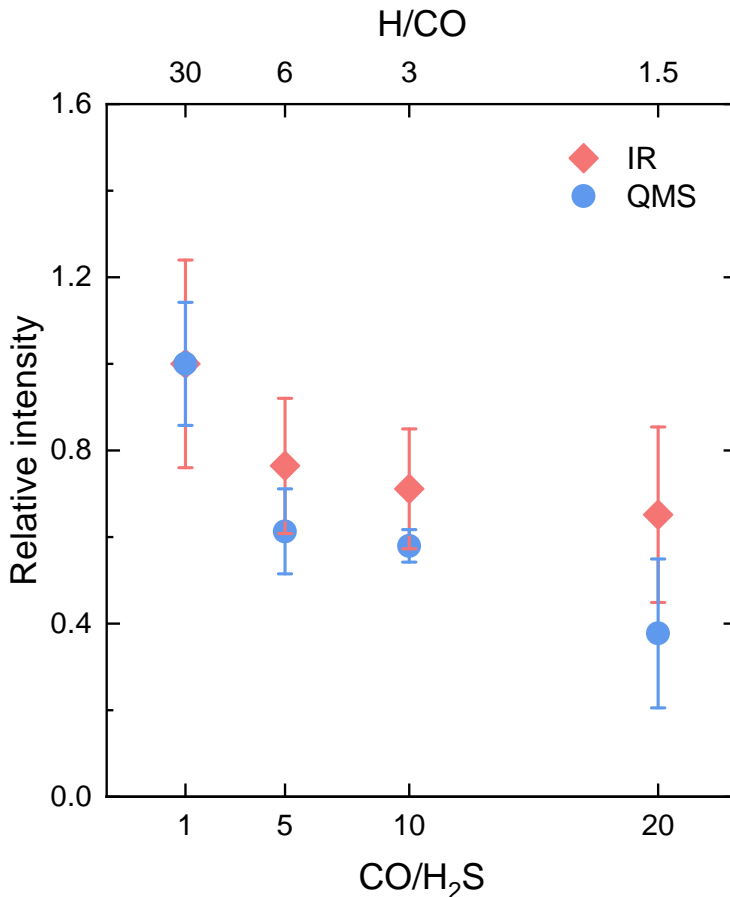
Figure 6.3: Integrated intensities of the infrared and QMS features of OCS for different flux conditions: CO:H$_2$S = 1:1, 5:1, 10:1, and 20:1. The infrared value is derived from the area of the ν_1 mode of OCS, while the QMS counterpart is calculated from the integrated desorption band for m/z = 60 peaking at $\sim$89 K. The resulting yields are normalized to that of experiment 1 (CO:H$_2$S = 1:1). The upper x-axis shows the corresponding ratios of H/CO, signaling the decrease in H-atom availability with increasing CO fractions.

Overall, the infrared and QMS data provide consistent OCS yields within their respective error bars, and signal that dilution of H$_2$S in CO reduces but does not impede OCS formation under our experimental conditions. Indeed, in the highest dilution case (5% H$_2$S with respect to CO), OCS production diminishes by $\sim$ 50% (the mean value between the infrared and QMS results) in comparison to the nondiluted reference experiment (100% H$_2$S with respect to CO). This decrease in OCS yield is likely governed by the reduced number of available H atoms in experiments with larger CO fractions, as opposed to a diminishing effectiveness of the OCS formation. As well established by previous works, the interaction of CO with H atoms in the solid state initiates a chain of reactions leading to H$_2$CO and CH$_3$OH (Tielens &

Hagen 1982; Charnley *et al.* 1992; Hiraoka *et al.* 1994; Watanabe & Kouchi 2002; Fuchs *et al.* 2009; Santos *et al.* 2022b), which efficiently consumes the available atomic hydrogen in the system. Increasing the CO deposition flux while maintaining a fixed H-atom flux therefore results in less hydrogen being able to react with other species. This decrease in available H atoms will have a greater impact on the formation of SH radicals (Reaction 6.5a) than on the final abstraction step (Reaction 6.7), as the latter is predicted to be barrierless (Adriaens *et al.* 2010), whereas the former requires quantum tunneling through a barrier of $\sim$1500 K (Lamberts & Kästner 2017). The slowly decreasing trend in Fig. 6.3 suggests that OCS can still be formed at 10 K in ice mixtures with CO:H_2S of higher than 20:1 and H:CO of as low as 1.5:1. The formation of OCS from CO + SH could therefore make a non-negligible contribution to the observed OCS in interstellar ices, as discussed below.

6.4 Astrophysical implications

The reaction network probed in this work is shown in Fig. 6.4. Aside from OCS, other closed-shell species also formed within this network are H_2S_2 (Santos *et al.* 2023b), H_2CO, and CH_3OH (Tielens & Hagen 1982; Charnley *et al.* 1992; Hiraoka *et al.* 1994; Watanabe & Kouchi 2002; Fuchs *et al.* 2009; Santos *et al.* 2022b). In our experiments, H_2S is used as a source of SH radicals via a hydrogen abstraction (Reaction 6.5a) to avoid reactions with S atoms to interfere with the analysis. In the ISM, however, SH will not only be produced from H_2S but also from the hydrogenation of sulfur atoms that adsorb onto dust grains (Reaction 6.3). Observations of singly and doubly deuterated H_2S in Class 0 sources suggest that the bulk of its formation takes place early in the evolution of a cloud, before the catastrophic CO freeze-out stage begins (Ceccarelli *et al.* 2014). Accordingly, SH radicals will be available in the ice as early as during the low-density prestellar core stage. As the cloud evolves and the density of the environment increases, most of the available S atoms will be converted into H_2S. Nonetheless, SH radicals can still be formed through Reaction 6.5a or through dissociation reactions induced by energetic processing. As a result, SH will remain a viable reactant throughout a large fraction of a cloud's lifetime.

Observations of OCS toward massive young stellar objects (MYSOs) reveal that its 4.9 μm feature is best fitted by reference spectra of OCS in a CH_3OH-rich environment (Palumbo *et al.* 1997; Boogert *et al.* 2022). Their column density ratios ($N(\text{OCS})/N(\text{CH}_3\text{OH})$) in both ice and gas have similarly narrow distributions and comparable median values (within a factor of 3, Santos *et al.* 2024c), strengthening the hypothesis that both coexist in similar ice environments. Moreover, observed ice abundances of OCS and CH_3OH are correlated (Boogert *et al.* 2022), suggesting a strong chemical link between the two molecules. As methanol is known to be formed via the hydrogenation of CO in the solid phase, such observations are in line with CO being a common precursor between the two. This would imply that the bulk of OCS ice likely originates deep into dense clouds, in a dense environment post catastrophic CO freeze-out. Conversely, a large portion of the free sulfur atoms will likely be readily converted into H_2S at such densities. The reaction route proposed here could partially circumvent this issue, as SH radicals can be efficiently produced through a top-down mechanism (Reaction 6.5a). Moreover, estimated H_2S upper limits in ices are larger than the detected OCS abundances (Palumbo *et al.* 1997; Jiménez-Escobar & Muñoz Caro 2011b; Boogert *et al.* 2022), and thus this route remains viable in light of the observational evidence available so far. Overall, both CO + S and CO + SH routes likely contribute to the observed OCS abundances in interstellar ices, and exploration of the extent of this contribution warrants dedicated chemical modeling.
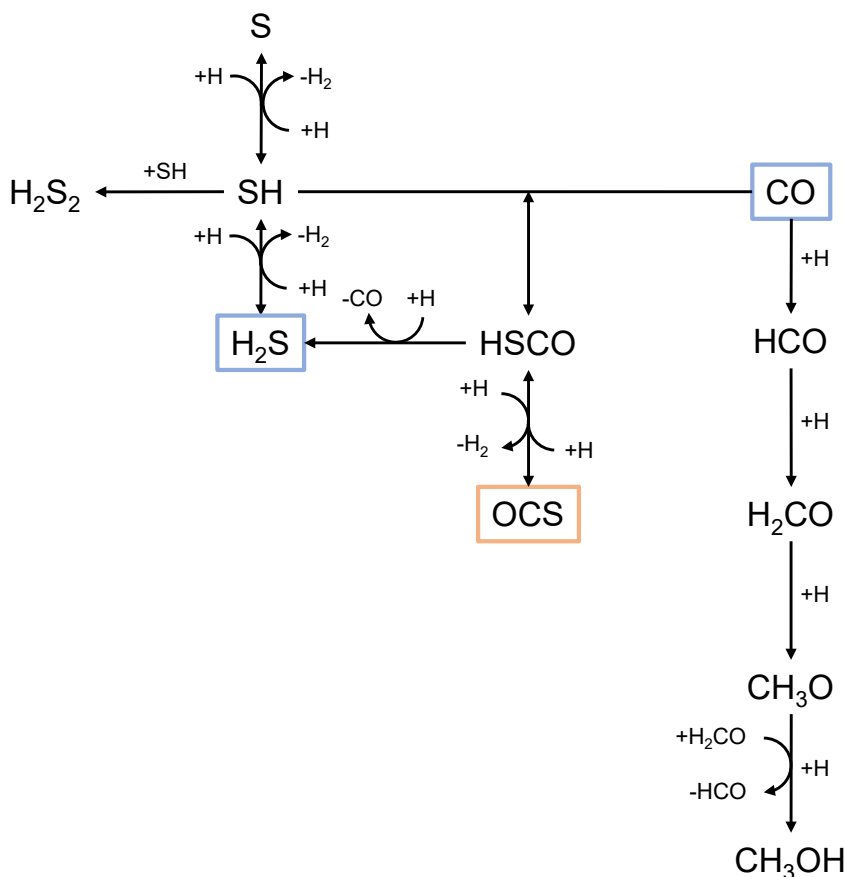
Figure 6.4: Reaction scheme proposed in this work. Blue boxes denote the deposited molecules and the orange box highlights the studied product, OCS. Hydrogen abstraction reactions from CH_3OH, H_2CO, and associated radicals are omitted for the sake of simplicity.

6.5   Conclusions

In this work, we conduct a systematic experimental investigation of the viability of forming OCS under dark cloud conditions from ice mixtures of CO, H_2S, and H atoms. Our main findings are summarized below:

- OCS can be efficiently formed at 10 K from solid-state reactions involving CO, H_2S, and H. The proposed underlying mechanism is via $CO + SH \rightarrow HSCO$ followed by $HSCO + H \rightarrow OCS + H_2$, analogously to CO_2 ice.

- The OCS product yield decreases slowly with increasing initial CO/H_2S ratios and decreasing H-atom availability, resulting in $\sim 50\%$ less OCS formation for a 20 times higher CO abundance relative to H_2S and fixed H-atom fluxes. This trend suggests that OCS can be efficiently formed via the proposed route in more representative interstellar ices, where H_2S is likely highly diluted in CO.

- SH can be produced both through bottom-up ($S + H \rightarrow SH$) and top-down ($H_2S + H \rightarrow$

SH + H$_2$) routes, thus making it a favorable reactant to form OCS during the high-density, post-CO-freeze-out stage of prestellar cores. This is in line with both ice and gas-phase observations of OCS in protostars.

These findings suggest that the CO + SH reaction is potentially responsible for a non-negligible share of the interstellar OCS ice and therefore could be a valuable new addition to gas-grain chemical models focusing on sulfur species. In turn, such models could help to disentangle the contributions of the CO + SH and CO + S routes to forming OCS.

6.6 Acknowledgements

7. FORMATION OF S-BEARING COMPLEX ORGANIC MOLECULES IN INTERSTELLAR CLOUDS VIA ICE REACTIONS WITH C_2H_2, HS, AND ATOMIC H

The chemical network governing interstellar sulfur has been the topic of unrelenting discussion for the past decades due to the conspicuous discrepancy between its expected and observed abundances in different interstellar environments. More recently, the astronomical detections of CH_3CH_2SH and CH_2CS highlighted the importance of interstellar formation routes for sulfur-bearing organic molecules with two carbon atoms. In this work, we perform a laboratory investigation of the solid-state chemistry resulting from the interaction between C_2H_2 molecules and SH radicals—both thought to be present in interstellar icy mantles—at 10 K. Reflection absorption infrared spectroscopy and quadrupole mass spectrometry combined with temperature-programmed desorption experiments are employed as analytical techniques. We confirm that SH radicals can kick-start a sulfur reaction network under interstellar cloud conditions and identify at least six sulfurated products: CH_3CH_2SH, CH_2CHSH, $HSCH_2CH_2SH$, H_2S_2, and tentatively CH_3CHS and CH_2CS. Complementarily, we utilize computational calculations to pinpoint the reaction routes that play a role in the chemical network behind our experimental results. The main sulfur-bearing organic molecule formed under our experimental conditions is CH_3CH_2SH and its formation yield increases with the ratios of H to other reactants. It serves as a sink to the sulfur budget within the network, being formed at the expense of the other unsaturated products. The astrophysical implications of the chemical network proposed here are discussed.

7.1 Introduction

Over 300 molecules have been detected in the interstellar and circumstellar medium to date Müller *et al.* (2005), with identifications increasing at a remarkably accelerating rate within the last decade McGuire (2022). Among such detections, the so-called "complex organic molecules" (COMs, i.e., organic molecules with six or more atoms) are observed in various sources at different stages of star and planet formation—from prestellar cores to comets Herbst & van Dishoeck (2009); Öberg *et al.* (2010a); Bacmann *et al.* (2012); Biver *et al.* (2014); Öberg *et al.* (2015); Walsh *et al.* (2016); Herbst (2017); Altwegg *et al.* (2017); Favre *et al.* (2018); Brunken *et al.* (2022). Their formation routes have been extensively investigated in both gas and solid phases (see the reviews by Linnartz *et al.* (2015); Öberg (2016); Herbst (2017)). Radical-induced reactions can lead to the formation of a wide range of complex organic molecules even at temperatures as low as 10 K Watanabe & Kouchi (2002); Linnartz *et al.* (2015); Butscher *et al.* (2015); Chuang *et al.* (2016); Fedoseev *et al.* (2017); Chuang *et al.* (2020); Qasim *et al.* (2020a); Ioppolo *et al.* (2021); Perrero *et al.* (2022). Alternatively, interactions with photons, electrons, or cosmic rays can also trigger chemical reactions in the ice. Investigating the different pathways to forming interstellar molecules, and especially COMs, is therefore crucial to understanding the evolution of the chemical inventory of different sources.

Sulfur-bearing species, in particular, have been a long-standing issue in astrochemistry. In dense environments such as cold clouds, the (observable) gas-phase sulfur is severely depleted by up to two orders of magnitude compared to cosmic values Tieftrunk *et al.* (1994); Anderson *et al.* (2013); Vastel *et al.* (2018); Fuente *et al.* (2019); Rivière-Marichalar *et al.* (2019), with the bulk of its content remaining largely unknown. In addition to the sulfur depletion problem, hydrogen sulfide (H_2S) specifically also exhibits a mismatch between its predicted abundances—based on astrochemical models—and observations. It is formed very efficiently in ices via the successive hydrogenation of S atoms, producing the radical SH as an intermediate (see, e.g., Garrod *et al.* 2007; Druard & Wakelam 2012; Esplugues *et al.* 2014; Vidal *et al.* 2017):

$$S \xrightarrow{+H} SH \xrightarrow{+H} H_2S. \tag{7.1}$$

Indeed, H_2S has been detected in the gas phase towards a range of different interstellar sources Thaddeus *et al.* (1972); Minh *et al.* (1989); van Dishoeck *et al.* (1995); Hatchell *et al.* (1998); Vastel *et al.* (2003); Wakelam *et al.* (2004); Neufeld *et al.* (2015); Le Roy *et al.* (2015); Biver *et al.* (2015); Calmonte *et al.* (2016); Phuong *et al.* (2018). It has also been observed in the comae of comets at the highest abundance amid all sulfur-bearing species Bockelée-Morvan *et al.* (2000b); Le Roy *et al.* (2015); Biver *et al.* (2015); Calmonte *et al.* (2016). However, it has not been detected in interstellar ices so far, and estimated upper limits are of only $\leq 0.7\%$ with respect to water Jiménez-Escobar & Muñoz Caro (2011b). This indicates that H_2S ice must be subjected to effective destruction mechanisms, among which chemical desorption and (photo)chemical conversion seem to be particularly promising Jiménez-Escobar & Muñoz Caro (2011b); Jiménez-Escobar *et al.* (2014b); Oba *et al.* (2018, 2019); Shingledecker *et al.* (2020); Cazaux *et al.* (2022); Santos *et al.* (2023b).

A prominent loss channel involves the interaction of H atoms with solid H_2S, resulting in the abstraction reaction:

$$H_2S + H \rightarrow SH + H_2 \tag{7.2}$$

which involves a barrier of ~ 1500 K that can be overcome by quantum tunneling Lamberts & Kästner (2017). This reaction has been shown to enrich the ice mantles with SH radicals, which in turn can kick-start sulfur-bearing ice chemistry at temperatures of relevance to molecular clouds Santos *et al.* (2023b). On a similar context, Laas & Caselli (2019) found that a significant portion of the missing sulfur reservoir would consist of simple organosulfur compounds (e.g., OCS, H_2CS, CS_2) locked-up in the ices. Solid-state reactions leading to

S-bearing molecules could thus play a significant role in unraveling the fate of interstellar sulfur.

Another important species to interstellar chemistry is the simplest alkyne acetylene (C_2H_2). It has been observed with infrared instruments in the gas phase towards young stellar objects and envelopes of C-rich stars, as well as at fairly high abundances in the inner parts of protoplanetary disks and in comets Ridgway *et al.* (1976); Lacy *et al.* (1989); Lahuis & van Dishoeck (2000); Gibb *et al.* (2007); Mumma & Charnley (2011); Bast *et al.* (2013); Pontoppidan *et al.* (2014); Tabone *et al.* (2023). It is also suggested to be present in pre-stellar clouds Taniguchi *et al.* (2017, 2019b). However, definitive detections in such environments require observations of gaseous molecules in submillimeter wavelengths, which are hindered for C_2H_2 due to its lack of a dipole moment. Since gas-phase formation routes cannot explain its observed abundances, sublimation from dust grains is usually suggested as a major source of gaseous C_2H_2 Charnley & Tielens (1992); Lahuis & van Dishoeck (2000); Nguyen *et al.* (2002). However, its main ice features at $\sim$3 μm and $\sim$13 μm overlap with H_2O and silicate bands, making its detection quite challenging Boudin *et al.* (1998); Knez *et al.* (2012). This is particularly true for water-rich ices, as evinced by its high upper limit of 10 % with respect to H_2O Boudin *et al.* (1998).

A top-down mechanism through the energetic processing of polycyclic aromatic hydrocarbons (PAHs) or bare carbonaceous grains has been shown experimentally to be particularly efficient in forming C_2H_2 (see, e.g., Jochims *et al.* (1994); Le Page *et al.* (2003); West *et al.* (2018)). Additionally, a bottom-up formation could be feasible through the diffusion and reaction of C atoms on dust grains yielding C_2, and its subsequent hydrogenation Tsuge *et al.* (2023). The widely detected C_2H radicals (e.g., Padovani *et al.* (2009); Sakai & Yamamoto (2013); Kastner *et al.* (2014)) could also contribute to forming C_2H_2 upon adsorption onto ice grains followed by hydrogenation. Its gas-phase abundances in prestellar cores can however be lower than C_2H_2 counterparts detected towards hot cores by up to one order of magnitude Lahuis & van Dishoeck (2000); Padovani *et al.* (2009), which might limit its role as a dominant C_2H_2 precursor. As the cloud becomes denser and the residence time of H atoms on the dust surfaces increases, C_2H_2 may be hydrogenated to form C_2H_4, C_2H_6, and the radicals in-between Hiraoka *et al.* (2000); Kobayashi *et al.* (2017); Molpeceres & Rivilla (2022).

The reactive nature of the triple bond in C_2H_2 makes it a versatile precursor to form interstellar molecules with a carbon backbone (see, e.g., the routes proposed by Charnley (2004); Molpeceres & Rivilla (2022)). Indeed, laboratory investigations of its reaction with thermalized OH radicals and H atoms on interstellar-ice analogues resulted in the formation of a variety of O-bearing COMs, such as acetaldehyde (CH_3CHO), vinyl alcohol (CH_2CHOH), ketene (CH_2CO), and ethanol (CH_3CH_2OH) Chuang *et al.* (2020). Furthermore, energetic processing of C_2H_2 ices mixed with other interstellar-relevant compounds (e.g., H_2O, CO, CO_2, and NH_3) have also been explored experimentally, probing efficient formation mechanisms to a wide range of O- and N-bearing molecules Hudson & Moore (2003); Bergner *et al.* (2019); Chuang *et al.* (2021); Canta *et al.* (2023); Zhang *et al.* (2023); Chuang *et al.* (2024). Its reactivity with sulfur-bearing species, however, remains to be explored under interstellar cloud conditions.

In a recent computational study, Molpeceres & Rivilla (2022) suggested a general mechanism in which C_2H_2 molecules could provide the carbon backbone to form a series of different organic molecules by reacting with a range of open shell species (e.g., H, OH, NH_2) on interstellar-ice surfaces. Among other cases, they speculate that its interaction with H atoms followed by SH radicals could serve as a potential route to forming S-bearing COMs in the solid state, albeit without exploring it computationally. In the present study, we conduct an experimental investigation of the formation of S-bearing COMs via the interactions of C_2H_2 with H atoms and SH radicals. We also employ quantum-chemical calculations to elucidate the reaction network behind our laboratory results. In Section 7.2, the experimental setup and computational methods are described. The main results are presented and discussed in Section 7.3, and their astrophysical implications are elaborated in Section 7.4. In Section 7.5

we summarize our main findings.

7.2 Methods

7.2.1 Experimental methods

This work is executed with the ultrahigh vacuum (UHV) setup SURFRESIDE[3], which has been described in detail elsewhere Ioppolo *et al.* (2013); Qasim *et al.* (2020c). Here, only the relevant information is presented. A gold-plated copper substrate is mounted on the tip of a closed-cycle helium cryostat at the center of the main chamber, which operates at a base pressure of $\sim 5 \times 10^{-10}$ mbar. The substrate temperature can be varied between 8 and 450 K using resistive heaters, and is monitored by two silicon diode sensors with a relative accuracy of 0.5 K. Gases of H_2S (Linde, purity 99.5%) and C_2H_2 (Linde, 5% in Helium) are simultaneously admitted into the chamber through all-metal leak valves. Concomitantly, a hydrogen atom beam source (HABS Tschersich (2000)) generates H atoms that are subsequently cooled down by colliding with a nose-shaped quartz pipe before reaching the substrate. Ice is deposited at 10 K and monitored by Fourier-transform reflection-absorption infrared spectroscopy (FT-RAIRS), with 1 cm^{-1}-resolution spectra acquired in the range of 700 to 4000 cm^{-1}. After deposition, the sample is heated at a ramping rate of 5 K min^{-1} during temperature-programmed desorption experiments (TPD). The sublimated ice species are immediately ionized by electron impact with an energy of 70 eV and are recorded by a quadrupole mass spectrometer (QMS), whilst the solid phase is concurrently monitored by RAIRS.

To quantify the abundances of products, two approaches are adopted. In the case of infrared spectroscopy, the IR integrated absorbance ($\int Abs(\nu)d\nu$) of the species in the ice can be converted to absolute abundance using a modified Beer-Lambert law:

$$N_X = \ln 10 \frac{\int Abs(\nu)d\nu}{A'(X)} \tag{7.3}$$

where N_X is the column density in molecules cm^{-2} and $A'(X)$ is the apparent absorption band strength in cm molecule^{-1} of a given species. For H_2S, we utilize $A'(H_2S)_{\sim 2553\ cm^{-1}} \sim (4.7 \pm 0.1) \times 10^{-17}$ cm molecule^{-1}, as measured for our reflection-mode IR settings using the laser-interference technique Santos *et al.* (2023b). The band strength of C_2H_2 is derived by multiplying the A value in transmission mode reported by Hudson *et al.* (2014) ($A(C_2H_2)_{\sim 3240\ cm^{-1}} \sim 2.39 \times 10^{-17}$ cm molecule^{-1}) by a transmission-to-reflection conversion factor of 3.2 measured with the same experimental setup (see Santos *et al.* (2023b) for the case of H_2S, that was later combined with the value for CO to derive the averaged conversion factor).

Due to the higher sensitivity of the QMS compared to the RAIRS employed in this work, some of the chemical species formed in our experiments were only detectable by the former technique. In order to quantify their relative abundances, column density ratios (N_X/N_Y) can be derived from the QMS data by the expression Martín-Doménech *et al.* (2015):

$$\frac{N_X}{N_Y} = \frac{A(m/z(X))}{A(m/z(Y))} \cdot \frac{\sigma^+(Y)}{\sigma^+(X)} \cdot \frac{I_F(z(Y))}{I_F(z(X))} \cdot \frac{F_F(m(Y))}{F_F(m(X))} \cdot \frac{S(m/z(Y))}{S(m/z(X))} \tag{7.4}$$

where $A(m/z)$ is the integrated desorption signal of a given mass fragment, $F_F(m/z)$ is its fragmentation fraction; and $S(m/z)$ is the corresponding sensitivity of the QMS. Moreover, σ^+ denotes the molecule's electronic ionization cross-section; and $I_F(z)$ is the fraction of ions with charge z (here corresponding to unity). The parameters employed for each of the products found in this work are summarized in Table 7.1. Given the overall lack of experimental values,

Table 7.1: List of parameters used to quantify the products' relative abundances with the QMS.

Species	α [Å^3] [a]	F_F (m/z) [b]	S (m/z) [b,c]
CH_3CHS	7.617 [d]	0.598 [g]	0.1
CH_2CHSH	7.578 [e]	0.200 [h]	0.1
CH_3CH_2SH	7.38 [f]	0.200 [i]	0.09
H_2S_2	6.828 [d]	0.330 [g]	0.08
$HSCH_2CH_2SH$	10.503 [d]	0.164 [i]	0.1

[a] CCCBDB

[b] Values are given for the molecular ions

[c] Chuang (2018)

[d] Derived by group additivity methods

[e] Computed with the B97D3/daug-cc-pVTZ level of theory

[f] Gussoni *et al.* (1998)

[g] Derived in this work

[h] Assuming the same as CH_3CH_2SH

[i] NIST

the ionization cross sections are estimated based on the molecule's polarizability volume (α) by the empirical correlation Hudson *et al.* (2006); Bull *et al.* (2012):

$$\sigma_{\max}^+(X) = c \cdot \alpha(X) \tag{7.5}$$

where X denotes a given species and c is a correlation constant of 1.48 Å^{-1}. It is expected that, for organic species, $\sigma^+(X)$ at 70 eV does not vary significantly ($< 5\%$) from the maximum ionization cross section ($\sigma_{\max}^+$) Hudson *et al.* (2003); Bull & Harland (2008). When available, fragmentation fractions are derived from NIST [1]. Otherwise they are estimated based on our QMS measurements. In the case of CH_2CHSH, isolating its peak during TPD is quite challenging (see Section 7.3.1). Thus, we assume the same fragmentation fraction as its fully-hydrogenated counterpart, CH_3CH_2SH. The polarizability values are obtained from CCCBDB[2]. Given sulfur's natural isotopic abundances, the contribution from ^{34}S-bearing species to the mass signals would be ~ 22 times weaker than the dominant ^{32}S-bearing counterparts and therefore are not further considered.

The experiments performed in this work are summarized in Table 7.2. Both molecule fluxes, as well as the H-atom flux, have an estimated relative error of $\lesssim 5\%$. As a control experiment, pure CH_3CH_2SH (Sigma-Aldrich, purity 97%) ice is grown through vapor deposition. Previous to dosing, it is purified by a series of freeze-pump-thaw cycles. The other identified products are not commercially available and therefore standard samples cannot be obtained. The instrumental uncertainties in the integrated QMS signals are derived from the corresponding integrated spectral noise for the same band width.

---

[1] https://webbook.nist.gov/chemistry/

[2] NIST Computational Chemistry Comparison and Benchmark Database (CCCBDB), NIST Standard Reference Database Number 101, http://cccbdb.nist.gov/

Table 7.2: Overview of the performed experiments.

Experiment	Label	C_2H_2 flux $(\text{cm}^{-2}\ \text{s}^{-1})$	H_2S flux $(\text{cm}^{-2}\ \text{s}^{-1})$	H flux $(\text{cm}^{-2}\ \text{s}^{-1})$	$C_2H_2:H_2S:H$	Time (min)
$C_2H_2 + H_2S + H$	1	5.0×10^{11}	5.0×10^{11}	1.0×10^{13}	1:1:20	360
$C_2H_2 + H_2S + H$	2	7.5×10^{11}	3.7×10^{12}	7.5×10^{12}	1:5:10	80
$C_2H_2 + H_2S + H$	3	8.0×10^{11}	8.0×10^{12}	4.0×10^{12}	1:1:5	60
$C_2H_2 + H_2S + H$	4	6.0×10^{11}	6.0×10^{11}	6.0×10^{12}	1:1:10	240
$C_2H_2 + H_2S + H$	5	2.0×10^{11}	2.0×10^{11}	1.0×10^{13}	0.4:0.4:2	360
$C_2H_2 + H$	6	6.0×10^{11}		6.0×10^{12}	1:0:10	240

Experiment	Label	CH_3CH_2SH flux $(\text{cm}^{-2}\ \text{s}^{-1})$				Time (min)
CH_3CH_2SH	7	7.0×10^{12}				60

7.2.2   Computational methods

We have complemented our experimental results with computational chemical simulations for selected cases. Specifically, we have employed ORCA 5.0.4Neese *et al.* (2020) to run density functional theory (DFT) calculations. The density functional of choice is M062X Zhao & Truhlar (2008b), combined with the def2-TZVP basis set. All the DFT calculations were done under the unrestricted formalism and the options VERYTIGHTSCF and NORI were used. The broken symmetry approximation was used in all open shell singlet systems (i.e., radical-radical reactions). We made sure M062X is an appropriate method by comparing its performance with CCSD(T)-F12/AUG-CC-PVTZ calculations in radical-molecule reactions. For these coupled cluster calculations we used MolproWerner *et al.* (2012, 2020); Knizia *et al.* (2009). The computational results can be found in Section 7.3.4.

7.3   Results and discussion

In Figure 7.1, the selected signals of m/z = 32, 45, 46, 47, 58, 59, 60, 62, and 66 recorded during TPD after the codeposition of C_2H_2, H_2S, and H (1:1:20) for six hours (experiment 1) are shown. The deposition experiment results in (at least) six reaction products as revealed by a prolific series of desorption peaks at, in decreasing order of signal intensity, $\sim$ 119 K, $\sim$ 131 K, $\sim$ 158 K, $\sim$ 84 K, and $\sim$ 72 K. These bands are identified as six sulfur-bearing molecules: respectively, ethanethiol (CH_3CH_2SH), vinyl mercaptan (CH_2CHSH), disulfane (H_2S_2), 1,2-ethanedithiol ($HSCH_2CH_2SH$), thioacetaldehyde (CH_3CHS), and thioketene (CH_2CS). Representative structures of the identified products are shown in Figure 7.2 as obtained from the MolView application[3]. In the following subsections, the assignments of the desorption bands depicted in Figure 7.1 are discussed in detail.

7.3.1 CH_2CHSH and CH_3CH_2SH

The TPD of experiment 2 (C_2H_2:H_2S:H = 1:5:10) is shown in panel a) of Figure 7.3. In contrast to experiment 1, for this mixing ratio two desorption peaks—at $\sim$117 K and $\sim$121 K—are clearly distinguishable, revealing that this band actually consists of two products. The first one is evinced by a peak in the signals for m/z = 58 and 60, whereas the second one is characterized by m/z = 46, 47, and 62. Given the elemental composition of the ice (i.e., C, S, and H atoms), these mass signals are consistent with the desorption of two sulfur-bearing organic molecules with general formula C_2H_XS. From the peak signals of m/z = 60 and 62—the largest mass-to-charge ratios detected for each peak respectively—it is inferred that the product desorbing at $\sim$117 K is described by the formula C_2H_4S, and the one at $\sim$121 K is described by C_2H_6S. Indeed, it is expected that the lighter species with four hydrogen atoms would be more volatile than the fully-saturated counterpart, albeit slightly. The contribution of the mass fragment m/z = 32 to these species cannot be measured since it is blended with the desorption profile of H_2S at $\sim$85 K (see, e.g., Santos *et al.* (2023b)).

Given the proposed chemical route involving C_2H_2, SH radicals, and H atoms, the most plausible candidates to the $\sim$117 K and $\sim$121 K peaks are, respectively, vinyl mercaptan (CH_2CHSH) and ethanethiol (CH_3CH_2SH). These assignments are fortified by a comparison with the molecules' standard fragmentation pattern, although deriving the mass fragments' relative intensities is not trivial in this case. Since the full desorption bands of the two products still overlap considerably, the quantification of the contribution from each species to a given integrated mass signal is challenging. To minimize errors induced by contamination from the blended molecule, only fingerprint m/z signals uniquely associated with each species
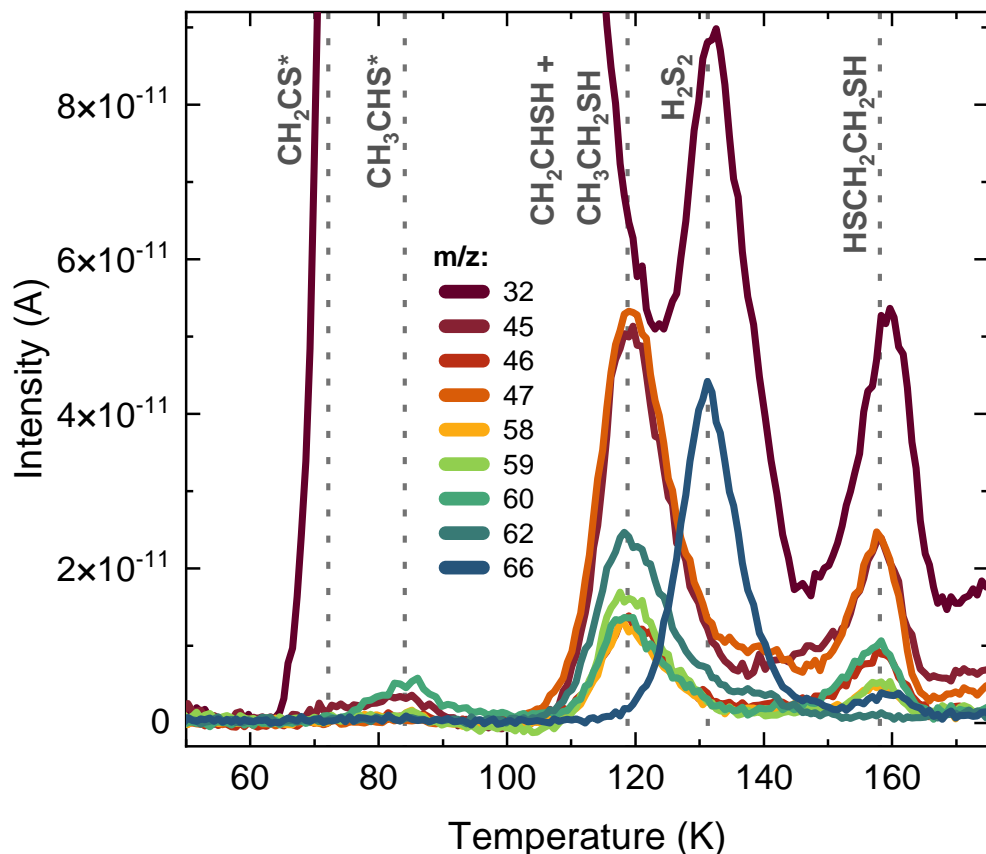
---

[3]https://molview.org/

Figure 7.1: Relevant QMS signals recorded during a TPD experiment after codepositon of C_2H_2:H_2S:H (1:1:20) at 10 K for six hours. The dotted lines mark the desorption peak of each band, and their assignments are denoted in grey. The asterisk indicates a tentative identification.

were considered in the product identification—i.e., mass fragments with a simultaneous relative intensity of $\geq 10\%$ in both standards of CH_2CHSH and CH_3CH_2SH were excluded from the analysis, leaving only the ones with minor contributions from the adjacent feature. Panels b) and c) of Figure 7.3 show the resulting fragmentation patterns of peaks ~ 117 K and ~ 121 K, respectively, as well as the reference values for CH_2CHSH and CH_3CH_2SH. The relative intensities of each peak match the references well, securing their assignments as CH_2CHSH and CH_3CH_2SH. Furthermore, the pure CH_3CH_2SH ice standard exhibits peak desorption at 119 K, in line with its identification in the C_2H_2 + H_2S + H experiments.

Infrared spectroscopy is used to further assist in the identification of the most abundant products. The red IR spectrum in panel a) of Figure 7.4 was acquired after a six-hours codeposition experiment with a flux ratio C_2H_2:H_2S:H = 1:1:20 (experiment 1). In the same panel, a control blank experiment of a C_2H_2 + H (1:10, experiment 6) deposition is shown in grey. All depositions were performed at 10 K. In comparison with the blank experiment, the IR spectrum of C_2H_2 + H_2S + H contains three additional features at ~ 1272 cm^{-1}, ~ 1450 cm^{-1}, and ~ 1591 cm^{-1} due to newly formed reaction products. The bands at ~ 1272 cm^{-1} and ~ 1450 cm^{-1}, respectively, are consistent with the peak positions and relative intensities of the CH_2 wagging and CH_3 bending modes of CH_3CH_2SH, as shown in panel b) by the

Thioacetaldehyde
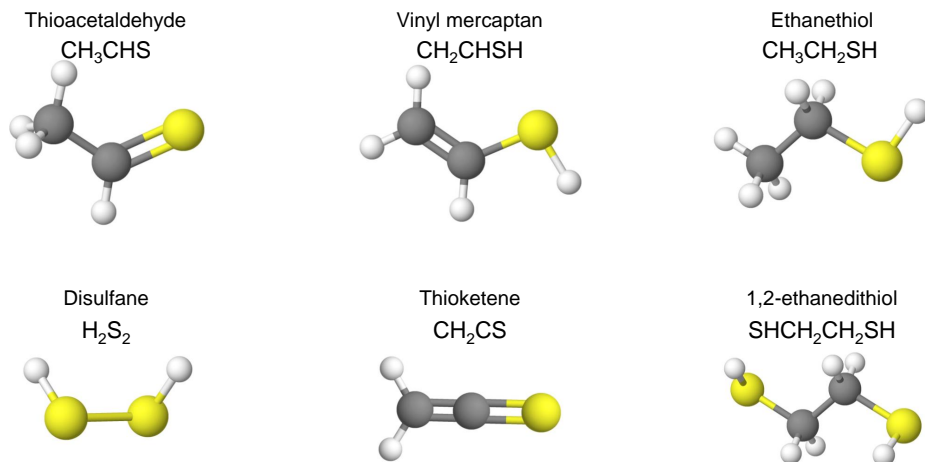CH₃CHS

Vinyl mercaptan
CH₂CHSH

Ethanethiol
CH₃CH₂SH

Disulfane
H₂S₂

Thioketene
CH₂CS

1,2-ethanedithiol
SHCH₂CH₂SH

Figure 7.2: Representative structures of the six S-bearing products identified in the experiments with C_2H_2 + H_2S + H. These are provided for visualization purposes and may not depict the accurate minimum-energy geometries of the species formed in the experiments.

standard spectrum in green (see also Smith *et al.* (1968)). The band at ~ 1591 cm^{-1} is compatible with the C=C stretching mode of CH$_2$CHSH, its strongest feature Almond *et al.* (1983).

Infrared spectra are also obtained during the TPD experiments, which allows to correlate peaks in mass signals with the disappearance of a molecule's vibrational modes. The difference spectrum between temperatures of 100 K and 140 K of the codeposition with C$_2$H$_2$:H$_2$S:H = 1:1:20 (experiment 1) is shown in red in Figure 7.4, panel b). This is obtained by subtracting the spectrum measured at 140 K from the one measured at 100 K, thus highlighting the vibrational modes that disappear during this temperature range. At 100 K, C$_2$H$_2$ and its hydrogenation products C$_2$H$_4$ and C$_2$H$_6$ are already desorbed from the ice, and only the bands of CH$_2$CHSH and CH$_3$CH$_2$SH are visible in the difference spectrum. These bands completely disappear from the spectra between 100 and 140 K. These desorption temperatures obtained from the IR data are consistent with the QMS measurement shown in Figure 7.3. During warm up, the areas of the bands remain constant until reaching the temperature in which they begin to desorb, indicating that no significant change in their concentration in the ice occurs upon heating. The combination of both the infrared and the QMS data provides unambiguous evidence for the identification of CH$_2$CHSH and CH$_3$CH$_2$SH, and signal that these molecules must be formed in the ice at 10 K and remain preserved until desorption.

7.3.2   H₂S₂ and HSCH₂CH₂SH

The second strongest desorption feature in Figure 7.1 peaks at 131 K and contains the mass signals m/z = 32 and 66 (see Figure 7.5, panel a). Both the peak desorption temperature and the relative intensities of the fragments are in full agreement with the reference values for disulfane (H$_2$S$_2$) Santos *et al.* (2023b) (Figure 7.5, panel b). Moreover, its characteristic SH stretching band is observed on the red wing of the H$_2$S feature peaking at $\sim$2491 cm^{-1}, as shown in panel c) of Figure 7.5. During TPD, the intensity of the H$_2$S$_2$ infrared feature remains constant until its complete desorption before 150 K, consistent with the desorption temperature observed for its mass fragments in the QMS data. This is highlighted by the
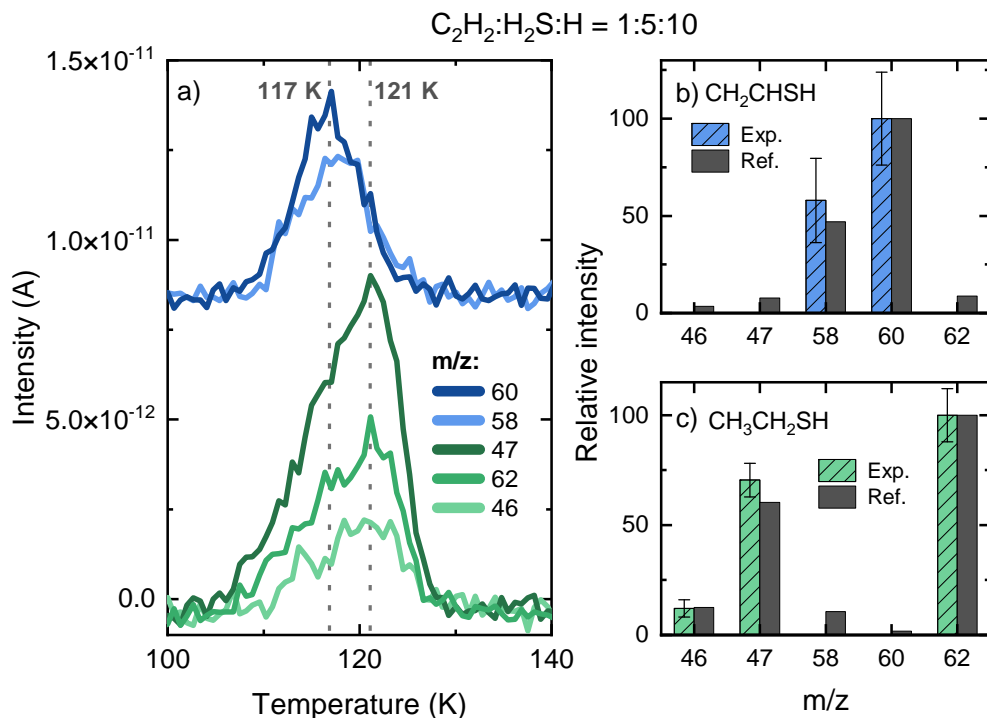
Figure 7.3: Assignment of the TPD-QMS peaks at ∼117 K and ∼121 K as vinyl mercaptan (CH_2CHSH) and ethanethiol (CH_3CH_2SH), respectively. The deposition is performed with a flux ratio of $C_2H_2:H_2S:H = 1:5:10$. Panel a): QMS signals showing two desorption peaks highlighted by the dotted grey lines. Panel b): Mass fragmentation pattern of the selected signals for the peak at ∼117 K corrected for the sensitivity of the QMS. The standard for CH_2CHSH is shown for comparison Strausz *et al.* (1965). Panel c): Same as panel b), but for the peak at ∼121 K in comparison with CH_3CH_2SH (standard measured in this work).

difference spectrum between 120 K and 150 K shown in grey in Figure 7.5, panel c). Indeed, the formation of this species is unsurprising, as it has been previously shown to form at 10 K in an H_2S ice exposed to H atoms as a result of SH radical recombination Santos *et al.* (2023b).

Subsequently to H_2S_2, a desorption feature appears at 158 K with contributions from m/z = 46, 47, 58, 59, 60, 61, and 94 (Figure 7.6, left panels). The mass-to-charge ratios of 92, 118, 120, and 122 were also recorded during the TPD experiment, but no increase in their signal was observed above the instrumental detection limit. Thus, it is reasonable to assume that m/z = 94 corresponds to the product's molecular ion defined by the general formula $C_2H_6S_2$. Among the possible structures associated with this formula, the most promising candidate for the assignment of the band at 158 K is 1,2-ethanedithiol ($HSCH_2CH_2SH$). The relative intensities of the mass fragments match well with the reference values for $HSCH_2CH_2SH$ provided by NIST (Figure 7.6, right panel), and the desorption temperature is also in line with a slightly higher value of 180 K measured by Roe & Schulz (1998) for one layer of $HSCH_2CH_2SH$ on a molybdenum (110) surface with adsorbed carbon.

No corresponding features of $HSCH_2CH_2SH$ are observed in the infrared spectra after deposition or during TPD, likely due to the significantly lower sensitivity of the infrared spectrometer in comparison with the QMS employed in our experiments. Moreover, this
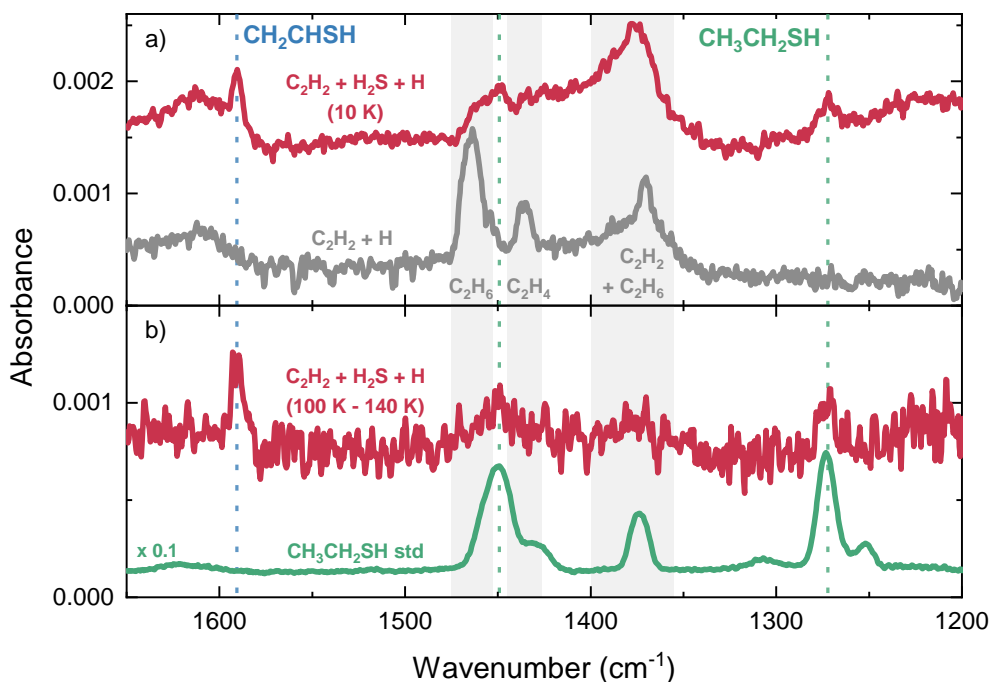
Figure 7.4: Infrared spectra utilized to assign CH_3CH_2SH and CH_2CHSH. Spectrum recorded after codeposition of a $C_2H_2 + H_2S + H$ ice (1:1:20; red), together with a $C_2H_2 + H$ (1:10; grey) blank experiment. Panel b): difference spectrum acquired during TPD between 100 K and 140 K (red) for the $C_2H_2 + H_2S + H$ codeposition, together with a CH_3CH_2SH standard spectrum (green). All depositions are performed at 10 K and the spectra are offset for clarity.

product's yield is relatively small, and its IR features heavily overlap with the other, more abundant S-bearing species sharing the same functional groups. Nonetheless, as will be discussed in detail in Section 7.4, the most probable route to form 1,2-ethanedithiol requires the consumption of a CH_2CHSH molecule as reactant. The fact that the infrared absorbance area of CH_2CHSH remains constant during TPD until its desorption indicates that no additional reactions involving this molecule take place as a result of the heat, thus suggesting that $HSCH_2CH_2SH$ formation should occur at 10 K.

7.3.3 CH_2CS and CH_3CHS

Prior to the sublimation of the most abundant products, a relatively small band appears with peak desorption temperature of $\sim$ 84 K (see Figure 7.7, panel a). It is characterized by $m/z = 45, 46, 58, 59,$ and 60, but without contribution from higher masses. Because its desorption temperature coincides with H_2S, we cannot probe the yield of $m/z = 32$ from this species. It is reasonable to assume $m/z = 60$ to be its molecular ion, described by the chemical formula C_2H_4S (i.e., an isomer of vinyl mercaptan). Besides CH_2CHSH, three other closed-shell structures can derive from this formula: thioacetaldehyde (CH_3CHS), thiirane ($c-(CH_2)_2S$), and thione S-methylide (CH_2SCH_2). The latter is significantly less stable than the other isomers Salta *et al.* (2021), and would require a cleavage of the C≡C bond in a C_2H_2 molecule. Thus, it is unlikely to be synthesized under our experimental conditions. Thiirane is also ruled out due to the incompatibilities of its standard fragmentation pattern from NIST
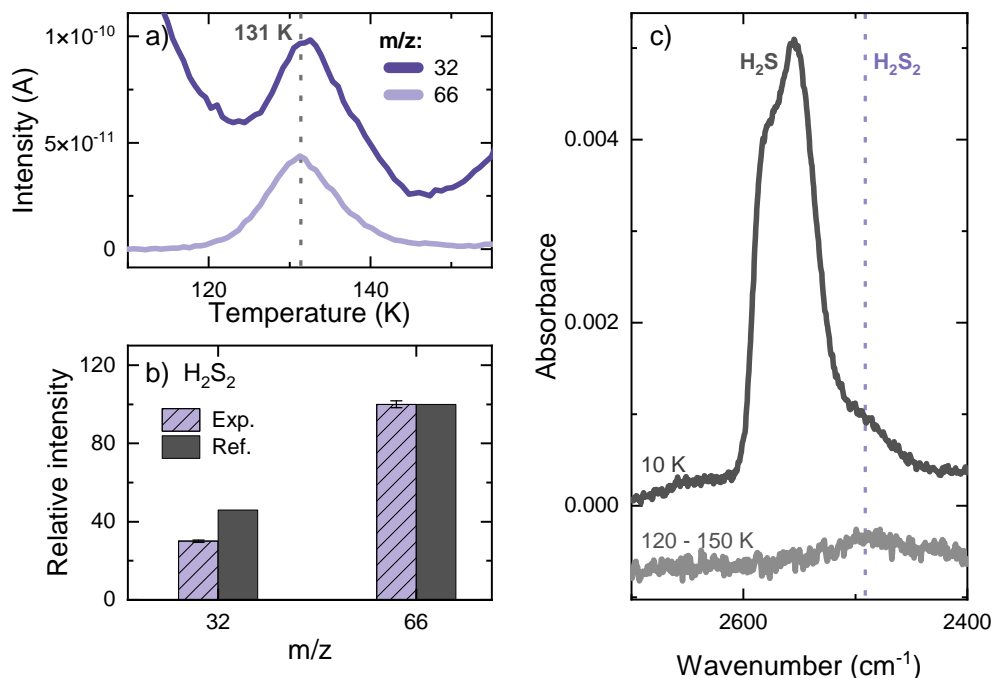
Figure 7.5: Assignment of the TPD-QMS peak at ∼131 K as disulfane (H_2S_2) after a codeposition experiment with a flux ratio of C_2H_2:H_2S:H = 1:1:20 (experiment 1). Panel a): QMS signals of the relevant fragments. Panel b): Mass fragmentation pattern corrected for the sensitivity of the QMS in comparison with the standard for H_2S_2 from Santos *et al.* (2023b). Panel c): Infrared spectrum at 10 K (black) and difference spectrum between 120 and 150 K (grey).

and the relative intensities of the recorded mass signals (panel b) in Figure 7.7)—in particular considering the large discrepancy in the dominant mass fragment between the two (i.e., m/z = 45 for thiirane, compared to m/z= 60 for our experiments). This leaves CH_3CHS as the most promising candidate for the desorption band at ∼84 K. To the best of our knowledge, no standard mass fragmentation patterns are available for this species in the literature—likely because of its extreme reactivity at room temperature. The fragments detected by the QMS are nevertheless all reasonable to arise upon electron-impact ionization of thioacetaldehyde. These are $[CHS]^+$ (m/z = 45), $[CH_2S]^+$ (m/z = 46), $[C_2H_2S]^+$ (m/z = 58), $[C_2H_3S]^+$ (m/z = 59), and $[C_2H_4S]^+$ (m/z = 60). Given the lack of standard measurements, this assignment is classified as tentative. Similarly to $HSCH_2CH_2SH$, the formation of CH_3CHS also requires CH_2CHSH as a reactant (see Section 7.3.4 for more details), and consequently it is most likely formed at 10 K.

At ∼74 K, a small shoulder appears in the signal of m/z = 45 (Figure 7.7 panel a), suggesting the desorption of another species containing the $[CHS^+]$ moiety. Its identification is however quite challenging given the very small yield of this product and its proximity to the more abundant CH_3CHS. For an ice mixture with mixing ratio C_2H_2:H_2S:H=1:1:5 deposited for one hour (experiment 3), the production of CH_3CHS can be significantly reduced with respect to the shoulder peak at ∼74 K (see Figure 7.7 panel c), revealing an otherwise undetectable contribution from m/z = 58 to the fragmentation of the more volatile product. This mass fragment is consistent with the formula $C_2H_2S^+$ and, together with m/z = 45, suggests that the peak is due to thioketene (CH_2CS). This is however only a tentative assignment,
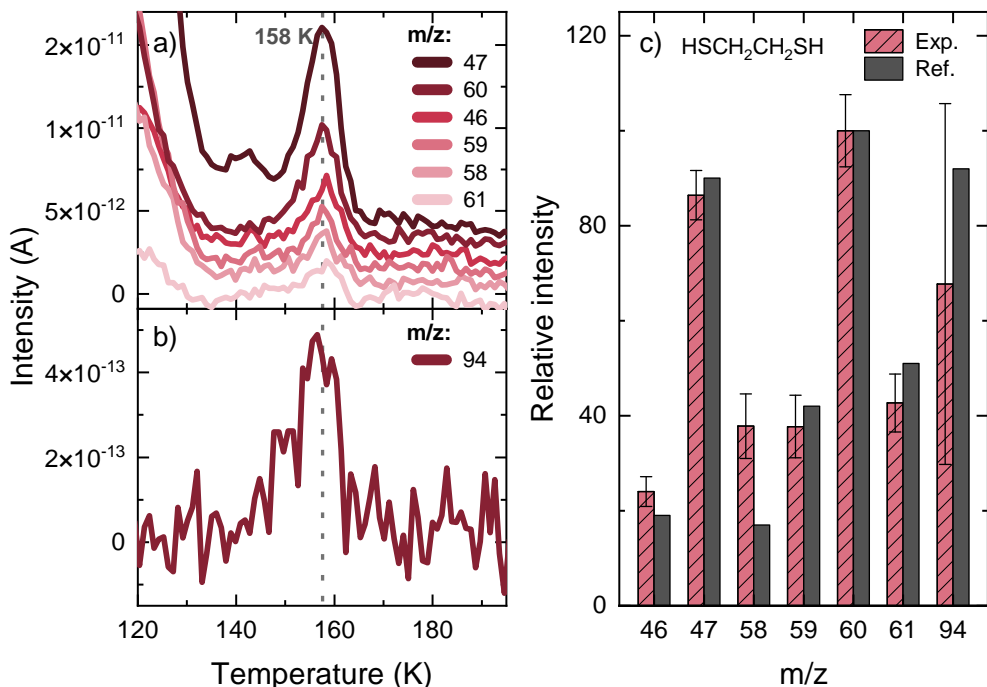
Figure 7.6: Assignment of the TPD-QMS peak at $\sim$158 K as 1,2-ethanedithiol (HSCH$_2$CH$_2$SH) after a codeposition experiment with a flux ratio of C$_2$H$_2$:H$_2$S:H = 1:1:20 (experiment 1). Panel a): QMS signals of the relevant fragments with m/z $\leq$ 61. Panel b): Signal for m/z = 94 measured during the same experiment. The dotted grey line indicates the peak desorption temperature. Panel c): Mass fragmentation pattern of the detected signals for the peak at $\sim$158 K corrected for the sensitivity of the QMS in comparison with the standard for HSCH$_2$CH$_2$SH from NIST. The larger error bar of m/z = 94 is a consequence of the significantly lower sensitivity of the QMS at this mass-to-charge ratio.

as a more secure identifications is alas not possible given the lack of literature standards on thioketene—presumably due to its high reactivity—and the difficulty in distinguishing this product from the more abundant peak at $\sim$84 K.

7.3.4 Computational results and chemical network

We combine theoretical calculations performed in-house and from the literature to constrain the reactions at play in our experiments. In both cases, care should be taken when interpreting the activation energies since they are obtained in vacuum and therefore could differ from more representative solid-state scenarios. Nonetheless, these values are still useful for an assessment of the feasibility of a given route. The proposed chemical network is summarized in Figure 7.8. The first step in forming sulfur-bearing species under our experimental conditions involves the association of SH to a hydrocarbon containing two C atoms (general formula C$_2$H$_x$). The radical-molecule reaction between C$_2$H$_2$ and SH is the most straightforward candidate to initiate the network:

$$C_2H_2 + SH \rightarrow CHCHSH. \tag{7.6}$$

Our DFT calculations in vacuum predict a fairly small energy barrier of only $\Delta E_a \sim$758 K for
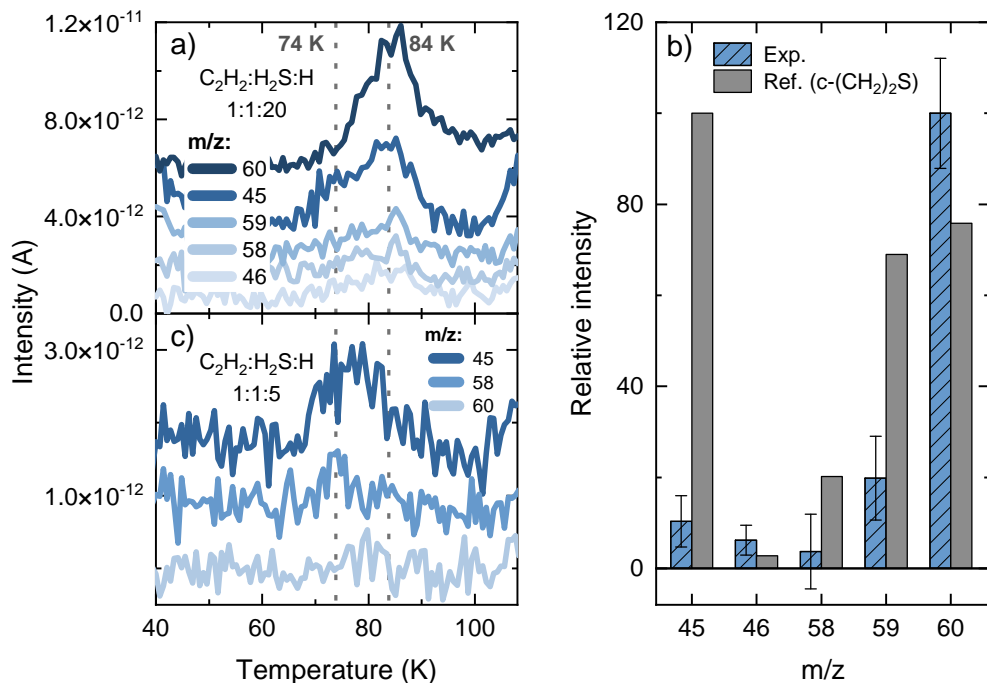
Figure 7.7: Tentative assignments of the TPD-QMS peaks at ∼74 K and ∼84 K as, respectively, thioketene (CH$_2$CS) and thioacetaldehyde (CH$_3$CHS). Panel a): QMS signals of the relevant fragments after a codeposition experiment with a flux ratio of C$_2$H$_2$:H$_2$S:H = 1:1:20 (experiment 1). The dotted gray lines indicates the peak desorption temperatures. Panel b): Mass fragmentation pattern of the detected signals for the peak at ∼84 K corrected for the sensitivity of the QMS (blue), assigned to CH$_3$CHS, in comparison to the standard fragmentation pattern of c−(CH$_2$)$_2$S from NIST (grey). Panel c): QMS signals of the relevant fragments after a codeposition experiment with a flux ratio of C$_2$H$_2$:H$_2$S:H = 1:1:5 (experiment 3), in which the CH$_3$CHS production is minimized. The dotted line highlights the contribution from the desorption peak at ∼74 K to the signals of m/z = 58 and m/z = 45.

this reaction. However, due to the extremely low temperatures of our experiments (10 K) and the high mass of the SH radical, quantum tunneling is largely restricted. Considering that Reaction 7.2 is exothermic, vibrationally excited SH radicals might play a role in overcoming such a barrier. However, energy dissipation in H$_2$O ices takes place typically within picosecond timescales (e.g., Ferrero *et al.* (2023)), and we extrapolate that it will also proceed in similarly short timescales for H$_2$S mixed with C$_2$H$_2$, since a variety of vibrational modes are present that could accept the energy that is dissipating. Thus, Reaction 7.6 is unlikely to initiate the chemical network probed here.

Alternatively, the network is proposed to be kick-started by the formation of C$_2$H$_3$ through a hydrogen addition reaction to C$_2$H$_2$ and its subsequent association with SH:

$$C_2H_2 + H \rightarrow C_2H_3 \tag{7.7}$$

$$C_2H_3 + SH \rightarrow CH_2CHSH. \tag{7.8}$$

Reaction 7.7 has been previously investigated in experimental as well as theoretical works and has been shown to proceed efficiently on icy surfaces at ∼10 K Hiraoka *et al.* (2000); Miller & Klippenstein (2004); Kobayashi *et al.* (2017); Molpeceres & Rivilla (2022), with a
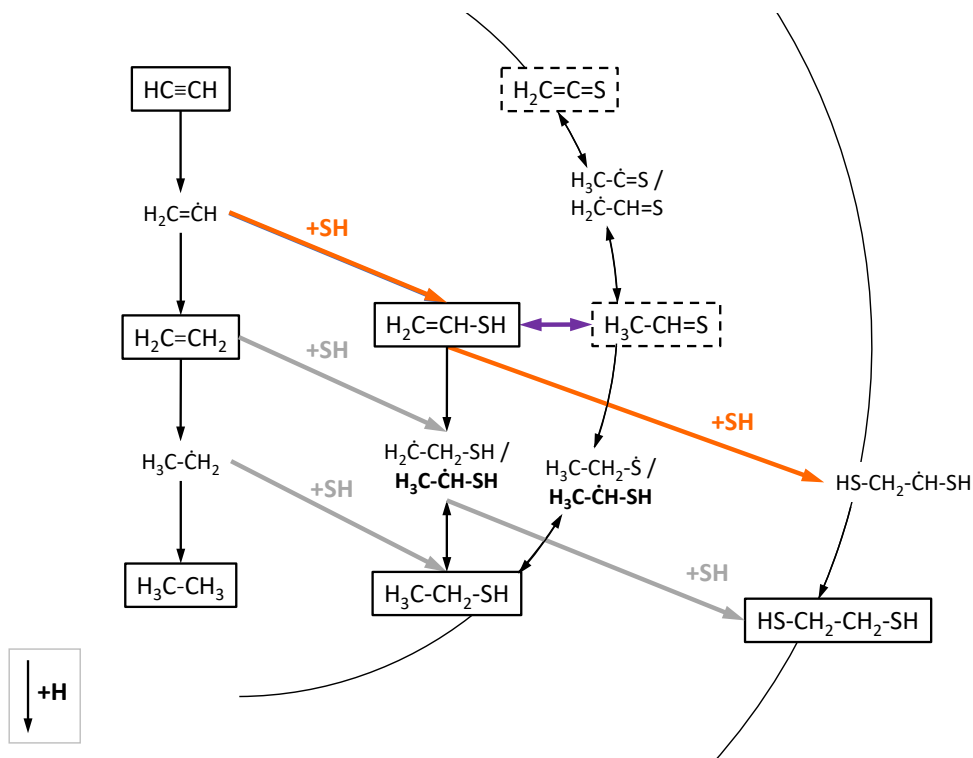
Figure 7.8: Chemical network explored in this work. Boxes denote closed-shell species, with solid and dashed lines indicating confirmed and tentative detections, respectively. Open-shell species in bold-face are formed barrierlessly Shingledecker *et al.* (2022). Reactions with SH radicals constrained in this work are indicated by orange arrows, grey arrows display potential reactions not investigated further in this work, and black arrows represent reactions with H atoms.The purple arrow highlights the speculated intermolecular isomerization process.

predicted activation energy of $\sim 2141 - 2430$ K depending on the level of theory utilized Molpeceres & Rivilla (2022). Despite being significantly larger than the activation energy for Reaction 7.6, it does not hinder Reaction 7.7 due to the much more efficient quantum tunneling of the light H atoms as opposed to the heavy SH radicals. Indeed, estimated rate constants for Reaction 7.7 in the solid phase are of the order of 10^4 s^{-1} Molpeceres & Rivilla (2022). The subsequent Reaction 7.8 takes place between two radicals, C$_2$H$_3$ and SH. The former is a non-polar species, and hence is expected to have a low binding energy to the H$_2$S ice. Since the ice is continuously grown, a randomized distribution of orientations is to be expected. Thus, reorientation barriers as predicted by Enrique-Romero *et al.* (2022) and observed by, e.g., Martín-Doménech *et al.* (2020), are less of a limitation. Consequently, nondiffusive interactions between C$_2$H$_3$ and SH radicals in the vicinity of one another are expected to efficiently form CH$_2$CHSH and initiate the sulfur chemical network in Figure 7.8. Such nondiffusive mechanisms have been extensively studied in the laboratory and through chemical modeling and are suggested to contribute significantly to ice chemistry under dark cloud conditions (Jin & Garrod (2020); Garrod *et al.* (2022), and references therein).

Following its formation via Reaction 7.8, CH$_2$CHSH can be hydrogenated to form CH$_3$CH$_2$SH:

$$CH_2CHSH + H \rightarrow CH_3CHSH \tag{7.9a}$$

$$CH_2CHSH + H \rightarrow CH_2CH_2SH \quad (7.9b)$$

$$CH_3CHSH + H \rightarrow CH_3CH_2SH \quad (7.10a)$$

$$CH_2CH_2SH + H \rightarrow CH_3CH_2SH, \quad (7.10b)$$
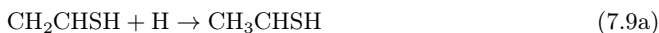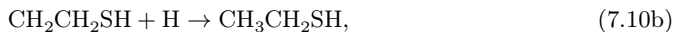
which proceeds by first forming either the radical CH_3CHSH (Reaction 7.9a, $\Delta E_a = 0$ in vacuum) or CH_2CH_2SH (Reaction 7.9b, $\Delta E_a \sim 1227$ K in vacuum) (Shingledecker et $al.$ 2022). The subsequent hydrogen additions in Reactions 7.10a and 7.10b proceed without an activation barrier.

Alternatively, CH_2CHSH can also react with nearby SH radicals to form the doubly-sulfurated radical $HSCH_2CHSH$:

$$CH_2CHSH + SH \rightarrow HSCH_2CHSH, \quad (7.11)$$

for which no activation energy barrier was observed in our vacuum DFT calculations. The hydrogenation of this radical will lead to the formation of $HSCH_2CH_2SH$:

$$HSCH_2CHSH + H \rightarrow HSCH_2CH_2SH. \quad (7.12)$$

Similarly, radical-radical coupling reactions between SH $+CH_2CH_2SH/CH_3CHSH$ could also form $HSCH_2CH_2SH$ efficiently.

A third possible fate for the CH_2CHSH molecule is that it is converted to its structural isomer CH_3CHS:
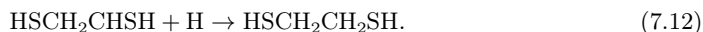
$$CH_2CHSH \leftrightarrow CH_3CHS. \quad (7.13)$$

Intramolecular isomerization (i.e., a transfer of a hydrogen atom within one molecule) is unlikely to occur at 10 K given its high energy barrier ($\Delta E_a \gtrsim 28000$ K in vacuum) (Salta et $al.$ 2021; Shingledecker et $al.$ 2022). Alternatively, transfers of hydrogen atoms in a concerted mechanism involving multiple molecules from the ice are associated with significantly lower activation energies and could arguably take place in our experiments. This process, known as "intermolecular isomerization", has been widely studied in both the gas and liquid phases for the oxygen-bearing counterparts CH_2CHOH and CH_3CHO Klopman & Andreozzi (1979); Capon & Zucco (1982); Lledos et $al.$ (1986); da Silva (2010), and is shown to be catalyzed by surrounding H_2O molecules Capon & Zucco (1982); Lledos et $al.$ (1986). This same mechanism has been proposed previously to explain the large abundances of CH_2CHOH and CH_3CHO in similar ice experiments involving C_2H_2 and OH radicals (Chuang et $al.$ 2020). However, Perrero et $al.$ (2022) found this mechanism to be hampered by high activation energy barriers ($\gtrsim 7000$ K) in pathways starting from both CH_2CHOH and its radical precursor CH_2CHO. Interestingly, theoretical calculations by Suenobu et $al.$ (1999) predict a faster conversion of CH_2CHSH into CH_3CHS mediated by H_2O molecules in the liquid phase compared to the oxygen-bearing counterparts. They argue that this is due to the larger electric dipole moment of the transition state in the sulfur-bearing case, causing it to be more stabilized by aqueous environments. We therefore speculate that such a mechanism could also proceed in the solid state under our experimental conditions facilitated by H_2S molecules in the vicinity of CH_2CHSH, although further theoretical work is warranted to accurately constrain this possibility.

We emphasize that CH_3CHS is tentatively detected in this work and contains relatively low abundances. Thus, its suggested formation by the intermolecular isomerization mechanism is probably not very efficient. Nonetheless, assuming that it can be formed, further hydrogenation will lead to CH_3CH_2SH via:

$$CH_3CHS + H \rightarrow CH_3CHSH \quad (7.14a)$$

$$CH_3CHS + H \rightarrow CH_3CH_2S \quad (7.14b)$$

$$CH_3CH_2S + H \rightarrow CH_3CH_2SH. \tag{7.15}$$
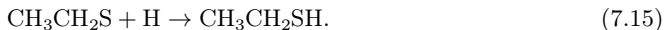
Reaction 7.14a proceeds barrierlessly, whereas Reaction 7.14b has a very small $\Delta E_a \sim 397$ K (Shingledecker *et al.* 2022). Both CH_3CHSH and CH_3CH_2S will be hydrogenated without an activation energy through Reactions 7.10a and 7.15 to form CH_3CH_2SH. Finally, CH_3CHS can potentially undergo two hydrogen-abstraction reactions to form CH_2CS, another tentative product of this work. This alluded abstraction route warrants dedicated experimental and theoretical investigations to be confirmed, as only a tentative detections of both reactants and products are provided here.

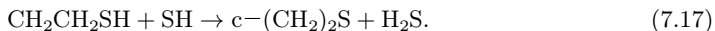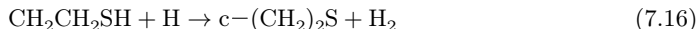Abstraction reactions from the radicals CH_2CH_2SH and CH_3CHSH are also possible a priori, and are explored computationally here. Our DFT calculations predict that CH_2CH_2SH can undergo abstraction routes induced by both H atoms and SH to form thiirane ($c-(CH_2)_2S$):

$$CH_2CH_2SH + H \rightarrow c-(CH_2)_2S + H_2 \tag{7.16}$$

$$CH_2CH_2SH + SH \rightarrow c-(CH_2)_2S + H_2S. \tag{7.17}$$

Likewise, CH_3CHSH can also form thiirane by reacting with H:

$$CH_3CHSH + H \rightarrow c-(CH_2)_2S + H_2 \tag{7.18}$$
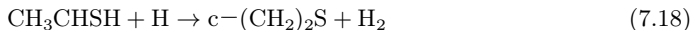
This structure, however, is excluded as a major product in our experiment on the basis of its mass fragmentation pattern (see section 7.3.3). The reason behind this discrepancy between theory and experiment may be related to the former being performed in vacuum, when interactions with other species in the ice could potentially hinder the formation of $c-(CH_2)_2S$.

Most of the hydrogenation steps in this network ultimately lead to the formation of CH_3CH_2SH. This molecule could in principle be further processed by reactions with H atoms to form the radicals CH_3CH_2S, CH_3CH_2, CH_3CHSH, or CH_2CH_2SH Zhang *et al.* (2006). The theoretical calculations by Zhang *et al.* (2006) predict that the hydrogen abstraction channel from the SH group ($CH_3CH_2SH + H \rightarrow CH_3CH_2S + H_2$) is the dominant route in vacuum ($\Delta E_a \sim 1610$ K), but that the C-S bond breaking channel ($CH_3CH_2SH + H \rightarrow CH_3CH_2 + H_2S$) is also likely to proceed ($\Delta E_a \sim 1761$ K). The contribution from these channels might vary when surfaces are considered (as was shown by Nguyen *et al.* (2023) within their work and in comparison to Lamberts (2018) for the analogue reactions involving CH_3SH). We do not find any evidence (such as a peak in mass signal) for the presence of $CH_3CH_2SSCH_2CH_3$ (diethyl-disulfide, DEDS) in our experiments—the presumed product of the recombination of two CH_3CH_2S radicals. This is rather unsurprising, since the addition routes to CH_3CH_2SH proceed effectively barrierlessly and multiple reaction steps, as well as close proximity of reactants, would be needed to form DEDS. Overall, the chemical network probed here converges into forming mostly CH_3CH_2SH as long as enough H is available. This conclusion can assist in explaining astronomical observations of S-bearing COMs with two carbon atoms (or lack thereof), as will be discussed in the following Section.

7.4   Astrophysical implications

Within interstellar clouds, low activation barriers are generally required for a chemical reaction to occur, as thermal hopping is not possible for most molecular radicals at the typical temperatures of those environments ($10 - 20$ K). The high reactivity associated with open shell species thus makes radicals important drivers of chemical complexity in such astronomical environments. This is particularly relevant for solid-state reactions facilitated by interstellar dust grains. In the case of sulfur, the SH radical can serve as an important pivot towards building a complex sulfur-bearing inventory, especially because it is expected to be

continuously formed in interstellar ices throughout a wide evolutionary span. During the earlier cloud stages, it can be readily produced by the hydrogenation of sulfur atoms accreted onto interstellar dust grains. As the density of the environment increases, most of the atomic sulfur is expected to be readily converted into H_2S. Abstraction reactions involving H atoms and H_2S can then efficiently reform SH, thus partially replenishing the supply of this radical in the ice.

The deuterium fractionation of H_2S observed in Class 0 sources points to an early formation in ices, before the CO catastrophic freeze-out stage Ceccarelli *et al.* (2014). Similarly, C_2H_2 is expected to be more abundantly present in earlier cloud stages, where atomic carbon is available to produce C_2H_2 via the bottom-up route, and before C_2H_2 is largely hydrogenated to form C_2H_4 and C_2H_6. Reactions involving the two species and the ubiquitous hydrogen atoms are therefore feasible given that they coexist in the same ice environment. As illustrated in Figure 7.8, these interactions can enrich interstellar ices with complex organic sulfur-bearing molecules. Furthermore, C_2H radicals could act as an additional source of carbon within our network upon adsorption onto ice grains. It should be noted, however, that the scheme proposed here could be further complicated in fully representative interstellar ices due to the presence of other species, in particular water.
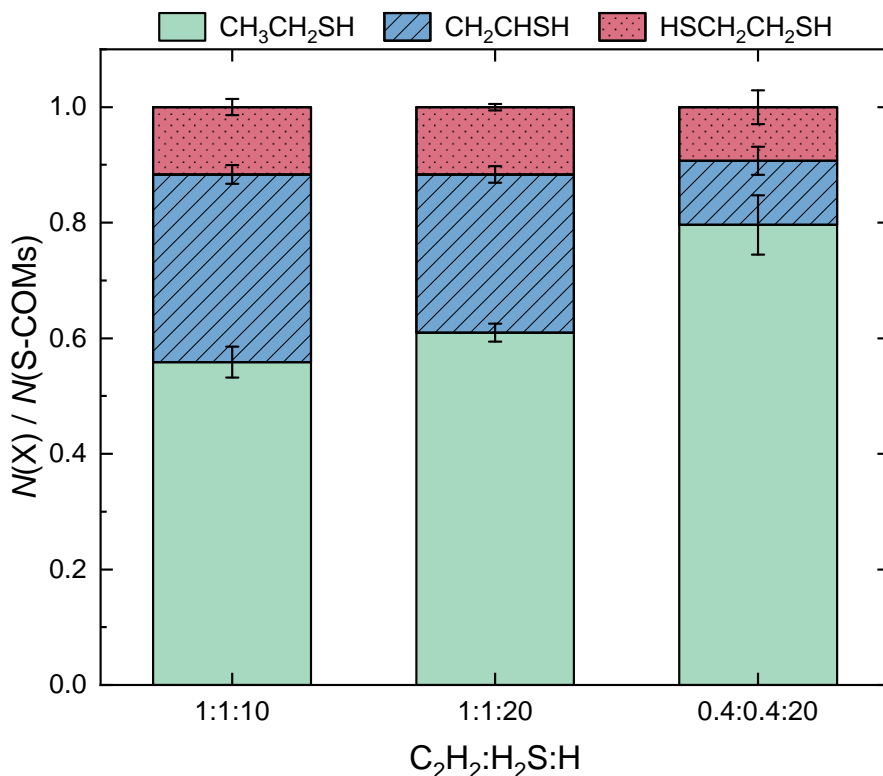
Figure 7.9: Relative abundances of the sulfur-bearing COMs formed during deposition as a function of the C_2H_2:H_2S:H ratio. The abundances are shown with respect to the total yield of sulfurated COMs positively identified at the end of each experiment.

For the three main organic products, CH_3CH_2SH, CH_2CHSH, and $HSCH_2CH_2SH$, the dependence of the product yield with the molecule-to-hydrogen ratio is shown in Figure 7.9. The products' relative column densities are derived from the mass signals of their molecular

ions using Equation 7.4 and the parameters in Table 7.1. Thioacetaldehyde and thioketene (CH_3CHS and CH_2CS, respectively) are not included in this analysis since they are tentative detections and minor products. For all explored deposition conditions, the most abundant S-bearing organic molecule resulting from the interaction of C_2H_2 with H_2S and H atoms is CH_3CH_2SH. The predominance of this species is in line with the conclusions drawn by Shingledecker *et al.* (2022) from their calculations and the computational results from this work. Once C_2H_2 is hydrogenated to form C_2H_3, it can react barrierlessly with SH radicals to form CH_2CHSH, which can subsequently be barrierlessly hydrogenated to form CH_3CH_2SH. The production of CH_3CH_2SH can therefore proceed very efficiently as long as there are H atoms in the vicinity available to react, and hence is increasingly favored for higher H-to-molecule ratios. Thus, our experiments show that CH_3CH_2SH acts as a sink in the chemical network explored here, meaning that the sulfur budget in this network will be mostly locked away into ethanethiol at the expense of the other products—in agreement with the theoretical predictions Shingledecker *et al.* (2022). These conclusions remain valid irrespective of the formation route behind CH_2CHSH, and thus are not exclusively dependent on the network being initiated by the interaction between C_2H_3 and SH. Indeed, as suggested by Shingledecker *et al.* (2022), the absence of CH_2CHSH in interstellar sources despite dedicated attempts to identify it towards Sgr B2(N2) Martin-Drumel *et al.* (2019), alongside the detections of CH_3CH_2SH towards both Orion KL and the G+0.693-0.027 molecular cloud Kolesniková *et al.* (2014); Rodríguez-Almeida *et al.* (2021b), might be related to the effective chemical conversion of the former to the latter.

Thioketene (CH_2CS) was also detected in interstellar environments, towards the cold core TMC-1 Cernicharo *et al.* (2021). The reaction routes proposed in this work could in principle contribute to forming it in the solid phase, albeit to a small extent. Nonetheless, its astronomical detection reinforces the relevance of investigating chemical networks that lead to sulfur-bearing organics with two carbon atoms.

7.5   Conclusions

In the present work, we explore the solid-state chemistry resulting from the interaction of C_2H_2, H_2S, and H atoms in interstellar ices at 10 K by means of laboratory experiments combined with theoretical calculations. The investigated chemical network is summarized in Figure 7.8, and our main findings are listed below:

- The codeposition of C_2H_2, H_2S, and H leads to the formation of several sulfur-bearing species at 10 K via radical-induced reactions involving SH. We securely identify the products CH_3CH_2SH, CH_2CHSH, $HSCH_2CH_2SH$, H_2S_2, and tentatively CH_3CHS and CH_2CS, by using infrared spectroscopy and mass spectrometry.

- Calculations at the M062X/def2-TZVP level of theory bechmarked with CCSD(T)-F12/AUG-CC-PVTZ predict an activation barrier of $\sim$758 K for the radical-molecule reaction $C_2H_2 + SH \rightarrow C_2H_2SH$, which is deterrent under molecular clouds conditions. Thus, the chemical network is likely initiated by the interaction between C_2H_3 and SH radicals.

- The product CH_2CHSH plays an important role as an intermediate as it can be hydrogenated to form CH_3CH_2SH or potentially converted to its isomer CH_3CHS. Given enough H-atom availability, it will be largely consumed to produce more stable species.

- For all explored deposition conditions, the main product formed is CH_3CH_2SH, with percentage yield with respect to the sum of S-bearing COMs ranging from $\sim$56% to $\sim$80%. The yield of CH_3CH_2SH increases with the H fraction due to its efficient formation through a series of barrierless hydrogenation reactions. It therefore acts as a sulfur sink in the present chemical network, being preferably formed at the expense of the other products.

Astronomical detections of CH_3CH_2SH and CH_2CS in the submillimiter range evince the importance of exploring the formation mechanisms of sulfur-bearing organic molecules with two carbon atoms under interstellar cloud conditions. In this work we experimentally investigate solid-phase formation routes that enrich the ice with the aforementioned products, in particular during the early cloud stages. Nonetheless, further laboratory, observational, and modelling works are warranted to better constrain the ice abundances of C_2H_2 and H_2S and the yield of products in more representative interstellar ices.

7.6   Acknowledgments

8. SO$_2$ AND OCS TOWARD HIGH-MASS PROTOSTARS: A COMPARATIVE STUDY OF ICE AND GAS

OCS and SO$_2$ are both major carriers of gaseous sulfur and are the only sulfurated molecules detected in interstellar ices to date. They are thus the ideal candidates for exploring the evolution of the volatile sulfur content throughout the different stages of star formation. We aim to investigate the chemical history of interstellar OCS and SO$_2$ by deriving a statistically significant sample of gas-phase column densities toward massive protostars and comparing them to observations of gas and ices toward other sources, from dark clouds to comets. We analyzed a subset of 26 line-rich massive protostars observed by ALMA in Band 6 as part of the High Mass Protocluster Formation in the Galaxy (ALMAGAL) survey. Column densities were derived for OCS and SO$_2$ from their rare isotopologs O^{13}CS and ^{34}SO$_2$ toward the compact gas around the hot cores. We compared the abundance ratios of gaseous OCS, SO$_2$, and CH$_3$OH with ice detections toward both high- and low-mass sources as well as dark clouds and comets. We find that gas-phase column density ratios of OCS and SO$_2$ with respect to methanol remain fairly constant as a function of luminosity between low- and high-mass sources, despite their very different physical conditions. In our dataset, OCS and SO$_2$ are weakly correlated. The derived gaseous OCS and SO$_2$ abundances relative to CH$_3$OH are overall similar to protostellar ice values, with a significantly larger scatter for SO$_2$ than for OCS. Cometary and dark-cloud ice values agree well with protostellar gas-phase ratios for OCS, whereas higher abundances of SO$_2$ are generally seen in comets compared to the other sources. Gaseous SO$_2$/OCS ratios are consistent with ices toward dark clouds, protostars, and comets, albeit with some scatter. The constant gas-phase column density ratios throughout low- and high-mass sources indicate an early-stage formation before intense environmental differentiation begins. Icy protostellar values are similar to the gas-phase medians and are compatible with an icy origin for these species followed by thermal sublimation. The larger spread in SO$_2$ compared to OCS ratios with respect to CH$_3$OH is likely due to a more water-rich chemical environment associated with the former, as opposed to a CO-rich origin for the latter. Post-sublimation gas-phase processing of SO$_2$ can also contribute to the large spread. Comparisons to ices in dark clouds and comets point to a significant inheritance of OCS from earlier to later evolutionary stages.

8.1   Introduction

Over 240 molecules have been detected in the interstellar medium to date, among which at least 30 contain one or more sulfur atoms (McGuire 2022). With an abundance of S/H$\sim$1.35$\times$10^{-5}, sulfur is one of the most common elements in space (Asplund *et al.* 2009). S-bearing species are observed in the gas phase throughout most stages of star and planet formation, from diffuse and dense clouds (e.g., Drdla *et al.* 1989; Navarro-Almaida *et al.* 2020; Spezzano *et al.* 2022; Esplugues *et al.* 2022) and protostars (e.g., Blake *et al.* 1987, 1994; van der Tak *et al.* 2003; Li *et al.* 2015; Drozdovskaya *et al.* 2018; Codella *et al.* 2021; Artur de la Villarmois *et al.* 2023; Fontani *et al.* 2023; Kushwahaa *et al.* 2023) to protoplanetary disks (Fuente *et al.* 2010; Phuong *et al.* 2018; Semenov *et al.* 2018; Le Gal *et al.* 2019; Rivière-Marichalar *et al.* 2021; Le Gal *et al.* 2021; Booth *et al.* 2024). They have also been detected in Solar System bodies such as comets (Smith *et al.* 1980; Bockelée-Morvan *et al.* 2000a; Biver *et al.* 2021a,b; Calmonte *et al.* 2016; Altwegg *et al.* 2022), planets (Moullet *et al.* 2013), and satellites (Hibbitts *et al.* 2000; Jessup *et al.* 2007; Moullet *et al.* 2008; Cartwright *et al.* 2020), as well as toward extragalactic sources (Henkel & Bally 1985; Petuchowski & Bennett 1992; Mauersberger *et al.* 1995; Heikkilä *et al.* 1999; Martín *et al.* 2003, 2005). Identified species range from simple diatomic molecules such as CS and SO to the complex organics methanethiol and ethanethiol (CH$_3$SH and CH$_3$CH$_2$SH; Linke *et al.* 1979; Gibb *et al.* 2000; Cernicharo *et al.* 2012; Kolesniková *et al.* 2014; Zapata *et al.* 2015; Müller *et al.* 2016; Majumdar *et al.* 2016; Rodríguez-Almeida *et al.* 2021a).

Despite this widespread detection, derived abundances in dense starless cores, protostars, and protoplanetary disks can only account for up to a few percent of the total expected cosmic value (Tieftrunk *et al.* 1994; Wakelam *et al.* 2004; Anderson *et al.* 2013; Vastel *et al.* 2018; Fuente *et al.* 2019; Le Gal *et al.* 2019; Rivière-Marichalar *et al.* 2019, 2020; Le Gal *et al.* 2021; Bouscasse *et al.* 2022; Fuente *et al.* 2023). The bulk of the sulfur content is largely thought to be locked away in or underneath the ice mantles that shroud interstellar dust grains, in a state that makes its detection challenging. Such icy mantles start to form early in the interstellar evolutionary sequence, during the so-called translucent-cloud phase. Atoms of H and O adsorb onto dust grains and react to form H$_2$O, resulting in a water-rich ice layer (Tielens & Hagen 1982; Hiraoka *et al.* 1998; Mokrane *et al.* 2009; Dulieu *et al.* 2010; Ioppolo *et al.* 2010; Cuppen *et al.* 2010; Romanzin *et al.* 2011; Öberg *et al.* 2011a). As the density of the collapsing cloud increases, carbon monoxide (CO) molecules present in the gas phase catastrophically freeze out on top of the water-rich ice, forming a second coating known as the CO-rich ice layer (Tielens *et al.* 1991; Boogert *et al.* 2002; Pontoppidan *et al.* 2003; Pontoppidan 2006; Öberg *et al.* 2011a). This CO ice is efficiently converted into methanol (CH$_3$OH) by reactions involving H atoms (Tielens & Hagen 1982; Charnley *et al.* 1992; Hiraoka *et al.* 1994; Watanabe & Kouchi 2002; Fuchs *et al.* 2009; Cuppen *et al.* 2009; Santos *et al.* 2022b). Complementarily, some smaller contribution to CH$_3$OH formation from ice chemistry in less dense environments, before the catastrophic CO freeze-out, is also often invoked (e.g., Wada *et al.* 2006; Hodyss *et al.* 2009; Öberg *et al.* 2010b; Bergner *et al.* 2017; Lamberts *et al.* 2017; Qasim *et al.* 2018), although it is likely not dominant.

Eventually, the environment close to the emerging young stellar object is warmed up to temperatures of 100$-$300 K, resulting in the complete thermal sublimation of the ices. This chemically rich region surrounding the protostar is known as the hot core for massive sources or the hot corino for low-mass counterparts (e.g., Herbst & van Dishoeck 2009), and is thought to be representative of the bulk ice content. For simplicity, we henceforth utilize "hot core" as an umbrella term for both high- and low-mass sources. By studying the compact emission originated from the hot core in comparison to ice observations, it is possible to gain insight into the formation and destruction mechanisms of molecules in both the gas and solid phases.

Compared to gaseous species, the unambiguous detection of solid-state molecules embed-

ded in interstellar ices poses significantly more challenges. Spectral features of species in the solid phase are intrinsically broad and highly degenerate, with properties such as peak position and width that vary considerably with the ice environment. Likely as a consequence of such inherent limitations, only two sulfur-bearing species have been identified in ices so far: carbonyl sulfide (OCS) and sulfur dioxide (SO_2). The former was first detected by Palumbo *et al.* (1995) toward the massive protostar W33A. Soon after, Boogert *et al.* (1997) suggested the presence of the latter toward both W33A and NGC 7538:IRS1—another massive young stellar object (MYSO). Since then, both species have been either inferred or detected in ices toward other protostars as well as dark clouds (Palumbo *et al.* 1997; Öberg *et al.* 2008; Zasowski *et al.* 2009; Yang *et al.* 2022; Boogert *et al.* 2022; McClure *et al.* 2023; Rocha *et al.* 2024). Recently, the presence of SO_2 ice was confirmed by *James Webb* Space Telescope (JWST) observations toward the solar-type protostar IRAS 2A by constraining the contribution of blended species, in particular OCN^-, to its 7.6 μm region (Rocha *et al.* 2024).

In the gas phase, both species are commonly detected. Gaseous SO_2 is observed toward protostellar systems both through its pure rotational transitions occurring at submillimeter wavelengths and through its rovibrational lines probed by the mid-infrared (Keane *et al.* 2001; Dungee *et al.* 2018; Nickerson *et al.* 2023; van Gelder *et al.* 2024). It is a good tracer of outflows, jets, and accretion shocks due to its enhanced gas-phase formation at high temperatures ($T \gtrsim 100$ K) combined with either sputtering or thermal sublimation of SO_2 or its precursors from icy dust grains (Pineau des Forêts *et al.* 1993; Sakai *et al.* 2014; Oya *et al.* 2019; Taquet *et al.* 2020; Tychoniec *et al.* 2021; van Gelder *et al.* 2021). It has also been shown to trace disk winds (Tabone *et al.* 2017). While this is the case for the main isotopolog (i.e., $^{32}SO_2$), the emission of minor isotopologs such as $^{34}SO_2$ is expected to be mostly compact, tracing the hot core region. Moreover, in contrast to SO_2, gaseous OCS emission is not expected to have significant contributions from outflows (van der Tak *et al.* 2003; Drozdovskaya *et al.* 2018), tracing predominately the envelope surrounding protostars (e.g., Herpin *et al.* 2009; Oya *et al.* 2016). As the only two sulfurated molecules detected in both gas and ices, SO_2 and OCS are the ideal targets for performing a comparative study between these two physical states.

In this work we explored the origin and fate of two of the most abundant sulfur species, OCS and SO_2, by directly comparing their solid and gaseous components during the evolution of star-forming regions. We utilized data from the ALMA Evolutionary study of High Mass Protocluster Formation in the Galaxy (ALMAGAL) survey and selected a subsample of 26 line-rich sources to perform the analysis. This is the first interferometric study on a statistically significant sample of detections for these two molecules in the gas phase. The molecular column densities were derived from the rare isotopologs $O^{13}CS$ and $^{34}SO_2$ to avoid contamination from extended emission and to limit line optical depth effects. We thus focused on the hot core region, which contains the molecular reservoir from the ices after complete thermal sublimation. We compared their ratios to other observations in the solid and gas phases taken from the literature. This includes recent work that utilized ground-based infrared observatories to investigate OCS ice abundances (among other species) in a large sample of MYSOs (Boogert *et al.* 2022), as well as space observations by JWST of both OCS and SO_2 ices toward sources ranging from background stars to protostars (McClure *et al.* 2023; Rocha *et al.* 2024). This work sets the stage for future studies of gas and ice enabled by the combination of data from the Atacama Large Millimeter/submillimeter Array (ALMA) and JWST on both low- and high-mass protostars, paving the way to a more thorough understanding of the sulfur chemical evolution of the interstellar medium.

In Sect. 8.2 we describe the observational parameters and details of the dataset, as well as the procedure for fitting a synthetic spectrum to the lines of interest. The resulting emission morphologies, kinematics, and column densities are presented in Sect. 8.3. The column density ratios with respect to methanol and in comparison to other observations are discussed in Sect. 8.4. Finally, our main findings and conclusions are summarized in Sect. 8.5.

8.2   Observations and methods

8.2.1   The observations

The ALMAGAL survey (2019.1.00195.L; PIs: P. Schilke, S. Molinari, C. Battersby, P. Ho) was observed by ALMA in Band 6 ($\sim$1 mm). It targeted over 1000 dense clumps across the Galaxy with $M > 500$ M$_\odot$ and $d < 7.5$ kpc, chosen based on the Herschel infrared Galactic Plane Survey (Hi-GAL; Molinari *et al.* 2010; Elia *et al.* 2017, 2021). ALMAGAL covers a statistically significant sample of sources in all stages of star formation, with many of them consisting of MYSOs. For this work we considered only archival data made publicly available before February 2021 and with beam sizes between 0.5$''$and 1.5$''$($\sim$1000–5000 au). The Common Astronomy Software Applications[1] (CASA; McMullin *et al.* 2007) version 5.6.1. was used to pipeline calibrate and image the data. The selection of sources was based on a subset studied in both Nazari *et al.* (2022) and van Gelder *et al.* (2022a), thus culling for particularly line-rich sources for which the CH$_3$OH column densities—our benchmark for comparison—are well constrained. In van Gelder *et al.* (2022a), the selection was based on sources with high bolometric luminosities ($L_{bol} > 1000$ $L_\odot$) where complex organic molecules such as CH$_3$OH and CH$_3$CN were detected. In Nazari *et al.* (2022), the selection criterium consisted of sources that contain the CH$_3$CN 12_7–11_7 line above the $2.5-3\sigma$ level. Within the subset studied by both Nazari *et al.* (2022) and van Gelder *et al.* (2022a), we excluded sources for which the line profiles of the targeted molecules differed significantly across species, to avoid probing distinct emitting regions. An example case of an excluded source is shown in Appendix 8.7.1. The final subset consists of 26 line-rich sources, whose properties and observational parameters are listed in Appendix 8.7.2.

In this work we made use of two out of the four spectral windows in ALMAGAL, encompassing frequencies of $\sim$217.00$-$218.87 GHz and $\sim$219.07$-$220.95 GHz with a spectral resolution of $\sim$0.5 MHz ($\sim$0.7 km s^{-1}). The spectral windows cover 4 transitions of ^{34}SO$_2$, 11 transitions of ^{33}SO$_2$, and 1 transition of O^{13}CS with upper energy $E_{up} < 800$ K and Einstein $A_{ij} > 1 \times 10^{-6}$ s^{-1} (see Appendix 8.7.3). However, only the $11_{1,11}$–$10_{0,10}$ transitions of ^{34}SO$_2$ and ^{33}SO$_2$ were detected in our sources ($E_{up} = 60.1$ K and 57.9 K, respectively). For ^{34}SO$_2$, this corresponds to only one line, whereas for ^{33}SO$_2$ it encompasses 7 hyperfine components caused by the nuclear spin $I = 3/2$ of the ^{33}S atom. The remaining ^{34}SO$_2$ and ^{33}SO$_2$ lines are rather weak ($A_{ij} < 2.6 \times 10^{-5}$ s^{-1}) and for the most part highly blended, hampering their detections. O^{13}CS is detected in its $18-17$ transition ($E_{up} = 99.5$ K). No other isotopologs of OCS, including O^{12}CS, are covered in the ALMAGAL range. One line of ^{32}SO$_2$ is covered, but it is not included in this work due to its likely contamination from outflow emission and because it is probably optically thick.

The spectra utilized in this work are the same as in van Gelder *et al.* (2022a). For all sources with the CH$_3$OH $8_{0,8}$–$7_{1,6}$ line ($E_{up} = 97$ K) above the 3σ level, the spectra were extracted from the peak pixel for this line in the integrated intensity maps. This particular transition of CH$_3$OH was chosen because it is the strongest methanol line within the sample with $E_{up} > 70$ K, to avoid contamination by the outflow or extended emission that are probed by lines with lower E_{up}. The choice of extracting the spectra from the methanol peak intends to maximize the signal-to-noise ratio of both ^{34}SO$_2$ and O^{13}CS originating from the hot core region. In G023.3891p00.1851, the peak emission of the methanol isotopolog CH$_2$DOH is offset by $\sim 0.6''$ (approximately half a beam) from that of CH$_3$OH, and thus the CH$_2$DOH $17_{1,16}e_0$–$17_{0,17}e_0$ ($E_{up} = 336$ K) peak is chosen to extract the spectrum since it is a more reliable tracer of the hot core. All sources probed here show line widths of $\gtrsim 3$ km s^{-1}, well above the spectral resolution of ~ 0.7 km s^{-1}, and the spectral sensitivity corresponds to ~ 0.2 K (for a list of rms values see Appendix 8.7.2).

---

[1]https://casa.nrao.edu

8.2.2   Spectral analysis

The target molecules of this study are SO_2 and OCS, the two sulfur-bearing species detected in both gas and ices so far. We analyzed them by means of their rare isotopologs $^{34}SO_2$ and $O^{13}CS$ in order to avoid issues with optically thick lines and contamination from extended emission and outflows. The $^{33}SO_2$ emission is also analyzed as a diagnostic tool to assess whether or not $^{34}SO_2$ is indeed optically thin (Sect. 8.3.3). We utilized the CASSIS[2] spectral analysis tool (Vastel *et al.* 2015) to fit the spectrum for each source and derive each species' column density (N) and full width at half maximum (FWHM) assuming that the excitation is under local thermodynamic equilibrium. Since we only detect one line per species per source, the excitation temperature was fixed to $T_{ex} = 150$ K in the spectral fittings—a roughly averaged value for hot cores (see, e.g., van Gelder *et al.* 2020; Yang *et al.* 2021; Nazari *et al.* 2022). Fixing the T_{ex} to $60-250$ K only changes the derived column densities by up to a factor of ~ 3, and both molecules in the same direction. Furthermore, for $\gtrsim 80\%$ of the sources in this work, excitation temperatures derived from CH_3CN lines range between 120 and 170 K (Nazari *et al.* 2022), corresponding to only up to a factor of 1.6 difference in column densities for SO_2 and OCS. Thus, the assumption of a fixed $T_{ex} = 150$ K does not interfere significantly with the column density ratios—the main focus of this work. The spectroscopic properties employed in the fittings of each species are obtained from the Cologne Database for Molecular Spectroscopy (CDMS; Müller *et al.* 2001, 2005).

The $^{34}SO_2$ and $O^{13}CS$ lines analyzed in this work are mostly unblended, which allows the utilization of the grid fitting method as explained in detail previously (van Gelder *et al.* 2020; Nazari *et al.* 2021; Chen *et al.* 2023). In summary, a grid of column densities and FWHMs is tested and the best-fit model is assigned to the combination with the lowest χ^2. In this work N was varied from 1×10^{13} cm^{-2} to 1×10^{17} cm^{-2} with a step of 0.1 on a logarithmic scale, and the FWHM was varied from 3 km s^{-1} to 11 km s^{-1} with a spacing of 0.1 km s^{-1} on a linear scale. The radial velocities (V_{lsr}) are derived by eye using increments of 0.1 km s^{-1} in a similar manner as described in Nazari *et al.* (2022) and Chen *et al.* (2023), and are fixed to the best manually derived values for the grid fits. Their median offsets are of 0.35 km s^{-1} from the velocities for CH_3OH in the same sources (see Sect. 8.3.2). The 2σ errors are derived from the reduced χ^2 calculated from the comparison between the resulting model of each grid point and the observed spectrum. If the 2σ uncertainties of the column densities are smaller than 20%, we assumed a 20% uncertainty as a conservative estimate to account for systematic sources of errors. In a few instances, such as for $^{34}SO_2$ in 693050, more severe blending or deviations from a Gaussian profile are observed (see Appendix 8.7.4). Nonetheless, the integrated line emissions are still encompassed by our models well within the adopted conservative uncertainties, and thus it does not affect our analysis. In the cases of G025.6498p01.0491 for $^{34}SO_2$, and 126348 and 707948 for $O^{13}CS$, the emission is better described by two components (see Appendix 8.7.4). However, obtaining column density ratios for each velocity component separately is not possible since they are not resolved for methanol. In such cases, we performed the grid fits assuming one Gaussian and fixing the V_{lsr} to the mean between the values derived by eye for each component. This procedure yields column densities within 20% of the ones obtained by manually fitting each component separately. Thus, to ensure a systematic approach to the line analysis, we utilized the column densities derived from the grid fittings to these sources. The exact source sizes are not known, so we assumed that the source fully fills the beam (i.e., a beam dilution factor of unity). Since this work focuses on comparing column density ratios, this assumption does not interfere with the analysis as long as the lines are optically thin (van Gelder *et al.* 2020; Nazari *et al.* 2021).

Fitting $^{33}SO_2$ is more challenging. It is considerably less abundant than $^{34}SO_2$, and its only detected transitions are blended with $CH_3^{13}CN$. The fitting was thus performed by eye on top of the best models for $CH_3^{13}CN$ derived by Nazari *et al.* (2022). The V_{lsr} values of $^{33}SO_2$ were fixed to those of $^{34}SO_2$, while its column densities and FWHMs were varied in

---

[2]http://cassis.irap.omp.eu/

steps of 0.1 in log space and 0.1 in linear space, respectively. For most sources, barely or no emission was left underfit after accounting for $CH_3^{13}CN$. In such cases we assigned $^{33}SO_2$ as upper limits. However, for four sources (615590, 644284A, 693050, and G343.1261-00.0623) the $CH_3^{13}CN$ model underfit the emission significantly ($\lesssim 50\%$), in which cases we could derive approximate column densities for $^{33}SO_2$.
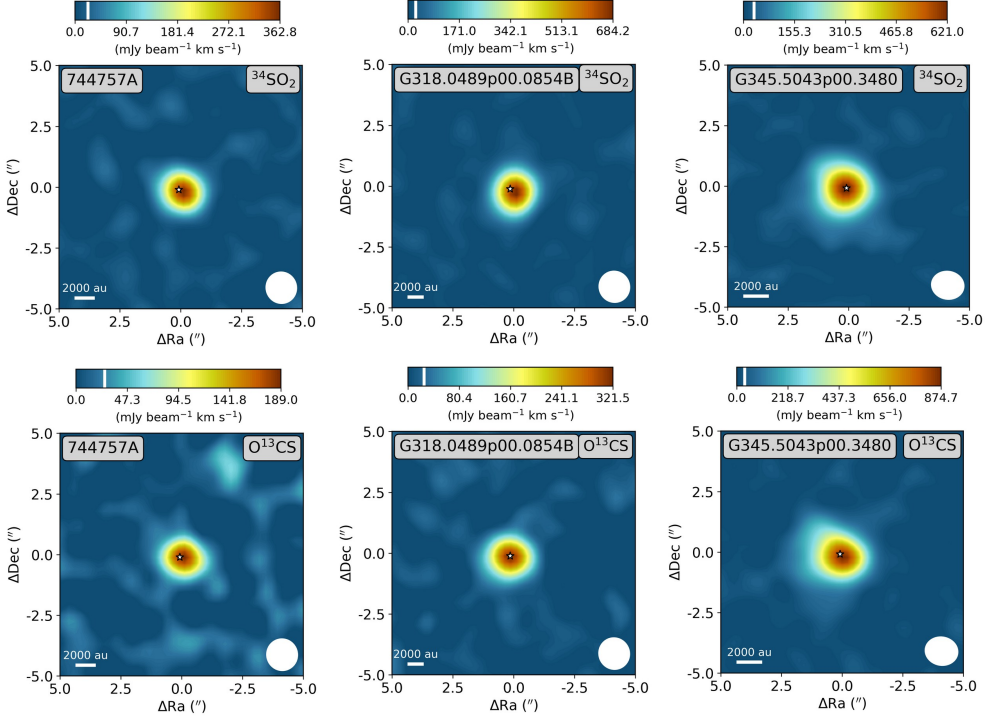
Figure 8.1: Integrated intensity maps of the $^{34}SO_2$ $11_{1,11}-10_{0,10}$ ($E_{up} = 60.1$ K, top) and $O^{13}CS$ $18-17$ ($E_{up} = 99.5$ K, bottom) lines for 744757A, G318.0489p00.0854B, and G345.5043p00.3480. The integration limits are set to [-2, 2] km s^{-1} with respect to the sources' V_{lsr}. The white star denotes the source positions derived from the peak continuum emission, and the 3σ threshold is denoted by the white line in the color bars. The beam size is shown in the lower-right corner of each panel, and a scale bar is depicted in the lower left.

8.2.3   Isotope ratio calibration

Isotopic abundances are dependent on the stellar population and therefore vary as a function of the distance to the Galactic center (D_{GC}). In order to obtain accurate column densities of the main SO_2 and OCS isotopologs, it is thus required to calibrate the isotope ratios of $(^{32}S/^{34}S)$, $(^{32}S/^{33}S)$, and $(^{12}C/^{13}C)$ accordingly. Recently, Yan *et al.* (2023) utilized CS lines in a wide variety of isotopologs observed toward 110 high-mass star-forming regions to derive the equations

$$(^{32}S/^{34}S) = (0.73 \pm 0.36)D_{GC} + (16.50 \pm 2.07), \tag{8.1}$$

$$(^{32}S/^{33}S) = (2.64 \pm 0.77)D_{GC} + (70.80 \pm 5.57), \tag{8.2}$$

$$(^{12}C/^{13}C) = (4.77 \pm 0.81)D_{GC} + (20.76 \pm 4.61). \tag{8.3}$$

The D_{GC} can be calculated based on the source's distance to Earth (d) and its coordinates. The resulting values for each source are listed in Appendix 8.7.2 and are used to derive $^{32}SO_2$ and $O^{12}CS$ from the isotopologs. For the solar neighborhood, the ratios are $(^{32}S/^{34}S)\sim22$, $(^{32}S/^{33}S)\sim92$, and $(^{12}C/^{13}C)\sim59$. The uncertainties in the final column densities of $^{32}SO_2$ and $O^{12}CS$ (henceforth simply SO_2 and OCS) are obtained by propagating the errors in the derived column densities of the minor isotopologs together with the uncertainties in Eqs. 8.1−8.3 and the typical error of ~0.5 kpc in D_{GC} (see Nazari *et al.* 2022).

8.3 Results

8.3.1 Morphology

The integrated intensity maps of $^{34}SO_2$ and $O^{13}CS$ for 744757A, G318.0489p00.0854B, and G345.5043p00.3480 are presented in Fig. 8.1. These are chosen as a representative sample of the sources analyzed in this work. The emission areas of both species are compact (with typical radii of $\sim1000-3000$ au considering all sources) and mostly unresolved, in accordance with the expectation that rare isotopologs likely trace the hot core region with little to no contribution from extended emission. The case of 693050 is an exception in which the $^{34}SO_2$ and $O^{13}CS$ peaks are offset from the continuum peak (as shown by the white star) by ~4000 au (see Appendix 8.7.5). This could be the result of optically thick dust at these wavelengths, leading to continuum over-substraction or dust attenuation toward the continuum peak, which has been shown to hide molecular emission in protostellar systems (De Simone *et al.* 2020). Indeed, the same behavior is observed for CH_3OH emission in 693050, in line with this hypothesis (van Gelder *et al.* 2022b). Higher spatial resolution is required to fully distinguish the species' emitting regions. Still, some spatial information can be acquired by comparing their best-fit parameters (see Sect. 8.3.2).

8.3.2 Fitting results

The best-fit parameters of $^{34}SO_2$ and $O^{13}CS$ for all sources are listed in Appendix 8.7.6, together with the corresponding column densities derived for SO_2 and OCS. The best-fit models are shown in Fig. 8.2 for a set of representative sources: 744757A, G318.0489p00.0854B, and G345.5043p00.3480. The models for the remaining sources are presented in Appendix 8.7.4. 3σ upper limits are provided when line intensities do not surpass this detection threshold. For most sources, the $^{34}SO_2$ column densities range between 10^{15} and 10^{16} cm^{-2}, which corresponds to SO_2 column densities of $10^{16}-10^{17}$ cm^{-2}. The only exceptions to this trend are the sources for which only $N(^{34}SO_2)$ upper limits could be derived.

In comparison, the $O^{13}CS$ column densities are roughly one order of magnitude lower, but given the larger ratios of $(^{12}C/^{13}C)$ compared to $(^{32}S/^{34}S)$, the corresponding N(OCS) values also range between 10^{16} and 10^{17} cm^{-2}. Absolute column densities are nevertheless subject to biases such as the assumed emitting area and thus are not ideal to be directly compared. Column density ratios are a more reliable form of comparison to provide information on the chemical inventories of different systems. The column densities derived in this work will be discussed in detail in Sect. 8.4.

Despite the emissions probed here being largely unresolved, line widths and velocities can be utilized to infer the kinematics of the gas. In Appendix 8.7.7, we present a comparison between the widths and velocities for both $^{34}SO_2$ and $O^{13}CS$ with respect to $CH_3^{18}OH$. The latter were obtained from the fittings performed by van Gelder *et al.* (2022a). For some sources, van Gelder *et al.* (2022a) did not detect $CH_3^{18}OH$, in which cases we compared them to the fitting parameters of the main CH_3OH isotopolog (signaled by empty markers). The median offsets of the line widths and peak velocities between the three different species are,
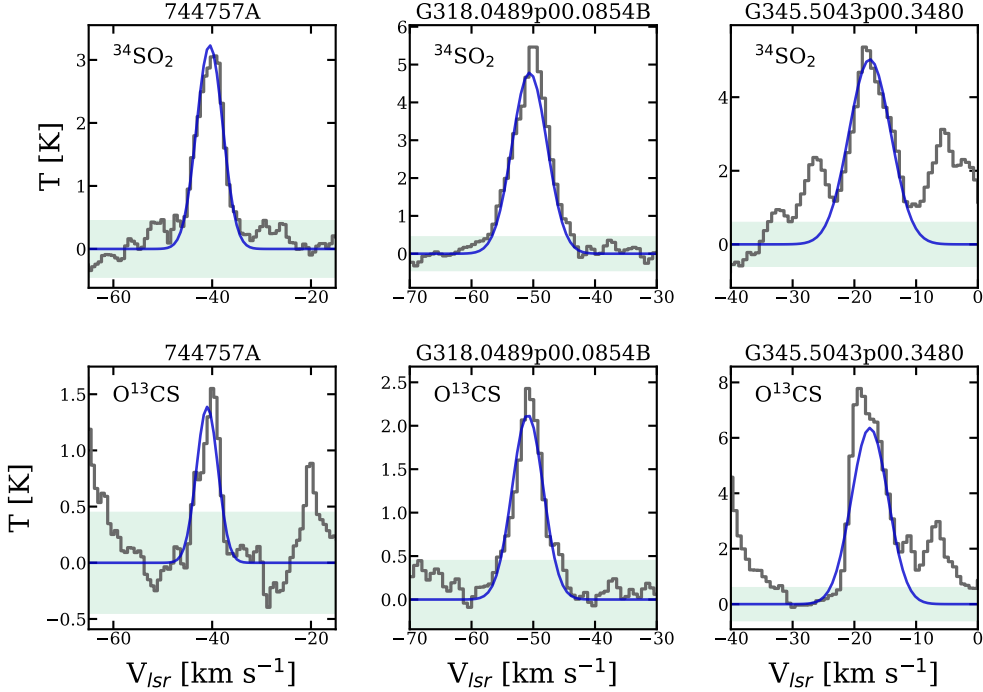
Figure 8.2: Observed spectra toward 744757A, G318.0489p00.0854B, and G345.5043p00.3480 (gray) superimposed by their best-fit models (blue). The upper panels show the lines of $^{34}SO_2$ ($11_{1,11}-10_{0,10}$), and the lower panels lines of $O^{13}CS$ ($18-17$). The green shadowed area delimits the 3σ threshold.

respectively, 0.15 and 0.35 km s^{-1}. This is in line with all three molecules tracing a similar compact gas within the hot core region and serves as validation for a comparative analysis of their column density ratios. The fact that no distinctively large discrepancy in FWHM and V_{lsr} is observed for $^{34}SO_2$ is an indication that any contribution from outflows to this line can be neglected.

8.3.3 Is $^{34}SO_2$ optically thin?

Line emissions from rare isotopologs are usually assumed to be optically thin. However, this is not necessarily always true, especially for abundant species such as SO_2. For this reason, we utilized the four sources in which $^{33}SO_2$ is detected to assess whether $^{34}SO_2$ is indeed optically thin. Their best-fit parameters are listed in Appendix 8.7.8. We derived the column densities of SO_2 (i.e., of the main isotopolog) from both $N(^{34}SO_2)$ and $N(^{33}SO_2)$ separately, using their isotope ratios as described in Sect. 8.2.3. Figure 8.3 shows the ratios of SO_2 column densities derived from $^{34}SO_2$ over the $^{33}SO_2$ counterparts for the four sources. The resulting values are all remarkably close to unity, confirming that both the $^{34}SO_2$ and $^{33}SO_2$ lines are indeed optically thin. In fact, the larger the $N(SO_2)/N(CH_3CN)$ ratios (indicated by the red arrow), the closer the values are to unity. Given that the $^{33}SO_2$ lines had to be fitted on top of $CH_3^{13}CN$ (see the discussion in Sect. 8.2.2), this strongly suggests that the small discrepancies in SO_2 column densities calculated from $N(^{33}SO_2)$ and $N(^{34}SO_2)$ are mostly due to $^{33}SO_2$ being heavily blended.
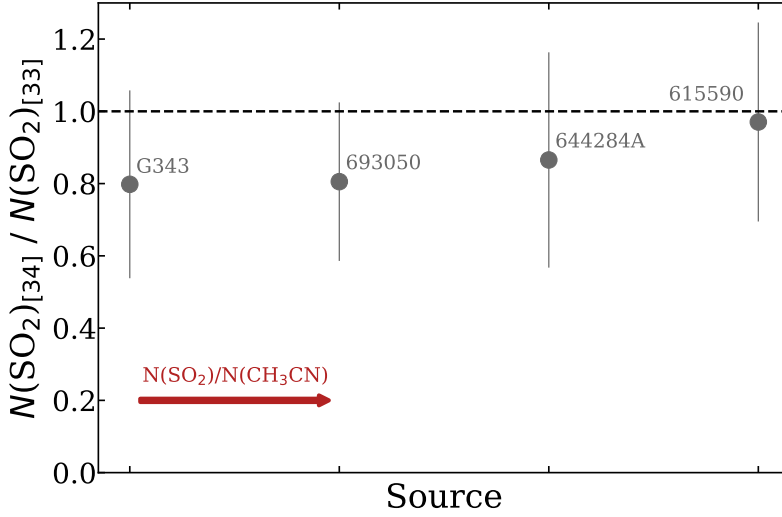
Figure 8.3: Ratios of $N(^{32}SO_2)$ derived from $N(^{34}SO_2)$ (numerator) over those derived from $N(^{33}SO_2)$ (denominator). The red arrow indicates that the sources are sorted in order of increasing $N(SO_2)/N(CH_3CN)$ relative abundances. The dashed line highlights the unity mark. G343 stands for source G343.1261-00.0623.

8.4 Discussion

As mentioned in Sect. 8.3.2, column density ratios are a good metric to compare the chemical content of different sources and types of environments. Here we utilized the CH_3OH column densities derived by van Gelder *et al.* (2022a) from minor isotopologs as a basis for comparison. Given the ice origin of methanol, it is possible to deduct information on the chemical history of OCS and SO_2 from their relative abundances with respect to CH_3OH. In the following subsections, we compare $N(OCS)/N(CH_3OH)$ and $N(SO_2)/N(CH_3OH)$ derived in this work with relative abundances taken from the literature. These encompass gas-phase observations toward both MYSOs and low-mass young stellar objects (LYSOs), ice observations toward protostars and dark clouds, as well as cometary ratios. A complete list of references from which these ratios are taken can be found in Appendix 8.7.9.

8.4.1 $N(OCS)/N(CH_3OH)$

Figure 8.4 shows a comparison of the column density ratios of $N(OCS)/N(CH_3OH)$ for various objects. It includes gas-phase observations in low- and high-mass sources as well as ice observations in MYSOs, in dark clouds, and in comets (see Appendix 8.7.9 for a list of references). The ratios derived in this work are shown in blue. In general, no trend in ratio versus luminosity is observed. Indeed, the data points for protostars (including both ice and gas phases) result in a Pearson correlation coefficient (r) of only -0.11. Spearman correlation tests are also performed and yield similar results to Pearson's for all cases explored in this work. Figure 8.4 also contain single-dish observations, but since these probe a much larger scale compared to interferometric counterparts, they are not included in the analysis. Furthermore, Kushwahaa *et al.* (2023) note that their observations could be subject to beam dilution, which could affect the gas-phase ratios for most of the low-mass sources shown in Fig. 8.4 (with the exception of IRAS 16293-2422 B). Nonetheless, they can still provide information on general trends in abundances. The fairly constant abundance ratios observed
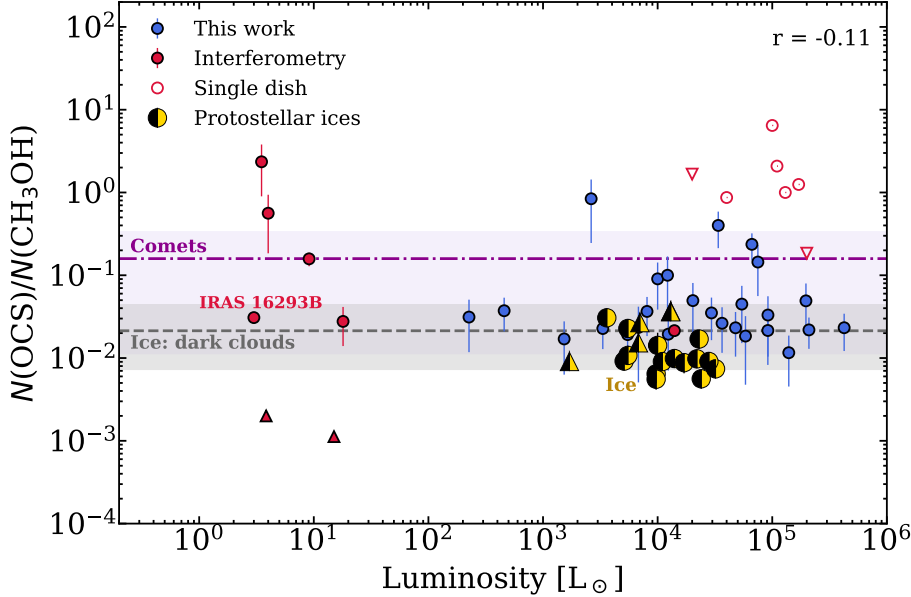
Figure 8.4: Column density ratios $N(\mathrm{OCS})/N(\mathrm{CH_3OH})$ derived in this work (blue markers) for 26 high-mass protostars as a function of luminosity. Literature gas-phase values are shown for comparison (red markers), together with ice values in protostars (yellow and black markers), dark clouds (gray dashed line), and comets (purple dash-dot line). The references can be found in Appendix 8.7.9. Upper and lower limits towards protostars are denoted by downward- and upward-facing triangles, respectively. The range of values for dark clouds and comets are shown by their respective shadowed areas. For gas-phase ratios, filled markers correspond to interferometric observations, whereas empty markers denote single dish counterparts. The Pearson correlation coefficient for protostellar ratios in both gas and ices, but excluding single-dish observations and lower limits, is displayed in the upper right corner. IRAS 16293B stands for the source IRAS 16293-2422 B.

throughout all sources indicate that OCS must be formed under similar conditions irrespective of the mass (or luminosity) of the protostar. Considering the drastically different physical conditions experienced by MYSOs and LYSOs during their evolution, particularly regarding their temperatures and UV fields, this lack of correlation with respect to luminosity points to an early formation of the bulk of OCS under cold and dense conditions, prior to the onset of star formation. More data points for low-mass sources would be useful to further constrain any potential trend obscured by the scatter in the ratios.

A considerable number of data points are available for $N(\mathrm{OCS})/N(\mathrm{CH_3OH})$ ratios in protostellar ices (Boogert *et al.* 2022), which enables a statistically significant analysis. Using abundance distribution histograms is an instructive approach to comparing different, large datasets (see, e.g., Öberg *et al.* 2011a). In Fig. 8.5, the log-transformed $N(\mathrm{OCS})/N(\mathrm{CH_3OH})$ ratios are presented for both ice and gas observations toward MYSOs, and are centered on the weighted median of the ALMAGAL dataset ($\sim$0.033). Ice lower limits affect the median value by $< 5\%$ and are thus not included in the analysis. Overall, the ice ratios in MYSOs are slightly lower than the gas-phase counterparts, with a difference of a factor of $\sim$3 between their weighted medians. This discrepancy is remarkably small, and could be due to the

uncertainties in the spectral analysis (especially considering the approximation of a fixed T_{ex}). Such strikingly similar ratios provide strong evidence of an icy origin for OCS.

Furthermore, both ice and gas datasets have small scatters, which suggests that the column densities of CH_3OH and OCS are subject to similar dependences. A spread factor f, defined by 10 to the power of the weighted 1σ standard deviation measured in log10 space, serves as a convenient comparison basis between distinct datasets (see, e.g., Nazari et al. 2023). Table 8.1 summarizes the weighted median gas-phase ratios and spread factors derived in this work for $N(\text{OCS})/N(\text{CH}_3\text{OH})$, $N(\text{SO}_2)/N(\text{CH}_3\text{OH})$, and $N(\text{SO}_2)/N(\text{OCS})$. For the ALMAGAL subset, the $N(\text{OCS})/N(\text{CH}_3\text{OH})$ ratios results in $f = 2.8$, whereas ice observations in MYSOs have $f = 1.9$. These small scatters suggest similar conditions during the formation of the bulk of OCS and CH_3OH, strengthening the conclusion of an icy origin to OCS followed by thermal sublimation. It is worth noting that the lower limits in the available ice ratios are either equivalent to or higher than the corresponding weighted median, so a high abundance tail similar to the gas-phase case could be plausible.

Table 8.1: Weighted medians of the column density ratios and spread factors derived in this work for gas-phase species in massive sources (not including upper limits).

Ratio	Weighted median	Spread factor
$N(\text{OCS})/N(\text{CH}_3\text{OH})$	0.033	2.8
$N(\text{SO}_2)/N(\text{CH}_3\text{OH})$	0.044	5.8
$N(\text{SO}_2)/N(\text{OCS})$	1.103	3.7

The small scatter for OCS points to an ice environment similar to CH_3OH. This agrees with the main proposed chemical routes to form OCS, which involve the sulfurization of CO ices. Laboratory experiments show that OCS ice can be readily formed by the reactions (Ferrante et al. 2008; Jiménez-Escobar et al. 2014a; Chen et al. 2015; Nguyen et al. 2021b; Santos et al. 2024b)

$$s-CO + s-S \rightarrow s-OCS \tag{8.4}$$

$$s-CO + s-HS \rightarrow s-OCS + s-H, \tag{8.5}$$
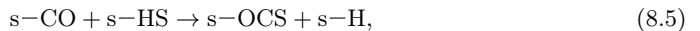
which can either be induced by thermalized S and SH adsorbed on the ice or as a result of the energetic processing of larger species (e.g., CO_2 and H_2S). Indeed, Boogert et al. (2022) analyzed a large sample of ice observations toward massive protostars and conclude that OCS and CH_3OH column densities are correlated, pointing to an OCS formation concomitant with CH_3OH during the dense pre-stellar core stage, with both sharing CO as a common precursor.

Comparisons with dark clouds prior to star formation and comets are also relevant to constrain the evolution of sulfur species in both solid and gas phases. Observed $N(\text{OCS})/N(\text{CH}_3\text{OH})$ ice ratios in dark clouds agree strikingly well with the protostellar observations toward both ice and gas. This is in full support of the hypothesis that OCS is formed in the ices within pre-stellar cores. Caution should be taken when comparing these values, however, since only two data points are available for ices in pre-stellar cores so far (McClure et al. 2023). Nonetheless, it can still provide the basis for an interesting preliminary comparison. Cometary ratios, in turn, are marginally higher (by a factor of ~ 4) than the weighted median for ALMAGAL, although their spread encompasses both gas and ice observations. This small discrepancy could be due to additional processing of OCS during the protostellar disk phase (as was also suggested by Boogert et al. 2022) or as a result of selective CH_3OH destruction before incorporation into comets. The latter has been previously suggested by Öberg et al. (2011a) as one explanation to the depletion of cometary CH_3OH, CH_4, and CO ices relative
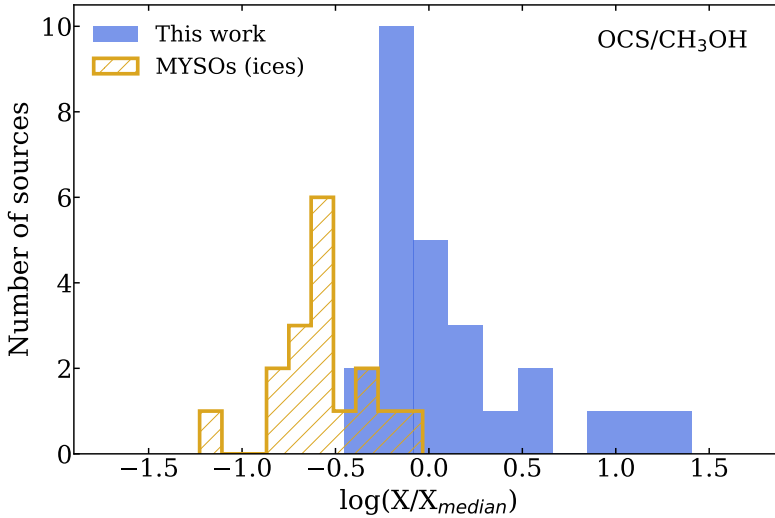
Figure 8.5: Relative abundance distributions of $N(\mathrm{OCS})/N(\mathrm{CH_3OH})$ for the gas-phase observations of massive sources analyzed in this work (blue) compared to ice observations toward 20 MYSOs by (Boogert *et al.* 2022, yellow). Both histograms are normalized to the weighted gas-phase median value derived from the ALMAGAL dataset for 26 high-mass protostars.

to H_2O compared to protostars. However, given that OCS and CH_3OH are mixed, it seems unlikely that a destruction mechanism could affect one but not the other.

8.4.2 $N(\mathrm{SO_2})/N(\mathrm{CH_3OH})$

Figure 8.6 shows a comparison of the column density ratios of $N(\mathrm{SO_2})/N(\mathrm{CH_3OH})$. Similarly to OCS, no correlation is observed for the column density ratios in protostars as a function of luminosity (Pearson $r = -0.08$), in support of the hypothesis of an early formation during the pre-stellar core stage. One caveat to this conclusion is that the gaseous SO_2 column densities in LYSOs are derived from its major isotopolog for most sources (light-red points in Fig. 8.6), which could contain appreciable contamination from outflow emission and could be optically thick. In fact, Artur de la Villarmois *et al.* (2023) estimate that $\sim$40% of the SO_2 emission in their study is extended. The only exception among low-mass sources is the data point corresponding to IRAS 16293–2422 B, for which SO_2 column densities are derived from $^{34}SO_2$ (dark-red point in Fig. 8.6). Further works focused on compact, optically thin SO_2 emission (as traced by, e.g., $^{34}SO_2$) in low-mass sources are warranted to further evaluate this hypothesis.

In contrast to OCS, ice ratios of $N(\mathrm{SO_2})/N(\mathrm{CH_3OH})$ in protostars are still scarce. However, the available values so far for both high-mass and low-mass sources taken from Boogert *et al.* (1997, 2022) and Rocha *et al.* (2024) agree fairly well with the median gas-phase ratios derived in this study. The weighted median for our subset of MYSOs (excluding upper limits) is $\sim$ 0.044, which is consistent with both ice ratios of 0.06±0.04 and 0.07±0.04 in a low- and high-mass source, respectively. This agrees with the hypothesis that SO_2 is primarily formed in ices prior to the onset of star formation, and later sublimates upon thermal heating by the protostar.

The scatter in the ALMAGAL values is considerably larger than that for OCS, which suggests that the column densities of CH_3OH and SO_2 are subject to different dependences.
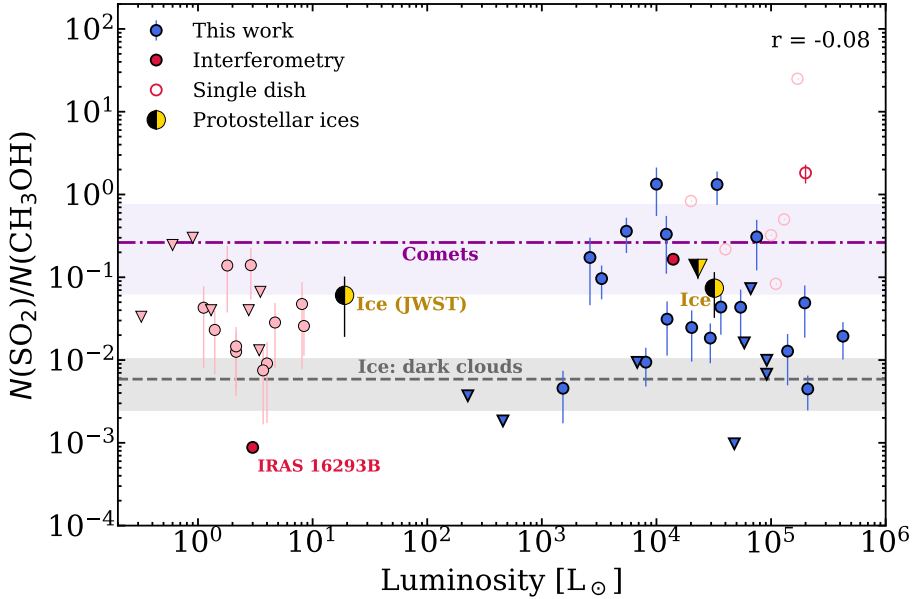
Figure 8.6: Same as Figure 8.4, but for $N(SO_2)/N(CH_3OH)$. Literature ratios with $N(SO_2)$ derived from the main isotopologue are signaled by light red markers to differentiate from values derived from $^{34}SO_2$, which are shown in darker red. The data point for the low-mass protostellar ice ratio corresponds to the JWST observations towards IRAS 2A (Rocha *et al.* 2024), and the high-mass ice ratios correspond to airborne (KAO) and ground-base (IRTF) observations towards W33A and NGC 7538 IRS 9 (upper limit) (Boogert *et al.* 1997, 2022).

For the ALMAGAL subset, $N(SO_2)/N(CH_3OH)$ ratios result in $f = 5.8$. For comparison, oxygen and nitrogen-bearing complex organic molecules typically have $N(X)/N(CH_3OH)$ spread factors of $f \lesssim 3.5$ (Nazari *et al.* 2022; Chen *et al.* 2023). There are likely two reasons behind this large scatter for SO_2: one related to both CH_3OH and SO_2 ice environments, and another related to post-desorption processing of SO_2.

Compared to methanol, the body of knowledge on interstellar SO_2 formation in cold environments is still somewhat scarce. Currently, its main proposed formation routes generally involve SO and a source of oxygen as reactants (Hartquist *et al.* 1980; Charnley 1997; Atkinson *et al.* 2004; Blitz *et al.* 2000; Woods *et al.* 2015; Vidal & Wakelam 2018; Laas & Caselli 2019):

$$SO + OH \rightarrow SO_2 + H \tag{8.6}$$

$$SO + O_2 \rightarrow SO_2 + O \tag{8.7}$$

$$SO + O \rightarrow SO_2. \tag{8.8}$$

In the gas phase, such routes are usually not viable at temperatures below 100 K (e.g., van Gelder *et al.* 2021). One exception might be Reaction 8.6, for which rate constants have been predicted to range from $\sim(2-3)\times10^{-10}$ cm^3 s^{-1} for temperatures between 10 and 100 K (Fuente *et al.* 2019). Still, observed gaseous abundances of SO_2 in both diffuse and dense

clouds are $\sim 10^{-6}$–10^{-5} with respect to CO (Turner 1995; Cernicharo *et al.* 2011, see also Table 4 in Laas & Caselli 2019), which are three to four orders of magnitude lower than ice abundances. Adsorption of SO_2 from the gas phase therefore cannot account for the ice observations. Rather, solid-phase routes to SO_2 must be considered, for which Reactions 8.6–8.8 are also good candidates (Smardzewski 1978; Moore *et al.* 2007; Ferrante *et al.* 2008; Chen *et al.* 2015; Vidal *et al.* 2017).

Like SO_2, gas-phase abundances of SO with respect to CO are still orders of magnitude smaller than those of SO_2 in the ices (Turner 1995; Lique *et al.* 2006; Neufeld *et al.* 2015). Thus, even if all SO adsorbed from the gas phase would be converted to SO_2, it would still be insufficient to explain SO_2 abundances. Alternatively, S atoms adsorbed on the ices could react with O or OH to form SO through

$$s-S + s-O \rightarrow s-SO, \tag{8.9}$$

$$s-S + s-OH \rightarrow s-SO + s-H, \tag{8.10}$$
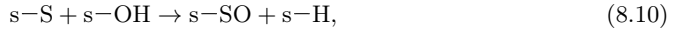
which in turn can lead to SO_2 ice via Reactions 8.6 − 8.8. Atomic S can also directly form SO_2 ice by reacting with O_2:

$$s-S + s-O_2 \rightarrow s-SO_2. \tag{8.11}$$

In addition to the atomic form, interactions of HS radicals with O can efficiently produce SO ice:

$$s-HS + s-O \rightarrow s-SO + s-H. \tag{8.12}$$
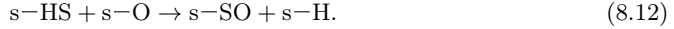
Most of these routes have been probed in the laboratory by a number of experimental works involving H_2S ices mixed with oxygen-bearing molecules (e.g., CO_2 or H_2O) and exposed to energetic processing (such as UV photons or protons) to generate the open-shell species (Smardzewski 1978; Moore *et al.* 2007; Ferrante *et al.* 2008; Chen *et al.* 2015). Indeed, HS radicals are thought to be formed in ices via both the hydrogenation of adsorbed S atoms and the destruction of H_2S molecules. The latter can occur either through energetic processing, as mentioned above, or due to H-induced abstraction reactions (Oba *et al.* 2018, 2019; Santos *et al.* 2023b). Furthermore, Laas & Caselli (2019) assert that Reactions 8.7 and 8.8 are hindered in ices due to the high diffusion and binding energies of the reactants. Radical and atom formation through energetic processing could partially circumvent this issue.

Irrespective of the mechanism to originate SO_2, all routes require an oxygen-rich environment to take place. Such an environment is more likely to occur in the earlier phases of the pre-stellar stage, during which H_2O ices grow from the hydrogenation of O, O_2, and O_3 (e.g., Tielens & Hagen 1982; Miyauchi *et al.* 2008; Ioppolo *et al.* 2008; Lamberts *et al.* 2016). Therefore, SO_2 should be formed simultaneously with H_2O during the low-density stage of pre-stellar cores. In contrast, CH_3OH is mainly formed at a much later stage, when densities are high enough for CO to catastrophically freeze-out onto the grains ($A_v > 9$, $n_H \gtrsim 10^5$ cm^{-3}). This discrepancy in the formation timeline of the two species means that they will be subject to different physical conditions and collapse timescales, which may explain the large scatter in the observed ratios. While it is true that ice observations of SO_2 have so far been best described by laboratory measurements of SO_2 in a CH_3OH-rich environment (Boogert *et al.* 1997; Rocha *et al.* 2024), the SO_2 ice feature at 7.6 μm was shown to be highly sensitive to ice mixtures and temperatures (Boogert *et al.* 1997). Hence, further systematic infrared characterizations of SO_2, perhaps with a combination of tertiary ice mixtures including H_2O, would be beneficial to better constrain the chemical environment of this molecule.

A complementary explanation for the scatter in $N(SO_2)/N(CH_3OH)$ is the reprocessing of SO_2 in the gas phase. The SO_2 emission probed in this work traces the hot core region surrounding the protostar, where thermal heating has led the volatile ice content to fully sublimate. At the typically warmer temperatures of such environments ($\gtrsim$100 K), the conditions

become favorable for Reactions 8.6−8.8 to take place in the gas phase (Hartquist *et al.* 1980; van Gelder *et al.* 2021). Given the large variation of source structures and physical conditions associated with massive protostars, the degree to which such reactions occur will likely vary considerably from source to source and are thus expected to result in a wide scatter of SO_2 column densities. Indeed, the models in Vidal & Wakelam (2018) predict that the gaseous SO_2 abundances in protostars are particularly subject to large variations depending on the composition of the parent cloud and the temperature. Furthermore, van Gelder *et al.* (2021) show that gas-phase SO_2 formation is strongly linked to the local UV radiation field since the strength of the latter will largely affect the distribution of reactants. These properties are expected to vary considerably from one massive source to another.

In addition to SO_2, CH_3OH ices typically show considerable variations in column density from source to source (Öberg *et al.* 2011a), which could be contributing to the scatter seen for $N(SO_2)/N(CH_3OH)$. Nonetheless, the larger spread for $N(SO_2)$ compared to other species relative to $N(CH_3OH)$ (e.g., Nazari *et al.* 2022; Chen *et al.* 2023 and the $N(OCS)/N(CH_3OH)$ ratios in this work) points to a significant effect directly associated with SO_2. Differences in the emitting area of SO_2 and CH_3OH could also play a part in the scatter (Nazari *et al.* 2024), albeit to a lesser extent since experimental laboratory sublimation temperatures of SO_2 and CH_3OH are generally quite similar (at ∼120 K and ∼145 K, respectively; Kaňuchová *et al.* 2017; Mifsud *et al.* 2023; Carrascosa *et al.* 2023). Co-desorption with H_2O can potentially raise the sublimation temperature of SO_2, but not enough to result in an appreciable difference to CH_3OH (see, e.g., Fraser *et al.* 2001 for sublimation temperatures of H_2O). Overall, both the origin of SO_2 in ices and its fate after sublimation are likely to play a part in the large scatter seen in Fig. 8.6.

In dark clouds, the ice ratios of $N(SO_2)/N(CH_3OH)$ are generally lower than in the protostellar phase (both for ice and gas observations) by about one order of magnitude. This discrepancy could indicate some additional production of SO_2 during the protostellar phase, conceivably due to the enhanced UV radiation field produced in such environments. Cometary ratios are marginally higher, but still in a reasonably good agreement with protostellar ices, and are larger than the weighted median for gas-phase MYSOs by a factor of ∼ 6. As for the case of OCS, causes for this enhancement could be additional processing of SO_2 during the protostellar disk phase, or as a result of selective CH_3OH destruction before incorporation into comets. Given that SO_2 and CH_3OH are proposed to inhabit different ice phases, this supposition is not a priori unreasonable. In summary, the ratios shown in Fig. 8.6 support the hypothesis of a moderate, but not complete inheritance of SO_2 ices from the pre-stellar phase into comets.

8.4.3 SO_2 versus OCS

The column density ratios for SO_2/OCS as a function of luminosity agree with the conclusions drawn in the previous subsections (see Appendix 8.7.10). Figure 8.7 presents the distribution histograms of $N(SO_2)$ and $N(OCS)$ with respect to $N(CH_3OH)$ derived in this work. Each $N(X)/N(CH_3OH)$ is normalized to its own weighted median, so that both distributions are centered on 1 (i.e., 0 in log space). This figure clearly shows the distinctive behaviors of SO_2 and OCS, emphasizing that the latter is likely much more strongly linked to CH_3OH than the former. Furthermore, it suggests that the reprocessing of SO_2 upon desorption is much more drastic than for OCS, in agreement with the models in Vidal & Wakelam (2018).

Another relevant source of information is to compare the direct correlation between SO_2 and OCS abundances with respect to CH_3OH (Fig. 8.8). Based on the derived Pearson coefficient ($r = 0.32$), a weak correlation appears to exist between $N(SO_2)/N(CH_3OH)$ and $N(OCS)/N(CH_3OH)$. This is supported by the Spearman's correlation test, which yields a coefficient of $\rho = 0.38$ with a p-value of 0.05. The fact that this association is weak is unsurprising, since the bulk of SO_2 and OCS probably originate from two different ice environments, which means that their chemistry cannot be strongly linked. Nonetheless,
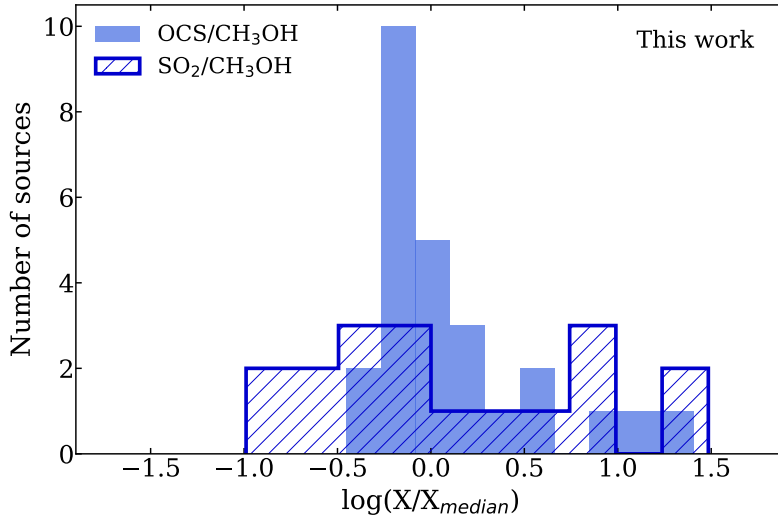
Figure 8.7: Same as Fig. 8.5, but for $N(SO_2)/N(CH_3OH)$ (hatched) and $N(OCS)/N(CH_3OH)$ (filled) gas-phase observations from the ALMAGAL dataset. In this case, each ratio is normalized to its own weighted median value.

some modest connection seems to be present between the two sulfur-bearing species. This could be due, for instance, to one species providing a source of sulfur that is converted into the other. Indeed, SO_2 ices can be dissociated into S atoms upon energetic processing, which could in turn react with CO to form OCS. Likewise, OCS molecules can also yield S atoms upon fragmentation, which in turn can react with H_2O to form SO_2 (Ferrante *et al.* 2008). Alternatively, this correlation could be the result of a common precursor to both species, such as atomic S or SH radicals. We emphasize, however, that the correlation is weak and reliant on the high-abundance end of the range of values, and thus should be considered with caution.

8.5   Conclusions

In this work we analyzed the emission of OCS and SO_2 toward 26 line-rich MYSOs observed as part of the ALMAGAL survey. We compared their abundances with respect to methanol with other gas-phase observations toward low-mass sources, as well as in interstellar ices and comets. Our main findings are as follows:

- The gaseous column density ratios of OCS/CH_3OH and SO_2/CH_3OH show no trend with respect to luminosity, pointing to an early onset formation of both sulfur-bearing molecules before star formation begins. The ratios in protostellar ices are consistent with the weighted medians of the ALMAGAL dataset, suggesting an icy origin for both OCS and SO_2 followed by thermal sublimation upon heating from the protostar.

- A large scatter in relative abundances is observed with ALMAGAL for gaseous SO_2/CH_3OH ($f = 5.8$), but not for OCS/CH_3OH ($f = 2.8$). We suggest that this is due to different chemical environments during the formation of SO_2 and OCS, with the former being formed during the low-density phase of cold clouds, and the latter's formation mostly taking place during the later, high-density pre-stellar stage. OCS and CH_3OH both originate from reactions with CO ice. Post-desorption processing likely
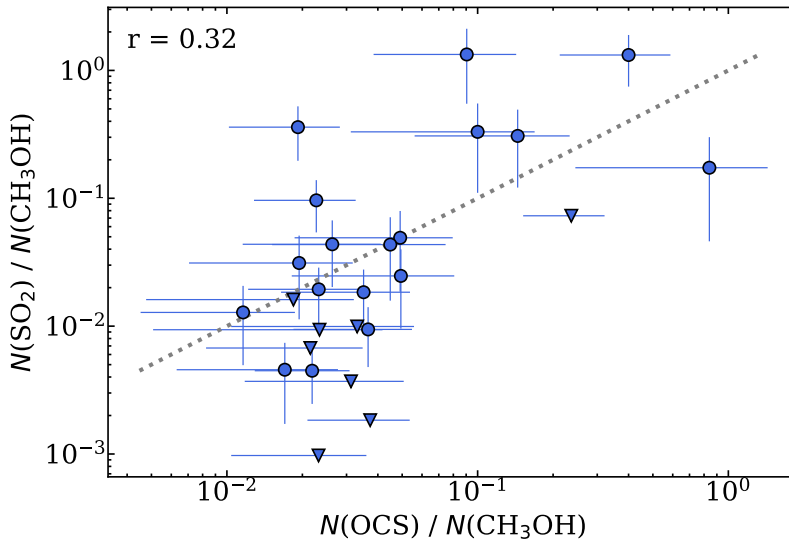
Figure 8.8: Relative abundances $N(SO_2)/N(CH_3OH)$ versus $N(OCS)/N(CH_3OH)$ for the ALMAGAL dataset analyzed in this work. Upper limits in the $N(SO_2)/N(CH_3OH)$ ratios are denoted by downward facing triangles. The Pearson correlation coefficient (excluding upper limits) is shown in the upper-left corner, and the dotted line traces the 1:1 relation.

also contributes to the spread in $N(SO_2)/N(CH_3OH)$.

- For OCS, dark cloud ice values are in remarkably good agreement with both protostellar ice and gas observations. Cometary ratios are also quite similar, at only a factor of $\sim$4 higher. Some extra formation of OCS during the protostellar disk phase has been suggested as a root for this difference, as well as selective destruction of CH_3OH. Nonetheless, all ratios point to a significant inheritance of OCS ices throughout the different stages of star formation.

- The gaseous abundances of SO_2 relative to CH_3OH derived in this work agree with both dark-cloud and cometary ice ratios. Values in comets are generally slightly higher (by a factor of $\sim$6) than in protostars, which in turn are higher than in dark clouds. This could indicate some additional formation of SO_2 during the protostellar and protoplanetary-disk phases, although selective destruction of CH_3OH could also explain such observations in the latter case.

- A weak correlation ($r = 0.32$) is found between $N(SO_2)/N(CH_3OH)$ and $N(OCS)/N(CH_3OH)$. While the bulk of these ices is likely formed in different environments on two distinct evolutionary timescales, some interconversion between SO_2 and OCS is possible and could lead to a weak association. This could also result from a common precursor of the two species, arguably S or HS.

Overall, our findings suggest that OCS and SO_2 differ significantly in both their formation and destruction pathways, but could still potentially share a common history. It should be noted that the dataset studied here is biased in favor of line-rich sources and therefore our results might not represent all massive protostars. Furthermore, it is clear that more observational constraints on interstellar ice column densities of sulfur-bearing species, and in particular of SO_2, are paramount to building a more complete understanding of the origin

and fate of sulfur. The JWST offers a unique opportunity for such constraints to be explored in depth.

8.6 Acknowledgments

8.7 Appendix

8.7.1 Example of an excluded source

Figure 8.9 contains an example of a source that was excluded from the analysis because of large divergences in the spectral properties between $^{34}SO_2$ and $O^{13}CS$, in this case potentially due to self absorption of the $^{34}SO_2$ lines.
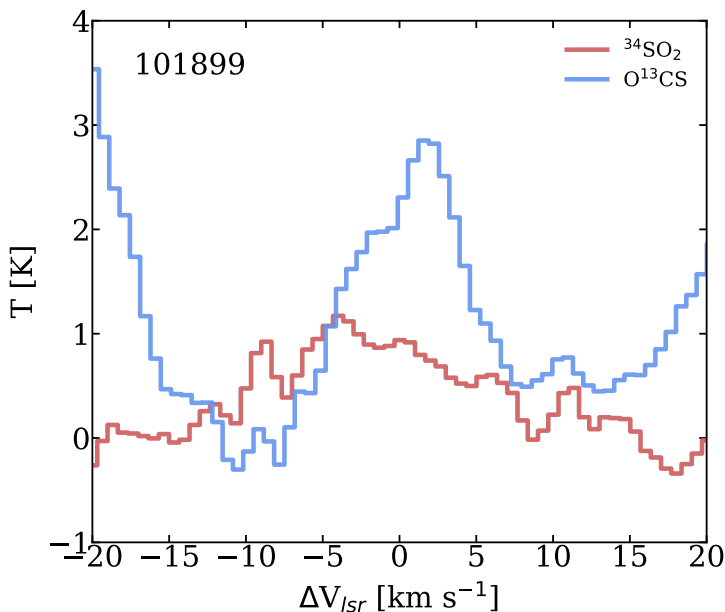
Figure 8.9: Superimposed lines of $^{34}SO_2$ (red) and $O^{13}CS$ (blue) observed toward 101899.

8.7.2 Source properties and observational parameters

The observational parameters for each source and their physical properties are listed in Table 8.2.

Table 8.2: Observational parameters and physical properties of the sources.

Source	R.A. (J2000)[a] (hh:mm:ss.s)	Dec. (J2000)[a] (dd:mm:ss.s)	Beam (″)	Line rms[b] (K)	d[c] (kpc)	D_{GC}[d] (kpc)	L_{bol}[e] ($L_\odot$)
126348	18:42:51.98	-03:59:54.37	1.26 × 1.08	0.16	4.41	4.67	6798
615590	09:24:41.96	-52:02:08.04	0.68 × 0.59	0.50	2.70	8.31	5470
644284A	10:31:29.78	-58:02:19.27	0.96 × 0.80	0.32	4.75	8.20	–
693050	12:35:35.05	-63:02:31.19	1.03 × 0.94	0.19	4.31	6.89	12200
705768	13:12:36.17	-62:33:34.43	0.93 × 0.81	0.24	6.88	6.93	91728
707948	13:16:43.19	-62:58:32.83	0.94 × 0.80	0.26	7.14	6.97	196800
717461A	13:43:01.68	-62:08:51.42	1.34 × 1.21	0.22	4.29	6.31	3323
721992	13:51:58.27	-61:15:41.04	0.90 × 0.79	0.37	5.38	6.16	2630
724566	13:59:30.92	-61:48:38.27	0.87 × 0.78	0.34	4.93	6.10	226
732038	14:13:15.05	-61:16:53.19	0.87 × 0.78	0.40	5.64	5.93	74930
744757A	14:45:26.35	-59:49:15.55	1.31 × 1.27	0.15	2.51	6.45	12381
767784	15:29:19.31	-56:31:22.02	1.31 × 1.24	0.16	4.04	5.37	139400
865468A	17:05:10.90	-41:29:06.99	1.32 × 1.14	0.22	3.04	5.17	47824
876288	17:11:51.02	-39:09:29.18	0.92 × 0.69	0.29	5.95	2.58	58410
881427C	17:20:06.12	-38:57:15.84	1.31 × 1.13	0.56	1.50	6.59	458
G023.3891p00.1851	18:33:14.32	-08:23:57.82	1.43 × 1.07	0.18	10.86	4.72	91560
G025.6498p01.0491	18:34:20.92	-05:59:42.08	1.24 × 1.07	0.15	12.20	6.05	424000
G305.2017p00.2072A1	13:11:10.45	-62:34:38.60	1.38 × 1.21	0.21	4.00	6.61	20301
G314.3197p00.1125	14:26:26.25	-60:38:31.26	1.36 × 1.23	0.21	8.25	6.33	66440
G316.6412-00.0867	14:44:18.35	-59:55:11.28	1.32 × 1.25	0.15	2.73	6.35	8080
G318.0489p00.0854B	14:53:42.64	-59:08:53.02	1.31 × 1.27	0.15	3.18	6.07	36480
G318.9480-00.1969A1	15:00:55.28	-58:58:52.60	1.30 × 1.27	0.15	10.40	6.83	209000
G323.7399-00.2617B2	15:31:45.45	-56:30:49.84	1.29 × 1.25	0.15	3.20	5.79	1529
G327.1192p00.5103	15:47:32.72	-53:52:38.60	0.90 × 0.72	0.34	4.74	4.81	54270
G343.1261-00.0623	16:58:17.22	-42:52:07.54	1.33 × 1.15	0.21	2.00	6.16	33800
G345.5043p00.3480	17:04:22.89	-40:44:23.06	1.34 × 1.15	0.20	2.00	6.13	29498

[a] The coordinates correspond to the pixel from which the spectra were extracted.

[b] Line rms as computed by Nazari et al. (2022).

[c] Distance to the source (Lumsden et al. 2013; Mège et al. 2021). Typical uncertainties are of ~0.5 kpc.

[d] Distance to the galactic center assuming the Sun's D_{GC} as 8.05 kpc (Honma et al. 2015).

[e] Bolometric luminosities corrected to the distances d (Lumsden et al. 2013; Elia et al. 2017). For regions with multiple cores, the fraction of each individual source was estimated by dividing the total luminosity over all the cores weighted by their peak continuum flux (see also van Gelder et al. 2022b and Nazari et al. 2022). No estimations for 644284A are available, so a generic $L_{bol} \sim 10^4$ $L_\odot$ is assumed.

8.7.3   List of transitions

Table 8.7.3 lists all the transitions of $^{34}SO_2$, $^{33}SO_2$, and $O^{13}CS$ with $E_{up} < 800$ K and $A_{ij} > 10^{-6}$ s^{-1} covered in the data.

Table 8.3: Covered transitions.

Species	Transition	Frequency (MHz)	E_{up} (K)	A_{ij} (s^{-1})
$^{34}SO_2$	26 8 18 − 27 7 21	217412.915	473.565	2.09×10^{-5}
$^{34}SO_2$	31 9 23 − 32 8 24	217902.353	646.797	2.17×10^{-5}
$^{34}SO_2$	11 1 11 − 10 0 10 *	219355.009	60.075	1.11×10^{-4}
$^{34}SO_2$	36 5 31 − 35 6 30	220451.866	675.942	2.61×10^{-5}
$^{33}SO_2$	6 4 2 4.5 − 7 3 5 5.5	217628.227	57.861	1.07×10^{-5}
$^{33}SO_2$	6 4 2 7.5 − 7 3 5 8.5	217628.440	57.861	1.04×10^{-5}
$^{33}SO_2$	6 4 2 5.5 − 7 3 5 6.5	217628.749	57.861	1.03×10^{-5}
$^{33}SO_2$	6 4 2 6.5 − 7 3 5 7.5	217628.884	57.861	1.03×10^{-5}
$^{33}SO_2$	11 1 11 9.5 − 10 0 10 9.5 *	220613.365	60.215	1.60×10^{-6}
$^{33}SO_2$	11 1 11 9.5 − 10 0 10 8.5 *	220617.426	60.215	1.11×10^{-4}
$^{33}SO_2$	11 1 11 12.5 − 10 0 10 11.5 *	220617.778	60.215	1.12×10^{-4}
$^{33}SO_2$	11 1 11 10.5 − 10 0 10 10.5 *	220619.743	60.215	1.93×10^{-6}
$^{33}SO_2$	11 1 11 10.5 − 10 0 10 9.5 *	220620.374	60.215	1.10×10^{-4}
$^{33}SO_2$	11 1 11 11.5 − 10 0 10 10.5 *	220620.716	60.215	1.11×10^{-4}
$^{33}SO_2$	11 1 11 11.5 − 10 0 10 11.5 *	220624.670	60.215	1.33×10^{-6}
$O^{13}CS$	18 − 17 *	218198.998	99.49	3.01×10^{-5}

* Detected transitions.

8.7.4   Best-fit models for all sources

Figures 8.10 and 8.11 show the best-fit models derived by the grid-fitting approach for each source in the ALMAGAL subset analyzed here. The former contains the results for $^{34}SO_2$, and the latter for $O^{13}CS$.

8.7.5   Integrated intensity map of 693050

Figure 8.12 shows the integrated intensity maps of source 693050 for $^{34}SO_2$ $11_{1,11}-10_{0,10}$ and $O^{13}CS$ 18−17. The offset in the emission to the continuum peak is likely due to effects of optically thick dust at these wavelengths.

8.7.6   Best-fit parameters of $^{34}SO_2$ and $O^{13}CS$

Tables 8.4 and 8.5 list the best-fit parameters for $^{34}SO_2$ and $O^{13}CS$, respectively, obtained with the grid fitting approach toward all sources. The isotope ratios for each source and corresponding estimated column densities of the main isotopologs are also reported.

Table 8.4: Fitting results for $^{34}SO_2$.

Source	$^{34}SO_2$ N ^{a} (cm^{-2})	FWHM ^{b} (km s^{-1})	V_{lsr} ^{b} (km s^{-1})	(^{32}S/^{34}S) ^{c}	SO$_2$ N ^{d} (cm^{-2})
126348	<4.5×10^{14}	[7.5]	76.9	20	<8.8×10^{15}
615590	(4.0±0.8)×10^{16}	4.3±0.4	40.5	23	(9.0±2.4)×10^{17}
644284A	(2.5±0.5)×10^{16}	7.4±0.5	2.60	22	(5.6±1.5)×10^{17}
693050	(2.0±0.4)×10^{16}	5.7±1.6	-41.2	22	(4.3±1.1)×10^{17}
705768	<6.0×10^{14}	[6.7]	-34.1	22	<1.3×10^{16}
707948	(2.5±0.7)×10^{16}	8.5±2.5	-32.6	22	(5.4±1.6)×10^{17}
717461A	(5.0±1.0)×10^{15}	5.7±0.5	-51.3	21	(1.1±0.3)×10^{17}
721992	(1.3±0.3)×10^{15}	3.2±0.7	-57.3	21	(2.6±0.8)×10^{16}
724566	<7.0×10^{14}	[6.0]	-57.3	21	<1.5×10^{16}
732038	(4.0±0.8)×10^{15}	5.2±0.6	-62.5	21	(8.3±2.0)×10^{16}
744757A	(2.5±0.5)×10^{15}	6.2±0.7	-40.5	21	(5.3±1.3)×10^{16}
767784	(1.6±0.3)×10^{15}	4.1±0.3	-67.9	20	(3.2±0.8)×10^{16}
865468A	<6.0×10^{14}	[8.0]	-27.3	20	<1.2×10^{16}
876288	<5.0×10^{14}	4.8±0.5	-96.2	18	<9.2×10^{15}
881427C	<1.1×10^{15}	[5.5]	-10.4	18	<2.0×10^{16}
G023.3891p00.1851	<2.5×10^{14}	[4.0]	75.5	21	<5.3×10^{15}
G025.6498p01.0491	(3.2±0.6)×10^{15}	6.2±0.9	42.4	21	(6.6±1.6)×10^{16}
G305.2017p00.2072A1	(1.0±0.2)×10^{15}	4.2±0.5	-40.9	21	(2.1±0.5)×10^{16}
G314.3197p00.1125	<3.8×10^{14}	5.0±0.5	-49.0	21	<8.0×10^{15}
G316.6412-00.0867	(1.6±0.3)×10^{15}	8.2±0.5	-20.5	21	(3.3±0.8)×10^{16}
G318.0489p00.0854B	(4.0±0.8)×10^{15}	6.6±0.4	-50.6	21	(8.3±2.1)×10^{16}
G318.9480-00.1969A1	(2.0±0.5)×10^{15}	7.0±4.0	-33.5	22	(4.3±1.3)×10^{16}
G323.7399-00.2617B2	(1.3±0.3)×10^{15}	6.6±0.5	-51.4	21	(2.6±0.6)×10^{16}
G327.1192p00.5103	(6.3±1.3)×10^{15}	6.0±0.7	-83.2	20	(1.3±0.3)×10^{17}
G343.1261-00.0623	(3.2±0.6)×10^{15}	7.3±0.5	-31.5	21	(6.6±1.6)×10^{17}
G345.5043p00.3480	(5.0±1.0)×10^{15}	7.9±0.6	-17.5	21	(1.1±0.3)×10^{17}

^{a} Column densities are calculated using the grid fitting method. 3σ upper limits are derived by manual fitting.

^{b} Square brackets denote FWHM values kept fixed during the fitting. For the sources where no $^{34}SO_2$ emission is detected, their FWHM and V_{lsr} are fixed to the values reported for CH$_3^{13}$CN toward the same source (Nazari *et al.* 2022). For the rest of the sources the velocities are fixed to the best-fitted values derived by the manual approach.

^{c} Values are rounded to zero decimals.

^{d} Column densities of the main isotopologs are derived from the fitting results of the rare isotopologs and considering the isotope ratios.

Table 8.5: Fitting results for O^{13}CS.

Source	O^{13}CS N (cm^{-2})	FWHM (km s^{-1})	V_{lsr} (km s^{-1})	(^{12}C/^{13}C)	OCS N (cm^{-2})
126348	$(5.0\pm1.3)\times10^{14}$	8.7 ± 2.3	75.1	43	$(2.2\pm0.6)\times10^{16}$
615590	$(7.9\pm2.1)\times10^{14}$	3.8 ± 1.6	40.0	60	$(4.8\pm1.4)\times10^{16}$
644284A	$(6.3\pm1.3)\times10^{14}$	6.2 ± 1.7	1.50	60	$(3.8\pm0.9)\times10^{16}$
693050	$(2.5\pm0.7)\times10^{15}$	4.8 ± 0.5	-41.4	54	$(1.3\pm0.4)\times10^{17}$
705768	$(7.9\pm2.1)\times10^{14}$	4.4 ± 0.9	-34.1	54	$(4.3\pm1.3)\times10^{16}$
707948	$(1.0\pm0.3)\times10^{16}$	11.0 ± 2.0	-31.3	54	$(5.4\pm1.6)\times10^{17}$
717461A	$(5.0\pm1.0)\times10^{14}$	4.4 ± 0.9	-51.5	51	$(2.5\pm0.6)\times10^{16}$
721992	$(2.5\pm0.5)\times10^{15}$	3.0 ± 0.1	-57.9	50	$(1.3\pm0.3)\times10^{17}$
724566	$(2.5\pm0.5)\times10^{15}$	4.6 ± 0.6	-56.4	50	$(1.3\pm0.3)\times10^{17}$
732038	$(7.9\pm1.6)\times10^{14}$	4.3 ± 1.2	-63.8	49	$(3.9\pm1.0)\times10^{16}$
744757A	$(6.3\pm1.3)\times10^{14}$	5.1 ± 1.2	-41.0	52	$(3.3\pm0.8)\times10^{16}$
767784	$(6.3\pm1.3)\times10^{14}$	4.0 ± 0.7	-67.2	46	$(2.9\pm0.7)\times10^{16}$
865468A	$(6.3\pm1.3)\times10^{15}$	5.8 ± 0.5	-26.8	45	$(2.9\pm0.7)\times10^{17}$
876288	$(3.2\pm0.8)\times10^{14}$	3.0 ± 0.6	-96.5	33	$(1.1\pm0.3)\times10^{16}$
881427C	$(7.9\pm1.6)\times10^{15}$	5.3 ± 0.4	-11.3	52	$(4.1\pm1.0)\times10^{17}$
G023.3891p00.1851	$(4.0\pm0.8)\times10^{14}$	3.0 ± 0.1	75.6	43	$(1.7\pm0.5)\times10^{16}$
G025.6498p01.0491	$(1.6\pm0.3)\times10^{15}$	6.0 ± 0.9	41.3	50	$(7.9\pm1.9)\times10^{16}$
G305.2017p00.2072A1	$(7.9\pm2.1)\times10^{14}$	3.5 ± 1.0	-41.7	52	$(4.2\pm1.2)\times10^{16}$
G314.3197p00.1125	$(5.0\pm1.0)\times10^{14}$	5.9 ± 0.8	-49.8	51	$(2.6\pm0.6)\times10^{16}$
G316.6412-00.0867	$(2.5\pm0.5)\times10^{15}$	5.5 ± 0.4	-19.4	51	$(1.3\pm0.3)\times10^{17}$
G318.0489p00.0854B	$(1.0\pm0.3)\times10^{15}$	5.7 ± 1.1	-50.9	50	$(5.0\pm1.5)\times10^{16}$
G318.9480-00.1969A1	$(4.0\pm0.8)\times10^{15}$	4.7 ± 0.3	-34.5	53	$(2.1\pm0.5)\times10^{17}$
G323.7399-00.2617B2	$(2.0\pm0.4)\times10^{15}$	3.9 ± 0.5	-52.1	48	$(9.7\pm2.4)\times10^{16}$
G327.1192p00.5103	$(2.5\pm0.5)\times10^{15}$	6.7 ± 1.7	-84.1	44	$(1.1\pm0.3)\times10^{17}$
G343.1261-00.0623	$(2.5\pm0.7)\times10^{15}$	8.9 ± 2.1	-32.5	50	$(1.3\pm0.4)\times10^{17}$
G345.5043p00.3480	$(4.0\pm1.0)\times10^{15}$	6.9 ± 1.9	-17.5	50	$(2.0\pm0.6)\times10^{17}$

$$^{34}SO_2\ (11_{1,10} - 10_{0,10})$$
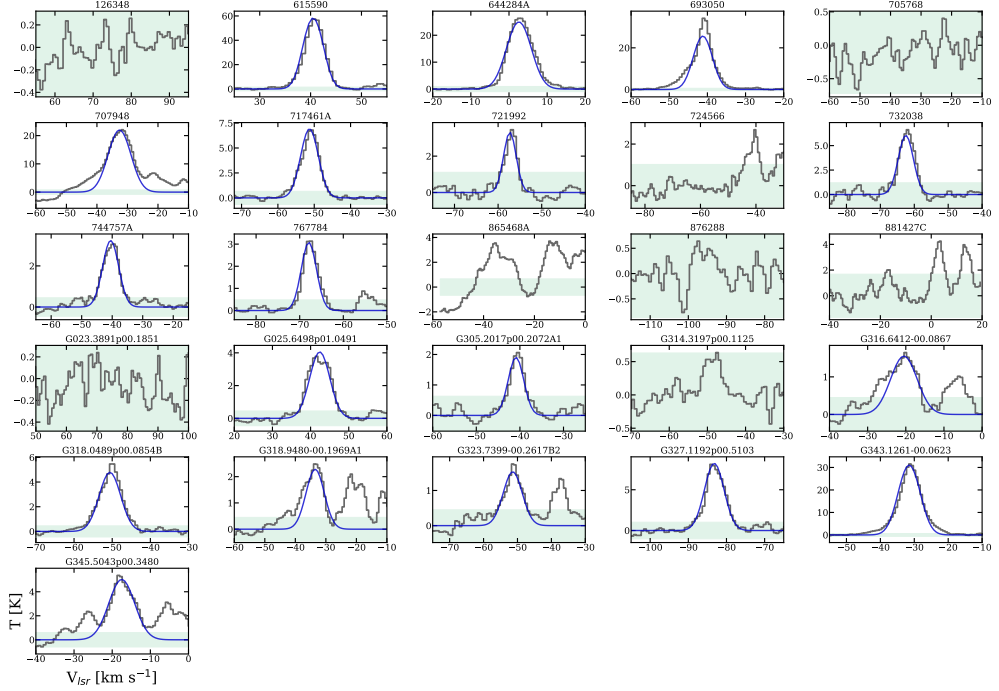
Figure 8.10: Observed spectra toward each source (gray) superimposed by its best-fit model for $^{34}SO_2$ (blue). The green shadowed area delimits the 3σ threshold. The name of each source is shown on the top of each panel.

8.7.7   FWHM and V_{lsr} of $^{34}SO_2$ and $O^{13}CS$ compared to CH_3OH

Figure 8.13 shows the ratios of FWHM and differences of V_{lsr} for $^{34}SO_2$ and $O^{13}CS$ with respect to CH_3OH.

8.7.8   Best-fit parameters of $^{33}SO_2$

Table 8.6 lists the best-fit parameters for the $^{33}SO_2$ transitions in the sources where it could be constrained.

8.7.9   Literature ratios

Table 8.7 lists the literature values for $N(SO_2)/N(CH_3OH)$, $N(OCS)/N(CH_3OH)$, and $N(SO_2)/N(OCS)$ gathered in this work.

8.7.10 $N(SO_2)/N(OCS)$

The ratios of the derived column densities for SO_2 and OCS are shown in Fig. 8.14 as a function of luminosity. For comparison, ratios measured in the gas phase of low-mass sources are also shown, together with ice observations toward comets, dark clouds, as well as both low- and high-mass protostars.

Table 8.6: Fitted parameters for $^{33}SO_2$.

Source	$^{33}SO_2$ N (cm^{-2})	FWHM [a] $(km\ s^{-1})$	V_{lsr} [a] $(km\ s^{-1})$	$(^{32}S/^{33}S)$ [b]	SO_2 from $^{33}SO_2$ N (cm^{-2})	SO_2 from $^{34}SO_2$ N (cm^{-2})
615590	$(1.0\pm0.2)\times10^{16}$	3.7	40.5	93	$(9.3\pm0.9)\times10^{17}$	$(9.0\pm2.4)\times10^{17}$
644284A	$(7.0\pm1.0)\times10^{15}$	6.0	2.6	92	$(6.5\pm1.4)\times10^{17}$	$(5.6\pm1.5)\times10^{17}$
693050	$(6.0\pm1.5)\times10^{15}$	3.5	-41.2	89	$(5.3\pm0.5)\times10^{17}$	$(4.3\pm1.1)\times10^{17}$
G343.1261-00.0623	$(9.5\pm1.5)\times10^{15}$	7.3	-31.5	87	$(8.3\pm1.8)\times10^{17}$	$(6.6\pm1.6)\times10^{17}$

[a] Uncertainties in the FWHMs and V_{lsr} are $\lesssim 0.5\ km\ s^{-1}$.
[b] Values are rounded to zero decimals.

Table 8.7: References of literature ratios.

Object	$N(SO_2)/N(CH_3OH)$	$N(OCS)/N(CH_3OH)$	$N(SO_2)/N(OCS)$
	Gas phase		
MYSOs [a]	(1), (2), (4), (10), (11)	(1), (2), (4), (10), (11)	(1) – (13)
LYSOs [b]	(15), (16), (22), (23)	(15) – (17), (19) – (23)	(14) – (16), (18), (22), (23), (24)
	Interstellar ices		
Dark clouds [c]	(25)	(25)	(25)
MYSOs [d]	(26), (27)	(27)	(26), (27)
LYSOs [e]	(28), (29)		
	Solar System		
Comets [f]	(30), (31), (33), (36), (37)	(30) – (38)	(30), (31), (33), (36), (37)

[a] (1) Hatchell et al. (1998); (2) van der Tak et al. (2000); (3) Hofner et al. (2001); (4) van der Tak et al. (2003); (5) Osorio et al. (2009); (6) Herpin et al. (2009); (7) Cesaroni et al. (2010); (8) Pillai et al. (2011); (9) van der Tak et al. (2013); (10) Gieser et al. (2019); (11) Fuente et al. (2021); (12) Minimni et al. (2021); (13) Fontani et al. (2023).

[b] (14) Tafalla et al. (2000); (15) Jørgensen et al. (2018); (16) Drozdovskaya et al. (2018); (17) Sahu et al. (2019); (18) Agúndez et al. (2019); (19) van Gelder et al. (2020); (20) Manigand et al. (2020); (21) Yang et al. (2020); (22) Artur de la Villarmois et al. (2023); (23) Kushwahaa et al. (2023); (24) Esplugues et al. (2023).

[c] (25) McClure et al. (2023).

[d] (26) Boogert et al. (1997); (27) Boogert et al. (2022).

[e] (28) Tobin et al. (2016); (29) Rocha et al. (2024).

[f] (30) Dello Russo et al. (1998); (31) Bockelée-Morvan et al. (2000a); (32) Mumma et al. (2011); (33) Le Roy et al. (2015); (34) Biver et al. (2015); (35) Dello Russo et al. (2016); (36) Calmonte et al. (2016); (37) Schuhmann et al. (2019); (38) Saki et al. (2020).

O^{13}CS (18 - 17)
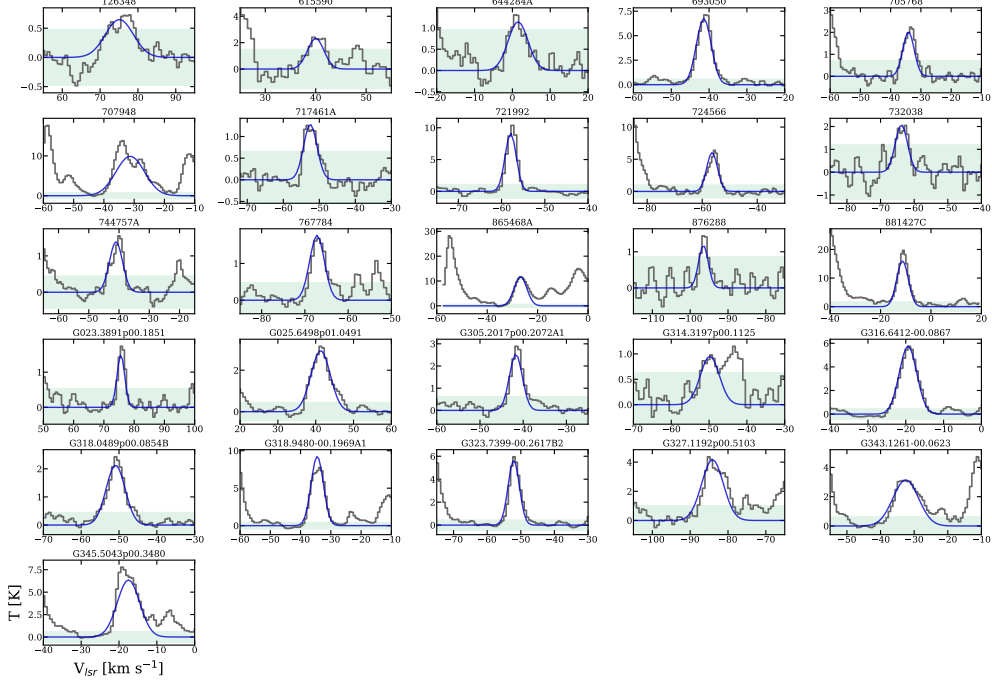
Figure 8.11: Same as Fig. 8.10, but for O^{13}CS.
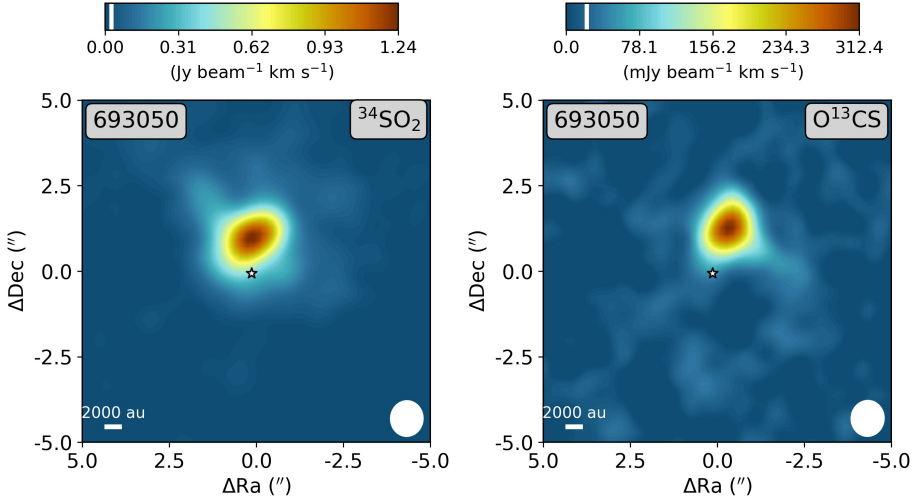
Figure 8.12: Integrated intensity maps of the $^{34}SO_2$ $11_{1,11}-10_{0,10}$ (left) and O^{13}CS $18-17$ (right) lines for 693050. The integration limits are set to [-5, 5] km s^{-1} with respect to the source's V_{lsr}. The white star denotes the source positions derived from the continuum emission, and the 3σ threshold is delimited by the white line in the color bars. The beam size is shown in the lower-right corner of each panel, and a scale bar is depicted in the lower left.
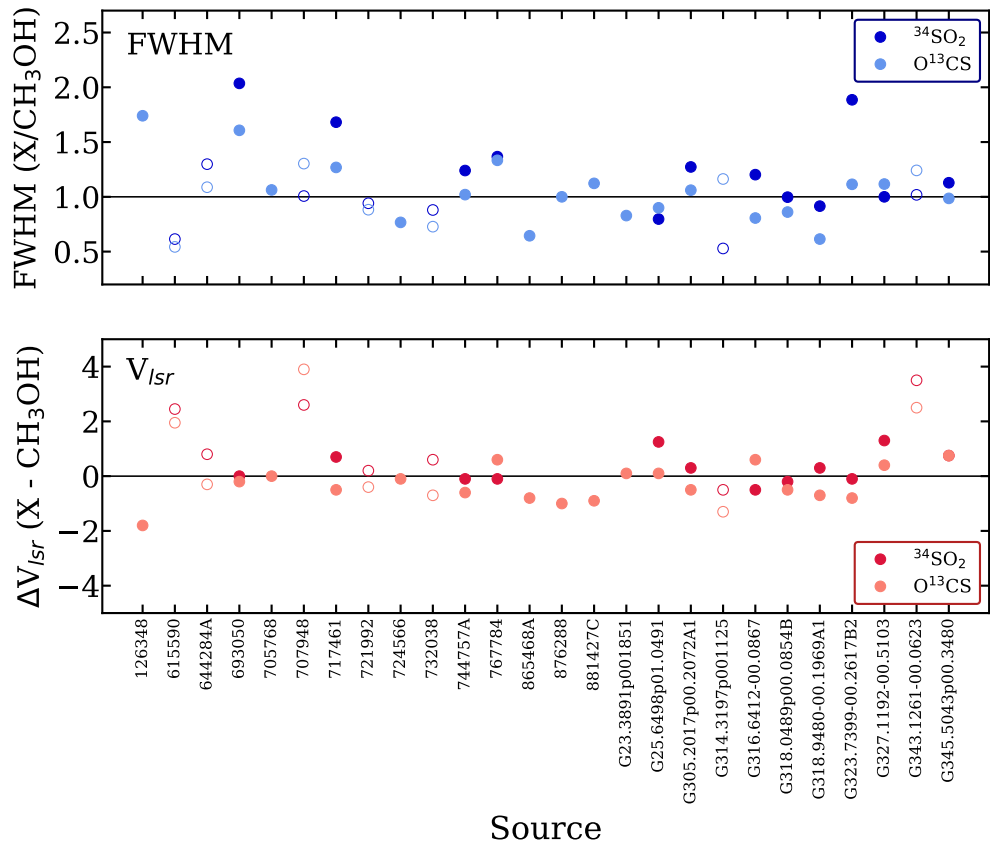
Figure 8.13: FWHM ratios (upper panel) and V_{lsr} differences (lower panel) with respect to $CH_3^{18}OH$. For sources in which $CH_3^{18}OH$ was not detected by van Gelder *et al.* (2022a), the main CH_3OH isotopolog was used (empty markers). Values for $^{34}SO_2$ are shown in darker colors and for $O^{13}CS$ in lighter colors.
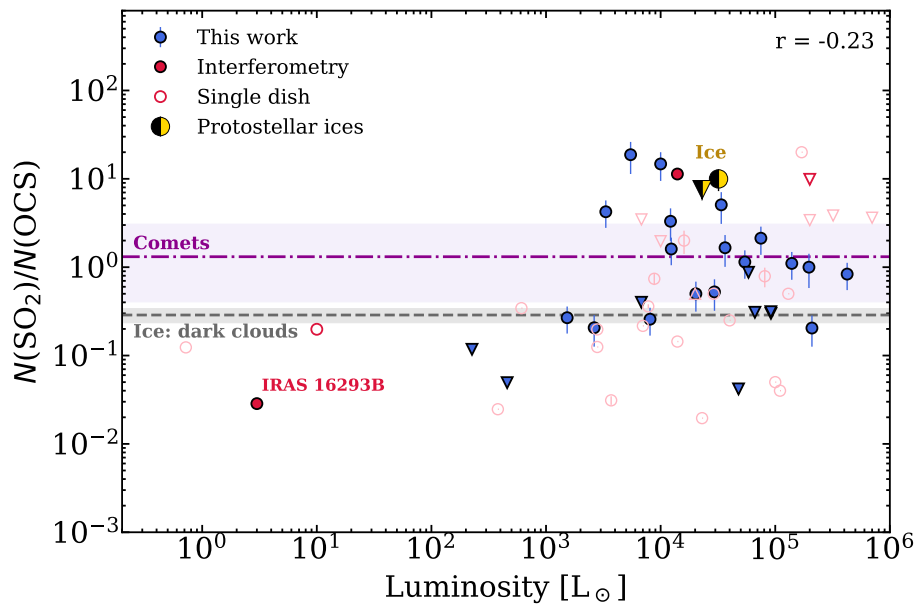
Figure 8.14: Same as Figure 8.4, but for $N(SO_2)/N(OCS)$. Literature ratios with $N(SO_2)$ derived from the main isotopologue are signaled by light red markers to differentiate from values derived from $^{34}SO_2$, which are shown in darker red.

9. A SPECTRAL SURVEY OF CH$_3$CCH IN THE HOT MOLECULAR CORE G331.512-0.103

A spectral survey of methyl acetylene (CH$_3$CCH) was conducted toward the hot molecular core/outflow G331.512-0.103. Our APEX observations allowed the detection of 41 uncontaminated rotational lines of CH$_3$CCH in the frequency range between 172–356 GHz. Through an analysis under the local thermodynamic equilibrium assumption, by means of rotational diagrams, we determined T_{exc}=50±1 K, N(CH$_3$CCH)=(7.5±0.4)×10^{15} cm^{-2}, X[CH$_3$CCH/H$_2$]≈(0.8–2.8)×10^{-8} and X[CH$_3$CCH/CH$_3$OH]≈0.42±0.05 for an extended emitting region ($\sim$10$''$). The relative intensities of the K=2 and K=3 lines within a given K-ladder are strongly negatively correlated to the transitions' upper J quantum-number (r=-0.84). Pure rotational spectra of CH$_3$CCH were simulated at different temperatures, in order to interpret this observation. The results indicate that the emission is characterized by a non-negligible temperature gradient with upper and lower limits of $\sim$45 and $\sim$60 K, respectively. Moreover, the line widths and peak velocities show an overall strong correlation with their rest frequencies, suggesting that the warmer gas is also associated with stronger turbulence effects. The K=0 transitions present a slightly different kinematic signature than the remaining lines, indicating that they might be tracing a different gas component. We speculate that this component is characterized by lower temperatures, and therefore larger sizes. Moreover, we predict and discuss the temporal evolution of the CH$_3$CCH abundance using a two-stage zero-dimensional model of the source constructed with the three-phase Nautilus gas-grain code.

9.1   Introduction

Star-forming regions play a key role in building the complex inventory of chemical species detected in astronomical environments, which in turn serve as powerful tools to study their surroundings. Through the observation of molecular emission lines, it is possible to constrain both the physical conditions and the chemical evolution of circumstellar sources, shedding light on the formation processes that connect different evolutionary stages of star-formation. Methyl acetylene (CH_3CCH), also known as propyne, is a particularly good temperature probe, and has therefore been widely explored toward various star-forming objects (e.g., Fontani *et al.* 2002; Bisschop *et al.* 2007; Fayolle *et al.* 2015; Giannetti *et al.* 2017; Andron *et al.* 2018; Calcutt *et al.* 2019).

Massive stars ($L > 10^3 L_\odot$; $M > 8 M_\odot$) greatly affect their surroundings through their feedback and the production of heavy elements. The formation process of those stars, however, is still less well-understood in comparison to the low-mass counterparts. Observational disadvantages, such as their complex cluster environments ($n_\star \gtrsim 100$ pc^{-3}) and large distances involved ($d \geq 1$ kpc), together with a considerably shorter evolutionary timescale ($t_{KH} \leq 10^4$ yr for O-type stars), substantially impair the development of a solid massive star-formation paradigm (Garay & Lizano 1999; Zinnecker & Yorke 2007; Tan *et al.* 2014; Krumholz 2015; Silva *et al.* 2017; Rosen *et al.* 2020).

Despite the lack of a thoroughly defined evolutionary sequence, some precursors of high-mass stars are well established. One example are Hot Molecular Cores (HMCs), which are one of the first manifestations of massive star formation (Cesaroni 2005). They are characterized by relatively high temperatures (>100 K) and high densities ($n_{H_2} \sim 10^5$–10^8 cm^{-3}), linked with a compact (<0.1 pc), luminous (>10^4 $L_\odot$) and massive ($\sim$10–1000 $M_\odot$) molecular core (Heaton *et al.* 1989; Gomez *et al.* 1995; Cesaroni *et al.* 1998; Cesaroni 2005; Bonfand *et al.* 2019). HMCs are associated with a rich molecular emission spectrum, which carries information on their chemical and physical properties, as well as their morphology and evolutionary stage (e.g., Caselli *et al.* 1993; Comito *et al.* 2005; Herbst & van Dishoeck 2009; Allen *et al.* 2018; Bonfand *et al.* 2019; Jørgensen *et al.* 2020; Gieser *et al.* 2021).

9.1.1   The source: G331.512-0.103

G331.512-0.103 (henceforth G331) is a massive and energetic hot molecular core/outflow system. It is located within the millimeter source G331.5-0.1 (see Merello *et al.* 2013b and references therein), at the tangent point of the Norma spiral arm ($\sim$ 7.5 kpc) (Bronfman *et al.* 1985, 2008), and which consists of a singularly extended and luminous complex at the center of a Giant Molecular Cloud (GMC). The parent GMC is located at the peak region of the southern molecular and massive-star-formation rings (i.e., the peaks of the azimuthally averaged radial distributions of molecular gas and of regions of massive star formation, Bronfman *et al.* 2000). Likewise, it is one of the most massive and active star forming clouds in the southern Galaxy (García *et al.* 2014). Observational evidence indicates that a Young Massive Stellar Object (YMSO) at the center of G331 drives a powerful outflow with $\sim$ 55 $M_\odot$ of mass and a momentum of $\sim 2.4 \times 10^3$ $M_\odot$ km s^{-1} (Bronfman *et al.* 2008), with lobes closely aligned with the line of sight. Observations with the Atacama Large Millimeter/submillimeter Array (ALMA) of the SiO(8-7), $H^{13}CO^+$(4-3), HCO^+(4-3) and CO(3-2) transitions revealed an expanding bubble geometry driven by stellar winds, which probably arises from the protostar confined in a compact HII region of $\sim$5 arcsec (projected size of $\sim$0.2 pc) (Merello *et al.* 2013a). Its emission spectrum exhibits great chemical lavishness, from common radicals and carbon-chain molecules to prebiotic and complex organic species (Merello *et al.* 2013a,b; Mendoza *et al.* 2018; Duronea *et al.* 2019; Hervías-Caimapo *et al.* 2019; Canelo *et al.* 2021). All those factors make G331 an exquisite source for astrochemical investigations by means of spectral surveys in sub-mm wavelenghts.

9.1.2   The molecule: Methyl acetylene

More than 200 molecules have been hitherto detected toward the interstellar and circumstellar media (e.g., McGuire 2018). Methyl acetylene (CH_3CCH) has been detected in a wide variety of sources. It has been proven to be a reliable tracer of physical conditions, such as temperature and density, and has been extensively studied toward star-forming regions (e.g., Buhl & Snyder 1973; Lovas *et al.* 1976; Hollis *et al.* 1981; Kuiper *et al.* 1984; Taniguchi *et al.* 2018; Guzmán *et al.* 2018; Bøgelund *et al.* 2019; Calcutt *et al.* 2019). It has also been observed toward extragalactic sources, such as M 82, NGC 253, and NGC 1068 (Mauersberger *et al.* 1991; Qiu *et al.* 2020), and toward a planetary nebula (Schmidt & Ziurys 2019).

The rotational transitions of CH_3CCH are characterized by two quantum numbers, namely the total angular momentum (J) and its projection on the principal symmetry axis (K) (Townes & Schawlow 1975; Müller *et al.* 2000). Because it is a symmetric rotor, CH_3CCH presents many transitions that are closely spaced in frequency: the so-called K-ladders. The capability to observe many lines in the same bandwidth reduces calibration uncertainties and yields more precise predictions. Moreover, due to its small electric dipole moment ($\mu = 0.75$ D) (Dubrulle *et al.* 1978), line thermalization occurs at densities as low as $\sim 10^4$ cm^{-3} (e.g., Bergin *et al.* 1994; Fontani *et al.* 2002; Molinari *et al.* 2016). Transitions with $\Delta K \neq 0$ are forbidden, and therefore the relative population of different K-ladders are dictated by collisions. As a result, CH_3CCH acts as an excellent temperature probe. Indeed, this molecule's temperature sensitivity makes it a reliable tracer of physical conditions and passive heating (Giannetti *et al.* 2017; Molinari *et al.* 2016).

Aside from observational advantages, the intrinsic spectroscopic properties of CH_3CCH can directly affect the observed spectra and therefore can give powerful insights on the physics of the emitting gas. Rotational spectroscopy is a conspicuously fruitful technique to infer information on the molecular species and its environment (e.g., Domenicano & Hargittai 1992; Winnewisser *et al.* 2003; Grubbs & Cooke 2010), and is nowadays highly assisted by quantum-chemistry (e.g., Puzzarini *et al.* 2012b,a; Cernicharo *et al.* 2015; McGuire *et al.* 2016; Cazzoli *et al.* 2016; Cerqueira *et al.* 2020; Santos *et al.* 2020). The rotational Hamiltonian is described in terms of the zeroth-order rotational constants (A, B, and C), and the higher-order centrifugal-distortion constants (e.g., D_J, D_{JK}, D_K, H_J, H_{JK}, H_{KJ} and H_K, for symmetric tops). These constants can be measured from laboratory experiments guided by theoretical simulations, which in turn play a fundamental role in line assignments of radioastronomical observations (e.g., Belloche *et al.* 2014; Coutens *et al.* 2016; Melli *et al.* 2018; Belloche *et al.* 2019).

In this work, we conducted a spectral survey of CH_3CCH toward G331, resulting in the detection of 41 uncontaminated lines. The goal of this work is to analyze the excitation conditions of methyl acetylene in this source, which gives information on the chemical and physical conditions of the gas and consequently helps unveiling the early stages of massive star-formation. Quantum-chemical properties associated with this molecule are especially relevant to explore the small-scale structure of the source. In section 9.2, we delineate the observational procedure. In section 9.3, we present our results on the line identifications and radiative analysis. Those results are then discussed in section 9.4. The observed abundance is discussed in the context of a chemical model of our source in section 9.5. Finally, our conclusions and perspectives are presented in section 9.6.

9.2   Observations

The observations were obtained with the Atacama Pathfinder EXperiment (APEX) telescope (Güsten *et al.* 2006) using the single-point mode toward the coordinates of the source (Bronfman *et al.* 2008) RA, DEC (J2000) = $16^h12^m10.1^s$, $-51°28'38.1''$. The Swedish-ESO PI Instrument (SEPIA180; Belitsky *et al.* 2018) was used, together with APEX-1 and APEX-2

receivers of the Swedish Heterodyne Facility Instrument (SHeFI; Vassilev *et al.* 2008b), to observe nine frequency setups within the intervals 170–205 GHz and 222–307 GHz, respectively. As backend for the APEX-1 and APEX-2 receivers, the eXtended bandwidth Fast Fourier Transform Spectrometer2 (XFFTS2) was used, which consists of two units with 2.5 GHz bandwidth divided into 32768 channels each. SEPIA180 is a dual-polarization sideband-separated (2SB) receiver, which is able to observe two 4 GHz band, separated by 12 GHz, simultaneously. Thus, it covers 100% of the SEPIA ALMA Band 5 receiver channel IF band (159–211 GHz). The spectral resolution, corresponding to velocity resolutions, was obtained between 0.06 and 0.13 km s^{-1} for a noise level of ∼30–50 mK. While all analyses were performed with the original data, for further clarity and uniformity in their graphical depiction, the resolution of the spectra exhibited in the present work were degraded to a common value of 1 km s^{-1}. The original intensity, obtained in a scale of antenna temperature corrected for atmospheric attenuation (T_A), was converted to the main-beam temperature (T_{mb}) scale using the main-beam efficiencies $\eta_{mb} = 0.80$ for SEPIA180[1], and $\eta_{mb} = 0.75$ and 0.73 for APEX-1 and APEX-2, respectively[2] (e.g. Canelo *et al.* 2021). The Half Power Beam Width (HPBW) values vary between ∼17–39″.[3] We adopted a calibration uncertainty of about 10% (Dumke & Mac-Auliffe 2010).

The data reduction was carried out using the CLASS package of the GILDAS software[4] (Pety *et al.* 2005; Gildas Team 2013). First-degree polynomial baselines were removed from each individual scan, which were subsequently averaged into a final spectrum. Line identifications were performed using the Weeds extension of CLASS, in combination with spectroscopic databases such as NIST[5] Recommended Rest Frequencies for Observed Interstellar Molecular Microwave Transitions (Lovas 2004), CDMS[6] (Müller *et al.* 2001, 2005; Endres *et al.* 2016), JPL[7] (Pickett *et al.* 1998), and Splatalogue[8]. The establishment of a molecular identification warrants the satisfaction of a set of standard requirements (Snyder *et al.* 2005). Accordingly, the following criteria were used in order to confirm a detection: the peak frequencies of the observed lines should be consistent with the systemic velocity of G331 ($V_{lsr} \sim -90$ km s^{-1}), the intensities of the observed lines should surpass the threshold of 3 rms noise, and lines predicted through Local Thermodynamic Equilibrium (LTE) modeling should agree with the observations. The radiative studies, including the optical depth estimation, were based on analyses carried out with the CASSIS software[9] (Vastel *et al.* 2015)—assuming LTE. CASSIS has been developed by IRAP-UPS/CNRS.

9.3 Results

9.3.1 Line analysis of CH$_3$CCH

We detected a total of 41 lines of CH$_3$CCH spread across the spectral band, from ∼170.84 GHz to ∼307.60 GHz. Considering that CH$_3$CCH exhibits a K-ladder spectral signature, in Figure 9.1 we have displayed all the observed K-ladder structures from the J=10–9 to J=18–17 rotational levels.

Spectroscopic parameters obtained through Gaussian fittings to the lines are summarized in Table 1 in Santos *et al.* (2022a) (omitted in this thesis). The fittings were performed to

---

[1] http://www.apex-telescope.org/telescope/efficiency/
[2] https://www.apex-telescope.org/telescope/efficiency/index.php.old
[3] https://www.apex-telescope.org/instruments/
[4] https://www.iram.fr/IRAMFR/GILDAS/
[5] https://physics.nist.gov/cgi-bin/micro/table5/start.pl
[6] https://cdms.astro.uni-koeln.de/
[7] https://spec.jpl.nasa.gov/
[8] https://www.cv.nrao.edu/php/splat/
[9] http://cassis.irap.omp.eu/

the spectra at their full resolution of $\sim$0.06–0.13 km s^{-1}.
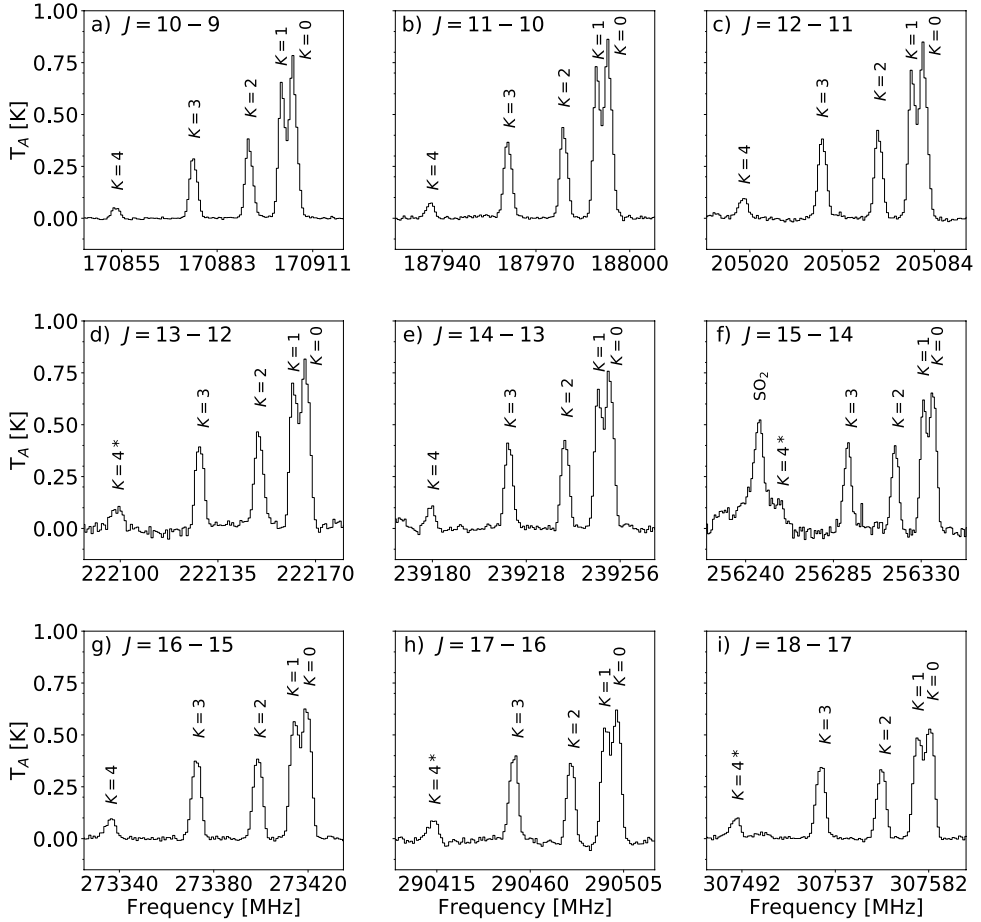
Figure 9.1: Spectral lines of CH$_3$CCH identified toward G331 across the frequency range of 170.850–307.590 GHz. Each panel displays the K-ladder lines for the rotational transitions a) $J = 10_K - 9_K$, b) $J = 11_K - 10_K$, c) $J = 12_K - 11_K$, d) $J = 13_K - 12_K$, e) $J = 14_K - 13_K$, f) $J = 15_K - 14_K$, g) $J = 16_K - 15_K$, h) $J = 17_K - 16_K$ and i) $J = 18_K - 17_K$. The asterisk ($*$) indicates lines below the 3σ threshold. Linear baselines were subtracted from each spectrum, and the spectral resolution was resampled to a common channel of approximately 1 km s^{-1}.

For each observed J_u level, all transitions with K=3–0 were detected. In some cases (see Table 1 in Santos *et al.* 2022a), lines with K=4 were not detectable above the 3 rms noise threshold, and were not considered in our analyses. Nevertheless, all K-ladders include a minimum of four detected transitions. The CH$_3$CCH lines present a low velocity dispersion ($\pm$0.68 km s^{-1}) around the systemic velocity of the source and a mean systemic velocity of $\bar{V}_{lsr}$ = -90.0 $\pm$ 0.3 km s^{-1}, obtained through averaging the velocities of all 41 lines. Line profiles are narrow, with average values of 4.9 $\pm$ 0.8 km s^{-1}, and observed line widths also show an overall small dispersion, with FWHM values ranging from 4.15 to 5.68 km s^{-1}. This indicates that the emission originates from a quiescent region, as will be discussed in § 9.4.1.

9.3.2   Rotational diagrams and physical properties

In order to estimate the excitation temperature (T_{exc}) and column density (N) of CH_3CCH, rotational diagrams were constructed. Under the assumption of LTE, one can derive the T_{exc} and N of an optically thin emission that uniformly fills the antenna beam from:

$$\ln\left(\frac{N_u}{g_u}\right) = \ln\left(\frac{N}{Q(T_{exc})}\right) - \frac{E_u}{k_B T_{exc}} \tag{9.1}$$

where Q is the species' partition function at T_{exc} and k_B is the Boltzmann constant. N_u, g_u and E_u are, respectively, the column density, the statistical weight and the energy of the upper level (Goldsmith & Langer 1999). A plot of $\ln(N_u/g_u)$ versus E_u of the observed lines will thus correspond to a straight line, whose slope and y-intercept are defined by $1/T_{exc}$ and $\ln(N/Q(\mathbf{T_{exc}}))$, respectively. For a spatially unresolved emitter, a beam-dilution correction factor, $(\Delta\Omega_a/\Delta\Omega_s)$, should be introduced on the right-hand side of Equation (9.1). For a preliminary analysis, we adopted an average source size of $5''$, in accordance with previous observations of G331 (e.g. Hervías-Caimapo *et al.* 2019; Canelo *et al.* 2021, and references therein).

The rotational diagram of CH_3CCH constructed under the assumption of optically thin lines is displayed in blue in the upper panel of Figure 9.2. We derived $N(CH_3CCH) = (2.5\pm0.1) \times 10^{16}$ cm^{-2} and $T_{exc} = 50\pm1$ K from the fit ($\chi^2_{red}=1.49$). The uncertainties were computed following the formalism of the CASSIS software[10], which takes into account the calibration error of 10%.

To explore the validity of the optically thin assumption, we estimated the lines' optical depths (τ) using CASSIS. The opacity correction is incorporated to Equation (9.1) through iterative calculations of the optical-depth correction factor C_τ (Goldsmith & Langer 1999), associated with the photon escape probability:

$$C_\tau = \frac{\tau}{1 - e^{-\tau}} \tag{9.2}$$

The optical-depth correction factor is introduced on the right-hand side of Equation (9.1). The iterations stop when a solution for T_{exc} and N converges. That is to say, when the difference between the last two iterations is smaller than 1%. The opacity-corrected rotational diagram of CH_3CCH is displayed in red in both panels of Figure 9.2. From the fit ($\chi^2_{red} = 2.57$) we obtained $N(CH_3CCH) = (4.5 \pm 0.3) \times 10^{16}$ cm^{-2} and $T_{exc} = 42 \pm 1.0$ K. This correction leads to a new scaling of the diagram's ordinate axis, resulting in a decrease of 17% and an increase of 80% in the values of T_{exc} and N, respectively.

Given the rather low temperatures derived from the rotational diagrams, we infer that the CH_3CCH emission is originated from a cooler gas in the outer envelope of the source, in accordance with other observational works toward star-forming regions (Churchwell & Hollis 1983; Nagy *et al.* 2015; Andron *et al.* 2018; Hervías-Caimapo *et al.* 2019). Thus, we expect CH_3CCH to trace a more extended region. The rotational diagram constructed for an extended source (size of $10''$) is displayed in the lower panel of Figure 9.2. From the fit under the optically thin assumption ($\chi^2_{red}=1.43$), we derived $N(CH_3CCH)=(6.9\pm0.4)\times10^{15}$ cm^{-2} and $T_{exc}=52\pm1$ K.

After including the opacity correction factor, we derived $N(CH_3CCH) = (7.5 \pm 0.4) \times 10^{15}$ cm^{-2} and $T_{exc} = 50 \pm 1$ K from the fit ($\chi^2_{red} = 1.51$). These values were employed to model the emission of CH_3CCH under LTE conditions with WEEDS (see Figure 9.3). Overall, the synthetic spectra are in good agreement with the observations, although the accordance is sensibly higher for K-ladders with lower J quantum-numbers (see the discussion in § 9.4.2). For the $10''$ source size, the contribution of C_τ to the diagram is much less significant than for more compact emissions. Indeed, the corrected fit yielded T_{exc} and N values only slightly different from the optically thin scenario, with respective changes of -2.09% and 8.69%.

---

[10]http://cassis.irap.omp.eu/docs/RadiativeTransfer.pdf
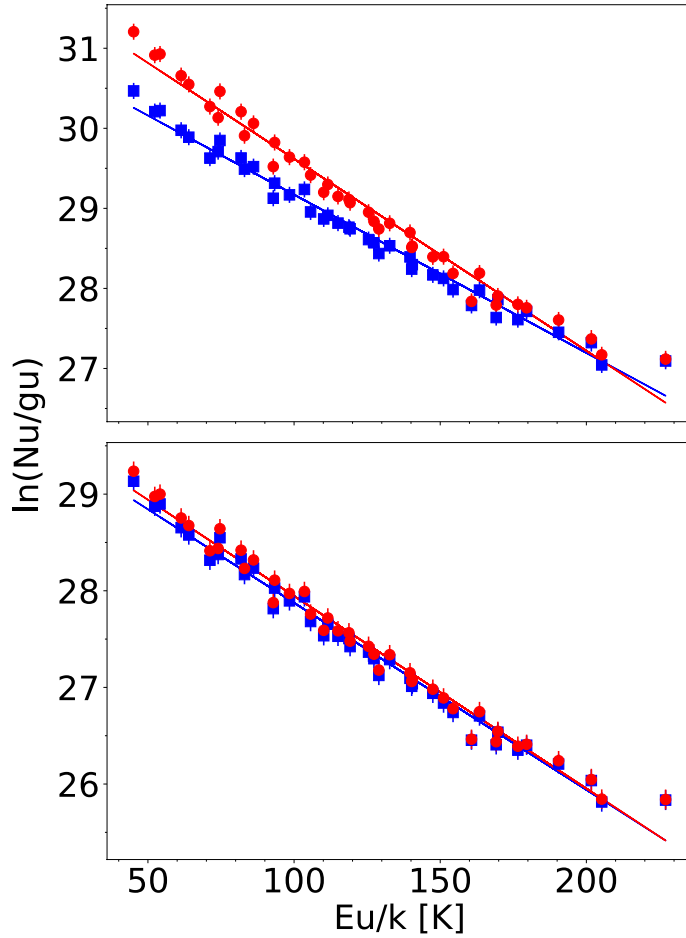
Figure 9.2: *Upper panel:* Rotational diagram of the CH$_3$CCH lines for a source size of 5″. Red circles and blue squares correspond to the lines with and without opacity corrections, respectively. Least squares fits to the points are also shown in their respective color. The error bars are propagated from the Gaussian fit to the lines and take into consideration a calibration uncertainty of 10% (Santos 2021) *Lower panel:* Same as the upper panel, but for a source size of 10″ in diameter.

Table 9.1 summarizes the excitation temperatures and column densities derived from the rotational-diagram analyses.
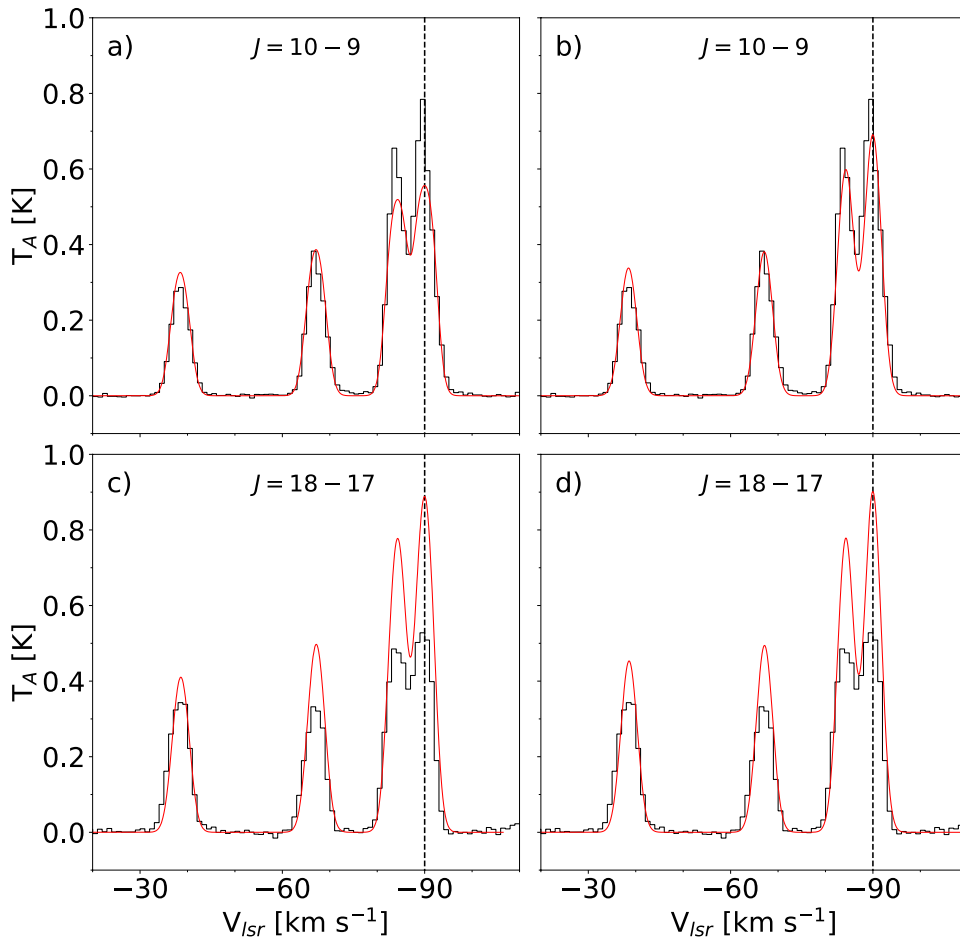
Figure 9.3: Spectra of CH_3CCH observed toward G331. *Upper pannels*: J=10–9, $\sim$ 170.87–170.91 GHz; *Lower pannels*: J=18–17, $\sim$ 307.52–307.59 GHz. *Left pannels*: LTE models simulated for a compact emission ($5''$). *Right pannels*: LTE models simulated for an extended emission ($10''$). For all panels, the black and red spectra correspond to the observations and the LTE models, respectively. The dashed line indicates the systemic velocity of the source. The abscissas of all spectra were adjusted to the systemic velocity of the K=0 transition.

In terms of the reduced χ^2 values, the fit of the $5''$ diagram with opacity corrections was less accurate in comparison with the uncorrected counterpart, whereas no significant change was observed for the $10''$ diagrams. This is a consequence of the underestimation of the source size in the $5''$ scenario, which is compensated by overestimating the lines' optical depth—in particular, for the K=0 and K=1 transitions at lower J values (see Figure 9.3). Indeed, the CH_3CCH emission seems to be optically thin (Churchwell & Hollis 1983; Fontani *et al.* 2002), especially for the range of J quantum-numbers observed in this work.

Table 9.1: Values of T_{exc} and N of CH_3CCH toward G331 obtained from the analysis of the rotational diagrams.

Parameter	Source size: $5''$		Source size: $10''$	
	With C_τ	Without C_τ	With C_τ	Without C_τ
T_{exc} [K]	42 ± 1	51 ± 1	50 ± 1	52 ± 1
N [$\times 10^{16}$ cm^{-2}]	4.5 ± 0.3	2.5 ± 0.1	0.75 ± 0.04	0.69 ± 0.04
χ^2_{red}	2.57	1.49	1.51	1.42

9.3.3   Relative intensities

The relative intensities of the lines within a K-ladder will change depending on the temperature of the environment. To explore this relation, the rotational spectra of CH_3CCH were simulated at temperatures ranging from 10 K to 100 K, using the PGOPHER general purpose software (Western 2016). The rotational constants (A and B), the quartic and sextic centrifugal distortion constants (D_J, D_{JK}, H_J, H_{JK} and H_{KJ}), and the dipole moment (μ) employed in the simulations are listed in Table 9.2.

Table 9.2: Spectroscopic parameters employed in the spectrum simulations. References: [a]JPL database; [b](Dubrulle *et al.* 1978); [c](Muenter & Laurie 1966).

Parameter	Value	Parameter	Value
A [MHz]	158590^a	H_J [Hz]	0.0097^b
B [MHz]	8545.87712^b	H_{JK} [Hz]	0.935^b
D_J [kHz]	2.9423^b	H_{KJ} [Hz]	5.23^b
D_{JK} [kHz]	163.423^b	μ [D]	0.75^c

The transition intensities are given by (Western 2016):

$$I = \frac{S}{Q(T)} \left[\exp\left(\frac{-E_l}{k_B T} \right) - \exp\left(\frac{-E_u}{\mathbf{k_B} T} \right) \right], \tag{9.3}$$

which is simply the line strength S times the Boltzmann factor, normalized to the partition function $Q(T)$ at the given temperature. E_l and E_u correspond to the energies of the lower and the upper states, respectively. In Figure 9.4, we plot the intensity ratios I[K=n]/I[K=0] of the predicted lines within a K-ladder versus the temperature, with $n = 1$, 2 and 3. We show the results for the J=10–9 and J=18–17 transitions, corresponding to the extremes of the observed bandwidth.

As seen in the plot, the behavior of the intensity ratios are overall analogous for the range of J values explored in this work. At low temperatures, the spectrum is dominated by the K=0 transitions, with small contributions from the other K levels. As the temperature rises, however, the ratios of all K transitions increase at different rates. The intensity ratios of both K=1 and K=2 transitions, compared to K=0, follow a similar trend. They show an initial stage of rapid growth, which becomes gradually slower as the temperature continues to rise. As can be seen for the K=1 transitions, the curve will eventually reach a plateau, which stabilizes the K=1/K=0 intensity ratios at values around 0.8–0.9. Comparatively, the ratios for K=3 present a more dramatic increase. At around 50 K, the K=3 lines become more intense than the K=2 transitions. Further, at around 100 K, their intensities surpass those of the K=1 transitions. At even higher temperatures, they ultimately become the most intense line of the given K-ladder.

This behavior can be explained by nuclear spin statistics: symmetric tops with three equivalent hydrogens, such as CH_3CCH, have two different spin symmetries—namely, A and
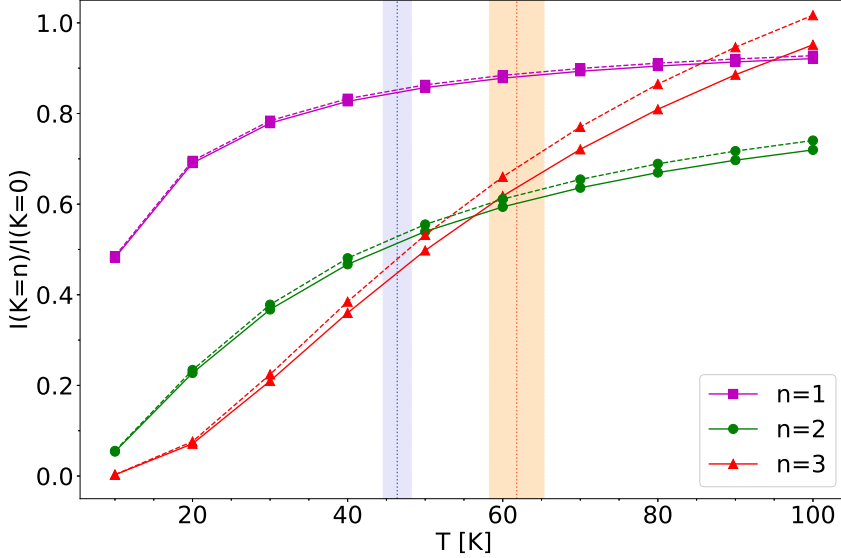
Figure 9.4: Intensity ratios I[K=n]/I[K=0] versus temperature for transitions within a given K-ladder. Purple squares represent ratios with $n = 1$, green circles represent ratios with $n = 2$, and red triangles represent ratios with $n = 3$. The solid and dashed lines correspond to, respectively, the J=10–9 and J=18–17 K-ladders. The red and blue regions represent upper and lower limits to the temperature profile of the source and are discussed in § 9.4.2.

E. The A states correlate with the transitions with K=0, 3, 6, 9, ..., whereas the E states correspond to the remaining transitions, such as K=1, 2, 4, 5, ... (e.g. Strom *et al.* 2020). Those states have relative statistical weights of A:E = 2:1 (Herzberg 1945), and therefore the population distribution of the transitions at higher temperatures will favor the K=3 states. At lower temperatures, however, the energy acts as a limiting factor. This phenomenon makes the CH_3CCH K-ladder profile highly sensitive to the local temperature, in particular with regards to the relative intensities of the K=3 transitions.

As can be seen in Figure 9.1, we serendipitously observed a frequency window in which the CH_3CCH K-ladder profiles gradually change as a function of the rotational quantum number. For low J values, which are associated with cooler regions, the K=2 lines are more intense than the K=3 (see panel a). However, as we observe transitions with higher J values, which are consequently associated with warmer regions, the K=2/K=3 intensity ratios consistently decrease. From J=15–14 onward, the K=3 lines become more intense than the K=2 (see panel i). In Figure 9.5, we plot the K=2/K=3 ratios of the observed areas listed in Table 1 in Santos *et al.* (2022a) as a function of the upper J value. This plot yields a Pearson correlation coefficient of r=-0.84, which, given the small FWHM dispersion of the observed lines, clearly indicates a decreasing trend of the K=2/K=3 intensity ratios with J. This result strongly suggests that the lines are tracing a region with a temperature gradient, as will be discussed in § 9.4.2.
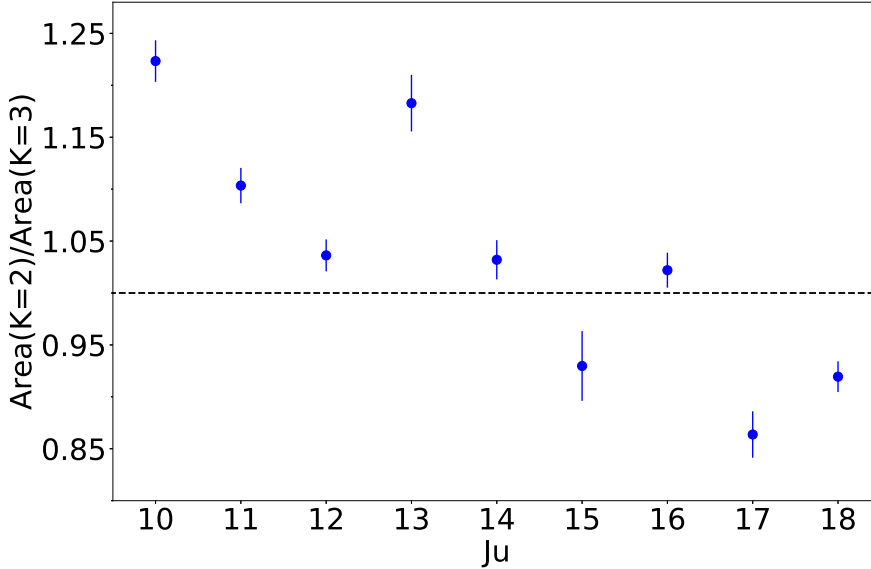
Figure 9.5: Ratios of the areas for $K=2$ and $K=3$ lines versus the upper J value of the transition. Areas and uncertainties were obtained through Gaussian fittings of the observed data using CLASS. The dashed line indicates a ratio of unity.

9.3.4   Search for the CH$_3$CCH isotopologues

The ^{13}C isotopologues of CH$_3$CCH, as well as its deuterated forms, have been successfully detected toward multiple interstellar sources (Gerin *et al.* 1992a; Markwick *et al.* 2002, 2005; Belloche *et al.* 2013; Potapov *et al.* 2016; Halfen *et al.* 2017; Schmidt & Ziurys 2019; Agúndez *et al.* 2019). Recently, Agundez *et al.* (2021) have detected the two doubly deuterated forms of methyl acetylene—CHD$_2$CCH and CH$_2$DCCD—toward the dense core L483. They derived abundance ratios of CH$_3$CCH/CHD$_2$CCH=34±10 and CH$_3$CCH/CH$_2$DCCD=42±13, which are only a few times less than the singly deuterated counterparts.

Motivated by the copious amount of CH$_3$CCH line detections in G331, we searched across the survey for the ^{13}C and D isotopologues of CH$_3$CCH. Only the 10_0–9_0 and 10_1–9_1 lines of ^{13}CH$_3$CCH were detected above the 3σ threshold. However, they are blended, and just marginally above the detection limit, and so we cannot reliably confirm these detections. Assuming a ratio of ^{12}C/^{13}C ~ 20, as estimated for G331 and other sources toward the Galactic center (Wilson & Rood 1994; Requena-Torres *et al.* 2006; Mendoza *et al.* 2018; Duronea *et al.* 2019; Yan *et al.* 2019), we derive a ^{13}CH$_3$CCH column density of $N \sim 3.75 \times 10^{14}$ cm^{-2}. This column density was used to model the emission of the 10_K–9_K K-ladder of ^{13}CH$_3$CCH under LTE conditions (Figure 9.6), which is shown to be consistent with the observed spectrum of G331.
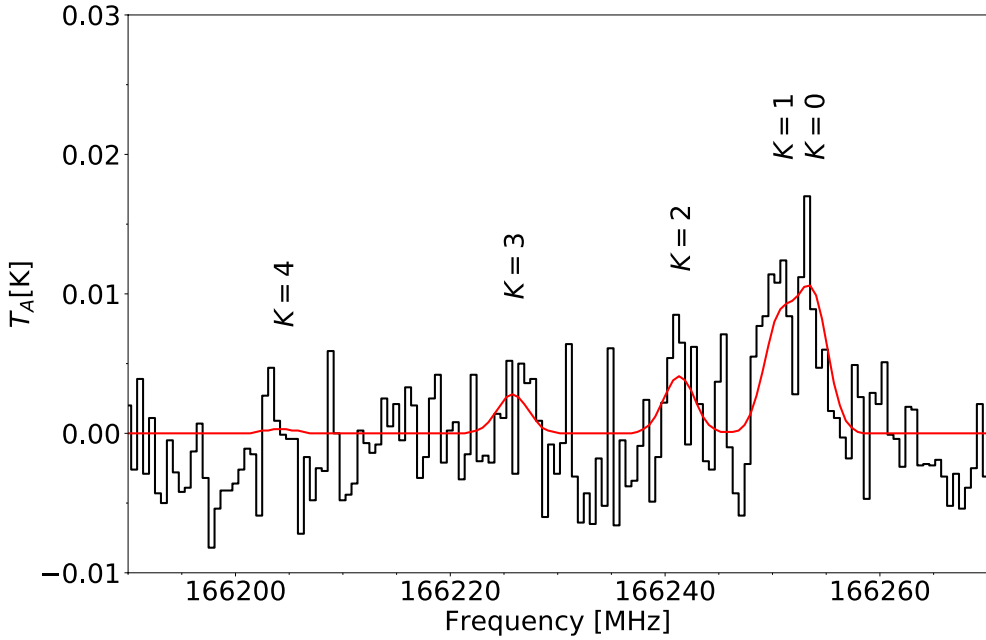
Figure 9.6: Modelled 10_K–9_K K-ladder of $^{13}CH_3CCH$ (in red) superimposed on the spectrum observed toward G331 (in black).

9.4 Discussion

9.4.1 Origin of the emission

Hervías-Caimapo *et al.* (2019) have observed several molecular lines toward G331 and classified them according to the line profile, with narrow lines tracing the emission from the core ambient medium and lines with broad wings tracing the outflow and shocked region. Accordingly, we expect from the narrow line profiles that the observed CH_3CCH emission is originated from a quiescent (not expanding) core medium. This region is also associated with lower temperatures (below 100 K), which is consistent with the excitation temperatures derived from the rotational diagram. A schematic view of the physical model of G331, which considers the emission of CH_3CCH and other molecular tracers, is presented in Figure 9.7.

9.4.2 Physical conditions: gas temperatures

In §9.3.4, we discussed the dependence of the $K=2/K=3$ intensity ratios of CH_3CCH with increasing temperatures. This inversion in relative populations within the same K-ladder is observed toward G331, and can be easily inferred by visual inspection (see Figure 9.1).

States with higher J quantum numbers require higher energies to be populated, and therefore tend to be associated with warmer regions than the lower J states. Given that the $K=2/K=3$ intensity ratios are negatively correlated with J (see Figure 9.5), we suggest that the CH_3CCH emission is in fact described by a temperature gradient, which explains the behavior seen in Figure 9.1. In order to estimate the extent of the temperature gradient, we have grouped the points in the rotational diagram into two subsets (Figure 9.8) separated at $E_{up} \approx 125$ K—according to the behavior of the $K=2/K=3$ intensity ratio of the K-ladder: the lower-energy group contains all $K=2$ transitions with $J \leq 14$, for which K=2/K=3 $\gtrsim 1$.
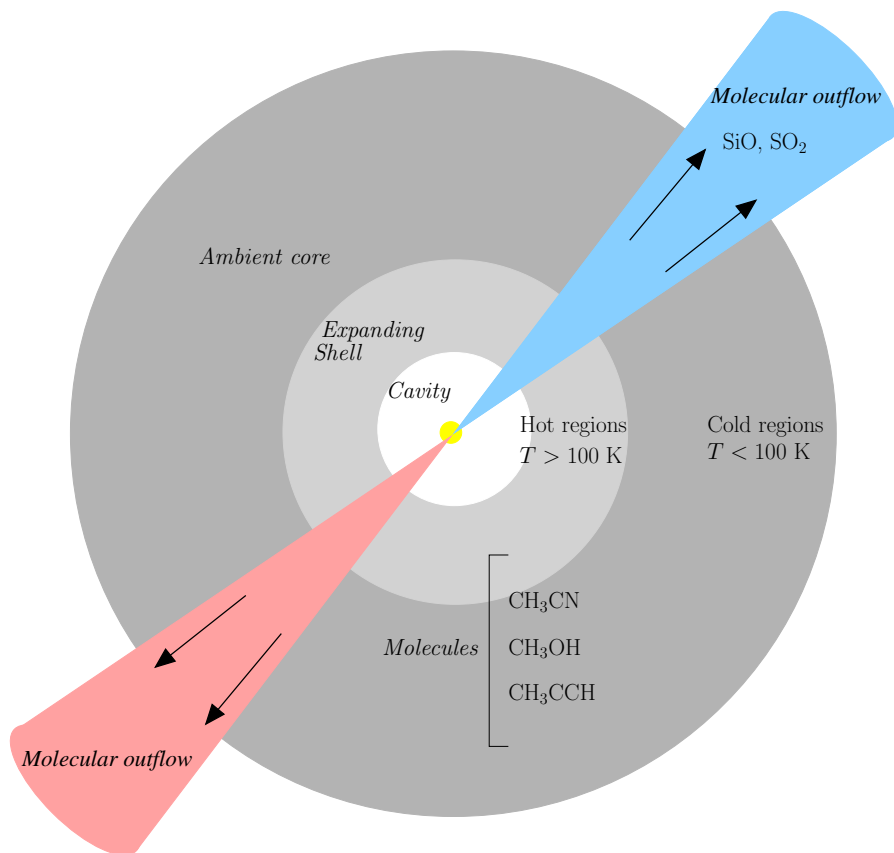
Figure 9.7: Schematic view of the physical model proposed for G331. Based on the models of Merello *et al.* (2013b); Duronea *et al.* (2019); Hervías-Caimapo *et al.* (2019).

Contrarily, the higher-energy subset encompasses all $K=2$ transitions with $J > 14$, for which $K=2/K=3 \lesssim 1$. The resulting T_{exc} and N obtained from the linear fit of each subset are listed in Table 9.3.
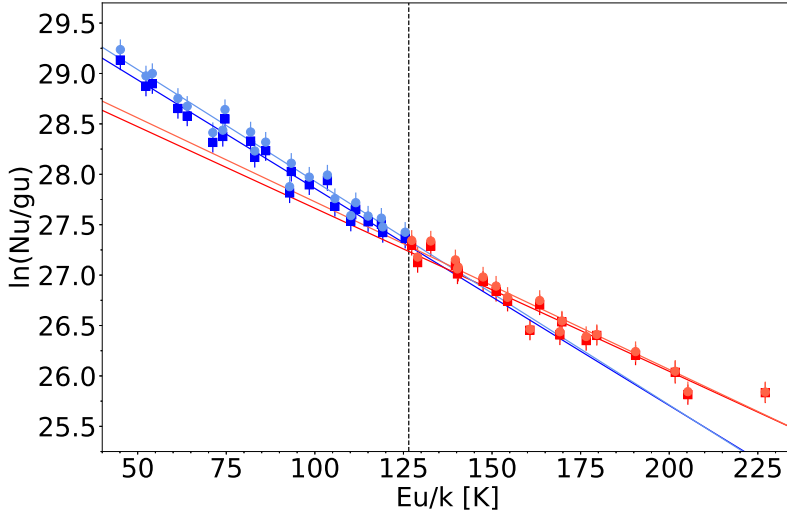
Figure 9.8: Rotational diagram of the CH_3CCH lines for a source size of $10''$. The points were divided into two subsets indicated by the dashed line. The points pertaining to the low- and high-energy subsets are shown in blue and red, respectively. Least squares fits to the points within each subset are shown. Circles and squares correspond to the lines with and without opacity corrections, respectively.

Table 9.3: Values of T_{exc} and N of CH_3CCH obtained from the 2-component rotational diagrams for a source size of $10''$.

Parameter	Lower-energy comp. (blue)		Higher-energy comp. (red)	
	With C_τ	Without C_τ	With C_τ	Without C_τ
T_{exc} [K]	45 ± 2	46 ± 2	60 ± 3	62 ± 3
N [$\times 10^{15}$ cm^{-2}]	7.9 ± 0.6	7.2 ± 0.5	5.7 ± 0.9	5.3 ± 0.8
χ^2_{red}	0.87	0.82	1.19	1.14

Assuming an optically thin scenario, the rotational diagram divided into two subsets yields temperature components of ~ 45 and ~ 60 K. Although the points in the rotational diagram show an overall fairly linear trend, the T_{exc} obtained from this analysis is highly sensitive to the fitted slope. Consequently, a difference of around 15 K arises between the derived values from the linear fittings of the two subsets. This temperature interval coincides with the region of Figure 9.4 where the intensity inversion of $K=2$ and $K=3$ occurs. Thus, one can regard the two temperature components extracted from the blue and red subsets in Figure 9.8 as, respectively, lower and upper limits to the temperature profile of the observed emitting region—indicated as the blue and red regions in Figure 9.4. The rotational diagram analysis of § 9.3.2 is therefore suited to evaluate the large-scale emission of CH_3CCH, yielding an averaged temperature of $T_{exc} \sim 50.2$ K. The intrinsic spectroscopic properties of methyl

acetylene, however, enabled us to perform a more direct and meticulous assessment of the temperature of the source. The same discussion is valid for the optically thick scenario.

The synthetic spectra under the LTE assumption shown in Figure 9.3 reproduces more accurately the observed data for lower J quantum-numbers. This gradual loss in accuracy for higher J transitions is likely a consequence of the temperature profile that leads to the intensity inversion around $J_u=14$ (see Figure 9.5). Indeed, throughout the entire $\sim$170840–307600 MHz frequency range, modeled transitions with $K=3$ are less intense than the $K=2$ counterparts. Since using only one temperature component is not completely adequate to describe our observations, the model will be increasingly amiss as the bulk of the emission transits to regions with different average gas temperatures. Hence, our LTE model seems to best describe the cooler environment, traced by the lines with lower J values.

Previously, Hervías-Caimapo *et al.* (2019) have used ALMA to observed four CH_3CCH lines within the $J=21$–20 K-ladder toward G331, which showed a peak of emission located at a radius of $\sim$1.2$''$. From the rotational diagram constructed with the CH_3CCH lines, they obtained an excitation temperature of $T_{exc} = 70 \pm 7$ K. Their results are in accordance with our hypothesis of a temperature gradient, which indeed predicts that transitions with higher J quantum-numbers will be associated with higher excitation temperatures and more compact regions.

9.4.3   Kinematics

The spectroscopic parameters (see Table 1 in Santos *et al.* 2022a), obtained through fitting a Gaussian profile to each line, are directly related to the kinematics of the emitting region—or, at least, of the gas where the bulk of the emission is originated. In Figure 9.9, we present a plot of the widths and peak velocities of the observed lines, which are listed in Table 1 in Santos *et al.* (2022a).

The line widths and peak velocities of transitions with the same quantum number K are overall strongly correlated. Indeed, the Pearson correlation coefficient of the $K=0$, $K=1$, $K=2$ and $K=3$ groups are, respectively, r=-0.85, r=-0.97, r=-0.78, and r=-0.80. This coefficient measures the linear correlation between two variants by means of the ratio of their covariance and the product of their standard deviation. Thus, $r=\pm1$ correspond to perfect linear correlations (either positive or negative) and $r=0$ corresponds to no correlation. The lines with $K=4$ are fainter and harder to observe, and therefore were not included in the comparison. Their smaller signal-to-noise ratios hampers their analysis, which is reflected in their higher associated uncertainties reported in Table 1 in Santos *et al.* (2022a). Nonetheless, for each K group, there is a clear tendency for broader lines to present increasingly blueshifted velocities. The same trend was also observed by Di Francesco *et al.* (2004) for bright ($T_B^{max} \geq 10\ \sigma$) N_2H^+ lines toward the Ophiuchus A star-forming core: they found that the higher velocity lines were systematically broader, which they associate to infalling motions that increase local rotation speeds.

Interestingly, the $K=0$ lines are systematically broader and less blueshifted than the other groups, indicating that they might be tracing a slightly different region than the bulk of the emission of the other K transitions. At low temperatures, the contributions from transitions with $K \neq 0$ to the rotational spectrum of CH_3CCH are minor (see Figure 9.4), and the emission is dominated by the $K=0$ lines. As the temperature rises, the relative intensities of the $K \neq 0$ transitions rapidly increase, resulting in richer K-ladders. Thus, it is likely that the bulk of the $K=0$ emission is originated from a cooler and more extended region, which does not contribute as significantly to the lines with $K \neq 0$. These, in turn, must be tracing a hotter and more compact environment, resulting in a different kinematic signature. The systematic redshift of the peak velocities for the $K=0$ lines compared to the other groups also suggests interesting velocity features of the cold component. It is worth mentioning that the mean velocity shift between lines with the same quantum number K within the $J=10$–9 and $J=18$–17 K-ladders is $\sim$0.49 km s^{-1}, which is more than three times the poorest
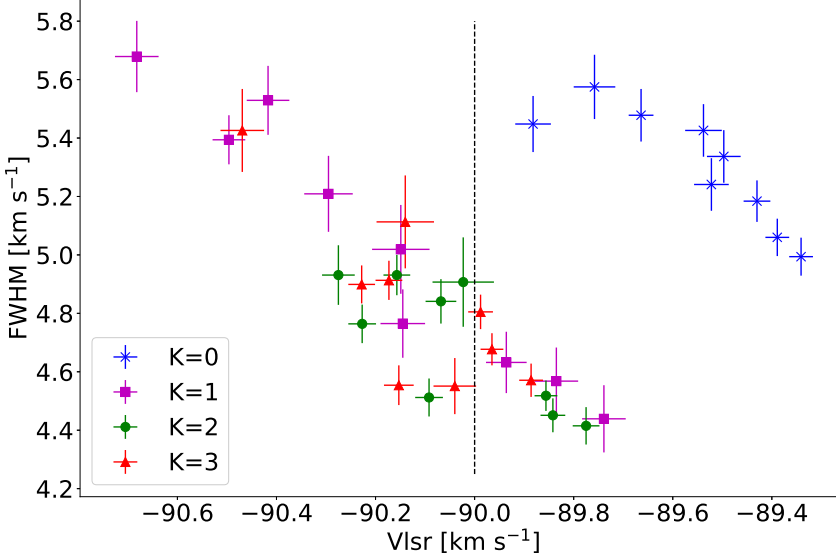
Figure 9.9: Line widths vs. peak velocities obtained from Gaussian fittings of the observed transitions. Blue crosses represent transitions with $K=0$, purple squares represent transitions with $K=1$, green circles represent transitions with $K=2$ and red triangles represent transitions with $K=3$. The black dashed line separates the blue- and redshifted regions relative to the adopted systemic velocity of G331 (-90 km s^{-1}).

obtained velocity resolution. Further surveys of the CH$_3$CCH emission toward G331 with higher angular resolution are imperative to better understand the different gas components, and the small-scale structure of the hot core.

In Figure 9.10, we show a comparison of the line widths versus the rest frequency, together with their Pearson coefficients. From the plots, it is clear that the FWHM is correlated to the line frequency, particularly for the lines with $K=0$ and $K=1$. Since thermal broadening effects are negligible for radio transitions at the considered temperature range (see, for example, the discussion of Fontani *et al.* 2002), the broader widths associated with higher J values indicate that the gas where the bulk of the emission is originated must become gradually more turbulent as the temperature increases. This is fairly reasonable, considering that the warmer emission comes from the inner parts of the envelope surrounding the Massive Young Stellar Object (MYSO).

9.4.4   CH$_3$CCH abundances

The abundance of CH$_3$CCH relative to H$_2$ (X(CH$_3$CCH)) is defined as the ratio of the column densities N(CH$_3$CCH)$/N$(H$_2$). We have estimated the H$_2$ column density in G331 from ALMA measurements of N(H^{13}CO$^+$)$\approx$(1.5–3.2)$\times10^{13}$ cm^{-2} (Merello *et al.* 2013a,b; Hervías-Caimapo *et al.* 2019), adopting an abundance ratio N(H^{13}CO$^+$)$/N$(H$_2$)=3.3$\times10^{-11}$, as measured by Blake *et al.* (1987) in Orion KL. Additionally, a hydrogen column density of N(H$_2$)=2.7$\times10^{23}$ cm^{-2} was reported for G331 from the continuum emission's surface density at 1.2 mm (Duronea *et al.* 2019). Considering those two limits for N(H$_2$), we derived a ratio
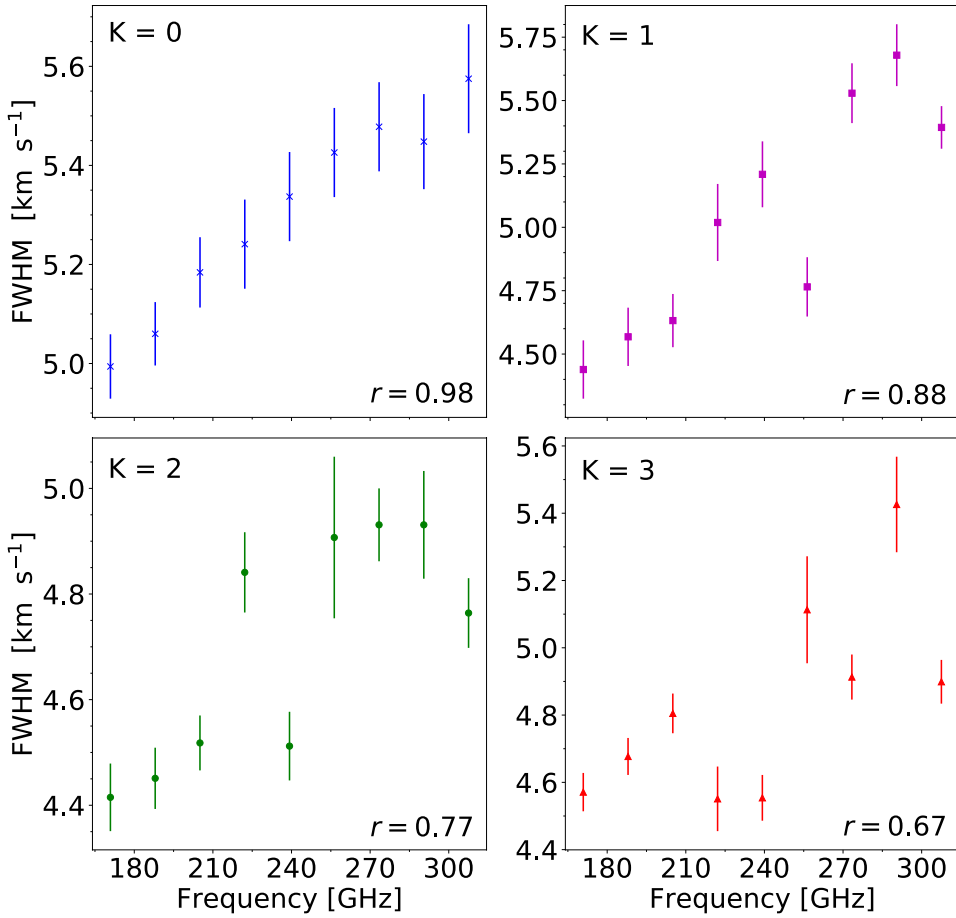
Figure 9.10: Line widths vs. rest frequencies obtained from Gaussian fittings of the observed transitions with $K=0$, $K=1$, $K=2$ and $K=3$.

of $X(\mathrm{CH_3CCH}) \approx (0.8–2.8) \times 10^{-8}$.

In Table 9.4, we present a comparison of the $\mathrm{CH_3CCH}$ abundances with respect to $\mathrm{H_2}$ in different massive star-forming regions, including G331. Our derived abundance and excitation temperature agree well with the ones obtained for similar sources, which indicates similarities in the formation pathway of this molecule at such environments. The fact that this abundance comes mostly from the enveloping gas reinforces the conclusions drawn by other works (e.g., Öberg *et al.* 2013; Fayolle *et al.* 2015; Giannetti *et al.* 2017; Taniguchi *et al.* 2018) that the formation of methyl acetylene is not limited by heat input, and should take place during the earlier stages of star-formation. In other words, $\mathrm{CH_3CCH}$ is likely a so-called zeroth-generation molecule (Herbst & van Dishoeck 2009). Nonetheless, in the case of solid-phase formation, heat will eventually be required in order for the molecule to desorb to the gas-phase.

We also estimate the fractional abundance of $\mathrm{CH_3CCH}$ with respect to methanol to be 0.42 ± 0.05. This value is listed in Table 9.4, together with the ratios obtained from the literature for other massive star-forming regions. The methanol column density in G331 is assumed to be of $\approx (1.8 \pm 0.2) \times 10^{16} \ \mathrm{cm^{-2}}$, as derived by Mendoza *et al.* (2018) under the

Table 9.4: Abundances of CH_3CCH relative to H_2 and CH_3OH observed toward high-mass star-forming sites. References: [a](Taniguchi *et al.* 2018), [b](Giannetti *et al.* 2017), [c](Fayolle *et al.* 2015). [*]Derived from the average abundances reported by Giannetti *et al.* (2017). n.p. = not provided. The excitation temperatures are given in units of K.

Source	$/N(H_2)$	$/N(CH_3OH)$	$T_{exc}^{CH_3CCH}$
G12.89+0.49[a]	$4.2^{+2.8}_{-2.2} \times 10^{-8}$	$0.34^{+0.28}_{-0.15}$	33^{+20}_{-9}
G16.86-2.16[a]	$3.2^{+1.9}_{-1.5} \times 10^{-8}$	$0.36^{+0.28}_{-0.18}$	29^{+15}_{-8}
G28.28-0.36[a]	$7.6^{+5.2}_{-4.4} \times 10^{-8}$	$1.61^{+1.4}_{-0.86}$	23^{+9}_{-6}
ATLASGAL[b]	$(0.5$–$2.5) \times 10^{-8}$ [b]	0.31^{*}	$34.5^{+24.6}_{-10.5}$
NGC 7538 IRS9[c]	n.p.	1.3 ± 0.4	47 ± 5
W3 IRS5[c]	n.p.	2.2 ± 0.7	58 ± 8
AFGL490[c]	n.p.	1.8 ± 0.8	41 ± 7
G331 (this work)	$(0.8$–$2.8) \times 10^{-8}$	0.42 ± 0.05	50 ± 1

LTE formalism and assuming the total CH_3OH abundance as the sum of the A-CH_3OH and E-CH_3OH contributions. This methanol emission, however, is thought to originate from a region of only $5''.3$, which is considerably more compact than the emitting region of CH_3CCH. Given that the envelope abundance of methanol in G331 is not fully known, the derived $N(CH_3CCH)/N(CH_3OH)$ ratio is likely artificially lower than in reality. Nonetheless, it is still fairly close to the ratios derived in other sources, further strengthening the conclusion that they present similar chemistry.

9.5   Chemical modeling

Formation pathways of CH_3CCH in the ISM include gas-phase ion-neutral routes with $C_2H_2^+$ as a precursor (Schiff & Bohme 1979; Millar & Freeman 1984), neutral-neutral reactions such as $CH + C_2H_4 \rightarrow CH_3CCH + H$ (Turner *et al.* 1999), as well as dissociative recombination reactions involving larger hydrocarbons (Calcutt *et al.* 2019). Grain-surface reactions are also proposed in order to explain the observed abundances of CH_3CCH (Hickson *et al.* 2016; Guzmán *et al.* 2018). Regarding massive environments, Taniguchi *et al.* (2019a) have constructed hot-core models to investigate the formation pathways of cyanopolyynes and other carbon-chain species, including CH_3CCH and c-C_3H_2, around MYSOs. They found chemical similarities between methyl acetylene, methane and cyanopolyynes, being all triggered by CH_4 sublimation from dust grains. Furthermore, those species are also shown to accumulate in the bulk of the ice until the temperature reaches their respective sublimation points. Comparatively, small reactive hydrocarbons such as CCH and CCS are shown not to accumulate onto dust grains, being readily destroyed in the gas-phase instead. Complementary, Andron *et al.* (2018) discuss the formation routes of methyl acetylene in the solar-type protostar IRAS 16293-2422. They show that, at large distances form the central star, the abundance of CH_3CCH in the solid phase is higher than in the gas-phase, which indicates that it is efficiently produced on dust grains at low temperatures through successive hydrogenation of C_3. Moreover, their models also indicates that reactions in the gas-phase with C_2H_4 and C_3H_5 as precursors can also effectively form methyl acetylene in the outer envelope.

In order to investigate the chemical evolution of CH_3CCH in G331, we constructed a time-dependent chemical model of the source using the three-phase gas-grain Nautilus code (Ruaud *et al.* 2016), in which the grain surface chemistry is distinguished from the bulk of the ice. The model consists of two zero-dimensional steps (i.e., the physical properties of the source are uniform and static), comprising the dark-cloud and the hot-core phases of

star formation. The 1st step, representing an initial dark-cloud phase, was computed using the elemental abundances listed in Table 9.5, as was computed in previous works about the chemistry of HNCO in G331 (Canelo *et al.* 2021). For the physical parameters, we adopted a gas temperature and density of 10 K and 1×10^4 cm^{-3}, respectively. Then, we employed the abundances derived from the dark-cloud model after 10^5 yr as initial parameters for the 2nd step: a "rapid" hot-core phase. For this second period we used $T = 80$ K and tested four different values for n_{H_2}: 1×10^6, 5×10^6, 1×10^7 and 5×10^7 cm^{-3}. The gas and dust temperatures were set as equal throughout the entire simulation, as they have been shown to be coupled in dense sources (Merello *et al.* 2019). Moreover, standard visual extinction ($A_V = 10$ mag) and cosmic ray ionization rates ($\zeta=1.3\times10^{-17}$ cm^{-3}) were used. The standard chemical network presented in the KInetic Database for Astrochemistry (KIDA)[11] (Wakelam *et al.* 2015) catalog was employed in the simulations.

Table 9.5: Initial gas-phase elemental abundances, with the format a(b) representing $a\times10^b$. References: 1. Wakelam & Herbst (2008); 2. Jenkins (2009); 3. Hincelin *et al.* (2011); 4. low-metal abundances from Graedel *et al.* (1982); 5. depleted value from Neufeld *et al.* (2005).

Element	n_i/n_H^a	Ref.	Element	n_i/n_H^a	Ref.
H_2	0.5		He	9.0(-2)	1
N	6.2(-5)	2	O	2.4(-4)	3
C^+	1.7(-4)	2	S^+	1.5(-5)	2
Fe^+	3.0(-9)	4	Si^+	8.0(-9)	4
Na^+	2.0(-9)	4	Mg^+	7.0(-9)	4
Cl^+	1.0(-9)	4	P^+	2.0(-10)	4
F	6.7(-9)	5			

The temporal-evolution of the CH$_3$CCH abundance derived from the hot-core model for the different hydrogen densitites is presented in Figure 9.11. The abundance derived from our observations is best predicted by the model with $n_{H_2} = 5 \times 10^6$ at timescales as early as $\sim 10^3$ yr, in agreement with the expected age of this source (Merello *et al.* 2013a). This is consistent with an extended and thus less dense emitting gas, as was inferred from the radiative analyses. Furthermore, the steady-state plateau in abundance reached after $\sim 10^3$ yr is consistent with the hypothesis of CH$_3$CCH accumulating onto dust grains and enriching the gas-phase upon desorption. Experiments on interstellar ice analogues exposed to energetic electrons ensued the formation of CH$_3$CCH, among other related molecules (Abplanalp *et al.* 2019), which supports this hypothesis. Complementary observations of different species with related chemical networks are desirable to build a comprehensive view on the properties of the source, and will be included in future works focused on constructing a thorough chemical and physical model of G331.

9.6   Conclusions

We have conducted a spectral survey of CH$_3$CCH toward the Hot Molecular Core G331.512 − 0.103, resulting in the detection of 41 lines without contamination. To the best of our knowledge, this was the first spectral survey of methyl acetylene toward the source, resulting in interesting insights on the physics of the source. The spectral analysis was performed through rotational diagrams, assuming LTE, from which we derived an averaged excitation temperature of $\sim$50 K for an extended emission. Thus, the bulk of the CH$_3$CCH emission is likely originated from a warm and extended gas, associated with the ambient core region of G331.

---

[11]http://kida.obs.u-bordeaux1.fr/
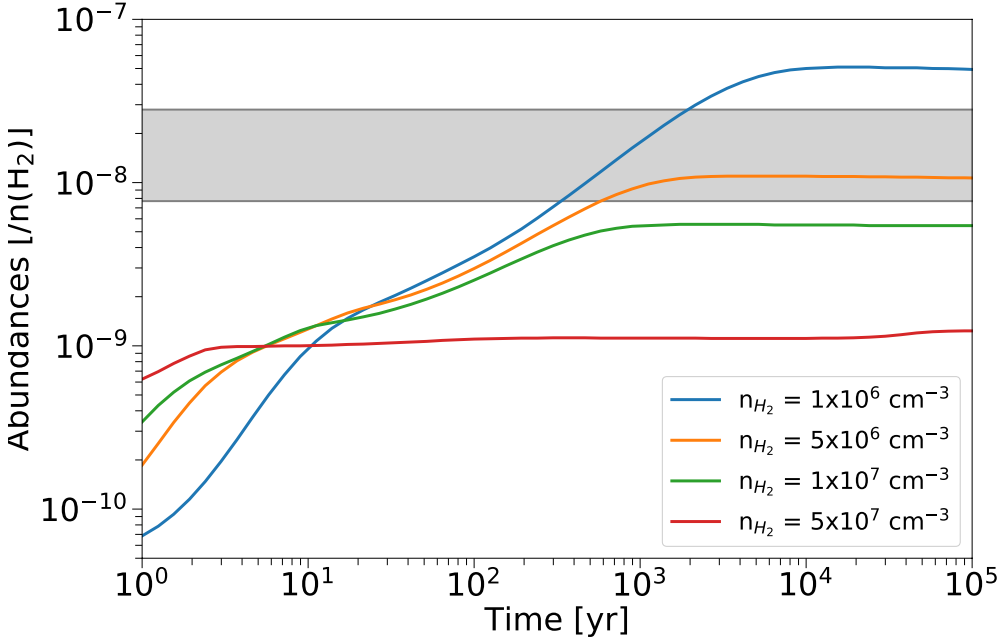
Figure 9.11: Abundance of CH_3CCH as a function of time, obtained from the hot-core model for different initial densities of H_2. The gray area indicates the methyl-acetylene abundance derived from the observations.

Moreover, we obtained $N(CH_3CCH)=7.5\times10^{15}cm^{-2}$, $X[CH_3CCH/H_2] \approx (0.77 - 2.8) \times 10^{-8}$ and $X[CH_3CCH/CH_3OH] \approx 0.42 \pm 0.05$ from the observations, which are consistent with other single-dish observational works toward massive star-forming regions and suggest that CH_3CCH is a zeroth-generation molecule with similar chemistry throughout these environments.

The $K=2/K=3$ line-intensity ratios of transitions within a given K-ladder are strongly negatively correlated with J_u, which firmly suggests that the emission is arising from a region with a temperature gradient. An analysis of the rotational diagram separated into two subsections provides upper and lower limits of, respectively, $\sim$60 and $\sim$45 K for the temperature gradient. This approach enables us to assess the small-scale structure of the source with data from single-dish facilities. For a thorough analysis of the temperature profile, however, it is imperative to observe a wide range of CH_3CCH lines with a high angular resolution, by means of interferometry instruments such as ALMA.

The line widths of transitions with the same K quantum number are strongly correlated to their rest frequencies and peak velocities. Thus, we infer that the warmer regions, traced by the higher-frequency lines, are also associated with higher turbulence effects. Moreover, the $K=0$ transitions seem to be tracing a slightly different region than the rest of the CH_3CCH lines, as indicated by its different kinematic signature. Surveys of this species with higher angular resolution are also fundamental to further explore the origin of this differentiation.

A chemical model of CH_3CCH in G331, comprising of a dark-cloud phase followed by a hot-core collapse, predicts CH_3CCH abundances that agree with our observations for timescales of $t \gtrsim 10^3$ yr and densities of $n_{H_2} \sim 5 \times 10^6$ cm^{-3}. This is in line with the expected age and size of this source.

9.7   Acknowledgments

9.8   Software

- CASSIS (Vastel *et al.* 2015);
- GILDAS (Pety *et al.* 2005; Gildas Team 2013);
- NAUTILUS (Ruaud *et al.* 2016);
- PGOPHER (Western 2016)

Bibliography

Abplanalp, M. J., Góbi, S. & Kaiser, R. I., 2019, Physical Chemistry Chemical Physics (Incorporating Faraday Transactions), 21, 10, 5378–5393, doi: 10.1039/C8CP03921F

Accolla, M., Congiu, E., Manicò, G., Dulieu, F., Chaabouni, H. *et al.*, 2013, MNRAS, 429, 4, 3200–3206, doi: 10.1093/mnras/sts578

Adriaens, D., Goumans, T., Catlow, C. & Brown, W., 2010, The Journal of Physical Chemistry C, 114, 4, 1892–1900

Agúndez, M., Marcelino, N., Cernicharo, J., Roueff, E. & Tafalla, M., 2019, A&A, 625, A147, doi: 10.1051/0004-6361/201935164

Agundez, M., Roueff, E., Cabezas, C., Cernicharo, J. & Marcelino, N., 2021, arXiv e-prints, arXiv:2104.04374

Agúndez, M., Molpeceres, G., Cabezas, C., Marcelino, N., Tercero, B. *et al.*, 2025, A&A, 693, L20, doi: 10.1051/0004-6361/202453459

Aikawa, Y., van Zadelhoff, G. J., van Dishoeck, E. F. & Herbst, E., 2002, A&A, 386, 622–632, doi: 10.1051/0004-6361:20020037

Allen, V., van der Tak, F. F. S. & Walsh, C., 2018, A&A, 616, A67, doi: 10.1051/0004-6361/201732553

Almond, V., Charles, S. W., MacDonald, J. N. & Owen, N. L., 1983, Journal of Molecular Structure, 100, 223–239

Altwegg, K., Balsiger, H., Berthelier, J. J., Bieler, A., Calmonte, U. *et al.*, 2017, Philosophical Transactions of the Royal Society of London Series A, 375, 2097, 20160253, doi: 10.1098/rsta.2016.0253

Altwegg, K., Balsiger, H., Berthelier, J.-J., Bieler, A., Calmonte, U. *et al.*, 2017, Monthly Notices of the Royal Astronomical Society, 469, Suppl_2, S130–S141

Altwegg, K., Combi, M., Fuselier, S. A., Hänni, N., De Keyser, J. *et al.*, 2022, MNRAS, 516, 3, 3900–3910, doi: 10.1093/mnras/stac2440

Álvarez-Barcia, S., Russ, P., Kästner, J. & Lamberts, T., 2018, MNRAS, 479, 2, 2007–2015, doi: 10.1093/mnras/sty1478

Anderson, D. E., Bergin, E. A., Maret, S. & Wakelam, V., 2013, ApJ, 779, 2, 141, doi: 10.1088/0004-637X/779/2/141

Andrews, S. M. & Williams, J. P., 2007, ApJ, 659, 1, 705–728, doi: 10.1086/511741

Andron, I., Gratier, P., Majumdar, L., Vidal, T. H. G., Coutens, A. *et al.*, 2018, MNRAS, 481, 4, 5651–5659, doi: 10.1093/mnras/sty2680

Anton, R., Wiegner, T., Naumann, W., Liebmann, M., Klein, C. & Bradley, C., 2000, Rev. Sci. Instrum., 71, 2, 1177–1180, doi: 10.1063/1.1150420

Arce, H. G., Santiago-García, J., Jørgensen, J. K., Tafalla, M. & Bachiller, R., 2008, ApJ, 681, 1, L21, doi: 10.1086/590110

Artur de la Villarmois, E., Guzmán, V. V., Yang, Y. L., Zhang, Y. & Sakai, N., 2023, A&A, 678, A124, doi: 10.1051/0004-6361/202346728

Asplund, M., Grevesse, N., Sauval, A. J. & Scott, P., 2009, ARA&A, 47, 1, 481–522, doi: 10.1146/annurev.astro.46.060407.145222

Atkinson, R., Baulch, D. L., Cox, R. A., Crowley, J. N., Hampson, R. F. *et al.*, 2004, Atmospheric Chemistry & Physics, 4, 6, 1461–1738, doi: 10.5194/acp-4-1461-200410.5194/acpd-3-6179-2003

Bacmann, A., Taquet, V., Faure, A., Kahane, C. & Ceccarelli, C., 2012, A&A, 541, L12, doi: 10.1051/0004-6361/201219207

Balucani, N., Ceccarelli, C. & Taquet, V., 2015, MNRAS, 449, L16–L20, doi: 10.1093/mnrasl/slv009

Bar-Nun, A., Kleinfeld, I. & Kochavi, E., 1988, Physical Review B, 38, 11, 7749–7754, doi: 10.1103/PhysRevB.38.7749

Bariosco, V., Pantaleone, S., Ceccarelli, C., Rimola, A., Balucani, N. *et al.*, 2024, MNRAS, 531, 1, 1371–1384, doi: 10.1093/mnras/stae1210

Bast, J. E., Lahuis, F., van Dishoeck, E. F. & Tielens, A. G. G. M., 2013, Astronomy and Astrophysics, 551, A118, doi: 10.1051/0004-6361/201219908

Behmard, A., Fayolle, E. C., Graninger, D. M., Bergner, J. B., Martín-Doménech, R. *et al.*, 2019, ApJ, 875, 1, 73, doi: 10.3847/1538-4357/ab0e7b

Belitsky, V., Lapkin, I., Fredrixon, M., Meledin, D., Sundin, E. *et al.*, 2018, A&A, 612, A23, doi: 10.1051/0004-6361/201731458

Belloche, A., Müller, H. S. P., Menten, K. M., Schilke, P. & Comito, C., 2013, A&A, 559, A47, doi: 10.1051/0004-6361/201321096

Belloche, A., Garrod, R. T., Müller, H. S. P. & Menten, K. M., 2014, Science, 345, 6204, 1584–1587, doi: 10.1126/science.1256678

Belloche, A., Garrod, R. T., Müller, H. S. P., Menten, K. M., Medvedev, I. *et al.*, 2019, A&A, 628, A10, doi: 10.1051/0004-6361/201935428

Bergin, E. A. & Langer, W. D., 1997, ApJ, 486, 1, 316–328, doi: 10.1086/304510

Bergin, E. A. & Tafalla, M., 2007, ARA&A, 45, 1, 339–396, doi: 10.1146/annurev.astro.45.071206.100404

Bergin, E. A., Goldsmith, P. F., Snell, R. L. & Ungerechts, H., 1994, ApJ, 431, 674, doi: 10.1086/174518

Bergner, J. B., Öberg, K. I., Rajappan, M. & Fayolle, E. C., 2016, ApJ, 829, 2, 85, doi: 10.3847/0004-637X/829/2/85

Bergner, J. B., Öberg, K. I. & Rajappan, M., 2017, ApJ, 845, 1, 29, doi: 10.3847/1538-4357/aa7d09

Bergner, J. B., Öberg, K. I. & Rajappan, M., 2019, The Astrophysical Journal, 874, 2, 115, doi: 10.3847/1538-4357/ab07b2

Bergner, J. B., Rajappan, M. & Öberg, K. I., 2022, ApJ, 933, 2, 206, doi: 10.3847/1538-4357/ac771e

Bertin, M., Fayolle, E. C., Romanzin, C., Poderoso, H. A. M., Michaut, X. *et al.*, 2013, ApJ, 779, 2, 120, doi: 10.1088/0004-637X/779/2/120

Bertin, M., Romanzin, C., Doronin, M., Philippe, L., Jeseck, P. *et al.*, 2016, ApJ, 817, 2, L12, doi: 10.3847/2041-8205/817/2/L12

Beuther, H., Churchwell, E. B., McKee, C. F. & Tan, J. C., 2007, B. Reipurth, D. Jewitt & K. Keil, editors, Protostars and Planets V, 165, doi: 10.48550/arXiv.astro-ph/0602012

Beuther, H., Kuiper, R. & Tafalla, M., 2025, arXiv e-prints, arXiv:2501.16866, doi: 10.48550/arXiv.2501.16866

Bisschop, S. E., Fraser, H. J., Öberg, K. I., van Dishoeck, E. F. & Schlemmer, S., 2006, A&A, 449, 3, 1297–1309, doi: 10.1051/0004-6361:20054051

Bisschop, S. E., Jørgensen, J. K., van Dishoeck, E. F. & de Wachter, E. B. M., 2007, A&A, 465, 3, 913–929, doi: 10.1051/0004-6361:20065963

Biver, N., Bockelée-Morvan, D., Debout, V., Crovisier, J., Boissier, J. *et al.*, 2014, Astronomy and Astrophysics, 566, L5, doi: 10.1051/0004-6361/201423890

Biver, N., Bockelée-Morvan, D., Moreno, R., Crovisier, J., Colom, P. *et al.*, 2015, Science Advances, 1, 9, 1500863, doi: 10.1126/sciadv.1500863

Biver, N., Bockelée-Morvan, D., Boissier, J., Moreno, R., Crovisier, J. *et al.*, 2021a, A&A, 648, A49, doi: 10.1051/0004-6361/202040125

Biver, N., Bockelée-Morvan, D., Lis, D. C., Despois, D., Moreno, R. *et al.*, 2021b, A&A, 651, A25, doi: 10.1051/0004-6361/202140765

Blake, G. A., Sutton, E. C., Masson, C. R. & Phillips, T. G., 1987, ApJ, 315, 621, doi: 10.1086/165165

Blake, G. A., van Dishoeck, E. F., Jansen, D. J., Groesbeck, T. D. & Mundy, L. G., 1994, ApJ, 428, 680, doi: 10.1086/174278

Blitz, M. A., McKee, K. W. & Pilling, M. J., 2000, Proceedings of the Combustion Institute, 28, 2, 2491–2497

Bockelée-Morvan, D., Lis, D. C., Wink, J. E., Despois, D., Crovisier, J. *et al.*, 2000a, A&A, 353, 1101–1114

Bockelée-Morvan, D., Lis, D. C., Wink, J. E., Despois, D., Crovisier, J. *et al.*, 2000b, Astronomy and Astrophysics, 353, 1101–1114

Bøgelund, E. G., Barr, A. G., Taquet, V., Ligterink, N. F. W., Persson, M. V. *et al.*, 2019, A&A, 628, A2, doi: 10.1051/0004-6361/201834527

Bonfand, M., Belloche, A., Garrod, R. T., Menten, K. M., Willis, E. *et al.*, 2019, A&A, 628, A27, doi: 10.1051/0004-6361/201935523

Bonnell, I. A. & Bate, M. R., 2006, MNRAS, 370, 1, 488–494, doi: 10.1111/j.1365-2966.2006.10495.x

Bonnell, I. A., Bate, M. R. & Zinnecker, H., 1998, MNRAS, 298, 1, 93–102, doi: 10.1046/j.1365-8711.1998.01590.x

Boogert, A. C. A., Schutte, W. A., Helmich, F. P., Tielens, A. G. G. M. & Wooden, D. H., 1997, A&A, 317, 929–941

Boogert, A. C. A., Blake, G. A. & Tielens, A. G. G. M., 2002, ApJ, 577, 1, 271–280, doi: 10.1086/342176

Boogert, A. C. A., Gerakines, P. A. & Whittet, D. C. B., 2015, ARA&A, 53, 541–581, doi: 10.1146/annurev-astro-082214-122348

Boogert, A. C. A., Brewer, K., Brittain, A. & Emerson, K. S., 2022, ApJ, 941, 1, 32, doi: 10.3847/1538-4357/ac9b4a

Booth, A. S., Temmink, M., van Dishoeck, E. F., Evans, L., Ilee, J. D. *et al.*, 2024, AJ, 167, 4, 165, doi: 10.3847/1538-3881/ad26ff

Boss, A. P., 1997, Science, 276, 1836–1839, doi: 10.1126/science.276.5320.1836

Bossa, J. B., Isokoski, K., de Valois, M. S. & Linnartz, H., 2012, A&A, 545, A82, doi: 10.1051/0004-6361/201219340

Bottinelli, S., Boogert, A. C. A., Bouwman, J., Beckwith, M., van Dishoeck, E. F. *et al.*, 2010, ApJ, 718, 2, 1100–1117, doi: 10.1088/0004-637X/718/2/1100

Boudin, N., Schutte, W. A. & Greenberg, J. M., 1998, Astronomy and Astrophysics, 331, 749–759

Bouilloud, M., Fray, N., Bénilan, Y., Cottin, H., Gazeau, M. C. & Jolly, A., 2015, MNRAS, 451, 2, 2145–2160, doi: 10.1093/mnras/stv1021

Bouscasse, L., Csengeri, T., Belloche, A., Wyrowski, F., Bontemps, S. *et al.*, 2022, A&A, 662, A32, doi: 10.1051/0004-6361/202140519

Breck, D., 1973, Zeolite Molecular Sieves: Structure, Chemistry, and Use, Wiley

Brittain, S. D., Kamp, I., Meeus, G., Oudmaijer, R. D. & Waters, L. B. F. M., 2023, Space Sci. Rev., 219, 1, 7, doi: 10.1007/s11214-023-00949-z

Bronfman, L., Cohen, R. S., Thaddeus, P. & Alvarez, H., 1985, H. van Woerden, R. J. Allen & W. B. Burton, editors, The Milky Way Galaxy, volume 106, 331

Bronfman, L., Casassus, S., May, J. & Nyman, L. Å., 2000, A&A, 358, 521–534

Bronfman, L., Garay, G., Merello, M., Mardones, D., May, J. *et al.*, 2008, ApJ, 672, 1, 391–397, doi: 10.1086/522487

Brunken, N. G. C., Booth, A. S., Leemker, M., Nazari, P., van der Marel, N. & van Dishoeck, E. F., 2022, Astronomy and Astrophysics, 659, A29, doi: 10.1051/0004-6361/202142981

Buhl, D. & Snyder, L. E., 1973, M. A. Gordon & L. E. Snyder, editors, Molecules in the Galactic Environment, 187

Bull, J. N. & Harland, P. W., 2008, International Journal of Mass Spectrometry, 273, 1, 53–57, doi: https://doi.org/10.1016/j.ijms.2008.03.003

Bull, J. N., Harland, P. W. & Vallance, C., 2012, The Journal of Physical Chemistry A, 116, 1, 767–777, doi: 10.1021/jp210294p, pMID: 22142325

Burke, D. J. & Brown, W. A., 2010, Physical Chemistry Chemical Physics (Incorporating Faraday Transactions), 12, 23, 5947, doi: 10.1039/b917005g

Butscher, T., Duvernay, F., Theule, P., Danger, G., Carissan, Y. *et al.*, 2015, Monthly Notices of the Royal Astronomical Society, 453, 2, 1587–1596, doi: 10.1093/mnras/stv1706

Calcutt, H., Willis, E. R., Jørgensen, J. K., Bjerkeli, P., Ligterink, N. F. W. *et al.*, 2019, A&A, 631, A137, doi: 10.1051/0004-6361/201936323

Calmonte, U., Altwegg, K., Balsiger, H., Berthelier, J. J., Bieler, A. *et al.*, 2016, MNRAS, 462, S253–S273, doi: 10.1093/mnras/stw2601

Canelo, C. M., Bronfman, L., Mendoza, E., Duronea, N., Merello, M. *et al.*, 2021, MNRAS, 504, 3, 4428–4444, doi: 10.1093/mnras/stab1163

Canta, A., Öberg, K. I. & Rajappan, M., 2023, The Astrophysical Journal, 953, 1, 81, doi: 10.3847/1538-4357/acda99

Capon, B. & Zucco, C., 1982, Journal of the American Chemical Society, 104, 26, 7567–7572

Carmack, R. A., Tribbett, P. D. & Loeffler, M. J., 2023, ApJ, 942, 1, 1, doi: 10.3847/1538-4357/aca76b

Carrascosa, H., Satorre, M. Á., Escribano, B., Martín-Doménech, R. & Muñoz Caro, G. M., 2023, MNRAS, 525, 2, 2690–2700, doi: 10.1093/mnras/stad2462

Cartwright, R. J., Nordheim, T. A., Cruikshank, D. P., Hand, K. P., Roser, J. E. *et al.*, 2020, ApJ, 902, 2, L38, doi: 10.3847/2041-8213/abbdae

Caselli, P. & Ceccarelli, C., 2012, A&A Rev., 20, 56, doi: 10.1007/s00159-012-0056-x

Caselli, P., Hasegawa, T. I. & Herbst, E., 1993, ApJ, 408, 548, doi: 10.1086/172612

Cazaux, S., Cobut, V., Marseille, M., Spaans, M. & Caselli, P., 2010, A&A, 522, A74, doi: 10.1051/0004-6361/201014026

Cazaux, S., Bossa, J. B., Linnartz, H. & Tielens, A. G. G. M., 2015, A&A, 573, A16, doi: 10.1051/0004-6361/201424466

Cazaux, S., Carrascosa, H., Muñoz Caro, G. M., Caselli, P., Fuente, A. *et al.*, 2022, A&A, 657, A100, doi: 10.1051/0004-6361/202141861

Cazzoli, G., Lattanzi, V., Kirsch, T., Gauss, J., Tercero, B. *et al.*, 2016, A&A, 591, A126, doi: 10.1051/0004-6361/201628745

Ceccarelli, C., Caselli, P., Bockelée-Morvan, D., Mousis, O., Pizzarello, S. *et al.*, 2014, H. Beuther, R. S. Klessen, C. P. Dullemond & T. Henning, editors, Protostars and Planets VI, 859–882, doi: 10.2458/azu_uapress_9780816531240-ch037

Cecchi-Pestellini, C. & Aiello, S., 1992, MNRAS, 258, 1, 125–133, doi: 10.1093/mnras/258.1.125

Cernicharo, J., Spielfiedel, A., Balança, C., Dayou, F., Senent, M. L. *et al.*, 2011, A&A, 531, A103, doi: 10.1051/0004-6361/201016216

Cernicharo, J., Marcelino, N., Roueff, E., Gerin, M., Jiménez-Escobar, A. & Muñoz Caro, G. M., 2012, ApJ, 759, 2, L43, doi: 10.1088/2041-8205/759/2/L43

Cernicharo, J., McCarthy, M. C., Gottlieb, C. A., Agúndez, M., Velilla Prieto, L. *et al.*, 2015, ApJ, 806, 1, L3, doi: 10.1088/2041-8205/806/1/L3

Cernicharo, J., Cabezas, C., Agúndez, M., Tercero, B., Pardo, J. R. *et al.*, 2021, Astronomy and Astrophysics, 648, L3, doi: 10.1051/0004-6361/202140642

Cerqueira, H. B. A., Santos, J. C., Fantuzzi, F., Ribeiro, F. d. A., Rocco, M. L. M. *et al.*, 2020, The Journal of Physical Chemistry A, 124, 34, 6845–6855, doi: 10.1021/acs.jpca.0c03529, pMID: 32702984

Cesaroni, R., 2005, R. Cesaroni, M. Felli, E. Churchwell & M. Walmsley, editors, Massive Star Birth: A Crossroads of Astrophysics, volume 227, 59–69, doi: 10.1017/S1743921305004369

Cesaroni, R., Hofner, P., Walmsley, C. M. & Churchwell, E., 1998, A&A, 331, 709–725

Cesaroni, R., Hofner, P., Araya, E. & Kurtz, S., 2010, A&A, 509, A50, doi: 10.1051/0004-6361/200912877

Charnley, S., 2004, Advances in Space Research, 33, 1, 23–30

Charnley, S. B., 1997, ApJ, 481, 1, 396–405, doi: 10.1086/304011

Charnley, S. B. & Tielens, A. G. G. M., 1992, P. D. Singh, editor, Astrochemistry of Cosmic Phenomena, volume 150, 317

Charnley, S. B., Tielens, A. G. G. M. & Millar, T. J., 1992, ApJ, 399, L71, doi: 10.1086/186609

Chen, L., Schwarzer, D., Verma, V. B., Stevens, M. J., Marsili, F. *et al.*, 2017, Accounts of Chemical Research, 50, 6, 1400–1409, doi: 10.1021/acs.accounts.7b00071, pMID: 28573866

Chen, L., Lau, J. A., Schwarzer, D., Meyer, J., Verma, V. B. & Wodtke, A. M., 2019, Science, 363, 6423, 158–161, doi: 10.1126/science.aav4278

Chen, Y., van Gelder, M. L., Nazari, P., Brogan, C. L., van Dishoeck, E. F. *et al.*, 2023, A&A, 678, A137, doi: 10.1051/0004-6361/202346491

Chen, Y. J., Chuang, K. J., Muñoz Caro, G. M., Nuevo, M., Chu, C. C. *et al.*, 2014, ApJ, 781, 1, 15, doi: 10.1088/0004-637X/781/1/15

Chen, Y. J., Juang, K. J., Nuevo, M., Jiménez-Escobar, A., Muñoz Caro, G. M. *et al.*, 2015, ApJ, 798, 2, 80, doi: 10.1088/0004-637X/798/2/80

Chiar, J. E., Tielens, A. G. G. M., Adamson, A. J. & Ricca, A., 2013, ApJ, 770, 1, 78, doi: 10.1088/0004-637X/770/1/78

Chuang, K.-J., 2018, Ph.D. thesis, Leiden University

Chuang, K. J., Fedoseev, G., Ioppolo, S., van Dishoeck, E. F. & Linnartz, H., 2016, MNRAS, 455, 2, 1702–1712, doi: 10.1093/mnras/stv2288

Chuang, K. J., Fedoseev, G., Qasim, D., Ioppolo, S., van Dishoeck, E. F. & Linnartz, H., 2018, ApJ, 853, 2, 102, doi: 10.3847/1538-4357/aaa24e

Chuang, K. J., Fedoseev, G., Qasim, D., Ioppolo, S., Jäger, C. *et al.*, 2020, Astronomy and Astrophysics, 635, A199, doi: 10.1051/0004-6361/201937302

Chuang, K. J., Fedoseev, G., Scirè, C., Baratta, G. A., Jäger, C. *et al.*, 2021, A&A, 650, A85, doi: 10.1051/0004-6361/202140780

Chuang, K.-J., Jäger, C., Santos, J. & Henning, T., 2024, arXiv preprint arXiv:2405.07855

Churchwell, E. & Hollis, J. M., 1983, ApJ, 272, 591–608, doi: 10.1086/161322

Codella, C., Bianchi, E., Podio, L., Mercimek, S., Ceccarelli, C. *et al.*, 2021, A&A, 654, A52, doi: 10.1051/0004-6361/202141485

Collings, M. P., Anderson, M. A., Chen, R., Dever, J. W., Viti, S. *et al.*, 2004, MNRAS, 354, 4, 1133–1140, doi: 10.1111/j.1365-2966.2004.08272.x

Comito, C., Schilke, P., Phillips, T. G., Lis, D. C., Motte, F. & Mehringer, D., 2005, ApJS, 156, 2, 127–167, doi: 10.1086/425996

Congiu, E., Minissale, M., Baouche, S., Chaabouni, H., Moudens, A. *et al.*, 2014, Faraday Discussions, 168, 151, doi: 10.1039/C4FD00002A

Cooke, I. R., Fayolle, E. C. & Öberg, K. I., 2016, ApJ, 832, 1, 5, doi: 10.3847/0004-637X/832/1/5

Corcelli, S. A. & Tully, J. C., 2002, The Journal of Chemical Physics, 116, 18, 8079–8092, doi: 10.1063/1.1467056

Coussan, S., Noble, J. A., Cuppen, H. M., Redlich, B. & Ioppolo, S., 2022, Journal of Physical Chemistry A, 126, 14, 2262–2269, doi: 10.1021/acs.jpca.2c00054

Coutens, A., Jørgensen, J. K., van der Wiel, M. H. D., Müller, H. S. P., Lykke, J. M. *et al.*, 2016, A&A, 590, L6, doi: 10.1051/0004-6361/201628612

Crapsi, A., Caselli, P., Walmsley, M. C. & Tafalla, M., 2007, A&A, 470, 1, 221–230, doi: 10.1051/0004-6361:20077613

Craw, J. S. & Bacskay, G. B., 1992, Journal of the Chemical Society, Faraday Transactions, 88, 16, 2315–2321

Cruz-Diaz, G. A., Martín-Doménech, R., Muñoz Caro, G. M. & Chen, Y. J., 2016, A&A, 592, A68, doi: 10.1051/0004-6361/201526761

Cuppen, H. M., van Dishoeck, E. F., Herbst, E. & Tielens, A. G. G. M., 2009, A&A, 508, 1, 275–287, doi: 10.1051/0004-6361/200913119

Cuppen, H. M., Ioppolo, S., Romanzin, C. & Linnartz, H., 2010, Physical Chemistry Chemical Physics (Incorporating Faraday Transactions), 12, 38, 12077, doi: 10.1039/C0CP00251H

Cuppen, H. M., Penteado, E. M., Isokoski, K., van der Marel, N. & Linnartz, H., 2011, MNRAS, 417, 4, 2809–2816, doi: 10.1111/j.1365-2966.2011.19443.x

Cuppen, H. M., Walsh, C., Lamberts, T., Semenov, D., Garrod, R. T. *et al.*, 2017, Space Sci. Rev., 212, 1-2, 1–58, doi: 10.1007/s11214-016-0319-3

Cuppen, H. M., Noble, J. A., Coussan, S., Redlich, B. & Ioppolo, S., 2022, The Journal of Physical Chemistry A, 0, 0, null, doi: 10.1021/acs.jpca.2c06314, pMID: 36383692

Cuppen, H. M., Linnartz, H. & Ioppolo, S., 2024, arXiv e-prints, arXiv:2407.06657, doi: 10.48550/arXiv.2407.06657

Dartois, E., Chabot, M., Id Barkach, T., Rothard, H., Augé, B. *et al.*, 2018, A&A, 618, A173, doi: 10.1051/0004-6361/201833277

Das, A., Sil, M., Gorai, P., Chakrabarti, S. K. & Loison, J. C., 2018, ApJS, 237, 1, 9, doi: 10.3847/1538-4365/aac886

De Simone, M., Ceccarelli, C., Codella, C., Svoboda, B. E., Chandler, C. *et al.*, 2020, ApJ, 896, 1, L3, doi: 10.3847/2041-8213/ab8d41

De Vos, R. M. & Verweij, H., 1998, Science, 279, 5357, 1710–1711

DeLeon, R. L. & Rich, J. W., 1986, Chemical Physics, 107, 2, 283–292, doi: 10.1016/0301-0104(86)85008-X

Dello Russo, N., DiSanti, M. A., Mumma, M. J., Magee-Sauer, K. & Rettig, T. W., 1998, ICARUS, 135, 2, 377–388, doi: 10.1006/icar.1998.5990

Dello Russo, N., Kawakita, H., Vervack, R. J. & Weaver, H. A., 2016, ICARUS, 278, 301–332, doi: 10.1016/j.icarus.2016.05.039

Delsemme, A. H., 1991, J. Newburn, R. L., M. Neugebauer & J. Rahe, editors, IAU Colloq. 116: Comets in the post-Halley era, volume 167 of *Astrophysics and Space Science Library*, 377, doi: 10.1007/978-94-011-3378-4_17

DeVine, J. A., Choudhury, A., Lau, J. A., Schwarzer, D. & Wodtke, A. M., 2022, Journal of Physical Chemistry A, 126, 14, 2270–2277, doi: 10.1021/acs.jpca.2c01168

Di Francesco, J., André, P. & Myers, P. C., 2004, ApJ, 617, 1, 425–438, doi: 10.1086/425264

Domenicano, A. & Hargittai, I., 1992, Accurate Molecular Structures: Their Determination and Importance, Oxford University Press

Doronin, M., Bertin, M., Michaut, X., Philippe, L. & Fillion, J. H., 2015, J. Chem. Phys., 143, 8, 084703, doi: 10.1063/1.4929376

Draine, B. T., 2003, ARA&A, 41, 241–289, doi: 10.1146/annurev.astro.41.011802.094840

Draine, B. T. & Li, A., 2001, ApJ, 551, 2, 807–824, doi: 10.1086/320227

Drdla, K., Knapp, G. R. & van Dishoeck, E. F., 1989, ApJ, 345, 815, doi: 10.1086/167953

Drozdovskaya, M. N., Walsh, C., Visser, R., Harsono, D. & van Dishoeck, E. F., 2015, MNRAS, 451, 4, 3836–3856, doi: 10.1093/mnras/stv1177

Drozdovskaya, M. N., van Dishoeck, E. F., Jørgensen, J. K., Calmonte, U., van der Wiel, M. H. D. *et al.*, 2018, MNRAS, 476, 4, 4949–4964, doi: 10.1093/mnras/sty462

Drozdovskaya, M. N., van Dishoeck, E. F., Rubin, M., Jørgensen, J. K. & Altwegg, K., 2019, MNRAS, 490, 1, 50–79, doi: 10.1093/mnras/stz2430

Druard, C. & Wakelam, V., 2012, MNRAS, 426, 1, 354–359, doi: 10.1111/j.1365-2966.2012.21712.x

Dubrulle, A., Boucher, D., Burie, J. & Demaison, J., 1978, Journal of Molecular Spectroscopy, 72, 1, 158 – 164, doi: https://doi.org/10.1016/0022-2852(78)90051-6

Dulieu, F., Amiaud, L., Congiu, E., Fillion, J. H., Matar, E. *et al.*, 2010, A&A, 512, A30, doi: 10.1051/0004-6361/200912079

Dulieu, F., Congiu, E., Noble, J., Baouche, S., Chaabouni, H. *et al.*, 2013, Scientific Reports, 3, 1338, doi: 10.1038/srep01338

Dumke, M. & Mac-Auliffe, F., 2010, Observatory Operations: Strategies, Processes, and Systems III, volume 7737 of *Proc. SPIE*, 77371J, doi: 10.1117/12.858020

Dungee, R., Boogert, A., DeWitt, C. N., Montiel, E., Richter, M. J. *et al.*, 2018, ApJ, 868, 1, L10, doi: 10.3847/2041-8213/aaeda9

Dunning Jr, T. H., 1989, The Journal of chemical physics, 90, 2, 1007–1023

Duronea, N. U., Bronfman, L., Mendoza, E., Merello, M., Finger, R. *et al.*, 2019, MNRAS, 489, 2, 1519–1532, doi: 10.1093/mnras/stz2087

Edridge, J. L., Freimann, K., Burke, D. J. & Brown, W. A., 2013, Philosophical Transactions of the Royal Society of London Series A, 371, 1994, 20110578–20110578, doi: 10.1098/rsta.2011.0578

Elia, D., Molinari, S., Schisano, E., Pestalozzi, M., Pezzuto, S. *et al.*, 2017, MNRAS, 471, 1, 100–143, doi: 10.1093/mnras/stx1357

Elia, D., Merello, M., Molinari, S., Schisano, E., Zavagno, A. *et al.*, 2021, MNRAS, 504, 2, 2742–2766, doi: 10.1093/mnras/stab1038

Endres, C. P., Schlemmer, S., Schilke, P., Stutzki, J. & Müller, H. S. P., 2016, Journal of Molecular Spectroscopy, 327, 95–104, doi: 10.1016/j.jms.2016.03.005

Enrique-Romero, J., Rimola, A., Ceccarelli, C., Ugliengo, P., Balucani, N. & Skouteris, D., 2022, The Astrophysical Journal Supplement Series, 259, 2, 39

Esplugues, G., Fuente, A., Navarro-Almaida, D., Rodríguez-Baras, M., Majumdar, L. *et al.*, 2022, A&A, 662, A52, doi: 10.1051/0004-6361/202142936

Esplugues, G., Rodríguez-Baras, M., San Andrés, D., Navarro-Almaida, D., Fuente, A. *et al.*, 2023, A&A, 678, A199, doi: 10.1051/0004-6361/202346721

Esplugues, G. B., Viti, S., Goicoechea, J. R. & Cernicharo, J., 2014, A&A, 567, A95, doi: 10.1051/0004-6361/201323010

Fathe, K., Holt, J. S., Oxley, S. P. & Pursell, C. J., 2006, The Journal of Physical Chemistry A, 110, 37, 10793–10798

Favre, C., Fedele, D., Semenov, D., Parfenov, S., Codella, C. *et al.*, 2018, The Astrophysical Journal Letters, 862, 1, L2, doi: 10.3847/2041-8213/aad046

Fayolle, E. C., Bertin, M., Romanzin, C., Michaut, X., Öberg, K. I. *et al.*, 2011, ApJ, 739, 2, L36, doi: 10.1088/2041-8205/739/2/L36

Fayolle, E. C., Bertin, M., Romanzin, C., Poderoso, H. A. M., Philippe, L. *et al.*, 2013, A&A, 556, A122, doi: 10.1051/0004-6361/201321533

Fayolle, E. C., Öberg, K. I., Garrod, R. T., van Dishoeck, E. F. & Bisschop, S. E., 2015, A&A, 576, A45, doi: 10.1051/0004-6361/201323114

Fayolle, E. C., Balfe, J., Loomis, R., Bergner, J., Graninger, D. *et al.*, 2016, ApJ, 816, 2, L28, doi: 10.3847/2041-8205/816/2/L28

Fedoseev, G., Cuppen, H. M., Ioppolo, S., Lamberts, T. & Linnartz, H., 2015a, MNRAS, 448, 2, 1288–1297, doi: 10.1093/mnras/stu2603

Fedoseev, G., Ioppolo, S. & Linnartz, H., 2015b, MNRAS, 446, 1, 449–458, doi: 10.1093/mnras/stu1852

Fedoseev, G., Chuang, K. J., Ioppolo, S., Qasim, D., van Dishoeck, E. F. & Linnartz, H., 2017, The Astrophysical Journal, 842, 1, 52, doi: 10.3847/1538-4357/aa74dc

Ferrante, R. F., Moore, M. H., Spiliotis, M. M. & Hudson, R. L., 2008, ApJ, 684, 2, 1210–1220, doi: 10.1086/590362

Ferrero, S., Zamirri, L., Ceccarelli, C., Witzel, A., Rimola, A. & Ugliengo, P., 2020, ApJ, 904, 1, 11, doi: 10.3847/1538-4357/abb953

Ferrero, S., Pantaleone, S., Ceccarelli, C., Ugliengo, P., Sodupe, M. & Rimola, A., 2023, The Astrophysical Journal, 944, 2, 142, doi: 10.3847/1538-4357/acae8e

Fillion, J.-H., Fayolle, E. C., Michaut, X., Doronin, M., Philippe, L. et al., 2014, Faraday Discussions, 168, 533–552, doi: 10.1039/C3FD00129F

Focsa, C., Chazallon, B. & Destombes, J., 2003, Surface Science, 528, 1, 189–195, doi: https://doi.org/10.1016/S0039-6028(02)02631-6, proceedings of the Ninth International Workshop on Desorption Induced by Electronic Transitions

Focsa, C., Mihesan, C., Ziskind, M., Chazallon, B., Therssen, E. et al., 2006, Journal of Physics Condensed Matter, 18, 30, S1357–S1387, doi: 10.1088/0953-8984/18/30/S02

Fontani, F., Cesaroni, R., Caselli, P. & Olmi, L., 2002, A&A, 389, 603–617, doi: 10.1051/0004-6361:20020579

Fontani, F., Roueff, E., Colzi, L. & Caselli, P., 2023, A&A, 680, A58, doi: 10.1051/0004-6361/202347565

Pineau des Forêts, G., Roueff, E., Schilke, P. & Flower, D. R., 1993, MNRAS, 262, 4, 915–928

Fraser, H. J., Collings, M. P., McCoustra, M. R. S. & Williams, D. A., 2001, MNRAS, 327, 4, 1165–1172, doi: 10.1046/j.1365-8711.2001.04835.x

Fredon, A., Groenenboom, G. C. & Cuppen, H. M., 2021, ACS Earth and Space Chemistry, 5, 8, 2032–2041, doi: 10.1021/acsearthspacechem.1c00116

Fredon, A., Radchenko, A. K. & Cuppen, H. M., 2021, Accounts of Chemical Research, 54, 4, 745–753, doi: 10.1021/acs.accounts.0c00636, pMID: 33502177

Frisch, M. J., Trucks, G. W., Schlegel, H. B., Scuseria, G. E., Robb, M. A. et al., 2016, Gaussian~16 Revision C.01, gaussian Inc. Wallingford CT

Fuchs, G. W., Cuppen, H. M., Ioppolo, S., Romanzin, C., Bisschop, S. E. et al., 2009, A&A, 505, 2, 629–639, doi: 10.1051/0004-6361/200810784

Fuente, A., Cernicharo, J., Agúndez, M., Berné, O., Goicoechea, J. R. et al., 2010, A&A, 524, A19, doi: 10.1051/0004-6361/201014905

Fuente, A., Navarro, D. G., Caselli, P., Gerin, M., Kramer, C. et al., 2019, A&A, 624, A105, doi: 10.1051/0004-6361/201834654

Fuente, A., Treviño-Morales, S. P., Alonso-Albi, T., Sánchez-Monge, A., Rivière-Marichalar, P. & Navarro-Almaida, D., 2021, MNRAS, 507, 2, 1886–1898, doi: 10.1093/mnras/stab2216

Fuente, A., Rivière-Marichalar, P., Beitia-Antero, L., Caselli, P., Wakelam, V. et al., 2023, A&A, 670, A114, doi: 10.1051/0004-6361/202244843

Furuya, K., Oba, Y. & Shimonishi, T., 2022, ApJ, 926, 2, 171, doi: 10.3847/1538-4357/ac4260

Garay, G. & Lizano, S., 1999, PASP, 111, 763, 1049–1087, doi: 10.1086/316416

García, P., Bronfman, L., Nyman, L.-Å., Dame, T. M. & Luna, A., 2014, ApJS, 212, 1, 2, doi: 10.1088/0067-0049/212/1/2

Garozzo, M., Fulvio, D., Kanuchova, Z., Palumbo, M. E. & Strazzulla, G., 2010, A&A, 509, A67, doi: 10.1051/0004-6361/200913040

Garrod, R., Park, I. H., Caselli, P. & Herbst, E., 2006, Faraday Discussions, 133, 51, doi: 10.1039/b516202e

Garrod, R. T. & Pauly, T., 2011, ApJ, 735, 1, 15, doi: 10.1088/0004-637X/735/1/15

Garrod, R. T., Wakelam, V. & Herbst, E., 2007, A&A, 467, 3, 1103–1115, doi: 10.1051/0004-6361:20066704

Garrod, R. T., Widicus Weaver, S. L. & Herbst, E., 2008, ApJ, 682, 1, 283–302, doi: 10.1086/588035

Garrod, R. T., Jin, M., Matis, K. A., Jones, D., Willis, E. R. & Herbst, E., 2022, The Astrophysical Journal Supplement Series, 259, 1, 1, doi: 10.3847/1538-4365/ac3131

Geppert, W., 2006, Complex Molecules in Space: Present Status and Prospects with ALMA, 37

Geppert, W. D., Hellberg, F., Österdahl, F., Semaniak, J., Millar, T. J. *et al.*, 2005, Proc. Int. Astron. Union, 1, S231, 117–124, doi: 10.1017/S1743921306007101

Gerakines, P. A. & Hudson, R. L., 2020, ApJ, 901, 1, 52, doi: 10.3847/1538-4357/abad39

Gerakines, P. A., Schutte, W. A., Greenberg, J. M. & van Dishoeck, E. F., 1995, A&A, 296, 810, doi: 10.48550/arXiv.astro-ph/9409076

Gerin, M., Combes, F., Wlodarczak, G., Encrenaz, P. & Laurent, C., 1992a, A&A, 253, L29–L32

Gerin, M., Viala, Y., Pauzat, F. & Ellinger, Y., 1992b, A&A, 266, 463–478

Gerin, M., Neufeld, D. A. & Goicoechea, J. R., 2016, ARA&A, 54, 181–225, doi: 10.1146/annurev-astro-081915-023409

Giannetti, A., Leurini, S., Wyrowski, F., Urquhart, J., Csengeri, T. *et al.*, 2017, A&A, 603, A33, doi: 10.1051/0004-6361/201630048

Gibb, E., Nummelin, A., Irvine, W. M., Whittet, D. C. B. & Bergman, P., 2000, ApJ, 545, 1, 309–326, doi: 10.1086/317805

Gibb, E. L., Van Brunt, K. A., Brittain, S. D. & Rettig, T. W., 2007, The Astrophysical Journal, 660, 2, 1572–1579, doi: 10.1086/513502

Gieser, C., Semenov, D., Beuther, H., Ahmadi, A., Mottram, J. C. *et al.*, 2019, A&A, 631, A142, doi: 10.1051/0004-6361/201935865

Gieser, C., Beuther, H., Semenov, D., Ahmadi, A., Suri, S. *et al.*, 2021, A&A, 648, A66, doi: 10.1051/0004-6361/202039670

Gildas Team, 2013, GILDAS: Grenoble Image and Line Data Analysis Software

Gillett, F. C. & Forrest, W. J., 1973, ApJ, 179, 483, doi: 10.1086/151888

Goicoechea, J. R., Aguado, A., Cuadrado, S., Roncero, O., Pety, J. *et al.*, 2021, A&A, 647, A10, doi: 10.1051/0004-6361/202039756

Goldsmith, P. F. & Langer, W. D., 1999, ApJ, 517, 1, 209–225, doi: 10.1086/307195

Goldsmith, P. F. & Li, D., 2005, ApJ, 622, 2, 938–958, doi: 10.1086/428032

Gomez, Y., Garay, G. & Lizano, S., 1995, ApJ, 453, 727, doi: 10.1086/176434

Goumans, T. P. M., 2011, MNRAS, 413, 4, 2615–2620, doi: 10.1111/j.1365-2966.2011.18329.x

Goumans, T. P. M., Uppal, M. A. & Brown, W. A., 2008, MNRAS, 384, 3, 1158–1164, doi: 10.1111/j.1365-2966.2007.12788.x

Graedel, T. E., Langer, W. D. & Frerking, M. A., 1982, ApJS, 48, 321–368, doi: 10.1086/190780

Grubbs, G. & Cooke, S., 2010, Journal of Molecular Spectroscopy, 259, 2, 120 – 122, doi: https://doi.org/10.1016/j.jms.2009.12.003

Gussoni, M., Rui, M. & Zerbi, G., 1998, Journal of molecular structure, 447, 3, 163–215

Güsten, R., Nyman, L. Å., Schilke, P., Menten, K., Cesarsky, C. & Booth, R., 2006, A&A, 454, L13–L16, doi: 10.1051/0004-6361:20065420

Guzmán, A. E., Guzmán, V. V., Garay, G., Bronfman, L. & Hechenleitner, F., 2018, ApJS, 236, 2, 45, doi: 10.3847/1538-4365/aac01d

Haas, M. R., Davidson, J. A. & Erickson, E. F., editors, 1995, Airborne Astronomy Symposium on the Galactic Ecosystem: From Gas to Stars to Dust, volume 73

Halfen, D. T., Woolf, N. J. & Ziurys, L. M., 2017, ApJ, 845, 2, 158, doi: 10.3847/1538-4357/aa816b

Harsono, D., Bjerkeli, P., van der Wiel, M. H. D., Ramsey, J. P., Maud, L. T. *et al.*, 2018, Nature Astronomy, 2, 646–651, doi: 10.1038/s41550-018-0497-x

Hartquist, T. W., Dalgarno, A. & Oppenheimer, M., 1980, ApJ, 236, 182–188, doi: 10.1086/157731

Hatchell, J., Thompson, M. A., Millar, T. J. & MacDonald, G. H., 1998, A&A, 338, 713–722

Haupa, K. A., Johnson, B. A., Sibert, E. L. & Lee, Y.-P., 2017, J. Chem. Phys., 147, 15, 154305, doi: 10.1063/1.4996951

He, J., Acharyya, K. & Vidali, G., 2016a, ApJ, 825, 2, 89, doi: 10.3847/0004-637X/825/2/89

He, J., Acharyya, K. & Vidali, G., 2016b, ApJ, 823, 1, 56, doi: 10.3847/0004-637X/823/1/56

He, J., Emtiaz, S. M. & Vidali, G., 2017, ApJ, 851, 2, 104, doi: 10.3847/1538-4357/aa9a3e

He, J., Simons, M., Fedoseev, G., Chuang, K.-J., Qasim, D. *et al.*, in press, A&A

Heaton, B. D., Little, L. T. & Bishop, I. S., 1989, A&A, 213, 148–154

Heikkilä, A., Johansson, L. E. B. & Olofsson, H., 1999, A&A, 344, 817–847

Henderson, B. L. & Gudipati, M. S., 2014, Journal of Physical Chemistry A, 118, 29, 5454–5463, doi: 10.1021/jp503111k

Henkel, C. & Bally, J., 1985, A&A, 150, L25–L27

Henning, T. & Semenov, D., 2013, Chemical Reviews, 113, 12, 9016–9042, doi: 10.1021/cr400128p

Herbst, E., 2017, International Reviews in Physical Chemistry, 36, 2, 287–331

Herbst, E. & Klemperer, W., 1973, Astrophysical Journal, Vol. 185, pp. 505-534 (1973), 185, 505–534

Herbst, E. & van Dishoeck, E. F., 2009, ARA&A, 47, 1, 427–480, doi: 10.1146/annurev-astro-082708-101654

Herpin, F., Marseille, M., Wakelam, V., Bontemps, S. & Lis, D. C., 2009, A&A, 504, 3, 853–867, doi: 10.1051/0004-6361/200811257

Hervías-Caimapo, C., Merello, M., Bronfman, L., Åke-Nyman, L., Garay, G. *et al.*, 2019, ApJ, 872, 2, 200, doi: 10.3847/1538-4357/aaf9ac

Herzberg, G., 1945, Molecular Spectra And Molecular Structure. Volume II, D. Van Nostrand Company, Inc.

Hibbitts, C., McCord, T. & Hansen, G., 2000, Journal of Geophysical Research: Planets, 105, E9, 22541–22557

Hickson, K. M., Wakelam, V. & Loison, J.-C., 2016, Molecular Astrophysics, 3, 1–9, doi: 10.1016/j.molap.2016.03.001

Hidaka, H., Kouchi, A. & Watanabe, N., 2007, J. Chem. Phys., 126, 20, 204707–204707, doi: 10.1063/1.2735573

Hidaka, H., Watanabe, M., Kouchi, A. & Watanabe, N., 2009, ApJ, 702, 1, 291–300, doi: 10.1088/0004-637X/702/1/291

Hincelin, U., Wakelam, V., Hersant, F., Guilloteau, S., Loison, J. C. *et al.*, 2011, A&A, 530, A61, doi: 10.1051/0004-6361/201016328

Hiraoka, K., Ohashi, N., Kihara, Y., Yamamoto, K., Sato, T. & Yamashita, A., 1994, Chem. Phys. Lett., 229, 4, 408–414, doi: 10.1016/0009-2614(94)01066-8

Hiraoka, K., Miyagoshi, T., Takayama, T., Yamamoto, K. & Kihara, Y., 1998, ApJ, 498, 2, 710–715, doi: 10.1086/305572

Hiraoka, K., Takayama, T., Euchi, A., Handa, H. & Sato, T., 2000, The Astrophysical Journal, 532, 2, 1029–1037, doi: 10.1086/308612

Hodyss, R., Johnson, P. V., Stern, J. V., Goguen, J. D. & Kanik, I., 2009, ICARUS, 200, 1, 338–342, doi: 10.1016/j.icarus.2008.10.024

Hofner, P., Wiesemeyer, H. & Henning, T., 2001, ApJ, 549, 1, 425–432, doi: 10.1086/319065

Holland, H. D., 1997, Science, 275, 5296, 38–39

Hollenbach, D., Kaufman, M. J., Bergin, E. A. & Melnick, G. J., 2009, ApJ, 690, 2, 1497–1521, doi: 10.1088/0004-637X/690/2/1497

Hollenberg, J. L. & Dows, D. A., 1961, J. Chem. Phys., 34, 3, 1061–1062, doi: 10.1063/1. 1731636

Hollis, J. M., Snyder, L. E., Blake, D. H., Lovas, F. J., Suenram, R. D. & Ulich, B. L., 1981, ApJ, 251, 541–548, doi: 10.1086/159495

Honma, M., Nagayama, T. & Sakai, N., 2015, PASJ, 67, 4, 70, doi: 10.1093/pasj/psv045

Hudgins, D. M., Sandford, S. A., Allamandola, L. J. & Tielens, A. G. G. M., 1993, ApJS, 86, 713, doi: 10.1086/191796

Hudson, J. E., Hamilton, M. L., Vallance, C. & Harland, P. W., 2003, Phys. Chem. Chem. Phys., 5, 3162–3168, doi: 10.1039/B304456D

Hudson, J. E., Weng, Z. F., Vallance, C. & Harland, P. W., 2006, International Journal of Mass Spectrometry, 248, 1, 42–46, doi: https://doi.org/10.1016/j.ijms.2005.11.003

Hudson, R. L. & Gerakines, P. A., 2018, ApJ, 867, 2, 138, doi: 10.3847/1538-4357/aae52a

Hudson, R. L. & Moore, M. H., 2003, The Astrophysical Journal Letters, 586, 1, L107–L110, doi: 10.1086/374580

Hudson, R. L., Ferrante, R. F. & Moore, M. H., 2014, Icarus, 228, 276–287, doi: 10.1016/j. icarus.2013.08.029

Ioppolo, S., Cuppen, H. M., Romanzin, C., van Dishoeck, E. F. & Linnartz, H., 2008, ApJ, 686, 2, 1474–1479, doi: 10.1086/591506

Ioppolo, S., Cuppen, H. M., Romanzin, C., van Dishoeck, E. F. & Linnartz, H., 2010, Physical Chemistry Chemical Physics (Incorporating Faraday Transactions), 12, 38, 12065, doi: 10.1039/C0CP00250J

Ioppolo, S., van Boheemen, Y., Cuppen, H. M., van Dishoeck, E. F. & Linnartz, H., 2011, MNRAS, 413, 3, 2281–2287, doi: 10.1111/j.1365-2966.2011.18306.x

Ioppolo, S., Fedoseev, G., Lamberts, T., Romanzin, C. & Linnartz, H., 2013, Rev. Sci. Instrum., 84, 7, 073112-073112-13, doi: 10.1063/1.4816135

Ioppolo, S., Fedoseev, G., Chuang, K. J., Cuppen, H. M., Clements, A. R. *et al.*, 2021, Nature Astronomy, 5, 197–205, doi: 10.1038/s41550-020-01249-0

Ioppolo, S., Noble, J. A., Traspas Muiña, A., Cuppen, H. M., Coussan, S. & Redlich, B., 2022, Journal of Molecular Spectroscopy, 385, 111601, doi: 10.1016/j.jms.2022.111601

Ismail, A. F., Khulbe, K. C. & Matsuura, T., 2015, Switz. Springer, 10, 973–978

Isoniemi, E., Pettersson, M., Khriachtchev, L., Lundell, J. & Räsänen, M., 1999, The Journal of Physical Chemistry A, 103, 6, 679–685, doi: 10.1021/jp9838893

Jakobsen, R. J., Mikawa, Y. & Brasch, J. W., 1967, Nature, 215, 1071, doi: 10.1038/ 2151071a0

Jenkins, E. B., 2009, The Astrophysical Journal, 700, 2, 1299–1348, doi: 10.1088/0004-637X/ 700/2/1299

Jensen, S. S., Jørgensen, J. K., Kristensen, L. E., Coutens, A., van Dishoeck, E. F. *et al.*, 2021, A&A, 650, A172, doi: 10.1051/0004-6361/202140560

Jessup, K. L., Spencer, J. & Yelle, R., 2007, ICARUS, 192, 1, 24–40, doi: 10.1016/j.icarus.2007.06.025

Jiang, G. J., Person, W. B. & Brown, K. G., 1975, The Journal of Chemical Physics, 62, 4, 1201–1211, doi: 10.1063/1.430634

Jiménez-Escobar, A. & Muñoz Caro, G. M., 2011a, A&A, 536, A91, doi: 10.1051/0004-6361/201014821

Jiménez-Escobar, A. & Muñoz Caro, G. M., 2011b, Astronomy and Astrophysics, 536, A91, doi: 10.1051/0004-6361/201014821

Jiménez-Escobar, A., Muñoz Caro, G. M. & Chen, Y. J., 2014a, MNRAS, 443, 1, 343–354, doi: 10.1093/mnras/stu1100

Jiménez-Escobar, A., Muñoz Caro, G. M. & Chen, Y. J., 2014b, Monthly Notices of the Royal Astronomical Society, 443, 1, 343–354, doi: 10.1093/mnras/stu1100

Jiménez-Serra, I., Vasyunin, A. I., Caselli, P., Marcelino, N., Billot, N. *et al.*, 2016, ApJ, 830, 1, L6, doi: 10.3847/2041-8205/830/1/L6

Jin, M. & Garrod, R. T., 2020, ApJS, 249, 2, 26, doi: 10.3847/1538-4365/ab9ec8

Jochims, H. W., Ruhl, E., Baumgartel, H., Tobita, S. & Leach, S., 1994, The Astrophysical Journal, 420, 307, doi: 10.1086/173560

Johnson, J. A., 2019, Science, 363, 6426, 474–478, doi: 10.1126/science.aau9540

Johnstone, D., Boonman, A. M. S. & van Dishoeck, E. F., 2003, A&A, 412, 157–174, doi: 10.1051/0004-6361:20031370

Jones, A. P., Fanciullo, L., Köhler, M., Verstraete, L., Guillet, V. *et al.*, 2013, A&A, 558, A62, doi: 10.1051/0004-6361/201321686

Jørgensen, J. K., Müller, H. S. P., Calcutt, H., Coutens, A., Drozdovskaya, M. N. *et al.*, 2018, A&A, 620, A170, doi: 10.1051/0004-6361/201731667

Jørgensen, J. K., Belloche, A. & Garrod, R. T., 2020, ARA&A, 58, 727–778, doi: 10.1146/annurev-astro-032620-021927

Kaifu, N., Ohishi, M., Kawaguchi, K., Saito, S., Yamamoto, S. *et al.*, 2004, PASJ, 56, 69–173, doi: 10.1093/pasj/56.1.69

Kama, M., Shorttle, O., Jermyn, A. S., Folsom, C. P., Furuya, K. *et al.*, 2019, ApJ, 885, 2, 114, doi: 10.3847/1538-4357/ab45f8

Kastner, J. H., Hily-Blant, P., Rodriguez, D. R., Punzi, K. & Forveille, T., 2014, The Astrophysical Journal, 793, 1, 55

Kaňuchová, Z., Boduch, P., Domaracka, A., Palumbo, M. E., Rothard, H. & Strazzulla, G., 2017, A&A, 604, A68, doi: 10.1051/0004-6361/201730711

Keane, J. V., Boonman, A. M. S., Tielens, A. G. G. M. & van Dishoeck, E. F., 2001, A&A, 376, L5–L8, doi: 10.1051/0004-6361:20011008

Keller, L. P., Hony, S., Bradley, J. P., Molster, F. J., Waters, L. B. F. M. *et al.*, 2002, Nature, 417, 6884, 148–150, doi: 10.1038/417148a

Klopman, G. & Andreozzi, P., 1979, Bulletin des Sociétés Chimiques Belges, 88, 11, 875–882

Knez, C., Moore, M. H., Ferrante, R. F. & Hudson, R. L., 2012, The Astrophysical Journal, 748, 2, 95, doi: 10.1088/0004-637X/748/2/95

Knizia, G., Adler, T. B. & Werner, H.-J., 2009, The Journal of chemical physics, 130, 5

Kobayashi, H., Hidaka, H., Lamberts, T., Hama, T., Kawakita, H. *et al.*, 2017, The Astrophysical Journal, 837, 2, 155, doi: 10.3847/1538-4357/837/2/155

Köhler, M., Jones, A. & Ysard, N., 2014, A&A, 565, L9, doi: 10.1051/0004-6361/201423985

Kolesniková, L., Tercero, B., Cernicharo, J., Alonso, J. L., Daly, A. M. *et al.*, 2014, ApJ, 784, 1, L7, doi: 10.1088/2041-8205/784/1/L7

Kouchi, A., 1990, Journal of Crystal Growth, 99, 1, Part 2, 1220–1226, doi: https://doi.org/10.1016/S0022-0248(08)80112-1

Kouchi, A. & Kuroda, T., 1990, Nature, 344, 6262, 134–135, doi: 10.1038/344134a0

Krasnokutski, S. A. & Huisken, F., 2014, Applied Physics Letters, 105, 11, 113506, doi: 10.1063/1.4895806

Krasnopoler, A. & George, S. M., 1998, The Journal of Physical Chemistry B, 102, 5, 788–794, doi: 10.1021/jp972016q

Kruczkiewicz, F., Dulieu, F., Ivlev, A. V., Caselli, P., Giuliano, B. M. *et al.*, 2024, A&A, 686, A236, doi: 10.1051/0004-6361/202346948

Krumholz, M. R., 2015, J. S. Vink, editor, Very Massive Stars in the Local Universe, volume 412 of *Astrophysics and Space Science Library*, 43, doi: 10.1007/978-3-319-09596-7_3

Kuiper, T. B. H., Kuiper, E. N. R., Dickinson, D. F., Turner, B. E. & Zuckerman, B., 1984, ApJ, 276, 211–220, doi: 10.1086/161604

Kurtz, S., Cesaroni, R., Churchwell, E., Hofner, P. & Walmsley, C. M., 2000, Protostars and Planets IV, 299

Kushwahaa, T., Drozdovskaya, M. N., Tychoniec, Ł. & Tabone, B., 2023, A&A, 672, A122, doi: 10.1051/0004-6361/202245097

Kuwahata, K., Hama, T., Kouchi, A. & Watanabe, N., 2015, Phys. Rev. Lett., 115, 13, 133201, doi: 10.1103/PhysRevLett.115.133201

Laas, J. C. & Caselli, P., 2019, A&A, 624, A108, doi: 10.1051/0004-6361/201834446

Lacy, J. H., Evans, I., Neal J., Achtermann, J. M., Bruce, D. E., Arens, J. F. & Carr, J. S., 1989, The Astrophysical Journal Letters, 342, L43, doi: 10.1086/185480

Lacy, J. H., Knacke, R., Geballe, T. R. & Tokunaga, A. T., 1994, ApJ, 428, L69, doi: 10.1086/187395

Lahuis, F. & van Dishoeck, E. F., 2000, Astronomy and Astrophysics, 355, 699–712

Lamberts, T., 2018, Astronomy & Astrophysics, 615, L2, doi: 10.1051/0004-6361/201832830

Lamberts, T. & Kästner, J., 2017, The Journal of Physical Chemistry A, 121, 51, 9736–9741, doi: 10.1021/acs.jpca.7b10296, pMID: 29190103

Lamberts, T., Samanta, P. K., Köhn, A. & Kästner, J., 2016, Physical Chemistry Chemical Physics (Incorporating Faraday Transactions), 18, 48, 33021–33030, doi: 10.1039/C6CP06457D

Lamberts, T., Fedoseev, G., Kästner, J., Ioppolo, S. & Linnartz, H., 2017, A&A, 599, A132, doi: 10.1051/0004-6361/201629845

Le Gal, R., Öberg, K. I., Loomis, R. A., Pegues, J. & Bergner, J. B., 2019, ApJ, 876, 1, 72, doi: 10.3847/1538-4357/ab1416

Le Gal, R., Öberg, K. I., Teague, R., Loomis, R. A., Law, C. J. *et al.*, 2021, ApJS, 257, 1, 12, doi: 10.3847/1538-4365/ac2583

Le Page, V., Snow, T. P. & Bierbaum, V. M., 2003, The Astrophysical Journal, 584, 1, 316–330, doi: 10.1086/345595

Le Roy, L., Altwegg, K., Balsiger, H., Berthelier, J.-J., Bieler, A. *et al.*, 2015, A&A, 583, A1, doi: 10.1051/0004-6361/201526450

Lefloch, B., Ceccarelli, C., Codella, C., Favre, C., Podio, L. *et al.*, 2017, MNRAS, 469, 1, L73–L77, doi: 10.1093/mnrasl/slx050

Li, A. & Draine, B. T., 2001, ApJ, 554, 2, 778–802, doi: 10.1086/323147

Li, J., Wang, J., Zhu, Q., Zhang, J. & Li, D., 2015, ApJ, 802, 1, 40, doi: 10.1088/0004-637X/802/1/40

Ligterink, N. F. W., Paardekooper, D. M., Chuang, K. J., Both, M. L., Cruz-Diaz, G. A. *et al.*, 2015, A&A, 584, A56, doi: 10.1051/0004-6361/201526930

Linke, R. A., Frerking, M. A. & Thaddeus, P., 1979, ApJ, 234, L139–L142, doi: 10.1086/183125

Linnartz, H., Ioppolo, S. & Fedoseev, G., 2015, International Reviews in Physical Chemistry, 34, 2, 205–237, doi: 10.1080/0144235X.2015.1046679

Lique, F., Cernicharo, J. & Cox, P., 2006, ApJ, 653, 2, 1342–1352, doi: 10.1086/508978

Lledos, A., Bertran, J. & Ventura, O. N., 1986, International journal of quantum chemistry, 30, 4, 467–477

Loeffler, M. J., Hudson, R. L., Chanover, N. J. & Simon, A. A., 2015, ICARUS, 258, 181–191, doi: 10.1016/j.icarus.2015.06.015

Loison, J.-C., Halvick, P., Bergeat, A., Hickson, K. M. & Wakelam, V., 2012, MNRAS, 421, 2, 1476–1484, doi: 10.1111/j.1365-2966.2012.20412.x

López-Gallifa, Á., Rivilla, V. M., Beltrán, M. T., Colzi, L., Mininni, C. *et al.*, 2024, MNRAS, 529, 4, 3244–3283, doi: 10.1093/mnras/stae676

Lovas, F. J., 2004, Journal of Physical and Chemical Reference Data, 33, 177–355, doi: 10.1063/1.1633275

Lovas, F. J., Johnson, D. R., Buhl, D. & Snyder, L. E., 1976, ApJ, 209, 770–777, doi: 10.1086/154774

Lumsden, S. L., Hoare, M. G., Urquhart, J. S., Oudmaijer, R. D., Davies, B. *et al.*, 2013, ApJS, 208, 1, 11, doi: 10.1088/0067-0049/208/1/11

Luna, R., Molpeceres, G., Ortigoso, J., Satorre, M. A., Domingo, M. & Maté, B., 2018, A&A, 617, A116, doi: 10.1051/0004-6361/201833463

Madhusudhan, N., 2019, ARA&A, 57, 617–663, doi: 10.1146/annurev-astro-081817-051846

Majumdar, L., Gratier, P., Vidal, T., Wakelam, V., Loison, J. C. *et al.*, 2016, MNRAS, 458, 2, 1859–1865, doi: 10.1093/mnras/stw457

Mandt, K. E., Mousis, O., Marty, B., Cavalié, T., Harris, W. *et al.*, 2015, Space Sci. Rev., 197, 1-4, 297–342, doi: 10.1007/s11214-015-0161-z

Manigand, S., Jørgensen, J. K., Calcutt, H., Müller, H. S. P., Ligterink, N. F. W. *et al.*, 2020, A&A, 635, A48, doi: 10.1051/0004-6361/201936299

Markwick, A. J., Millar, T. J. & Charnley, S. B., 2002, A&A, 381, 560–565, doi: 10.1051/0004-6361:20011381

Markwick, A. J., Charnley, S. B., Butner, H. M. & Millar, T. J., 2005, ApJ, 627, 2, L117–L120, doi: 10.1086/432415

Martín, S., Mauersberger, R., Martín-Pintado, J., García-Burillo, S. & Henkel, C., 2003, A&A, 411, L465–L468, doi: 10.1051/0004-6361:20031442

Martín, S., Martín-Pintado, J., Mauersberger, R., Henkel, C. & García-Burillo, S., 2005, ApJ, 620, 1, 210–216, doi: 10.1086/426888

Martín-Doménech, R., Muñoz Caro, G. M., Bueno, J. & Goesmann, F., 2014, A&A, 564, A8, doi: 10.1051/0004-6361/201322824

Martín-Doménech, R., Manzano-Santamaría, J., Muñoz Caro, G. M., Cruz-Díaz, G. A., Chen, Y. J. *et al.*, 2015, A&A, 584, A14, doi: 10.1051/0004-6361/201526003

Martín-Doménech, R., Öberg, K. I. & Rajappan, M., 2020, The Astrophysical Journal, 894, 2, 98, doi: 10.3847/1538-4357/ab84e8

Martin-Drumel, M. A., Lee, K. L. K., Belloche, A., Zingsheim, O., Thorwirth, S. *et al.*, 2019, Astronomy & Astrophysics, 623, A167, doi: 10.1051/0004-6361/201935032

Mathis, J. S., Mezger, P. G. & Panagia, N., 1983, A&A, 128, 212–229

Matteucci, S., Yampolskii, Y., Freeman, B. D. & Pinnau, I., 2006, Materials science of membranes for gas and vapor separation, 1–47

Mauersberger, R., Henkel, C., Walmsley, C. M., Sage, L. J. & Wiklind, T., 1991, A&A, 247, 307

Mauersberger, R., Henkel, C. & Chin, Y. N., 1995, A&A, 294, 23–32

Mayer, E. & Pletzer, R., 1986, Nature, 319, 6051, 298–301, doi: 10.1038/319298a0

McAnally, M., Bocková, J., Herath, A., Turner, A. M., Meinert, C. & Kaiser, R. I., 2024, Nature Communications, 15, 1, 4409

McClure, M. K., Rocha, W. R. M., Pontoppidan, K. M., Crouzet, N., Chu, L. E. U. *et al.*, 2023, Nature Astronomy, 7, 431–443, doi: 10.1038/s41550-022-01875-w

McCord, T. B., Hansen, G. B., Clark, R. N., Martin, P. D., Hibbitts, C. A. *et al.*, 1998, Journal of Geophysical Research, 103, E4, 8603–8626, doi: 10.1029/98JE00788

McGuire, B. A., 2018, ApJS, 239, 2, 17, doi: 10.3847/1538-4365/aae5d2

McGuire, B. A., 2022, ApJS, 259, 2, 30, doi: 10.3847/1538-4365/ac2a48

McGuire, B. A., Martin-Drumel, M.-A., Thorwirth, S., Brünken, S., Lattanzi, V. *et al.*, 2016, Phys. Chem. Chem. Phys., 18, 22693–22705, doi: 10.1039/C6CP03871A

McMullin, J. P., Waters, B., Schiebel, D., Young, W. & Golap, K., 2007, R. A. Shaw, F. Hill & D. J. Bell, editors, Astronomical Data Analysis Software and Systems XVI, volume 376 of *Astronomical Society of the Pacific Conference Series*, 127

Mège, P., Russeil, D., Zavagno, A., Elia, D., Molinari, S. *et al.*, 2021, A&A, 646, A74, doi: 10.1051/0004-6361/202038956

Melli, A., Melosso, M., Tasinato, N., Bosi, G., Spada, L. *et al.*, 2018, ApJ, 855, 2, 123, doi: 10.3847/1538-4357/aaa899

Mendoza, E., Bronfman, L., Duronea, N. U., Lépine, J. R. D., Finger, R. *et al.*, 2018, ApJ, 853, 2, 152, doi: 10.3847/1538-4357/aaa1ec

Merello, M., Bronfman, L., Garay, G., Lo, N., Evans, I., Neal J. *et al.*, 2013a, ApJ, 774, 1, L7, doi: 10.1088/2041-8205/774/1/L7

Merello, M., Bronfman, L., Garay, G., Nyman, L.-Å., Evans, I., Neal J. & Walmsley, C. M., 2013b, ApJ, 774, 1, 38, doi: 10.1088/0004-637X/774/1/38

Merello, M., Molinari, S., Rygl, K. L. J., Evans, N. J., Elia, D. *et al.*, 2019, MNRAS, 483, 4, 5355–5379, doi: 10.1093/mnras/sty3453

Mifsud, D. V., Herczku, P., Rácz, R., Rahul, K. K., Kovács, S. T. S. *et al.*, 2022, Frontiers in Chemistry, 10, 1003163, doi: 10.3389/fchem.2022.1003163

Mifsud, D. V., Herczku, P., Rahul, K. K., Ramachandran, R., Sundararajan, P. *et al.*, 2023, Physical Chemistry Chemical Physics (Incorporating Faraday Transactions), 25, 38, 26278–26288, doi: 10.1039/D3CP03196A

Mifsud, D. V., Herczku, P., Ramachandran, R., Sundararajan, P., Rahul, K. K. *et al.*, 2024, Spectrochimica Acta Part A: Molecular Spectroscopy, 319, 124567, doi: 10.1016/j.saa.2024.124567

Mihesan, C., Ziskind, M., Chazallon, B., Therssen, E., Desgroux, P. *et al.*, 2006, Applied Surface Science, 253, 3, 1090–1094, doi: 10.1016/j.apsusc.2006.01.082

Millar, T. J. & Freeman, A., 1984, MNRAS, 207, 405–423, doi: 10.1093/mnras/207.3.405

Millar, T. J. & Williams, D. A., 1993, T. J. Millar & D. A. Williams, editors, Dust and Chemistry in Astronomy, Institute of Physics Publishing: London, 1–8

Miller, J. A. & Klippenstein, S. J., 2004, Physical Chemistry Chemical Physics, 6, 6, 1192–1202

Minh, Y. C., Irvine, W. M. & Ziurys, L. M., 1989, ApJ, 345, L63, doi: 10.1086/185553

Minh, Y. C., Ziurys, L. M., Irvine, W. M. & McGonagle, D., 1990, ApJ, 360, 136, doi: 10.1086/169103

Mininni, C., Fontani, F., Sánchez-Monge, A., Rivilla, V. M., Beltrán, M. T. *et al.*, 2021, A&A, 653, A87, doi: 10.1051/0004-6361/202040262

Minissale, M. & Dulieu, F., 2014, J. Chem. Phys., 141, 1, 014304, doi: 10.1063/1.4885847

Minissale, M., Dulieu, F., Cazaux, S. & Hocuk, S., 2016a, A&A, 585, A24, doi: 10.1051/0004-6361/201525981

Minissale, M., Moudens, A., Baouche, S., Chaabouni, H. & Dulieu, F., 2016b, MNRAS, 458, 3, 2953–2961, doi: 10.1093/mnras/stw373

Minissale, M., Aikawa, Y., Bergin, E., Bertin, M., Brown, W. A. *et al.*, 2022, ACS Earth and Space Chemistry, 6, 3, 597–630, doi: 10.1021/acsearthspacechem.1c00357

Mispelaer, F., Theule, P., Duvernay, F., Roubin, P. & Chiavassa, T., 2012, A&A, 540, A40, doi: 10.1051/0004-6361/201117128

Miyauchi, N., Hidaka, H., Chigai, T., Nagaoka, A., Watanabe, N. & Kouchi, A., 2008, Chemical Physics Letters, 456, 1-3, 27–30, doi: 10.1016/j.cplett.2008.02.095

Mokrane, H., Chaabouni, H., Accolla, M., Congiu, E., Dulieu, F. *et al.*, 2009, ApJ, 705, 2, L195–L198, doi: 10.1088/0004-637X/705/2/L195

Molinari, S., Swinyard, B., Bally, J., Barlow, M., Bernard, J. P. *et al.*, 2010, A&A, 518, L100, doi: 10.1051/0004-6361/201014659

Molinari, S., Merello, M., Elia, D., Cesaroni, R., Testi, L. & Robitaille, T., 2016, ApJ, 826, 1, L8, doi: 10.3847/2041-8205/826/1/L8

Molpeceres, G. & Rivilla, V. M., 2022, Astronomy and Astrophysics, 665, A27, doi: 10.1051/0004-6361/202243892

Molpeceres, G., García de la Concepción, J. & Jiménez-Serra, I., 2021, ApJ, 923, 2, 159, doi: 10.3847/1538-4357/ac2ebc

Molpeceres, G., Kästner, J., Fedoseev, G., Qasim, D., Schömig, R. *et al.*, 2021, The Journal of Physical Chemistry Letters, 12, 44, 10854–10860, doi: 10.1021/acs.jpclett.1c02760, pMID: 34727500

Molpeceres, G., Enrique-Romero, J. & Aikawa, Y., 2023, A&A, 677, A39, doi: 10.1051/0004-6361/202347097

Moore, M. H., Hudson, R. L. & Carlson, R. W., 2007, ICARUS, 189, 2, 409–423, doi: 10.1016/j.icarus.2007.01.018

Mottram, J. C., Hoare, M. G., Davies, B., Lumsden, S. L., Oudmaijer, R. D. *et al.*, 2011, ApJ, 730, 2, L33, doi: 10.1088/2041-8205/730/2/L33

Moullet, A., Lellouch, E., Moreno, R., Gurwell, M. A. & Moore, C., 2008, A&A, 482, 1, 279–292, doi: 10.1051/0004-6361:20078699

Moullet, A., Lellouch, E., Moreno, R., Gurwell, M., Black, J. H. & Butler, B., 2013, ApJ, 776, 1, 32, doi: 10.1088/0004-637X/776/1/32

Muñoz Caro, G. M. & Martín Doménech, R., 2018, G. M. Muñoz Caro & R. Escribano, editors, Astrophysics and Space Science Library, volume 451 of *Astrophysics and Space Science Library*, 133, doi: 10.1007/978-3-319-90020-9_9

Muñoz Caro, G. M., Jiménez-Escobar, A., Martín-Gago, J. Á., Rogero, C., Atienza, C. *et al.*, 2010, A&A, 522, A108, doi: 10.1051/0004-6361/200912462

Muñoz Caro, G. M., Chen, Y. J., Aparicio, S., Jiménez-Escobar, A., Rosu-Finsen, A. *et al.*, 2016, A&A, 589, A19, doi: 10.1051/0004-6361/201628121

Muenter, J. S. & Laurie, V. W., 1966, The Journal of Chemical Physics, 45, 3, 855–858, doi: 10.1063/1.1727694

Müller, B., Giuliano, B. M., Goto, M. & Caselli, P., 2021, A&A, 652, A126, doi: 10.1051/0004-6361/202039139

Müller, H. S. P., Thorwirth, S., Bizzocchi, L. & Winnewisser, G., 2000, Zeitschrift Naturforschung Teil A, 55, 491, doi: 10.1515/zna-2000-0503

Müller, H. S. P., Thorwirth, S., Roth, D. A. & Winnewisser, G., 2001, A&A, 370, L49–L52, doi: 10.1051/0004-6361:20010367

Müller, H. S. P., Schlöder, F., Stutzki, J. & Winnewisser, G., 2005, Journal of Molecular Structure, 742, 1-3, 215–227, doi: 10.1016/j.molstruc.2005.01.027

Müller, H. S. P., Belloche, A., Xu, L.-H., Lees, R. M., Garrod, R. T. *et al.*, 2016, A&A, 587, A92, doi: 10.1051/0004-6361/201527470

Mumma, M. J. & Charnley, S. B., 2011, ARA&A, 49, 1, 471–524, doi: 10.1146/annurev-astro-081309-130811

Mumma, M. J., Bonev, B. P., Villanueva, G. L., Paganini, L., DiSanti, M. A. *et al.*, 2011, ApJ, 734, 1, L7, doi: 10.1088/2041-8205/734/1/L7

Nagaoka, A., Watanabe, N. & Kouchi, A., 2005, ApJ, 624, 1, L29–L32, doi: 10.1086/430304

Nagaoka, A., Watanabe, N. & Kouchi, A., 2007, J. Phys. Chem. A, 111, 16, 3016–3028, doi: 10.1021/jp068978r

Nagy, Z., van der Tak, F. F. S., Fuller, G. A. & Plume, R., 2015, A&A, 577, A127, doi: 10.1051/0004-6361/201425014

Nash, D. B. & Howell, R. R., 1989, Science, 244, 4903, 454–457, doi: 10.1126/science.244.4903.454

Navarro-Almaida, D., Le Gal, R., Fuente, A., Rivière-Marichalar, P., Wakelam, V. *et al.*, 2020, A&A, 637, A39, doi: 10.1051/0004-6361/201937180

Nazari, P., 2024, Ph.D. thesis, Leiden University

Nazari, P., van Gelder, M. L., van Dishoeck, E. F., Tabone, B., van't Hoff, M. L. R. *et al.*, 2021, A&A, 650, A150, doi: 10.1051/0004-6361/202039996

Nazari, P., Meijerhof, J. D., van Gelder, M. L., Ahmadi, A., van Dishoeck, E. F. *et al.*, 2022, A&A, 668, A109, doi: 10.1051/0004-6361/202243788

Nazari, P., Tabone, B., van't Hoff, M. L. R., Jørgensen, J. K. & van Dishoeck, E. F., 2023, ApJ, 951, 2, L38, doi: 10.3847/2041-8213/acdde4

Nazari, P., Tabone, B., Rosotti, G. P. & van Dishoeck, E. F., 2024, A&A, 687, A263, doi: 10.1051/0004-6361/202347033

Neese, F., Wennmohs, F., Becker, U. & Riplinger, C., 2020, The Journal of chemical physics, 152, 22, doi: 10.1063/5.0004608

Neufeld, D. A., Wolfire, M. G. & Schilke, P., 2005, ApJ, 628, 1, 260–274, doi: 10.1086/430663

Neufeld, D. A., Falgarone, E., Gerin, M., Godard, B., Herbst, E. *et al.*, 2012, A&A, 542, L6, doi: 10.1051/0004-6361/201218870

Neufeld, D. A., Godard, B., Gerin, M., Pineau des Forêts, G., Bernier, C. *et al.*, 2015, A&A, 577, A49, doi: 10.1051/0004-6361/201425391

Nguyen, T., Baouche, S., Congiu, E., Diana, S., Pagani, L. & Dulieu, F., 2018, A&A, 619, A111, doi: 10.1051/0004-6361/201832774

Nguyen, T., Oba, Y., Shimonishi, T., Kouchi, A. & Watanabe, N., 2020, ApJ, 898, 2, L52, doi: 10.3847/2041-8213/aba695

Nguyen, T., Oba, Y., Sameera, W. M. C., Kouchi, A. & Watanabe, N., 2021a, ApJ, 918, 2, 73, doi: 10.3847/1538-4357/ac0cf4

Nguyen, T., Oba, Y., Sameera, W. M. C., Kouchi, A. & Watanabe, N., 2021b, ApJ, 922, 2, 146, doi: 10.3847/1538-4357/ac2238

Nguyen, T., Oba, Y., Sameera, W. M. C., Furuya, K., Kouchi, A. & Watanabe, N., 2023, The Astrophysical Journal, 944, 2, 219, doi: 10.3847/1538-4357/acafde

Nguyen, T. K., Viti, S. & Williams, D. A., 2002, Astronomy and Astrophysics, 387, 1083–1091, doi: 10.1051/0004-6361:20020457

Nickerson, S., Rangwala, N., Colgan, S. W. J., DeWitt, C., Monzon, J. S. *et al.*, 2023, ApJ, 945, 1, 26, doi: 10.3847/1538-4357/aca6e8

Noble, J. A., Dulieu, F., Congiu, E. & Fraser, H. J., 2011, ApJ, 735, 2, 121, doi: 10.1088/0004-637X/735/2/121

Noble, J. A., Congiu, E., Dulieu, F. & Fraser, H. J., 2012, MNRAS, 421, 1, 768–779, doi: 10.1111/j.1365-2966.2011.20351.x

Noble, J. A., Cuppen, H. M., Coussan, S., Redlich, B. & Ioppolo, S., 2020, The Journal of Physical Chemistry C, 124, 38, 20864–20873, doi: 10.1021/acs.jpcc.0c04463

Oba, Y., Watanabe, N., Kouchi, A., Hama, T. & Pirronello, V., 2010a, ApJ, 712, 2, L174–L178, doi: 10.1088/2041-8205/712/2/L174

Oba, Y., Watanabe, N., Kouchi, A., Hama, T. & Pirronello, V., 2010b, ApJ, 712, 2, L174–L178, doi: 10.1088/2041-8205/712/2/L174

Oba, Y., Tomaru, T., Lamberts, T., Kouchi, A. & Watanabe, N., 2018, Nature Astronomy, 2, 228–232, doi: 10.1038/s41550-018-0380-9

Oba, Y., Tomaru, T., Kouchi, A. & Watanabe, N., 2019, ApJ, 874, 2, 124, doi: 10.3847/1538-4357/ab0961

Öberg, K. I., 2016, Chemical reviews, 116, 17, 9631–9663

Öberg, K. I. & Bergin, E. A., 2021, Phys. Rep., 893, 1–48, doi: 10.1016/j.physrep.2020.09.004

Öberg, K. I., van Broekhuizen, F., Fraser, H. J., Bisschop, S. E., van Dishoeck, E. F. & Schlemmer, S., 2005, ApJ, 621, 1, L33–L36, doi: 10.1086/428901

Öberg, K. I., Fuchs, G. W., Awad, Z., Fraser, H. J., Schlemmer, S. *et al.*, 2007, ApJ, 662, 1, L23–L26, doi: 10.1086/519281

Öberg, K. I., Boogert, A. C. A., Pontoppidan, K. M., Blake, G. A., Evans, N. J. *et al.*, 2008, ApJ, 678, 2, 1032–1041, doi: 10.1086/533432

Öberg, K. I., Fayolle, E. C., Cuppen, H. M., van Dishoeck, E. F. & Linnartz, H., 2009a, A&A, 505, 1, 183–194, doi: 10.1051/0004-6361/200912464

Öberg, K. I., van Dishoeck, E. F. & Linnartz, H., 2009b, A&A, 496, 1, 281–293, doi: 10.1051/0004-6361/200810207

Öberg, K. I., Bottinelli, S., Jørgensen, J. K. & van Dishoeck, E. F., 2010a, ApJ, 716, 1, 825–834, doi: 10.1088/0004-637X/716/1/825

Öberg, K. I., van Dishoeck, E. F., Linnartz, H. & Andersson, S., 2010b, ApJ, 718, 2, 832–840, doi: 10.1088/0004-637X/718/2/832

Öberg, K. I., Boogert, A. C. A., Pontoppidan, K. M., van den Broek, S., van Dishoeck, E. F. *et al.*, 2011a, ApJ, 740, 2, 109, doi: 10.1088/0004-637X/740/2/109

Öberg, K. I., Murray-Clay, R. & Bergin, E. A., 2011b, ApJ, 743, 1, L16, doi: 10.1088/2041-8205/743/1/L16

Öberg, K. I., Boamah, M. D., Fayolle, E. C., Garrod, R. T., Cyganowski, C. J. & van der Tak, F., 2013, ApJ, 771, 2, 95, doi: 10.1088/0004-637X/771/2/95

Öberg, K. I., Guzmán, V. V., Furuya, K., Qi, C., Aikawa, Y. *et al.*, 2015, Nature, 520, 7546, 198–201, doi: 10.1038/nature14276

Öberg, K. I., Facchini, S. & Anderson, D. E., 2023, ARA&A, 61, 287–328, doi: 10.1146/annurev-astro-022823-040820

Olson, K. R. & Straub, K. D., 2016, Physiology, 31, 1, 60–72

Osorio, M., Anglada, G., Lizano, S. & D'Alessio, P., 2009, ApJ, 694, 1, 29–45, doi: 10.1088/0004-637X/694/1/29

Oya, Y., Sakai, N., López-Sepulcre, A., Watanabe, Y., Ceccarelli, C. *et al.*, 2016, ApJ, 824, 2, 88, doi: 10.3847/0004-637X/824/2/88

Oya, Y., López-Sepulcre, A., Sakai, N., Watanabe, Y., Higuchi, A. E. *et al.*, 2019, ApJ, 881, 2, 112, doi: 10.3847/1538-4357/ab2b97

Paardekooper, D. M., Fedoseev, G., Riedo, A. & Linnartz, H., 2016, A&A, 596, A72, doi: 10.1051/0004-6361/201629063

Padovani, M., Walmsley, C., Tafalla, M., Galli, D. & Müller, H., 2009, Astronomy & Astrophysics, 505, 3, 1199–1211

Pagani, L., Bacmann, A., Cabrit, S. & Vastel, C., 2007, A&A, 467, 1, 179–186, doi: 10.1051/0004-6361:20066670

Palumbo, M. E., Tielens, A. G. G. M. & Tokunaga, A. T., 1995, ApJ, 449, 674, doi: 10.1086/176088

Palumbo, M. E., Geballe, T. R. & Tielens, A. G. G. M., 1997, ApJ, 479, 2, 839–844, doi: 10.1086/303905

Penteado, E. M., Boogert, A. C. A., Pontoppidan, K. M., Ioppolo, S., Blake, G. A. & Cuppen, H. M., 2015, MNRAS, 454, 1, 531–540, doi: 10.1093/mnras/stv1987

Penteado, E. M., Walsh, C. & Cuppen, H. M., 2017, ApJ, 844, 1, 71, doi: 10.3847/1538-4357/aa78f9

Perrero, J., Enrique-Romero, J., Martínez-Bachs, B., Ceccarelli, C., Balucani, N. *et al.*, 2022, ACS Earth and Space Chemistry, 6, 3, 496–511, doi: 10.1021/acsearthspacechem.1c00369

Pesciotta, C., Simon, A., Rajappan, M. & Öberg, K. I., 2024, ApJ, 973, 2, 166, doi: 10.3847/1538-4357/ad684d

Petuchowski, S. J. & Bennett, C. L., 1992, ApJ, 391, 137, doi: 10.1086/171330

Pety, J., Teyssier, D., Fossé, D., Gerin, M., Roueff, E. *et al.*, 2005, A&A, 435, 3, 885–899, doi: 10.1051/0004-6361:20041170

Phuong, N. T., Chapillon, E., Majumdar, L., Dutrey, A., Guilloteau, S. *et al.*, 2018, A&A, 616, L5, doi: 10.1051/0004-6361/201833766

Piacentino, E. L. & Öberg, K. I., 2022, ApJ, 939, 2, 93, doi: 10.3847/1538-4357/ac96e2

Pickett, H. M., Poynter, R. L., Cohen, E. A., Delitsky, M. L., Pearson, J. C. & Müller, H. S. P., 1998, Journal of Quantitative Spectroscopy and Radiative Transfer, 60, 883–890, doi: 10.1016/S0022-4073(98)00091-0

Pillai, T., Kauffmann, J., Wyrowski, F., Hatchell, J., Gibb, A. G. & Thompson, M. A., 2011, A&A, 530, A118, doi: 10.1051/0004-6361/201015899

Pineau des Forets, G., Roueff, E. & Flower, D. R., 1990, MNRAS, 244, 668–674

Polman, J., Waters, L. B. F. M., Min, M., Miguel, Y. & Khorshid, N., 2023, A&A, 670, A161, doi: 10.1051/0004-6361/202244647

Pontoppidan, K. M., 2006, A&A, 453, 3, L47–L50, doi: 10.1051/0004-6361:20065569

Pontoppidan, K. M., Fraser, H. J., Dartois, E., Thi, W. F., van Dishoeck, E. F. *et al.*, 2003, A&A, 408, 981–1007, doi: 10.1051/0004-6361:20031030

Pontoppidan, K. M., Salyk, C., Bergin, E. A., Brittain, S., Marty, B. *et al.*, 2014, H. Beuther, R. S. Klessen, C. P. Dullemond & T. Henning, editors, Protostars and Planets VI, 363–385, doi: 10.2458/azu_uapress_9780816531240-ch016

Porter, T. A. & Strong, A. W., 2005, 29th International Cosmic Ray Conference (ICRC29), Volume 4, volume 4 of *International Cosmic Ray Conference*, 77

Potapov, A., Sánchez-Monge, Á., Schilke, P., Graf, U. U., Möller, T. & Schlemmer, S., 2016, A&A, 594, A117, doi: 10.1051/0004-6361/201628426

Potapov, A., Krasnokutski, S. A., Jäger, C. & Henning, T., 2021, ApJ, 920, 2, 111, doi: 10.3847/1538-4357/ac1a70

Prasad, S. S. & Tarafdar, S. P., 1983, ApJ, 267, 603–609, doi: 10.1086/160896

Puzzarini, C., Cazzoli, G. & Gauss, J., 2012a, J. Chem. Phys., 137, 15, 154311–154311, doi: 10.1063/1.4758316

Puzzarini, C., Cazzoli, G., López, J. C., Alonso, J. L., Baldacci, A. *et al.*, 2012b, J. Chem. Phys., 137, 2, 024310–024310, doi: 10.1063/1.4731284

Qasim, D., Chuang, K. J., Fedoseev, G., Ioppolo, S., Boogert, A. C. A. & Linnartz, H., 2018, A&A, 612, A83, doi: 10.1051/0004-6361/201732355

Qasim, D., Lamberts, T., He, J., Chuang, K. J., Fedoseev, G. *et al.*, 2019, A&A, 626, A118, doi: 10.1051/0004-6361/201935068

Qasim, D., Fedoseev, G., Chuang, K. J., He, J., Ioppolo, S. *et al.*, 2020a, Nature Astronomy, 4, 781–785, doi: 10.1038/s41550-020-1054-y

Qasim, D., Witlox, M. J. A., Fedoseev, G., Chuang, K. J., Banu, T. *et al.*, 2020b, Rev. Sci. Instrum., 91, 5, 054501, doi: 10.1063/5.0003692

Qasim, D., Witlox, M. J. A., Fedoseev, G., Chuang, K. J., Banu, T. *et al.*, 2020c, Review of Scientific Instruments, 91, 5, 054501, doi: 10.1063/5.0003692

Qasim, D. N., 2020, Ph.D. thesis, Leiden University

Qiu, J., Zhang, J., Zhang, Y., Jia, L. & Tang, X., 2020, A&A, 634, A125, doi: 10.1051/0004-6361/201935800

Raut, U., Famá, M., Teolis, B. D. & Baragiola, R. A., 2007, J. Chem. Phys., 127, 20, 204713–204713, doi: 10.1063/1.2796166

Requena-Torres, M. A., Martín-Pintado, J., Rodríguez-Franco, A., Martín, S., Rodríguez-Fernández, N. J. & de Vicente, P., 2006, A&A, 455, 3, 971–985, doi: 10.1051/0004-6361:20065190

Ridgway, S. T., Hall, D. N. B., Wojslaw, R. S., Kleinmann, S. G. & Weinberger, D. A., 1976, Nature, 264, 345–346, doi: 10.1038/264345a0

Rivière-Marichalar, P., Fuente, A., Goicoechea, J. R., Pety, J., Le Gal, R. *et al.*, 2019, A&A, 628, A16, doi: 10.1051/0004-6361/201935354

Rivière-Marichalar, P., Fuente, A., Le Gal, R., Baruteau, C., Neri, R. *et al.*, 2020, A&A, 642, A32, doi: 10.1051/0004-6361/202038549

Rivière-Marichalar, P., Fuente, A., Le Gal, R., Arabhavi, A. M., Cazaux, S. *et al.*, 2021, A&A, 652, A46, doi: 10.1051/0004-6361/202140470

Rivière-Marichalar, P., Fuente, A., Esplugues, G., Wakelam, V., le Gal, R. *et al.*, 2022, A&A, 665, A61, doi: 10.1051/0004-6361/202142906

Rocha, W. R. M., Rachid, M. G., Olsthoorn, B., van Dishoeck, E. F., McClure, M. K. & Linnartz, H., 2022, A&A, 668, A63, doi: 10.1051/0004-6361/202244032

Rocha, W. R. M., van Dishoeck, E. F., Ressler, M. E., van Gelder, M. L., Slavicinska, K. *et al.*, 2024, A&A, 683, A124, doi: 10.1051/0004-6361/202348427

Rodríguez-Almeida, L. F., Jiménez-Serra, I., Rivilla, V. M., Martín-Pintado, J., Zeng, S. *et al.*, 2021a, ApJ, 912, 1, L11, doi: 10.3847/2041-8213/abf7cb

Rodríguez-Almeida, L. F., Jiménez-Serra, I., Rivilla, V. M., Martín-Pintado, J., Zeng, S. *et al.*, 2021b, The Astrophysical Journal Letters, 912, 1, L11, doi: 10.3847/2041-8213/abf7cb

Roe, C. L. & Schulz, K. H., 1998, Journal of Vacuum Science & Technology A: Vacuum, Surfaces, and Films, 16, 3, 1066–1072

Romanzin, C., Ioppolo, S., Cuppen, H. M., van Dishoeck, E. F. & Linnartz, H., 2011, J. Chem. Phys., 134, 8, 084504–084504, doi: 10.1063/1.3532087

Rosen, A. L., Offner, S. S. R., Sadavoy, S. I., Bhandare, A., Vázquez-Semadeni, E. & Ginsburg, A., 2020, Space Sci. Rev., 216, 4, 62, doi: 10.1007/s11214-020-00688-5

Roueff, E., Ruaud, M., Le Petit, F., Godard, B. & Le Bourlot, J., 2014, J. Cami & N. L. J. Cox, editors, The Diffuse Interstellar Bands, volume 297, 311–320, doi: 10.1017/S1743921313016050

Ruaud, M., Wakelam, V. & Hersant, F., 2016, MNRAS, 459, 4, 3756–3767, doi: 10.1093/mnras/stw887

Rubin, M., Altwegg, K., Balsiger, H., Bar-Nun, A., Berthelier, J.-J. *et al.*, 2018, Science Advances, 4, 7, eaar6297, doi: 10.1126/sciadv.aar6297

Rybicki, G. B. & Lightman, A. P., 1985, Radiative processes in astrophysics, John Wiley & Sons

Sahu, D., Liu, S.-Y., Su, Y.-N., Li, Z.-Y., Lee, C.-F. *et al.*, 2019, ApJ, 872, 2, 196, doi: 10.3847/1538-4357/aaffda

Sakai, N. & Yamamoto, S., 2013, Chemical Reviews, 113, 12, 8981–9015, doi: 10.1021/cr4001308

Sakai, N., Sakai, T., Hirota, T., Watanabe, Y., Ceccarelli, C. *et al.*, 2014, Nature, 507, 7490, 78–80, doi: 10.1038/nature13000

Saki, M., Gibb, E. L., Bonev, B. P., Roth, N. X., DiSanti, M. A. *et al.*, 2020, AJ, 160, 4, 184, doi: 10.3847/1538-3881/aba522

Salta, Z., Segovia, M. E., Katz, A., Tasinato, N., Barone, V. & Ventura, O. N., 2021, The Journal of Organic Chemistry, 86, 3, 2941–2956

Salyk, C., Blake, G. A., Boogert, A. C. A. & Brown, J. M., 2011, ApJ, 743, 2, 112, doi: 10.1088/0004-637X/743/2/112

Santos, J. C., 2021, Master's thesis, University of Sao Paulo

Santos, J. C., Rocha, A. B. & Oliveira, R. R., 2020, Journal of Molecular Modeling, 26, 278, doi: 10.1007/s00894-020-04523-0

Santos, J. C., Bronfman, L., Mendoza, E., Lépine, J. R. D., Duronea, N. U. *et al.*, 2022a, ApJ, 925, 1, 3, doi: 10.3847/1538-4357/ac36cc

Santos, J. C., Chuang, K.-J., Lamberts, T., Fedoseev, G., Ioppolo, S. & Linnartz, H., 2022b, ApJ, 931, 2, L33, doi: 10.3847/2041-8213/ac7158

Santos, J. C., Chuang, K.-J., Lamberts, T., Fedoseev, G., Ioppolo, S. & Linnartz, H., 2022c, ApJ, 931, 2, L33, doi: 10.3847/2041-8213/ac7158

Santos, J. C., Chuang, K. J., Schrauwen, J. G. M., Traspas Muiña, A., Zhang, J. *et al.*, 2023a, A&A, 672, A112, doi: 10.1051/0004-6361/202245704

Santos, J. C., Linnartz, H. & Chuang, K. J., 2023b, A&A, 678, A112, doi: 10.1051/0004-6361/202347348

Santos, J. C., Enrique-Romero, J., Lamberts, T., Linnartz, H. & Chuang, K.-J., 2024a, ACS Earth and Space Chemistry, 8, 8, 1646–1660, doi: 10.1021/acsearthspacechem.4c00150

Santos, J. C., Linnartz, H. & Chuang, K. J., 2024b, A&A, 690, A24, doi: 10.1051/0004-6361/202451368

Santos, J. C., van Gelder, M. L., Nazari, P., Ahmadi, A. & van Dishoeck, E. F., 2024c, A&A, in press, doi: 10.1051/0004-6361/202347097

Schiff, H. I. & Bohme, D. K., 1979, ApJ, 232, 740–746, doi: 10.1086/157334

Schmidt, D. R. & Ziurys, L. M., 2019, ApJ, 881, 2, L38, doi: 10.3847/2041-8213/ab3663

Schopf, J. W., 1993, Science, 260, 5108, 640–646, doi: 10.1126/science.260.5108.640

Schopf, J. W., 1994, Proceedings of the National Academy of Science, 91, 15, 6735–6742, doi: 10.1073/pnas.91.15.6735

Schuhmann, M., Altwegg, K., Balsiger, H., Berthelier, J.-J., De Keyser, J. *et al.*, 2019, ACS Earth and Space Chemistry, 3, 9, 1854–1861, doi: 10.1021/acsearthspacechem.9b00094

Scibelli, S. & Shirley, Y., 2020, ApJ, 891, 1, 73, doi: 10.3847/1538-4357/ab7375

Semenov, D., Favre, C., Fedele, D., Guilloteau, S., Teague, R. *et al.*, 2018, A&A, 617, A28, doi: 10.1051/0004-6361/201832980

Shannon, R. J., Blitz, M. A., Goddard, A. & Heard, D. E., 2013, Nature Chemistry, 5, 9, 745–749, doi: 10.1038/nchem.1692

Shimanouchi, T., 1972, Tables of Molecular Vibrational Frequencies Consolidated Volume I, National Bureau of Standards

Shingledecker, C. N., Lamberts, T., Laas, J. C., Vasyunin, A., Herbst, E. *et al.*, 2020, ApJ, 888, 1, 52, doi: 10.3847/1538-4357/ab5360

Shingledecker, C. N., Banu, T., Kang, Y., Wei, H., Wandishin, J. *et al.*, 2022, The Journal of Physical Chemistry A, 126, 32, 5343–5353

Sie, N.-E., Cho, Y.-T., Huang, C.-H., Muñoz Caro, G. M., Hsiao, L.-C. *et al.*, 2022, ApJ, 938, 1, 48, doi: 10.3847/1538-4357/ac922a

Silva, A., Zhang, Q., Sanhueza, P., Lu, X., Beltran, M. T. *et al.*, 2017, ApJ, 847, 2, 87, doi: 10.3847/1538-4357/aa88c6

da Silva, G., 2010, Angewandte Chemie, 122, 41, 7685–7687

Simon, A., Öberg, K. I., Rajappan, M. & Maksiutenko, P., 2019, ApJ, 883, 1, 21, doi: 10.3847/1538-4357/ab32e5

Simon, A., Rajappan, M. & Öberg, K. I., 2023, ApJ, 955, 1, 5, doi: 10.3847/1538-4357/aceaf8

Simons, M. A. J., Lamberts, T. & Cuppen, H. M., 2020, A&A, 634, A52, doi: 10.1051/0004-6361/201936522

Slavicinska, K., van Dishoeck, E. F., Tychoniec, Ł., Nazari, P., Rubinstein, A. E. *et al.*, 2024, A&A, 688, A29, doi: 10.1051/0004-6361/202449785

Slavicinska, K., Boogert, A. C. A., Tychoniec, Ł., van Dishoeck, E. F., van Gelder, M. L. *et al.*, 2025, A&A, 693, A146, doi: 10.1051/0004-6361/202451383

Smardzewski, R. R., 1978, J. Chem. Phys., 68, 6, 2878–2888, doi: 10.1063/1.436085

Smith, A. M., Stecher, T. P. & Casswell, L., 1980, ApJ, 242, 402–410, doi: 10.1086/158473

Smith, D., Devlin, J. P. & Scott, D. W., 1968, Journal of Molecular Spectroscopy, 25, 2, 174–184

Smith, I. W. M., 2011, ARA&A, 49, 1, 29–66, doi: 10.1146/annurev-astro-081710-102533

Smith, R. G., 1991, MNRAS, 249, 172, doi: 10.1093/mnras/249.1.172

Smith, R. S., Huang, C., Wong, E. K. L. & Kay, B. D., 1997, Phys. Rev. Lett., 79, 5, 909–912, doi: 10.1103/PhysRevLett.79.909

Snow, T. P. & McCall, B. J., 2006, ARA&A, 44, 1, 367–414, doi: 10.1146/annurev.astro.43.072103.150624

Snyder, L. E., Lovas, F. J., Hollis, J. M., Friedel, D. N., Jewell, P. R. *et al.*, 2005, ApJ, 619, 2, 914–930, doi: 10.1086/426677

Song, L. & Kästner, J., 2017, ApJ, 850, 2, 118, doi: 10.3847/1538-4357/aa943e

Spezzano, S., Sipilä, O., Caselli, P., Jensen, S. S., Czakli, S. *et al.*, 2022, A&A, 661, A111, doi: 10.1051/0004-6361/202243073

Strausz, O., Hikida, T. & Gunning, H., 1965, Canadian Journal of Chemistry, 43, 3, 717–721

Strom, A. I., Gutiérrez-Quintanilla, A., Chevalier, M., Ceponkus, J., Crépin, C. & Anderson, D. T., 2020, The Journal of Physical Chemistry A, 124, 22, 4471–4483, doi: 10.1021/acs.jpca.0c02900, pMID: 32401028

Suenobu, K., Nagaoka, M. & Yamabe, T., 1999, Journal of Molecular Structure: THEOCHEM, 461, 581–588

Tabone, B., Cabrit, S., Bianchi, E., Ferreira, J., Pineau des Forêts, G. *et al.*, 2017, A&A, 607, L6, doi: 10.1051/0004-6361/201731691

Tabone, B., Bettoni, G., van Dishoeck, E. F., Arabhavi, A. M., Grant, S. *et al.*, 2023, Nature Astronomy, 7, 805–814, doi: 10.1038/s41550-023-01965-3

Tafalla, M., Myers, P. C., Mardones, D. & Bachiller, R., 2000, A&A, 359, 967–976, doi: 10.48550/arXiv.astro-ph/0005525

Tait, S. L., Dohnálek, Z., Campbell, C. T. & Kay, B. D., 2005, J. Chem. Phys., 122, 16, 164708–164708, doi: 10.1063/1.1883630

Tan, J. C., Beltrán, M. T., Caselli, P., Fontani, F., Fuente, A. *et al.*, 2014, H. Beuther, R. S. Klessen, C. P. Dullemond & T. Henning, editors, Protostars and Planets VI, 149–172, doi: 10.2458/azu_uapress_9780816531240-ch007

Taniguchi, K., Ozeki, H. & Saito, M., 2017, The Astrophysical Journal, 846, 1, 46, doi: 10.3847/1538-4357/aa82ba

Taniguchi, K., Saito, M., Majumdar, L., Shimoikura, T., Dobashi, K. *et al.*, 2018, ApJ, 866, 2, 150, doi: 10.3847/1538-4357/aade97

Taniguchi, K., Herbst, E., Caselli, P., Paulive, A., Maffucci, D. M. & Saito, M., 2019a, ApJ, 881, 1, 57, doi: 10.3847/1538-4357/ab2d9e

Taniguchi, K., Herbst, E., Ozeki, H. & Saito, M., 2019b, The Astrophysical Journal, 884, 2, 167, doi: 10.3847/1538-4357/ab3eb8

Taquet, V., Codella, C., De Simone, M., López-Sepulcre, A., Pineda, J. E. *et al.*, 2020, A&A, 637, A63, doi: 10.1051/0004-6361/201937072

Thaddeus, P., Kutner, M. L., Penzias, A. A., Wilson, R. W. & Jefferts, K. B., 1972, ApJ, 176, L73, doi: 10.1086/181023

Theule, P., Duvernay, F., Ilmane, A., Hasegawa, T., Morata, O. *et al.*, 2011, A&A, 530, A96, doi: 10.1051/0004-6361/201016051

Thompson, A. R., Moran, J. M. & Swenson, G. W., 2017, Interferometry and synthesis in radio astronomy, Springer Nature

Tieftrunk, A., Pineau des Forets, G., Schilke, P. & Walmsley, C. M., 1994, A&A, 289, 579–596

Tielens, A. G. G. M. & Hagen, W., 1982, A&A, 114, 2, 245–260

Tielens, A. G. G. M., Tokunaga, A. T., Geballe, T. R. & Baas, F., 1991, ApJ, 381, 181, doi: 10.1086/170640

Tobin, J. J. & Sheehan, P. D., 2024, ARA&A, 62, 1, 203–241, doi: 10.1146/annurev-astro-052920-103752

Tobin, J. J., Looney, L. W., Li, Z.-Y., Chandler, C. J., Dunham, M. M. *et al.*, 2016, ApJ, 818, 1, 73, doi: 10.3847/0004-637X/818/1/73

Townes, C. H. & Schawlow, A. L., 1975, Microwave Spectroscopy, Dover Publications

Tsai, S.-M., Lee, E. K. H., Powell, D., Gao, P., Zhang, X. *et al.*, 2023, Nature, 617, 7961, 483–487, doi: 10.1038/s41586-023-05902-2

Tschersich, K. G., 2000, J. Appl. Phys., 87, 5, 2565–2573, doi: 10.1063/1.372220

Tsuge, M., Molpeceres, G., Aikawa, Y. & Watanabe, N., 2023, Nature Astronomy, doi: 10.1038/s41550-023-02071-0

Turner, B. E., 1995, ApJ, 455, 556, doi: 10.1086/176604

Turner, B. E., Terzieva, R. & Herbst, E., 1999, ApJ, 518, 2, 699–732, doi: 10.1086/307300

Tychoniec, Ł., Manara, C. F., Rosotti, G. P., van Dishoeck, E. F., Cridland, A. J. *et al.*, 2020, A&A, 640, A19, doi: 10.1051/0004-6361/202037851

Tychoniec, Ł., van Dishoeck, E. F., van't Hoff, M. L. R., van Gelder, M. L., Tabone, B. *et al.*, 2021, A&A, 655, A65, doi: 10.1051/0004-6361/202140692

van der Tak, F. F. S., van Dishoeck, E. F. & Caselli, P., 2000, A&A, 361, 327–339, doi: 10.48550/arXiv.astro-ph/0008010

van der Tak, F. F. S., Boonman, A. M. S., Braakman, R. & van Dishoeck, E. F., 2003, A&A, 412, 133–145, doi: 10.1051/0004-6361:20031409

van der Tak, F. F. S., Chavarría, L., Herpin, F., Wyrowski, F., Walmsley, C. M. *et al.*, 2013, A&A, 554, A83, doi: 10.1051/0004-6361/201220976

van der Tak, F. F. S., Lique, F., Faure, A., Black, J. H. & van Dishoeck, E. F., 2020, Atoms, 8, 2, 15, doi: 10.3390/atoms8020015

van Dishoeck, E. F., 2004, ARA&A, 42, 1, 119–167, doi: 10.1146/annurev.astro.42.053102.134010

van Dishoeck, E. F., 2014, Faraday Discussions, 168, 9, doi: 10.1039/C4FD00140K

van Dishoeck, E. F. & Black, J. H., 1986, ApJS, 62, 109, doi: 10.1086/191135

van Dishoeck, E. F. & Black, J. H., 1988, ApJ, 334, 771, doi: 10.1086/166877

van Dishoeck, E. F., Blake, G. A., Jansen, D. J. & Groesbeck, T. D., 1995, ApJ, 447, 760, doi: 10.1086/175915

van Dishoeck, E. F., Herbst, E. & Neufeld, D. A., 2013, Chemical Reviews, 113, 12, 9043–9085, doi: 10.1021/cr4003177

van Gelder, M. L., Tabone, B., Tychoniec, Ł., van Dishoeck, E. F., Beuther, H. *et al.*, 2020, A&A, 639, A87, doi: 10.1051/0004-6361/202037758

van Gelder, M. L., Tabone, B., van Dishoeck, E. F. & Godard, B., 2021, A&A, 653, A159, doi: 10.1051/0004-6361/202141591

van Gelder, M. L., Jaspers, J., Nazari, P., Ahmadi, A., van Dishoeck, E. F. *et al.*, 2022a, A&A, 667, A136, doi: 10.1051/0004-6361/202244471

van Gelder, M. L., Nazari, P., Tabone, B., Ahmadi, A., van Dishoeck, E. F. *et al.*, 2022b, A&A, 662, A67, doi: 10.1051/0004-6361/202142769

van Gelder, M. L., Ressler, M. E., van Dishoeck, E. F., Nazari, P., Tabone, B. *et al.*, 2024, A&A, 682, A78, doi: 10.1051/0004-6361/202348118

van Hemert, M. C., Takahashi, J. & van Dishoeck, E. F., 2015, Journal of Physical Chemistry A, 119, 24, 6354–6369, doi: 10.1021/acs.jpca.5b02611

Vassilev, V., Meledin, D., Lapkin, I., Belitsky, V., Nyström, O. *et al.*, 2008a, A&A, 490, 3, 1157–1163, doi: 10.1051/0004-6361:200810459

Vassilev, V., Meledin, D., Lapkin, I., Belitsky, V., Nyström, O. *et al.*, 2008b, A&A, 490, 1157–1163, doi: 10.1051/0004-6361:200810459

Vastel, C., 2014, Formalism of the CASSIS software, `https://cassis.irap.omp.eu/docs/RadiativeTransfer.pdf`, accessed: 2025-02-13

Vastel, C., Phillips, T. G., Ceccarelli, C. & Pearson, J., 2003, ApJ, 593, 2, L97–L100, doi: 10.1086/378261

Vastel, C., Ceccarelli, C., Lefloch, B. & Bachiller, R., 2014, ApJ, 795, 1, L2, doi: 10.1088/2041-8205/795/1/L2

Vastel, C., Bottinelli, S., Caux, E., Glorian, J. M. & Boiziot, M., 2015, SF2A-2015: Proceedings of the Annual meeting of the French Society of Astronomy and Astrophysics, 313–316

Vastel, C., Quénard, D., Le Gal, R., Wakelam, V., Andrianasolo, A. *et al.*, 2018, MNRAS, 478, 4, 5514–5532, doi: 10.1093/mnras/sty1336

Vasyunin, A. I. & Herbst, E., 2013, ApJ, 769, 1, 34, doi: 10.1088/0004-637X/769/1/34

Vidal, T. H. G. & Wakelam, V., 2018, MNRAS, 474, 4, 5575–5587, doi: 10.1093/mnras/stx3113

Vidal, T. H. G., Loison, J.-C., Jaziri, A. Y., Ruaud, M., Gratier, P. & Wakelam, V., 2017, MNRAS, 469, 1, 435–447, doi: 10.1093/mnras/stx828

Vidali, G., 2013, Chemical Reviews, 113, 12, 8752–8782, doi: 10.1021/cr400156b

Viti, S., Collings, M. P., Dever, J. W., McCoustra, M. R. S. & Williams, D. A., 2004, MNRAS, 354, 4, 1141–1145, doi: 10.1111/j.1365-2966.2004.08273.x

Vitorino, J., Loison, J. C., Wakelam, V., Congiu, E. & Dulieu, F., 2024, MNRAS, doi: 10.1093/mnras/stae1747

Wada, A., Mochizuki, N. & Hiraoka, K., 2006, ApJ, 644, 1, 300–306, doi: 10.1086/503380

Wagner, A. F. & Graff, M. M., 1987, ApJ, 317, 423, doi: 10.1086/165287

Wakelam, V. & Herbst, E., 2008, ApJ, 680, 1, 371–383, doi: 10.1086/587734

Wakelam, V., Castets, A., Ceccarelli, C., Lefloch, B., Caux, E. & Pagani, L., 2004, A&A, 413, 609–622, doi: 10.1051/0004-6361:20031572

Wakelam, V., Ceccarelli, C., Castets, A., Lefloch, B., Loinard, L. *et al.*, 2005, A&A, 437, 1, 149–158, doi: 10.1051/0004-6361:20042566

Wakelam, V., Loison, J. C., Herbst, E., Pavone, B., Bergeat, A. *et al.*, 2015, ApJS, 217, 2, 20, doi: 10.1088/0067-0049/217/2/20

Wakelam, V., Loison, J. C., Mereau, R. & Ruaud, M., 2017, Molecular Astrophysics, 6, 22–35, doi: 10.1016/j.molap.2017.01.002

Walsh, C., Millar, T. J., Nomura, H., Herbst, E., Widicus Weaver, S. *et al.*, 2014, A&A, 563, A33, doi: 10.1051/0004-6361/201322446

Walsh, C., Loomis, R. A., Öberg, K. I., Kama, M., van 't Hoff, M. L. R. *et al.*, 2016, The Astrophysical Journal Letters, 823, 1, L10, doi: 10.3847/2041-8205/823/1/L10

Wang, J., Marks, J. H., Tuli, L. B., Mebel, A. M., Azyazov, V. N. & Kaiser, R. I., 2022, The Journal of Physical Chemistry A, 126, 51, 9699–9708

Watanabe, N. & Kouchi, A., 2002, ApJ, 571, 2, L173–L176, doi: 10.1086/341412

Watanabe, N. & Kouchi, A., 2008, Progress In Surface Science, 83, 439–489, doi: 10.1016/j. progsurf.2008.10.001

Watanabe, N., Mouri, O., Nagaoka, A., Chigai, T., Kouchi, A. & Pirronello, V., 2007, ApJ, 668, 2, 1001–1011, doi: 10.1086/521421

Werner, H.-J., Knowles, P. J., Knizia, G., Manby, F. R. & Schütz, M., 2012, Wiley Interdisciplinary Reviews: Computational Molecular Science, 2, 2, 242–253

Werner, H.-J., Knowles, P. J., Manby, F. R., Black, J. A., Doll, K. *et al.*, 2020, The Journal of chemical physics, 152, 14

West, B., Castillo, S. R., Sit, A., Mohamad, S., Lowe, B. *et al.*, 2018, Physical Chemistry Chemical Physics, 20, 10, 7195–7205

Western, C. M., 2016, J. Quant. Spectrosc. Radiat. Transf., 186, 221–242

Westley, M. S., Baratta, G. A. & Baragiola, R. A., 1998, J. Chem. Phys., 108, 8, 3321–3326, doi: 10.1063/1.475730

Whittet, D. C. B., Poteet, C. A., Chiar, J. E., Pagani, L., Bajaj, V. M. *et al.*, 2013, ApJ, 774, 2, 102, doi: 10.1088/0004-637X/774/2/102

Widicus Weaver, S. L., 2019, ARA&A, 57, 79–112, doi: 10.1146/ annurev-astro-091918-104438

Williams, J. P. & Cieza, L. A., 2011, Annual Review of Astronomy and Astrophysics, 49, 1, 67–117

Willner, S. P., Gillett, F. C., Herter, T. L., Jones, B., Krassner, J. *et al.*, 1982, ApJ, 253, 174–187, doi: 10.1086/159622

Wilson, T. L. & Rood, R., 1994, ARA&A, 32, 191–226, doi: 10.1146/annurev.aa.32.090194. 001203

Winnewisser, G., Lewen, F., Thorwirth, S., Behnke, M., Hahn, J. *et al.*, 2003, Chemistry – A European Journal, 9, 22, 5501–5510, doi: 10.1002/chem.200305192

Woods, P. M., Occhiogrosso, A., Viti, S., Kaňuchová, Z., Palumbo, M. E. & Price, S. D., 2015, MNRAS, 450, 2, 1256–1267, doi: 10.1093/mnras/stv652

Yan, Y. T., Zhang, J. S., Henkel, C., Mufakharov, T., Jia, L. W. *et al.*, 2019, ApJ, 877, 2, 154, doi: 10.3847/1538-4357/ab17d6

Yan, Y. T., Henkel, C., Kobayashi, C., Menten, K. M., Gong, Y. *et al.*, 2023, A&A, 670, A98, doi: 10.1051/0004-6361/202244584

Yang, Y.-L., Evans, I., Neal J., Smith, A., Lee, J.-E., Tobin, J. J. *et al.*, 2020, ApJ, 891, 1, 61, doi: 10.3847/1538-4357/ab7201

Yang, Y.-L., Sakai, N., Zhang, Y., Murillo, N. M., Zhang, Z. E. *et al.*, 2021, ApJ, 910, 1, 20, doi: 10.3847/1538-4357/abdfd6

Yang, Y.-L., Green, J. D., Pontoppidan, K. M., Bergner, J. B., Cleeves, L. I. *et al.*, 2022, ApJ, 941, 1, L13, doi: 10.3847/2041-8213/aca289

Yarnall, Y. Y. & Hudson, R. L., 2022, ApJ, 931, 1, L4, doi: 10.3847/2041-8213/ac6b32

Zapata, L. A., Palau, A., Galván-Madrid, R., Rodríguez, L. F., Garay, G. *et al.*, 2015, MNRAS, 447, 2, 1826–1833, doi: 10.1093/mnras/stu2527

Zasowski, G., Kemper, F., Watson, D. M., Furlan, E., Bohac, C. J. *et al.*, 2009, ApJ, 694, 1, 459–478, doi: 10.1088/0004-637X/694/1/459

Zhang, C., Wang, J., Turner, A. M., Marks, J. H., Chandra, S. *et al.*, 2023, The Astrophysical Journal, 952, 2, 132, doi: 10.3847/1538-4357/acd451

Zhang, Q., Wang, H., Sun, T. & Wang, W., 2006, Chemical physics, 324, 2-3, 298–306

Zhao, Y. & Truhlar, D. G., 2008a, Theoretical chemistry accounts, 120, 215–241

Zhao, Y. & Truhlar, D. G., 2008b, Theoretical chemistry accounts, 120, 215–241, doi: 10.1007/s00214-007-0310-x

Zhou, Q., Simon, A., Öberg, K. I. & Rajappan, M., 2024, ApJ, 972, 2, 189, doi: 10.3847/1538-4357/ad6322

Zinnecker, H. & Yorke, H. W., 2007, ARA&A, 45, 1, 481–563, doi: 10.1146/annurev.astro.44.051905.092549

Zukowski, S. R., Mitev, P. D., Hermansson, K. & Ben-Amotz, D., 2017, The journal of physical chemistry letters, 8, 13, 2971–2975

Nederlandse Samenvatting

Sterren ontstaan in immense, inhomogene wolken van gas en stof die door de ruimte zweven. Na verloop van tijd verzamelen de dichtere delen binnen deze wolken genoeg materiaal om onder hun eigen zwaartekracht in te storten, waardoor een jonge ster ontstaat. Rond elke pasgeboren ster bevindt zich een draaiende schijf van achtergebleven materiaal, waarin planeten, manen, asteroïden en kometen geleidelijk hun vorm krijgen (Figuur 1).
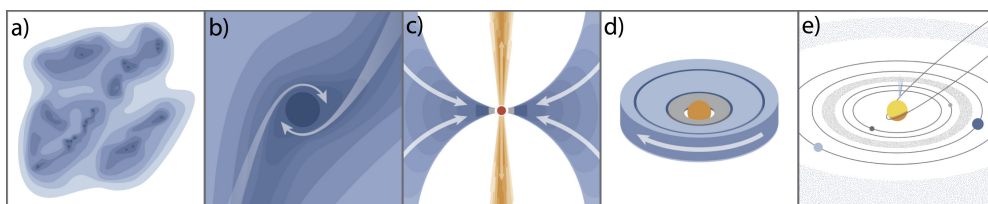
Figuur 1: Fasen van ster- en planeetvorming in zonachtige systemen. (a) Er ontstaan dichte delen in inhomogene wolken van gas en stof. (b en c) Deze delen storten in onder de zwaartekracht en vormen een jonge ster. (d) Het omringende materiaal wordt verspreid, waarna een jonge ster met een schijf overblijft waarin planeten kunnen ontstaan. (e) Uiteindelijk verdwijnt de schijf en ontstaat een planetenstelsel. Afkomstig van Öberg & Bergin (2021).

Deze sterrenkraamkamers—waaruit uiteindelijk de onderdelen van een planetenstelsel ontstaan—bestaan voor ongeveer 99% uit gas en slechts 1% uit stof. Ondanks het feit dat stof schaars is vergeleken met gas, speelt het een grote rol: het biedt oppervlak voor verschillende chemische reacties. Op deze kleine deeltjes, kleiner dan de breedte van een menselijk haar, combineren atomen en moleculen zich om essentiële ingrediënten voor het leven te vormen, zoals water en organische verbindingen. Terwijl deze soorten zich ophopen, creëren ze een laag van bevroren materiaal—bekend als interstellair ijs—die de stofdeeltjes omhult. Wanneer een jonge ster ontstaat en zijn omgeving opwarmt, ervaren de bevroren stofdeeltjes die dicht genoeg bij de ster komen hogere temperaturen. Dit veroorzaakt dat het ijs sublimeert, waardoor het materiaal dat voorheen in vaste vorm was, vrijkomt als gas.

Interstellaire ijsprocessen

Stofdeeltjes—en het ijs dat zich erop vormt—creëren een vruchtbare omgeving waar chemie kan gedijen. Ten eerste, omdat de temperaturen in interstellaire wolken extreem laag zijn (rond de 10 K, of –263°C), blijven gasfase-moleculen gemakkelijk plakken aan het koude oppervlak van het stof. Dit maakt het mogelijk voor moleculen en atomen om zich op te hopen, makkelijker met elkaar in contact te komen en te reageren. Ten tweede biedt het oppervlak een manier om de overtollige energie die vrijkomt bij een reactie kwijt te raken. Dit helpt de pas gevormde moleculen om zich te stabiliseren, zodat ze niet meteen uit elkaar vallen—een veelvoorkomend probleem voor chemische reacties in de gasfase in interstellaire wolken.

Al met al spelen de fysisch-chemische processen die plaatsvinden in interstellair ijs een centrale rol bij het bepalen van de moleculaire samenstelling van de gebieden waar

sterren en planeten beginnen te vormen. Deze ijsprocessen kunnen in het algemeen worden onderverdeeld in vier hoofdgroepen (Figuur 2): adsorptie, desorptie, diffusie en reactie. Wanneer een gasfase-molecuul een koud stofdeeltje tegenkomt en aan het oppervlak blijft kleven, noemen we dit adsorptie. Tegenovergesteld, als een geadsorbeerd molecuul genoeg energie krijgt om de krachten die het aan het oppervlak vasthouden te overwinnen, komt het in de gasfase in een proces dat desorptie wordt genoemd. Moleculen op het oppervlak kunnen zich ook verplaatsen zonder het oppervlak te verlaten, in een reeks bewegingen die diffusie wordt genoemd. Ten slotte, wanneer twee atmen of moleculen onder de juiste omstandigheden met elkaar in contact komen, kan een reactie plaatsvinden, wat resulteert in de vorming van nieuw molecuul.
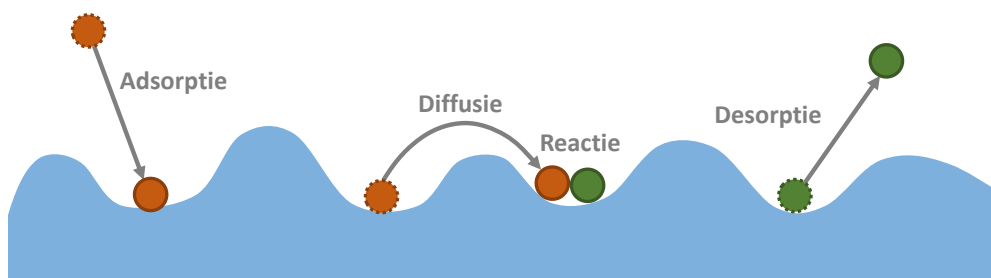
Figuur 2: Cartoon van de vier categorieën van ijsprocessen: adsorptie, desorptie, diffusie en reactie.

De interactie tussen deze ijsprocessen bepaalt welke moleculen worden gevormd of vernietigd op stofdeeltjes, evenals hoe en wanneer ze in de gasfase komen. Het ontrafelen van de uitkomsten van deze ijsprocessen is daarom essentieel voor het begrijpen van welke moleculen worden geproduceerd in pre-stellaire en proto-stellaire omgevingen en in welke mate ze kunnen worden opgenomen in vormende planetesimalen. Dit is het hoofddoel van dit proefschrift.

Astrochemie in het laboratorium

Vanwege de grote afstand tussen de aarde en de interstellaire wolken waar ijs groeit (meestal meer dan 100 pc, of 325 lichtjaar), is direct experimenteren met de bevroren stofdeeltjes in deze regio's niet mogelijk. Ruimtemissies zoals Rosetta, die de komeet 67P/Churyumov–Gerasimenko bestudeerde, en sample-return missies zoals Hayabusa en OSIRIS-REx, kunnen enig inzicht bieden in het lot van interstellair ijs nadat het onderdeel is geworden van kometen of asteroïden; maar de eerdere fasen blijven buiten bereik. Om de chemie die plaatsvindt in deze eerdere fasen te bestuderen, recreëren we de fysische omstandigheden van hun omgevingen in laboratoria hier op aarde. Dit wordt mogelijk gemaakt door geavanceerde experimentele opstellingen die extreem lage temperaturen (rond de 10 K, of –263°C) en druk (rond de 10^{-10} mbar, of bijna een biljard keer lager dan atmosferische druk) kunnen bereiken. Deze apparaten stellen ons in staat niet alleen de vorming en evolutie van interstellair ijs te simuleren, maar ook processen te versnellen die normaal gesproken minstens miljoenen jaren zouden duren, en deze te verkorten tot tijdschalen van slechts een paar uur. Deze gecontroleerde experimenten stellen ons ook in staat specifieke mechanismes in vereenvoudigde systemen te isoleren en te bestuderen, wat een meer gerichte kijk biedt op de bestudeerde chemie.

In dit proefschrift zijn verschillende van dergelijke vacuüm-cryogene apparaten gebruikt. Het belangrijkste apparaat was SURFRESIDE[3], dat zich bevindt in de Universiteit Leiden in Nederland, dat speciaal is gebouwd om oppervlakte-reacties op interstellaire ijsanalogen te bestuderen die in gang worden gezet door atomen en radicalen. Andere opstellingen die in dit proefschrift worden gepresenteerd zijn LISA (Radboud Universiteit, Nederland), dat zich richt op de interactie van interstellaire ijsanalogen met infraroodlicht; en SPACE-KITTEN (Harvard University, Verenigde Staten), ontworpen om te onderzoeken hoe ijs reageert op thermische processen die opwarming door een jonge ster nabootsen.

Observationele astrochemie

Om zinvolle experimenten te bedenken, moeten we eerst weten welke moleculen aanwezig zijn in verschillende gebieden in de ruimte, en in welke fysische toestand. Hiervoor zijn waarnemingen essentieel, omdat deze het enige directe, empirische bewijs leveren van de chemische inventaris van gebieden waar sterren en planeten zich vormen. Waarnemingen stellen ons ook in staat om hypothesen te testen en te valideren die zijn afgeleid van laboratoriumexperimenten en modellen van interstellaire chemische evolutie. Op deze manier vormen waarnemingen een fundamenteel onderdeel van astrochemisch onderzoek, en verankeren ze experimentele en theoretische onderzoeken in echte astronomische gegevens.

In dit proefschrift zijn twee soorten astronomische waarnemingen bijzonder relevant: die gedaan op radiofrequenties en die gedaan met behulp van infraroodlicht. Radio-waarnemingen stellen ons in staat moleculen te detecteren die aanwezig zijn in de gasfase van interstellaire omgevingen, waaronder soorten die ooit in ijs waren bevroren en sindsdien zijn gesublimeerd. Deze waarnemingen worden uitgevoerd met behulp van radio-antennes, hetzij individueel of in gecoördineerde verzamelingen van telescopen die interferometers worden genoemd. Infraroodwaarnemingen zijn daarentegen cruciaal voor het detecteren van moleculen in ijs, die onzichtbaar blijven bij radiofrequenties. Samen bieden deze twee technieken complementaire inzichten in de chemische samenstelling van ster- en planeetvormingsgebieden.

Dit proefschrift

Dit proefschrift onderzoekt de fysisch-chemische evolutie van interstellair ijs tijdens de verschillende stadia van ster- en planeetvorming. Dit omvat het begrijpen van hun vormingsmechanismen in koude moleculaire wolken, hun transformatie tijdens ster- en planeetvorming, en hun uiteindelijke sublimatie en mogelijke incorporatie in vormende planeten en planetesimalen. Om dit te bereiken combineren we experimenten die gebruik maken van apparatuur die interstellaire omstandigheden nabootsen met astronomische waarnemingen van de moleculaire samenstelling in deze omgevingen. De chemische paden die in dit proefschrift zijn ontdekt, worden benadrukt in Figuur 3, en hieronder volgt een samenvatting van de belangrijkste bevindingen uit elk hoofdstuk:

Hoofdstuk 2. In dit hoofdstuk bestuderen we de vorming van methanol (CH_3OH) ijs, een cruciaal bestanddeel van interstellair ijs dat fungeert als een belangrijke voorganger van complexe organische moleculen in de ruimte. Onze experimentele resultaten tonen aan dat de dominante laatste stap in het pad voor methanolvorming plaatsvindt via een reactie tussen CH_3O en H_2CO, in plaats van het eerder voorgestelde mechanismen waarbij CH_3O en H betrokken zijn. Deze bevindingen komen overeen
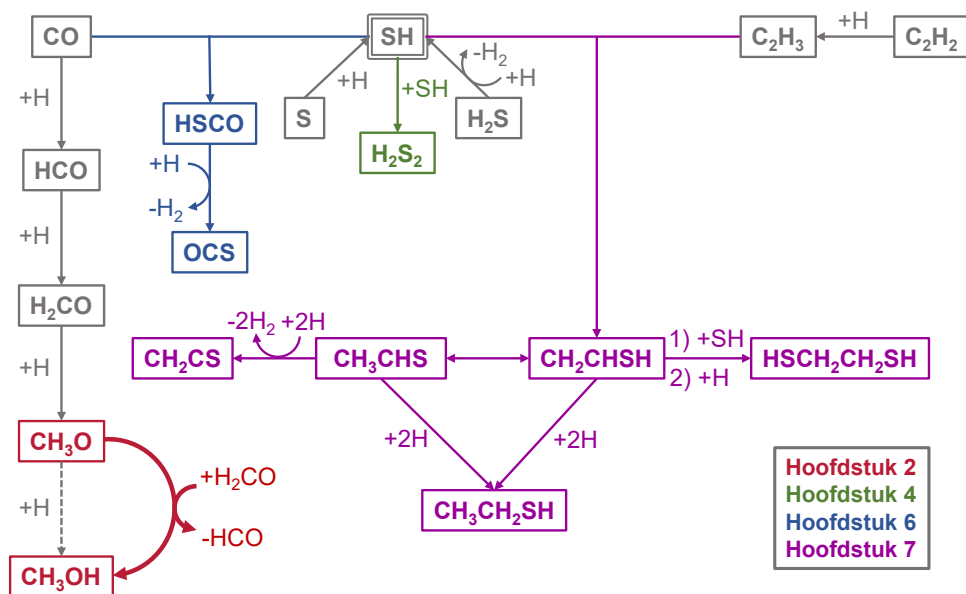
Figuur 3: Samenvatting van de interstellaire ijsreactie routes die in dit proefschrift zijn ontdekt.

met theoretische modelvoorspellingen onder laboratoriumomstandigheden, die vervolgens uitgebreid kunnen worden naar situaties die representatief zijn voor interstellaire wolken, en die suggereren dat dit alternatieve mechanisme ook het dominante proces in de ruimte is. Dit heeft belangrijke implicaties voor het modelleren van de chemie van deze omgevingen en het interpreteren van de verdeling van gedeutereerd methanol in deze gebieden.

Hoofdstuk 3. Dit hoofdstuk onderzoekt experimenteel de invloed van infrarode straling op interstellair ijs, waarbij wordt aangetoond dat infraroodlicht dat in resonantie is met de vibraties van ijsmoleculen, structurele herschikkingen kan induceren en zelfs de desorptie van ijsmateriaal kan veroorzaken. Deze effecten hebben mogelijke implicaties voor de waargenomen hoeveelheden complexe moleculen, met name degenen die vermoedelijk in ijs worden gevormd, en die in de gasfase worden gezien in gebieden waar thermische sublimatie niet mogelijk is.

Hoofdstuk 4. In dit hoofdstuk onderzoeken we de interactie tussen vast H_2S, een belangrijke vluchtige zwaveldrager in interstellair ijs, en waterstofatomen in het laboratorium. We tonen aan dat H_2S reageert met waterstof om HS radicalen en H_2 te vormen, waarbij het meeste van de HS ofwel combineert om H_2S_2 te vormen of opnieuw reageert met waterstof om H_2S te hervormen. Een significant deel van het hervormde H_2S sublimeert onmiddellijk door de overtollige vormingsenergie, wat leidt tot een verlies van H_2S ijs. In deze studie ontwikkelen we een nieuwe manier om deze door chemie geïnduceerde desorptie direct te kwantificeren en de bijdrage hiervan in de vorming van H_2S_2 te onderscheiden van de vernietiging van het oorspronkelijke H_2S ijs.

Hoofdstuk 5. In dit hoofdstuk karakteriseren we experimenteel het desorptiegedrag van H_2S ijs. We bepalen hoe sterk H_2S hecht aan zichzelf en aan waterijs –het belangrijkste bestanddeel van interstellair ijs– door het desorptiegedrag te meten wanneer het wordt gedeponeerd als puur H_2S ijs op waterijs. We onderzoeken ook het desorptiegedrag van H_2S in gemengd ijs dat veelal water bevat en vinden dat een verrassend groot deel van het H_2S gevangen blijft, zelfs boven de normale sublimatie-temperatuur. Met behulp van deze resultaten maken we een schatting van de locatie van de fase-overgang van ijs naar gas van H_2S in een planeetvormende schijf en vinden we dat H_2S waarschijnlijk in vaste vorm blijft in het gebied waar kometen en ijzige planetesimalen zich vormen.

Hoofdstuk 6. In dit hoofdstuk bouwen we voort op de bevindingen uit Hoofdstuk 4 en onderzoeken we experimenteel het chemische netwerk dat ontstaat door interacties tussen HS, CO en H. We vinden dat dit netwerk leidt tot de vorming van OCS ijs–een belangrijk vluchtig zwavelhoudend molecuul in interstellair ijs–zelfs onder ongunstige omstandigheden zoals een schaarste aan H-atomen. We stellen ook dat deze nieuwe potentiële route om OCS in ijs te vormen zich kan voordoen gedurende een lang deel van de levensduur van een wolk, en meer overeenkomt met de voorgestelde ijsfase (en dus de tijdschaal van de instorting van de wolk) waarin OCS wordt gedacht te worden waargenomen, dan andere veelvoorkomende voorgestelde mechanismen voor OCS vorming.

Hoofdstuk 7. Dit hoofdstuk breidt de zwavel-ijschemie uit die werd onderzocht in Hoofdstukken 4 en 6 door experimenteel de vorming van zwavelhoudende complexe organische moleculen met twee koolstofatomen te onderzoeken. We bestuderen de reacties van HS met C_2H_2 en H en vinden dat dit netwerk leidt tot een rijke chemie, waarbij minstens zes zwavelhoudende producten worden gevormd, waarvan vijf organisch. Het dominante product is ethaanthiol (CH_3CH_2SH) –een molecuul dat al is gedetecteerd in de interstellaire gasfase– dat lijkt te fungeren als een chemische put, en dus efficiënt wordt gevormd zolang er waterstofatomen aanwezig zijn, ten koste van de andere producten.

Hoofdstuk 8. In dit hoofdstuk presenteren we gasfase waarnemingen van twee belangrijke vluchtige zwaveldragers, OCS en SO_2, rondom een groot aantal massieve jonge, vormende sterren. We vinden dat hun hoeveelheid ten opzichte van methanol (CH_3OH; een veelvoorkomend referentiemolecuul dat in ijzen wordt aangetroffen), geen consistente trend met de helderheid van de sterren. Dit suggereert dat beide moleculen voornamelijk in ijs worden gevormd voordat de ster zelf is gevormd –in wolken dus. Ondanks deze gedeelde oorsprong wijzen hun abundantie verdelingen, en hoe ze zich verhouden tot ijs waarnemingen, op verschillende historische paden: OCS lijkt later in de evolutie van de wolk te vormen, samen met CH_3OH ijs, terwijl SO_2 waarschijnlijk eerder wordt gevormd, gelijktijdig met H_2O ijs, en/of mogelijk significant verandert nadat het sublimeert, door gasfasereacties dicht bij de vormende ster.

Hoofdstuk 9. In dit hoofdstuk presenteren we gasfase waarnemingen van het organische molecuul CH_3CCH rondom een massieve jonge ster die wordt gevormd. Dit molecuul, dat wordt gedacht te worden gevormd via een combinatie van gas- en ijschemie, wordt vaak gebruikt om gas temperaturen te traceren. Door de kinematica van het gas te analyseren, concluderen we dat de emissie waarschijnlijk wordt gedomineerd door de rustige, buitenste lagen van het omhulsel rond de protoster en waarschijnlijk twee verschillende componenten bevat – de ene warmer dan de andere. Daarnaast

kunnen we dankzij de spectroscopische eigenschappen van CH_3CCH indirect het hele temperatuurbereik van dit gas in meer detail traceren dan normaal mogelijk is met waarnemingen van een enkele radio-telescoop.

Toekomstperspectief

Samenvattend toont dit proefschrift aan hoe laboratoriumexperimenten en telescoopwaarnemingen samenwerken om het chemische verhaal te onthullen van het ijs en gas waaruit sterren en planeten vormen. Dit is een opwindend tijdperk voor dit veld, dankzij de geavanceerde laboratoriumtechnologie en krachtige telescopen zoals ALMA en JWST, die een ongekende blik bieden op de bouwstenen van planeten en planetesimalen, zowel in gas als in ijs. JWST biedt ook nieuwe inzichten in de materialen die aanwezig zijn in gebieden waar planeten zich vormen. Deze gezamenlijke inspanningen van waarnemingen, laboratoriumwerk en computermodellen zullen ons binnenkort het beste beeld geven van de chemie die speelt in de geboorteplaatsen van planeten.

English summary

Stars are born within immense, inhomogeneous clouds of gas and dust that drift through space. Over time, denser pockets within these clouds accumulate enough material to collapse under their own gravity, giving rise to a young star. Surrounding each newborn star is a swirling disk of leftover cloud material, where planets, moons, asteroids, and comets gradually take shape (Figure 1).
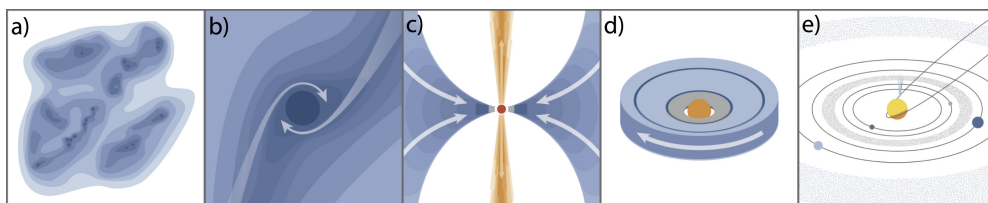
Figure 1: Stages of star and planet formation in Sun-like systems. (a) Dense pockets exists in inhomogeneous clouds of gas and dust. (b and c) These pockets collapse under gravity to form a young star. (d) The surrounding cloud material is dispersed, leaving a young star with a disk where planets can form. (e) Eventually, the disk disappears and gives rise to a planetary system. Adapted from Öberg & Bergin (2021).

These stellar nursery clouds—whose material eventually forms solar system bodies—are made up of about 99% gas and just 1% dust. Yet, despite being scarce compared to gas, dust grains play an outsized role: they provide surfaces where various chemical reactions take place. On these tiny particles, smaller than the width of a human hair, atoms and molecules combine to form essential ingredients for life, including water and organic compounds. As these species accumulate, they create a coating of frozen material—known as interstellar ices—that envelops the dust grains. When a young star forms and heats its surroundings, the icy grains that drift close enough to it experience rising temperatures. This causes the ices to sublimate, releasing into the gas the material that was previously locked in solid form.

Interstellar ice processes

Dust grains—and the ices that form on them—create a fertile environment where chemistry can thrive. First, because temperatures in interstellar clouds are extremely low (around 10 K, or –263°C), gas-phase molecules readily stick to the cold dust surfaces. This allows chemical species to accumulate, come into contact more easily, and react. Second, the solid surface provides a way for the excess energy released during molecule formation to dissipate. This helps stabilize the newly formed molecules, preventing them from immediately breaking apart—a common hindrance to gas-phase chemical reactions in interstellar environments.

Altogether, the physicochemical processes taking place in interstellar ices play a central role in shaping the molecular makeup of the environments where stars and

planets begin to form. These ice processes can generally be grouped into four main categories (Figure 2): adsorption, desorption, diffusion, and reaction. When a gas-phase molecule encounters a cold dust grain and sticks to its surface, this is called adsorption. On the other hand, if an adsorbed molecule gains enough energy to overcome the forces holding it to the surface, it is released into the gas phase in a process known as desorption. Molecules on the surface can also move around without detaching from it, in a set of motions called diffusion. Finally, when two species come into contact under the right conditions, a reaction can take place, resulting in the formation of a new molecule.
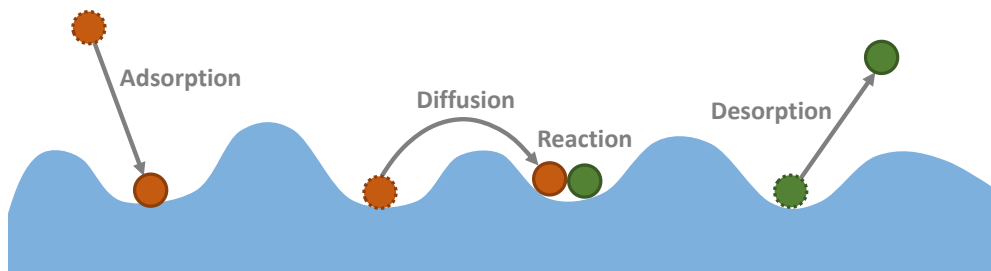
Figure 2: Cartoon of the four categories of ice processes: adsorption, desorption, diffusion, and reaction.

The interplay among these ice processes determines which molecules are formed or destroyed on dust grains, as well as how, and when, they are released into the gas phase. Unraveling the outcomes of these ice processes is therefore essential for understanding which molecules are produced in prestellar and protostellar environments and to what extent they can be incorporated into forming planetesimals. This is the central goal of the present thesis.

Laboratory astrochemistry

Due to the large distance between the Earth and the interstellar clouds where ices grow (typically over 100 pc, or 325 light years), direct experimentation on the icy dust grains within these regions is not possible. Space missions such as Rosetta, which targeted comet 67P/Churyumov–Gerasimenko, and sample-return missions like Hayabusa and OSIRIS-REx can offer some insight into the fate of interstellar ices after they have become part of comets or asteroids; but the earlier stages remain out of reach. To study the physicochemistry taking place in these earlier stages, we recreate the physical conditions of their environments in laboratory settings here on Earth. This is made possible by advanced experimental setups that can reach extremely low temperatures (around 10 K, or –263°C) and pressures (around 10^{-10} mbar, or nearly a quadrillion times below atmospheric pressure). These apparatuses allow us not only to simulate the formation and evolution of interstellar ices, but also to accelerate processes that would naturally take at least millions of years, condensing them into timescales of just a few hours. These controlled experiments also allow us to isolate and study specific mechanisms in simplified systems, offering a more focused view of the chemistry under investigation.

In this thesis, several such vacuum cryogenic apparatuses were utilized. The main one was SURFRESIDE[3], located at Leiden University in the Netherlands, which is

specifically built to study surface reactions on interstellar ice analogues triggered by atoms and radicals. Other setups featured in this thesis are LISA (Radboud University, the Netherlands), which focuses on the interaction of interstellar ice analogues with infrared light; and SPACE-KITTEN (Harvard University, United States), designed to investigate how ices respond to thermal processing that mimics heating by a young star.

Observational astrochemistry

To design meaningful experiments, we first need to know which molecules are present in different space environments, and in what physical state. Observations are crucial for this, as they provide the only direct, empirical evidence of the chemical inventory of regions where stars and planets are forming. They also allow us to test and validate hypotheses drawn from laboratory experiments and models of interstellar chemical evolution. In this way, observations form a fundamental pillar of astrochemical research, anchoring experimental and theoretical studies in real astronomical data.

In this thesis, two types of astronomical observations are particularly relevant: those made at radio frequencies and those using infrared light. Radio observations allow us to detect molecules present in the gas phase of interstellar environments, including species that were once frozen in ices and have since sublimated. These observations are carried out using radio antennas, either individually or in coordinated arrays known as interferometers. Infrared observations, on the other hand, are crucial for detecting molecules in ices, which mostly remain invisible at radio frequencies. Together, these two techniques offer complementary views of the chemical composition of star- and planet-forming regions.

This thesis

This thesis investigates the physicochemical evolution of interstellar ices across the various stages of star and planet formation. This includes understanding their formation mechanisms in cold molecular clouds, their transformation during star and planet formation, and their eventual sublimation and potential incorporation into forming planets and planetesimals. To achieve this, we combine experiments using apparatuses that mimic interstellar conditions with astronomical observations of the molecular content in these environments. The chemical pathways discovered in this thesis are highlighted in Figure 3, and below is a summary of the key findings from each chapter:

Chapter 2. In this chapter, we study the formation of methanol (CH_3OH) ice, a major component of interstellar ices that serves as a key precursor to complex organic molecules in space. Our experimental results demonstrate that the dominant final step in the pathway for methanol formation occurs through a reaction between CH_3O and H_2CO, rather than the previously proposed mechanism involving CH_3O and H. These findings align with theoretical model predictions under laboratory settings, which in turn extend to conditions representative of interstellar clouds and suggest that this alternative mechanism is also the dominant process in space. This has significant implications for modeling the chemistry of these environments and interpreting the distribution of deuterated methanol in these regions.

Chapter 3. This chapter investigates experimentally the influence of infrared radiation on interstellar ices, finding that infrared light in resonance with the vibrations of
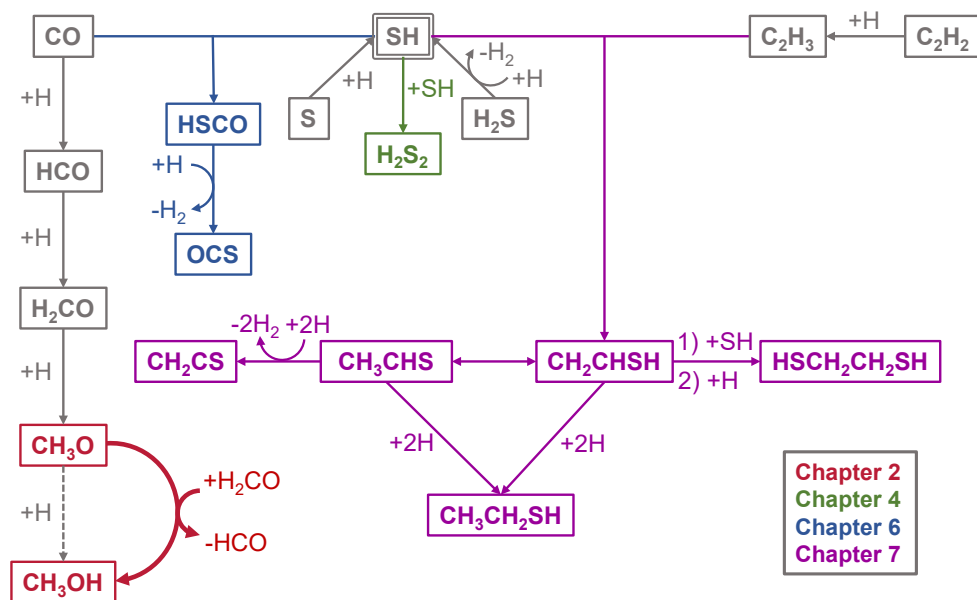
Figure 3: Summary of the interstellar ice reaction routes discovered in this thesis.

ice molecules can induce structural rearrangements and even trigger the desorption of ice material. These effects have potential implications for the observed abundances of complex molecules, particularly those thought to be formed in ices, in the gas phase of regions where thermal sublimation is not feasible.

Chapter 4. This chapter explores the interaction between solid H_2S, a key volatile sulfur carrier in interstellar ices, and hydrogen atoms in the laboratory. We show that H_2S reacts with hydrogen to form HS radicals and H_2, with most of the HS either recombining to form H_2S_2 or reacting again with hydrogen to reform H_2S. A significant fraction of the reformed H_2S promptly desorbs due to its excess formation energy, resulting in a loss of H_2S ice. In this study, we develop a novel approach to directly quantify this chemistry-induced desorption and disentangle its contribution from that of H_2S_2 formation in the net destruction of the original H_2S ice.

Chapter 5. This chapter experimentally characterizes the desorption behavior of H_2S ice. We determine how strongly H_2S adheres to itself and to water ice—the main constituent of interstellar ices—by measuring its desorption behavior when deposited as pure H_2S ice and on top of water ice. We also investigate the desorption behavior of H_2S in mixed ices dominated by water and find that a surprisingly large fraction of H_2S remains trapped well above its normal sublimation temperature. Using these results, we estimate the location in a planet-forming disk where H_2S transitions from ice to gas and find that it likely remains solid within the region where comets and icy planetesimals form.

Chapter 6. In this chapter we build on the findings from Chapter 4 and investigate experimentally the chemical network initiated by interactions between HS, CO, and H. We find that this network leads to the formation of OCS ice—a major volatile

sulfur carrier in interstellar ices—even at unfavorable conditions such as in scarcity of H atoms. We also argue that this new potential route to form OCS in ices can occur throughout a wide range of a cloud lifespan, and is more consistent with the proposed ice phase (and therefore cloud collapse timescale) in which OCS is thought to be observed than other commonly invoked OCS formation mechanisms.

Chapter 7. This chapter extends the sulfur ice chemistry explored in Chapters 4 and 6 by experimentally investigating the formation of sulfur-bearing complex organic molecules with two carbon atoms. We study the reactions of HS with C_2H_2 and H and find that this network leads to a rich chemistry, producing at least six sulfur-containing products, five of which are organic. The dominant product is ethanethiol (CH_3CH_2SH)—a molecule already detected in the interstellar gas phase—which appears to act as a chemical sink, forming efficiently as long as hydrogen atoms are present, at the expense of the other products.

Chapter 8. In this chapter, we present gas-phase observations of two major volatile sulfur carriers, OCS and SO_2, around a large sample of massive young, forming stars. We find that their abundances with respect to methanol (CH_3OH; a common reference molecule found in ices), do not display any trends across stars of different brightnesses. This suggests that both molecules are predominantly formed in ices before the star itself is formed—that is, in clouds. However, despite this shared origin, their abundance distributions and how they compare to ice observations point to different histories: OCS appears to form later in the cloud's evolution, in tandem with CH_3OH ice, while SO_2 likely forms earlier, simultaneously to H_2O ice, and/or may be significantly altered after it sublimates due to gas-phase reactions happening close to the newly forming star.

Chapter 9. This chapter presents gas-phase observations of the organic molecule CH_3CCH around a massive young star in formation. This molecule is thought to form through a combination of gas and ice chemistry and is commonly used to trace gas temperatures. By analyzing the kinematics of the gas, we find that the emission is dominated by the quiescent, outer layers surrounding the protostar and likely contains two distinct components—one warmer than the other. Additionally, thanks to the spectroscopic properties of CH_3CCH, we are able to indirectly trace the overall temperature range of this gas in more detail than is typically achievable with observations from a single-antenna radio telescope.

Future look

Overall, this thesis shows how laboratory experiments and telescope observations work together to reveal the chemical story of the ices and gases that form stars and planets. This is an exciting era for this field: thanks to cutting-edge laboratory technology and powerful telescopes like ALMA and JWST, we are offered an unprecedented look at the building blocks of planets and planetesimals in both gas and ice. With JWST also providing new insights into the materials present where planets are forming, the combined efforts of observations, lab work, and computer models will soon give us our best picture yet of the chemistry at play in the birthplaces of planets.

Resumo em Português

As estrelas nascem em imensas nuvens inhomogêneas de gás e poeira que flutuam pelo espaço. Com o tempo, bolsões mais densos dentro dessas nuvens acumulam material suficiente para colapsar sob sua própria gravidade, dando origem a uma estrela jovem. Ao redor de cada estrela recém-nascida existe um disco giratório de material remanescente da nuvem, onde planetas, luas, asteroides e cometas começam a se formar gradualmente (Figura 1).
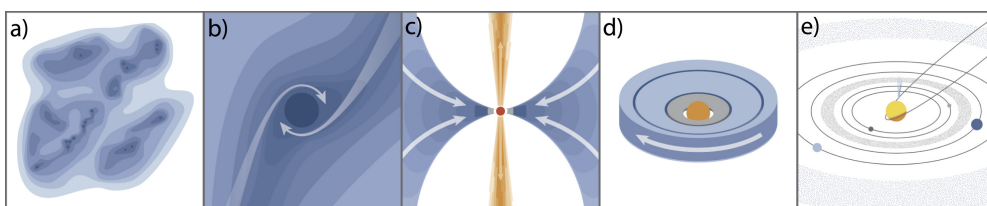
Figura 1: Estágios da formação de estrelas e planetas em sistemas semelhantes ao Sol. (a) Bolsões densos existem em nuvens inhomogêneas de gás e poeira. (b e c) Esses bolsões colapsam sob a própria gravidade para formar uma estrela jovem. (d) O material da nuvem ao redor é disperso, deixando uma estrela jovem com um disco onde planetas podem se formar. (e) Eventualmente, o disco desaparece e dá origem a um sistema planetário. Adaptado de Öberg & Bergin (2021).

Essas nuvens de estrelas em formação — cujo material eventualmente forma os corpos do sistema solar — são compostas por cerca de 99% de gás e apenas 1% de poeira. No entanto, apesar de sua escassez em relação ao gás, os grãos de poeira desempenham um papel desproporcional: eles fornecem superfícies onde várias reações químicas ocorrem. Nesses pequenos grãos, menores que a largura de um fio de cabelo humano, átomos e moléculas se combinam para formar ingredientes essenciais para a vida, incluindo água e compostos orgânicos. À medida que essas espécies se acumulam, elas criam uma camada de material congelado — conhecida como gelo interestelar — que envolve os grãos de poeira. Quando uma estrela jovem se forma e aquece seus arredores, os grãos congelados que se aproximam o suficiente experienciam um aumento de temperatura que faz com que os gelos sublimem, liberando para o gás o material que estava anteriormente preso na forma sólida.

Processos em gelos interestelar

Os grãos de poeira — e os gelos que se formam sobre eles — criam um ambiente fértil para que a química possa florescer. Primeiramente, porque as temperaturas nas nuvens interestelares são extremamente baixas (cerca de 10 K, ou –263°C), as moléculas na fase gasosa se aderem facilmente às superfícies frias dos grãos de poeira. Isso permite que espécies químicas se acumulem, entrem em contato de maneira mais

fácil e reagam. Em segundo lugar, a superfície sólida oferece uma maneira de dissipar a energia extra liberada durante a formação das moléculas. Isso ajuda a estabilizar as moléculas recém-formadas, impedindo que se quebrem imediatamente — um obstáculo comum nas reações químicas na fase gasosa em ambientes interestelares.

No geral, os processos físico-químicos que ocorrem nos gelos interestelares desempenham um papel central na composição molecular dos ambientes onde as estrelas e os planetas começam a se formar. Esses processos podem ser agrupados em quatro categorias principais (Figura 2): adsorção, dessorção, difusão e reação. Quando uma molécula da fase gasosa encontra um grão de poeira frio e se adere à sua superfície, isso é chamado de adsorção. Por outro lado, se uma molécula adsorvida ganha energia suficiente para superar as forças que a mantêm presa à superfície, ela é liberada para a fase gasosa em um processo conhecido como dessorção. As moléculas na superfície também podem se mover sem se soltar dela, em um conjunto de movimentos chamado difusão. Finalmente, quando duas espécies entram em contato nas condições certas, uma reação pode ocorrer, resultando na formação de uma nova molécula.
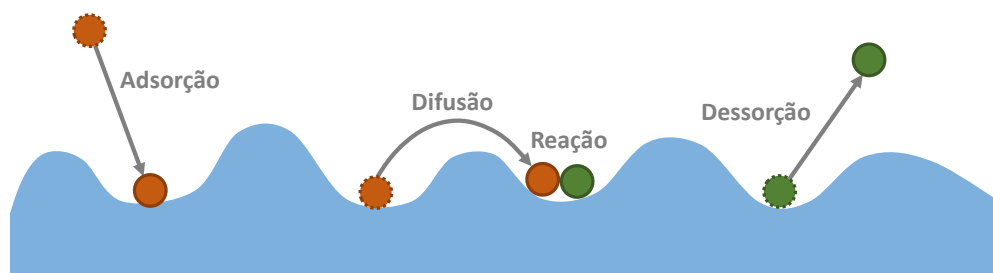
Figura 2: Cartoon dos quatro tipos de processos que ocorrem nos gelos: adsorção, dessorção, difusão e reação.

A interação entre esses processos ocorrendo nos gelos determina quais moléculas são formadas ou destruídas nos grãos de poeira, bem como quando e como elas são liberadas para a fase gasosa. Desvendar os resultados desses processos é, portanto, essencial para entender quais moléculas são produzidas nos ambientes pré-estelares e protostelares e até que ponto elas podem ser incorporadas em planetesimais em formação. Este é o objetivo central desta tese.

Astroquímica experimental

Devido à grande distância entre a Terra e as nuvens interestelares onde os gelos se formam (geralmente a mais de 100 pc, ou 325 anos-luz), experimentos conduzidos diretamente nos grãos de poeira nessas regiões não são viáveis. Missões espaciais como a Rosetta, que visitou o cometa 67P/Churyumov–Gerasimenko, e missões de coleta de amostras como a Hayabusa e a OSIRIS-REx podem oferecer algumas informações sobre o destino dos gelos interestelares depois que se tornam parte de cometas ou asteroides; mas as fases iniciais permanecem fora de alcance. Por isso, para estudar a físico-química que ocorre nessas etapas iniciais, é preciso recriar as condições físicas de seus ambientes em configurações laboratoriais aqui na Terra. Isso é possível graças a experimentos avançados que podem atingir temperaturas e pressões extremamente baixas (cerca de 10 K, ou —263°C; e cerca de 10^{-10} mbar, ou quase um quatrilhão de vezes abaixo da pressão atmosférica). Esses aparelhos não só simulam a formação

e evolução dos gelos interestelares, mas também aceleram processos que naturalmente levariam milhões de anos, condensando-os em poucas horas. Esses experimentos controlados também nos permitem isolar e estudar mecanismos específicos em sistemas simplificados, oferecendo uma visão mais focada da química sendo investigada.

Nesta tese, vários desses aparelhos criogênicos de vácuo foram utilizados. O principal deles foi o SURFRESIDE[3], localizado na Universidade de Leiden, na Holanda, especialmente projetado para estudar as reações de superfície em análogos de gelo interestelar desencadeadas por átomos e radicais. Outros aparatos utilizados nesta tese são o LISA (Universidade Radboud, na Holanda), que foca na interação dos análogos de gelo interestelar com luz infravermelha; e o SPACE-KITTEN (Universidade de Harvard, nos Estados Unidos), projetado para investigar como os gelos respondem ao processamento térmico que imita o aquecimento por uma estrela jovem.

Astroquímica observacional

Para projetar experimentos significativos, precisamos primeiro saber quais moléculas estão presentes em diferentes ambientes espaciais, e em que estado físico elas se encontram. As observações são cruciais para isso, pois fornecem a única evidência empírica direta do inventário químico das regiões onde estrelas e planetas estão se formando. Elas também nos permitem testar e validar hipóteses extraídas de experimentos laboratoriais e modelos de evolução química interestelar. Dessa forma, as observações formam um pilar fundamental da pesquisa astroquímica, ancorando estudos experimentais e teóricos em dados astronômicos reais.

Nesta tese, dois tipos de observações astronômicas são particularmente relevantes: aquelas feitas em radiofrequências e aquelas usando luz infravermelha. Observações de rádio nos permitem detectar moléculas presentes na fase gasosa dos ambientes interestelares, incluindo espécies que estavam outrora congeladas em gelos e que já sublimaram. Essas observações são realizadas usando antenas de rádio, individualmente ou em conjuntos coordenados conhecidos como interferômetros. Observações infravermelhas, por outro lado, são cruciais para detectar moléculas em gelos, que geralmente permanecem invisíveis nas observações em rádio. Juntas, essas duas técnicas oferecem visões complementares da composição química das regiões de formação de estrelas e planetas.

Esta tese

Esta tese investiga a evolução físico-química dos gelos interestelares nas várias etapas da formação de estrelas e planetas. Isso inclui entender seus mecanismos de formação em nuvens moleculares frias, sua transformação durante a formação de estrelas e planetas, e sua eventual sublimação e possível incorporação em planetas e planetesimais em formação. Para alcançar isso, combinamos experimentos utilizando aparelhos que simulam as condições interestelares com observações astronômicas do conteúdo molecular nesses ambientes. As vias químicas descobertas nesta tese estão destacadas na Figura 3, e abaixo está um resumo dos principais achados de cada capítulo:

Capítulo 2. Neste capítulo, estudamos a formação do gelo de metanol (CH_3OH), um dos principais componentes dos gelos interestelares que serve como precursor chave para moléculas orgânicas complexas no espaço. Nossos resultados experimentais demonstram que a etapa final dominante no caminho para a formação do metanol ocorre por meio de uma reação entre CH_3O e H_2CO, em vez do mecanismo previamente

Figura 3: Resumo das rotas de reação em gelos interestelares descobertas nesta tese.

proposto envolvendo CH_3O e H. Esses achados estão alinhados com as previsões de modelos teóricos em condições de laboratório, que por sua vez se estendem para condições representativas de nuvens interestelares e sugerem que esse mecanismo alternativo também seja o processo dominante no espaço. Isso tem implicações significativas para a modelagem da química desses ambientes e para a interpretação da distribuição de metanol deuterado nessas regiões.

Capítulo 3. Este capítulo investiga experimentalmente a influência da radiação infravermelha nos gelos interestelares, descobrindo que a luz infravermelha em ressonância com as vibrações das moléculas de gelo pode induzir rearranjos estruturais e até mesmo desencadear a desorção do material do gelo. Esses efeitos têm implicações potenciais para as abundâncias observadas de moléculas complexas, particularmente aquelas que se pensa serem formadas em gelos, na fase gasosa de regiões onde a sublimação térmica não é viável.

Capítulo 4. Este capítulo explora, em laboratório, a interação entre o H_2S sólido — um reservatório volátil importante de enxofre nos gelos interestelares — e átomos de hidrogênio. Mostramos que H_2S reage com hidrogênio para formar radicais HS e H_2, com a maior parte do HS recombinando-se para formar H_2S_2 ou reagindo novamente com hidrogênio para reformar H_2S. Uma fração significativa do H_2S reformado desorve prontamente devido à sua energia de formação excessiva, resultando em perda do gelo de H_2S. Neste estudo, desenvolvemos uma abordagem inovadora para quantificar diretamente essa desorção induzida pela química e separar sua contribuição da formação de H_2S_2 na destruição líquida do gelo original de H_2S.

Capítulo 5. Este capítulo caracteriza experimentalmente o comportamento de desorção do gelo de H_2S. Determinamos como o H_2S se adere a si mesmo e ao gelo de

água—o principal componente dos gelos interestelares—medindo seu comportamento de desorção quando depositado como gelo puro de H_2S e sobre gelo de água. Também investigamos o comportamento de desorção do H_2S em gelos mistos dominados por água e descobrimos que uma fração surpreendentemente grande de H_2S permanece presa muito acima de sua temperatura normal de sublimação. Usando esses resultados, estimamos a localização em um disco formador de planetas onde H_2S transita do gelo para o gás e encontramos que provavelmente permanece sólido na região onde cometas e planetesimais congelados se formam.

Capítulo 6. Neste capítulo, damos continuidade aos achados do Capítulo 4 e investigamos experimentalmente a rede química iniciada pelas interações entre HS, CO e H. Descobrimos que essa rede leva à formação de gelo de OCS—um importante transportador volátil de enxofre nos gelos interestelares—mesmo em condições desfavoráveis, como a escassez de átomos de hidrogênio. Também argumentamos que essa nova rota potencial para formar OCS em gelos pode ocorrer durante um longo intervalo de tempo na vida de uma nuvem. Ela também é mais consistente com a fase do gelo proposta (e, portanto, o tempo de colapso da nuvem) na qual se pensa que o OCS é observado do que outros mecanismos de formação de OCS comumente invocados.

Capítulo 7. Este capítulo amplia a química dos gelos de enxofre explorada nos Capítulos 4 e 6, investigando experimentalmente a formação de moléculas orgânicas complexas contendo enxofre e dois átomos de carbono. Estudamos as reações de HS com C_2H_2 e H e descobrimos que essa rede leva a uma química rica, produzindo pelo menos seis produtos contendo enxofre, cinco dos quais são orgânicos. O produto dominante é o etanotiol (CH_3CH_2SH)—uma molécula já detectada na fase gasosa interestelar—que parece atuar como um ralo químico, formando-se de maneira eficiente enquanto átomos de hidrogênio estiverem presentes, em detrimento dos outros produtos.

Capítulo 8. Neste capítulo, apresentamos observações na fase gasosa de dois principais reservatórios voláteis de enxofre, OCS e SO_2, em torno de uma grande amostra de estrelas massivas jovens em formação. Descobrimos que suas abundâncias em relação ao metanol (CH_3OH; uma molécula de referência comumemte encontrada em gelos) permanecem surpreendentemente consistentes entre estrelas de diferentes brilho. Isso sugere que ambas as moléculas são predominantemente formadas em gelos antes da formação da própria estrela—ou seja, nas nuvens. No entanto, apesar dessa origem comum, suas distribuições de abundância e como elas se comparam com observações de gelos indicam histórias diferentes: OCS parece se formar mais tarde na evolução da nuvem, em paralelo com o gelo de CH_3OH, enquanto SO_2 provavelmente se forma mais cedo, simultaneamente ao gelo de H_2O, e/ou pode ser significativamente alterado após sublimação devido a reações na fase gasosa ocorrendo perto da estrela em formação.

Capítulo 9. Este capítulo apresenta observações na fase gasosa da molécula orgânica CH_3CCH em torno de uma estrela massiva jovem em formação. Esta molécula, que provavelmente se forma por uma combinação de química gasosa e de gelo, é comumente usada para rastrear temperaturas do gás. Ao analisar a cinemática do gás, descobrimos que a emissão provavelmente é dominada pelas camadas externas quiescentes ao redor da protoestrela e contém provavelmente dois componentes distintos—um mais quente do que o outro. Além disso, graças às propriedades espectroscópicas do CH_3CCH, conseguimos rastrear indiretamente a faixa de temperatura geral desse gás com mais detalhes do que normalmente é possível com observações de um telescópio de rádio com uma única antena.

Olhar para o Futuro

De maneira geral, esta tese mostra como os experimentos de laboratório e as observações astronômicas trabalham juntos para revelar a história química dos gelos e gases que formam estrelas e planetas. Esta é uma era empolgante para este campo, graças às tecnologias de ponta disponíveis aos laboratórios e aos telescópios poderosos como o ALMA e o JWST, que oferecem uma visão sem precedentes sobre os blocos de construção dos planetas e planetesimais, tanto no gás quanto no gelo. Com o JWST também oferecendo novas percepções sobre os materiais presentes nas regiões onde os planetas estão se formando, os esforços combinados de observações, trabalhos em laboratório e modelos computacionais em breve nos darão a melhor imagem já vista da química em ação nos locais de nascimento dos planetas.

PUBLICATIONS

Refereed publications as lead author

1. *H_2S ice sublimation dynamics: experimentally constrained binding energies, entrapment efficiencies, and snowlines*
   Santos, J. C., Piacentino, E. L., Bergner, J. B., Rajappan, M., Öberg, K. I., 2025, Astronomy & Astrophysics, in press. (Chapter 5)

2. *Formation of carbonyl sulfide (OCS) via SH radicals in interstellar CO-rich ice under dense cloud conditions*
   Santos, J. C., Linnartz, H., Chuang, K.-J., 2024c, Astronomy & Astrophysics, 690, A24. (Chapter 6)

3. *SO_2 and OCS toward high-mass protostars: A comparative study between ice and gas*
   Santos, J. C., van Gelder, M. L., Nazari, P., Ahmadi, A., van Dishoeck, E. F., 2024b, Astronomy & Astrophysics, 689, A248. (Chapter 8)

4. *Formation of S-bearing complex organic molecules in molecular clouds via ice reactions with C_2H_2, HS, and atomic H*
   Santos, J. C., Enrique-Romero, J., Lamberts, T., Linnartz, H., Chuang, K.-J., 2024a, ACS Earth and Space Chemistry, 8, 1646. (Chapter 7)

5. *Interaction of H_2S with H atoms on grain surfaces under molecular cloud conditions*
   Santos, J. C., Linnartz, H., Chuang, K.-J., 2023b, Astronomy & Astrophysics, 678, A112. (Chapter 4)

6. *Resonant infrared irradiation of CO and CH_3OH interstellar ices*
   Santos, J. C., Chuang, K.-J., Schrauwen, J. G. M., Muiña, A. T., Zhang, J., Cuppen, H. M., Redlich, B., Linnartz, H., Ioppolo, S., 2023a, Astronomy & Astrophysics, 672, A112. (Chapter 3)

7. *Experimental confirmation of a new formation route to CH_3OH in interstellar ices: $CH_3O + H_2CO \rightarrow CH_3OH + HCO$*
   Santos, J. C., Chuang, K.-J., Lamberts, T., Fedoseev, G., Ioppolo, S., Linnartz, H., 2022c, The Astrophysical Journal Letters, 931, L33. (Chapter 2)

8. *Structure and stability of multiply charged naphthalene and its $C_{10}H_8$ isomers: bonding, spectroscopy, and astrophysical implications*
   Santos, J. C.[‡], Fantuzzi, F.[‡], Quitián-Lara, H. M., Martins-Franco, Y., Menéndez-Delmestre, K., Boechat-Roberty, H. M., Oliveira, R. R., 2022b, Monthly Notices of the Royal Astronomical Society, 512, 4669. (not included in this thesis)

[‡]These authors contributed equally

9. *A spectral survey of CH$_3$CCH in the Hot Molecular Core G331.512-0.103*
   Santos, J. C., Bronfman, L., Mendoza, E., Lépine, J. R. D., Duronea, N. U., Merello, M., Finger, R. A., 2022a, The Astrophysical Journal, 925, 3. (Chapter 9)

10. *Rotational spectrum simulations of asymmetric tops in an astrochemical context*
    Santos, J. C., Rocha, A. B., Oliveira, R. R., 2020b, Journal of Molecular Modeling, 26, 278. (not included in this thesis)

11. *Structure, stability, and spectroscopic properties of small acetonitrile cation clusters*
    Cerqueira, H. B. A.[‡], **Santos, J. C.**[‡], Fantuzzi, F., Ribeiro, F. de A., Rocco, M. L. M., Oliveira, R. R., Rocha, A. B., 2020a, The Journal of Physical Chemistry A, 124, 6845. (not included in this thesis)

Refereed publications as co-author

1. *IR-induced CO photodesorption from pure CO ice and CO on amorphous solid water (ASW)*
   Slumstrup, L., Thrower, J., Schrauwen, J. G. M., Lamberts, T., Ingman, E., Laurinavicius, D., DeVine, J., Terwisscha van Scheltinga, J., **Santos, J. C.**, Wenzel, G., Noble, J., McCoustra, M., Brown, W., Linnartz, H., Hornekær, L., Cuppen, H. M., Redlich, B., Ioppolo, S., 2025, ACS Earth and Space Chemistry, in press.

2. *Ammonium hydrosulfide (NH$_4$SH): a potential significant sulfur sink in interstellar ices*
   Slavicinska, K., Boogert, A. C. A, Tychoniec, Ł., van Dishoeck, E. F., van Gelder, M. L., Navarro, M. G., **Santos, J. C.**, Klaassen, P. D., Kavanagh, P. J., Chuang, K.-J., 2025, Astronomy & Astrophysics, 693, A146.

3. *A systematic FTIR and VUV spectroscopic investigation of ion, electron, and thermally processed ethanolamine ice*
   Zhang, J.[‡], Muiña, A. T.[‡], Mifsud, D. V., Kaňuchová, Z., Cielinska, K., Herczku, P., Rahul, K. K., Kovács, S. T. S., Rácz, R., **Santos, J. C.**, Hopkinson, A. T., Craciunescu, L., Jones, N. C., Hoffmann, S. V., Biri, S., Vajda, I., Rajta, I., Dawes, A., Sivaraman, B., Juhász, Z., Sulik, B., Linnartz, H., Hornekær, L., Fantuzzi, F., Mason, N. J., Ioppolo, S., 2024, Monthly Notices of the Royal Astronomical Society, 533, 826.

4. *Formation of N-bearing complex organic molecules in molecular clouds: keten-imine, acetonitrile, acetaldimine, and vinylamine via the UV photolysis of C$_2$H$_2$ ice*
   Chuang, K.-J., Jäger, C., **Santos, J. C.**, Henning, Th., 2024, Astronomy & Astrophysics, 687, A7.

5. *Methane formation in cold regions from carbon atoms and molecular hydrogen*
   Lamberts, T., Fedoseev, G., van Hemert, M., Qasim, D., Chuang, K.-J., **Santos, J. C.**, Linnartz, H., 2022, The Astrophysical Journal, 928, 48.

[‡]These authors contributed equally

CURRICULUM VITAE

I was born on the 17$^{\text{th}}$ of September, 1995, in Rio de Janeiro, Brazil, to an engineer mother and an astronomer father. Having a parent with a Bachelor's degree in astronomy is a rare privilege for a young science enthusiast, and I certainly took full advantage of it. My childhood was filled with long, lively conversations with my father about physics, astronomy, and the other fields within the natural sciences, and I remember waiting impatiently for the day I would finally get to study those subjects in school. But although astronomy was always a big part of my life, it was chemistry that ultimately stole my heart. That love began when I received a children's chemistry kit as a gift, which I used obsessively until every reagent was gone—at which point I cried inconsolably in frustration, devastated that I could no longer "do science".

My passion for STEM remained strong throughout my childhood and adolescence. I attended a traditional school in Rio de Janeiro, Colégio Santo Inácio, for both my primary and secondary education. There, I had the privilege of accessing well-equipped science laboratories, and hands-on STEM classes quickly became my favorite part of the curriculum. Still, I didn't realize that being a scientist could be a real profession—"that's something from the movies," my younger self thought, "certainly not something that exists here in Brazil." With that mindset, I decided to pursue a Bachelor's degree in chemical engineering, which at the time seemed like the ideal way to combine my passion for chemistry with a prestigious major that offered strong prospects for financial stability. I applied to the Federal University of Rio de Janeiro and was accepted.

The few years I spent studying chemical engineering were nothing short of dreadful. I had no interest—and frankly, no aptitude—for the industrial sector, and I found the chemistry portion of the curriculum far too superficial. At the same time, I began to notice that many of my professors were, in fact, scientists, which made me realize that science was, indeed, a viable career path. Around the same time, I also discovered the field of astrochemistry, which perfectly combined two of my greatest scientific passions: chemistry and astronomy. It was then that I mustered the courage and decided to fully commit to becoming a scientist. After three years studying chemical engineering, I resolved to transfer into the Chemistry major, scoring the highest grades in the transfer exam and securing the only available spot that semester. From there, I began seeking out supervisors for undergraduate research opportunities in astrochemistry.

I started my scientific career in laboratory astrochemistry, exploring vacuum cryogenic experiments on interstellar ice analogues. To pursue this project, I was awarded a two-years' undergraduate research scholarship. However, towards the end of my Bachelor's degree, I was also eager to explore other facets of astrochemistry, which led me to change topics for my final research project. Building on the results of my experimental work, I used computational chemistry methods to simulated the rotational spectra of molecules relevant to astrophysical environments. Both projects earned me several presentation awards at local as well as national conferences, and the latter

project also resulted in my first two first-author publications in peer-reviewed journals.

I then recognized that to become a well-rounded astrochemist, I needed to complement my education with a solid foundation in astronomy. With this goal in mind, I applied for the Master's program in Astronomy at São Paulo University—the largest university in Latin America, and one that I am immensely proud to be an alumna. As part of the admissions process, I was required to take a continent-wide graduate-level physics exam, which prompted me to independently study and fill the gaps in my chemistry-focused education. My efforts paid off when I scored above the 90th percentile and was accepted into the program as the top-ranked candidate, also earning a graduate-level scholarship for the duration of my Master's degree. Excited for the challenge of living on my own for the first time, I left my hometown to pursue my Master's in São Paulo. During this period, I shifted my focus once again—this time, to observational astrochemistry—where I explored molecular emission lines in star-forming regions observed in submillimeter wavelengths.

After successfully defending my Master's remotely due to the COVID-19 pandemic, I started a PhD position with Prof. Dr. Harold Linnartz at Leiden University. Having explored various aspects of astrochemistry, I ultimately decided to return to experimental work, an area I've always found immensely satisfying. There's a special type of gratification in immersing yourself fully in the hands-on nature of experimental science. My laboratory endeavors extended beyond Leiden, with opportunities to conduct experiments at the FELIX Laboratory at Radboud University in Nijmegen, the Netherlands, as well as the ASTRID synchrotron light source and the low-temperature scanning tunneling microscope at Aarhus University in Denmark. Aarhus also served as the central hub for the InterCat consortium, which I was a part of throughout my doctorate. Additionally, I was fortunate to undertake a short-term research stay in Prof. Dr. Karin Öberg's lab at Harvard University, in the United States—a time that was particularly meaningful after the loss of my supervisor, Harold. Although the primary focus of my PhD was experimental, I have always maintained a passion for observations, so I continued pursuing observational research as a secondary field under the guidance of Prof. Dr. Ewine van Dishoeck.

The work conducted during my PhD culminated in this thesis and was presented at conferences around the world, including in Italy, Denmark, France, the United States, the Netherlands, Brazil, Spain, Iceland, and Japan. Concomitantly, I was the teaching assistant for the Bachelor's Research Project for three consecutive years, and have supervised two Master's students and co-supervised another Master's student. Following my defense, I will return to Harvard University to continue investigating the role of interstellar ices in the chemical evolution of star- and planet-forming regions—this time hosted by Prof. Dr. Karin Öberg as a 51 Pegasi b Fellow.

ACKNOWLEDGEMENTS

There's something wry about how humans experience time—somehow, four years can feel like both a lifetime and the blink of an eye, all at once. My PhD journey was long and short, and not always easy, but looking back, I realize it was filled with moments of joy. These were only possible thanks to the people who supported, challenged, and inspired me along the way. Just as it takes a village to raise a child, it also takes a village to shape an independent researcher—and with this section, I'd like to thank mine.

The first person I'd like to thank is, sadly, no longer here to read this. Harold, thank you for offering me the incredible opportunity to work with SURFRESIDE[3], and for always being so supportive of me. You were right—I did get the prize fellowships I so deeply hoped for. I only wish you were here to know it.

Ewine, thank you for welcoming me so openly when I first reached out about pursuing an observational project; and again, for embracing me into your group with such generosity after we lost Harold. You have been an inspiration to me ever since I first discovered this amazing field we're in, and I'm deeply grateful to have had the opportunity to learn from your guidance.

Throughout my time in Leiden, I've met some incredible people. Katie, I'm so glad our paths crossed. You're a brilliant researcher and a wonderful friend. Thank you for making me feel less alone in this world. Brian—please don't cringe—you remind me so much of Luffy. Thank you for your friendship and for reminding me that it's okay to stand up for yourself. Fran, Nashanty, Yuan, your companionship has meant a lot to me. Jerry, I've always admired your big heart. Thank you for sharing your kindness and good humor with me. Will, you're one of the most steadfast people I know; I hope life brings you all the fulfillment you deserve. Martijn, Pooneh, and Łukasz, thank you for teaching me everything I know about ALMA observations. If I can now candidly call myself an observer, it's all thanks to you. To my fellow LfA folks—Carlos, Jeroen, Jessalyn, Ko-Ju, Marina, Martijn, Michał, Milan, Pranjal, Robin, and Thanh—thank you for the time we shared, I've learned a lot from you. Iara, Kelly, and Lina, thank you for teaching me what it means to be a supervisor. I hope I lived up to what you deserved. I'm also grateful to the astrochemistry community at Leiden for the many stimulating discussions: Andrew, Andrés, Ardjan, Joan, Lukas, Lucas, Logan, Margot, Marissa, Marten, Melissa, Marie, Mathilde, Milou, Serena, Thanja, Tobias, Tere, Xunchuan, and Zak.

To the InterCat team, thank you for opening so many doors for me. I'm sorry I don't have the space to name all of you. Signe, I'm so grateful for your friendship. Despite spending most of our PhDs apart, I've always felt close to you. I think I would've gone crazy watching the STM scan line by line without your company. Alfie, thank you for always making me laugh. Ale, you're one of the sweetest people I know, I'll never forget our epic chair race during our ASTRID beamtime.

Though I only spent five weeks at the CfA, I feel fortunate to have many people to

thank from my time there. Karin, thank you for welcoming me so warmly into your lab and for supporting me throughout postdoc applications. I've long admired your work, but after witnessing your dedication to your mentees, I've come to appreciate you even more on a personal level. Elettra, I truly admire your authenticity and your drive to support others. Alexandra, Alexia, Alice, Bea, Jenny, Marissa, Michelle, and Suchi, you are all powerhouses, and I've learned so much from you. Mahesh, having your support is a privilege that made all the difference in my experiments.

To my dojo, Daidokan, thank you for welcoming me with such inclusiveness. Being the only expat in a Dutch-speaking dojo felt daunting at first, but your warmth quickly put me at ease. I even ended up as treasurer! Thank you for your patience as I fumbled through figuring out what a voorziening was. Ilia sensei, Roek sensei, thank you for sharing some of your budo knowledge with me. To my fellow dojo mates—Esmée, Gabija, Iris, Julia K., Julia van V., Juul, Lisette, Marthe, Miriam, Nienke, Nikki, Noortje, Rosa, Sabina, Sandra, Sanne de J., Sanne de V., Saar, Thirza, and Yalda—thank you for making this space both challenging and safe, and for being such dedicated training partners. Though I'll be leaving Daidokan, karate will always be part of my life—and I have you all to thank for that.

Mom, dad, thank you for always being in my corner. Knowing I could always count on your safety net gave me the strength to take risks and keep going. To my in-laws—Sônia, Flávio, Camila, Juca, Caio, and Ciça—thank you for embracing me into the family. You're so much fun to be around, and I truly cherish our Sunday gatherings whenever we're back home.

Finally, Fabio, my love, I still can't believe how lucky I am to have you. You left our home country to be with me in the Netherlands, and now you're ready to upend your life once again to come with me to the U.S. You are my rock, my best friend, and my greatest source of support. Whatever comes next, I know I can handle it—because I have you by my side.